NON-HEME METAL COMPLEXES- A VERSATILE DESIGN FOR PHARMACEUTICAL REACTION, ENVIRONMENTAL POLLUTANTS AND CHEMICAL WARFARE DETOXIFICATION: A QUANTUM MECHANICAL STUDY

THESIS SUBMITTED FOR THE AWARD OF THE DEGREE OF

Doctor of Philosophy

in
Applied Physics

By
Devendra Singh
Enrolment No.: 926/13

Under the Supervision of
Dr. Devesh Kumar

BABASAHEB
BHIMRAO
AMBEDKAR
UNIVERSITY
LUCKNOW
प्रज्ञा शील करुणा
ESTABLISHED 1996

Department of Applied Physics
School for Physical Sciences
Babasaheb Bhimrao Ambedkar University, Lucknow,
U.P., (India) – 226025
August, 2017

THIS THESIS IS DEDICATED

TO

DEVESH SIR

AND

MY FAMILY

DECLARATION

I declare that the thesis titled **"Non-Heme Metal Complexes- A Versatile Design for Pharmaceutical Reaction, Environmental Pollutants and Chemical Warfare Detoxification: A Quantum Mechanical Study"** has been prepared by me under the supervision of Dr. Devesh Kumar, Associate Professor, Department of Applied Physics, School for Physical Sciences, Babasaheb Bhimrao Ambedkar University Lucknow. No part of this thesis has formed the basis for the award of any degree, diploma or fellowship previously. Further, I declare that the material embodied in the present work is based on original research work and the indebtedness to others has been duly acknowledged at relevant places. This is also declared that the thesis is essentially free from all kinds of plagiarism

(Devendra Singh)

Department of Applied Physics
School for Physical Sciences
Babasaheb Bhimrao Ambedkar University
Vidya Vihar, Raebareili Road
Lucknow, (U.P.), India- 226025

Date: 25th August, 2017
Place: Lucknow

CERTIFICATE

This is to certify that the thesis titled **"Non-Heme Metal Complexes- A Versatile Design for Pharmaceutical Reaction, Environmental Pollutants and Chemical Warfare Detoxification: A Quantum Mechanical Study"** submitted by Mr. Devendra Singh is an original research work and has not been previously submitted in part or full for the award of any other degree or diploma to this or any other university.

The thesis submitted to Babasaheb Bhimrao Ambedkar University Lucknow satisfies all the requirements as stipulated in the Doctor of Philosophy (Ph.D.) Regulations – 1999 as amended in ~~2008~~/~~2010~~/2013 and it is fit for submission and evaluation for the award of the degree of Doctor of Philosophy of the University.

25/8/17

Date: 25th August, 2017

Supervisor

25/8/17

Head of Department

ACKNOWLEDGEMENT

I would like to thank the Almighty for His blessings continuously showered on me without which it would have been a Herculean task to begin this work, complete it and compile in the form of a thesis. Thank you God for this Day.

I feel obliged to take this opportunity to express my heartfelt reverences towards my supervisor and mentor **Dr. Devesh Kumar**, Associate Professor and Head, Department of Applied Physics who took it as a challenge to help me sail this boat smoothly even in most turbulent times. Without him, this thesis would not have taken this apt form. Besides guiding and encouraging me throughout the course of this research work, he was always there watching cautiously for any barrier that could hinder the progress or rather completion of this Ph.D. work.

Next I would like to express my deep sense of gratitude towards my family. My parents have been constant torch bearers for me constantly encouraging and providing all necessary guidance, support and inspiration towards acquiring new skills. My wife's support needs no mention, without her it would have not been such a smooth task. My son has been an inspiration throughout the work. I am highly indebted to all my family members, they helped me glide smoothly during times of despair.

I am highly grateful to the help and support provided by faculties of the department: Dr. B. C. Yadav, Dr. Ramesh Chandra, Dr. A. K. Yadav and Dr. K. B. Thapa for helping me complete this task. They were always available for fruitful discussions culminating into successful results. I feel extremely enlightened by the company of their thought provoking deliberations.

I would not like to feel guilty by not mentioning the help provided by my research group. Dr. Jitendra Kumar, Dr. Pranav Upadhyay, Dr. Suresh Kumar, Mr. Deep Kumar, Mr. Dharmveer Singh, Mr. Asheesh Kumar, Mr Narinder Kumar and Mr. Ankur Trivedi were ever willing to lend helping hand even during odd hours. The help provided during course of Ph.D. research and manuscript preparation is highly acknowledged. Miss Ruchi Mishra and Miss Rolly Yadav are also thanked for their help. Paucity of space does not allow me to mention names of other researchers of the department, their support is highly acknowledged. I thank one and all who have directly or indirectly helped me or inspired me towards achievement of my goal.

Finally I would like to appreciate support and facilities extended by staff at Library and Computer Center of the Department as well as the University for necessary literature survey and other requirements.

(Devendra Singh)

ABSTRACT

The enzymes have important biological functions. Metalloenzymes have metal as cofactor bound to proteins. The metal ions in active site of enzymes allow it to perform redox reactions. Metals were used in most developed civilizations since ages in therapeutic purposes but the mechanism was not known properly. With advent of computer, the theoreticians could compute structures and reaction pathways within reasonable time. The quantum mechanical methods have been of great help in devising competing methods for explaining involved phenomena. With advancement in technology, these theoretical results were validated by experimentalists as well. Hence both began working in close collaboration. Their concerted efforts have helped develop highly benchmarked computational methods that produce reliable results. Now modeled structures have grown in size and complexity.

Metalloenzymes may be broadly classified into heme and non-heme enzymes. While former have been well documented, latter is in growing phase but has immense potential for exploring various reaction pathways that may further be fine-tuned. In this work, iron(IV)-oxo species have been studied in great detail. Reaction pathways have been proposed that closely match with experimental results. Aliphatic hydroxylation catalysis reactions by synthetic models of variously ligated complexes have been considered that exhibited low activation barriers compared to known efficient catalysts. Also, comparative study between iron(IV)-oxo versus iron(V)-oxo complexes has been attempted for the first time. In another work, alkane synthesis by intramolecular methyl and hydrogen atom transfer has been studied and reaction mechanism has also been deduced.

PREFACE

Metalloenzymes are found in many life forms having a variety of functions. Primarily they act as vital catalysts in many crucial metabolic and biosynthetic biological pathways. Iron being most abundant in earth's crust is also found in prominence in most enzymes. Iron containing enzymes are classified as heme and non-heme enzymes. These enzymes may also contain other transition or non-transition metals (homo/hetero-nuclear metals systems). Man has known therapeutic applications of these metal complexes but their mechanism was unknown until chemistry developed both experimentally as well as theoretically. Lack of technology may impair characterization of given substrate but theoretician emerged with promising tools that blossomed fruitful results and gave deep insights into reaction mechanisms of these complexes and their impact on health of living organisms as well as ecosystem. Nowadays computational techniques have matured to a level that one has various sets of extensively tested and benchmarked methods and procedures that produce reliable results that predate experimental data by many years. There are many instances when experimentalists have reproduced and validated theoretical results once technological advancements allowed them to do so. In study of transition metal complexes, the basic hindrance in experiment is their short life time. Computational study helps in studying the properties of short lived intermediates and transition state complexes and help in determining reaction pathways or in fine-tuning a known reaction mechanism. This thesis will focus on reaction mechanism of metalloenzymes having transition metal (iron) into their active sites. Activation of molecular oxygen in hydroxylation reactions is main focus. Various synthetic models are used to models reactions. This thesis contains six chapters.

Chapter 1 presents a literature survey of work done so far on heme and non-heme enzymes with a focus on various computational quantum mechanical techniques prevalent in the arena.

Chapter 2 discusses mathematical details of quantum mechanical methods. It also gives a glimpse of the theoretical methods helpful in study of transition metal complexes.

Chapter 3 attempts at exploring effects of axially coordinated nitride iron porphyrin ligand in molecular orbital interactions of the metal(IV)-oxo group. It reports complexes that are efficient oxidants of aliphatic hydroxylation reactions and suggests design of efficient and powerful oxidants of hydrogen-atom-abstraction reactions.

Chapter 4 is focused on study of methane hydroxylation by axially ligated iron(IV)-oxo porphyrin cation radical models. It emerges that axial ligand dramatically reduces activation barriers and gives an scheme for design of efficient oxidant.

Chapter 5 describes one of the first attempt at comparison of the reactivities of non-heme iron(IV)-oxo versus iron(V)-oxo species. Here effect of outer-sphere (long range) electron transfer on C-H bond strength of the substrate was studied in relation to a more efficient H-transfer.

Chapter 6 deals with exploring reaction mechanism for intra-molecular methyl and hydrogen atom transfer in a tri-metal carbine complex that act as precursor to alkane synthesis.

LIST OF ABBREVIATIONS

1	α-KG	α-Ketoglutarate dependent enzymes
2	ADH	Alcohol dehydrogenase
3	BDE	Bond Dissociation Energy
4	BDFE	Bond Dissociation Free Energy
5	BDO	Benzene dioxygenase
6	BLM	Bleomycin
7	BQEN	N,N’-dimethyl-N,N’-bis(8-quinolyl) ethane-1,2-diamine
8	BS1	Basis set 1 – UB3LYP in combination with LACVP or LANL2DZ basis set on iron and 6-31G on rest of atoms
9	BS2	Basis set 2 – LACV3P+ basis set on iron and 6-311+G* on rest of the atoms
10	CCD	Chlorocatechol dioxygenase
11	CTD	Catechol dioxygenase
12	CDO	Cysteine Dioxygenase
13	Cpd0	Compound 0, Iron-Hydroperoxo Intermediate
14	CpdI	Compound I, Iron-oxo Ferryl Species
15	CI	Configuration-Interaction
16	CT	Charge-Transfer
17	CYP	Cytochrome P450
18	CYP2E1	Cytochrome P450 2E1
19	CWA	Chemical Warfare Agent
20	DAOCS	Deacetoxycephalosporin C synthase
21	DFT	Density Functional Theory
22	DHBD	Dihydroxybiphenyl dioxygenase
23	DNA	Deoxyribonucleic acid
24	EA	Electron Affinity
25	EB	Ethyl Benzene
26	ECP	Effective Core Potential
27	EPR	Electron Paramagnetic Resonance

28	GTO	Gaussian type Orbital
29	HAT	Hydrogen Atom Abstraction
30	HF	Hartree-Fock
31	HOMO	Highest Occupied Molecular Orbital
32	Hr	Hemerythrin
33	HSAB	Hard and Soft Acids and Bases principle
34	IE	Ionization Energy
35	IPNS	Isopenicillin N Synthase
36	KIE	Kinetic Isotope Effect
37	LACVP	Basis sets that include effective core potential
38	LCAO	Linear Combination of Atomic Orbital
39	LO	Lipoxygenase
40	LUMO	Lowest Occupied Molecular Orbital
41	MDB	Metalloprotein Databank
42	MM	Molecular Mechanics
43	MMO	Methane Monooxygenase
44	MMOH	Methane Monooxygenase Hydroxylase
45	MS	Mass Spectrometry
46	MNHID	Mononuclear Nonheme Iron Dioxygenase
47	MTFE	Methylenium Transfer Gibbs Free Energy
48	NADH	Nicotinamide Adenine Dinucleotide
49	NDO	Naphthalene dioxygenase
50	NOR	Nitric Oxide Reductase
51	OAT	Oxygen Atom Transfer
52	P450	Cytochrome P450 enzyme
53	P450cam	Cytochrome P450 from Pseudomonas putida, hydroxylase of camphor
54	PAH	Phenylalanine hydroxylase
55	PCD	Protocatechuate dioxygenase
56	PDB	Protein Data Bank
57	PDO	Phthalate dioxygenase
58	PES	Potential Energy Surface
59	PKU	Phenyl ketonuria

60	Por	Porphine Dianion
61	PTFE	Proton Transfer Gibbs Free Energy
62	QM	Quantum Mechanics
63	RC	Reactant Complex
64	RHF	Restricted Hartree-Fock
65	RNA	Ribonucleic Acid
66	RR	Ribonucleotide Reductase
67	SCF	Self Consistent Field
68	SET	Single Electron Transfer
69	SLO	Soybean Lipoxygenase
70	SORCI	Spectra Oriented Configuration Interaction
71	STO	Slater Type Orbital
72	TMC	Tetramethyl Cyclam ligand (1,4,8,11-tetramethyl-1,4,8,11-tetraazacyclotetradecane)
73	TS	Transition State
74	TrpH	Tryptophan hydroxylase
75	TyrH	Tyrosine hydroxylase
76	UB3LYP	Unrestricted Becke Lee Yang Parr basis set
77	UHF	Unrestricted Hartree-Fock
78	ZPE	Zero Point Energy

LIST OF AMINO ACID ABBREVIATIONS

S. No.	Amino Acid	Three letter code
1	Alanine	Ala
2	Arginine	Arg
3	Asparagine	Asn
4	Aspartic Acid	Asp
5	Cysteine	Cys
6	Glutamine	Gln
7	Glutamic Acid	Glu
8	Glycine	Gly
9	Histidine	His
10	Isoleucine	Ile
11	Leucine	Leu
12	Lysine	Lys
13	Methionine	Met
14	Phenylalanine	Phe
15	Proline	Pro
16	Serine	Ser
17	Threonine	Thr
18	Tryptophan	Trp
19	Tyrosine	Tyr
20	Valine	Val

LIST OF TABLES

LIST OF FIGURES

TABLE OF CONTENTS

CHAPTER 1: Introduction

CHAPTER 2: Methodology

CHAPTER 3: Origin of the enhanced reactivity of a synthetic N-bridged diiron(IV)-oxo porphyrin complex over cytochrome P450 Compound I

CHAPTER 4: Methane Hydroxylation by axially ligated iron(IV)-oxo porphyrin cation radical models

CHAPTER 5: Properties and reactivities of non-heme iron(IV)-oxo versus iron(V)-oxo: Long-range electron transfer versus hydrogen atom abstraction

CHAPTER 1

INTRODUCTION

CHAPTER 1

INTRODUCTION

1.1: Role of Metals in life

Metals play a vital role in living organisms. They form functional components (cofactors) of several essential enzymes. In humans, they perform a variety of tasks: oxygen transport, electron transport, (hemoglobin- an iron containing protein), formation of bones that form structural framework of human body, protein stabilization (calcium containing enzymes), electron mediation, catalysis of redox reactions, storage and/or activation (copper containing enzymes), specific functions in metabolism and DNA stabilization (zinc containing enzymes), skeletal development, detoxification of free radicals (manganese containing enzymes), free radical reactions (cobalt containing enzymes) etc. These metals find crucially important role in animal as well as plant kingdom. It is believed that precursors of metalloenzymes may have played a key role in catalyzing reactions necessary for synthesis of prebiotic macromolecules. As metals have been extensively used by nature in biological systems, it seems obvious to think of their potential medicinal usage. Although medicinal inorganic chemistry has been practiced since long (Indians, Egyptians, Arabs, Chinese, Europeans and others), the reaction mechanism is poorly understood. There is huge potential for drug design and discovery once the properties have been well understood.

Enzymes are understood to be biological catalysts that play major role in chemical reactions in living systems. Metals easily lose their electron to become an ion while enzymes are assumed to be electron rich. Thus metal ions are potent enough to bind to enzymes. Transition metals have large ionic volumes and display multi oxidation states, thus they have tendency to bind to large number of proteins and assist in electron/proton transfer mechanism. Metals are so inevitable to enzymes that the catalyzed reactions would proceed very slowly without them. Hence they are called metalloenzymes and constitute more than one third of enzymes.[1]

Various metabolic functions play key role in all living forms, e.g. methane hydroxylation in methanotrophs (bacteria), fatty acids desaturation (plants), DNA and RNA repairs, biosynthesis of β-lactam antibiotics (animals) etc. These functions require controlled oxidation of organic substrates which is carried out by activation of dioxygen (O_2) and is mediated by metals.[2-6] Transition metals activate dioxygen to facilitate oxidative transformation. This gains importance industrially as it helps in making efficient use of naturally abundant oxidant (i.e. O_2) in oxidation reactions.[7-9] Consequently, research is focused on understanding mechanism of activation of dioxygen in a number of heme and non-heme monooxygenase enzymes which contain mononuclear and homo- and hetero-dinuclear active sites.[3,10-24] Although active site of enzymes is quite diverse in nature, a common mechanistic hypothesis may quite be helpful in understanding dioxygen activation.

1.2: Metal Complexes

Organic compounds form a large class of compounds vital to all life forms. More sophisticated compounds may be created by redistribution of C–C and C–H bonds in hydrocarbons which generally requires activation of bonds. Such bond activation may be selectively controlled efficiently in catalysis regulated by transition metals. Though such reactions are not new to experimentalists, selective bond activation was a severe drawback. Different situations arise depending on transition metal and substrate under study. While oxidative mechanism is the most common process, σ-bond metathesis, electrophilic substitution and 1,2-substitution are other methods proposed for such reactions. Transition metal ions play innumerable and varied essential roles in the chemistry of living systems, in particular at the active sites of metalloenzymes.[25] The transition metal ions behave as electrophiles and are capable of accommodating multiple ligands. The metal ion plays dominant role in chemistry exhibited by metal complexes. Over the years, it has now been established that metal active centre interacts with substrate to form metal-oxo, metal-hydroxo, metal-peroxo, metal-hydroperoxo, and metal-alkoxo or bimetal μ-oxo species during reaction. These transition states proceed in a number of ways via electron transfer, hydrogen abstraction or rebound mechanism to get products. Even if reaction mechanism has been fully established by a theoretician in collaboration with experimentalist, it has been found that ligand substitution plays dominant role in fine tuning these reactions.

Nature performs regioselective as well as stereospecific substrate conversions vide efficient catalysts and is capable of speeding up biochemical reactions successfully through chemical systems known as enzymes. In general, latter contain transition metal as catalytic centres. Due to abundance of iron in earth’s crust, iron comprises active sites in most enzymes,[2,3,26-40] besides numerous other examples of copper-,[41-43] vanadium-,[44,45] molybdenum-,[46,47] and other transition- as well as non-transition metal-containing enzymes. Also some enzymes have clusters of two or more transition metal atoms as active sites, for instance, diiron enzyme ribonucleotide reductase [48-50] or the multi-center cluster in photosystem II.[51-54]

The mononuclear iron-containing enzymes can be classified as heme [26-33] and non-heme.[2,3,34-40] Two typical examples of these categories are cytochrome P450 and taurine/α-ketoglutarate dioxygenase,[55,56] whose active site structure is shown in figure 1.1. The crystal structure coordinates of P450 were taken from human enzyme cytochrome P450 2A13 found in liver responsible for detoxification of endogenous compounds. The heme group is linked to protein via a direct bond of the metal with the thiolate group of Cys439. The latter acts as a ligand and is found to fine-tune the electronic properties of the oxidant and attributes it the functional properties to act as a monooxygenase.[57] Other heme enzymes include peroxidases typically having histidine group as axial ligand [58-62] and catalases have a tyrosinate group.[63-65] The intermediates of catalytic cycles of enzymes are difficult to detect and characterize as they are short-lived which necessitates completion of experimental work in the field to be done by theoretical studies. Computational modeling has come as a useful aid in assisting experimentalists by establishing fundamental properties and successfully predicting changes upon ligand substitution in metalloenzymes and their catalytic features.[66-69] As an example, one can see that theory proposed a high valent iron(IV)-oxo heme cation radical, known as Compound I (Cpd I), reacting with substrates via radical mechanism with low barriers [70-72], 10 years before first characterization of the active species of P450 enzymes. It should be noted that Rittle *et al.* have characterized Cpd I using electron paramagnetic resonance (EPR), absorption and Mössbauer spectroscopy recently.[73]

The crystal structure of taurine/α-ketoglutarate dioxygenase, a non-heme iron enzyme , is shown in Figure 1(b) where metal is bound via a facial triad represented by two histidine (His) and an aspartate amino acid (Asp). This enzyme performs biodegradation of taurine and functions as sulphur source. Computational modeling was instrumental in comparison of properties between heme and non-heme iron enzymes and origin of efficiency of hydrogen-atom abstraction.[74-77] Effects of axial and equatorial ligand in oxidation of substrate by heme and nonhme iron complexes have been extensively reviewed [78,79] and it seems obvious that theory assists experimental studies in biocatalysis and biotransformation and gives insight into reaction mechanism and pathways.

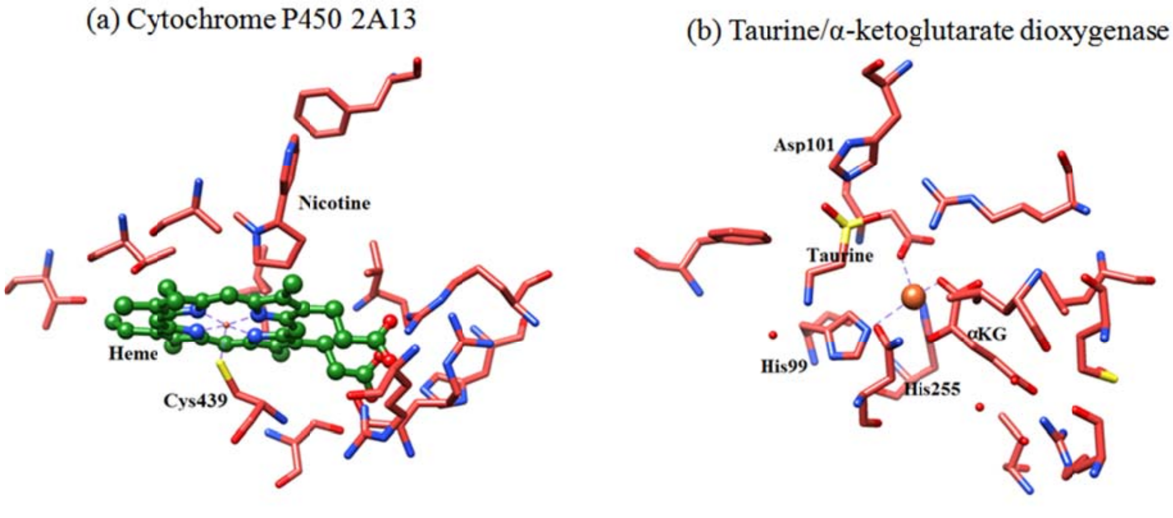

Figure 1.1: Active site structures of typical mononuclear iron enzymes: (a) cytochrome P450 (PDB: 4EJG), (b) taurine/α-ketoglutarate dioxygenase (PDB: 1OS7).

High valent metal-oxo complexes have been found to be the key oxidizing intermediates in various oxidation reactions catalyzed by heme and non-heme enzymes.[3,29,33,80-88]

An iron(IV)-oxo porphyrin π-radical cation species is implicated to be a reactive oxidizing intermediate in the catalytic cycle of P450 monooxygenase family of enzymes.[29-83-85] Oxygen evolving center of photosystem II (PSII) involves high valent manganese-oxo radicals.[89-92] Non-heme iron(IV)-oxo intermediates are believed to be oxidizing species in the catalytic cycles of taurine α-ketoglutarate dioxygenase (TauD), prolyl-4-hydroxylase, and halogenase CytC3.[93-97] Various groups have put in tremendous efforts in examining the biomimetic reactivities of high-valent metal-oxo complexes in respective enzymatic activities [98-108] and are trying to systematically overview the fundamental electron-transfer properties of high-valent metal-oxo species.

Besides iron(IV)-oxo species, iron(III)-superoxo, iron(III)-peroxo and iron(III)-hydroperoxo complexes have often been detected as key intermediates in the catalytic cycles of dioxygen activation by heme and non-heme iron enzymes. Studies of structural and spectroscopic properties and reactivities of synthetic analogues of these key intermediates have greatly improved our understanding of their chemistry.

A mononuclear non-heme iron(IV)-oxo complex of the tetraazamacrocyclic TMC ligand (TMC, 1,4,8,11-tetramethyl-1,4,8,11-tetraazacyclotetradecane) was one of the first biomimetic model systems, where an iron(IV)-oxo species was trapped and structurally characterized and has since been intensively studied to gain valuable insights into its physical properties, axial ligand effects and its reactivities with substrates.[109] This iron complex has since been intensely studied, and valuable insights into its physical properties, axial ligand influences, and reactivities with substrates have been gained from this work. Studies of reactivity patterns in ligand influences have unveiled considerable differences with respect to analogous intermediates in the catalytic cycle of CYP 450 enzymes. Various models of other ligated heme or non-heme enzymes have been characterized for their reactivity patterns over recent years. A combination of experimental and computational techniques has helped gain new insights into intrinsic properties of non-heme metal-oxygen complexes. Thus short-lived catalytic cycle intermediates such as the iron(IV)-oxo, iron(III)-superoxo, iron(III)-peroxo and iron(III)-hydroperoxo species have been synthesized and spectroscopically characterized via biomimetic non-heme ligand systems. Furthermore a comparison between heme and non-heme iron systems has been established and remarkable differences have been discovered. For instance, in some biomimetic porphyrin complexes, Cpd I was found to be the only viable oxidant in oxygen atom transfer reactions, in such systems, studies have suggested the existence of a single active oxidant in heme enzymes (e.g. P450). By contrast, some non-heme based superoxo and hydroperoxo complexes have revealed reactivity patterns that are considerably different from those of their heme analogues with occasionally higher reactivities for these intermediates than for the corresponding iron(IV)-oxo complexes.[101]

In recent years, many workers have reported significant progress in understanding the geometric and electronic structure of the active sites of non-heme iron enzymes and the contributions of these sites to molecular mechanisms. These enzymes have been found to participate in a range of reactions as extensive as those found in heme chemistry but are much less well understood. Dioxygen is one of the reactants for most of the enzymes. The uncatalyzed reactions of O_2 with organic substrates are thermodynamically favorable. The reaction is found to be kinetically slow as it is spin forbidden and the one-electron reduction potential of O_2 is low. While the mononuclear non-heme iron enzymes catalyze reaction either by a high spin ferrous site which is involved in dioxygen activation or by a high-spin ferric site which activates substrates. In some of the ferrous enzymes, an additional organic cofactor (e.g. α-ketoglutarate or pterin) may participate in a coupled reaction with dioxygen where both the substrate and cosubstrate are oxygenated.

1.3: Metalloenzymes

Metalloenzymes are known to catalyze many difficult reactions under mild conditions and with selectivity.[110] For instance, nitrogen fixation,[111] hydrocarbon oxidation [112,113] generation of radicals for subsequent catalysis,[114] and dismutation of superoxide (a radical anion) [115,116] require metalloenzymes at play. The transition metals form catalytic sites in them, some of which are Fe, Zn, Mn, and Cu (in order of prominence based on a current analysis utilizing the metalloprotein data bank-MDB).[117] Generally, the transition metal active sites are redox active, and there can be coupling between electron transfer (eT) and proton transfer (pT) as well.[118] These redox active sites aid in typical forming and breaking of bonds in catalytic reaction cycles. While in 'pure' eT metalloproteins, geometric reorganization is usually kept at a minimum to facilitate efficient eT, many redox active metalloenzymes undergo significant conformational changes at or near the active site.[119] Fe and Mn metalloenzymes (and related eT proteins) usually have high-spin (HS) metal sites in some or all steps of their catalytic cycles.[118,120] In dinuclear or polynuclear enzymes, these metal sites are often spin-coupled.[121] In other cases, as in Zn-Fe or Cu-Zn enzymes, bridging ligands link the metal sites electronically.[122,123] The positively charged metal ions and the negatively charged first shell ligands exhibit strong metal-ligand covalency, which can either tune the redox potential of the active site and/or shift the acidity of bound ligands.[25,118] In other non-redox case, the catalytic cycle is initiated either by some charge transfer to the metal (glyoxalase I, Zn), or spin coupling between a metal and a ligand radical (Cu-tyrosine in galactose oxidase). Here the ligands are 'noninocent', and can be radicals in some cases.

The monooxygenases and the dioxygenases are two types of oxygen-using metalloenzymes in nature. The monooxygenases bind molecular oxygen and transfers one atom of O_2 to a substrate, while the other atom is reduced to water. By contrast, in the dioxygenases both atoms of molecular oxygen are relayed to one or two substrate(s).

1.3.1: Heme enzymes

In heme enzymes, the proteins contain a heme cofactor, i.e., a porphyrin ring with an iron ion in the center. This heme cofactor functions to transfer electrons, to store and transfer molecular oxygen and plays major role in catalysis. The heme group can alternate oxidation states between the Fe(II) and Fe(III). This makes it suitable for an electron transfer cofactor either in electron transfer proteins (e.g. cytochromes) or as cofactors inside an enzyme for transporting electrons to an active site in the same enzyme.[124]

Cytochrome P450 is a large family of heme enzymes. This superfamily has many different enzymes (isoforms). Heme group is the main part of their active site in all isoforms. The heme-copper oxidase superfamily is another family of enzymes in which the heme cofactor also plays a catalytic role. The heme-copper oxidases are membrane enzymes.[30,125,126] This superfamily also contains different types of cytochrome c oxidase and nitric oxide reductase. These enzymes have a binuclear active site. Apart from the heme group they also contain a non-heme metal, either copper or iron.

The cytochrome P450 (commonly termed P450s or CYPs) are a superfamily of heme-binding enzymes that have immense biotechnological potential and are widely studied as a consequence of their multitude of physiological functions in organisms (from prokaryotes through to man).[30] The P450s catalyze the reduction of dioxygen bound to their heme iron and the insertion of an atom of oxygen into organic substrates bound in their active site and proximal to the heme.[127] It performs this function in a regio- and (usually) stereoselective manner so that it is a highly prized chemically process as synthetic chemistry methods are not able to achieve such otherwise difficult regioselective oxidation of non-activated C–H bonds. The P450s are found predominantly in endoplasmic reticulum and mitochondria, and in greatest abundance in liver. They catalyze a variety of reactions and convert chemicals to potentially reactive product as well as make compounds less toxic. They are best known for their functions in the metabolism of drugs and other xenobiotics in humans. Thus they aid in catalyzing a variety of reactions, conversion of chemical to potentially reactive products and making compounds less toxic. The hepatic isoforms are known to play pivotal roles in chemical detoxification and health.

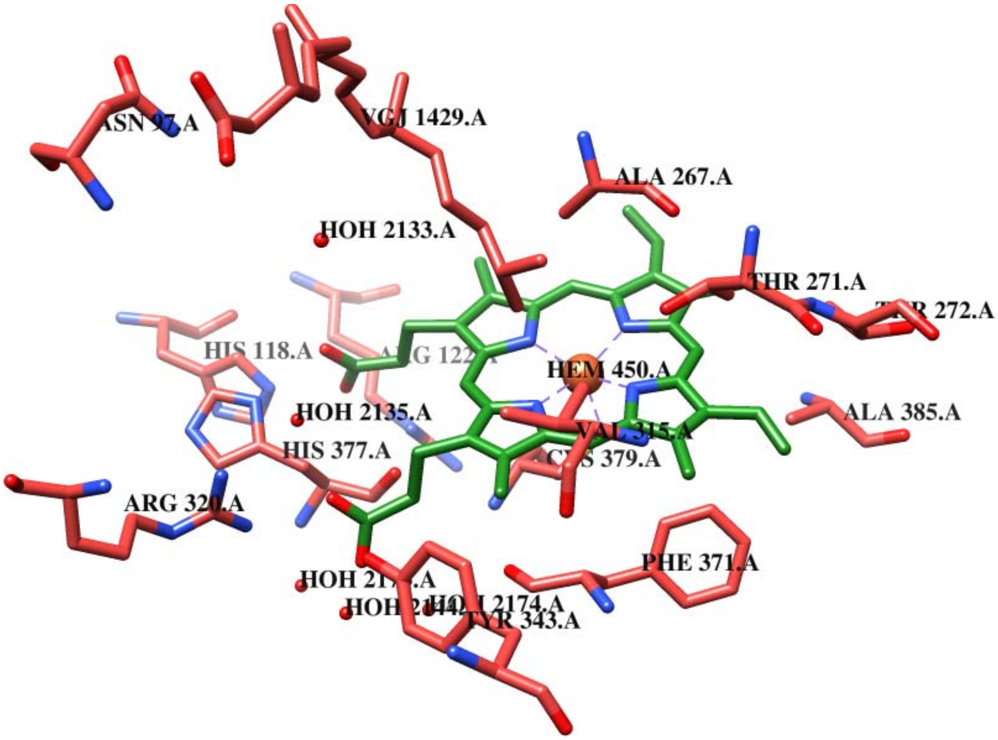

Figure 1.2: Active site of P450 (2WM4 pdb file).

Cytochrome c oxidase is located in the mitochondrial or bacterial membrane. It is the terminal enzyme found in the respiratory chain which has a binuclear center (BNC) consisting of a heme group and a histidine-ligated copper as active site. One of the histidine has a cross-linked tyrosine, which employs four electrons in the process of reducing molecular oxygen to water. These electrons are delivered to the BNC through two cofactors, one copper complex and another heme group located near the binuclear center. The membrane provides protons needed for charge compensation.[128] With difference in the exact form of the heme cofactors, the cytochrome c oxidase enzymes can be divided into subfamilies on the basis of the presence of different numbers of channels for proton transfer and in the number of pumped protons per electron.

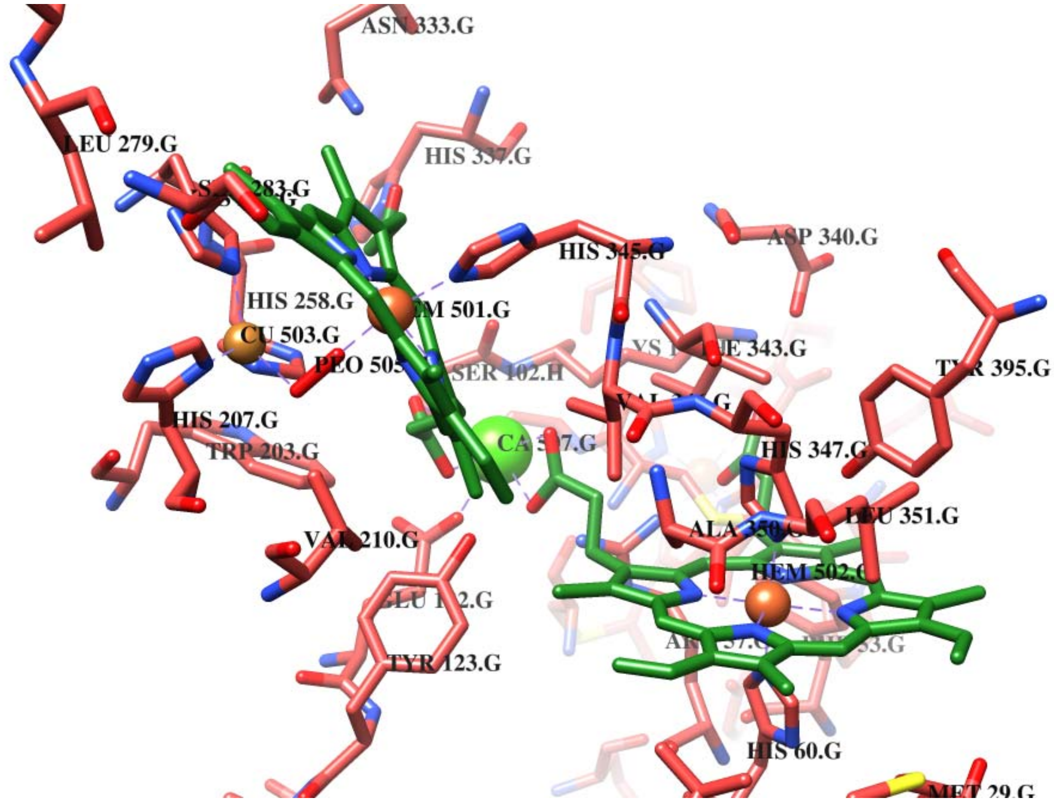

Figure 1.3: Active site of Cytochrome c Oxidase (5DJQ pdb file).

Nitric oxide reductase (NOR) catalyzes the nitric oxide to nitrous oxide and water by reduction of two-electrons. The active site of NOR is very similar to that of cytochrome c oxidase, with a non-heme Fe_B. Using a synthetic model of the BNC based on the X-ray determined structure of NOR, a DFT study of the catalytic NO reduction revealed that calculated energy profile was in agreement with the most important points with experimental information.[129] The calculations also explained the non electrogenicity of NO reduction reaction.[130]

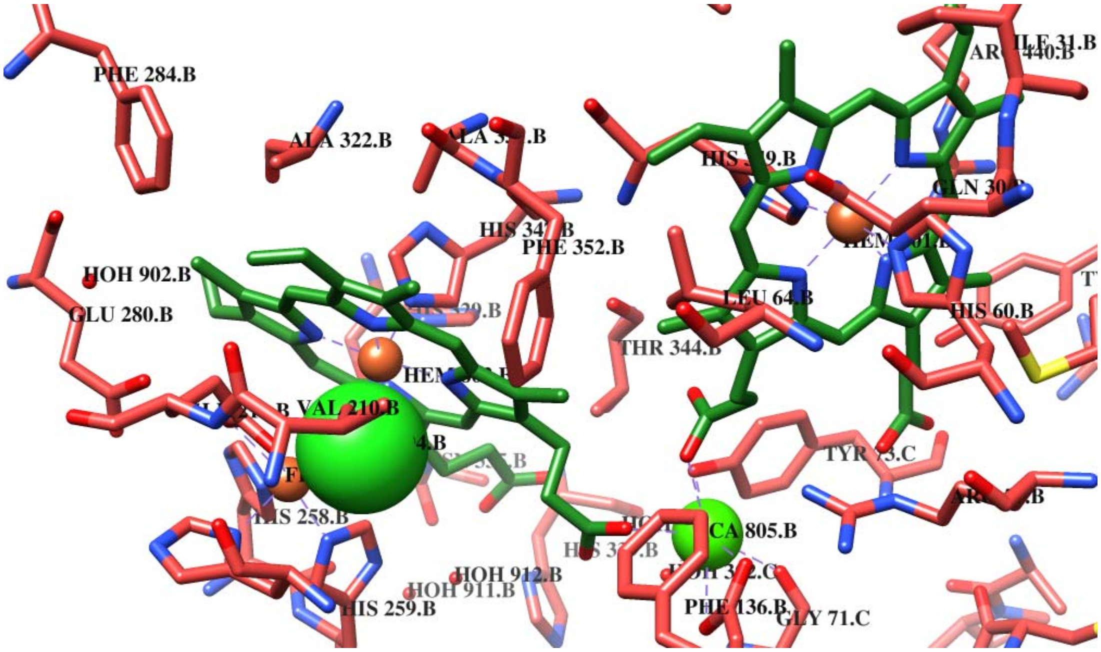

Figure 1.4: Active site of Nitric oxide reductase (3WFB pdb file).

1.3.1.1: Recent DFT model calculations of drug metabolism by cytochrome P450

Cytochrome P450 enzymes are the major catalysts involved in the oxidative metabolism of most drugs, steroids, carcinogens, and other chemicals.[131,132] They have been stated to be among “the most versatile biological catalysts known” [133] and its capability of oxidizing xenobiotic substances (e.g. drugs) has motivated scientists to focus on its viability in toxicology, drug metabolism and pharmacology. In pharmacology, knowledge of drug metabolism and its mechanism plays indispensible role in early phases of drug discovery process. More than 75% of drugs in clinical use are metabolized by P450s in phase I metabolism.[134] The effects of these oxidations may be manifested in poor drug bioavailability and various acute and chronic toxicities, including adverse drug interactions, cancer susceptibility, and birth defects.[135] The catalytic cycle of P450s is quite complicated and requires proper understanding for drug discovery.[20,86,133,136,137] After the substrate binds to the heme center, a series of events are triggered. These events lead to two reduction and two protonation steps and the formation of a high-valent oxo-ferryl species. This oxo-iron species (Compound I, Cpd I) in P450 enzymes has ultrashort lifetime and degenerate multiple ground spin states and hence is declared as an elusive oxidant due to difficulties in its detection experimentally until successful determination by Green's group in 2010.[73] A revelation by theoretical studies of Shaik's group have implicated, Cpd I of P450 as an elusive "chameleon",[138,139] for its ability to adapt its electronic structure as a response to the variation of the environment, making the chemical process catalyzed by P450 much more complicated.

1.3.1.2: DFT studies on the chemical process of drug metabolism catalyzed by P450

(a) Ethanol oxidation

Ethanol is an intoxicating ingredient, serves as a central nervous system depressant and a primary constituent of liquor. It is rapidly absorbed from the gastrointestinal tract into the bloodstream and is oxidized primarily in the liver. Earlier it was believed that alcohol dehydrogenase (ADH) was the only significant enzyme involved in ethanol metabolism until Lieber *et al.* suggested the microsomal ethanol oxidizing system, mainly involving cytochrome P450 2E1 (CYP2E1), as being responsible for alcohol oxidation.[140–142] Extensive experimental studies of ethanol oxidation by P450 were carried sooner [143–146] due to its key role in toxicology (e.g. in acidosis, fatty liver disease etc.). Three mechanisms have been proposed for ethanol oxidation by P450 (shown in Figure 1.5). The conventional mechanism is the gem-diol mechanism (Figure 1.5A) [143–148], in which the rate determining H-abstraction from the C_α of ethanol is followed by oxygen rebound to C_α radical to form the gem-diol intermediate, which then undergoes dehydration to form the acetaldehyde and water. The second mechanism (Figure 1.5B) involves an initial H-abstraction from C_α of ethanol, like the gem-diol mechanism, followed by a second H-abstraction from the hydroxyl group of the radical, and is hence called the dual hydrogen abstraction (DHA) mechanism.[147,148] The third mechanism (Figure 1.5C) is called reverse dual hydrogen abstraction (R-DHA) mechanism and starts with a H-abstraction from the hydroxyl group of ethanol, followed by a second H-abstraction from C_α. DFT calculations were carried out to explore all the three mechanistic hypotheses. R-DHA mechanism was the one discovered for the first time in computational study by de Visser *et al.* [149] and is shown diagrammatically below:

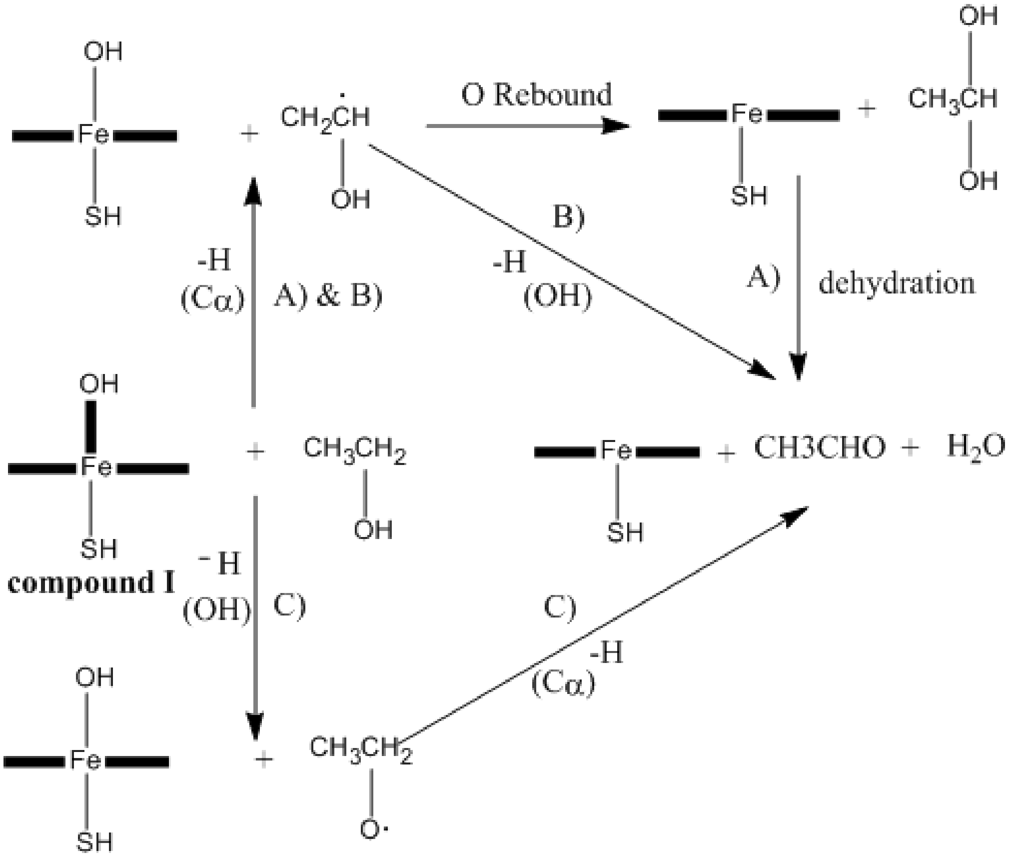

Figure 1.5: Three mechanistic hypothesis for ethanol oxidation by CYP2E1.[149]

(b) Acetaldehyde oxidation

Acetaldehyde is the primary product of ethanol oxidation and is more active. CYP2E1 could catalyze both ethanol and acetaldehyde.[150] It is considered to be responsible for many of the toxic effects caused by ethanol (acidosis, fatty livers etc.).[151] CYP2E1, accompanies the well-known acetaldehyde dehydrogenase (ALDH), in efficient oxidation and detoxification of acetaldehyde in the human body. The mechanism of CYP2E1-catalyzed acetaldehyde oxidation was investigated experimentally using kinetic deuterium isotope reactions.[146] A theoretical study was performed by using both the PorFe-SH model and the PorFe SMe model.[152] It was proposed that the reaction starts with hydrogen transfer from the aldehyde group of acetaldehyde to the oxygen of Cpd I on both HS and LS states, leading to a pair of transition states, ^{2,4}TS. This H-abstraction step is then followed by an O-rebound process, which leads to C–O bonding and formation of the ferric-acetic acid products, ^{2,4}PC. The rate determining step is H-abstraction step. The activation energy is 11.7/14.0 kcal/mol and 11.8/13.8 kcal/mol in the PorFe SMe model system and the PorFe SH model system respectively. The C–H bond activation barrier of acetaldehyde hydroxylation is about one-third to one-half of that needed for alkane hydroxylation due to weaker C–H bond of acetaldehyde than that of alkane.[153] The PorFe-SH model exhibits a barrier-less rebound phase, while PorFe SMe model system shows a quite low rebound barrier on both HS and LS states (0.6 kcal/mol for HS and 0.7 kcal/mol for LS). As such, the reaction proceeds in an effectively concerted rebound pattern. Consequently, acetaldehyde hydroxylation by CYP2E1 follows the TSR rebound mechanism,[153-156] similar to that of alkane hydroxylation, showing a much lower C-H bond activation barrier (about one-third to one-half of that of alkane hydroxylation) and a barrierless rebound process on both HS and LS state.

(c) Amine N-dealkylation

The alkylamine structure is found in numerous natural products, drugs and drug candidates, many of which undergo P450-catalyzed N-dealkylation with loss of the alkyl group.[157,158] The N-dealkylation reaction of amine has been the subject of several experimental and theoretical investigations.[158–173] It is proposed that N-dealkylation of amine results from hydroxylation of a carbon adjacent to the N atom, forming the unstable carbinolamine, which decomposes subsequently to give rise to a carbonyl product and a dealkylated amine. N-Dealkylation reaction of amine has been of great interest and is one of the most intriguing reactions debated for many decades. After years of discourse, two alternative mechanisms (Figure 1.6) have survived. One is a hydrogen atom transfer (HAT) reaction,[159–162] labeled as (i), on the carbon adjacent to the N atom, followed by oxygen rebound to form the carbinolamine, which decomposes subsequently to formaldehyde and a dealkylated amine. An alternative mechanism involves a single electron transfer (SET) on the N atom itself,[163,164,171] labeled as (ii), followed by proton transfer, and then oxygen rebound to form the carbinolamine, which then decomposes as outlined above. A theoretical study on a series of p-X-DMAs which were used in experimental studies also supported the HAT mechanism and explained the experimental observations that had been considered to be typically associated with the SET mechanism on the basis of HAT process.[174] This DFT study resolves the HAT-SET controversy and provides a consistent mechanistic view on the mechanism of the N-dealkylation reaction of amines.

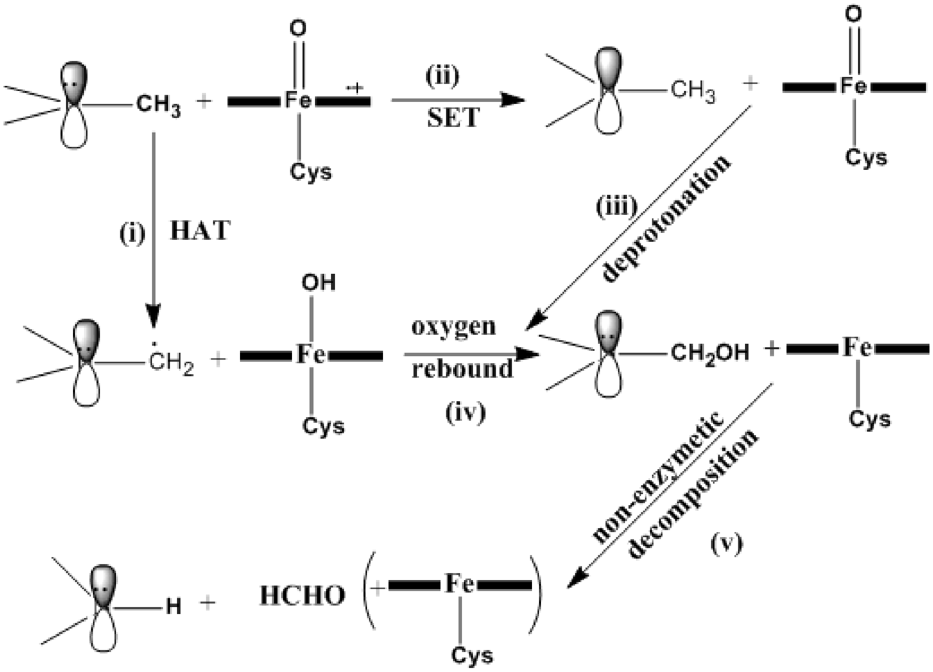

Figure 1.6: Mechanistic hypothesis for N-dealkylation of amine hydrogen atom transfer (HAT) mechanism and single electron transfer (SET) mechanism.[174]

(d). Amide N-demethylation

Amide compounds exist in insect repellents, industrial solvents and drugs, possessing important biological activities.[175–177] Many of these compounds undergo oxidative N-dealkylation mainly by P450.[178–183] The amide N-demethylation is understood in continuation of amine N-dealkylation. In the dimethylaniline N-demethylation study, the π_{Ph}–$\pi_{N\text{-}C}$ conjugated system in the p-X-DMAs (X =H, Cl, CN, NO_2) bridges the p-X substituent and the C-H moiety that undergoes cleavage in the transition state, and thus, make the transition state acquire a polar character.[184] To interrogate the precise role of the π_{Ph}–$\pi_{N\text{-}C}$ conjugation, an analogous series of substrates, para-substituted N,N-dimethylbenzamides (p-X-DMBAs, X=MeO, H, Cl, NO_2, shown in Figure 1.7), in which the conjugative interaction is disconnected and will thus not show the “polar-type” substituent effect on the reactivity, were studied by Wang *et al.* following the p-X-DMAs work.[185]

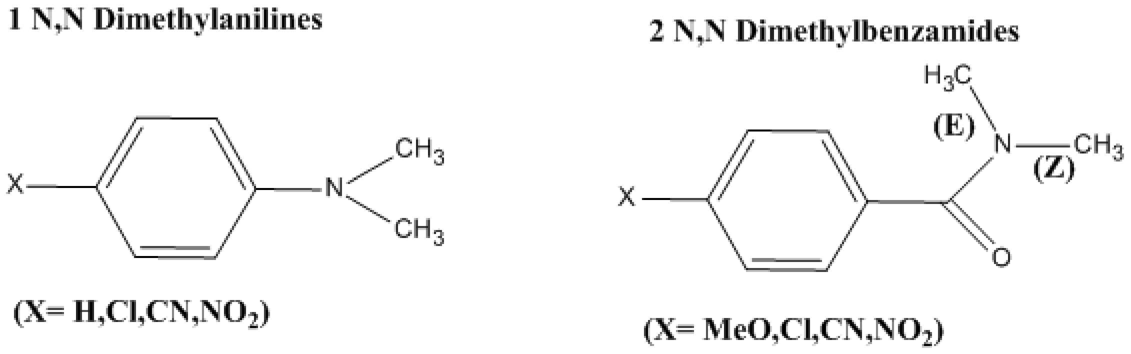

Figure 1.7: N,N-Dimethylanilines (DMA) and N,N-Dimethylbenzamides (DMBA).

1.3.2: Non-heme enzymes

Our understanding of how non-heme iron enzymes catalyze the activation of dioxygen in the course of oxidizing a range of substrate has progressed significantly.[3,102,186,187] Now protein crystallography has made it possible to visualize the metalloenzymes' active site not only in its isolated state but also in various other states leading to and deriving from the activated oxygen species. Generally there are one of the two types of active sites in oxygen activating non-heme iron enzymes: (a) the first comprises a mononuclear iron center coordinated to two histidines and a carboxylate that occupy one face of an octahedron, (b) the second active site is a diiron center with two histidines and four carboxylates as ligands and is associated with methane and toluene monooxygenases, fatty acid desaturases, and ribonucleotide reductase.[187] At one hand, in (a) the arrangement is called a 2-His-1-carboxylate facial triad recognized as a common structural motif for many mononuclear non-heme iron enzymes,[188] this motif is known to confer mechanistic flexibility by allowing three coordination sites on the metal center to be available for binding exogenous ligands such as substrate, cofactor, and/or O_2; on the other hand, in (b) at least one coordination site on each iron is available for exogenous ligand binding, and it has been shown that O_2 binds to both iron centers in the course of catalysis.

1.3.2.1: Mononuclear Non-heme iron

1.3.2.1.1: Lipoxygenases

Lipoxygenases (LOs) are non-heme iron dioxygenases that catalyze the regio- and stereo-specific hydroperoxidation of 1,4-Z,Z-pentadiene-containing polyunsaturated carboxylic acids.[189-193] They are found in all plants and animals and some lower organisms (alga, molds, and corals) but have not yet been found in bacteria or yeast.[194] Arachidonic acid is a major substrate of LOs in mammalian systems and its positional specificity serves as its basis of classification (e.g., 5-LOs biosynthesize leukotrienes and lipoxins which act as mediators of anaphylactic and inflammatory disorders,[192] 15-LOs aid pore formation in organelle membranes to initiate organelle degradation,[195] 12-LOs may play a role in tumor cell metastasis [196] etc.). All LOs are monomers containing one iron atom. The molecular weight of plant LOs is higher than their mammalian LOs.[191] Sequence alignment of known LOs exhibits the conservation of a set of histidines found to be clustered in a His(X)4His(X)4His(X)17His motif.[197]

Crystal structures of the ferrous form of two of the Soybean LOs (SLOs): SLO-1 were characterized by Boyington *et al.* at 2.6 Å resolution at room temperature (PDB ID: 2SBL) [198] and by Minor *et al.* at 1.4 Å resolution at 100K (PDB ID: 1YGE) [199] while SLO-3 structure was characterized by Skrzypczak-Jankun *et al.* at a resolution of 2.6 Å at room temperature (PDB ID: 1LNH).[200] Gillmor *et al.* characterized mammalian LOs by structure available for the inhibited ferrous form of reticulocytic rabbit 15-LO at 2.4 Å resolution at liquid N_2 temperature (PDB ID: 1LOX)

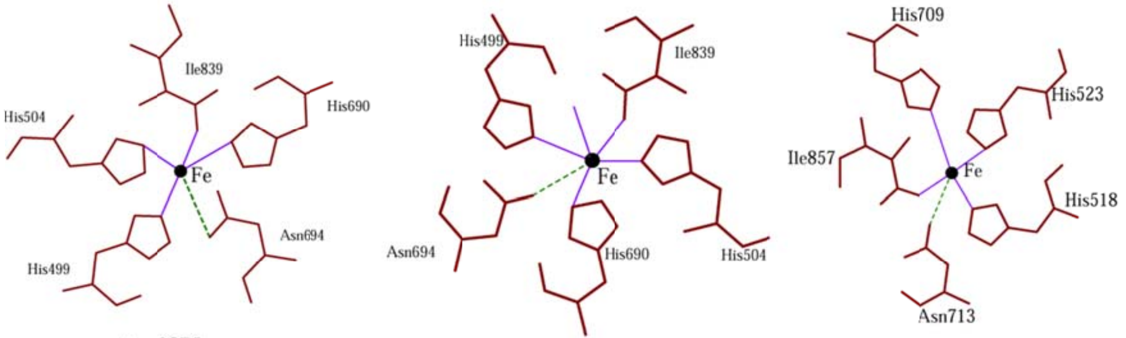

(a) 2SBL (b) 1YGE (c) 1LNH

Figure 1.8: Structures of active site of ferrous LO: (a) SLO-1 (PDB: 2SBL) (b) SLO-1 (PDB: 1YGE) (c) 15-RLO (PDB: 1LNH).

A single ferrous ion contained in an isolated LO is activated to ferric by the hydroperoxide product. The intermediate formed in the reaction of ferric enzyme with substrate has not been characterized. A mechanism of hemolytic cleavage of the C–H bond to produce a substrate radical and a ferrous species is argued by many.[201] Others favor production of a carbanion coordinated to the ferric center in heterolytic cleavage of the C–H bond. A hybrid mechanism is also proposed in which the formation of an organo-iron complex follow the hydrogen-atom abstraction step.[202-204]

1.3.2.1.2: Intradiol dioxygenases

Aromatic ring cleaving dioxygenases are found predominantly in aerobic soil bacteria besides vertebrates. In bacteria, these enzymes degrade lignin, terpene, tannin, and xenobiotic pollutants while in mammals they catabolise tryptophan and tyrosine. They insert both atoms from dioxygen into the substrate aromatic ring leading to ring cleavage.[205-208] Based on the position of the ring cleavage, it is divided into intra- and extradiol dioxygenases. Figure 1.9 shows its correlation to the metal ion oxidation state.

Sequence homology comparisons show that the intra- and extradiol dioxygenases have evolved independently;[209-211] however, in some cases a slow substrate (3-chloro-catechol) may be cleaved by an intradiol dioxygenase in an extradiol fashion. This indicates that the redox state is not the sole determining factor in specificity.[212]

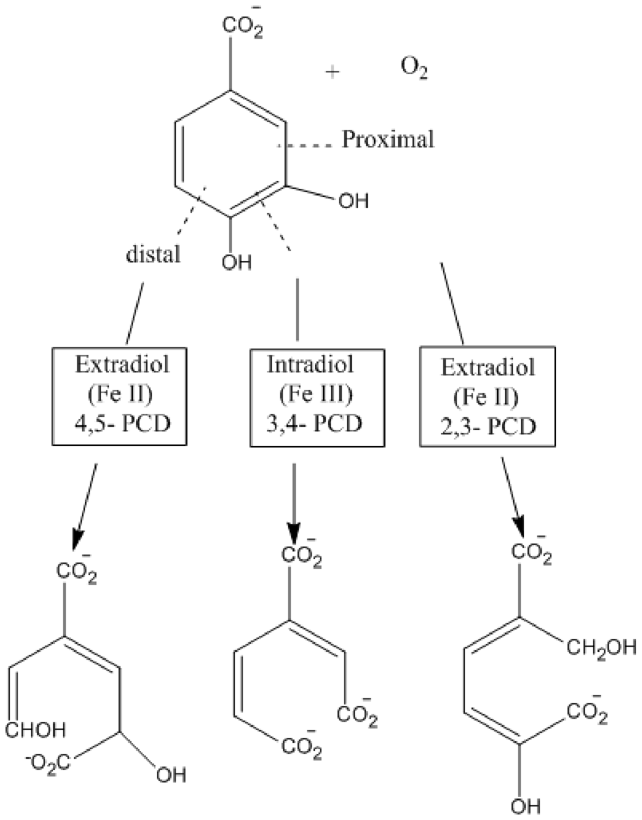

Figure 1.9: Classification of intradiol and extradiol dioxygenases.

Intradiol dioxygenases cleave a more limited set of aromatic substrates than extradiol dioxygenases. The most well-studied intradiol dioxygenases are protocatechuate 3,4-dioxygenases (3,4-PCD), catechol 1,2-dioxygenases (pyrocatechase; 1,2-CCD); and chlorocatechol 1,2-dioxygenases (1,2-CCD). They cleave catecholic substrates to produce muconic acid derivatives. The 3,4-PCD enzymes are found in divergent bacterial sources. They usually consist of 4-12 $\alpha\beta Fe^{III}$ protomer units.[211,213-216]

X-ray crystallography (via infra) has indicated the active site of 3,4-PCD containing an axial tyrosine which dissociates upon substrate binding. The crystallographic structure of 3,4-PCD from *Pseudomonas putida* has been characterized at 2.15 Å resolution indicating highly symmetric nature of enzyme with numerous 2- and 3-fold axes. The active site occurs at the subunit interface; however, all of the ligands originate from the β-subunit. 3,4-PCD has a 5C distorted trigonal-bipyramidal active site with Tyr447 and His462 coordinated in the axial positions, and His460, Tyr408 and water (i.e. hydroxide) are coordinated in the equatorial plane.[217,218] The reaction of intradiol dioxygenases has been shown to have a sequential order, with substrate binding before dioxygen.

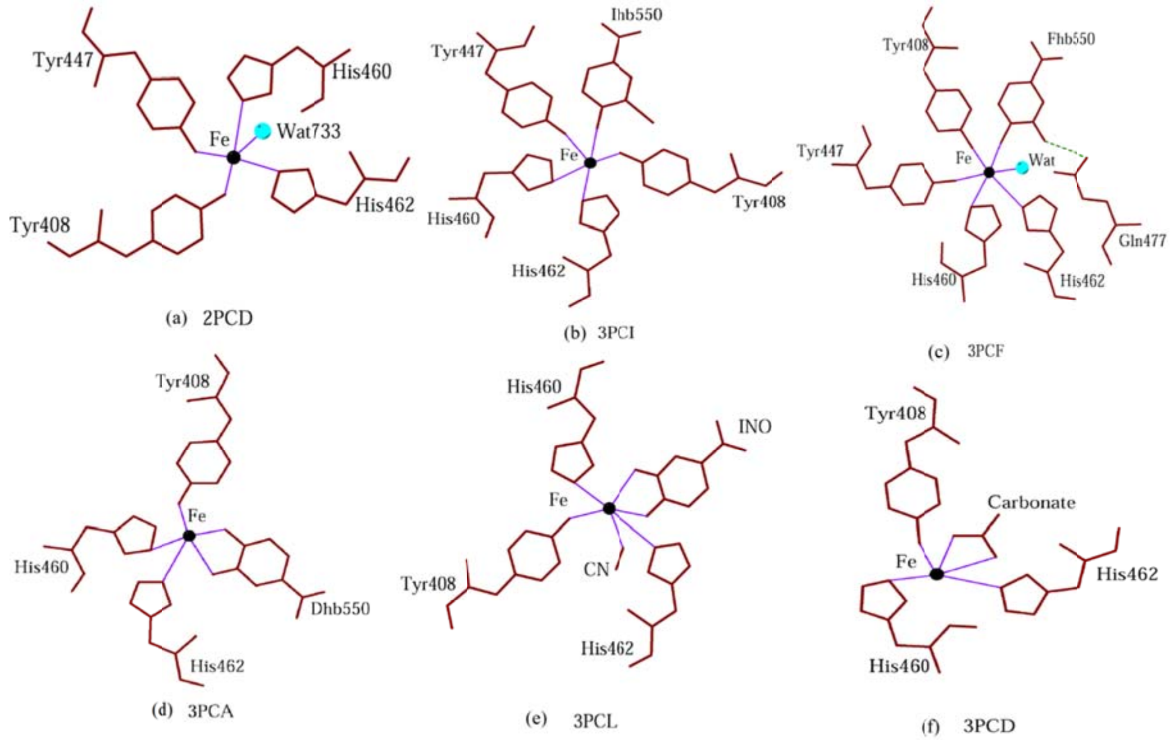

Figure 1.10: Active-site of X-ray crystallographic structures of (a) 3,4-PCD, (b) 3,4-PCD-IHB, (c) 3,4-PCD-FHB, (d) 3,4-PCD-PCA, (e) 3,4-PCD-INO-CN, and (f) Y447H 3,4-PCD. (PDB files 2PCD, 3PCI, 3PCF, 3PCA, 3PCL, 3PCD, respectively).

1.3.2.1.3: Extradiol dioxygenases

Extradiol dioxygenases, successfully isolated form many divergent soil bacteria (*Pesudomonads*), have Fe^{II} active site [219] (or rarely, Mn^{II}).[220-222] They catalyze the insertion of both atoms of dioxygen into catechol derivatives, thus forming the ring-cleavage product 2-hydroxymuconaldehyde acid.[205,223-225] They are classified into proximal or distal dioxygenase based on position of ring cleavage relative to the substituent (Figure 1.9). They are being investigated for their directed evolution to facilitate degradation of specific pollutants: the recalcitrant polychlorinated biphenyls (PCBs).[207,226] The bacteria appears to evolve quickly to degrade new substrates supposedly due to the location of the gene on a plasmid rather than in chromosomal DNA; latter is assumed to evolve more slowly.[227] These have been divided into one- and two-domain enzymes.[228] Representative bacterial extradiol dioxygenases, 2,3-dihydroxybiphenyl 1,2-dioxygenase (1,2-DHBD), catechol 2,3-dioxygenase (2,3-CTD), and protocatechuate 4,5-dioxygenase (4,5-PCD,) which have $(\alpha Fe)_8$, $(\alpha Fe)_4$ and $\alpha_2\beta_2Fe$ quaternary structures.[229-232] have been reviewed excellently.

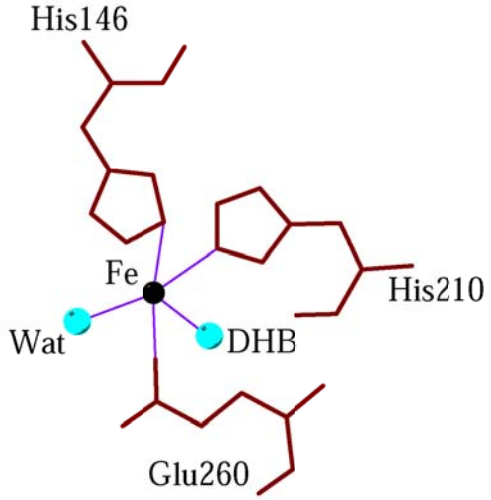

Figure 1.11: Active-site X-ray crystallographic structure of 1,2-DHBD (PDB: 1HAN).

Crystal structure of 1,2-DHBD has been reported for different forms: active ferrous (1.9 Å resolution) and inactive ferric (1.8 Å resolution), substrate-bound ferrous, and substrate-bound ferric (2.6 Å),[230,233-235] and more recently determined ferrous 2,3-CTD (2.8 Å resolution), ferric 4,5-PCD (2.2 Å resolution), and substrate bound to ferric 4,5-PCD (2.2 Å resolution).[236,237]

The extradiol dioxygenases are 5C in the resting ferrous form yet they are not highly reactive towards dioxygen in the absence of substrate. Similar to intradiol dioxygenase, these and related enzymes appear to have an ordered mechanism in which substrate binds before dioxygen.[238-240]

1.3.2.1.4: Pterin-Dependent Hydroxylases

Several tetrahydropterin-dependent monooxygenases have been isolated. Some of them are phenylalanine hydroxylase, PAH (phenylalanine 4-monooxygenase);[241-243] tyrosine hydroxylase, TyrH (tyrosine 3-monooxygenase);[244] anthranilate hydroxylase (anthranilate 3-monooxygenase);[245,246] tryptophan hydroxylase, TrpH (tryptophan 3-monooxygenase);[247,248] mandelate hydroxylase (mandelate 4-monooxygenase) [249] etc. They require mononuclear Fe^{II} for function. Anthranilate and mandelate enzymes have not been characterized much, but the three amino acid hydroxylases (PAH, TyrH, and TrpH) are known to share many physical, structural, and catalytic properties.[250-253] Several neurological disorders, including schizophrenia and Parkinson’s disease are suspectedly attributed to disruption of TyrH function, while dysfunction of PAH is known to lead to severe mental retardation (phenylketonuria, PKU). Of the PKU-inducing PAH mutants, most appear to affect protein stability.[254-259] The active site of PAH is in the Fe^{III} oxidation state in isolated state, which may be an artifact of purification. The enzyme is reduced from the Fe^{III} to the catalytically active Fe^{II} state by BH_4 and analogues.[260-263] This reduction is postulated to occur at a site distinct from either the regulatory or catalytic sites.[264] Several crystal structures have appeared on truncated forms of both PAH and TyrH.[252]

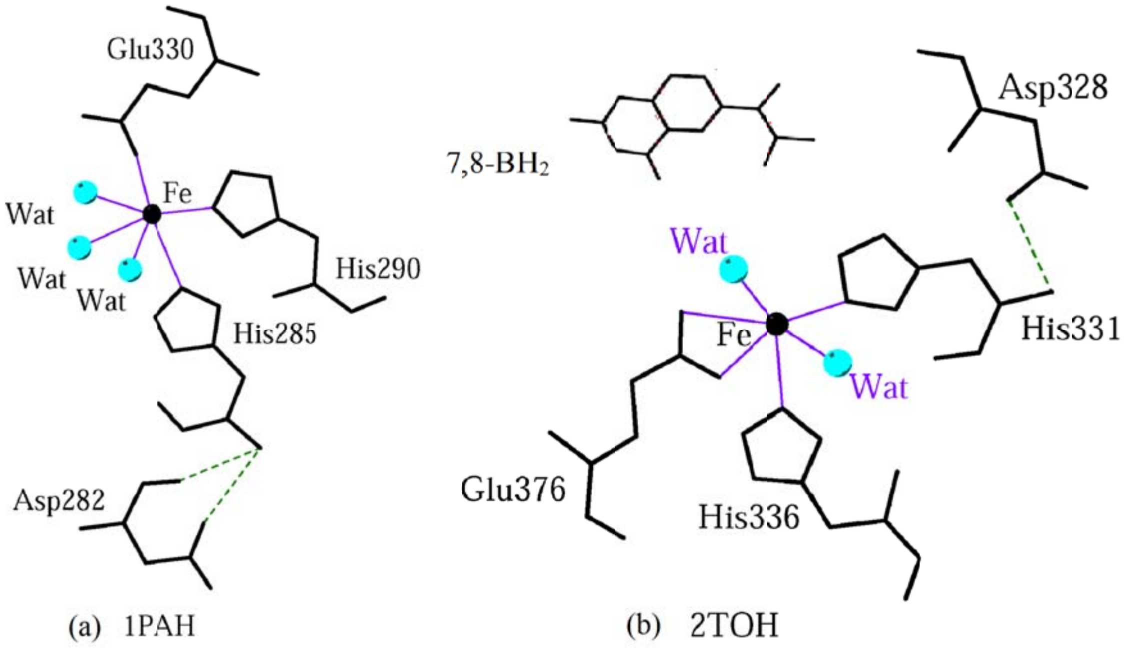

Figure 1.12: Structure of the active sites of (a) Fe^{III}PAH. (PDB: 1PAH) (b) Fe^{III}TyrH with cofactor analogue 7,8-BH2.(PDB: 2TOH).

The first published structure of PAH consists of the catalytic and C-terminal tetramerization domains of the enzyme, minus the N-terminal regulatory domain. A 5C site is formed upon substrate and cofactor binding, this directly implicates the iron in coupled hydroxylation and this fact is also consistent with the ordered mechanism of PAH wherein substrate and cofactor must be present before any product is released.[250]

1.3.2.1.5: α-Ketoglutarate-Dependent and related enzymes

The α-ketoglutarate (α-KG or 2-oxoglutarate) is required as a cosubstrate in a large class of mononuclear non-heme iron enzymes.[265-267] They are present in animals, plants, and microorganisms, and play important roles in an array of primary and secondary metabolic pathways. Prolyl 3-hydroxylase, prolyl 4-hydroxylase, and lysyl hydroxylase are involved in post-translational processing of collagen in animals.[268] In plants, Prolyl 4-hydroxylase is critical in the synthesis of hydroxyproline-rich glycoproteins responsible for regulating the extensibility and digestibility of the cell wall.[269] Aspartyl β-hydroxylase is known to catalyze the post-translational hydroxylation of aspartyl residues in many epidermal growth factors in mammalian systems.[270] Deacetoxycephalosporin C synthase (DAOCS) catalyzes the first committed step in the biosynthesis of antibiotic cephalosporin to deacetoxycephalosporin C.

All α-KG-dependent non-heme iron enzymes require ferrous ion, α-KG, and O_2 for reactivity but have different quarternary strucutres.[265]

The enzymes of this class are known to catalyze the reaction where α-KG decarboxylation is uncoupled from the substrate oxidation, either in the absence of substrate or in the presence of a substrate analogue.[271-275]

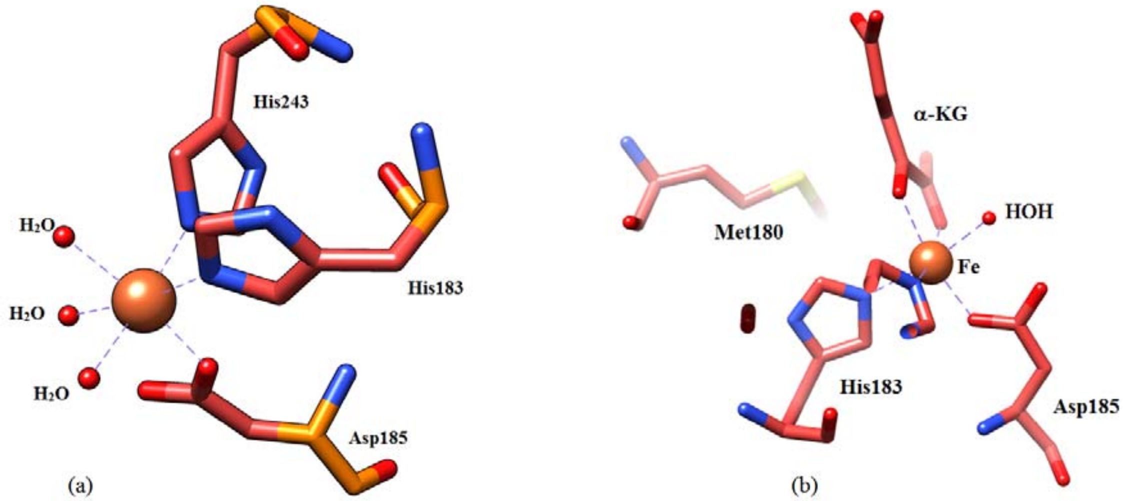

Figure 1.13: Structure of the active site in DAOCS: (a) the apoenzymes, (PDB: 1DCS) (b) the complex of DAOCS/FeII, (PDB: 1RXF).[276]

Valegard *et al.* have reported the first crystal structure of DAOCS.[276] Figure 1.13 shows apo (i.e., metal removed) DAOCS (PDB ID: 1DCS) and the DAOCS complex with Fe^{II} (PDB ID: 1RXF).

1.3.2.1.6: Rieske-Type Dioxygenases

The Rieske iron-sulfur center is a two iron-two sulfur cluster ([2Fe-2S]) having a 2His (on one iron), 2Cys (on the other iron) coordination environment, instead of the 4Cys present in plant ferredoxins. It assists prominently in electron transport pathway in membrane bound cytochrome complexes as well as in some dioxygenases.[277] The latter are mainly comprised of two protein components, namely a reductase containing flavin and a ferredoxin, [2Fe-2S] and a terminal oxygenase containing a Rieske [2Fe-2S] cluster and a non-heme iron active site.[278] Most of the Rieske-type oxygenases have a mononuclear iron site. This is known to be the site of dioxygen activation and substrate oxygenation.[278,279] Alkene monooxygenase was reported to have a binuclear iron site in its terminal oxygenase by F. J. Small and S. A. Ensign in 1997.

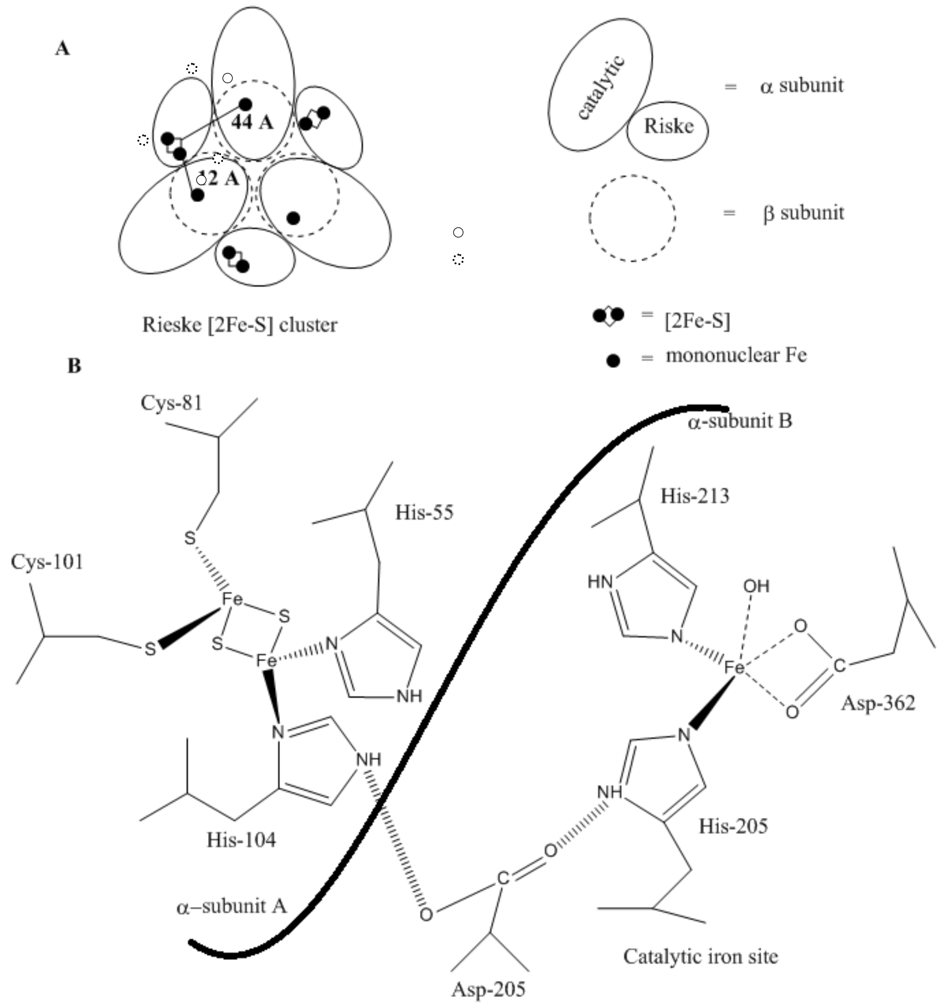

Figure 1.14: (a) Schematic overall protein structure of NDO showing α and β subunits and the inter- and intra-subunit distance between the Rieske site and the non-heme iron site. (b) Schematic structure of the Rieske site, the non-heme iron site, and the posposed route of ET between them in NDO (Adapted from work by Kauppi *et al.* (1998) and Kurtz *et al.* (1999).

The majority of the Rieske-type mononuclear non-heme oxygenases are known to be aromatic-ring-hydroxylating dioxygenases. These catalyze the regio- and stereospecific cis-dihydroxylation of an aromatic ring using dioxygen and NAD(P)H. For instance, benzene dioxygenase (BDO),[280] phthalate dioxygenase (PDO),[281] toluene dioxygenase,[282] and naphthalene 1,2-dioxygenase (NDO),[283] which initiate the aerobic degradation of aromatic compounds in the soil bacteria. They have been proved to be targets for bioengineering in bioremediation. This step in the reaction pathway (cis-dihydroxylation) ultimately leads to ring cleavage by the intra- and extradiol dioxygenases.[279] Besides these bacterial dioxygenases, other Rieske-type mononuclear non-heme oxygenases are anthranilate 1,2-dioxygenase,[284] which deaminates and decarboxylates the substrate to produce catechol; chlorophenylacetate 3,4-dioxygenase,[285] which converts substrate to catechol with chloride elimination; and 4-methoxybenzoate O-demethylase (putidamonooxin),[286] which catalyzes the conversion of 4-methoxybenzoic acid to 4-hydroxybenzoic acid and formaldehyde.

1.3.2.1.7: Bleomycin

Investigation of bleomycin (BLM) as a cancer chemotherapy agent began in 1965. This antibiotic possesses therapeutic benefit against squamous cell carcinoma and malignant lymphoma.[287] Since then, this drug has been characterized clinically and chemically.[288-294] BLM is isolated from *Streptomyces verticillus* as a copper complex. It is administered clinically in a metal-free form to reduce irritation and is believed to cleave DNA as an Fe^{II} complex in vivo.[295] BLM is shown to have reactivity with other metals like Cu, Co, Mn, Ru, and V.[293] The structure of this glycopeptide antibiotic has typically three domains (Figure 1.15): the bithiazole tail, which intercalates into DNA; the sugar moiety, believed to be involved in drug uptake into cells; and the β-aminoalanine, pyrimidine, and β-hydroxyhistidine groups, collectively known as the metal-binding region. There is some controversy regarding the β-aminoalanine and/or mannose carbamoyl ligands (vide infra).

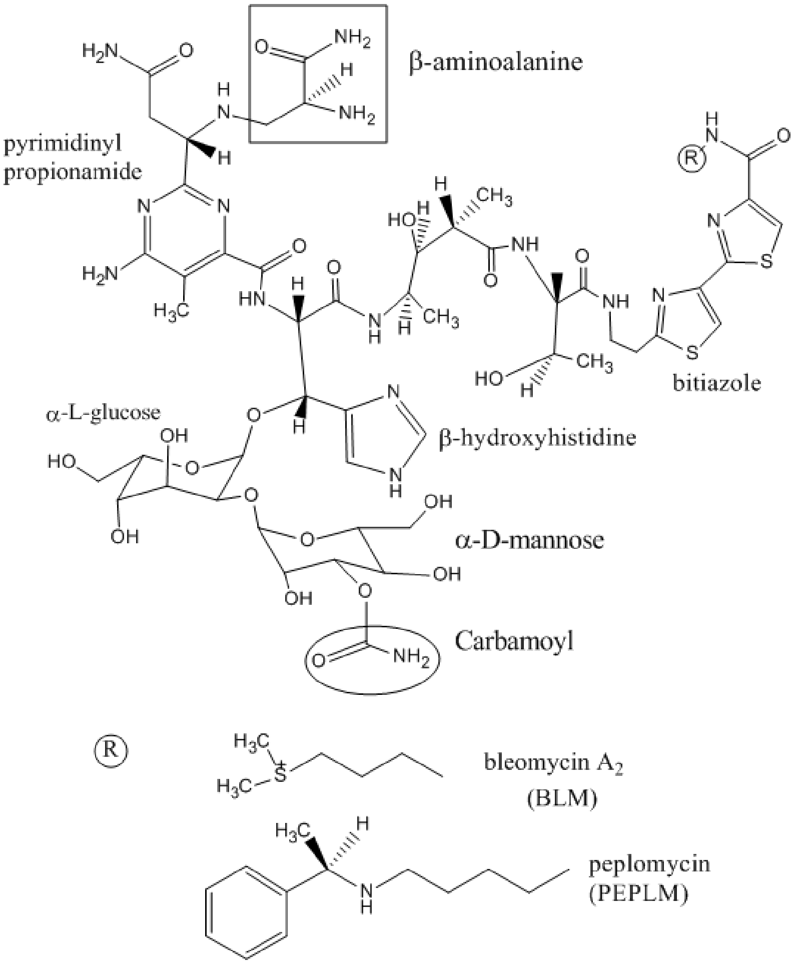

Figure 1.15: Structure of BLM.

The association constant of BLM with DNA is of the order of 10^5 M^{-1},[296,297] while the ratio of DNA base pairs to BLM in the cell nucleus are estimated as 10^{5-8}:1.[298,299] It is quite likely that virtually all of BLM is bound to DNA once it enters the nucleus and it is the DNA-bound species that is activated.[292]

The three-dimensional structure of BLM has been interpreted from the crystal structures of the Cu^{II} complex of the BLM synthetic precursor P-3A and model complexes (Cu^{II}, Co^{III}, Zn^{II}) [300-305] and from multinuclear NMR studies with and without a bound oligonucleotide.[306-325] There is no crystal structure on the complete BLM molecule.

1.3.2.2: Binuclear Non-heme iron

1.3.2.2.1: Hemerythrin

Hemerythrin (Hr) is the first characterized binuclear non-heme iron protein,[326-328] This metalloprotein is capable of reversible O_2 binding that also includes hemoglobin [329] (possessing a heme-iron active site) and hemocyanin [330] (having a binuclear Cu active site). Hr was first recognized as a dioxygen carrier in 1873.[331]

It is found in four phyla of invertebrates. It usually occurs as an octamer of virtually identical subunits. But sequences of monomeric (myoHr), dimeric, trimeric, and tetrameric proteins and a number of other Hr species have also been reported.[326-328] In addition to the iron ligands (vide infra) there are other conserved residues that are also believed to be of direct relevance for proper functioning of the protein.[328]

There were indications that two iron centers are involved in binding one dioxygen molecule during early experiments on Hr.[332] Two physiologically relevant forms of Hr as deoxyHr were identified by Klotz *et al.* [333], containing a diferrous site, and oxyHr, possessing a two-electron-reduced O_2 species bound to an oxo-bridged diferric site. Loehr and Klotz *et al.* [334-336] were successful to show that the O_2 moiety in oxy-Hr is a hydroperoxide, terminally bound to one Fe center and exhibiting a hydrogen-bond interaction with the bridging oxide. A third form of extensively studied Hr is met-Hr. It is the most stable form of the protein.[326-328] This physiologically irrelevant form also contains a diferric site but lacks the peroxide moiety.[328]

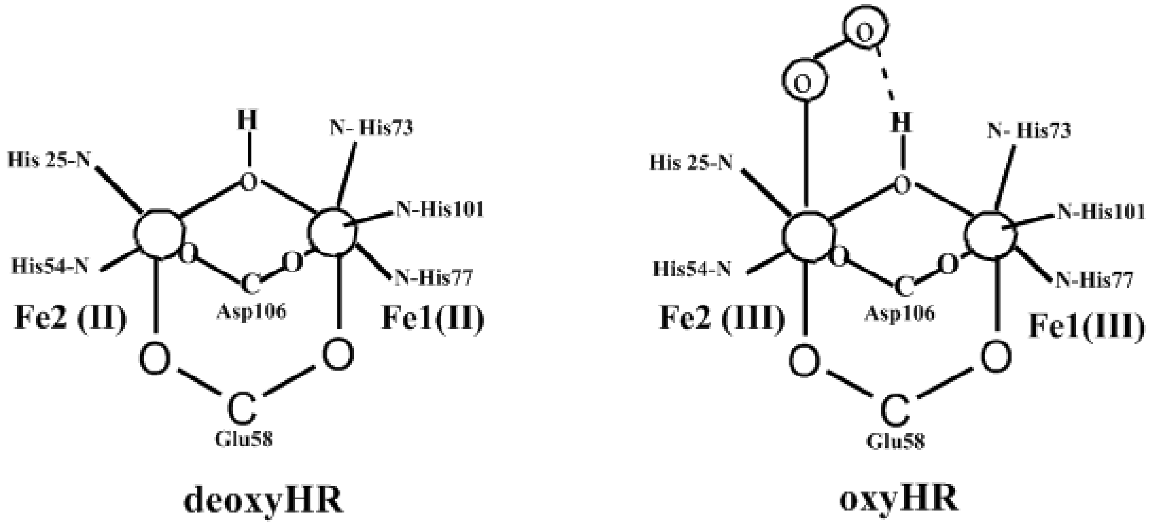

Figure 1.16: First coordination spheres of the diiron sites in deoxyHr and oxyHr [Adapted from Brunold *et al.* (1999)].

The three-dimensional molecular structures of myoHr and several octameric Hr species have been determined by X-ray crystallography at 2 Å resolution.[328] The folding of the polypeptide chain in the monomeric subunits is fairly simple. It consists of four R-helices that pack roughly parallel to one another. One characteristic of this packing is that there is only one small close-contact region, and the helices slightly diverge from one another away from the contact region. Thus a channel between the helices is produced that can accommodate the heme group in cytochromes and the binuclear iron cluster in Hr. The interior of the channel is very hydrophobic. It provides a suitable binding environment for dioxygen.

The active site of Hr consists of two iron centers roughly 3.25-3.50 Å apart. In deoxyHr (Figure 1.16), the ferrous ions are bridged by two carboxylates and an exogenous hydroxide ligand.[328,337]

To gain molecular-level insight into proton-coupled two-ET process associated with the interconversion of deoxyHr and oxyHr, the corresponding reaction coordinate was explored through DFT calculations evaluated and calibrated by the experimental data.[338]

1.3.2.2.2: Methane Monooxygenase

Methane monooxygenase (MMO) catalyzes NADH-dependent dioxygen activation and the insertion of an oxygen atom into the exceptionally stable C–H bond of methane (bond dissociation energy 104 kcal mol^{-1}) to form methanol.[339-341] Subsequently, methanol dehydrogenase converts methanol to formaldehyde which in turn may be catalyzed to formate by formaldehyde dehydrogenase in concert with NAD+ reduction. Finally, formate dehydrogenase oxidizes formate CO_2 with help of NAD^+ as an oxidant. Methanotrophs grow on methane through this pathway as the sole source of carbon and energy.[340,342,343] Methanotrophs have been classified as type I, II, or X on the basis of metabolic pathway utilized, their morphology, and types of MMO expressed.[342,343] Types I and X methanotrophs utilize a ribulose bisphosphate pathway (ribulose 5-phosphate is condensed with formaldehyde), while type II methanotrophs utilize a serine pathway (glycine is condensed with formaldehyde to initiate carbon assimilation). Type I methanotrophs possess only a particulate, membrane-bound form of MMO. In types II and X methanotrophs, either a particulate (pMMO) or a soluble (sMMO) form of the enzyme is expressed depending on growth conditions.[340,342,343] When the growth media contains a high concentration of copper and a low concentration of iron, the particulate form is exclusively expressed.[344,345] Less is known about pMMOs because of difficulties in purification of active enzyme.[346-351] However, there has been some recent progress towards the more detailed characterization of pMMO chemistry.[352-360] X-ray crystal structures of MMOH have been reported for both the *M. trichosporium* [113] and *M. capsulatus* enzymes.[361-363]

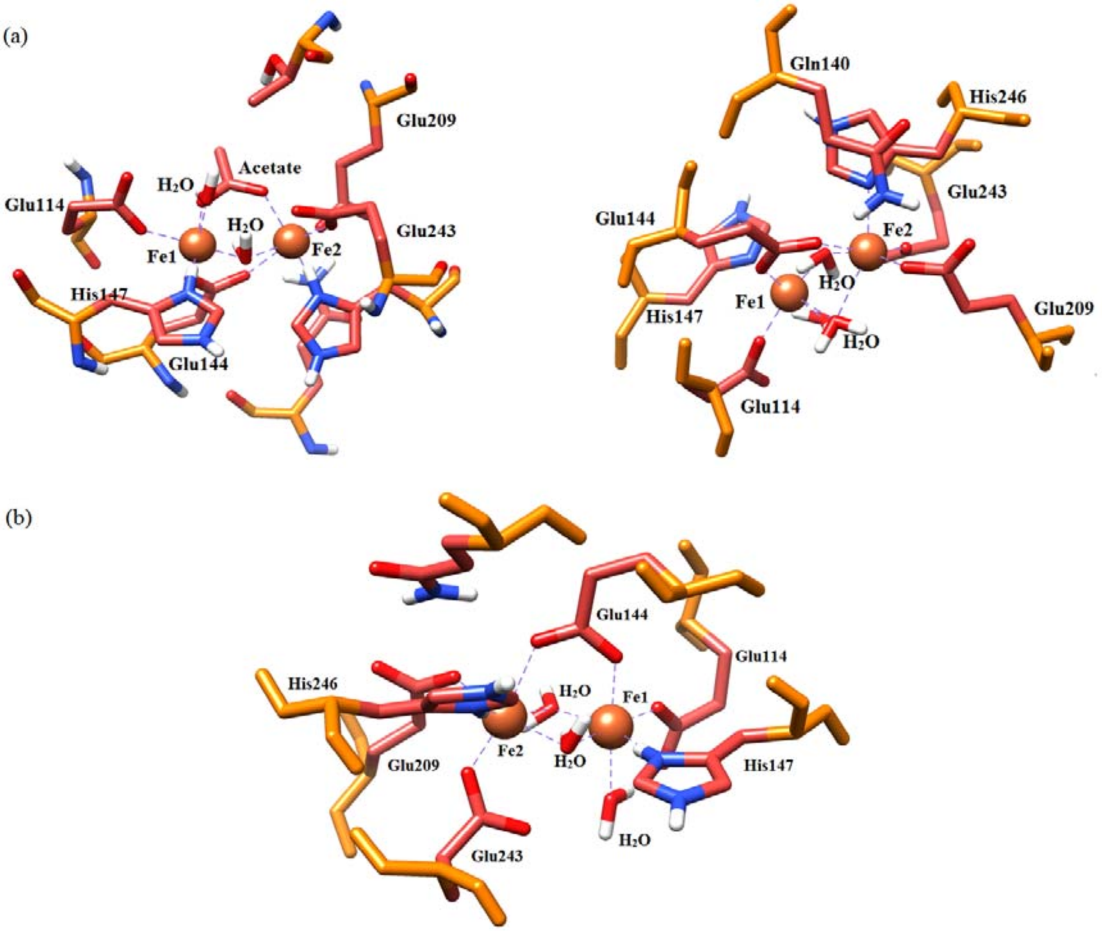

Figure 1.17: Representation of the crystallographically determined binuclear active sites of MMOH. (a) Diferric MMOH with (PDB: 1MTY, right) and without (PDB: 1MMO, left) acetate bound from *M. capsulatus*. (b) Diferric MMOH (PDB: 1MHY) from *M. trichosporium*.[362])

1.3.2.2.3: Ribonucleotide Reductase

The enzymatic reduction of ribonucleotides is catalyzed by ribonucleotide reductase (RR). It generates deoxyribonucleotides, that are essential for DNA synthesis.[364-366]

This involves reduction of the hydroxyl group on the 2'-carbon of the ribose moiety of nucleoside diphosphates and triphosphates.[367,368] There are at least four classes of RR.[368,369] Each class has its unique composition and cofactor requirement, but all contain a metal site and involve radical chemistry.[368-370] Class I has an $\alpha_2\beta_2$ quaternary structure.[371,372] Homodimers α_2 and β_2 are generally referred to as R1 and R2. Each R1 contains one substrate-binding site and two separate allosteric sites, and each R2 contains a binuclear non-heme iron active site with a stable tyrosyl radical essential for enzymatic reactivity.[364,371-376] Dioxygen is required in this class of RR to generate the binuclear active site and the radical. Hence it does not function under anaerobic conditions.[377-379] They are found in all eukaryotes and some microorganisms. RR from *E. coli* is characterized the most.[380] Class II RR has an α or α_2 homodimer structure. The radical required for reactivity is generated by adenosyl cobalamin.[381,382] This class of RR functions both aerobically and anaerobically. It is found in some microoganisms but not in higher organisms. The most characterized enzyme is from *Lactobacillus leichmannii*.[383] Class III RR is also found in *E. coli* and functions only anaerobically. [368,384-386] These class of enzymes are iron-sulfur proteins with a glycyl radical and have an $\alpha_2\beta_2$ quaternary structure. [387,388] Structures of R2 proteins in different oxidation states and from various sources have been determined by X-ray crystallography.[371,372,389-395]

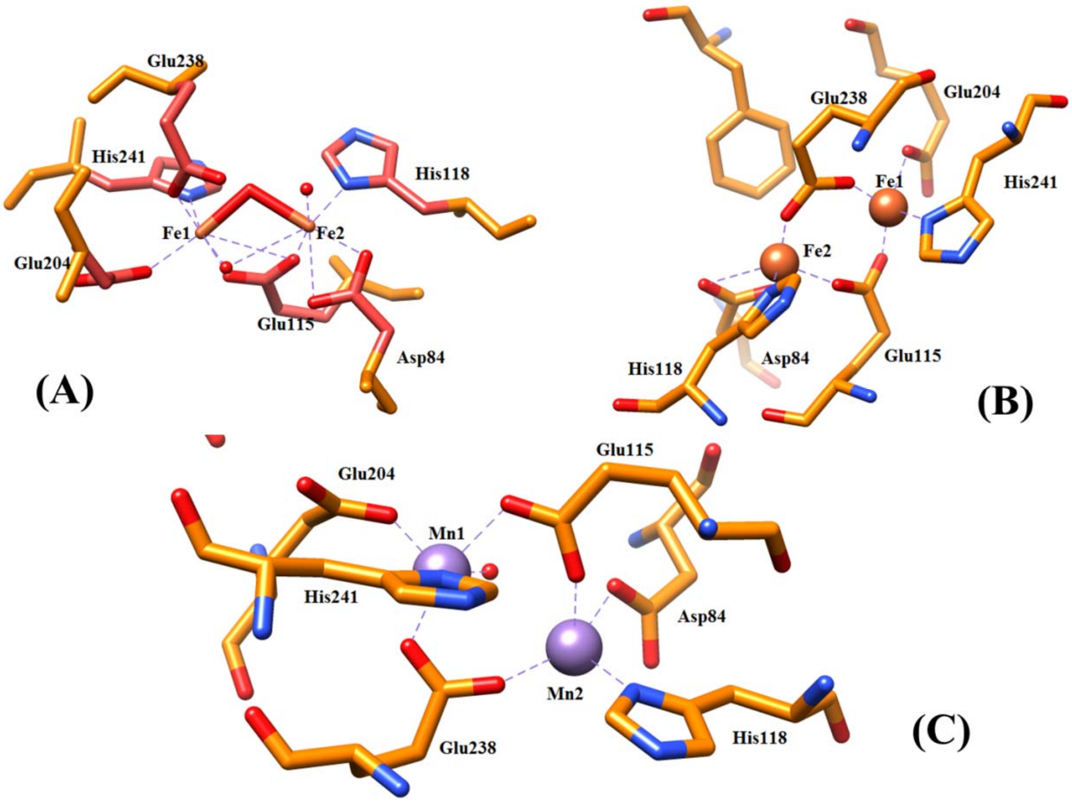

Figure 1.18: Representation of the crystallographically determined binuclear active sites of the R2 subunit of ribonucleotide reductase: (A) Binuclear oxidized [$Fe^{III}Fe^{III}$] active site from *E. coli* (PDB: 1RIB), (B) Binuclear reduced [Fe^{II}-Fe^{II}] active site from *E. coli* (PDB: 1XIK), and (C) Binuclear [Mn^{II}-Mn^{II}] active site from *E. coli* (PDB: 1MRR).

1.3.2.2.4: Δ^9 Desturase

The acyl-bound acyl carrier protein (acyl-ACP) desaturases activate dioxygen in a desaturation reaction involving the insertion of a cis (or Z) double bond. Desaturation is an essential step in fatty acid biosynthesis. In eukaryotes, desaturation is a post synthetic modification catalyzed by NADPH- and dioxygen-dependent binuclear non-heme iron enzymes. Both membrane bound and soluble enzymes have been identified, besides a large variety of isoforms varying in substrate specificity and regiospecificity.[396-398] The number and position of double bonds in fatty acids is known to have profound effects on their physical and, therefore, physiological properties.[399-402]

The three-dimensional structure of reduced Δ^9D from castor seeds has been determined by X-ray crystallography at a resolution of 2.4 Å (PDB ID 1AFR).[403]

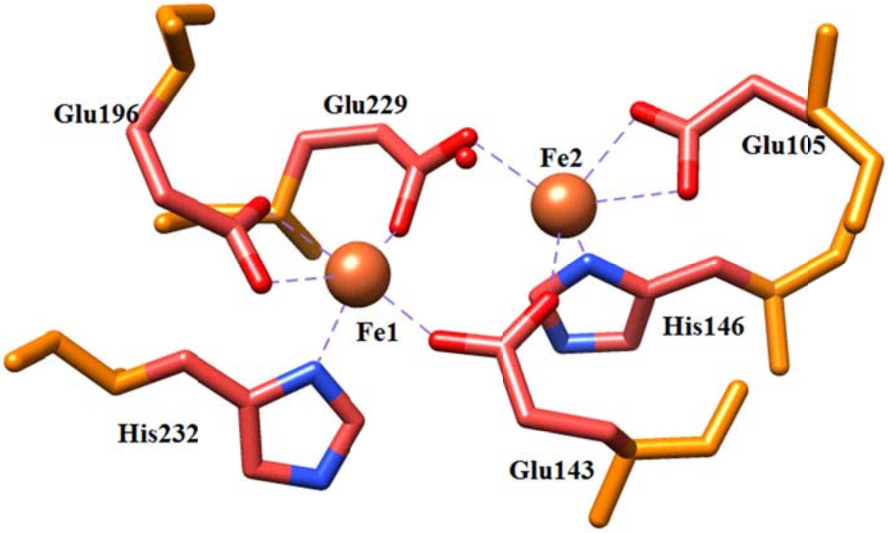

Figure 1.19: Representation of the crystallographically determined binuclear $Fe^{II}Fe^{II}$ active site of stearoyl-acyl carrier protein Δ^9 desaturase from caster seed (PDB:1AFR).

1.4: Computation of structure and properties of transition metal complexes

The computation of electronic structures of transition metal complexes has been developed in recent years to such an extent that with the help of ab initio and semi-empiricial quantum-chemical methods, a large variety of spectroscopic properties and reactivities of mono- and oligonuclear transition metal compounds can be computed efficiently and interpreted reliably. These computations are often based on known structural data. The electronic structures are usually interpreted by the comparison of computed and experimentally observed spectroscopic data and/or reactivities. This helps in proposing new models and refining existing theories that may lead to rules for improving relevant properties of a new class of compounds. Many a times, close collaboration of theoretically oriented chemists with experimentalists has culminated into novel types of compounds or novel mechanistic ideas, e.g. the discovery of the first molecular Fe^{VI} species,[404] the experimental characterization of HgF_4,[405] the prediction and observation of multi-state reactivity in iron-based oxygen activation,[406,407] the discovery of an elusive, biologically relevant $Cu\text{-}O_2$ complex,[408,409] the investigation of copper-oxygen intermediates, capable of hydroxylating areas [410] and the search for elusive high-spin $Fe^{IV}{=}O$ model system.[101,411-414]

An initial protein structure derived from crystallography, where possible, serves as starting point for calculations. Then geometry and self-consistent-field (SCF) optimizations are performed. The complete system is generally divided into the quantum cluster and the environment.[415-417] For the environment, dielectric and electrostatics approaches are employed. Either direct geometric constraints on the location of the active site cluster are imposed or force field derived approaches for steric constraints are implemented.

1.4.1: Correlation of molecular structure and properties

Structure correlation is a classical method for the thorough analysis and interpretation of molecular properties.[418] In transition metal coordination chemistry, the properties of a complex are largely determined by the type of donor atoms and their arrangement around a metal center, which may be tuned by structural modifications due to (a) the variation of substituents at the periphery of a ligand to modify solubility (used, e.g., for metal-ion-selective extractions;[419] note that hydrophobicity has also been proposed to change the properties of the metal center,[420] and charged peripheral substituents have been shown to influence the electronics of the metal center in a similar way as electrostatic fields in metalloproteins are tuning the electronics of the reactive center [421]); (b) the substitution at the ligand periphery to modify the ligand conformation and the complex stability;[422,423] and (c) the modulation of the shape of the active transition metal ion site to stabilize specific substrate-catalyst interactions and destabilize others (used, e.g., in the area of enantioselective catalysis [424] and for the stabilization of meta-stable intermediates in mechanistic biomimetic studies [425]). The role of the protein in enzymes in shaping the environment is another well-appreciated structural aspect of importance, and there are various examples of modeling these particular structural features.[426-428] In this section, the coordination geometry and its influence on the electronics of the coordination center is concentrated upon.

Classical methods for interpreting the properties of transition metal complexes are (a) the Hard and Soft Acids and Bases principle (HSAB): the types of donor atoms and metal centers are classified and rules for preferences in metal-donor combination have been derived,[429-432] and (b) ligand-field-theory-based approaches: one analyses the geometric arrangement of the donors around the metal center and uses to interpret spectroscopic and magnetic data [433] and also stabilites and reactivies,[434] e.g., using the empirical Irving-Williams series.[435-437] A demonstration of how various properties can be derived from the type and geometric arrangement of the donors around a metal ion, an example is given in Table 1.1 [438-440] and Fig. 1.20.[438] It is shown that donor set (N vs S) and the size of the macrocycles (13- to 16-membered) correlates with the redox potentials as well as electronic and EPR spectra of macrocyclic-ligand-copper(II) complexes.

Table 1.1: Electronic parameters and redox potentials of copper(II) complexes containing macrocyclic ligands with various donor sets (the $Me(NO_2)[n]aneN_4$ ligands are those shown in Fig. 1.20a.[438-440]

Compound	Electronic transition (cm^{-1})	EPR		$E_{½}$(V) vs NHE
		$g_{\parallel}$	$g_{\perp}$	
$[Cu\{Me(NO_2)[13]aneN_4\}]^{2+}$	18,020	2.18	2.05	-0.34
$[Cu\{Me(NO_2)[14]aneN_4\}]^{2+}$	20,830	2.19	2.05	-0.54
$[Cu\{[14]aneN_4\}]^{2+}$	19,610	2.19	2.05	-0.47
$[Cu\{Me(NO_2)[15]aneN_4\}]^{2+}$	18,180	2.21	2.06	-0.42
$[Cu\{Me(NO_2)[16]aneN_4\}]^{2+}$	17,240	2.21	2.06	-0.22
$[Cu\{Me(NO_2)[14]aneN_2\text{-cis}S_2\}]^{2+}$	18,730	2.16	2.038	-0.025
$[Cu\{[14]aneN_2\text{-cis}S_2\}]^{2+}$	18,760	2.145		+0.075
$[Cu\{[14]aneS_4\}]^{2+}$	17,540	2.10		+0.60
$[Cu\{Me(NO_2)[14]aneN_2\text{-cis}O_2\}]^{2+}$	17,300			-0.51

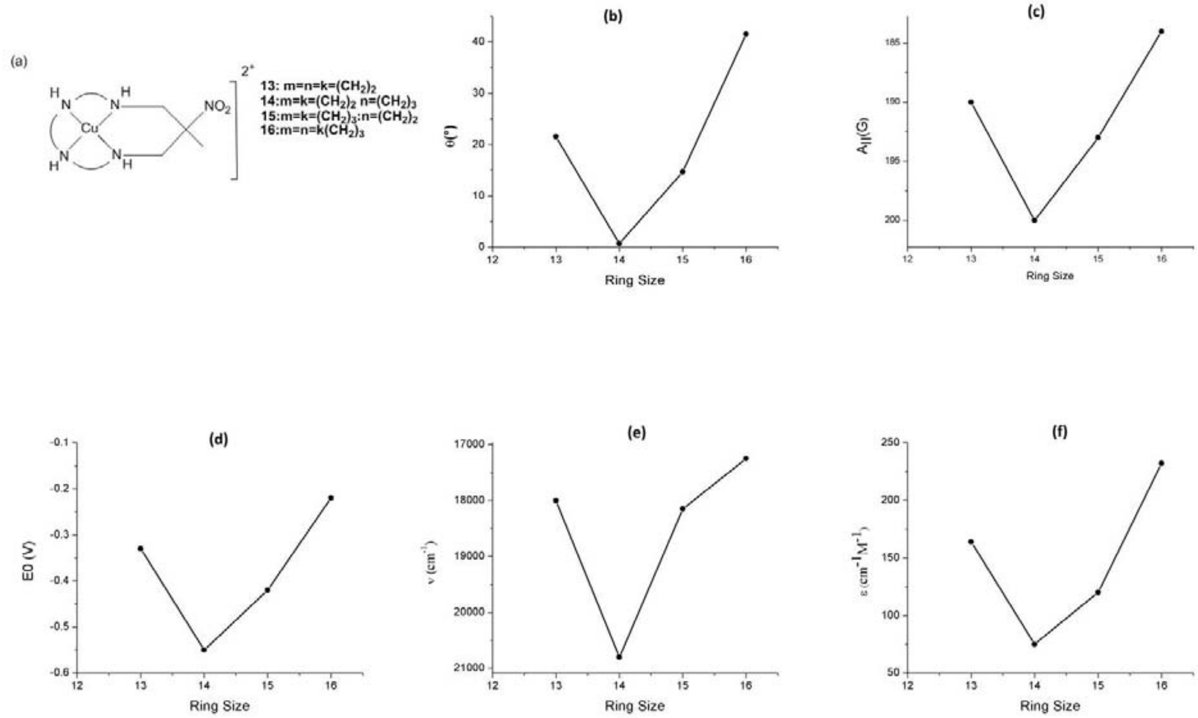

Figure 1.20: Correlations of spectroscopic and electrochemical data of a series of copper(II) compounds in (a), with tetrahedral twist (b), EPR parallel hyperfine coupling (c), redox potential (d), dd transition energy (e), dd transition intensity (f).[438]

The important observation is that the structure of these copper(II) complexes is enforced by the ligand (square pyramidal vs square planar vs. tetrahedral, described by the angle θ in Fig. 1.20b; the 14-membered macrocycle has the right size for square planar coordination to Cu^{II}, the 13-membered ring is too small and leads to a square pyramidal distortion, the 15- and 16- membered rings are too large and lead to tetrahedral distortions), and this define the redox and spectroscopic properties, i.e. there is a good linear correlation of θ with the various molecular properties (Fig. 1.20c-f).[441-444] These correlations might be accepted as a particularly well-behaved quantitative structure-property relationship (QSPR), others have been described in the area of metal-ion-selective extractions.[445-448] Empirical force field calculations (molecular mechanics, MM) were quite expectedly shown in most of these examples to be reliable predictive approach for the various QSPRs.

It is obvious that prediction and interpretation of properties is possible only by a detailed understanding and knowledge of how to influence molecular structures. In transition metal complexes, the metal-ligand distances and the ligand-metal-ligand angles are much more elastic than the organic backbone of the ligands. Due to this, the coordination geometries and, hence, the properties of the metal center may be enforced by a careful choice of ligands.[438, 449-451]

1.4.2: Computation of molecular properties

MM may be used to compute properties directly derived form steric effects and has proved to be an appropriate and efficient approach in relevant areas and is quite reliable and accurate. It also proves to be competitive and quite often the only approach which allows to fully separate steric from electronic effects.[452] Major contributions to complex stabilities and metal ion selectivities such as ligand preorganization and complementarity, derived from the shape and size of ligand cavities (host molecules) and their flexibility and elasticity, as well as the corresponding preferences of metal ions (the guest) have been successfully predicted.[450,453-455] Redox potentials have been shown to be related to complex stabilities (Fig. 1.20). For particular classes of metal complexes, it has been successful in computing redox properties with acceptable accuracies.[456-458] MM helps in optimizing transition states and, serves as an efficient way to optimize catalyst selectivities.[459] Conformational searches, based on MM and data mining, have been used to explain novel mechanistic details of metalloprotein-catalyzed reactions.[460,461]

Often quantum-mechanical methods (QM) compute bonding, spectroscopy and reaction pathways efficiently and reliably; approximate density functional theory (DFT) is generally used for mechanistic work, and time-dependent DFT (TD-DFT), spectra-oriented CI (SORCI) and ligand-filed-based DFT methods (LFDFT) are the methods appropriate for computing the spectroscopic parameters that were developed, validated and used during the last decade.[462-474]

Electronic structure calculations are typically used for interpreting experimental data. Therefore, when experimental structural data are available, the QM methods then used are single point calculations based on the data. The challenge arises when these are not available from experiments; it is obvious to demand the sources of accurate structural data. Obvious possibilities are structures optimized by MM or QM methods. One must however be careful regarding efficiency, reliability and accuracy of these methods. Where structure optimization is based on QM methods, the electronic properties may be refined with the help of a more expensive single point QM calculation, based on structure data obtained by a less costly QM model.[475] The basic disadvantage is that the structure may not be a minimum on the potential energy surface (wavefunction is slightly distorted) but the errors are small and generally reliable. It is generally believed that the approximations used in DFT lead to a situation where it is apt to use slightly different methods for structure optimization, the calculation of energetic properties and various electronic features. This methodology becomes handy particularly in the field of transition metal complexes.

1.4.3: Molecular structure optimization

Reliable structure prediction is required for the design of novel compounds possessing improved properties, in general and of transition metal complexes in particular. It is observed that empirical force-field-based methods (MM) are highly efficient, reliable and accurate if appropriate methods are employed for conformational analysis and structure optimization.[451,476-482] MM have undisputably higher efficiency with respect to electronic-structure-based methods. The QM structure optimization fails to be competitive enough for more than average sized molecules for molecular design purposes with current hardware and software capabilities. Also, the reliability of an optimized structure is related to the global energy minimum structure on a warped potential energy surface or to a set of structures with similar energy. This necessitates a conformational search to define the relevant structure,[477,483] which proves to be computationally expensive with QM methods. In terms of accuracy, it is believed that MM calculations may be equivalent or even superior to QM structure optimizations, provided a well-tuned force field is used.[451,477,484-487] This proves to be the major drawback of MM as parameter sets for specific problems are missing, additionally the parameterization procedure is tedious if published force fields are not available,[488] although different force-field fitting schemes have been described.[489-501]

Generally, in QM studies, accuracy of the optimized structures is not the point of contention. However when accurate structural data are required, the tuning of the model used (functional and basis set) may also be difficult,[502-504] and a thorough comparison of experimental with computed data based on MM on one hand and DFT on the other quite often indicates that the former are of superior quality.[458,476,505] The quality of both MM and DFT calculations depend on the method used (force field, functions and parameterization; functional and basis set), this is obvious from the fact that both are empirical and semi-empirical methods, respectively.

Transition metal complexes have long proved notorious that applied methods could not probe their properties correctly because of (a) the multifarious coordination numbers and geometries, resulting into difficulties in defining the coordination angles and functional forms to describe them,[449,451,484] (b) the many possible oxidation states and corresponding electronic structures,[451,484,485,506,507] and (c) the electronic influence exerted by the partially filled d-shell.[493,508-514] Thus theoretical methods may require some adaptation for efficient, reliable and accurate methods for prediction of structures of specific type of transition metal complexes

1.5: C–H bond activation in transition metal species

Homogeneous catalysis mediated by transition metal complexes acts as one of the most efficient ways to achieve high activity as well as control of the selectivity in C–H activation. Different situations may occur depending on the nature of the metal M and ligand set L_n in the active L_nM species. Thus the C–H activation processes are classified into four main different mechanisms, extensively studied and reviewed by David *et al.*[522]

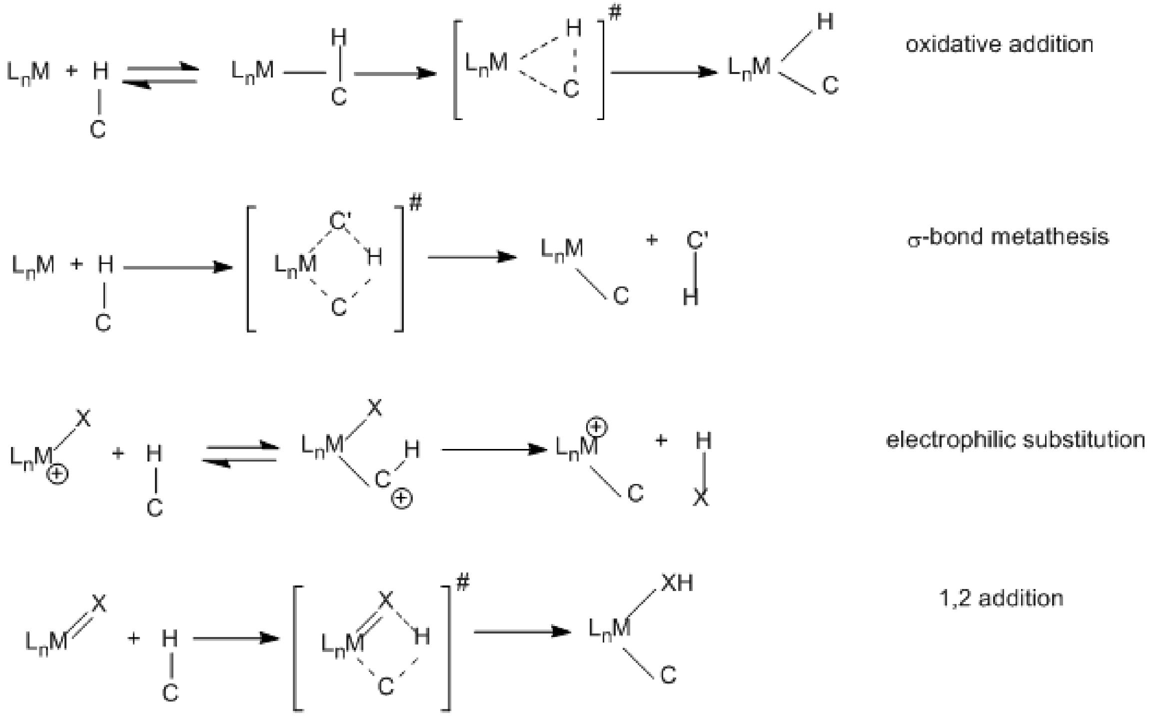

Figure 1.21: Schematic representation of the different mechanisms for C–H activation.

Oxidative addition is typically common in electron-rich, low-valent complexes of the late transition metals (Re, Fe, Ru, Os, Ir, Pt) for which the higher oxidation state of the metal in the product and the necessary change in geometry upon formation of the two new bonds are not energetically penalizing. Oxidative process is not possible for early transition metals (groups 3 and 4, lanthanides and actinides) with d^0 electronic configuration. The preferred mechanism is σ-bond metathesis which usually involves an alkyl or a hydride complex. In σ-bond metathesis mechanism, there is essentially the concerted formation (M–C and C′–H) and breaking (M–C′ and C–H) of bonds at the transition state. A reactivity formally equivalent to σ-bond metathesis is observed for late- or post-transition metals (Pd^{2+}, Pt^{2+} or Pt^{4+}, Hg^{2+}), usually in a strongly polar medium. The electrophilic attack of the metal forms the putative intermediate. In the product, the hydrogen atom of the substrate is seen to be formally substituted by the metal center acting only as a Lewis acid, due to this it is classified as electrophilic substitution. Finally, the C–H bond can add across an unsaturated M–X bond in a 1,2 addition (Figure 1.21). This mechanism is similar to σ-bond metathesis but differs in fact that the newly formed X-H bond does not lead to release of X–H because of the presence of the M–X σ-bond in the product. The functional groups X leading to such reactivity are generally amido and alkylidene complexes of early to middle transition metals, but C–H bonds have also been shown to be activated by alkoxy and alkylidyne complexes.

In homogeneous catalysis, computational studies of the structure and reactivity of organometallic complexes serves as an essential tool.[515–519] Density functional theory (DFT) has been proved and established to be a reliable method of studying organometallic activity by various comparative studies.[520,521] Since the seminal review by Niu and Hall,[516] the majority of the computational studies have employed DFT methods in general and the hybrid B3LYP approach in particular. With rise in computing power, systems could now be modelled closer to the actual experimental situation thus allowing access to information difficult to obtain directly from experiment. One key piece of information obtained in such studies of reaction mechanisms is the characterization of the transition state (TS) on the potential energy surface (PES), which is not accessible in other methods. The energy barrier (ΔE or ΔH) or the activation barrier (ΔG) can be evaluated from the energy of transition state, which may be compared with experimental values from kinetic studies, if (or when) available.[522] The electronic structure of the TS allows a more detailed characterization of the mechanism of the reaction in terms of bonds that are broken and made during the process. The reactants and products connected by a given TS can be easily obtained from calculations, thus the thermodynamics of the reaction may be well understood. Generally intermediates are short lived and unobservable, so calculations help locate intermediates and suggest modifications to the experimental systems to favor or disfavor the intermediate enabling the discovery of new pathways for C–H activation. Thus one can improve activity and selectivity by proposing modifications of the catalyst and experimental conditions. However computing energy profile for the entire catalytic cycle is a tough task, which if accomplished, may lead to understanding of the relative activation barriers for the individual steps and rate-determining step for transformation of interest. It should however be noted that C–H bond is inert in nature and one of the most difficult transformation. Hence emphasis is often put on the C–H bond-breaking step.

1.5.1: Mechanisms of C–H Bond Activation

The breaking of a σ(C–H) bond in the coordination sphere of a transition metal complex occurs due to the weakening and cleavage of σ(C–H) bond and is attributed to two synergic transfers of electron density: σ-donation from the bonding σ(C–H) molecular orbital (MO) into a symmetry adapted vacant orbital on L_nM and π-back donation from an occupied d_π MO on L_nM into the antibonding σ*(C–H) MO. However, a vacant site is required to be created on the metal to allow coordination of the σ bond. The observation of a σ-complex is experimentally challenging because the interaction between the metal and the C–H bond is usually weak.[523–527] Computationally, such intermediates often occur prior to the C–H cleavage step. The back donation from the metal is usually effective from a non-bonding dπ MO on L_nM, but in principle, any high-lying occupied MO could be involved in electron transfer into σ*(C–H) if symmetry allows. The actual nature and magnitude of the σ-donation from σ(C–H) and π-back donation into σ*(C–H) determines the various mechanisms for C–H activation.

(a) Oxidative Addition

The oxidative addition mechanism is mainly characterized by the concerted breaking of C–H and formation of M–C and M–H in the TS, the formal increase by 2 units of the oxidation state of the metal, and the change of geometry of the complex to accommodate the two new σ bonds. Efficient C–H activation through the oxidative addition mechanism depends on the electronic configuration of the metal in the fragment L_nM.

(b) σ-Bond Metathesis

The σ-bond metathesis is a one-step reaction wherein two σ bonds are broken and two new σ bonds are formed in a concerted manner without any change of the metal oxidation state (Figure 1.22a). A review describes the current understanding for this reaction.[528] This mechanism has been proposed for early and late transition metal complexes. However, in the case of the late transition metal complexes exhibiting multi-oxidation states, the transformation can be formally achieved either by σ-bond metathesis or by successive oxidative addition and reductive elimination (Figure 1.22b). Preference for either of these mechanisms has been the topic of a number of theoretical studies.

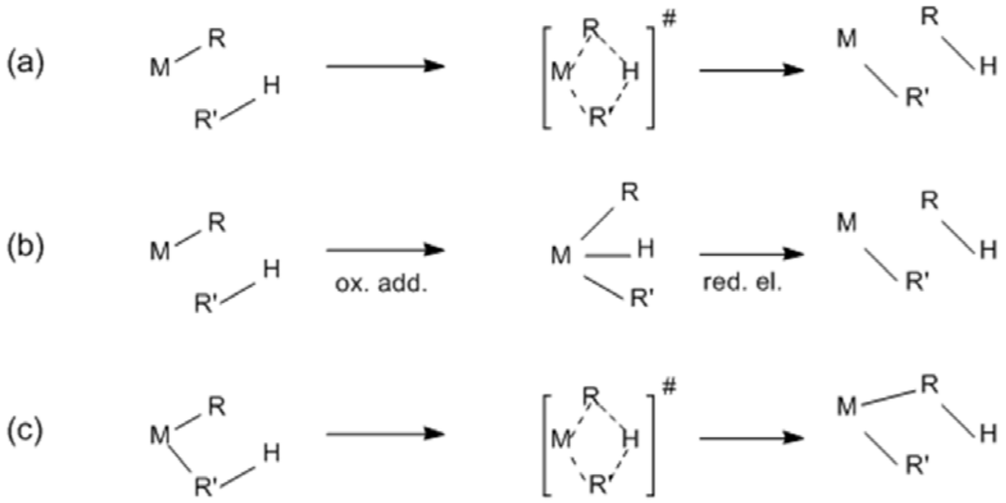

Figure 1.22: Various mechanisms for formal σ-bond metathesis.

(c) Electrophilic Substitution

This pathway for C–H activation is closely related to the σ-bond metathesis pathway. Here, coordination of the alkane C−H bond at an electrophilic metal center leads to a C−H bond weakening that facilitates the following loss of a proton and generates the M−CH_3 species. An external base or solvent or a sufficiently basic group in the coordination sphere of the metal may act as the proton acceptor. It is anticipated that soft electrophiles with low-lying, polarizable LUMOs should be most effective for this mode of C−H activation.[529]

(d) 1,2 Addition

If an early transition metal is coordinated to a ligand with π-bonding capability (alkylidene, alkylidyne, amide, imide, alkoxide, aryloxide), π-donation from the ligand stabilizes the unsaturation at the metal center. The M=X functionality (X= CR_2, CR, NR_2, NR, OR) adds to a C–H bond in a $[2_\sigma + 2_\pi]$-type reaction (Figure 1.23). The 1,2-addition product M(XH)(R) could lead to a hetero-functionalized hydrocarbon upon reductive elimination. If the regeneration of the M=X group could be made catalytic, this would constitute a major advance. The net 1,2-addition of a C–H bond across a metal-oxygen or metal-nitrogen bond is a key step in this catalytic cycle. Similar to oxidative addition, vacant site on the metal should be created for the C–H bond to coordinate and engage in an interaction with M=X.

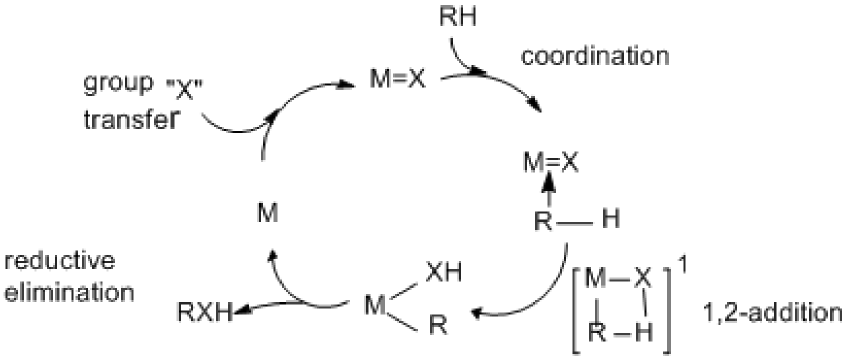

Figure 1.23: Hypothetical catalytic cycle for hydrocarbon heterofunctionalization through C–H 1,2-addition across M=X.

1.5.2: Substrate-activation by dehydrogenation in homogeneous transition metal catalysis

The substrate has been reported to be activated by catalytic dehydrogenative oxidation. A bond construction step follows this activation. These steps proceed under 'one-pot' conditions generally with a single catalyst or at most two catalysts acting together. In alkane substrate, alkanes are dehydrogenated to alkenes, which react further to give final products. In alcohol case, alcohol dehydrogenation leads to aldehydes or ketones that react further with nucleophiles. Besides these two best established reactants, amines also figure in dehydrogenative activation reactions, although to a lesser extent. Here, reactive imines are generated as intermediates.

A number of characteristics are common to these reactions. In each case a less reactive species, such as an alkane or alcohol, is converted to a more reactive one, an alkene or organic carbonyl compound, that then reacts further in a tandem ‘one-pot’ procedure. Tansition metal complexes catalyze the first step wherein a C–H bond is cleaved; next steps may or may not be catalyzed. The green chemistry has emerged and drawn attention to bond construction strategies that promote atom economy and avoid mutagenic reagents.[530] This is termed green in sense that atom economy is very high (minimize waste formation) and helps avoid the need to introduce activating groups (bromide or tosylate) by using unfunctionalized alkanes and alcohols.

These types of reactions can best be illustrated by taking examples of alkane metathesis and amine alkylation (Figure 1.24), where ‘cata’ refers to the dehydrogenation/ hydrogenation catalyst. While the initial dehydrogenation is endoergic, particularly for alkane dehydrogenation, third step is necessarily as exoergic approximately as the first step is endoergic but with the opposite sign. Thus third step may help drive the first step and the resulting arrangement has a great thermodynamic advantage.

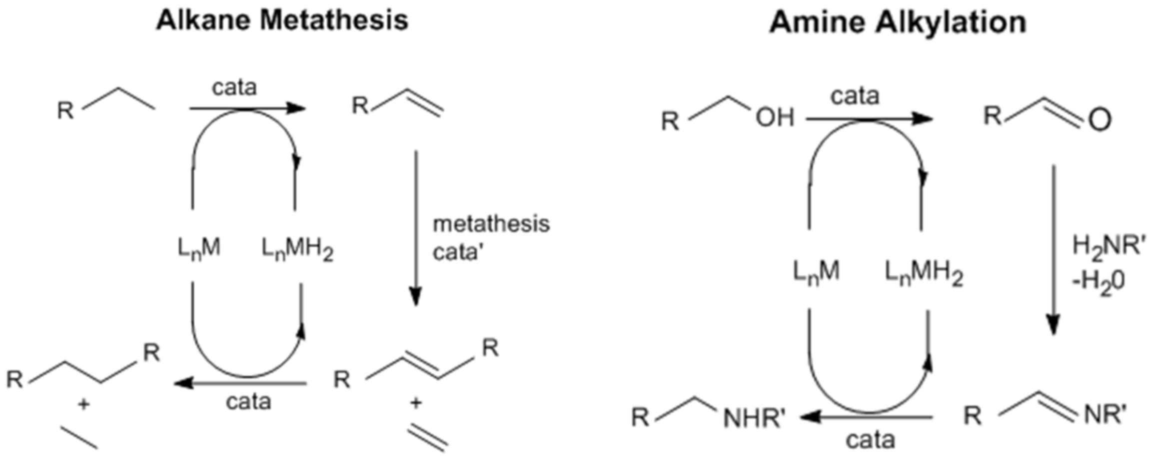

Figure 1.24: Representative reactions featuring Dehydrogenative activation.

1.6: High valent Non-heme Iron-oxo Complexes

In a superfamily of enzymes, mononuclear non-heme iron centers carry out vital metabolic processes by activating O_2 (oxidative transformations) [3,186] and are known to catalyze substrate oxidations, including hydroxylation, halogenation, desaturation, epoxidation and cis-dihydroxylation. Electron donors for O_2 activation include the commonly used reductant NADH, α-ketoglutarate (α-KG),[4] tetrahydrobiopterin, [250,531] and ascorbate.[532,533] In isopenicillin N synthase (IPNS), the substrate is reported to undergo 4-e^- oxidation, thus providing all necessary electrons required for O_2 activation.[534–536] An $Fe^{IV}=O$ species is the oxidant most commonly postulated for these enzymes, while a cis-HO-$Fe^{V}=O$ oxidant is proposed for the Rieske dioxygenases which catalyze cis-dihydroxylation of arene double bonds.[186,537,538] However no experimental evidence was reported for the putative $Fe^{IV}=O$ oxidizing intermediate in this enzyme superfamily until 2003.[87,411,539]

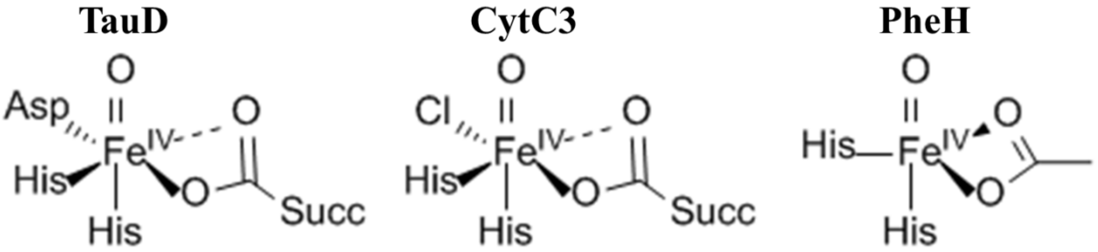

Figure 1.25: Proposed structures for $Fe^{IV}=O$ intermediates for TauD, CytC3, and PheH.

The non-heme iron enzymes were found to catalyze substrate oxidations similar to those by heme enzymes. This encouraged chemists to investigate the use of synthetic non-heme iron complexes as oxidation catalysts. Thus began the search for evidence for high-valent Fe=O species in these oxidations. Costas *et al.* have seminally reviewed the extensive work carried out prior to 2000.[540] Ascertaining the involvement of a metal-based oxidant rather than metal-free oxy radical species proved to be considerable challenge for long.[540] It was overcome in 1997 with a discovery that $[Fe^{II}(TPA)(NCCH_3)_2]^{2+}$ catalyzed stereospecific alkane hydroxylation with H_2O_2.[541] With cis-1,2-dimethylcyclohexane as substrate, the tertiary alcohol product showed complete retention of configuration, thereby establishing absence of an oxy radical as oxidant. Subsequently, this system was established as catalyst in epoxidation and cis-dihydroxylation of olefin substrates with high stereoselectivity.[542]

Borovik's report in 2000 of an unprecedented oxoiron(III) complex, $[Fe^{III}(O)(H_3buea)]^{2-}$ proved to be a milestone in synthetic efforts to make high-valent non-heme Fe=O complexes.[543] This breakthrough initiated intense investigations into non-heme Fe=O chemistry with many excellent reports detailing their generation and the characterization of their structural, electronic, and spectroscopic features.[14,101,103,104]

1.6.1: Synthesis

The first direct evidence for the generation of a non-heme Fe^{IV}=O complex was reported by Wieghardt.[544] A green chromophore was yielded by reaction of $[Fe^{III}(cyclam-CH_2CO_2)(OTf)]PF_6$ with ozone (O_3) at −80°C in acetone/H_2O. This was assigned to an S=1 Fe^{IV} species by Mössbauer spectroscopy. However the yield was very low. Although one could not obtain any evidence for an Fe^{IV}=O moiety, the green chromophore was postulated to be $[Fe^{IV}(O)(cyclam-CH_2CO_2)]^{+}$, its assignment as an Fe^{IV}=O complex was proven to be correct by favorable comparison of its characteristic NIR absorption band and the Mössbauer parameters with those of better characterized Fe^{IV}=O complexes subsequently prepared. Another breakthrough in non-heme Fe^{IV}=O chemistry came with the high-yield synthesis of $[Fe^{IV}(O)(TMC)(NCCH_3)]^{2+}$ and the solution of its crystal structure in 2003 and its thorough characterization of an Fe^{IV}=O species for the first time. $[Fe^{IV}(O)(TMC)(NCCH_3)]^{2+}$ was generated by the reaction between $[Fe^{II}(TMC)(OTf)_2]$ and iodosylbenzene (PhIO) in CH_3CN at −40°C. More than 90% yield of Fe^{IV}=O complex was reported.[109] The half life of $[Fe^{IV}(O)(TMC)(NCCH_3)]^{2+}$ was 10 h at 25°C and persisted for at least a month at −40°C, this facilitated its crystallization.[109] It represents the first crystallographically characterized synthetic complex with an Fe^{IV}=O unit. de Visser *et al.* have presented a seminal review on intrinsic properties and reactivities of Fe=O complexes bearing the TMC ligand.[78]

Bakac and co-workers characterized a synthetic S = 2 Fe^{IV}=O complex for the first time, and did it without a supporting polydentate ligand.[545] The reaction between aqueous $[Fe^{II}(H_2O)_6]^{2+}$ at pH 1.0 and O_3 yielded $[Fe^{IV}(O)(H_2O)_5]^{2+}$ in 50% efficiency, with a mononuclear Fe^{III} by-product. Its S = 2 spin state was established by high-field Mössbauer analysis, its Fe^{IV} oxidation state was further corroborated by the X-ray absorption which was reported to be 1–2 eV higher than observed for other synthetic Fe^{IV}=O complexes. In Fe^{IV}=O, though both S=1 and S=2 are d^4 systems, their electronic configuration is $(xy)^2(xz,yz)^2$ and $(xy)^1(xz/yz)^2(x^2\text{-}y^2)^1$ respectively.

1.7: Corrole derivatives

Corrole is fully aromatic analogue of the corrin ligand found in B_{12} cofactors. It was first synthesized by Hohnson and Kay via photocyclization of an a,c-biladiene,[546] which was itself the end product of a many-step synthesis. Multiple stable, formal Fe(IV) derivatives of octaethylcorrole were reported by Vogel and co-workers.[547] Will *et al.*

reported formal Ni(III) and Cu(III) corroles soon thereafter.[548] A number of synthetic routes have since been reported for synthesis.

The coordination chemistry of corroles is quite extensive and quite different from that of porphyrins.[549] Latter generally behave as dianionic ligands but free-base corroles are triprotic acids and coordinate as formally trianionic ligands.[550] As contracted porphyrins, they provide tight, sterically constrained environments for coordinated atoms.

Even as late as the year 2000, only few people, besides a handful of well-informed porphyrin specialists, had heard of corrole. Now its chemistry has grown explosively due to dedicated efforts of many. Corroles are important because of strong fluorescence of their lighter main-group element complexes, ubiquitous ligand non-innocence among first-row transition-metal corroles (Mn, Fe, Co, Cu etc.). It exhibits remarkable efficacy as group transfer catalyst. Although huge theoretical investigation has been reported for corroles, this area offers immense potential for research.

1.8: Importance of metal complexes

Metals have been used in treatment purposes since ancient times. As positive charge of metals readily interacts with proteins, some metal containing drugs are being developed which interact with active sites in metalloproteins to get desired reaction pathways for disease control.[551] Living organisms have evolved CYP 450 that serves in catalysis of specific chemical processes of drug metabolism.

Environment is infected with pollutants originating form industrial activities (mining, industry effluents, chemical weapons production etc.), anthropogenic activities (agriculture, traffic etc.), scientific activities (chemical, nuclear or other experiments) etc. which affect living forms (animals or plants alike) in various ways. The quality of life is linked directly to quality of environment. Besides incineration or chemical decomposition, bioremediation is important arena of research. It refers to microorganism mediated transformation of contaminants wherein pollutants are attacked enzymatically to convert them into innocuous products. Various metalloenzymes like methane monooxygenases (hydrolysis of methane), peroxidases (degradation of phenols, chlorophenols etc.), catechol dioxygenases (chlorophenol oxidation), aromatic hydrocarbon dioxygenases (oxidation) etc. have great potential in controlling pollutants. Also understanding their mechanism serves in search of environmentally benign procedures for synthesizing useful chemicals (green chemistry- atom economic reactions minimize waste formation).

Chemical warfare agents (CWAs) are a serious threat to living world. While usually prepared on mass scale during war (mustard gas, cyanide gas, sarin etc.), Nations are left with huge stocks posing severe threat to life during times of peace worldwide. Agents capable of detoxification of CWAs must be reactive to them and produce non-toxic (or less toxic) byproducts. Decontamination proceeds in multiple pathways, mostly by hydrolysis [552] and oxidation.[553] Water and Oxygen are ubiquitious in atomosphere and serve as excellent reactant/oxidant. While enzymes have come to rescue in eliminating these weapons of mass destruction (for instance, cyanidase hydrolyses cyanide gas to formate and ammonia), a comprehensive study in this area is the need of the hour. Terrorists may get a hand on these lethal weapons which may prove disastrous.

References:

1 J. J. R. F. D. Silva, R. J. P. Williams, *The Biological Chemistry of the Elements*, Clarendon Press, Oxford (1991).

2 E. I. Solomon, T. C. Brunold, M. I. Davis, J. N. Kemsley, S.-K. Lee, N. Lehnert, F. Neese, A. J. Skulan, Y.-S. Yang, J. Zhou, *Chem. Rev.*, **100**, 235 (2000).

3 M. Costas, M. P. Mehn, M. P. Jensen, L. Que Jr., *Chem. Rev.*, **104**, 939 (2004).

4 R. P. Hausinger, *Crit. Rev. Biochem. Mol. Biol.*, **39**, 21 (2004).

5 E. G. Kovaleva, J. D. Lipscomb, *Nat. Chem. Biol.*, **4**, 186 (2008).

6 C. Loenarz, C. J. Schofield, *Nat. Chem. Biol.*, **4**, 152 (2008).

7 H. Arakawa, M. Aresta, J. N. Armor, M. A. Barteau, E. J. Beckman, A. T. Bell, J. E. Bercaw, C. Creutz,E. Dinjus, D. A. Dixon, K. Domen, D. L. DuBois, J. Eckert, E. Fujita,D. H. Gibson,W. A. Goddard,D. W. Goodman, J. Keller, G. J. Kubas,H. H. Kung, J. E. Lyons,L. E. Manzer,T. J. Marks, K. Morokuma, K. M. Nicholas, R. Periana, L. Que, J. Rostrup-Nielson,W. M. Sachtler, L. D. Schmidt,A. Sen,G. A. Somorjai, P. C. Stair, B. R. Stults, W.Tumas, *Chem. Rev.*, **101**, 953 (2001).

8 A. E. Shilov,G. B. Shul, G. B. Shul'pin, *Chem. Rev.*, **97**, 2879, (1997).

9 B. L. Conley, W. J. Tenn, K. J. H. Young, S. Ganesh, S. Meier,V. Ziatdinov, O. Mironov, J. Oxgaard, J. Gonzales, W. A. Goddard, R. A. Periana, in *Activation of Small Molecules: Organometallic and Bioinorganic Perspectives*; W. B. Tolman (Ed.), Wiley-VCH: Weinheim, Germany, pp 235 (2006).

10 W. Nam, *Acc. Chem. Res.*, **40**, 465 (2007).

11 J. M. Bollinger Jr., C. Krebs, *Curr. Opin. Chem. Biol.*, **11**, 151 (2007).

12 M. Rolff, F. Tuczek, *Angew. Chem. Int. Ed.*, **47**, 2344 (2008).

13 E. I. Solomon, J. W. Ginsbach, D. E. Heppner, M. T. Kieber-Emmons, C. H. Kjaergaard, P. J. Smeets, L. Tian, J. S. Woertink, *Faraday Discuss.*, **148**, 11 (2011).

14 J. Hohenberger, K. Ray, K. Meyer, *Nat. Commun.*, **3**, 720 (2012).

15 P. C. A. Bruijnincx, G. van Koten, R. J. M. Klein Gebbink, *Chem. Soc. Rev.*, **37**, 2716 (2008).

16 C. E. Tinberg, S. J. Lippard, *Acc. Chem. Res.*, **44**, 280 (2011).

17 F.-H. Li, G.-H. Zhao, H.-X. Wu, H. Lin, X.-X. Wu, S.-R. Zhu, H.-K. Lin, *J. Inorg. Biochem.*, **100**, 36 (2006).

18 C. Jung, *Biochim. Biophys. Acta*, **1814**, 46 (2011).

19 C. Krebs, J. C. Price, J. Baldwin, L. Saleh, M. T. Green, J. M. Bollinger Jr., *Inorg. Chem.*, **44**, 742 (2005).

20 S. Shaik, S. Cohen, Y. Wang, H. Chen, D. Kumar, W. Thiel, *Chem. Rev.*, **110**, 949 (2010).

21 E. I. Solomon, S. D. Wong, L. V. Liu, A. Decker, M. S. Chow, *Curr. Opin. Chem. Biol.*, **13**, 99 (2009).

22 E. I. Solomon, D. E. Heppner, E. M. Johnston, J. W. Ginsbach, J. Cirera, M. Qayyum, M. T. Kieber-Emmons, C. H. Kjaergaard, R. G. Hadt, L. Tian, *Chem. Rev.*, **114**, 3659 (2014).

23 T. L. Poulos, *Chem. Rev.*, **114**, 3919 (2014).

24 Z. Halime, K. D. Karlin, in Copper-Oxygen Chemistry; K. D. Karlin, S.Itoh (Eds.), *Wiley Series of Reactive Intermediates in Chemistry and Biology*, John Wiley & Sons: New York, pp 283 (2011).

25 S.J. Lippard, J.M. Berg, *Principles of Bioinorganic Chemistry*, University Science Books, Mill Valley, CA, (1994).

26 M. Sono, M. P. Roach, E. D. Coulter, J. H. Dawson, *Chem. Rev.*, **96**, 2841 (1996).

27 J. T. Groves, *Proc. Natl. Acad. Sci.* U. S. A., **100**, 3569 (2003).

28 P. R. Ortiz de Montellano (Ed.), *Cytochrome P450: Structure, Mechanism and Biochemistry*, 3rd edition, Kluwer Academic/Plenum Publishers, NY, (2004).

29 B. Meunier, S. P. de Visser, S. Shaik, *Chem. Rev.*, **104**, 3947 (2004).

30 A. W. Munro, H. M. Girvan, K. J. McLean, *Nat. Prod. Rep.*, **24**, 585 (2007) .

31 K. M. Kadish, K. M. Smith, R. Guilard (Eds.), *Handbook of Porphyrin Science*, World Scientific Publishing Co., New Jersey, (2010).

32 P. R. Ortiz de Montellano, *Chem. Rev.*, **104**, 932 (2010).

33 S. P. de Visser, D. Kumar (Eds.), *Iron-containing enzymes: Versatile catalysts of hydroxylation reaction in nature*, RSC Publishing, Cambridge (UK), (2011).

34 T. D. H. Bugg, *Curr. Opin. Chem. Biol.*, **5**, 550 (2001).

35 M. J. Ryle, R. P.Hausinger, *Curr. Opin. Chem. Biol.*, **6**, 193 (2002).

36 S. V. Kryatov, E. V.Rybak-Akimova, S. Schindler, *Chem. Rev.*, **105**, 2175 (2005).

37 M. M. Abu-Omar, A. Loaiza, N. Hontzeas, *Chem. Rev.*, **105**, 2227 (2005).

38 A. R. McDonald, L. Que Jr., *Coord. Chem. Rev.*, **257**, 414 (2013).

39 D. Buongiorno, G. D. Straganz, *Coord. Chem. Rev.*, **257**, 541 (2013).

40 S. Al-Attar, S. de Vries, *Coord. Chem. Rev.*, **257**, 64 (2013).

41 L. Quintanar, L. Rivillas-Acevedo, R. Grande-Aztatzi, C. Z. Gómez-Castro, T. Arcos-López, A. Vela, *Coord. Chem. Rev.*, **257**, 42 (2013).

42 S. Fukuzumi, K. D. Karlin, *Coord. Chem. Rev.*, **257**, 187 (2013).

43 L. Rulíšek, U. Ryde, *Coord. Chem. Rev.*, **257**, 445 (2013).

44 V. Conte, A. Coletti, B. Floris, G. Licini, C. Zonta, *Coord. Chem. Rev.*, **255**, 2165 (2011).

45 G. Licini, V. Conte, A. Coletti, M. Mba, C. Zonta, *Coord. Chem. Rev.*, **255**, 2345 (2011).

46 P. J. Gonzalez, M. G. Rivas, C. S. Mota, C. D. Brondino, I. Moura, J. J. G. Moura, *Coord. Chem. Rev.*, **257**, 315 (2013).

47 H. Broda, S. Hinrichsen, F. Tuczek, *Coord. Chem. Rev.*, **257**, 587 (2013).

48 A. B. Tomter, G. Zoppellaro, N. H. Andersen, H.-P. Hersleth, M. Hammerstad, Å. K. Røhr, G. K. Sandvik, K. R. Strand, G. E. Nilsson, C. B. Bell III, A.-L. Barra, E. Blasco, L. Le Pape, E. I. Solomon, K. K. Andersson, *Coord. Chem. Rev.*, **257**, 3 (2013).

49 P. Nordlund, P. Reichard, *Annu. Rev. Biochem.*, **75**, 681 (2006).

50 J. Herrick, B. Sclavi, *Mol. Microbiol.*, **63**, 22 (2007).

51 N. Nelson, C. F. Yokum, *Annu. Rev. Biochem.*, **57**, 521 (2006).

52 C. W. Cady, R. H. Crabtree, G. W. Brudvig, *Coord. Chem. Rev.*, **252**, 444 (2008).

53 D. J. Vinyard, G. M. Ananyev, G. C. Dismukes, *Annu. Rev. Biochem.*, **82**, 577 (2013).

54 P. E.M. Siegbahn, *Chem.–Eur. J.*, **14**, 8290 (2008).

55 N. M. DeVore, E. E. Scott, *J. Biol. Chem.*, **287**, 26576 (2012).

56 J. R. O'Brien, D. J. Schuller, V. S. Yang, B. D. Dillard, W. N. Lanzilotta, *Biochemistry*, **42**, 5547 (2003).

57 J. H. Dawson, R. H. Holm, J. R. Trudell, G. Barth, R. E. Linder, E. Bunnenberg, C. Djerassi, S. C. Tang, *J. Am. Chem. Soc.*, **98**, 3707 (1976).

58 P. R. Ortiz de Montellano, *Annu. Rev. Pharmacol. Toxicol.*, **32**, 89 (1992).

59 M. Hofrichter, *Enzyme Microb. Technol.*, **30**, 454 (2002).

60 E. L. Raven, *Nat. Prod. Rep.*, **20**, 367 (2003).

61 T. L. Poulos, *Arch. Biochem. Biophys.*, **500**, 3 (2010).

62 F. Hollmann, I. W. C. E. Arends, K. Buehler, A. Schallmey, B. Bühler, *Green Chem.*, **13**, 226 (2011).

63 P. Nicholls, I. Fita, P. C. Loewen, *Adv. Inorg. Chem.*, **51**, 51 (2000).

64 N. G. Veitch, A. T. Smith, *Adv. Inorg. Chem.*, **51**, 107 (2000).

65 H.-P. Hersleth, U. Ryde, P. Rydberg, C. H. Görbitz, K. K. Andersson, *J. Inorg. Biochem.*, **100**, 460 (2006).

66 F. Ogliaro, S. P. de Visser, S. Shaik, *J. Inorg. Biochem.*, **91**, 554 (2002).

67 P. Rydberg, E. Sigfridsson, U. Ryde, *J. Biol. Inorg. Chem.*, **9**, 203 (2004).

68 D. Kumar, B. Karamzadeh, G. N. Sastry, S. P. de Visser, *J. Am. Chem. Soc.*, **132**, 7656 (2010).

69 D. Kumar, R. Latifi, S. Kumar, E. V. Rybak-Akimova, M. A. Sainna, S. P. de Visser, *Inorg. Chem.*, **52**, 7968 (2013).

70 M. T. Green, *J. Am. Chem. Soc.*, **121**, 7939 (1999).

71 S. P. de Visser, S. Shaik, P. K. Sharma, D. Kumar, W. Thiel, *J. Am. Chem. Soc.*, **125**, 15779 (2003).

72 K. Yoshizawa, Y. Shiota, T. Yamabe, *J. Am. Chem. Soc.*, **121**, 147 (1999).

73 J. Rittle, M. T. Green, *Science*, **330**, 933 (2010).

74 S. P. de Visser, *Angew. Chem. Int. Ed.*, **45**, 1790 (2006).

75 S. P. de Visser, *J. Am. Chem. Soc.*, **128**, 9813 (2006).

76 A. Decker, M. D. Clay, E. I. Solomon, *J. Inorg. Biochem.*, **100**, 697 (2006).

77 R. Latifi, M. Bagherzadeh, S. P. de Visser, *Chem.–Eur. J.*, **15**, 6651 (2009).

78 S. P. de Visser, J.-U. Rohde, Y.-M. Lee, J. Cho, W. Nam, *Coord. Chem. Rev.*,

257, 381 (2013).

79 K. P. Jensen, P. Rydberg, J. Heimdal, U. Ryde, A comparison of the tetrapyrrole cofactors in nature and their tuning by axial ligands, in *Computational modeling for homogeneous and enzymatic catalysis*, K. Morokuma and J. Musaev (Eds.), Wiley-VCH, Weinheim, pp. 27 (2008).

80 R. van Eldik, *Coord. Chem. Rev.*, **251**, 1649 (2007).

81 A.R. McDonald, L. Que Jr., *Nat. Chem.*, **3**, 761 (2011).

82 J.M. Bollinger, C. Krebs, *J. Inorg. Biochem.*, **200**, 586 (2006).

83 E.G. Hrycay, S.M. Bandiera, *Arch. Biochem. Biophys.*, **522**, 71 (2012).

84 P. R. Ortiz de Montellano, J. J. De Voss, in *Cytochrome P450: Structure, Mechanism, and Biochemistry*, P. R. Ortiz de Montellano (ed.), 3rd edition, Kluwer Academic/Plenum Publishers, New York, pp. 183 (2005).

85 D. F. V. Lewis, *Guide to Cytochromes P450: Structure and Function*, Taylor and Francis, London, UK, (2001).

86 I.G. Denisov, T.M. Makris, S.G. Sligar, I. Schlichting, *Chem. Rev.*, **105**, 2253 (2005).

87 C. Krebs, D. Galonicĭ Fujimori, C. T. Walsh, J. M. Bollinger Jr., *Acc. Chem. Res.*, **40**, 484 (2007).

88 C. E. Tinberg, S. Lippard, *Acc. Chem. Res.*, **44**, 280 (2011).

89 M. Yagi, M. Kaneko, *Chem. Rev.*, **101**, 21 (2001).

90 C. S. Mullins, V. L. Pecoraro, *Coord. Chem. Rev.*, **252**, 416 (2008).

91 Y. Umena, K. Kawakami, J.-R. Shen, N. Kamiya, *Nature*, **473**, 55 (2011).

92 J. P. McEvoy, G.W. Brudvig, *Chem. Rev.*, **106**, 4455 (2006).

93 S. P. de Visser, *Coord. Chem. Rev.*, **253**, 754 (2009).

94 O. Weinreb, T. Amit, S. Mandel, L. Kupershmidt, M.B.H. Youdim, *Antioxid. Redox Signal.*, **13**, 919 (2010).

95 C. Wong, D.G. Fujimori, C.T. Walsh, C.L. Drennan, *J. Am. Chem. Soc.*, **131**, 4872 (2009).

96 F. H. Vaillancourt, E. Yeh, D. A. Vosburg, S. Garneau-Tsodikova, C.T. Walsh, *Chem. Rev.*, **106**, 3364 (2006).

97 A. Butler, M. Sandy, *Nature*, **460**, 848 (2009).

98 Y. Watanabe, H. Fujii, *Struct. Bond.*, **97**, 61 (2000).

99 S. Shaik, W. Lai, H. Chen, Y. Wang, *Acc. Chem. Res.*, **43**, 1154 (2010).

100 R. Zhang, M. Newcomb, *Acc. Chem. Res.*, **41**, 468 (2008).

101 W. Nam, *Acc. Chem. Res.*, **40**, 522 (2007).

102 M. M. Abu-Omar, A. Loaiza, N. Hontzeas, *Chem. Rev.*, **105**, 2227 (2005).

103 L. Que Jr., *Acc. Chem. Res.*, **40**, 493 (2007).

104 X. Shan, L. Que Jr., *J. Inorg. Biochem.*, **100**, 421 (2006).

105 J. Cho, R. Sarangi, W. Nam, *Acc. Chem. Res.*, **45**, 1321 (2012).

106 D. Goldberg, *Acc. Chem. Res.*, **40**, 626 (2007).

107 Z. Gross, *J. Biol. Inorg. Chem.*, **6**, 733 (2001).

108 F. Neese, W. Ames, G. Christian, M. Kampa, D.G. Liakos, D.A. Pantazis, M. Roemelt, P. Surawatanawong, S. Ye, *Adv. Inorg. Chem.*, **62**, 301 (2010).

109 J.-U. Rohde, J.-H. In, M. H. Lim, W. W. Brennessel, M. R. Bukowski, A. Stubna, E. Münck, W. Nam, L. Que Jr., *Science*, **299**, 1037 (2003).

110 J. J. R. Frausto da Silva, R. J. P. Williams, *The Biological Chemistry of the Elements*, Clarendon Press, Oxford, (1991).

111 B. K. Burgess, D. J. Lowe, *Chem. Rev.*, **96**, 2983 (1996).

112 B. J. Wallar, J.D. Lipscomb, *Chem. Rev.*, **96**, 2625 (1996).

113 N. Elango, R. Radhakrishnan, W. A. Froland, B. J. Wallar, C. A. Earhart, J. D. Lipscomb, D. Ohlendorf, *Protein Sci.*, **6**, 556 (1997).

114 P. Richard, A. Ehrenberg, *Science*, **221**, 514 (1983).

115 M. S. Lah, M. M. Dixon, K. A. Pattridge, W. C. Stallings, J. A. Fee, M. L. Ludwig, *Biochemistry*, **34**, 1646 (1995).

116 A. F. Miller, D. L. Sorkin, *Comments Mol. Cell. Biophy.*, **9**, 1 (1997).

117 J. M. Castagnetto, S. W. Hennessy, V. A. Roberts, E. D. Getzoff, J. A. Tainer, M. E. Pique, *Nucleic Acids Res.*, **30**, 379 (2002).

118 R. H. Holm, P. Kennepohl, E. I. Solomon, *Chem. Rev.*, **96**, 2239 (1996).

119 A. M. Valentine, S. J. Lippard, *J. Chem. Soc. Dalton Trans.*, 3925 (1997).

120 J. W. Whittaker, M. M. Whittaker, *J. Am. Chem. Soc.*, **113**, 5528 (1991).

121 H. Beinert, R. H. Holm, E. Munck, *Science*, **277**, 653 (1997).

122 A. Mondragon, E. C. Griffith, L. Sun, F. Xiong, C. Armstrong, J. O. Liu,

Biochemistry, **36**, 4934 (1997).

123 N. L. Ogihara, H. E. Parge, P. J. Hart, M. S. Weiss, J. J. Goto, B. R. Crane, J. Tsang, K. Slater, J. A. Roe, J. S. Valentine, D. Eisenberg, J. A. Tainer, *Biochemistry*, **35**, 2316 (1996).

124 T. L. Poulos, *Nat. Prod. Rep.*, **24**, 504 (2007).

125 M. R. Mauk, F. I. Rosell, A. G. Mauk, *Nat. Prod. Rep.*, **24**, 523 (2007).

126 M. Unno, T. Matsui, M. Ikeda-Saito, *Nat. Prod. Rep.*, **24**, 553 (2007).

127 I. G. Denisov, T. M. Makris, S. G. Sligar, I. Schlichting, *Chem. Rev.*, **105**, 2253, (2005).

128 M. K. F. Wikstrom, *Nature*, **266**, 271 (1977).

129 M. R. A. Blomberg, P. E. M. Siegbahn, *Biochemistry*, **51**, 5173 (2012).

130 M. R. A. Blomberg, P. E. M. Siegbahn, *Biochim. Biophys. Acta, Bioenerg.*, **1827**, 826 (2013).

131 P. R. Ortiz de Montellano, *Mechanism and Biochemistry*, 2nd edition, Plenum, New York, (1995).

132 F. P. Guengerich, *Chem. Res. Toxicol.*, **14**, 611 (2001).

133 M. J. Coon, *Annu. Rev. Pharmacol. Toxicol.*, **45**, 1 (2005).

134 W. E. Evans, M.V. Relling, *Science*, **286**, 487 (1999).

135 F. P. Guengerich, *Drug Dev. Res.*, **49**, 4 (2000).

136 E. M. Isin, F.P. Guengerich, *Biochim. Biophys. Acta*, **1770**, 314 (2007).

137 P. R. Ortiz de Montellano, *Chem. Rev.*, **110**, 932 (2009).

138 S. P. de Visser, F. Ogliaro, P.K. Sharma, S. Shaik, *Angew. Chem. Int. Ed.*, **41**, 1947 (2002).

139 S. P. de Visser, F. Ogliaro, P.K. Sharma, S. Shaik, *J. Am. Chem. Soc.*, **124**, 11809 (2002).

140 C. S. Lieber, L.M. DeCarli, *Science*, **162**, 917 (1968).

141 C. S. Lieber, *Physiol. Rev.*, **77**, 517 (1997).

142 C. S. Lieber, *Drug Metab. Rev.*, **36**, 511 (2004).

143 G. Ekstroem, C. Norsten, T. Cronholm, M. Ingelman-Sundberg, *Biochemistry (Mosc.)*, **26**, 7348 (1987).

144 A. D. N. Vaz, M. J. Coon, *Biochemistry (Mosc.)*, **33**, 6442 (1994).

145 L. C. Bell, F. P. Guengerich, *J. Biol. Chem.*, **272**, 29643 (1997).

146 L. C. Bell-Parikh, F. P. Guengerich, *J. Biol. Chem.*, **274**, 23833 (1999).

147 A. W. Wood, D. C. Swinney, P. E. Thomas, D. E. Ryan, P. F. Hall, W. Levin, W. A. Garland, *J. Biol. Chem.*, **263**, 17322 (1988).

148 G. Bellucci, C. Chiappe, L. Pucci, P. G. Gervasi, *Chem. Res. Toxicol.*, **9**, 871 (1996).

149 Y. Wang, C. L. Yang, H. M.Wang, K. L. Han, S. Shaik, *Chembiochem.*, **8**, 277 (2007).

150 Y. Terelius, C. Norsten-Höög, T. Cronholm, M. Ingelman-Sundberg, *Biochem. Biophys. Res. Commun.*, **179**, 689 (1991).

151 R. G. Rahwan, *Toxicol. Appl. Pharmacol.*, **34**, 3 (1975).

152 Y. Wang, H. Wang, Y. Wang, C. Yang, L. Yang, K. Han, *J. Phys. Chem. B*, **110**, 6154 (2006).

153 F. Ogliaro, N. Harris, S. Cohen, M. Filatov, S. P. de Visser, S. Shaik, *J. Am. Chem. Soc.*, **122**, 8977 (2000).

154 S. Shaik, M. Filatov, D. Schroder, H. Schwarz, *Chem. Eur. J.*, **4**, 193 (1998).

155 M. Filatov, N. Harris, S. Shaik, *Angew. Chem. Int. Ed.*, **38**, 3510 (1999).

156 N. Harris, S. Cohen, M. Filatov, F. Ogliaro, S. Shaik, *Angew. Chem. Int. Ed.*, **39**, 2003 (2000).

157 G. Chouinard, K. Lefko-Singh, E. Teboul, *Cell. Mol. Neurobiol.*, **19**, 533 (1999).

158 W. Daher, L. Pelinski, S. Klieber, F. Sadoun, V. Meunier, M. Bourrié, C. Biot, F. Guillou, G. Fabre, J. Brocard, L. Fraisse, J.-P. Maffrand, J. Khalife, D. Dive, *Drug Metab. Dispos.*, **34**, 667 (2006).

159 M. M. Abdel-Monem, *J. Med. Chem.*, **18**, 427 (1975).

160 M. N. Bhakta, P. F. Hollenberg, K. Wimalasena, *Chem. Commun.*, **265** (2005).

161 M. N. Bhakta, P.F. Hollenberg, K. Wimalasena, *J. Am. Chem. Soc.*, **127**, 1376 (2005).

162 M. N. Bhakta, K. Wimalasena, *Eur. J. Org. Chem.*, **4801** (2005).

163 L. T. Burka, F. P. Guengerich, R. J. Willard, T. L. Macdonald, *J. Am. Chem. Soc.*, **107**, 2549 (1985).

164 T. L. Macdonald, W. G. Gutheim, R. B. Martin, F. P. Guengerich, *Biochemistry*

(Mosc.), **28**, 2071 (1989).

165 J. I. Manchester, J. P. Dinnocenzo, L. Higgins, J. P. Jones, *J. Am. Chem. Soc.*, **119**, 5069 (1997).

166 G. T. Miwa, W. A. Garland, B. J. Hodshon, A. Y. Lu, D. B. Northrop, *J. Biol. Chem.*, **255**, 6049 (1980).

167 G. T. Miwa, J. S. Walsh, G. L. Kedderis, P. F. Hollenberg, *J. Biol. Chem.*, **258**, 14445 (1983).

168 Y. Goto, Y. Watanabe, S. Fukuzumi, J. P. Jones, J. P. Dinnocenzo, *J. Am. Chem. Soc.*, **120**, 10762 (1998).

169 J. P. Dinnocenzo, S. B. Karki, J. P. Jones, *J. Am. Chem. Soc.*, **115**, 7111 (1993).

170 S. B. Karki, J. P. Dinnocenzo, J. P. Jones, K. R. Korzekwa, *J. Am. Chem. Soc.*, **117**, 3657 (1995).

171 F. P. Guengerich, C.-H. Yun, T. L. Macdonald, *J. Biol. Chem.*, **271**, 27321 (1996).

172 U. Jurva, P. Bissel, E. M. Isin, K. Igarashi, S. Kuttab, N. Castagnoli, *J. Am. Chem. Soc.*, **127**, 12368 (2005).

173 S. B. Karki, J. P. Dinnocenzo, *Xenobiotica*, **25**, 711 (1995).

174 Y. Wang, D. Kumar, C. Yang, K. Han, S. Shaik, J. Phys. Chem. B, **111**, 7700 (2007).

175 P. J. Robbins, M. G. Cherniack, *J. Toxicol. Environ. Health*, **18**, 503 (1986).

176 D. Ross, P. B. Farmer, A. Gescher, J. A. Hickman, M. D. Threadgill, *Biochem. Pharmacol.*, **32**, 1773 (1983).

177 G. L. Kennedy, R. D. Short, *Crit. Rev. Toxicol.*, **17**, 129 (1986).

178 L. R. Hall, R. P. Hanzlik, *J. Biol. Chem.*, **265**, 12349 (1990).

179 L. R. Hall, R. T. Iwamoto, R. P. Hanzlik, *J. Org. Chem.*, **54**, 2446 (1989).

180 J. Iley, L. Constantino, F. Norberto, E. Rosa, *Tetrahedron Lett.*, **31**, 4921 (1990).

181 J. Iley, L. Constantino, *Biochem. Pharmacol.*, **47**, 275 (1994).

182 J. Iley, R. Tolando, *J. Chem. Soc. Perk. Trans.*, **2**, 2328 (2000).

183 L. Constantino, J. Iley, *Org. Biomol. Chem.*, **2**, 1894 (2004).

184 Y. Wang, D. Kumar, C. Yang, K. Han, S. Shaik, *J. Phys. Chem. B*, **111**, 7700 (2007).

185 Y. Wang, D. Li, K. Han, S. Shaik, *J. Phys. Chem. B*, **114**, 2964 (2010).

186 E. I. Solomon, T. C. Brunold, M. I. Davis, J. N. Kemsley, S.-K. Lee, N. Lehnert, F. Neese, A. J. Skulan, Y.-S. Yang, J. Zhou, *Chem. Rev.*, **100**, 235 (2000).

187 M. Merkx, D. A. Kopp, M. H. Sazinsky, J. L. Blazyk, J. Müller, S. J. Lippard, *Angew. Chem., Int. Ed.*, **40**, 2782 (2001).

188 K. D. Koehntop, J. P. Emerson, L. Que Jr., *J. Biol. Inorg. Chem.*, **10**, 87 (2005).

189 H. W. Gardner, *Biochim. Biophys. Acta*, **1084**, 221 (1991).

190 J. N. Siedow, *Annu. Rev. Plant Physiol. Plant Mol. Biol.*, **42**, 145 (1991).

191 S. Yamamoto, *Biochim. Biophys. Acta*, **1128**, 117 (1992).

192 A. W. Ford-Hutchinson, M. Gresser, R. N. Young, *Annu. Rev. Biochem.*, **63**, 383 (1994).

193 H. Kühn, S. Borngräber, in *Lipoxgenases and Their Metabolites*; S. Nigam, C. R. Pace-Asciak, (Eds.), Plenum: New York, (1999).

194 A. R. Brash, *J. Biol. Chem.*, **274**, 23679 (1999).

195 K. van Leyen, R. M. Duvoisin, H. Engelhardt, M. Wiedmann, *Nature*, **395**, 392 (1998).

196 K. V. Honn, D. G. Tang, X. Gao, I. A. Butovich, B. Liu, J. Timar, W. Hagmann, *Cancer Metastasis Rev.*, **13**, 365 (1994).

197 D. L. Sloane, in *Lipoxygenase Lipoxygenase Pathway Enzymes*, G. Piazza, (Ed.), American Oil Chemists' Society: Champaign, IL, pp 57 (1996).

198 J. C. Boyington, B. J. Gaffney, L. M. Amzel, *Science*, **260**, 1482 (1993).

199 W. Minor, J. Steczko, B. Stec, Z. Otwinowski, J. T. Bolin, R. Walter, B. Axelrod, *Biochemistry*, **35**, 10687 (1996).

200 E. Skrzypczak-Jankun, L. M. Amzel, B. A. Kroa, M. O. Funk Jr., *Proteins: Struct. Funct. Genet.*, **29**, 15 (1997).

201 E. I. Solomon, J. Zhou, F. Neese, E. G. Pavel, *Chem. Biol.*, **4**, 795 (1997).

202 E. J. Corey, R. Nagata, *J. Am. Chem. Soc.*, **109**, 8107 (1987).

203 E. J. Corey, C. Walker, *J. Am. Chem. Soc.*, **109**, 8108 (1987).

204 M. J. Nelson, S. P. Seitz, *Curr. Opin. Struct. Biol.*, **4**, 878 (1994).

205 T. D. H. Bugg, C. J. Winfield, *Nat. Prod. Rep.*, 513 (1998).

206 S. Dagley, *Am. Sci.*, **63**, 681 (1975).

207 B. R. Glick, J. J. Pasternak, in *Molecular Biotechnology: Principles and Applications of Recombinant DNA*, 2nd edition, American Society for Microbiology: Washington, DC, (1998).

208 J. D. Lipscomb, A. M. Orville, in *Degradation of Environmental Pollutants by Microorganisms and Their Metalloenzymes*, H. Sigel, A. Sigel, (Eds.), Marcel Dekker: New York, Vol. 28 (Metal Ions in Biological Systems), pp 243 (1992).

209 B. Hofer, L. D. Eltis, D. N. Dowling, K. N. Timmis, *Gene*, **130**, 47-55 (1993).

210 S. Harayama, M. Rekik, *J. Biol. Chem.*, **264**, 15328-15333 (1989).

211 D. R. Durham, L. A. Stirling, L. N. Ornston, J. J. Perry, *Biochemistry*, **19**, 149-155 (1980).

212 M. Fujiwara, L. A. Golovleva, Y. Saeki, M. Nozaki, O. Hayaishi, *J. Biol. Chem.*, **250**, 4848-4855 (1975).

213 C. Bull, D. P. Ballou, S. Otsuka, *J. Biol. Chem.*, **256**, 12681 (1981).

214 H. Fujisawa, O. Hayaishi, *J. Biol. Chem.*, **243**, 2673 (1968).

215 C. Hartnett, E. L. Niedle, K.-L. Ngai, L. N. Ornston, *J. Bacteriol.*, **172**, 956 (1990).

216 J. R. van der Meer, R. I. L. Eggen, A. J. B. Zehnder, W. M. de Vos, *J. Bacteriol.*, **173**, 2425 (1991).

217 D. H. Ohlendorf, P. C. Weber, J. D. Lipscomb, *J. Mol. Biol.*, **195**, 225 (1987).

218 D. H. Ohlendorf, A. M. Orville, J. D. Lipscomb, *J. Mol. Biol.*, **244**, 586 (1994).

219 Y. Tatsuno, Y. Saeki, M. Nozaki, S. Otsuka, Y. Maeda, *FEBS Lett.*, **112**, 83 (1980).

220 Y. R. Boldt, M. J. Sadowsky, L. B. M. Ellis, L. Que Jr., L. P. Wackett, *J. Bacteriol.*, **177**, 1225 (1995).

221 L. Que Jr., J. Widom, R. L. Crawford, *J. Biol. Chem.*, **256**, 10941 (1981).

222 A. K. Whiting, Y. R. Boldt, M. P. Hendrich, L. P. Wackett, L. Que Jr., *Biochemistry*, **35**, 160 (1996).

223 J. D. Lipscomb, A. M. Orville, R. W. Frazee, M. A. Miller, D. H. Ohlendorf, in *Oxygen Homeostasis and Its Dynamics*, Y. Ishimura, H. Shimada, M. Suematsu (Eds.), Springer- Verlag: New York, Vol. 1, pp 263 (1998).

224 L. Que Jr., *Chem. Rev.*, **96**, 2607 (1996).

225 I. Bertini, F. Briganti, S. Mangani, H. F. Nolting, A. Scozzafava, *Coord. Chem. Rev.*, **144**, 321 (1995).

226 Y. Hrywna, T. V. Tsoi, O. V. Maltseva, J. F. Quensen III, J. M. Tiedje, *Appl. Environ. Microbiol.*, **65**, 2163 (1999).

227 F. Brühlmann, W. Chen, *Biotechnol. Bioeng.*, **63**, 544 (1999).

228 L. D. Eltis, J. T. Bolin, *J. Bacteriol.*, **178**, 5930 (1996).

229 D. M. Arciero, J. D. Lipscomb, B. H. Huynh, T. A. Kent, E. Münck, *J. Biol. Chem.*, **258**, 14981 (1983).

230 S. Han, L. D. Eltis, K. N. Timmis, S. W. Muchmore, J. T. Bolin, *Science*, **270**, 976 (1995).

231 S. Takemori, T. Komiyama, M. Katagiri, *Eur. J. Biochem.*, **23**, 178 (1971).

232 M. Nozaki, H. Kagamiyama, O. Hayaishi, *Biochem. Z.*, **23**, 582 (1963).

233 T. Senda, K. Sugiyama, H. Narita, T. Yamamoto, K. Kimbara, M. Fukuda, M. Sato, K. Yano, Y. Mitsui, *J. Mol. Biol.*, **255**, 735 (1996).

234 J. T. Bolin, Personal communication.

235 K. Sugiyama, T. Senda, H. Narita, T. Yamamoto, K. Kimbara, M. Fukuda, K. Yano, Y. Mitsui, *Proc. Jpn. Acad., Ser. B*, **71**, 32 (1995).

236 K. Sugimoto, T. Senda, H. Aoshima, E. Masai, M. Fukuda, Y. Mitsui, *Struct. Folding Design*, **7**, 953 (1999).

237 A. Kita, S.-I. Kita, I. Fujisawa, K. Inaka, T. Ishida, K. Horiike, M. Nozaki, K. Miki, *Structure*, **7**, 25 (1998).

238 K. Hori, T. Hashimoto, M. Nozaki, *J. Biochem.*, **74**, 375 (1973).

239 D. M. Arciero, A. M. Orville, J. D. Lipscomb, *J. Biol. Chem.*, **260**, 14035 (1985).

240 P. A. Mabrouk, A. M. Orville, J. D. Lipscomb, *J. Am. Chem. Soc.*, **113**, 4053 (1991).

241 S. Kaufman, *Adv. Enzymol.*, **35**, 245 (1971).

242 R. Shiman, in *Chemistry and Biochemistry of Pterins*, R. L. Blakley, S. J. Benkovic, (Eds.), Wiley: New York, Vol. 2 (Folates and Pterins), pp 179 (1985).

243 S. Kaufman, Adv. Enzymol. Relat. Areas *Mol. Biol.*, **67**, 77 (1993).

244 S. Kaufman, Adv. Enzymol. Relat. Areas *Mol. Biol.*, **70**, 103 (1995).

245 P. M. Nair, C. S. Vaidyanathan, *Biochim. Biophys. Acta*, **110**, 521 (1965).

246 H. Baran, R. Schwarcz, *Adv. Exp. Med. Biol.*, **294**, 485 (1991).

247 D. M. Kuhn, W. Lovenberg, in *Chemistry and Biochemistry of Pterins*, R. L. Blakley, S. J. Benkovic, (Eds.), Wiley: New York, Vol. 2 (Folates and Pterins), pp 353 (1985).

248 G. R. Moran, S. C. Daubner, P. F. Fitzpatrick, *J. Biol. Chem.*, **273**, 12259 (1998).

249 S. G. Bhat, C. S. Vaidyanathan, *Arch. Biochem. Biophys.*, **176**, 314 (1976).

250 T. J. Kappock, J. P. Caradonna, *Chem. Rev.*, **96**, 2659 (1996).

251 S. E. Hufton, I. G. Jennings, R. G. H. Cotton, *Biochem. J.*, **311**, 353 (1995).

252 T. Flatmark, R. C. Stevens, *Chem. Rev.*, **99**, 2137 (1999).

253 P. F. Fitzpatrick, *Annu. Rev. Biochem.*, **68**, 355 (1999).

254 M. Weinstein, R. C. Eisensmith, V. Abadie, S. Avigad, S. Lyonnet, G. Schwartz, A. Munnich, S. L. C. Woo, Y. Shiloh, *Hum. Genet.*, **90**, 645 (1993).

255 H. G. Eiken, P. M. Knappskog, J. Apold, T. Flatmark, *Hum. Mutat.*, **7**, 228 (1996).

256 P. M. Knappskog, H. G. Eiken, A. Martínez, O. Bruland, J. Apold, T. Flatmark, *Hum. Mutat.*, **8**, 236 (1996).

257 S. Ellingsen, P. M. Knappskog, H. G. Eiken, *Hum. Mutat.*, **9**, 88 (1997).

258 E. Bjørgo, P. M. Knappskog, A. Martínez, R. C. Stevens, T. Flatmark, *Eur. J. Biochem.*, **257**, 1 (1998).

259 P. J. Waters, M. A. Parniak, B. R. Akerman, A. O. Jones, C. R. Scriver, *J. Inherited Metab. Dis.*, **22**, 208 (1999).

260 R. Shiman, *J. Biol. Chem.*, **255**, 10029 (1980).

261 J. J. A. Marota, R. Shiman, *Biochemistry*, **23**, 1303 (1984).

262 D. E. Wallick, L. M. Bloom, B. J. Gaffney, S. J. Benkovic, *Biochemistry*, **23**, 1295 (1984).

263 M. A. Hill, J. J. A. Marota, R. Shiman, *J. Biol. Chem.*, **263**, 5646 (1988).

264 R. Shiman, D. W. Gray, M. A. Hill, *J. Biol. Chem.*, **269**, 24637 (1994).

265 E. De Carolis, V. De Luca, *Phytochemistry*, **36**, 1093 (1994).

266 P. Hedden, *Biochem. Soc. Trans.*, **20**, 373 (1992).

267 A. G. Prescott, *J. Exp. Bot.*, **44**, 849 (1993).

268 K. I. Kivirikko, R. Myllylä, in *The Enzymology of Posttranslational Modification of Proteins*, R. B. Freedman, H. C. Hawkins, (Eds.), Academic: London, Vol. 1, pp 53 (1980).

269 M. J. Chrispeels, *Methods Enzymol.*, **107**, 361 (1984).

270 Q. Wang, W. J. VanDusen, C. J. Petroski, V. M. Garsky, A. M. Stern, P. A. Friedman, *J. Biol. Chem.*, **253**, 1654 (1991).

271 L. Tuderman, R. Myllyla¨, K. I. Kivirikko, *Eur. J. Biochem.*, **80**, 341 (1977).

272 U. Puistola, T. M. Turpeenniemi-Hujanen, R. Myllyla¨, K. I. Kivirikko, *Biochim. Biophys. Acta*, **611**, 40 (1980).

273 E. Holme, S. Lindstedt, I. Nordin, *Biochem. Biophys. Res. Commun.*, **107**, 518 (1982).

274 R. S. Wehbie, N. S. Punekar, H. A. Lardy, *Biochemistry*, **27**, 2222 (1988).

275 C.-A. Hsu, M. D. Saewert, L. F. Polsinelli Jr., M. T. Abbott, *J. Biol. Chem.*, **256**, 6098 (1981).

276 K. Valegard, A. C. T. Vanscheltinga, M. D. Lloyd, T. Hara, S. Ramaswamy, A. Perrakis, A. Thompson, H. J. Lee, J. E. Baldwin, C. J. Schofield, J. Hajdu, I. Andersson, *Nature*, **394**, 805 (1998).

277 T. A. Link, in *Advances in Inorganic Chemistry*, Academic: New York, Vol. 47, pp 83 (1999).

278 I. Bertini, M. A. Cermonini, S. Ferretti, I. Lozzi, C. Luchinat, M. S. Viezzoli, *Coord. Chem. Rev.*, **151**, 145 (1996).

279 D. Ballou, C. Batie, *Prog. Clin. Biol. Res.*, **274**, 211 (1988).

280 S. E. Crutcher, P. J. Geary, *Biochem. J.*, **177**, 393 (1979).

281 C. J. Batie, E. LaHaie, D. P. Ballou, *J. Biol. Chem.*, **262**, 1510 (1987).

282 D. T. Gibson, W.-K. Yeh, T.-N.Liu, V. Subramanian, in *Oxygenases and Oxygen Metabolism*, M. Nozaki, S. Yamamoto, Y. Ishimura, M. J. Coon, L. Ernster, R W. Estabrook, (Eds.), Academic: New York, pp 51 (1982).

283 B. D. Ensley, D. T. Gibson, *J. Bacteriol.*, **155**, 505 (1983).

284 B. M. Bundy, A. L. Campbell, E. L. Neidle, *J. Bacteriol.*, **180**, 4466 (1998).

285 A. Markus, D. Krekel, F. Lingens, *J. Biol. Chem.*, **261**, 12883 (1986).

286 F.-H. Bernhardt, E. Heymann, P. S. Traylor, *Eur. J. Biochem.*, **92**, 209 (1978).

287 H. Umezawa, *Gann Monogr. Cancer Res.*, **19**, 3 (1976).

288 S. M. Hecht, *Acc. Chem. Res.*, **19**, 383 (1986).

289 J. Stubbe, J. W. Kozarich, *Chem. Rev.*, **87**, 1107 (1987).

290 D. H. Petering, R. W. Byrnes, W. E. Antholine, *Chem.-Biol. Interact.*, **73**, 133 (1990).

291 J. Stubbe, J. W. Kozarich, W. Wu, D. E. Vanderwall, *Acc. Chem. Res.*, **29**, 322 (1996).

292 D. H. Petering, Q. Mao, W. Li, E. DeRose, W. E. Antholine, in *Probing of Nucleic Acids by Metal Ion Complexes of Small Molecules*, A. Sigel, H. Sigel, (Eds.), *Metal Ions in Biological Systems*, Marcel Dekker: New York, Vol. 33 pp 619 (1996).

293 R. M. Burger, *Chem. Rev.*, **98**, 1153 (1998).

294 C. A. Claussen, E. C. Long, *Chem. Rev.*, **99**, 2797 (1999).

295 K. Radtke, F. A. Lornitzo, R. W. Byrnes, W. E. Antholine, D. H. Petering, *Biochem. J.*, **302**, 655 (1994).

296 M. Chien, A. P. Grollman, S. B. Horwitz, *Biochemistry*, **16**, 3641 (1977).

297 L. F. Povirk, M. Hogan, N. Dattagupta, M. Buechner, *Biochemistry*, **20**, 665 (1981).

298 E. A. Rao, L. A. Saryan, W. E. Antholine, D. H. Petering, *J. Med. Chem.*, **23**, 1310 (1980).

299 S. N. Roy, S. B. Horwitz, *Cancer Res.*, **44**, 1541 (1984).

300 Y. Iitaka, H. Nakamura, T. Nakatani, Y. Muraoka, A. Fujii, T. Takita, H. J. Umezawa, *J. Antiobiot.*, **31**, 1070 (1978).

301 S. J. Brown, P. K. Mascharak, *J. Am. Chem. Soc.*, **110**, 1996 (1988).

302 J. D. Tan, S. E. Hudson, S. J. Brown, M. M. Olmstead, P. K. Mascharak, *J. Am. Chem. Soc.*, **114**, 3841 (1992).

303 E. Farinas, J. D. Tan, N. Baidya, P. K. Mascharak, *J. Am. Chem. Soc.*, **115**, 2996 (1993).

304 H. Kurosaki, K. Hayashi, Y. Ishikawa, M. Goto, *Chem. Lett.*, 691 (1995).

305 H. Kurosaki, K. Hayashi, Y. Ishikawa, M. Goto, K. Inada, I. Taniguchi, M. Shionoya, E. Kimura, *Inorg. Chem.*, **38**, 2824 (1999).

306 N. J. Oppenheimer, L. O. Rodriguez, S. M. Hecht, Proc. Natl. Acad. Sci. U.S.A., **76**, 5616 (1979).

307 M. A. J. Akkerman, C. A. G. Haasnoot, U. K. Pandit, C. W. Hilbers, *Magn. Reson. Chem.*, **26**, 793 (1988).

308 M. A. J. Akkerman, C. A. G. Haasnoot, C. W. Hilbers, *Eur. J. Biochem.*, **173**, 211 (1988).

309 M. A. J. Akkerman, E. W. J. F. Neijman, S. S. Wijmenga, C W. Hilbers, W. Bermel, *J. Am. Chem. Soc.*, **112**, 7462 (1990).

310 R. A. Manderville, J. F. Ellena, S. M. Hecht, *J. Am. Chem. Soc.*, **116**, 10851 (1994).

311 W. Wu, D. E. Vanderwall, J. Stubbe, J. W. Kozarich, C. J. Turner, *J. Am. Chem. Soc.*, **116**, 10843 (1994).

312 R. X. Xu, D. Nettesheim, J. D. Otvos, D. H. Petering, *Biochemistry*, **33**, 907 (1994).

313 R. A. Manderville, J. F. Ellena, S. M. Hecht, *J. Am. Chem. Soc.*, **117**, 7891 (1995).

314 Q. Mao, P. Fulmer, W. Li, E. F. DeRose, D. H. Petering, *J. Biol. Chem.*, **271**, 6185 (1996).

315 J. D. Otvos, W. E. Antholine, S. Wehrli, D. H. Petering, *Biochemistry*, **35**, 1458 (1996).

316 W. Wu, D. E. Vanderwall, S. M. Lui, X.-J. Tang, C. J. Turner, J. W. Kozarich, J. Stubbe, *J. Am. Chem. Soc.*, **118**, 1268 (1996).

317 W. Wu, D. E. Vanderwall, C. J. Turner, J. W. Kozarich, J. Stubbe, *J. Am. Chem. Soc.*, **118**, 1281 (1996).

318 J. Caceres-Cortes, H. Sugiyama, K. Ikudome, I. Saito, A. H.-J. Wang, *Eur. J. Biochem.*, **244**, 818 (1997).

319 J. Caceres-Cortes, H. Sugiyama, K. Ikudome, I. Saito, A. H.-J. Wang, *Biochemistry*, **36**, 9995 (1997).

320 A. M. Calafat, H. Won, L. G. Marzilli, *J. Am. Chem. Soc.*, **119**, 3656 (1997).

321 T. E. Lehmann, L.-J. Ming, M. E. Rosen, L. Que Jr., *Biochemistry*, **36**, 2807 (1997).

322 S. M. Lui, D. E. Vanderwall, W. Wu, X.-J. Tang, C. J. Turner, J. W. Kozarich, J. Stubbe, *J. Am. Chem. Soc.*, **119**, 9603 (1997).

323 D. E. Vanderwall, S. M. Lui, W. Wu, C. J. Turner, J. W. Kozarich, J. Stubbe, *Chem. Biol.*, **4**, 373 (1997).

324 S. J. Sucheck, J. F. Ellena, S. M. Hecht, *J. Am. Chem. Soc.*, **120**, 7450 (1998).

325 W. Wu, D. E. Vanderwall, S. Teramoto, S. M. Lui, S. T. Hoehn,X. J. Tang,C. J. Turner, D. L. Boger, J. W. Kozarich, J. Stubbe, *J. Am. Chem. Soc.*, **120**, 2239 (1998).

326 I. M. Klotz, D. M. Kurtz, *Acc. Chem. Res.*, **17**, 16 (1984).

327 P. C. Wilkins, R. G. Wilkins, *Coord. Chem. Rev.*, **79**, 195 (1987).

328 R. E. Stenkamp, *Chem. Rev.*, **94**, 715 (1994).

329 E. C. Niederhoffer, J. H. Timmons, A. E. Martell, *Chem. Rev.*, **84**, 137 (1984).

330 E. I. Solomon, M. J. Baldwin, M. D. Lowery, *Chem. Rev.*, **92**, 521 (1992).

331 E. R. Lankester, *Proc. R. Soc.*, London, **21**, 71 (1873).

332 E. Boeri, A. Ghiretti-Magaldi, *Biochim. Biophys. Acta*, **23**, 489 (1957).

333 I. M. Klotz, T. A. Klotz, H. A. Fiess, *Arch. Biochem. Biophys.*, (1957).

334 A. K. Shiemke, T. M. Loehr, J. Sanders-Loehr, *J. Am. Chem. Soc.*, **106**, 4951 (1984).

335 K. M. Dunn, D. F. Shriver, I. M. Klotz, *Proc. Natl. Acad. Sci. U.S.A.*, **70**, 2852 (1973).

336 D. M. Kurtz, D. F. Shriver, I. M. Klotz, *Coord. Chem. Rev.*, **24**, 145 (1977).

337 M. A. Holmes, I. Le Trong, S. Turley, L. C. Sieker, R. E. Stenkamp, *Biochemistry*, **30**, 583 (1991).

338 T. C. Brunold, E. I. Solomon, *J. Am. Chem. Soc.*, **121**, 8288 (1999).

339 B. J. Wallar, J. D. Lipscomb, *Chem. Rev.*, **96**, 2625 (1996).

340 H. Dalton, *Adv. Appl. Microbiol.*, **26**, 71 (1980).

341 A. M. Valentine, S. J. Lippard, *J. Chem. Soc., Dalton Trans.*, 3925 (1997).

342 C. Anthony, *The Biochemistry of Methylotrophs*, Academic: London, (1982).

343 J. D. Lipscomb, *Annu. Rev. Microbiol.*, **48**, 371 (1994).

344 S. H. Stanley, S. D. Prior, D. J. Leak, H. Dalton, *Biotechnol. Lett.*, **5**, 487 (1983).

345 D. J. Leak, H. Dalton, *Appl. Microbiol. Biotechnol.*, **23**, 470 (1986).

346 S. Lontoh, A. A. DiSpirito, J. D. Semrau, *Arch. Microbiol.*, **171**, 301 (1999).

347 H. H. T. Nguyen, S. J. Elliott, J. H. K. Yip, S. I. Chan, *J. Biol. Chem.*, **273**, 7957 (1998).

348 H. H .T. Nguyen, A. K. Shiemke, S. J. Jacobs, B. J. Hales, M. E. Lidstrom, S. I. Chan, *J. Biol. Chem.*, **269**, 14995 (1994).

349 I. A. Tukhvatullin, L. A. Korshunova, R. I. Gvozdev, H. Dalton, *Biochemistry (Moscow)*, **61**, 886 (1996).

350 M. Takeguchi, K. Miyakawa, I. Okura, *Biometals*, **11**, 229 (1998).

351 M. Takeguchi, K. Miyakawa, I. Okura, *J. Mol. Catal., Ser. A*, **132**, 145 (1998).

352 M. Takeguchi, K. Miyakawa, I. Okura, *J. Mol. Catal., Ser. A*, **137**, 161 (1999).

353 M. Takeguchi, M. Ohashi, I. Okura, *Biometals*, **12**, 123 (1999).

354 H. Yuan, M. L. P. Collins, W. E. Antholine, *Biophys. J.*, **76**, 2223 (1999).

355 H. Yuan, M. L. P. Collins, W. E. Antholine, *J. Am. Chem. Soc.*, **119**, 5073 (1997).

356 S. J. Elliott, D. W. Randall, R. D. Britt, S. I. Chan, *J. Am. Chem. Soc.*, **120**, 3247 (1998).

357 B. Wilkinson, M. Zhu, N. D. Priestley, H. H. T. Nguyen, H. Morimoto, P. G. Williams, S. I. Chan, H. G. Floss, *J. Am. Chem. Soc.*, **118**, 921 (1996).

358 H. H. T. Nguyen, K. H. Nakagawa, B. Hedman, S. J. Elliott, M. E. Lidstrom, K. O. Hodgson, S. I. Chan, *J. Am. Chem. Soc.*, **118**, 12766 (1996).

359 S. J. Elliott, M. Zhu, L. Tso, H. H. T. Nguyen, J. H. K. Yip, S. I. Chan, *J. Am. Chem. Soc.*, **119**, 9949 (1997).

360 B. Katterle, N. Abudu, T. Ljones, R. Gvozdev, K. K. Andersson, *J. Inorg. Biochem.*, **74**, 189 (1999).

361 A. C. Rosenzweig, H. Brandstetter, D. A. Whittington, P. Nordlund, S. J. Lippard, C. A. Frederick, *Proteins: Struct. Funct. Genet.*, **29**, 141 (1997).

362 A. C. Rosenzweig, P. Nordlund, P. M. Takahara, C. A. Frederick, S. J. Lippard, *Chem. Biol.*, **2**, 409 (1995).

363 A. C. Rosenzweig, C. A. Frederick, S. J. Lippard, P. Nordlund, *Nature*, **366**, 537 (1993).

364 J. Stubbe, *J. Biol. Chem.*, **265**, 5329 (1990).

365 B.-M. Sjöberg, A. Gräslund, in *Advances in Inorganic Biochemistry*, E. C. Theil, G. L. Eichorn, L. G. Marzilli, (Eds.), Elsevier: Vol. 5, pp 87 (1983).

366 P. Reichard, A. Ehrenberg, *Science*, **221**, 514 (1983).

367 M. Lammers, H. Follmann, *Struct. Bonding*, **54**, 27 (1983).

368 P. Reichard, *Science*, **260**, 1773 (1993).

369 J. Stubbe, W. A. van der Donk, *Chem. Rev.*, **98**, 705 (1998).

370 E. Mulliez, M. Fontecave, *Coord. Chem. Rev.*, **185-186**, 775 (1999).

371 P. Nordlund, B.-M. Sjöberg, H. Eklund, *Nature*, **45**, 593 (1990).

372 P. Nordlund, H. Eklund, *J. Mol. Biol.*, **232**, 123 (1993).

373 U. von Döbeln, P. Reichard, *J. Biol. Chem.*, **251**, 3616 (1976).

374 N. C. Brown, P. Reichard, *J. Biol. Chem.*, **244**, 39 (1969).

375 L. Thelander, *J. Biol. Chem.*, **249**, 4858 (1974).

376 U. Uhlin, H. Eklund, *Nature*, **370**, 533 (1994).

377 T. Barlow, R. Eliasson, A. Platz, P. Reichard, B.-M. Sjöberg, *Proc. Natl. Acad. Sci. U.S.A.*, **80**, 1492 (1983).

378 L. Petersson, A. Gräslund, A. Ehrenberg, B.-M. Sjöberg, P. Reichard, *J. Biol. Chem.*, **255**, 6706 (1980).

379 M. Fontecave, R. Eliasson, P. Reichard, *J. Biol. Chem.*, **262**, 12325 (1987).

380 M. Fontecave, P. Nordlund, H. Eklund, P. Reichard, *Adv. Enzymol. Relat. Areas Mol. Biol.*, **65**, 147 (1992).

381 S. Licht, G. J. Gerfen, J. Stubbe, *Science*, **271**, 477 (1996).

382 S. Booker, S. Licht, J. Broderick, J. Stubbe, *Biochemistry*, **33**, 12626 (1994).

383 S. Booker, J. Stubbe, *Proc. Natl. Acad. Sci., U.S.A.*, **90**, 8352 (1993).

384 M. Fontecave, R. Eliasson, P. Reichard, *Proc. Natl. Acad. Sci. U.S.A.*, **86**, 2147 (1989).

385 T. Barlow, *Bichem. Biophys. Res. Commun.*, **155**, 747 (1988).

386 F.-D. Yang, R. A. Spanevello, I. Celiker, R. Hirschmann, H. Rubin, B. S. Cooperman, *FEBS Lett.*, **272**, 61 (1990).

387 E. Mulliez, M. Fontecave, J. Gaillard, P. Reichard, *J. Biol. Chem.*, **268**, 2296 (1993).

388 S. Ollangnier, E. Mulliez, J. Gaillard, R. Eliasson, M. Fontecave, P. Reichard, *J.*

Biol. Chem., **271**, 9410 (1996).

389 B. Kauppi, B. B. Nielsen, S. Ramaswamy, I. K. Larsen, M. Thelander, L. Thelander, H. Eklund, *J. Mol. Biol.*, **262**, 706 (1996).

390 A. Åberg, P. Nordlund, H. Eklund, *Nature*, **361**, 276 (1993).

391 D. T. Logan, X.-D. Su, A. Åberg, K. Regnström, J. Hajdu, H. Eklund, P. Nordlund, *Structure*, **4**, 1053 (1996).

392 M. E. Andersson, M. Högbom, A. Rinaldo-Matthis, K. K. Andersson, B.-M. Sjöberg, P. Nordlund, *J. Am. Chem. Soc.*, **121**, 2346 (1999).

393 M. Atta, P. Nordlund, A. Åberg, H. Eklund, M. Fontecave, *J. Biol. Chem.*, **267**, 20682 (1992).

394 W. C. Voegtli, N. Khidekel, J. Baldwin, B. A. Ley, J. M. Bollinger Jr., A. C. Rosenzweig, *J. Am. Chem. Soc.*, **122**, 3255 (2000).

395 D. T. Logan, F. deMaré, B. O. Persson, A. Slaby, B.-M. Sjöberg, P. Nordlund, *Biochemistry*, **37**, 10798 (1998).

396 S. Numa, *Fatty Acid Metabolism and Its Regulation*, Elsevier: New York, (1984).

397 F. D. Gunstone, *Fatty Acid and Lipid Chemistry*, 1st edition, Blackie: London, (1996).

398 J. Shanklin, E. B. Cahoon, *Annu. Rev. Plant Physiol. Plant Mol. Biol.*, **49**, 611 (1998).

399 E. Heinz, in *Lipid Metabolism in Plants*, T. S. Noore, (Ed.), CRC: Boca Raton, FL, pp 34 (1993).

400 N. Murata, H. Wada, *Biochem. J.*, **308**, 1 (1995).

401 E. B. Cahoon, Y. Lindqvist, G. Schneider, J. Shanklin, *Proc. Natl. Acad. Sci. U.S.A.*, **94**, 4872 (1997).

402 D. J. Schultz, E. B. Cahoon, J. Shanklin, R. Craig, D. L. Cox-Foster, R. O. Mumma, J. I. Medford, *Proc. Natl. Acad. Sci. U.S.A.*, **93**, 8771 (1996).

403 Y. Lindqvist, W. J. Huang, G. Schneider, J. Shanklin, *EMBO J.*, **15**, 4081 (1996).

404 J. F. Berry, E. Bill, E. Bothe, S. DeBeer George, B.Mienert, F. Neese, K. Wieghardt, *Science*, **312**, 1937 (2006).

405 X.Wang, L. Andrews, S. Riedel, M. Kaupp, *Angew. Chem. Int. Ed. Engl.*, **46**, 8371 (2007).

406 S. Shaik, D. Danovich, A. Fiedler, D. Schröder, H. Schwarz, *Helv. Chim. Acta*, **78**, 1393 (1995).

407 S. Shaik, H. Hirao, D. Kumar, *Acc. Chem. Res.*, **40**, 532 (2007).

408 M. Schatz, V. Raab, S. Foxon, G. Brehm, S. Schneider, M. Reiher, M. C. Holthausen, J. Sundermeyer, S. Schindler, *Angew. Chem. Int. Ed.*, **43 (33)**, 4360 (2004).

409 C. Würtele, E. Gaoutchenova, K. Harms, M. C. Holthausen, J. Sundermeyer, S. Schindler, *Angew. Chem.*, **118**, 3951 (2006).

410 S. Hong, S. M. Huber, L. Gagliardi, C. C. Cramer,W. B. Tolman, *J. Am. Chem. Soc.*, **129**, 14190 (2007).

411 J. C. Price, E. W. Barr, B. Tirupati, M. Bollinger Jr., C. Krebs, *Biochemistry*, **42**, 7497 (2003).

412 P. Comba, G. Rajaraman, H. Rohwer, *Inorg. Chem.*, **46**, 3826 (2007).

413 A. Anastasi, P. Comba, J. McGrady, A. Lienke, H. Rohwer, *Inorg. Chem.*, **46**, 6420 (2007).

414 J. Bautz, P. Comba, C. Lopez de Laorden, M. Menzel, G. Rajaraman, *Angew. Chem. Int. Ed.*, **46**, 8067 (2007).

415 J. Li, C. L. Fisher, R. Konecny, D. Bashford, L. Noodleman, *Inorg. Chem.*, **38**, 929 (1999).

416 J. Li, M. R. Nelson, C. Y. Peng, D. Bashford, L. Noodleman, *J. Phys. Chem. A*, **102**, 6311 (1998).

417 R. Konecny, J. Li, C. L. Fisher, V. Dillet, D. Bashford, L. Noodleman, *Inorg. Chem.*, **38**, 940 (1999).

418 H.-B. Bürgi, J.D. Dunitz, *Structure Correlation*, VCH, Weinheim NewYork, (1994).

419 F. Kubota, K. Shinohara, K. Shimojo, T. Oshima, M. Goto, S. Furusaki, T. Hano, *Sep. Purif. Technol.*, **24**, 93 (2001).

420 G. Golub, H. Cohen, D. Meyerstein, *J. Chem. Soc., Chem. Commun.*, 397, (1992).

421 N. D. Villanueva, M. Y. Chiang, J. R. Bocarsly, *Inorg. Chem.*, **37**, 685 (1998).

422 J. L. Sessler, D. Seidel, A. E. Vivian, V. Lynch, B. L. Scott, D. W. Keogh, *Angew. Chem. Int. Ed.*, **40**, 591 (2001).

423 G. A. Shamov, G. Schreckenbach, *Inorg. Chem.*, **47**, 805 (2008).

424 G. Helmchen, A. Pfaltz, *Acc. Chem. Res.*, **33**, 336 (2000).

425 J. A. Halfen, B. A. Jazdzewski, S. Mahapatra, L. M. Berreau, E. C. Wilkinson, L.J. Que,W.B. Tolman, *J. Am. Chem. Soc.*, **119**, 8217 (1997).

426 T. Darbre, J.-L. Reymond, *Acc. Chem. Res.*, **29**, 925 (2006).

427 R. Fiammengo, M. Crego-Calama, D. N. Reinhoudt, *Curr. Opin. Chem. Biol.*, **5**, 660 (2001).

428 A. Thapper, C. Lorber, J. Fryxelius, A. Behrens, E. Nordlander, *J. Inorg. Biochem.*, **79**, 67 (2000).

429 R. G. Pearson, *J. Am. Chem. Soc.*, **85**, 3533 (1963).

430 R. G. Pearson, *Hard and Soft Acids and Bases*, Dowsen, Hutchinson & Ross, Stroudsburg, (1973).

431 R. D. Hancock, *J. Chem. Educ.*, **73**, 654 (1996).

432 R. B. Martin, *Inorg. Chim. Acta*, **339**, 27 (2002).

433 B. N. Figgis, M. A. Hitchman, *Ligand Field Theory and its Applications*, Wiley-VCH, Weinheim, New York, (2000).

434 M. Gerloch, E. C. Constable, *Transition Metal Chemistry—The Valence Shell in d-Block Chemistry*, VCH,Weinheim New York, (1994).

435 H. Irving, R. J. P.Williams, *Nature*, **162**, 746 (1948).

436 H. Irving, R. J. P.Williams, *J. Chem. Soc.*, 3192 (1953).

437 D. A. Johnson, P. G. Nelson, *Inorg. Chem.*, **34**, 5666 (1995).

438 P. Comba, *Coord. Chem. Rev.*, **182**, 343 (1999).

439 P. Comba, G. A. Lawrance, M. Rossignoli,B. W. Skelton,A. H. White, *Aust. J. Chem.*, **41**, 773 (1988).

440 M. Salavati-Niasari, *Polyhedron*, **24**, 1405 (2005).

441 P. Comba, N. F. Curtis, G. A. Lawrance, M. A. O'Leary, B. W. Skelton, A. H. White, *J. Chem. Soc., Dalton Trans.*, 2145 (1988).

442 P. Comba, T. W. Hambley, M. A. Hitchman, H. Stratemeier, *Inorg. Chem.*, **34**,

3903 (1995).
443 P. Comba, *Coord. Chem. Rev.*, **200–202**, 217 (2000).
444 K. Born, P. Comba, R. Ferrari, S. Kuwata, G. A. Lawrance, H. Wadepohl, *Inorg. Chem.*, **46**, 458 (2007).
445 P. Comba, K. Gloe, T. Inoue, H. Stephan, K. Yoshizuka, *Inorg. Chem.*, **37**, 3310 (1998).
446 R. D. Hancock, G. J. McDougall, F. Marsicano, *Inorg. Chem.*, **18**, 2847 (1979).
447 R. D. Hancock, A.E. Martell, *Chem. Rev.*, **89**, 1875 (1989).
448 B. P. Hay, J. R. Rustad, C. J. Hostetler, *J. Am. Chem. Soc.*, **115**, 11158 (1993).
449 P. Comba, T. W. Hambley, N. Okon, G. Lauer, *MOMEC97, A Molecular Modeling Package for Inorganic Compounds*, Heidelberg, (1997).
450 P. Comba,W. Schiek, *Coord. Chem. Rev.*, **238–239**, 21 (2003).
451 P. Comba, T. W. Hambley, *Molecular Modeling of Inorganic Compounds*, 2nd edition, With a Tutorial, based on MOMEClite, Wiley-VCH,Weinheim, (2001).
452 P. Comba, in *Fundamental Principles of Molecular Modeling*, W. Gans,A. Amann, J.C.A. Boeyens (Eds.), Plenum Press, New York, , p. 167 (1996).
453 B. P. Hay, *Coord. Chem. Rev.*, **126**, 177 (1993).
454 P. Comba, A. Fath, A. Kühner, B. Nuber, *J. Chem. Soc., Dalton Trans.*, 1889 (1997).
455 P. Comba, *Coord. Chem. Rev.*, **185**, 81 (1999).
456 P. Comba, H. Jakob, *Helv. Chim. Acta.*, **80**, 1983 (1997).
457 T.W. Hambley, *Inorg. Chem.*, **27**, 2496 (1988).
458 P. Comba, A.F. Sickmüller, *Inorg. Chem.*, **36**, 4500 (1997).
459 P.-O.Norrby, *ACS Symp. Ser. 721 Transition State Modeling for Catalysis*, 163 (1999).
460 M. Zimmer, *J. Biomol. Struct. Dyn.*, **11**, 203 (1993).
461 M. Zimmer, *J. Biomol. Struct. Dyn.*, **17**, 787 (2000).
462 L. Noodleman, T. Lovell, W. G. Han, J. Li, F. Himo, *Chem. Rev.*, **104**, 459 (2004).
463 F. Neese, *Coord. Chem. Rev.*, **253**, 526 (2009).
464 C. Boehme, S. Dapprich, D. Deubel,U. Pidun, M. Stahl, R. Stegmann, G.

Frenking, *ACS Symp. Ser.*, **721**, 114 (1999).

465 O. Eisenstein, L. Maron, *J. Organomet. Chem.*, **647**, 190 (2002).

466 S. Shaik, D. Kumar, S. P. De Visser, A. Altum, W. Thiel, *Chem. Rev.*, **105** 2279 (2005).

467 F. Neese, *J. Biol. Inorg. Chem.*, **11**, 702 (2006).

468 M. Seth, J. Autschbach, T. Ziegler, *J. Chem. Theory Comput.*, **3**, 343 (2007).

469 J. Schirmer, A. Dreuw, *Phys. Rev. A*, **75**, 022513/1 (2007).

470 F. Neese, *J. Chem. Phys.*, **119**, 9428 (2003).

471 M. Atanasov, C. A. Daul, C. Rauzy, *Struct. Bonding*, **106**, 97 (2004).

472 B. Kirchner, F. Wennmohs, S. Ye, F. Neese, *Curr. Opin. Chem. Biol.*, **11**, 134 (2007).

473 F. Neese, T. Petrenko, D. Ganyushin, G. Olbrich, *Coord. Chem. Rev.*, **251**, 288 (2007).

474 M. Atanasov, P. Comba, C. A. Daul, F. Neese, in *Models, Mistery and Magic of Molecules*, J. C. A. Boeyens, J. Ogilvie (Eds.), Springer, pp. 411 (2008).

475 P. Comba, M. Kerscher, *Coord. Chem. Rev.*, **253**, 564 (2009).

476 P. Comba, B. Martin, in *Macrocyclic Chemistry, Current Trends and Future Perspectives*, K. Gloe (Ed.), Springer, Heidelberg, New York, p. 303(2005).

477 M. Zimmer, *Chem. Rev.*, **8**, 2629 (1995).

478 C. R. Landis, D. M. Root, T. Cleveland, in *Reviews in Computational Chemistry*, K.B. Lipkowitz, D.B. Boyd (Eds.),VCH Verlag, New York, Weinheim, pp. 73(1995).

479 R. J. Deeth, *Struct. Bonding (Berlin)*, **82**, 1 (1995).

480 T. R. Cundari, *J. Chem. Soc., Dalton Trans.,* 2771 (1998).

481 R. J. Deeth, *Coord. Chem. Rev.*, **212**, 11 (2001).

482 M. U. Schmidt, in *Crystal Engineering: From Molecules and Crystals to Materials*, D. Braga, F. Grepioni, A. G. Orpen (Eds.), Kluwer Academic Publishers, Dordrecht, The Netherlands, p. 331 (1999).

483 J. Bartol, P. Comba, M. Melter, M. Zimmer, *J. Comput. Chem.*, **20**, 1549 (1999).

484 P. Comba, M. Zimmer, *J. Chem. Educ.*, **73**, 108 (1996).

485 J. C. A. Boeyens, P. Comba, *Coord. Chem. Rev.*, **212**, 3 (2001).

486 R. J. Deeth, Struct. *Bonding*, **113**, 37 (2004).

487 U. Burkert, N. L. Allinger, *Molecular Mechanics*, American Chemical Society, New York, (1982).

488 P. Comba, R. Remenyi, *Coord. Chem. Rev.*, **238–239**, 9, (2003).

489 H. M. Marques, I. Cukrowski, *Phys. Chem. Chem. Phys.*, **5**, 5499 (2003).

490 C. E. Skopec, J. M. Robinson, I. Cukrowski, H. M. Marques, *J. Mol. Struct.*, **738**, 67 (2005).

491 C. E. Skopec, I. Cukrowski, H. M. Marques, *J. Mol. Struct.*, **783**, 21 (2006).

492 A.J. Hopfinger, R.A. Pearlstein, *J. Comput. Chem.*, **5**, 486 (1984).

493 V.S. Allured, C.M. Kelly, C.R. Landis, *J. Am. Chem. Soc.*, **113**, 1 (1991).

494 M. Orozco, F. J. Luque, *J. Comput. Chem.*, **14**, 881 (1993).

495 J. Sabolovic, C. S. Tautermann, T. Loerting, K. R. Liedl, *Inorg. Chem.*, **42**, 2268 (2003).

496 A. Liwo, S. Oldziej, C. Czaplewski, U. Kozlowska, H. A. Scheraga, *J. Phys. Chem. B*, **108**, 9421 (2004).

497 D. Dubbeldam, S. Calero, T. J. H. Vlugt, R. Krishna, T. L. M. Maesen, E. Beerdsen, B. Smit, *Phys. Rev. Lett.*, **93**, 088302/1 (2004).

498 A. C. Vaiana, Z. Cournia, I. B. Costescu, J. C. Smith, *Comp. Phys. Commun.*, **167**, 34 (2005).

499 T. R. Cundari, W. Fu, E. W. Moody, L. L. Slavin, L. A. Snyder, S. O. Sommerer, T. R. Klickman, *J. Phys. Chem.*, **100**, 18057 (1996).

500 J. Hunger, G. Huttner, *J. Comput. Chem.*, **20**, 455 (1999).

501 P. Norrby, K. Warmark, B. Akermark, C. Moberg, *J. Comput. Chem.*, **16**, 620 (1995).

502 M. Atanasov, P. Comba, B. Martin, V. Müller, G. Rajaraman, H. Rohwer, S.Wunderlich, *J. Comp. Chem.*, **27**, 1263 (2006).

503 M. Reiher, O. Salomon, B. A. Hess, *Theor. Chem. Acc.*, **107**, 48 (2001).

504 P. Comba, G. Rajaraman, *Inorg. Chem.*, **47**, 78 (2008).

505 C. Diedrich, R. J. Deeth, *Inorg. Chem.*, **47**, 2494 (2008).

506 P. V. Bernhardt, P. Comba, *Inorg. Chem.*, **31**, 2638 (1992).

507 P. Comba, *Coord. Chem. Rev.*, **123**, 1 (1993).

508 R. J. Deeth, A. Anastasi, C. Diedrich, K. Randell, *Coord. Chem. Rev.*, 253, 795 (2009).

509 D. M. Root, C. R. Landis, T. Cleveland, *J. Am. Chem. Soc.*, **115**, 4201 (1993).

510 C. R. Landis, T. K. Firman, T. Cleveland, D. M. Root, in *Molecular Modeling and Dynamics of Bioinorganic Systems*, L. Banci, P. Comba (Eds.), Kluwer, Dordrecht, pp. 49 (1997).

511 T. K. Firman, C. Landis, *J. Am. Chem. Soc.*, **123**, 11728 (2001).

512 D. L. Kepert, *Inorganic Stereochemistry*, Springer, Berlin (1982).

513 T.W. Hambley, C.J. Hawkins, J.A. Palmer, M.R. Snow, *Aust. J. Chem.*, **34**, 45 (1981).

514 S.G. Taylor, M.R. Snow, T.W. Hambley, *Aust. J. Chem.*, **36**, 2359 (1983).

515 A. Dedieu, *Top. Organomet. Chem.*, **4**, 69 (1999).

516 S. Niu, M. B. Hall, *Chem. Rev.*, **100**, 353 (2000).

517 M. Torrent, M. Solà, G. Frenking, *Chem. Rev.*, **100**, 439 (2000).

518 A. Dedieu, *Chem. Rev.*, **100**, 543 (2000).

519 S. Sakaki, *Top. Organomet. Chem.*, **12**, 31 (2005).

520 P. E. M. Siegbahn, *Adv. Chem. Phys.*, **93**, 333 (1996).

521 A. Görling, S. B. Trickey, P. Gisdakis, N. Rösch, *Top. Organomet. Chem.*, **4**, 109 (1999).

522 D. Bacells, E. Clot, O. Eisenstein, *Chem. Rev.*, **110**, 749 (2010).

523 E. P. Wasserman, C. B. Moore, R. G. Bergman, *Science*, **255**, 315 (1992).

524 C. Hall, R. N. Perutz, *Chem. Rev.*, **96**, 3125 (1996).

525 S. Geftakis, G. E. Ball, *J. Am. Chem. Soc.*, **120**, 9953 (1998).

526 A. J. Cowan, P. Portius, H. K. Kawanami, O. S. Jina, D. C. Grills, X.-Z. Sun, J. McMaster, M. W. George, *Proc. Natl. Acad. Sci.*, U.S.A., **104**, 6933 (2007).

527 W. H. Bernskoetter, C. K. Schauer, K. I. Goldberg, M. Brookhart, *Science*, **326**, 553 (2009).

528 Z. Lin, Coord. *Chem. Rev.*, **251**, 2280 (2007).

529 R. A. Periana, G. Bhalla, W. J. Tenn, K. J. H. Young, X. Y. Liu, O. Mironov, C. Jones, V. R. Ziatdinov, *J. Mol. Catal. A*, **220**, 7 (2004).

530 P. T. Anastas, J. C. Warner, *Green Chemistry: Theory and Practice*; Oxford

University Press: Oxford, England; New York, (1998).

531 P. F. Fitzpatrick, *Annu. Rev. Biochem.*, **68**, 355 (1999).

532 A. M. Rocklin, D. L. Tierney, V. Kofman, N. M. W. Brunhuber, B. M. Hoffman, R. E. Christofferson, N. O. Reich, J. D. Lipscomb, L. Que Jr., *Proc. Natl. Acad. Sci.*, U. S. A., **96**, 7905 (1999).

533 L. M. Mirica, J. P. Klinman, *Proc. Natl. Acad. Sci.*, U. S. A., **105**, 1814 (2008).

534 J. E. Baldwin, M. Bradley, *Chem. Rev.*, **90**, 1079 (1990).

535 P. L. Roach, I. J. Clifton, C. M. Hensgen, N. Shibata, C. J. Schofield, J. Hajdu, J. E. Baldwin, *Nature*, **387**, 827 (1997).

536 W. A. Schenk, *Angew. Chem. Int. Ed.*, **39**, 3409 (2000).

537 M. D. Wolfe, J. D. Lipscomb, *J. Biol. Chem.*, **278**, 829 (2003).

538 M. B. Neibergall, A. Stubna, Y. Mekmouche, E. Münck, J. D. Lipscomb, *Biochemistry*, **46**, 8004 (2007).

539 J. M. Bollinger Jr., C. Krebs, *J. Inorg. Biochem.*, **100**, 586 (2006).

540 M. Costas, K. Chen, L. Que Jr., *Coord. Chem. Rev.*, **517**, 200–202, (2000).

541 C. Kim, K. Chen, J. Kim, L. Que Jr., *J. Am. Chem. Soc.*, **119**, 5964 (1997).

542 K. Chen, M. Costas, J. Kim, A. K. Tipton, L. Que Jr., *J. Am. Chem. Soc.*, **124**, 3026 (2002).

543 C. E. MacBeth, A. P. Golombek, V. G. Young Jr., C. Yang, K. Kuczera, M. P. Hendrich, A. S. Borovik, *Science*, **289**, 938 (2000).

544 C. A. Grapperhaus, B. Mienert, E. Bill, T. Weyhermüller, K. Wieghardt, *Inorg. Chem.*, **39**, 5306 (2000).

545 O. Pestovsky, S. Stoian, E. L. Bominaar, X. Shan, E. Münck, L. Que Jr., A. Bakac, *Angew. Chem. Int. Ed.*, **44**, 6871 (2005).

546 A. W. Johnson, I. T. Kay, *J. Chem. Soc.*, 1620 (1965).

547 E. Vogel, S. Will, A. S. Tilling, L. Neumann, J. Lex, E. Bill, A. X. Trautwein, K. Wieghardt, *Angew. Chem., Int. Ed. Engl.*, **33**, 731 (1994).

548 S. Will, J. Lex, E. Vogel, H. Schmickler, J. P. Gisselbrecht, C. Haubtmann, M. Bernard, M. Gross, *Angew. Chem., Int. Ed. Engl.*, **36**, 357 (1997).

549 J. H. Palmer, *Struct. Bonding* (Berlin, Ger.), **142**, 49 (2011).

550 R. Guilard, J.-M. Barbe, C. Stern, K. M. Kadish, in *The Porphyrin Handbook*, K.

M. Kadish, K. M. Smith, R. Guilard (Eds.), Elsevier Science: San Diego, Vol. 18; pp 303 (2003).

551 J. C. Dabrowiak, *Inor. Chim. Acta.*, **393**, 1 (2012).

552 G. W. Peterson, G. W. Wagner, *J. Porous Mater*, **21**, 121 (2014).

553 Y. C. Yang, J. A. Baker, J. R. Ward, *Chem. Rev.*, **92**, 1729 (1992).

CHAPTER 2

METHODOLOGY

CHAPTER 2

METHODOLOGY

2.1: Quantum mechanical calculations of atomic orbitals

The aim of a scientist is to explore new properties in a known material or to discover and characterize a novel substance displaying unique characteristics for service of the living world. These materials are made up of molecules, which are made up of atoms, which in turn are composed of electrons, protons and neutrons; classification may go on continuously through quark theory, field theory etc. While each nucleon possesses energy in its own manner, materials properties may primarily be attributed to electronic structure. While classical mechanics is capable of predicting trajectory of atoms, it finds itself inadequate to explain most properties at atomic level; quantum mechanics comes to the rescue. Though former aims at describing trajectory of a particle under study, latter aims at finding not an accurate motion but probability distribution function.While earlier works of Born, Hartree, Pauli, Dirac etc. helped in formal development of the subject during early stage, Schrodinger is undoubtedly the premier who helped build the foundation of the mechanics that was to have severe influence in what science has become today.[1] Modern day science is indebted deeply to Schrodinger for his celebrated wave equation [2]

$$H\psi = E\psi \qquad (2.1)$$

Here H represents Hamiltonian operator of the system-comprising of kinetic energy and potential energy term, E is eigen value representing energy and ψ represents eigen function. ψ is well behaved mathematical function such that $\psi^*\psi$ represents probability density.[3] While this equation is solvable for hydrogen or hydrogen-like atom easily-with little or no approximation- depending on property of interest. Howsoever simple equation it may be and capable of correctly describing the system fully, the only problem lies in solving it for a given system. In fact, it is beauty of this equation that almost any molecular system can be explained by merely solving it completely and yet, the basic problem lies with method of solving it.

Even for the simplest system like Hydrogen atom, the motion of constituents of system viz electrons and nucleus (the eigen function) may be represented by total wave function comprising of electronic as well as nuclear wave function. The Hamiltonian may be expanded as:

$$H = -\sum_i \frac{\hbar^2}{2m_e}\nabla^2 - \sum_A \frac{\hbar^2}{2m_A}\nabla^2 - \sum_i \sum_A \frac{Z_A e^2}{r_{iA}} + \sum_{i<j} \frac{e^2}{r_{ij}} + \sum_{A<B} \frac{Z_A Z_B e^2}{r_{AB}} \qquad (2.2)$$

where i, j represent summation over electrons while A, B stand for nucleus. First and second terms represent kinetic energy of electrons and nucleus, third term stands for electron-nucleus potential energy, while fourth and fifth terms denote inter-electron and inter-nucleon interaction energy. After Born-Oppenheimer's realization that electrons adjust instantaneously with any changes in nucleus, the Schrodinger's equation was resolved by variable separable method, it got solvable for electronic wave function separately for a given arrangement of nucleus.[4-6]

Changing nuclear positions necessitates addition of nuclear repulsion term to electronic energy to get correct total energy of new configuration. Although variation in nuclear position may be dealt-with easily in atoms, scenario complicates in energy levels of even the simplest molecule (e.g. diatomic or linear multi-atomic etc.). As has been discussed earlier that Hamiltonian comprises of (a) kinetic energy as well as (b) potential energy term also, which is sub-divided into (i) nucleus-nucleus interactions (ignored due to Born-Oppenheimer approximation), (ii) electron-nucleus potential energy and (ii) inter-electron interaction energy; it is this last term that creates complexity. Hamiltonian due to electrons only is written as:

$$H_e = -\sum_i \frac{1}{2}\nabla_i^2 - \sum_A \sum_i \frac{Z_A}{r_{iA}} + \sum_{i<j} \frac{1}{r_{ij}} \qquad (2.3)$$

Here first term is kinetic energy, second term is nucleus-electron potential energy and last term is electron-electron interaction energy. With this H_e in hand, one gets E_e and ψ_e as solution. Thus the modified Schrodinger wave equation for n electron system is written as: [7]

$$H_e(1,2,...,n)\psi_e(1,2,...,n) = E_e\psi_e(1,2,...,n) \qquad (2.4)$$

It should be noted, this gives only the electronic part and not the nuclear part. The results obtained at electronic equation are used to get total energy and total wave function of given system. Nuclear interactions do not play important role in atomic wave functions but become important in molecular wave functions (commonly called as molecular orbitals).

Multi-electron systems are solvable only with approximation methods and many workers have proposed numerous methods for solving it. D. R. Hartree made earliest attempts in 1928 by assuming the total wave function to be product of wave functions of individual electrons (assuming Z-electron atom): [8]

$$\psi_e(r_1,\theta_1,\phi_1;r_2,\theta_2,\phi_2;\ldots;r_z,\theta_z,\phi_z)=\psi_1(r_1,\theta_1,\phi_1)\psi_2(r_2,\theta_2,\phi_2)\ldots\psi_z(r_z,\theta_z,\phi_z) \quad (2.5)$$

As Schrodinger's equation involves potential energy operator which if known will provide wave function and eigen value. But potential energy term is not known fully for such system. Also wave function must carry coordinates for all Z-electrons. Variable separable method would guarantee Z-independent linear differential equations from a single Schrodinger's equation for Z-electron atom (ignoring electron-electron potential term), which may later be solved by beginning with an approximate trial solution and solving for a field which converges to certain value after substantial number of iterations, commonly called as self consistent field. Alternatively, variational principle may be used to get desired solutions. However application of such trial wave function was soon discarded due to such total wave function not being anti-symmetric- a condition imposed by Pauli's exclusion principle. After Fermi-Dirac statistics,[9] electrons were assumed to possess spatial as well spin functions:

$$\Psi_{tot}=\psi(\vec{r})\times\xi(s) \quad (2.6)$$

Here $\psi(\vec{r})$ represents spatial wave function while $\xi(\vec{s})$ stands for spin wave function (commonly represented by α .or β).[10] Slater devised a method for obtaining such total electron wave functions (anti-symmetric) [11] from spatial and spin coordinates with the help of so-called Slater determinant: [12]

$$\psi = \frac{1}{\sqrt{N!}} \begin{vmatrix} \phi_1(r_1)\alpha(s_1) & \phi_2(r_1)\beta(s_1) & \cdots & \cdots & \cdots & \phi_n(r_1)\beta(s_1) \\ \phi_1(r_2)\alpha(s_2) & \phi_2(r_2)\beta(s_2) & \cdots & \cdots & \cdots & \phi_n(r_2)\beta(s_2) \\ \cdots & \cdots & \cdots & & & \cdots \\ \cdots & \cdots & & \cdots & & \cdots \\ \cdots & \cdots & & & \cdots & \cdots \\ \phi_1(r_n)\alpha(s_n) & \phi_2(r_n)\beta(s_n) & & & & \phi_n(r_n)\beta(s_n) \end{vmatrix} \tag{2.7}$$

Alternatively,

$$\psi = \frac{1}{\sqrt{N!}} \begin{vmatrix} \chi_1(1) & \chi_2(1) & \cdots & \cdots & \cdots & \chi_N(1) \\ \chi_1(2) & \chi_2(2) & \cdots & \cdots & \cdots & \chi_N(2) \\ \cdots & \cdots & \cdots & & & \cdots \\ \cdots & \cdots & & \cdots & & \cdots \\ \cdots & \cdots & & & \cdots & \cdots \\ \chi_1(N) & \chi_2(N) & & & & \chi_N(N) \end{vmatrix} \tag{2.8}$$

Using Slater's method, Hartree and Fock improvised the method of Self-consistent field theory, whereby each electron is assumed as moving in a fixed field arising due to nucleus and remaining electrons. This method proved to be a great success as the electron-electron interaction term posed a severe hindrance in variable separation method. The energy of the atom or molecule is given by:

$$E = \frac{\int \psi^* H \psi d\tau}{\int \psi^* \psi d\tau} \tag{2.9}$$

or, in Dirac Notation,[13-15]

$$E = \frac{\langle \psi \mid H \mid \psi \rangle}{\langle \psi \mid \psi \rangle} \tag{2.10}$$

Besides being anti-symmetric, the wave functions are assumed to be ortho-normal:

$$\int \psi_m^* \psi_n d\tau = \delta_{mn} \qquad \text{OR} \qquad \langle \psi_m | \psi_n \rangle = \delta_{mn} \tag{2.11}$$

2.2: Hartree Self-consistent field method

As stated earlier, nucleus is much heavier than electron, hence nuclear contribution in Hamiltonian does not play important role in atoms. However in molecules, configuration of nucleus of atoms adds to nuclear potential. Though Born-Oppenheimer helped in resolving such problem, this field (having constant value for a given geometry) must be added appropriately to get total energy and total wave function of the molecule.[16-17]

The Hamiltonian for N-electron system may be re-written as:

$$H_e = \sum_i h_i + \sum_i \sum_{j>i} g_{ij} + V_{nn} \tag{2.12}$$

where

$$h_i = -\frac{1}{2}\nabla^2 - \sum_A \frac{Z_A}{|R_A - r_i|} \tag{2.13}$$

and

$$g_{ij} = \frac{1}{|r_i - r_j|} \tag{2.14}$$

Note that one electron operator h_i describes the motion of the ith electron in the field of all nuclei of given molecule and must be the only operator in absence of any inter electronic or inter nuclear interaction, g_{ij} is two electron operator giving mutual repulsion between two electrons while V_{nn} is nuclear-nuclear interaction energy. From Dirac's notation for energy,

$$E = \sum_i \langle \chi_i \mid h_i \mid \chi_i \rangle + \frac{1}{2} \sum_{i,j} \left(\langle \chi_i \chi_i \mid g_{ij} \mid \chi_j \chi_j \rangle - \langle \chi_i \chi_j \mid g_{ij} \mid \chi_i \chi_j \rangle \right) + V_{nn} \qquad (2.15)$$

Alternatively, it may be written as

$$E = \sum_i \langle \chi_i \mid h_i \mid \chi_i \rangle + \sum_{i<j} \left(J_{ij} - K_{ij} \right) + V_{nn} \qquad (2.16)$$

Here first term represents energy due core Hamiltonian operator in absence of any interaction, J_{ij} represents Coulomb operator (classically it is repulsion between two charge distributions), K_{ij} represents exchange operator (for which there is no classical analogue and is a result of Pauli's exclusion principle).[18] Evidently, this is many body problem (unlike Hydrogen atom, which is at most a two body problem) for which there is no 'exact' solution. Hence one solution can only be 'better' than another. To determine the Molecular Orbital (MO) which has minimum energy (stable configuration), variational principle is used. A better wave function will have minimum energy lesser than a less 'correct' one. Such type of optimization is obtained subject to constraint that MOs should remain orthogonal and normalized. For this, Lagrange's method of undetermined multipliers may be used.[16,19] Thus the problem is minimization of energy subject to orthonormality constraint:

$$S_{ij} = \int \chi_i \chi_j d\tau = \langle \chi_i \mid \chi_j \rangle = \delta_{ij} \qquad (2.17)$$

The Lagrange function will now be stationary with respect to variations in orbitals:

$$L = E - \sum_{i,j} \lambda_{ij} \left(\langle \chi_i \mid \chi_j \rangle - \delta_{ij} \right) \qquad (2.18)$$

For extremum of Lagrange function:

$$\delta L = \delta E - \delta \sum_{i,j} \lambda_{ij} \left(\langle \chi_i \mid \chi_j \rangle - \delta_{ij} \right) = 0 \qquad (2.19)$$

Here λ_{ij} is often identified as energy and related to molecular orbital energies. Under such formulation, one is now forced to find solution which takes into consideration motion of all electrons simultaneously, which in turn are so interconnected that change in one's coordinates (spatial or spin) is bound to affected others as well. To avoid such difficulty, one is forced to consider motion of one electron under the influence of field of nuclei and other electrons in their fixed orbitals χ_j. The resulting equation may then be tidied up as follows:[16,20]

$$F_i \chi_i = \sum_j \varepsilon_{ij} \chi_j \qquad (2.20)$$

where F_i is called Fock operator:

$$F_i(1) = h_i(1) + \sum_j \left(J_j(1) - K_j(1) \right) \qquad (2.21)$$

Here 1 in parentheses denotes operator for one particular electron, J is Coulomb operator (electron repulsion term) and K is exchange operator (spin correlation term). If Lagrangian multipliers are chosen zero unless indices i and j are same, one gets standard eigen value problem:

$$F_i \chi_i = \varepsilon_i \chi_i \qquad (2.22)$$

It should be noted that solutions of above equations are not unique as determinant is unaffected by row/column transformations. Also, Fock operator is evaluable only if orbitals of remaining electrons are known. To counteract this vicious cycle, iterative method is employed which assumes trial solutions to get Fock operator (via Coulomb and Exchange operators) till solutions are 'self-consistent'. The Hartree Fock method is also known as mean field approximation method in which average electron-electron repulsion is taken into account.[21]

2.3: Roothaan Hall equation

Fock proposed extension of Hartree's SCF procedure by introducing Slater's determinantal wave functions (obeying Pauli's exclusion principle). Although very elegant method for solving atoms, direct solution of Hartree Fock equation was not so practical for molecules. Roothaan and Hall independently recast the HF equation in matrix form by expanding MOs in terms of basis functions, conveniently called as atomic orbitals. This method is advantageous as it also helps in interpretability of results as properties of molecules are commonly traced back to those of constituent atoms. In this scheme, spatial wave function is expressed as linear combination of basis functions:

$$\phi_i = \sum c_{\mu i} \theta_\mu \qquad (2.23)$$

Energy minimization techniques help in evaluation of coefficients $c_{\mu i}$. Thus one gets a set of self consistent LCAO molecular orbitals ϕ_i. Such orbital will be best for any particular set of basis function. Roothaan Hall equation is obtained after variational technique: [22]

$$\sum_{\nu}\left(F_{\nu\mu}-\varepsilon_i S_{\nu\mu}\right)C_{\nu i}=0 \qquad (2.24)$$

where $F_{\nu\mu}$ is the Fock operator and $S_{\nu\mu}$ is the overlap integral:

$$F_{\nu\mu}=\left\langle\theta_\nu \mid h \mid \theta_\mu\right\rangle+\sum_{\gamma}^{AO}\sum_{\delta}^{AO}D_{\gamma\delta}\left(\left\langle\theta_\nu\theta_\gamma \mid g \mid \theta_\mu\theta_\delta\right\rangle-\left\langle\theta_\nu\theta_\gamma \mid g \mid \theta_\delta\theta_\mu\right\rangle\right) \qquad (2.25)$$

$$S_{\nu\mu}=\left\langle\theta_\nu \mid \theta_\mu\right\rangle \qquad (2.26)$$

The density matrix is defined as

$$D_{\gamma\delta}=\sum_{j}^{occ.MO}C_{\gamma j}C_{\delta j} \qquad (2.27)$$

These equations were originally developed by Roothaan [22] and Hall [23] independently. Equations as mentioned above are a set of algebraic equations conveniently written as a matrix equation:

$$FC=SCE \qquad (2.28)$$

The Fock matrix and C matrix are square matrix while E is a diagonal matrix whose elements are the orbital energies. Here the elements of Fock matrix depend on orbital coefficients $c_{\mu i}$ which appears on both sides of matrix equation, hence iterative procedure is adopted.[16]

Roothaan-Hall equation can be simplified to a form solvable by standard methods:

$$F'C'=C'E \qquad (2.29)$$

where $F'=S^{-1/2}FS^{-1/2}$ and $C'=S^{1/2}C$ (2.30) and solution exists only if determinant $\left|F'-EI\right|$ is zero. For larger matrices, diagonalization of matrix F' is preferred. The matrix of coefficients C' gives eigen vectors of F'.

2.4: Computational scheme for solving Roothaan Hall equation

Schrodinger equation is solved in Hartree-Fock method by setting up equations to solve all individual one-electron wavefunctions:

$$F_i(1)\phi_i(1) = \varepsilon_i \phi_i(1) \tag{2.31}$$

where 1 within parenthesis represents one electron equation. With certain basis set at hand, trial wave functions are formulated to get overlap matrix S_{ij} and Fock matrix F_{ij}. These are then used to calculate energy ε_i and coefficients $c_{\nu i}$ and iteration is followed until desired convergence is achieved. The motion of electrons is not correlated in HF equations.[24] The electron correlation is included in configuration interaction (CI) [25,26] and Møller-Plesset [27] perturbation theory.

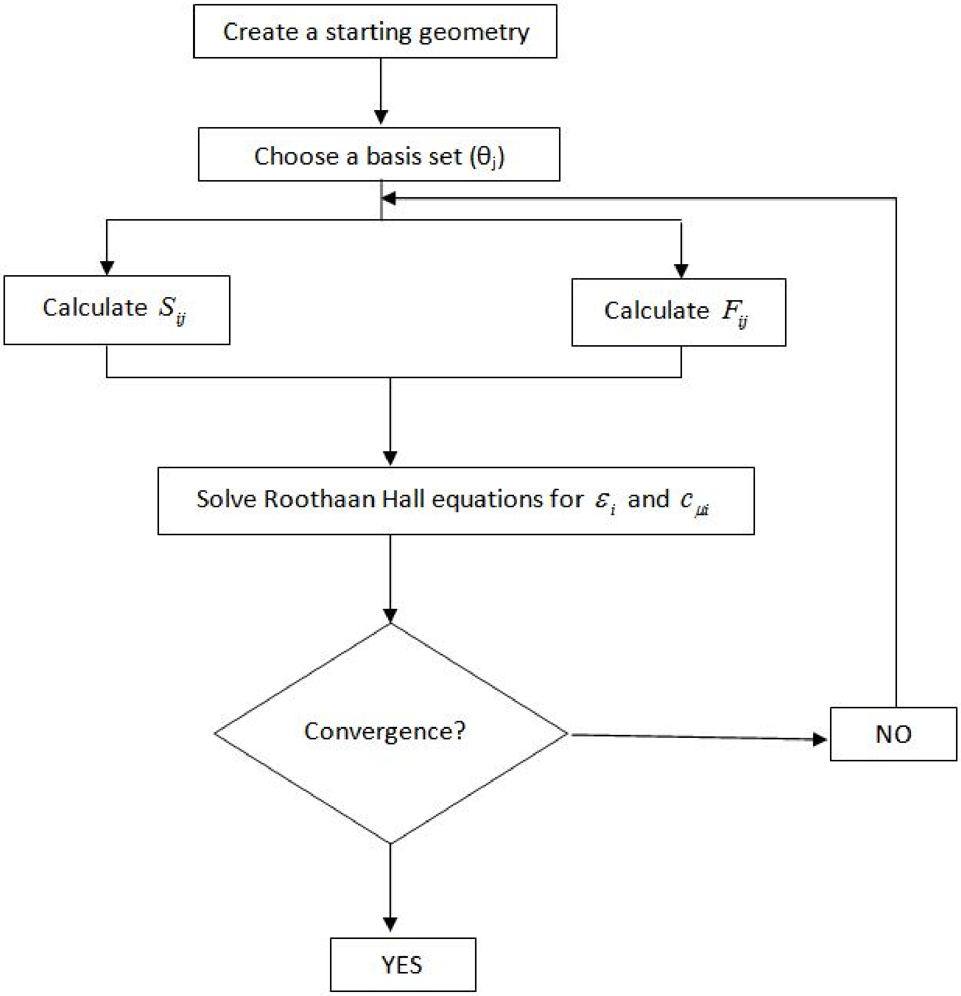

Figure 2.1: Algorithm for solving Roothaan Hall equation

2.5: Basis set

A basis set is a set of functions used to describe the shape of orbitals in an atom or a molecule. In principle, a complete set must represent orbitals completely and use of infinite number of basis functions may be necessary to get Hartree Fock energy close to that given by variational principle. Such proposition is not computationally feasible leading to unavoidable basis set truncation error. Hence it will be necessary to choose lesser basis functions set (to reduce computational costs) and to choose them cleverly (to minimize computational effort by getting simpler integrals) yet getting least possible error. The atomic functions prove to be the obvious choice for basis functions. For diatomic molecules, atomic orbitals are chosen as basis functions, some centered on one atom, others on the other atom. In an approach commonly called as Linear Combination of Atomic Orbitals (LCAO),[28] each atomic orbital can be represented as a linear combination of one or more Slater-type Orbitals (STOs); [29,30] and is used to describe the molecular wave functions. Here a set of virtual atomic orbitals is also chosen besides all occupied orbitals:

$$\phi_i = \sum_r c_{ri} \chi_r \tag{2.32}$$

Clearly, the number of active and virtual orbitals taken decides the quality of molecular orbitals thus obtained. This choice is crucial so that calculated energy gets converged within the basis set limit.

STOs are a general class of chosen basis sets. The STO for an s-type atomic orbital has form:

$$S(r) = N_s e^{-\zeta r} \tag{2.33}$$

where r is radial distance from the nucleus, N_s is normalization constant, and constant ζ is known as the orbital exponent governing the size of the orbital. Another popular choice of basis set is Gaussian-type Orbital (GTO) [16,31] which has given form for s-type atomic orbital:

$$g(r) = N_g e^{-\zeta r^2} \tag{2.34}$$

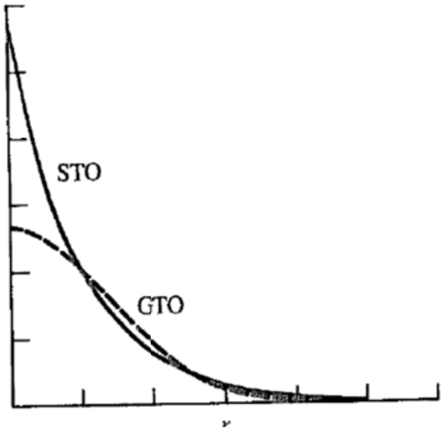

Figure 2.2(a): 1s STO and best Gaussian equivalent.

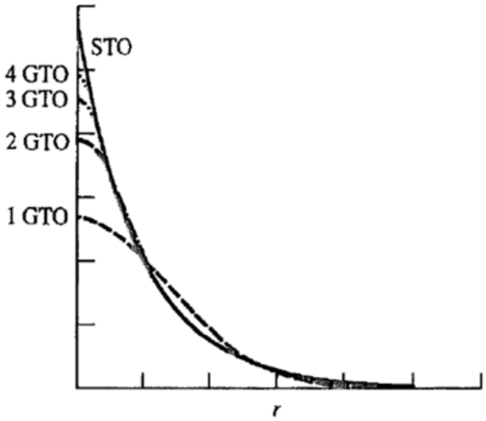

Figure 2.2(b): Comparison of 1s STO and Gaussian expansions with upto four terms.

To obtain higher orbital basis functions, the STO or GTO is multiplied by appropriate exponents of coordinates to produce p-type, d-type or higher functions. A general GTO has following form in Cartesian:

$$g(r) = N_g x^a y^b z^c e^{-\zeta r^2} \tag{2.35}$$

where values of a, b and c are chosen appropriately for desired orbital type. During the SCF convergence of a molecule, atomic orbitals mix to form molecular orbitals.

The STO basis set provides direct physical interpretation and is naturally good basis set for molecular orbitals. Unfortunately they are not implemented in molecular orbital calculations because required integrals to be calculated in SCF procedure are computationally expensive. The corresponding integrals are quite simple in GTO basis set, although it is susceptible to underestimating values near and far away from nucleus. This problem may however be solved by using linear combination of Gaussian functions.

It can be seen that Gaussian expansion contains two parameters: contraction coefficients and exponents. In molecular orbital calculations, both parameters are allowed to vary and such calculation is said to use uncontracted or primitive Gaussians. If these are predetermined and remain constant and number of terms in expansion is contracted, this is called contracted Gaussian function.

A minimal basis set is a set constructed with just the number of functions required to accommodate all filled orbitals in the shell.[32] It uses one basis function for each type of occupied orbital. It has been found that at least three Gaussian functions are required to represent STO closely. STO-3G is the most commonly used minimal basis set. This notation indicates that basis set approximates shape of STO by single contraction of three GTO orbitals. It has been proved to be absolute minimum in molecular orbital calculations. In general STO-nG basis set is minimal basis set in which n Gaussian functions are used to represent each orbital (in general n=2-6). However, such minimal basis set is not helpful in representing compounds containing atoms at the end of a period and are unable to describe non-spherical electronic distribution. This problem is solved by using more than one function for each orbital. Such an increase in the number of basis functions also helps in getting closer to exact energy value.

One is thus led to construct basis sets which have more basis function than the number of basis functions in minimal basis set. The Double Zeta (DZ) basis set uses two basis functions of each type of minimal basis functions for the separated atoms, differing in their orbital exponents ζ. This type of basis set is generally sufficient in DFT calculations for geometry optimizations.[33] The coefficients of hybrid density functional theory were benchmarked against the experimental data using calculations through double-ζ quality basis set. In a slight variation of this method, only double number of functions is used to describe valence electrons but single function is used for inner shell. It is called slit valence double-ζ basis set and is useful in non-isotropic charge distribution. For instance in 3-21G, three Gaussian functions describe the core orbitals, while valence electrons are represented by three Gaussians: the contracted part by two Gaussians and the diffuse part by one Gaussian. Other methods include triple-ζ, quadrupole-ζ etc. which may not necessarily improve the calculations.

The charge around atom in a molecule is usually perturbed than in an isolated atom. This distortion can be attributed to mixing of character of other type of orbitals (occupied or unoccupied) into occupied orbitals. Use of polarization functions into basis set helps in solving problem and generally comprises of higher angular momentum orbital (normally unoccupied) and are indicated by '*'. They give wave functions with more flexibility to change shape. For molecular systems having electron density significantly away from nucleus (anions, lone pairs etc.), highly diffuse functions are added to the basis set and are indicated by '+'. These diffuse functions are primitives with small exponents (resulting in large spread of Gaussian function). The effect of adding diffuse functions is to usually change the relative energies of the various geometries associated with these systems. Such basis sets with diffuse functions are also called augmented basis sets.[34,35]

The Pople basis set [34,36] is another family of basis sets denoted by 6-31G, popular for organic molecules. It indicates that each core orbital is described by a single contraction of six GTO primitives which describe each core orbital and two contractions, of which one with three primitives and another with one primitive describe each valence shell orbital. It is sometimes modified to 6-31G* or 6-31G**. A single asterisk (*) indicates addition of d primitives to atoms other than hydrogen while two asterisks mean that a set of p primitives has been added to hydrogen as well. One or two plus signs can also be added (6-31+G* or 6-31++G*). A single plus (+) sign indicates addition of diffuse functions to atoms other than hydrogen while two plus signs indicate diffuse function for all atoms.

To account for presence of large number of electrons in transition metals, several special basis sets have also been developed. They include an effective core potential (ECP) [37] for accounting all electrons. As core electrons do not participate in bond formation, an electric potential in Hamiltonian replaces such orbitals in the ECP treatment. Relativistic corrections may also be incorporated to improve energies. For iron, typical ECP containing basis sets are from Los Alamos type, eg., LACVP or LANL2DZ.[38] In our work, triple-ζ basis set (LACV3P+) has also been used that employs diffuse and polarization functions on metal. Kumar *et al.* [39] have used two different basis sets, namely BS1 (double-ζ on iron and 6-31G on the rest of the atoms) and BS2 (triple-ζ on iron and 6-311+G* on the rest of the atoms) in a test calculation on substrate hydroxylation potential energy profile by a Cpd I model of cytochrome P450. This resulted in very little changes in optimized geometries and virtually identical relative energies along a reaction profile. As such, geometries are usually optimized using double-ζ basis set followed by single point energy calculations with a triple-ζ basis set.

2.6: Density functional theory

The *ab initio* methods provide excellent technique in molecular orbital calculation using HF approximation but are computationally difficult due to involvement of large basis sets. In contrast to obtaining eigen functions and eigen values by this quantum mechanical method, Kohn *et al.* argued for obtaining such results using functional of electron density.[40] A functional enables a function to be mapped to number:

$$Q[f(r)] = \int f(r)dr \tag{2.36}$$

The key idea is that the energy of a given electronic system can be written in terms of electron probability density. It was proved that ground-state molecular energy, wave function and all other molecular electronic properties are uniquely determined by the ground state electron probability density. This methodology has proven quite successful due to being computationally inexpensive while providing results in close agreement with experimental values for relatively large systems.[41] It is popular because it acts as an alternative to HF methods and takes care of electron correlation as well. The concept of electron density proved extremely useful in early but approximate model by Thomas and Fermi. A major development in DFT came when a set of one-electron equations were derived from which electron density could be obtained. In this calculation, total energy is split into kinetic energy term, electron-nucleus interaction energy term, electron-electron Coulombic term and an exchange correlation term (E_{XC}).[41,42] The first three terms resemble terms in Hartree-Fock Hamiltonian:

$$H_e = -\sum_i \frac{1}{2}\nabla_i^2 - \sum_A \sum_i \frac{Z_A}{|R_A - r_i|} + \sum_{i<j} \frac{1}{|r_i - r_j|} + E_{XC} \tag{2.37}$$

$$E_{el} = \sum_{i=1}^{N} \int \psi_i(r) \left(-\frac{\nabla^2}{2} \right) \psi_i(r) dr - \sum_{A=1}^{M} \int \frac{Z_A}{|R_A - r|} \rho(r) dr + \frac{1}{2} \iint \frac{\rho(r_1)\rho(r_2)}{|r_1 - r_2|} dr_1 dr_2 + E_{XC}(\rho(r)) \tag{2.38}$$

Hohenberg and Kohn proved that for an extremely slowing varying density with position, $E_{XC}[\rho]$ is accurately given by

$$E_{XC}^{LDA}[\rho] = \int_V \rho(r) \varepsilon_{XC}(\rho) d\tau \tag{2.39}$$

where LDA stands for Local-Density Approximation, $\varepsilon_{XC}(\rho)$ is the exchange plus correlation energy per electron in a homogeneous electron gas with electron density ρ.

Kohn and Sham assumed the density of the system as the sum of square moduli of a set of one-electron orthonormal orbitals:

$$\rho(r) = \sum_i |\psi_i(r)|^2 \tag{2.40}$$

Using such electron density and applying variational principles gives one-electron equation as:

$$\left\{ -\frac{1}{2}\nabla^2 - \left(\sum_{A=1}^{M} \frac{Z_A}{r_{1A}} \right) + \int \frac{\rho(r_2)}{r_{12}} dr_2 + V_{XC}[r_1] \right\} \psi_i(r_1) = \varepsilon_i \psi_i(r_1) \tag{2.41}$$

where

$$V_{XC}[r] = \left(\frac{\delta E_{XC}[\rho(r)]}{\delta \rho(r)} \right) \tag{2.42}$$

Now self-consistent approach may be adopted in above equation beginning with trial electron density to get a set of orbitals. Convergence for density is tested and total energy is hence evaluated.

The exchange-correlation functional is not known *apriori*, so approximate equations are set-up to estimate its contribution. It is generally split into an exchange functional (E_X) and a correlation functional (E_C). While former represents interactions of two ferromagnetic spins in different orbital, latter denotes pairing energy of electrons in same orbital.[43,44] The exchange energy is usually estimated from the Slater exchange function:

$$E_X^{Slater} = -\frac{9}{4\alpha_{ex}}\left(\frac{3}{4\pi}\right)^{1/3}\sum_{\gamma}\int\left[\rho_1^{\gamma}(r_1)\right]^{4/3}dr_1 \qquad (2.43)$$

Here, α_{ex} is an exchange scale factor, which has the value 2/3 for electron gas.

Commonly used correlation energy functional E_C^{VWN} is attributed to works by Vosko, Wilk and Nusair. For a gas with spin densities ρ_1^{α} and ρ_1^{β} , it represents correlation energy per electron $\varepsilon_c\left[\rho_1^{\alpha},\rho_1^{\beta}\right]$:

$$E_C^{VWN} = \int \rho_1(r_1)\varepsilon_c\left[\rho_1^{\alpha}(r_1),\rho_1^{\beta}(r_1)\right]dr_1 \qquad (2.44)$$

Combination of Slater exchange and Vosko-Wilk-Nusair correlation gives Local Density Approximation. Both are derived directly from homogeneous electron gas equations. To correct the non-local terms, better exchange and correlation functionals have been developed by various workers. Lee, Yang and Parr (LYP correlation functional),[44] Perdew and Wang (PW91 correlation functional) [45] and Becke (B96 correlation functional) [46] are the popular ones among others, each having their own merits and/or demerits.

Becke developed the hybrid density functional procedures.[47] This proved a great breakthrough in DFT as he was able to benchmark DFT methods against a test set of experimentally known ionization energies, electron affinities and proton affinities with high accuracy. Contributions of exchange and correlation functions were estimated using a three parameter (hybrid) density functional method. These fit parameters (A, B and C) were optimized against the experimental data in the test set. Out of many possibilities combining the various exchange and correlation functionals, B3LYP method has emerged as most popular one throughout the years, although it may not necessarily be the most accurate one. Essentially the hybrid density functional method B3LYP has the following form:

$$E_{XC}^{B3LYP} = AE_X^{Slater} + (1-A)E_X^{HF} + B\Delta E_X^{Becke} + E_C^{VWN} + C\Delta E_C^{LYP} \tag{2.45}$$

Thus it is hybrid in sense that it takes the LDA functions of Slater and Vosko-Wilk-Nusair, the Hartree-Fock exchange, a correction term to the exchange due to Becke and, Lee-Yang-Parr correction for non-local correlation factors. The coefficients A, B and C are essentially fit-parameters obtained through fitting the energies of B3LYP/6-31G* calculations against experimentally obtained ionization energies and electron affinities. Consequently, B3LYP method is not truly an *ab initio* method. In strict sense, the term *ab initio* means starting from scratch without prior knowledge of experiment. However, these fit-parameters have created an accurate and low-cost computational method and as a result B3LYP has emerged as one of the widest used techniques in science over the past decade. The hybrid as well as non-hybrid DFT methods (including B3LYP) have been tested to be extremely accurate and versatile in computational techniques. Although high level *ab initio* methods such as coupled cluster method (CC, CCD, CCSD,…), Møller

Plesset perturbation theory (MBPT, MP, MP2, …) etc. promise good results than DFT calculations, their speed in combination with reasonable accuracy makes them a very popular and useful methodology.

This technique has developed over years so much that fitting parameters have improved considerably by enlarging the test set. In his original paper, Becke already published calculated energies within 2 kcal/mol of experimental values. Pople *et al.* have defined ultimate accuracy goal of computational chemisty to 1 kcal/mol.[7] Hence DFT has become one of the most extensively used methods in Chemistry which combines reasonable accuracy with speed. In fact, B3LYP methodology presents a considerable improvement over HF as well as MP2 calculations.[48] In some cases DFT is capable of reproducing results obtained with much more computationally demanding G2 methodology of Pople *et al.* Clearly DFT provides a low-cost alternative to quantum mechanical procedures and is highly suitable candidate for performing calculations on biochemical systems.[49]

2.7: Solvent effects

The quantum mechanical calculations refer to an isolated molecule or for gas-phase. However reactions in a laboratory generally occur in solutions. The molecule under study may induce polarization in the solvent molecules lying in its vicinity, generating an electric field that may tend to distort the solute's molecular electronic wave function from what it was in the gas phase. Thus molecular properties in solution will tend to differ to some extent from those in gas-phase. Solvent effect may be dealt with by rigorous calculations on molecular properties on system comprising of solute molecule surrounded by many solvent molecules and re-optimizing resulting structures. But solvent molecules may exist in several conformations.[50] Various methods are proposed for mimicking solvent into the calculations (Continuum solvent model, Quantum-Onsager self consistent reaction field method, multipole expansion method etc.) but they prove computationally expensive and time consuming. Hence instead of adding solvent molecule, it is deemed better to add solvent corrections to energetics using implicit solvent model. This can be done at single point level (energy is recalculated with a solvent model on gas-phase optimized geometry) or by re-optimizing structure using a solvent model.

Software packages like Gaussian and Jaguar include solvent models like Polarizable Continuum Model (PCM) [51] wherein calculations are done by assuming solvent as a perturbation of the molecule with a dielectric constant. The molecular structure of the solvent is ignored and the solvent is modeled as a continuous dielectric of infinite extent that surrounds a cavity containing the solute molecule. The molecule is assumed to be placed in a cavity surrounded by dielectric continuum. The cavity is described as the area around the molecule that contains less than pre-defined amount of electron density of the molecule and is often based on van der Waals radii of atoms. The classical Poisson equations are then used to calculate the electronic potential arising from the molecule-solvent interactions using a defined dielectric constant.

References:

1 L. I. Shiff, *Quantum Mechanics*, 3rd edition, McGraw- Hill, NewYork (1968).

2 E. Schroedinger, *Ann. Physik,***79**, 361 (1926).

3 L. Pauling, E. B. Wilson, *Introduction to Quantum Mechanics,* McGraw-Hill, New York (1935).

4 M. Born, J. R. Oppenheimer, *Ann. Physik,* **84**, 457 (1927).

5 W. Kolos, L.Wolniewicz, *J. Chem. Phys.,***41**, 3663 (1964).

6 B. T. Sutsliffe, *Adv. Quantum. Chem.,***28**, 65 (1997).

7 J. A. Pople , D. L. Beveridge, *Approximate Molecular Orbital Theory*, McGraw-Hill Book Co., New York (1970).

8 D. R. Hartree, *Proc. Cambridge Phil. Soc.,* **24:** 89, 111, 426 (1928).

9 G. Uhlenbeck, S. Goudsmit, *Nature wissenschaften*, **13**, 953 (1925).

10 J. A. Pople, D. L. Beveridge, P. A. Dobosh, *J. Chem. Phys.*, **47**, 2026 (1967).

11 W. Pauli, *Z. Physik.*, **31**, 765 (1925).

12 J. C. Slater, *Phys. Rev.*, **35**, 509 (1930) and **34**, 1239 (1959).

13 P. A. M. Dirac, *The Principle of Quantum Mechanics*, Oxford University Press, London (1958).

14 J. K. L. McDonald, *Phys. Rev*., **43**, 830 (1933).

15 R. H. Young*, Int. J. Quant. Chem*., **6**, 596 (1972).

16 F. Jenson, *Introduction to Computational Chemistry,* 2nd edition, John Wiley & Sons Ltd., Chichester (2007).

17 I. N. Levine, *Quantum Chemistry*; Chapter-11, *"The HartreeFock Self- Consistent Method"*, 5th edition, Pearson, (2000).

18 I. N. Levine, *Quantum Chemistry.*, Chapter-8, "Perturbation Theory", Pearson, 5th edition (2000).

19 J. A. Pople, D. L Beveridge, *Z. Physik.*, **61**, 126 (1930).

20 J. E. Lennard-Jones, *Proc. Roy. Soc. (London)*, **A198,** 14 (1949).

21 C. Edimiston, K. Ruedenberg, *Rev. Mol. Phys.,* **34**, 457 (1963); J. *Chem. Phys.,***43**, 597 (1965).

22 C. C. Roothan, *J. Rev. Mod. Phys.,* **23**, 69 (1951).

23 G. G. Hall, *Proc. Roy. Soc., (London),* **A205**, 541 (1951).

24 W. J. Hehre, L. Radom, J. A. Pople, P.v.R. Schleyer, *Ab Initio Molecular Orbital Theory*, Wiley (1986).

25 B. O. Roos, (Ed.) *Lecture Notes in Quantum Chemistry,* Springer –Verleg (1992).

26 J. Olsen, O. Christiansen, H. Koch, P. Jorgensen, *J. Chem. Phys. Lett.*, **261**, 369 (1996).

27 C. Moller, M. S. Plesset, *Phys. Rev.,* **46**, 618 (1934).

28 E. Hückel, *Z. Physik.*, **70**, 204 (1931).

29 D. Feller, E. R. Davidson*, Rev. Comp. Chem.,* 1 (1990).

30 T. Helgaker, P. R. Taylor, "*Modern Electronic Structure Theory*", Part II, D. Yarkony (Ed.), World Scientific, pp. 727 (1995).

31 S. F. Boys, *Proc. Roy. Soc.,* (London), **A 200**, 542 (1950).

32 W. J. Hehre, R. F. Stewart, J. A. Pople, *J. Chem. Phys.*, **51**, 2657 (1969).

33 T. H. Dunning Jr. and P. J. Hay, *Modern Theoretical Chemistry*, H. F. Schaefer III (Ed.), Vol. 3, pp. 1, Plenum, New York (1977).

34 J. S. Binkley, J. A. Pople, *J. Am. Chem. Soc.*, **102**, 939 (1980).

35 W. J. Hehre, R. Ditchfield, J. A. Pople, *J. Chem. Phys*., **56**, 2257 (1972).

36 M. J. Frisch, J. A. Pople, Binkley, *J. Chem. Phys.,* **80**, 3265 (1984).

37 H. Hellmann, *J. Chem. Phys*., **3**, 61 (1935).

38 P. J. Hay and W. R. Wadt, *J. Chem. Phys*., **82**, 270 (1985).

39 D. Kumar, B. Karamzadeh, G. N. Sastry and S. P. de Visser, *J. Am. Chem. Soc.*, **132**, 7656 (2010).

40 T. Ziegler*, Chem. Rev*., **91**, 651 (1991).

41 W. Khon, L.Sham, *J. Phys. Rev.,***140**, 1133 (1965).

42 P. Hohenberg, W. Khon, *Phys. Rev.,***136**, B864 (1964).

43 S. H. Vosko, L. Wilk, M. Nusair, *Can. J. Phys*., **58**, 1200 (1980).

44 C. Lee, W. Yang, R. G. Parr, *Phys. Rev*., **B37**, 785 (1988).

45 J. P. Perdew, Y. Wang, *Phys. Rev*., **B45**, 13244 (1992).

46 A. D. Becke, *J. Chem. Phys.*, **104**, 1040 (1996).

47 A. D. Becke, *J. Chem. Phys*., **98**, 5648 (1993).

48 R. G. Parr, W. Yang, *Density Functional Theory*, Oxford University Press (1989).

49 P. E. M. Siegbahn, *Quaet. Rev. Biophys.*, **36**, 91 (2003).

50 J. H. Jensen, *Molecular Modeling Basics*, CRC Press, Boca Raton (2010).

51 J. Tomasi, B. Mennucci, R. Cammi, *Chem. Rev.*, **105**, 2999 (2005).

CHAPTER 3

ORIGIN OF THE ENHANCED REACTIVITY OF A SYNTHETIC N-BRIDGED DIIRON(IV)-OXO PORPHYRIN COMPLEX OVER CYTOCHROME P450 COMPOUND I

CHAPTER 3

ORIGIN OF THE ENHANCED REACTIVITY OF A SYNTHETIC N-BRIDGED DIIRON(IV)-OXO PORPHYRIN COMPLEX OVER CYTOCHROME P450 COMPOUND I

3.1: Introduction

Cytochrome P450 enzymes are versatile enzymes in human physiology that mainly react with compounds through oxygen atom transfer to substrates with the aim to initiate their metabolism and detoxification, but, on the other hand, also assist in biosynthetic pathways of, e.g., hormones.[1-7] For instance, the biodegradation of long chain fatty acids and xenobiotics is catalyzed by P450 liver isozymes through a mechanism that is considered to proceed via an iron(IV)-oxo heme cation radical intermediate called Compound I (CpdI). To understand the fundamental features of the oxidant in the P450 enzyme structure, synthetic models have been prepared that contain the critical features of the enzyme active sites.[8-12] These, so-called biomimetic model complexes enable one to study the reactivity patterns and the intrinsic chemical properties of the iron-porphyrins and gain understanding on the intricate structural and electronic features of the active site. Biomimetic work indeed confirmed a high-valent iron(IV)-oxo porphyrin cation radical to be the active oxidant and ruled out many alternative suggestions.[13-15]

Recent biochemical studies isolated and characterized Compound I in a P450 isozyme and established the electronic configuration with spectroscopic methods.[16] Although the P450s are known to be efficient and powerful oxidants in nature, native enzymes do not catalyze the conversion of methane to methanol, which requires the breaking of a very strong C–H bond. Using PhIO as an oxidant, it was shown that CYP153A6 is able to oxidize CH_4 although with very low turnover numbers of 0.02–0.05.[17] Guest/host activation of P450 BM3 using perfluorocarboxilic acids was proposed to initiate the oxidation of light alkanes including methane.[18] However, Watanabe *et al.* showed that this approach failed in methane oxidation even under 0.5 MPa methane pressure.[19-20]

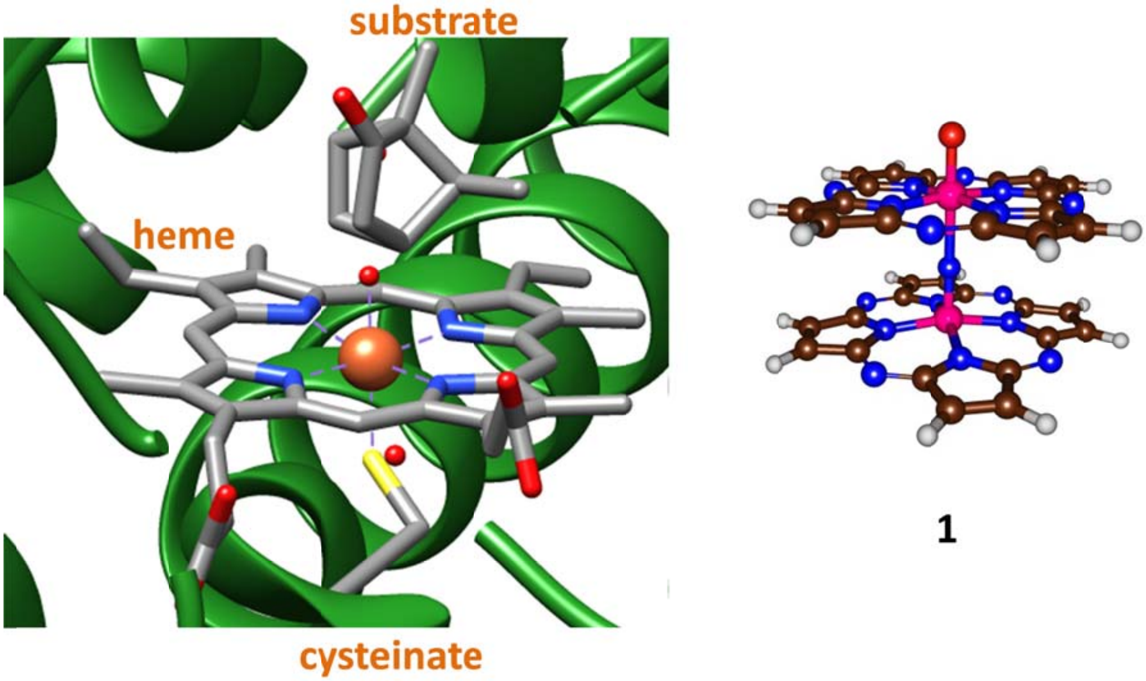

Figure 3.1: Comparative structural features of the active site of $P450_{cam}$ and N-bridged diiron-oxo porphyrazine complex 1 used as the model for N-bridged diiron-oxo phthalocyanine A.

Over the years, work on synthetic iron-porphyrins has focused on improving the oxidative power of the active species through modifications of the porphyrin scaffold, in particular with the aim to find a metal-porphyrin system able to hydroxylate methane, but so far only a few of these studies have been successful. Thus, N-bridged diiron-oxo phthalocyanine **A** was shown to be able to hydroxylate methane efficiently.[21-23] It appears, therefore, that this diiron complex is a more potent oxidant than the active species of P450 enzymes of which we show the active site structure from P450$_{\mathrm{cam}}$ as taken from the protein databank [24] for structural comparison in Figure 3.1.

The question is, then, what makes **A** a better oxidant than the enzyme, and what is the effect of the bridging nitrido group on the chemical properties of the oxidant and the catalysis? To understand the differences between **A**, modeled with the corresponding porphyrazine dimer **1** having simpler pyrrole units instead of the isoindole moieties of the phthalocyanine core (Figure 3.1), and an iron(IV) oxo-porphyrin cation radical (**2**, $[\mathrm{Fe^{IV}(O)(Por^{+\bullet})SH}]$) as a mimic of the active species of P450 enzymes, it was decided to do a computational study on methane hydroxylation using both complexes.

3.2: Methods

Extensively benchmarked and calibrated methods were used by us and others [25-26] on analogous chemical systems that are known to give the correct spin-state ordering and kinetics. Alternative DFT methods (Table 3.1) were tested but all give similar electronic configurations and the same spin state ordering, which gives us confidence that the results represent the chemical system well. The electronic properties and reactivity of **1** with **2** were compared and an active site model complex was taken because previous QM/MM studies showed these complexes represent the enzyme features well.[27] Furthermore, the small model complexes enable one to understand the fundamental chemical differences between the active site of P450 and the synthetic model **1** by elimination of the protein interactions. Our initial studies focused on the low-lying electronic configuration of reactant **1**, in which the lowest lying doublet, quartet, sextet and octet spin states were calculated. In addition, we calculated it with an acetate ion ligated in the axial ligand position of the second iron atom (${}^{2,4}\mathbf{1}_{\mathrm{Ac}}$) as well as an elaborate model containing the N-bridged diiron-oxo tetraphenylporphyrin (${}^{2}\mathbf{3}$).

Table 3.1: A breakdown of relative spin state ordering, in kcal mol^{-1}, reported for several different DFT methods. All values are related to the doublet (${}^{2}1$) energies for each of the methods, whilst values for the quartet (${}^{4}1$), sextet (${}^{6}1$) and octet (${}^{8}1$) were also determined. Values are recorded for the systems; electronic energy ΔE, zero point corrected energy ΔE+ZPE and free energy ΔG.

B3LYP	ΔE	ΔE+ZPE	ΔG	B3LYP*	ΔE	ΔE+ZPE	ΔG
${}^{2}1$	0.00	0.00	0.00	${}^{2}1$	0.00	0.00	0.00
${}^{4}1$	0.58	0.52	-0.24	${}^{4}1$	0.55	0.50	-0.10
${}^{6}1$	14.42	13.80	12.31	${}^{6}1$	25.52	25.95	28.18
${}^{8}1$	49.73	46.51	45.48	${}^{8}1$	63.76	62.17	66.97
BP86	ΔE	ΔE+ZPE	ΔG	M06	ΔE	ΔE+ZPE	ΔG
${}^{2}1$	0.00	0.00	0.00	${}^{2}1$	0.00	0.00	0.00
${}^{4}1$	3.94	3.82	0.74	${}^{4}1$	1.99	1.65	0.84
${}^{6}1$	47.39	48.79	53.80	${}^{6}1$	13.32	12.29	8.74
${}^{8}1$	47.15	45.50	42.14	${}^{8}1$	44.86	41.33	39.14

3.3: Results and Discussion

In agreement with experimental electron paramagnetic resonance (EPR) spectra the electronic ground state for all three complexes is a doublet spin state.[28] The optimized geometries of ${}^{2}\mathbf{1}$, ${}^{2}\mathbf{1}_{\mathrm{Ac}}$ and ${}^{2}\mathbf{3}$ are given in Figure 3.2 and are in line with crystal structure coordinates of [Fe$^{\mathrm{III}}$(Por)–N=Fe$^{\mathrm{IV}}$(Por)],[28] as well as with iron(IV)-oxo complexes calculated before with a porphyrin ligand.[29-31] As such the optimized geometry of **3** does not give hints on why it would be a better oxidant than **2**. However, **1** and **3**, have an electronic configuration and orbital occupation different from **2**, which has an electronic ground state with $\pi^*_{xz}{}^1\ \pi^*_{yz}{}^1\ a_{2u}{}^1$ configuration with close lying ferromagnetically coupled quartet and anti-ferromagnetically coupled doublet spin states that represented a triplet spin on the iron(IV)-oxo group coupled with a doublet spin on the macrocyclic ligand.[32] By contrast, the orbital interactions in **1** have changed due to the addition of an axial nitrido-iron-phthalocyanine group as shown in Figure 3.2. The center of Figure 3.2 highlights the orbital interactions of the key valence orbitals of **1**. Due to alignment of the O, Fe1, N and Fe2 atoms in **1**, their atomic orbitals interact and form new molecular orbitals that span the complete z-axis. The orbital interactions of the two iron $3d_{xz}/3d_{yz}$ with the $2p_x/2p_y$ orbitals on the oxo and bridging nitrido group leads to a set of bonding and antibonding combinations. This gives rise to a set of four pairs of molecular orbitals labeled as $\pi_{1,x}/\pi_{1,y}$, $\pi_{2,x}/\pi_{2,y}$, $\pi_{3,x}/\pi_{3,y}$ and $\pi^*_{4,x}/\pi^*_{4,y}$, which is fundamentally different from the orbital energy splitting in P450 Cpd I, where only a pair of π/π^* orbitals is found. Therefore, the difference in molecular valence orbitals between **1**, on the one hand, with **2**, on the other hand, will affect the relative energies of the molecular orbitals, such as the HOMO-LUMO energy gap, and as a consequence also the ionization potential, the electron affinity and pK_a values of the oxidant. As the H-atom abstraction involves a combined proton and electron transfer, these factors influence the reactivity patterns with substrates.

In agreement with earlier DFT studies on complex **1**,[29] an electronic ground state with orbital occupation $\pi_{3,x}{}^{\uparrow}\ \pi_{3,y}{}^{\downarrow}\ \pi^*_{4,x}{}^{\uparrow}\ a_{2u}{}^2$ for ^{2}**1**and $\pi_{3,x}{}^{\uparrow}\ \pi_{3,y}{}^{\uparrow}\ \pi^*_{4,x}{}^{\uparrow}\ a_{2u}{}^2$ for ^{4}**1** was found, therefore, complex **1** can be formally described as $[O{=}Fe^{IV}(Pz){-}(N^{-\bullet})Fe^{IV}(Pz)]$, Pz = porphyrazine. By contrast, Compound I of P450 was found to have a ground state described as [O=Fe^{IV}(Por$^{+\bullet}$)Cys]. An alternative doublet spin state of **1** with radical character on the porphyrazine ring was also calculated, but it was considerably higher in energy than the state mentioned above (+26 kcal mol^{-1}), which implies that the orbital energy splitting shown in Figure 3.2 will raise the π* orbitals in energy and as a consequence double occupation of the Pz a_{1u} and a_{2u} orbitals is favored. It appears, therefore, that the axially ligated nitrido-iron group affects the molecular orbital interactions and removes radical character from the macrocycle and changes the electronic configuration from that found for mononuclear iron(IV)-oxo complexes such as Compound I of P450, where the a_{2u} orbital is singly occupied. Thus, the alignment of the axial N–Fe unit with the iron(IV)-oxo group destabilizes the π* orbitals well above the a_{2u} orbital of the porphyrazine ring and creates a [O=Fe^{IV}(Pz)–(N$^{-\bullet}$)–Fe^{IV}(Pz)] state rather than the expected Compound I-like state [O=Fe^{IV}(Pz$^{+\bullet}$)–N=Fe^{IV}(Pz)].

Our assignment of the electronic ground state of ^{2}**1** disagrees with that reported in Ref 28 for an analogous N-bridged diiron-oxo porphyrin species, where a [O=Fe^{IV}(Por$^{+\bullet}$)–N=Fe^{IV}(Por)]^0 electronic state with significant radical character on the Por ligand was proposed on the basis of EPR, Mössbauer and UV-vis data. In particular, EPR spectroscopic data implicated considerable radical character on non-metal atoms. To find out whether our calculated doublet spin state could be represented by these spectroscopic results, a detailed study into the electronic and spectroscopic features of ^{2}**1** and $^2\mathbf{1}_{Ac}$ was done.

Firstly, the group spin densities of ^{2}**1** was analysed by us, and, although no significant spin density on the two porphyrazine rings was found, there is considerable spin located on non-metal atoms, and, in particular, the bridging nitrogen atom has accumulated –1.52 (1.51) spin density in ^{2}**1** (^{4}**1**). Indeed, the singly occupied orbital shown on the right-hand-side of Figure 3.2 gives considerable amount of electron density on the nitrido-bridge.

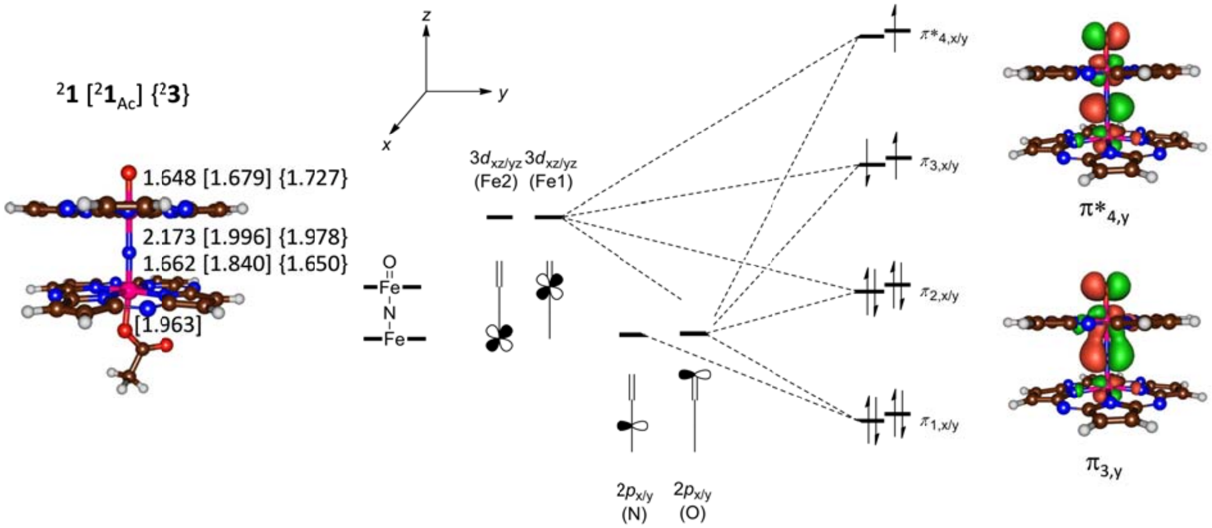

Figure 3.2: Optimized geometry of $^{2}1$, $^{2}1_{Ac}$ and $^{2}3$ and orbital splitting observed for the mixing of metal $3d_{xz/yz}$ with $2p_{x/y}$ on N and O. Also given are two singly occupied valence orbitals.

The spin densities further indicate values of about 1 (Fe1) and about 0.5 (Fe2). The spin density on Fe1, N and Fe2 is consistent with orbital occupation $\pi_{3,x}^{\uparrow}\ \pi_{3,y}^{\downarrow}\ \pi^{*}_{4,x}{}^{\uparrow}\ a_{2u}^{2}$. Note as well that due to an additional axial ligand the optimized geometry of ^{2}**1**$_{Ac}$ has the nitrido group almost midway between the two iron atoms, whereas it forms a double bond with Fe2 in ^{2}**1** and ^{2}**3**.

Subsequently, we investigated the hydrogen atom abstraction from methane by ^{2,4,6,8}**1** and ^{2,4}**2**. Thus, methane hydroxylation by all oxidants was found to occur via a stepwise mechanism via a radical intermediate with an initial hydrogen atom abstraction via a transition state (**TS**$_{H}$) followed by hydroxyl rebound to form methanol. For ^{2}**1** a solvent and dispersion corrected barrier of ΔE + ZPE = 6.7 kcal mol^{-1} on the doublet spin state is found, which implies efficient hydrogen atom transfer even from methane in agreement with experiment. By contrast, at the same level of theory the P450 model gives barriers of 17.8 (18.5) kcal mol^{-1} for ^{2}**TS**$_{H}$ (^{4}**TS**$_{H}$), respectively.[33-34] Therefore, **1** is a considerably better oxidant than **2** for aliphatic hydroxylation reactions. To understand the electronic differences between the transition states **TS**$_{H}$(**1**) and **TS**$_{H}$(**2**), their optimized geometries, group spin densities and dipole moments is displayed in Figure 3.3.

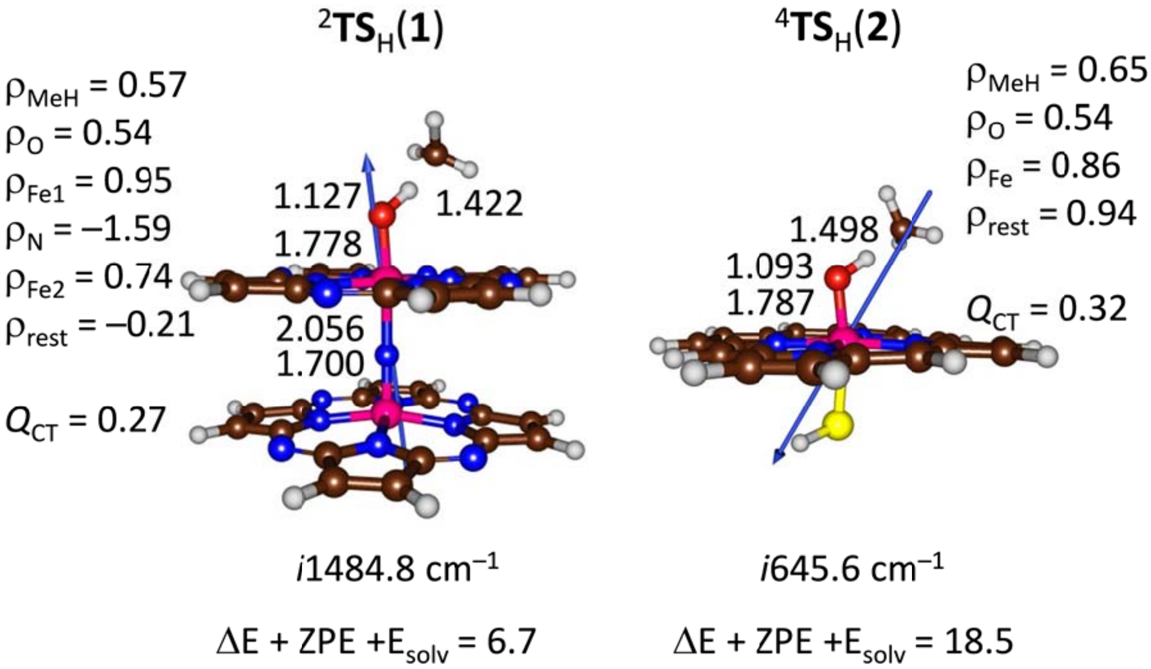

Figure 3.3: Optimized geometries with bond distances in angstroms and the imaginary frequency in wavenumbers of ^{2}TS1(1) and ^{2}TS1(2). Also given are group spin densities (ρ) and the degree of charge-transfer (Q_{CT}) as taken from the UB3LYP/ B2//UB3LYP/B1 calculations. The dipole vector is indicated with an arrow sign.

Geometrically, there are no dramatic differences between the two transition states and the O–H and H–C distances are very similar. This is also the case for the degree of charge transfer from substrate to oxidant and the resulting spin density accumulated on the methyl group. However, a considerably larger dipole moment is found for $\mathbf{TS}_H(1)$ of 4.7 Debye versus that for $\mathbf{TS}_H(2)$ [0.8 Debye], and, additionally, it points in the opposite direction. Obviously, an enlarged dipole moment will lead to stabilization of the complex in solution and interactions with polar solvent molecules; this may further enlarge the gap between $\mathbf{TS}_H(1)$ and $\mathbf{TS}_H(2)$. Note as well the considerably larger imaginary frequency in the transition state for ${}^2\mathbf{TS}_H(1)$ as compared to ${}^2\mathbf{TS}_H(2)$, which should lead to dramatic kinetic isotope effects (KIE) for the replacement of the transferring hydrogen atom by deuterium.

Experimental studies on hydrogen atom abstraction reactivities showed that the rate constant generally correlates with the strength of the C–H bond of the substrate that is broken (BDE_{CH}) as well as with the strength of the O–H bond that is formed (BDE_{OH}).[35-37] However, the latter can be split into an electron transfer (electron affinity, EA of the oxidant) and a proton affinity of the reduced oxidant (ΔH_{acid}) that are connected via the thermodynamic cycle as shown in Figure 3.4 with IE_H (the ionization potential of a hydrogen atom) as taken from the NIST database.[38] Extensive experimental studies, however, implicated a dominant component related to the acidity of the oxo group, i.e. ΔH_{acid}.[39-41] Thus, the values of BDE_{OH}, EA and ΔH_{acid} for **1** and **2** were calculated. In the gas-phase, a value of $BDE_{OH}(1) = 88.3$ kcal mol^{-1} was calcualted, which is almost identical to the value we calculated before for **2**, $BDE_{OH}(2) = 88.9$ kcal mol^{-1}.[42] However, **1** has an electron affinity that is about 10 kcal mol^{-1} lower than that for **2**, and as a consequence has an 11.4 kcal mol^{-1} larger ΔH_{acid} value. It is this acidity change that will make **1** a better oxidant than **2** for substrate hydroxylation reactions.

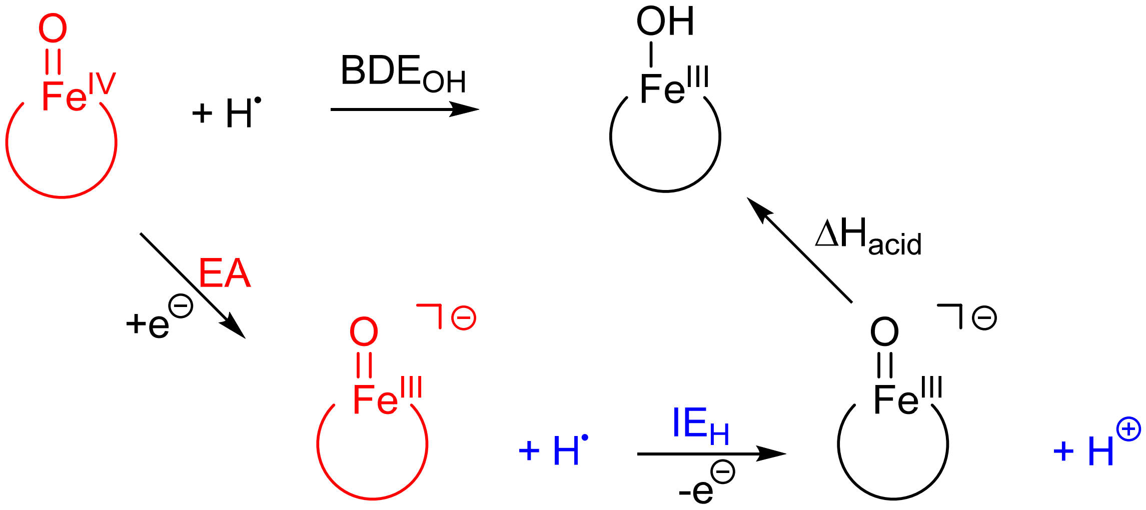

Figure 3.4: Definition of thermodynamic variables.

3.4: Conclusions

In summary, the calculations presented in this work highlight how small external perturbations, such as those of an axially coordinated nitride-porphyrin ligand can lead to changes in molecular orbital interactions of the metal(IV)-oxo group with aligned ligand-orbitals as well as the dipole moment of the oxidant. In particular, an N-bridged diiron-oxo complex, with either porphyrin or phthalocyanine, has an increased basicity of the oxo group that is highly susceptible to hydrogen atom abstraction. Indeed, very low activation barriers are calculated in agreement with experiment.

References:

1 M. Sono, M. P. Roach, E. D. Coulter, J. H. Dawson, *Chem. Rev.*, **96**, 2841 (1996).

2 F. P. Guengerich, *Chem. Res. Toxicol.*, **14**, 611 (2001).

3 J. T. Groves, *Proc. Natl. Acad. Sci. USA*, **100**, 3569 (2003).

4 P. R. Ortiz de Montellano, (Ed.) *Cytochrome P450: Structure, Mechanism and Biochemistry*, 3rd edition, Kluwer Academic/Plenum Publishers, New York (2005).

5 A. W. Munro, H. M. Girvan, K. J. McLean, *Nat. Prod. Rep.*, **24**, 585 (2007).

6 K. M. Kadish, K. M. Smith, R. Guilard, R. (Eds.) *Handbook of Porphyrin Science*. World Scientific Publishing Co., New Jersey (2010).

7 S. P. de Visser, D. Kumar, (Eds.) *Iron-containing enzymes: Versatile catalysts of hydroxylation reaction in nature*. RSC Publishing, Cambridge, UK (2011).

8 M. Costas, *Coord. Chem. Rev.*, **255**, 2912 (2011).

9 M. M. Abu-Omar, A. Loaiza, N. Hontzeas, *Chem. Rev.*, **105**, 2227 (2005).

10 P. C. A. Bruijnincx, G. van Koten, R. J. M. Klein Gebbink, *Chem. Soc. Rev.*, **37**, 2716 (2008).

11 S. V. Kryatov, E. V. Rybak-Akimova, S. Schindler, *Chem. Rev.*, **105**, 2175 (2005).

12 A. R. McDonald, L. Que Jr.,. *Coord. Chem. Rev.*, **257**, 414 (2013).

13 J. T. Groves, *Cytochrome P450: Structure, Mechanism and Biochemistry.* Chapter-1, *"Models and Mechanisms of Cytochrome P450 Action."* P. R. Ortiz de Montellano (Ed.), 3rd Ed., Kluwer Academic/Plenum Publishers:
New York (2005).

14 W. Nam, *Acc. Chem. Res.*, **40**, 522 (2007).

15 I. G. Denisov, T. M. Makris, S. G. Sligar, I. Schlichting, *Chem. Rev.* **105**, 2253 (2005).

16 J. Rittle, M. T. Green, *Science*, **330**, 933 (2010).

17 M. M. Chen, P. S. Coelho, F. H. Arnold, *Adv. Synth. Catal.*, **354**, 964 (2012).

18 F. E. Zilly, J. P. Acevedo, W. Augustyniak, A. Deege, U. W. Häusig, M. T. Reetz, *Angew. Chem. Int. Ed.*, **50**, 2720 (2011).

19 N. Kawakami, O. Shoji, Y. Watanabe, *Angew. Chem. Int. Ed.*, **50**, 5315 (2011).

20 N. Kawakami, O. Shoji, Y. Watanabe, *Chem. Sci.*, **4**, 2344 (2013).

21 A. B. Sorokin, E. V. Kudrik, D. Bouchu, *Chem. Commun.*, 2562 (2008).

22 A. B. Sorokin, E. V. Kudrik, L. X. Alvarez, P. Afanasiev, J. M. Millet, D. Bouchu, *Catal. Today*, **157**, 149 (2010).

23 A. B. Sorokin, *Chem. Rev.*, **113**, 8152 (2013).

24 H. M. Berman, J. Westbrook, Z. Feng, G. Gilliland, T. N. Bhat, H. Weissig, I. N. Shindyalov, P. E. Bourne, *Nucleic Acids Res.*, **28**, 235 (2000).

25 S. Shaik, S. Cohen, Y. Wang, H. Chen, D. Kumar, W. Thiel, *Chem. Rev.*, **110**, 949 (2010).

26 D. Kumar, W. Thiel, S. P. de Visser, *J. Am. Chem. Soc.*, **133**, 3869 (2011).

27 C. Li, S. Shaik, *RSC Adv.*, **3**, 2995 (2013).

28 E.V. Kudrik, P. Afanasiev, L. X. Alvarez, P. Dubourdeaux, M. Clémancey, J.-M. Latour, G. Blondin, D. Bouchu, F. Albrieux, S. E. Nefedov, A. B. Sorokin, *Nature Chem.*, **4**, 1024 (2012).

29 R. Silaghi-Dumitrescu, S. V. Makarov, M.-M. Uta, I. A. Dereven'kov, P. A. Stuzhin, *New J. Chem.*, **35**, 1140 (2011).

30 D. Kumar, B. Karamzadeh, G. N. Sastry, S. P. de Visser, *J. Am. Chem. Soc.*, **132**, 7656 (2010).

31 T. Kamachi, K. Yoshizawa, *J. Am. Chem. Soc.*, **125**, 4652 (2003).

32 M. T. Green, *J. Am. Chem. Soc.*, **121**, 7939 (1999).

33 S. P. de Visser, D. Kumar, S. Cohen, R. Shacham, S. Shaik, *J. Am. Chem. Soc.*, **126**, 8362 (2004).

34 S. Shaik, D. Kumar, S. P. de Visser, *J. Am. Chem. Soc.*, **130**, 10128 (2008).

35 L. E. Friedrich, *J. Org. Chem.*, **48**, 3851 (1983).

36 F. G. Bordwell, J. P. Cheng, *J. Am. Chem. Soc.*, **113**, 1736 (1991).

37 J. M. Mayer, *Acc. Chem. Res.*, **31**, 441 (1998).

38 P. J. Linstrom, W. G. Mallard, (Eds.), *NIST Chemistry WebBook, NIST Standard Reference Database Number 69, National Institute of Standards and Technology,* Gaithersburg MD, 20899, http://webbook.nist.gov.

39 M. T. Green, J. H. Dawson, H. B. Gray, *Science*, **304**, 1653 (2004).

40 T. H. Parsell, M. Y. Yang, A. S. Borovik, *J. Am. Chem. Soc*., **131**, 2762 (2009).

41 K. A. Prokop, S. P. de Visser, D. P. Goldberg, *Angew. Chem. Int. Ed*., **49**, 5091 (2010).

42 S. P. de Visser, L. S. Tan, *J. Am. Chem. Soc*., **130**, 12961 (2008).

CHAPTER 4

METHANE HYDROXYLATION BY AXIALLY LIGATED IRON(IV)-OXO PORPHYRIN CATION RADICAL MODELS

CHAPTER 4

METHANE HYDROXYLATION BY AXIALLY LIGATED IRON(IV)-OXO PORPHYRIN CATION RADICAL MODELS

4.1: Introduction

Methane hydroxylation is a challenging chemical process that few enzymatic systems are able to perform due to the strength of the methyl C–H bond that needs to be broken in the process. Nature has developed only a single class of enzymes that perform this task efficiently, namely the methane monoxygenases.[1-3] These are generally dicopper enzymes that utilize molecular oxygen and convert methane to methanol. Nature utilizes a large range of metalloenzymes with a broad functional scope, yet most of these enzymes cannot activate methane. For instance, non-heme iron dioxygenases are efficient oxidants of hydrogen atom abstraction and oxygen atom transfer reactions and therefore are well studied. In particular, the non-heme iron enzymes taurine/α-ketoglutarate dioxygenase,[4-7] prolyl-4-hydroxylase [8] and cysteine dioxygenase [9-13] are known to react with substrates efficiently with large turnovers. Our computational modelling predicted relatively small hydrogen atom abstraction barriers of methane by the high-valent iron(IV)-oxo intermediate of taurine/α-ketoglutarate dioxygenase,[14] but so far no experimental support of methane hydroxylation by non-heme iron enzymes exists. Similarly, heme monoxygenases, which are considered as highly efficient in hydrogen atom abstraction processes, do not naturally utilize methane during their activity either.[15-19]

Cytochrome P450 enzymes are heme-based monoxygenases found in all forms of life and have important biochemical functions that essentially include the chemical modification of substrates. Thus, they are involved in the biosynthesis of hormones, such as estrogen. In addition, the P450s catalyze the metabolism of drugs [20] and the detoxification of xenobiotics in the liver.[21] The P450s have a characteristic structure with a central protoporphyrin IX group (heme) that is attached to the protein via an Fe–S linkage using a conserved cysteinate residue of the protein; the axial ligand. Figure 4.1 displays the active site structure of the mammalian P450 isozyme $P450_{2C5}$ with the drug molecule diclofenac bound, as taken from the crystal structure coordinates.[22] The substrate is located in a tight binding pocket and is positioned in such a way that promotes a regioselective and stereospecific oxidation. The heme is linked to the protein via an interaction of the metal with a cysteinate group in the axial position. In addition, the heme is placed in position through a number of hydrogen bonding interactions, for instance, toward the propionate side chains of the heme. Molecular oxygen binds *trans* to the cysteinate moiety, i.e. on the distal site. Prior to substrate hydroxylation, however, the heme needs to be activated and an active species is generated. This process includes the binding of molecular oxygen, two reduction and two protonation steps and ultimately leads to the formation of a high-valent iron(IV)-oxoheme cation radical species, called Compound I (Cpd I).[15,18] The P450s, therefore, have an intricate hydrogen bonding network surrounding the heme active site that delivers protons.[23] Interestingly, hydrogen bonding interactions, for instance through water molecules, were found to affect also reaction barriers of substrate activation, and, hence they are often non-innocent.[24-26] Moreover, the spin state ordering and relative energies often gives a dependence on environmental effects, such as hydrogen bonding [27] or a point charge.[28]

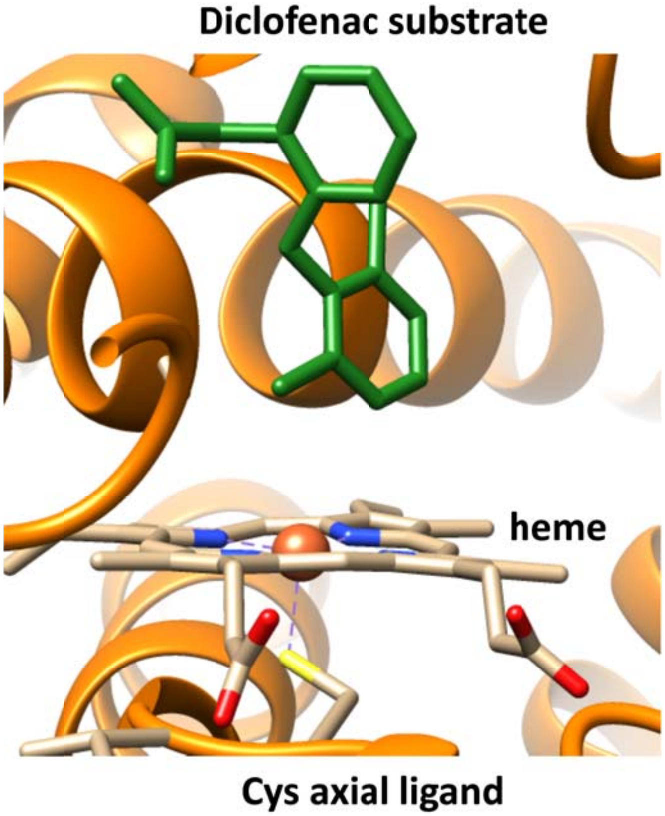

Figure 4.1: Extract of the active site of $P450_{2C5}$ with substrate diclofenac bound.

P450s are efficient oxidants in nature and react with substrates via aliphatic hydroxylation,[18] aromatic hydroxylation,[29-36] olefin epoxidation [4,5,37-54] and sulfoxidation.[24,55-57]

Enzymes with a structure closely resembling the P450 active site feature are, for instance, the peroxidases and catalases, but these systems lack the cysteinate axial ligand of P450. Instead, the peroxidases and catalases contain either a histidine or a tyrosinate axial ligand, respectively.[58,59] The difference in chemical structure of the P450s, on the one hand, and peroxidases and catalases, on the other hand, has led to speculation that the axial ligand is responsible for the change in reactivity and the chemical properties of these enzymes. Indeed, quantum chemical calculations of Cpd I with either a cysteinate, a histidine or a tyrosinate axial ligand as mimics of Cpd I of P450, horseradish peroxidase and catalase, respectively, showed dramatic differences in their electron affinities, and, consequently their ability to pick up electrons from substrates.[28,60,61] This was further highlighted through a push-effect of electron density from the axial ligand upon the heme and, in particular, the mixing of a lone pair of the axial ligand with the heme a_{2u} orbital.[62]

In order to understand spectroscopic and reactivity differences of these enzyme classes, synthetic model complexes have been developed: the so-called biomimetic models.[63-64] Thus, Gross *et al.* [65] showed that for synthetic iron(III)-porphyrins, there was an axial ligand effect on the reactivity differences of the various complexes but there also were spectroscopic differences as a result of binding an alternative axial ligand. Theoretical modelling can assist in understanding the fundamental differences in reactivities and establish the key factors that determine the reaction mechanism. To gain insight into the axial ligand effect of iron-porphyrins, we investigated the properties and reactivities of a range of iron(IV)-oxo porphyrin cation radical models with varying axial ligand description: $\mathbf{1}_X$, X = F^-, Cl^-, CN^-, OH^-, CH_3COO^-, CF_3COO^- and SH^-, (Figure

4.2). Then the reaction of a selection of these oxidants with methane on the doublet and quartet spin state surfaces was studied and reactivity differences were compared and how this is affected by the axial ligand of the oxidant.

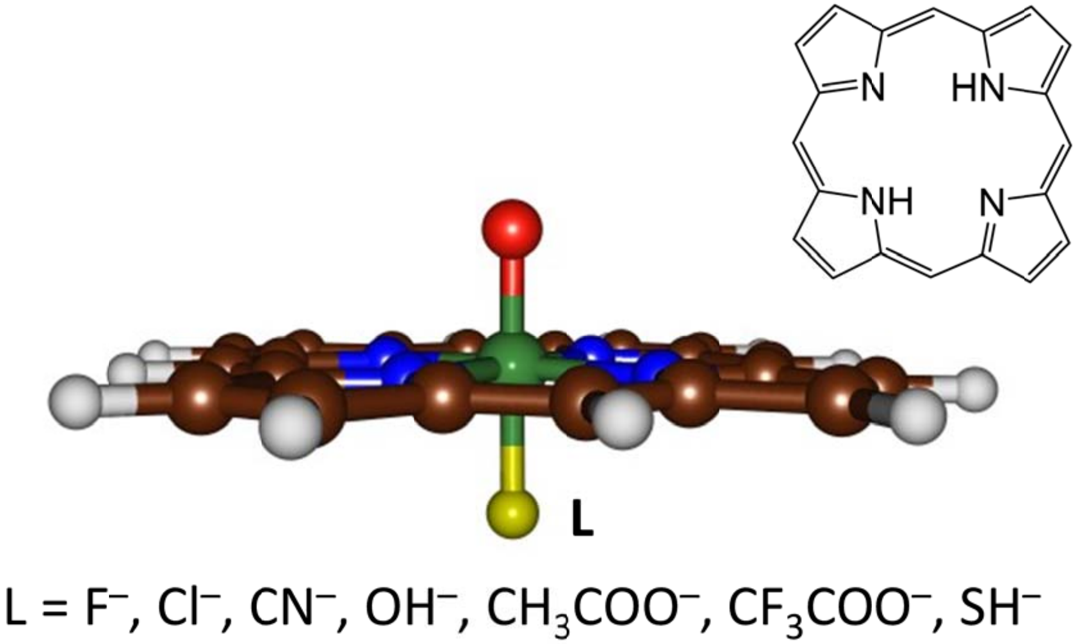

Figure 4.2: Chemical structure of the reactants studied in this work.

4.2: Methods

The studies presented in this work use density functional theory methods as implemented in the *Gaussian*-03 program package.[66] Following previous experience in the field,[67-69] the unrestricted hybrid density functional method UB3LYP [70-71] was used in combination with a double-ζ quality LACVP basis set on iron and 6-31G on the rest of the atoms: basis set BS1.[72] A full geometry optimization (without constraints) followed by an analytical frequency was performed. All reactant structures were confirmed as local minima and had no imaginary frequencies. Single point calculations using a triple-ζ

quality LACV3P+ basis set on iron and 6-311+G* on the rest of the atoms were used throughout: basis set BS2. All data reported here include zero-point corrections and solvent corrections using an acetonitrile solvent.

Subsequently, methane hydroxylation by several iron(IV)-oxo oxidants was investigated. Thereafter a reactant complex, radical intermediate and product complex at UB3LYP/BS1 on the doublet and quartet spin state surfaces were optimized. Extensive geometry scans linking reactants with radical intermediates and of radical intermediates with products were performed. The maxima of these scans were used as starting points for the transition state searches and established first order saddle points characterized by a single imaginary frequency for the correct mode.

Previously, the effect of substituents to the periphery of the porphyrin scaffold was tested and few changes to the chemical structures and reactivities were found.[73,74] Furthermore, full geometry optimization with basis set BS2 reproduced all calculations well. The methods and procedures used here were extensively tested and benchmarked and, for instance, were found to reproduce experimental rate constants within about 4 kcal mol^{-1} [75-77] but also reproduced experimental infrared spectra [50] and resonance Raman spectra.[78]

4.3: Results and Discussion

Before going through the reactivity studies, let us first discuss one of the reactant complexes, namely [Fe^{IV}(O)(Por$^{+\bullet}$)F] or $\mathbf{1}_{F}$, in more detail as an example of a Compound I model. Figure 4.3 displays the high-lying occupied and low-energy virtual orbitals that are relevant for the electronic description and the subsequent reactivity with methane. The molecular orbitals follow close analogy to those found for P450 Compound I.[54, 79-81] The metal orbitals form bonding and antibonding pairs of orbitals, e.g. there is a pair of π_{xz}/π^*_{xz} set of orbitals for the interaction of the $3d_{xz}$(Fe) with $2p_x$(O). Similarly, the atomic $3d_{yz}$(Fe) and $2p_y$(O) mix to form the π_{yz}/π^*_{yz} pair of orbitals. In addition, there is a nonbonding orbital in the plane of the porphyrin ring: δ_{x2-y2}. Finally, two virtual orbitals for the σ^* interactions along the O–Fe axis (σ^*_{z2}) and in the plane of the porphyrin ring (σ^*_{xy}) complete the set of iron-type orbitals. In addition to the metal-type orbitals there are two π-orbitals for the conjugated porphyrin system high-lying, which under D_{4h} symmetry have the labels a_{1u} and a_{2u}. The latter orbital strongly mixes with a lone-pair orbital on the axial ligand and influences the electron affinity of the oxidant strongly.

The set of orbitals displayed in Figure 4.3 is occupied with the following configuration: ^{4,2}Compound I = $\pi_{xz}{}^2\pi_{yz}{}^2\delta_{x2-y2}{}^2\pi^*_{xz}{}^1\pi^*_{yz}{}^1\sigma^*_{z2}{}^0\sigma^*_{xy}{}^0a_{1u}{}^2\ a_{2u}{}^1$. The three unpaired electrons in the system are either ferromagnetically coupled into a quartet spin state ($^4A_{2u}$ state) or the two π^* electrons are up-spin and the a_{2u} electron down-spin to give it an overall doublet spin state ($^2A_{2u}$ state). These two spin states are close in energy and for all systems considered here they fall within 1 kcal mol^{-1}.

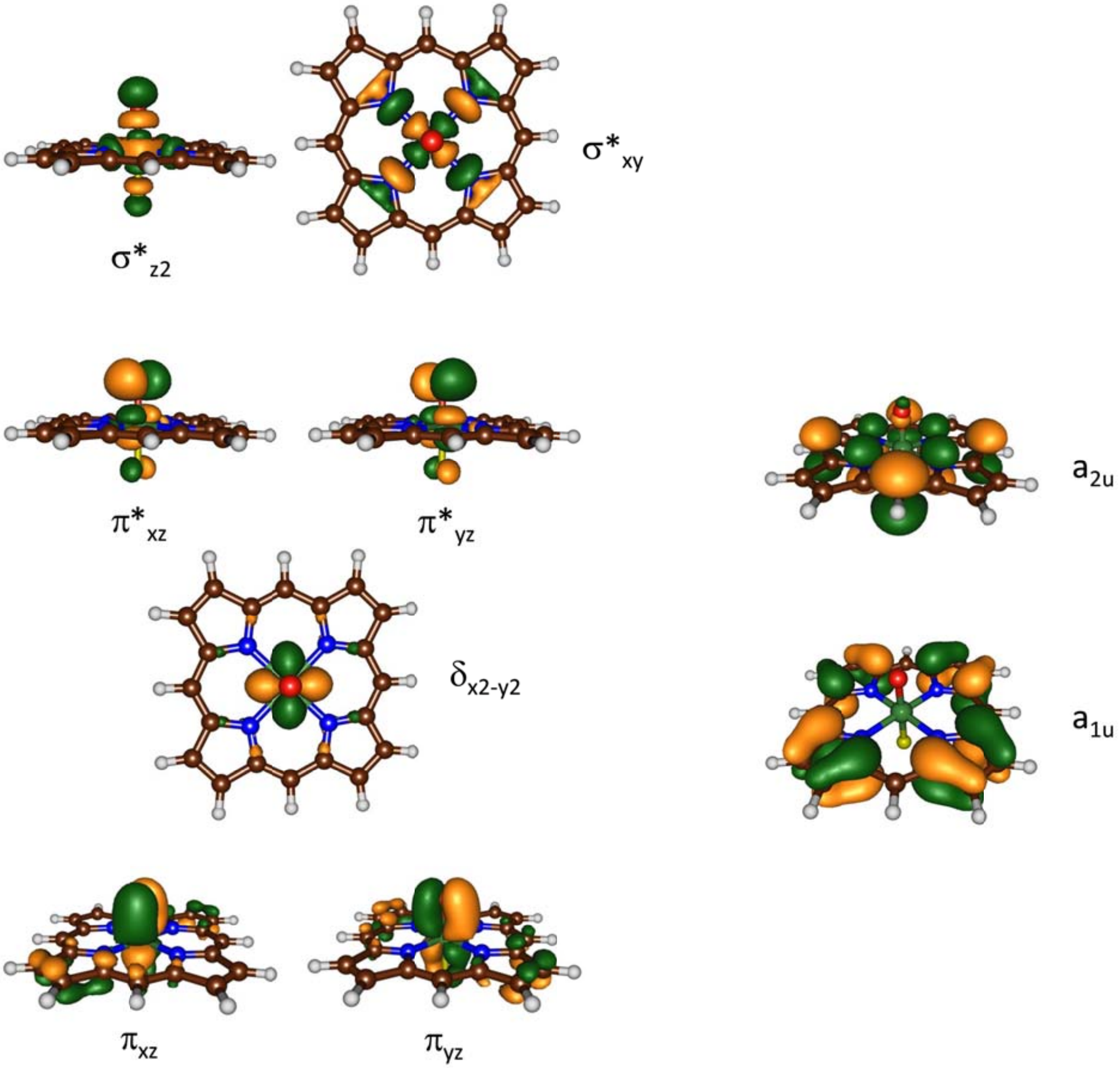

Figure 4.3: Molecular orbitals of $\mathbf{1}_F$.

Next, a geometry optimization of doublet and quartet iron(IV)-oxo porphyrin cation radical models with varying axial ligands, namely, $^{2,4}\mathbf{1}_X$ with X = CF_3COO^-, CH_3COO^-, Cl^-, F^-, ImH (imidazole), acetonitrile, OH^- and SH^- was done. Key geometric and vibrational parameters obtained for the doublet spin state structures are given in Figure

4.4. As follows from the data shown in Figure 4.4, the Fe–O distances vary strongly dependent on the axial ligand bound to the iron-porphyrin system. Thus, an axially ligated fluoride ligand gives a relatively long Fe–O distance of 1.681 Å, whereas a neutral acetonitrile molecule bound gives a much shorted Fe–O bond of 1.645 Å. This is further reduced to 1.630 Å when the axial ligand is removed altogether.[54] The opposite trends are found for the Fe–O stretch vibration (ν_{FeO}), whereby an axial thiolate ligand gives the highest mode at 870.6 cm^{-1}. Strong electron-donating axial ligands, such as F^{-} and OH^{-}, by contrast, give dramatically reduced Fe–O stretch vibrations of the order of 817.7 and 816.6 cm^{-1}, respectively. Note that without an axial ligand the Fe–O vibration is located at 920.0 cm^{-1}. Consequently, the axial ligand affects the strength of the Fe–O bond and as a result the Fe–O frequency is shifted by about 100 cm^{-1}. This will have major effects on the oxygen atom transfer reaction with substrates.

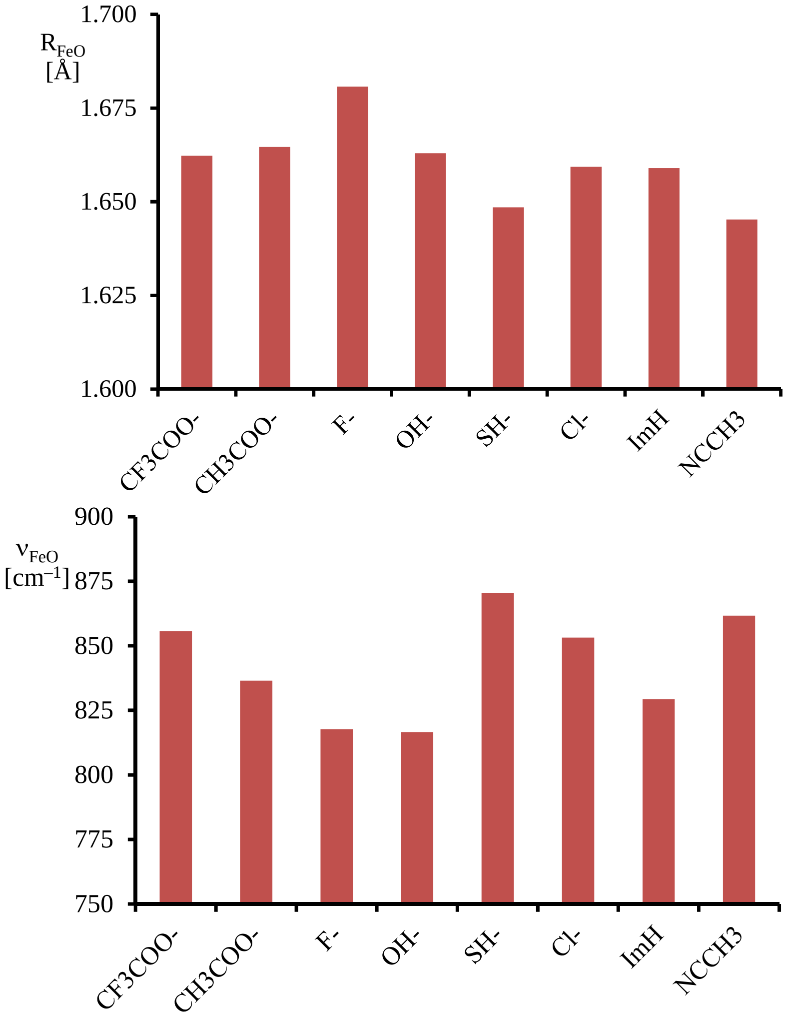

Figure 4.4: (a) Fe–O bond distance (R_{FeO}) for various complexes $^{2}\mathbf{1}_{X}$. (b) Fe–O stretch vibration (ν_{FeO}) for various complexes $^{2}\mathbf{1}_{X}$.

Subsequently the methane hydroxylation mechanism by $^{2,4}\mathbf{1}_{X}$ with X = OH^{-}, F^{-} and CN^{-} was investigated. As an example, the potential energy profile of methane hydroxylation by $^{2,4}\mathbf{1}_{OH}$ is shown in Figure 4.5, the results for $^{2,4}\mathbf{1}_{F}$ and $^{2,4}\mathbf{1}_{CN}$ are very similar. The reaction is stepwise with an initial hydrogen atom abstraction via transition state $\mathbf{TS}_{HA}$ leading to an iron(IV)-hydroxo complex with a radical, **IM**. The OH and radical are combined via a rebound transition state $\mathbf{TS}_{reb}$ to form the alcohol products **P**. This mechanism is analogous to earlier hydrogen atom abstraction reactions calculated for similar complexes and substrates.[4,5,8,14,20,30,35,41,42,45,47,48,73,79,82-110]. As described before, the rebound barriers are small on the high-spin surface and negligible on the low-spin surface, which is also seen here.[111]

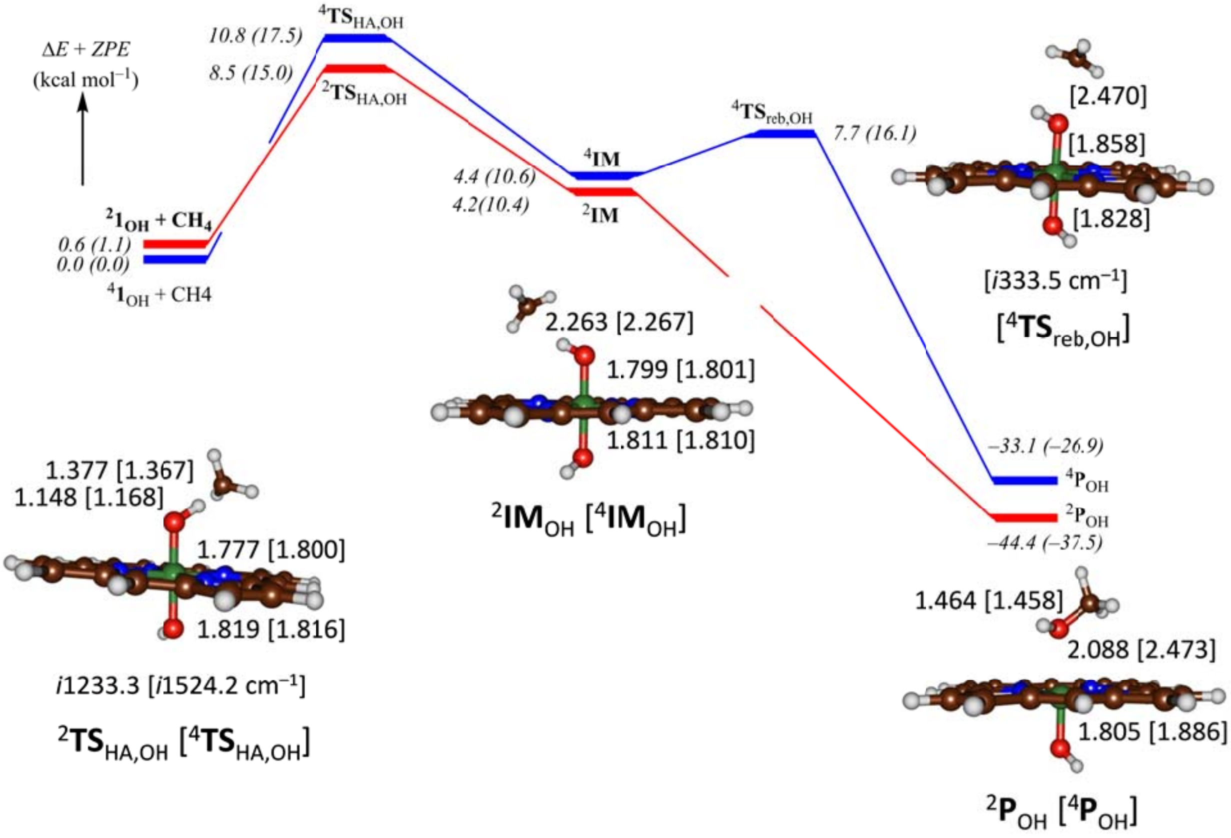

Figure 4.5: Potential energy landscape of methane hydroxylation by $^{2,4}\mathbf{1}_{\mathrm{OH}}$ with energies in kcal mol^{-1}. All energies obtained with UB3LYP/BS2//UB3LYP/BS1 and contain ZPE corrections. Values given out of parenthesis refer to gas-phase data and those inside parenthesis include solvent corrections. Optimized geometries of local minima and transition states give bond lengths in angstroms and the imaginary frequency in the transition state in wave numbers.

For $^{2,4}\mathbf{1}_{\mathrm{OH}}$, small hydrogen atom abstraction barriers of 8.5 (10.8) kcal mol^{-1} on the doublet (quartet) spin states are found in the gas-phase, whereas those with a dielectric continuum included with $\varepsilon = 4.7$ are raised to 15.0 (17.5) kcal mol^{-1}. Nevertheless, these barriers are accessible at room temperature and imply that $^{2,4}\mathbf{1}_{\mathrm{OH}}$ should be able to hydroxylate methane efficiently. The hydrogen atom abstraction barriers are narrow with a large imaginary frequency of *i*1233.3 (*i*1524.2) cm^{-1}, which implies they will proceed with a large kinetic isotope effect for replacing the transferring hydrogen atom by deuterium.[30,84] Geometrically, the barriers are late with long C–H bonds and much shorter O–H bonds, similarly to H-atom abstraction barriers calculated before for methane by [Fe$^{\mathrm{IV}}$(O)(Por$^{+\bullet}$)SH].[44,86]

After H-atom abstraction a radical intermediate is formed representing an [Fe$^{\mathrm{IV}}$(OH)(Por)OH] complexed to $CH_3^{\bullet}$ with a small exothermicity of 4.2 (4.4) kcal mol^{-1} for $^{2}\mathbf{IM}_{\mathrm{OH}}$ ($^{4}\mathbf{IM}_{\mathrm{OH}}$), respectively. The rebound barrier is negligible on the low-spin surface, whereas a OH rebound barrier of 3.5 kcal mol^{-1} is obtained in the high-spin state. The overall mechanism to form alcohols is strongly exothermic as expected.

Subsequently, we replaced the OH axial ligand of $^{2,4}\mathbf{1}_{\mathrm{L}}$ by alternative ligands, namely L = F^{-} and CN^{-} and the results are given in Table 4.1. In general, the potential energy profile for all complexes follows the same pattern as that seen in Figure 4.5, with a rate determining hydrogen atom abstraction barrier and negligible rebound barrier at the low-spin pathway. The only differences obtained are due to the axial ligand interactions with the metal and oxygen atom.

Table 4.1: Relative energies (ΔE+ZPE, in kcal mol^{-1}) of local minima and transition states for methane hydroxylation by $^{2,4}1_L$, L = OH$^-$, F$^-$, and CN$^-$. Values in the gas-phase and in solvent are in given.

	L = OH$^-$		L = F$^-$		L = CN$^-$	
	gas	solvent	gas	solvent	gas	solvent
$^4\mathbf{1}_L$	0.0	0.0	0.0	0.0	0.0	0.0
$^2\mathbf{1}_L$	0.6	1.1	2.1	2.6	0.6	1.1
$^4\mathbf{TS}_{HA}$	10.8	17.5	15.5	22.2	18.4	25.1
$^4\mathbf{IM}$	4.4	10.6	9.2	15.4	13.0	19.2
$^4\mathbf{TS}_{reb}$	7.7	16.1	ND	ND	ND	ND
$^4\mathbf{P}_L$	-33.1	-26.9	ND	ND	ND	ND
$^2\mathbf{TS}_{HA}$	8.5	15.0	26.2	32.7	16.3	22.8
$^2\mathbf{IM}$	4.2	10.4	9.0	15.2	13.2	19.4
$^2\mathbf{P}_L$	-44.4	-37.5	ND	ND	ND	ND

ND = not determined.

The studies presented in Table 4.1 implicate that the axial ligand has a profound effect on the catalytic efficiency and performance of the active oxidant. This is not surprising and has been seen before for the reactivity of iron(IV)-oxo porphyrin radical cation models with substrates.[33,48,53,88,96] To understand the electronic features of the reaction mechanism and find factors that determine the rate constant we set up a valence bond (VB) curve crossing diagram (Figure 4.6). Previously, the VB technique to rationalize the hydrogen atom abstraction reactions of heme and non-heme iron(IV)-oxo-complexes [14,20,92,96] as well as double bond epoxidation reactions [52,54] and sulfoxidation reactions was used.[56]

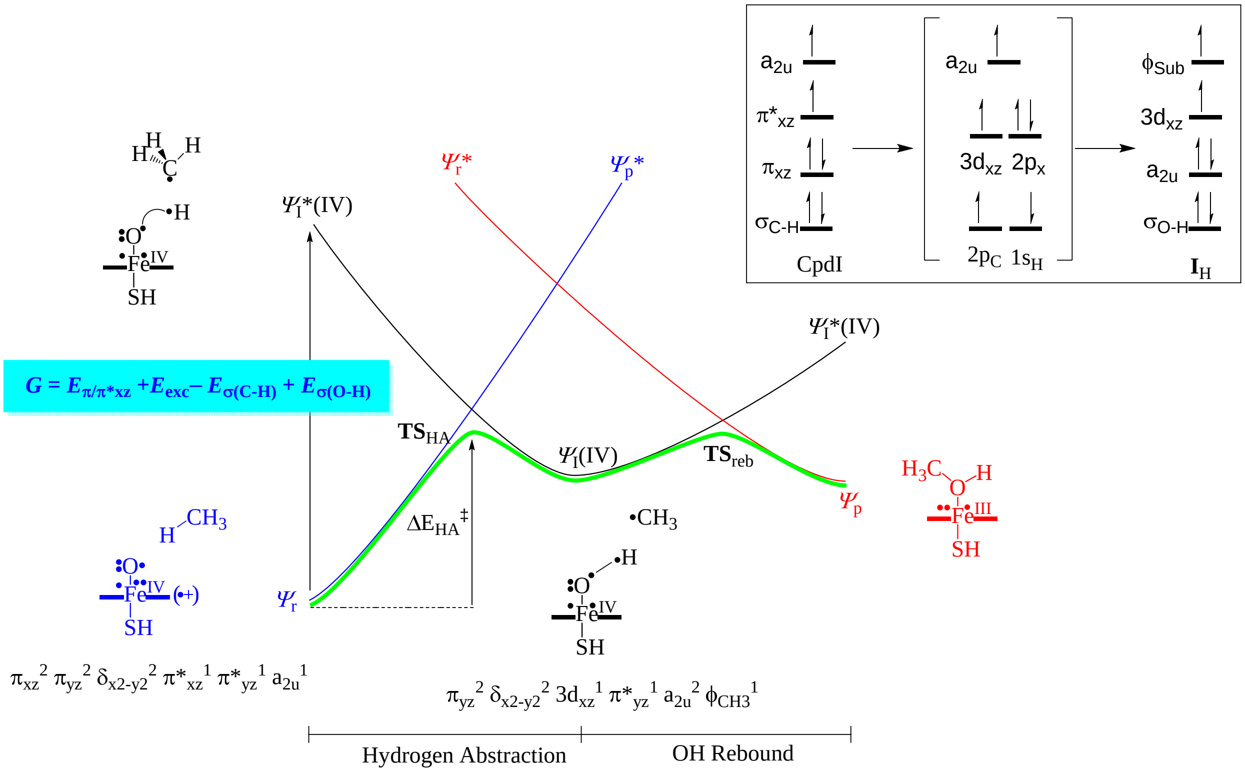

Figure 4.6: Valence bond curve crossing diagram rationalizing the methane hydroxylation reaction by P450 Cpd I. Dots represent valence electrons and lines (curved or straight) are chemical bonds.

Thus, in VB one starts on the left-hand-side with the reactant state Ψ_r, which in our case is Compound I and substrate (methane). The reactant state is connected to an excited state in the radical intermediate as well as in the product geometry. Similarly, the product state Ψ_p, although the ground state in the product geometry, is an excited state in the radical intermediate and reactant geometries. The radical intermediate state (Ψ_I) bisects the reactant and product wave functions and creates a stepwise hydrogen atom abstraction-radical rebound mechanism by creating a stable radical intermediate. The height of the barrier for hydrogen atom abstraction ($\Delta E_{HA}^‡$) is equal to the energy where the two curves cross, e.g. crossing point of the blue and black lines, minus the geometric distortion (resonance energy *B*) upon moving from reactants to the transition state. It has been shown previously [92] that the curve crossing energy is a fraction (usually with value of 0.3) of the excitation energy (*G*) from the reactant state (Ψ_r) to the radical intermediate state (Ψ_I*) in the geometry of the reactants. The analysis of the VB structures for the reactant and excited states enables one to determine the factors that influence the barrier. The VB structures give dots for key valence electrons. For instance, in Compound I the π_{xz}/π^*_{xz} set of orbitals has three electrons, which is given on the right-hand-side of the Fe–O bond with three dots. Similarly, the π_{yz}/π^*_{yz} pair of orbitals have three electrons and these are given with three dots on the left-hand-side of the Fe–O bond. In addition, there is of course a radical on the porphyrin ring for single occupation of the a_{2u} orbital. Two electrons occupy the C–H bond of the substrate.

A look at the VB structure of the radical intermediate shows the same π_{yz}/π^*_{yz} occupation with three electrons, however, the π_{xz}/π^*_{xz} set of orbitals has ceased to exist and has reverted back into atomic orbitals ($3d_{xz}$ and $2p_x$). The $3d_{xz}$ orbitals remains as a nonbonding orbital and singly occupied, while the $2p_x$ orbital on the oxo group pairs up with the 1s orbital of the incoming hydrogen atom to form the new O–H bond (σ_{OH}). As the π_{xz}/π^*_{xz} set of orbitals had three electrons, this implies that one of these electrons will have to move to another orbital and indeed fills the a_{2u} orbital with a second electron. This change in orbitals is summarized and highlighted in the inset of Figure 4.6.

As a result, the hydrogen atom abstraction barrier will depend on the energy to split the π_{xz}/π^*_{xz} orbitals back into atomic orbitals (E_{π/π^*xz}) and an electron excitation from π_{xz} to a_{2u} (E_{exc}). In addition, the excitation energy refers to the breaking of the C–H bond and the formation of the O–H bond. The bond dissociation energy (BDE_{CH}) of the C–H bond of methane is ΔE+ZPE = 101.6 kcal mol^{-1}.[92] The O–H bond strength from Eq 4.1 for $\mathbf{1}_L$ with L = F^-, Cl^-, OH^-, CH_3COO^-, CF_3COO^- and SH^- was calculated, (Table 4.2). As follows the strength of the O–H bond that is formed varies by as much as 14 kcal mol^{-1} between L = CF_3COO^- and L = OH^-.

$$[Fe^{IV}(OH)(Por)L] \rightarrow [Fe^{IV}(O)(Por^{+\bullet})L] + H^{\bullet} + BDE_{OH} \qquad (4.1)$$

Table 4.2: Calculated thermochemical properties (ΔE+ZPE) for selected 1_L species (L = CF_3COO^-, Cl^-, SH^-, CH_3COO^-, F^- and OH^-). All energies are in kcal mol^{-1}.

	BDE_{OH}	EA($\mathbf{1}_L$)	ΔH_{acid}	BDE_{FeL}	E_{π/π^*xz}	E_{exc}
CF_3COO^-	85.4	85.8	314.3	90.7	ND	ND
Cl^-	87.6	79.2	305.5	ND	ND	ND
SH^-	89.3	71.6	296.3	112.2	81.2	88.2
CH_3COO^-	89.4	80.5	305.0	103.6	75.5	84.8
F^-	94.0	78.9	298.8	128.4	86.3	86.0
OH^-	99.4	76.0	290.5	137.5	75.2	79.4

In addition to the BDE_{OH} values for the oxidants, we calculated several other thermochemical properties. Firstly, the electron affinity (EA) of all complexes $\mathbf{1}_L$ from the difference in energy of $^4\mathbf{1}_L$ and its one-electron reduced species ($^3\mathbf{1}_L^-$) was calculated. Technically, a hydrogen atom transfer is the sum of an electron and a proton transfer, so that the BDE_{OH} can be split into a the electron affinity of the oxidant, the acidity of the iron(IV)-hydroxo complex (ΔH_{acid}) and the ionization potential of a hydrogen atom (IE_H), Eq 4.2. The latter was taken from the NIST database [112] and has a value IE_H = 313.9 kcal mol^{-1}.

$$BDE_{OH} = EA(\mathbf{1}_L) - \Delta H_{acid} + IE_H \tag{4.2}$$

As discussed above, the electron affinity of $\mathbf{1}_L$ is dependent on the amount of mixing of the axial ligand orbitals with the a_{2u} orbital on the porphyrin. With L = SH$^-$ this interaction is strong and as a consequence $\mathbf{1}_{SH}$ has a very low EA of 71.6 kcal mol^{-1}. A weak anionic ligand like CF_3COO^- gives weak interactions with the a_{2u} orbital and has a considerably higher EA of 85.8 kcal mol^{-1}. Neutral axial ligands, such as a solvent molecule or an imidazole group of a histidine give a further rise in electron affinity and removal of the axial ligand altogether gives a maximum electron affinity of about 8.2 eV [54] as determined by mass spectrometry.

The BDE_{OH} value of the various complexes depends on the electron affinity and ΔH_{acid} differences of the complex. As mentioned the electron affinity differences depend on the mixing of axial ligand and a_{2u} orbitals. The ΔH_{acid} value, however, contains an electronic component for the splitting of the π_{xz}/π^*_{xz} orbitals back into atomic orbitals and formation of the O–H bond. We analyzed the orbitals of the complexes in detail and determined the E_{π/π^*xz} and E_{exc} energy gaps and report those in the last two columns of Table 4.2. Both parameters vary by as much as 10 kcal mol^{-1} for the four iron(IV)-oxo species studied. The smaller the π_{xz}/π^*_{xz} energy splitting and the smaller the excitation energy from π_{xz} to a_{2u}, the lower in energy the hydrogen atom abstraction barrier will be.

4.4: Conclusions

In this work a series of computational studies are presented on the methane hydroxylation mechanism of models of Compound I of cytochrome P450, whereby the axial ligand is replaced by alternative anionic ligands. The work shows that an axial ligand at a distance well over 4 Å from the reaction center has a profound effect on the catalytic properties of the oxidant. We identified several key components. Firstly, there are thermochemical impacts on the electron affinity and iron(IV)-hydroxo acidity due to differences in orbital occupation. In addition, during the rate determining hydrogen atom abstraction the π-bond of the iron-oxo group needs to be broken and the π_{xz}/π^*_{xz} energy splitting affect the hydrogen atom abstraction. Finally, during the hydrogen atom abstraction step an electron migrates from the oxo group to the heme. In general, a hydroxide axial ligand gives small reaction barriers, and should be the best oxidant.

References:

1 R. Balasubramanian, A. C. Rosenzweig, *Acc. Chem. Res*., **40**, 573 (2007).

2 Y. Shiota, K. Yoshizawa, *Inorg. Chem*., **48**, 838 (2009).

3 R. A. Himes, K.Barnese, K. D. Karlin, *Angew. Chem. Int. Ed*., **49**, 6714 (2010).

4 S. P. de Visser, *J. Am. Chem. Soc*., **128**, 9813 (2006).

5 S. P. de Visser, *Angew. Chem. Int. Ed*., **45**, 1790 (2006).

6 S. P. de Visser, *Chem. Commun*., 171 (2007).

7 S. P. de Visser, *Coord. Chem. Rev*., **253**, 754 (2009).

8 B. Karamzadeh, D. Kumar, G. N. Sastry, S. P. de Visser, *J. Phys. Chem. A*, **114**, 13234 (2010).

9 S. Aluri, S. P. de Visser, *J. Am. Chem. Soc*., **129**, 14846 (2007).

10 S. P. de Visser, G. D. Straganz, *J. Phys. Chem. A*, **113**, 1835 (2009).

11 D. Kumar, W. Thiel, S. P. de Visser, *J. Am. Chem. Soc*., **133**, 3869 (2011).

12 D. Kumar, G. N. Sastry, D. P. Goldberg, S. P. de Visser, *J. Phys. Chem. A*, **116**, 582 (2012).

13 M. Sallmann, S. Kumar, P. Chernev, J. Nehrkorn, A. Schnegg, D. Kumar, H. Dau, C. Limberg, S. P. de Visser. *Chem. Eur. J*., **21**, 7470. (2015).

14 R. Latifi, M. Bagherzadeh, S. P. de Visser,*Chem. Eur. J*., **15**, 6651 (2009).

15 B. Meunier, S. P. de Visser, S. Shaik,*Chem. Rev*., **104**, 3947 (2004).

16 M. M. Abu-Omar, A. Loaiza, N. Hontzeas, *Chem. Rev*., **105**, 2227 (2005).

17 S. V. Kryatov, E. V. Rybak-Akimova, S. Schindler, *Chem. Rev*., **105**, 2175 (2005).

18 S. Shaik, D. Kumar, S. P. de Visser, A. Altun, W. Thiel, *Chem. Rev*., **105**, 2279 (2005).

19 S. P. de Visser, D. Kumar (eds) *Iron-containing enzymes: Versatile catalysts of hydroxylation reactions in nature*, Royal Society of Chemistry Publishing: Cambridge (UK) (2011).

20 L. Ji, A. S. Faponle, M. G. Quesne, M. A. Sainna,J. Zhang, A. Franke, D. Kumar, R. van Eldik, W. Liu, S. P. de Visser, *Chem. Eur. J*., **21**, 9083 (2015).

21 A. W. Munro, H. M. Girvan, K. J. McLean, *Nat. Prod. Rep*., **24**, 585 (2007).

22 M. R. Wester, E. F. Johnson, C. Marques-Soares, S. Dijols, P. M. Dansette, D. Mansuy, C. D. Stout, *Biochemistry*, **42**, 9335 (2003).

23 D. Kumar, H. Hirao, S. P. de Visser, J. Zheng, D. Wang, W. Thiel, S. Shaik, *J. Phys. Chem. B*, **109**, 19946 (2005).

24 P. K. Sharma, S. P. de Visser, S. Shaik, *J. Am. Chem. Soc*., **125**, 8698 (2003).

25 P. K. Sharma, R. Kevorkiants, S. P. de Visser, D. Kumar, S. Shaik, *Angew. Chem. Int. Ed*., **43**, 1129 (2004).

26 D. Kumar, S. P. de Visser, S. Shaik, *J. Am. Chem. Soc*., **127**, 8204 (2005).

27 D. Sahoo, M. G. Quesne, S. P. de Visser, S. P. Rath, *Angew. Chem. Int. Ed*., **54**, 4796 (2015).

28 S. P. de Visser, *J. Phys. Chem. A*, **109**, 11050 (2005).

29 S. P. de Visser, S. Shaik, *J. Am. Chem. Soc*., **125**, 7413 (2003).

30 S. P. de Visser, *Chem. Eur. J*., **12**, 8168 (2006).

31 S. P. de Visser, K. Oh, A-R. Han, W. Nam, *Inorg. Chem*., **46**, 4632 (2007).

32 C. Hazan, D. Kumar, S. P. de Visser, S. Shaik, *Eur. J. Inorg. Chem*., 2966 (2007).

33 S. P. de Visser, L. Tahsini, W. Nam, *Chem. Eur. J*., **15**, 5577, (2009).

34 D. Kumar, G. N. Sastry, S. P. de Visser, *J. Phys. Chem. B*, **116**, 718 (2012).

35 R. Latifi, L. Tahsini, W. Nam, S. P. de Visser, *Phys. Chem. Chem. Phys*., **14**, 2518 (2012).

36 S. Sahu, L. R. Widger, M. G. Quesne, S. P. de Visser, H. Matsumura, P. Moënne-Loccoz, M. A. Siegler, D. P. Goldberg, *J. Am. Chem. Soc*., **135**, 10590 (2013).

37 S. P. de Visser, F. Ogliaro, N. Harris, S. Shaik, *J. Am. Chem. Soc*., **123**, 3037 (2001).

38 S. P. de Visser, F. Ogliaro,S. Shaik, *Angew. Chem. Int. Ed*., **40**, 2871 (2001).

39 S. P. de Visser, F. Ogliaro,S. Shaik, *Chem. Commun*., 2322 (2001).

40 F. Ogliaro, S. P. de Visser, S. Cohen, P. K. Sharma, S. Shaik, *J. Am. Chem. Soc*., **124**, 2806 (2002).

41 S. P. de Visser, F. Ogliaro, P. K. Sharma, S. Shaik, *Angew. Chem. Int. Ed*., **41**, 1947 (2002).

42 S. P. de Visser, F. Ogliaro, P. K. Sharma, S. Shaik, *J. Am. Chem. So*c., **124**, 11809

(2002).

43 S. P. de Visser, J. Kaneti, R. Neumann,S. Shaik, *J. Org. Chem.*, **68**, 2903 (2003).

44 S. P. de Visser, D. Kumar, S. Shaik, *J. Inorg. Biochem.*, **98**, 1183 (2004).

45 D. Kumar, S. P. de Visser, P. K. Sharma, E. Derat, S. Shaik, *J. Biol. Inorg. Chem.*, **10**, 181 (2005).

46 D. Kumar, S. P. de Visser, S. Shaik, *Chem. Eur. J.*, **11**, 2825 (2005).

47 S. P. de Visser, *J. Am. Chem. Soc.*, **128**, 15809 (2006).

48 S. P. de Visser, *J. Biol. Inorg. Chem.*, **11**, 168 (2006).

49 S. P. de Visser, *J. Phys. Chem. B*, **110**, 20759 (2006).

50 S. P. de Visser, *Chem. Eur. J.*, **14**, 4533 (2008).

51 S. P. de Visser,W. Nam, *J. Phys. Chem. A*, **112**, 12887 (2008).

52 D. Kumar, B. Karamzadeh, G. N. Sastry, S. P. de Visser, *J. Am. Chem. Soc.*, **132**, 7656 (2010).

53 D. Kumar, R. Latifi, S. Kumar, E. V. Rybak-Akimova, M. A. Sainna, S. P. de Visser, *Inorg. Chem.*, **52**, 7968 (2013).

54 M. A. Sainna, S. Kumar, D. Kumar, S. Fornarini, M. E. Crestoni, S. P. de Visser, *Chem. Sci.*, **6**, 1516 (2015).

55 D. Kumar, S. P. de Visser, P. K. Sharma, H. Hirao, S. Shaik, *Biochemistry*, **44**, 8148 (2005).

56 D. Kumar, G. N. Sastry, S. P. de Visser, *Chem. Eur. J.*, **17**, 6196 (2011).

57 K. A. Prokop, H. M. Neu, S. P. de Visser, D. P. Goldberg, *J. Am. Chem. Soc.*, **133**, 15874 (2011).

58 N. C. Veitch, A. T. Smith, *Adv. Inorg. Chem.*, **51**, 107 (2000).

59 P. Vidossich, M. Mercedes Alfonso-Prieto, C. Rovira, *J. Inorg. Biochem.*, **117**, 292 (2012).

60 S. P. de Visser, S. Shaik, P. K. Sharma, D. Kumar,W. Thiel, *J. Am. Chem. Soc.*, **125**, 15779 (2003).

61 S. P. de Visser, *Inorg. Chem.*, **45**, 9551 (2006).

62 F. Ogliaro, S. P. de Visser, S. Shaik, *J. Inorg. Biochem.*, **91**, 554 (2002).

63 P. C. A. Bruijnincx, G. van Koten, R. J. M. Klein Gebbink, *Chem. Soc. Rev.*, **37**,

2716 (2008).

64 M. Costas, *Coord. Chem. Rev.*, **255**, 2912 (2011).

65 Z. Gross, S. Nimri, *Inorg. Chem.*, **33**, 1731 (1994).

66 M. J. Frisch, G. W. Trucks, H. B. Schlegel, G. E. Scuseria, M. A. Robb, J. R. Cheeseman, G. Scalmani, V. Barone, B. Mennucci, G. A. Petersson, H. Nakatsuji, M. Caricato, X. Li, H. P. Hratchian, A. F. Izmaylov, J. Bloino, G. Zheng, J. L. Sonnenberg, M. Hada, M. Ehara, K. Toyota, R. Fukuda, J. Hasegawa, M. Ishida, T. Nakajima, Y. Honda, O. Kitao, H. Nakai, T. Vreven, J. A. Montgomery Jr., J. E. Peralta, F. Ogliaro, M. Bearpark, J. J. Heyd, E. Brothers, K. N. Kudin, V. N. Staroverov, T. Keith, R. Kobayashi, J. Normand, K. Raghavachari, A. Rendell, J. C. Burant, S. S. Iyengar, J. Tomasi, M. Cossi, N. Rega, J. M. Millam, M. Klene, J. E. Knox, J. B. Cross, V. Bakken, C. Adamo, J. Jaramillo, R. Gomperts, R. E. Stratmann, O. Yazyev, A. J. Austin, R. Cammi, C. Pomelli, J. W. Ochterski, R. L. Martin, K.Morokuma, V. G.Zakrzewski, G. A. Voth, P. Salvador, J. J. Dannenberg, S. Dapprich, A. D. Daniels, O. Farkas, J. B. Foresman, J. V. Ortiz, J. Cioslowski,D. J. Fox, *Gaussian 09*, *Revision D.01*, Gaussian, Inc., Wallingford CT (2013).

67 M. G. Quesne, R. Latifi, L. E. Gonzalez-Ovalle, D. Kumar, S. P. de Visser, *Chem. Eur. J.*, **20**, 435 (2014).

68 S. P. de Visser, M. G. Quesne, B. Martin, P. Comba, U. Ryde, *Chem. Commun.*, **50**, 262 (2014).

69 M. A. Sainna, D. Sil, D. Sahoo, B. Martin, S. P. Rath, P. Comba, S. P. de Visser, *Inorg. Chem.*, **54**, 1919 (2015).

70 A. D. Becke, *J. Chem. Phys.*, **98**, 5648 (1993).

71 C. Lee, W. Yang, R. G. Parr, *Phys. Rev. B*, **37**, 785 (1988).

72 P. J. Hay, W. R. Wadt, *J. Chem. Phys.*, **82**, 299 (1985).

73 D. Kumar, L. Tahsini, S. P. de Visser, H. Y. Kang, S. J. Kim, W. Nam, *J. Phys. Chem. A*, **113**, 11713 (2009).

74 H. M. Neu, M. G. Quesne, T. Yang, K. A. Prokop-Prigge, K. M. Lancaster, J. Donohoe, S. DeBeer, S. P. de Visser, D. P. Goldberg, *Chem. Eur. J.*, **20**, 14584 (2014).

75 A. K. Vardhaman, C. V. Sastri, D. Kumar, S. P. de Visser,*Chem. Commun.*, **47**, 11044 (2011).

76 A. K. Vardhaman, P. Barman, S. Kumar, C. V. Sastri, D. Kumar, S. P. de Visser, *Chem. Commun.*, **49**, 10926 (2013).

77 R. Jastrzebski, M. G. Quesne, B. M. Weckhuysen, S. P. de Visser, P. C. A. Bruijnincx, *Chem. Eur. J.*, **20**, 15686 (2014).

78 A. Draksharapu, D. Angelone, M. G. Quesne, S. K. Padamati, L. Gómez, R. Hage, M. Costas, W. R. Browne,S. P. de Visser, *Angew. Chem. Int. Ed.*, **54**, 4357 (2015).

79 F. Ogliaro, S. Cohen, S. P. de Visser,S. Shaik, *J. Am. Chem. Soc.*, **122**, 12892 (2000).

80 F. Ogliaro, S. P. de Visser, J. T. Groves, S. Shaik, *Angew. Chem. Int. Ed.*, **40**, 2874 (2001).

81 F. Ogliaro, S. P. de Visser, S. Cohen, J. Kaneti, S. Shaik, *Chem. Bio. Chem.*, **2**, 848 (2001).

82 P. K. Sharma, S. P. de Visser, F. Ogliaro, S. Shaik, *J. Am. Chem. Soc.*, **125**, 2291 (2003).

83 D. Kumar, S. P. de Visser, S. Shaik, *J. Am. Chem. Soc.*, **125**, 13024 (2003).

84 D. Kumar, S. P. de Visser, P. K. Sharma, S. Cohen, S. Shaik, *J. Am. Chem. Soc.*, **126**, 1907 (2004).

85 D. Kumar, S. P. de Visser, S. Shaik, *J. Am. Chem. Soc.*, **126**, 5072 (2004).

86 S. P. de Visser, D. Kumar, S. Cohen, R. Shacham, S. Shaik, *J. Am. Chem. Soc.*, **126**, 8362 (2004).

87 S. Shaik, S. P. de Visser, D. Kumar, *J. Am. Chem. Soc.*, **126**, 11746 (2004).

88 R. Wang, S. P. de Visser, *J. Inorg. Biochem.*, **101**, 1464 (2007).

89 S. P. de Visser, *J. Phys. Chem. B*, **111**, 12299 (2007).

90 S. P. de Visser, L. S. Tan, *J. Am. Chem. Soc.*, **130**, 12961 (2008).

91 E. Godfrey, C. S. Porro, S. P. de Visser, *J. Phys. Chem. A*, **112**, 2464 (2008).

92 S. Shaik, D. Kumar,S. P. de Visser, *J. Am. Chem. Soc.*, **130**, 10128 (2008).

93 D. J. Heyes, M. Sakuma, S. P. de Visser, N. S. Scrutton, *J. Biol. Chem.*, **284**, 3762 (2009).

94 S. J. Kim, R. Latifi, H. Y. Kang, W. Nam, S. P. de Visser, *Chem. Commun.*, 1562 (2009).

95 L. Tahsini, M. Bagherzadeh, W. Nam, S. P. de Visser, *Inorg. Chem.*, **48**, 6661 (2009).

96 S. P. de Visser, *J. Am. Chem. Soc.*, **132**, 1087 (2010).

97 K. A. Prokop, S. P. de Visser, D. P. Goldberg, *Angew. Chem. Int. Ed.*, **49**, 5091 (2010).

98 S. P. de Visser, R. Latifi, L. Tahsini, W. Nam, *Chem. Asian J.*, **6**, 493 (2011).

99 R. Latifi, L. Tahsini, B. Karamzadeh, N. Safari, W. Nam, S. P. de Visser, *Arch. Biochem. Biophys.*, **507**, 4 (2011).

100 R. Latifi, L. Tahsini, D. Kumar, G. N. Sastry, W. Nam, S. P. de Visser, *Chem. Commun.*, **47**, 10674 (2011).

101 S. P. de Visser, *Adv. Inorg. Chem.*, **64**, 1 (2012).

102 R. Latifi, J. S. Valentine, W. Nam, S. P. de Visser, *Chem. Commun.*, **48**, 3491 (2012).

103 S. P. de Visser, *J. Porph. Phthalocyanines*, **17**, 954 (2013).

104 S. P. de Visser, J-U.Rohde, Y-M. Lee, J. Cho, W. Nam, *Coord. Chem. Rev.*, **257**, 381 (2013).

105 R. Latifi, M. A. Sainna, E. V. Rybak-Akimova, S. P. de Visser, *Chem. Eur. J.*, **19**, 4058 (2013).

106 S. M. Pratter, C. Konstantinovics, C. L. M. DiGiuro, E. Leitner, D. Kumar, S. P. de Visser, G. Grogan, G. D.Straganz, *Angew. Chem. Int. Ed.*, **52**, 9677 (2013).

107 A. K. Vardhaman, P. Barman, S. Kumar, C. V. Sastri, D. Kumar, S. P. de Visser,*Angew. Chem. Int. Ed.*, **52**, 12288 (2013).

108 S. Kumar, A. S. Faponle, P. Barman, A. K. Vardhaman, C. V. Sastri, D. Kumar, S. P. de Visser, *J. Am. Chem. Soc.*, **136**, 17102 (2014).

109 B. Karamzadeh, D. Singh, W. Nam, D. Kumar, S. P. de Visser, *Phys. Chem. Chem. Phys.*, **16**, 22611 (2014).

110 F. Ogliaro, N. Harris, S. Cohen, M. Filatov, S. P. de Visser, S. Shaik, *J. Am. Chem. Soc.*, **122**, 8977 (2000).

111 S. Shaik, S. Cohen, S. P. de Visser, P. K. Sharma, D. Kumar, S. Kozuch, F. Ogliaro, D. Danovich, *Eur. J. Inorg. Chem.*: 207 (2004).

112 P. J. Linstrom, W. G. Mallard, *NIST Chemistry WebBook, NIST Standard Reference Database, Number 69,* National Institute of Standards and Technology, Gaithersburg MD, 20899 (2015) (http://webbook.nist.gov).

CHAPTER 5

PROPERTIES AND REACTIVITIES OF NONHEME IRON(IV)-OXO VERSUS IRON(V)-OXO: LONG RANGE ELECTRON TRANSFER VERSUS HYDROGEN ATOM ABSTRACTION

CHAPTER 5

PROPERTIES AND REACTIVITIES OF NONHEME IRON(IV)-OXO VERSUS IRON(V)-OXO: LONG-RANGE ELECTRON TRANSFER VERSUS HYDROGEN ATOM ABSTRACTION

5.1: Introduction

Nonheme iron dioxygenases are important enzymes for human health with essential functions that include DNA base repair mechanisms and oxidative cleavage of carotenoids.[1-7] In several organisms, natural product biosynthesis is catalysed by nonheme iron dioxygenases, and, therefore, they have important functions in biology as well as in biotechnology. In order to understand enzymatic reaction processes, synthetic model complexes have been developed and designed.[8-14] These biomimetic model complexes of nonheme iron oxidants are well studied and many biomimetic high-valent catalytic intermediates have been characterized in recent years.[15-20] For instance, to tackle the controversy in Rieske dioxygenases regarding the active oxidant in the reaction process, several biomimetic model complexes with iron(V)-oxo(hydroxo) as reactive features have been studied and their reactivity patterns were also established.[21-26]

All biomimetic Rieske dioxygenase models contain a hydroxo group in a *cis*-position of the iron(IV/V)-oxo group. Only few examples exist of biomimetic iron(V)-oxo intermediates without this *cis*-hydroxo ligand and spectroscopic studies gave indirect evidence of its existence.[27,28] Thus, McKenzie and co-workers reported the structural characterization of an iron(V)-oxo species with a monoionic multidentate ligand and found it to react with thioanisole efficiently.[29,30] Kim and co-workers used a tetradentate ligand system and formed the corresponding iron(V)-oxo species by heterolytic cleavage of an iron-acylperoxo intermediate.[31] They determined kinetic isotope effects (KIE, k_H/k_D), $H_2{}^{18}O$ exchange reactions and measured product distributions. Using a tetraamido macrocyclic ligand, Collins and co-workers studied the sulfoxidation of substrates by an iron(V)-oxo species and compared the rates with analogous iron(IV)-oxo species.[32] Finally, Nam and co-workers studied the reaction of $[Fe^{II}(BQEN)]^{2+}$, BQEN = *N*,*N*'-dimethyl-*N*,*N*'-bis(8-quinolyl) ethane-1,2-diamine, with CH_3CO_3H and found evidence of competing reaction mechanisms originating from two oxidants in the reaction mixture that were tentatively assigned as $[Fe^{IV}(O)(BQEN)]^{2+}$ and $[Fe^{V}(O)(BQEN)]^{3+}$.[33] Their studies failed to unequivocally assign the active oxidant in the reaction mechanism, and therefore could not assign the relative reactivity of iron(IV)-oxo versus iron(V)-oxo. In order to resolve this dichotomy and gain general insight into the relative reactivity of iron(IV)-oxo versus iron(V)-oxo with nonheme ligand systems a computational study was conducted using the $[Fe^{IV}(O)(BQEN)(NCCH_3)]^{2+}$ (**1**) and $[Fe^{V}(O)(BQEN)(NCCH_3)]^{3+}$ (**2**) systems, Figure 5.1.

Currently, very little is known on the catalytic activity of iron(V)-oxo intermediates and to the best of our knowledge, no direct comparison in reactivity between iron(IV)-oxo and iron(V)-oxo has been reported. We present here a DFT study to to gain insight into the potential use of iron(V)-oxo intermediates as catalytic oxidant with ethylbenzene as the selected substrate. Here, we present the first comparative study of the aliphatic hydroxylation by iron(IV)-oxo versus iron(V)-oxo using the BQEN ligand system in Figure 5.1 and follow the mechanism of ethylbenzene activation leading to benzyl alcohol product complexes.

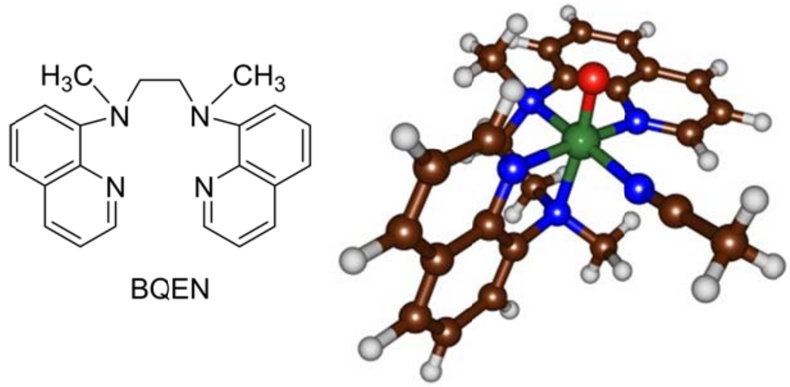

1: $[Fe(O)(BQEN)(NCCH_3)]^{2+}$
2: $[Fe(O)(BQEN)(NCCH_3)]^{3+}$

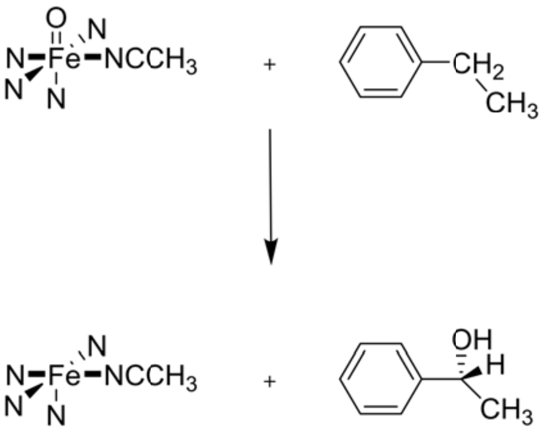

Figure 5.1: Iron-oxo oxidants and ligand system studied in this chapter.

5.2: Methods

All studies reported here utilize density functional theory (DFT) methods as implemented in the *Jaguar* and *Gaussian* program packages.[34,35] We initially did exploratory gas-phase optimizations on $[Fe(O)(BQEN)(NCCH_3)]^{3+/2+}$ in *Jaguar* at the UB3LYP level of theory [36,37] and explored the catalytic mechanism of ethylbenzene hydroxylation. However, as most of our chemical systems are multiply charged ions we decided to do a subsequent set of calculations, where the complete project was done using a polarized continuum solvent model included during the geometry optimizations. These studies gave considerable differences from the gas-phase results and therefore our focus will be on the solvent optimized calculations mainly. Thus, all geometry optimizations and frequencies were performed with a solvent model included with a dielectric constant mimicking acetonitrile. All local minima are characterized with a frequency calculation and have real frequencies only, whereas the transition states have one imaginary frequency for the correct mode. As transition metal containing complexes give close-lying electronic and spin states,[38,39] the $[Fe(O)(BQEN)(NCCH_3)]^{3+}$ complexes in the lowest lying doublet, quartet and sextet spin states and the $[Fe(O)(BQEN)(NCCH_3)]^{2+}$ complexes in the singlet, triplet and quintet spin states were calculated.

The reproducibility and reliability of the density functional method by applying a range of unrestricted DFT methods have been tested, including B3LYP,[36,37] B3LYP-D3,[40] B3LYP*,[41] and OPBE.[42,43] There is a certain degree of fluctuation observed in the relative energies, spin state ordering and geometric details as commonly observed in nonheme iron complexes.[44] However, the results confirmed the assignment of the electron configuration of all complexes and reproduced experimental trends.

All optimizations and frequencies use a triple-ζ quality basis set (BS2) with LACV3P+ on iron and 6-311+G* on the rest of the atoms.[45,46] Previously, these methods were extensively used for the description of nonheme iron complexes and reproduced experimental free energies of activation within several kcal mol^{-1}.[47-49] To test the effect of the overall charge on the calculations, we performed a set of test calculations to neutralize the reactants and rate determining transition states by adding counter-ions at a fixed distance of 15Å from the axial nitrogen atom and with an angle of 120 degrees with respect to iron and the axial nitrogen atom. Point charges, Cl^- counter-ions and OH^- counter-ions were applied, but all results reproduced the solvent optimized results and did not give changes to the charge and spin distributions.

Kinetic isotope effects (KIEs) were calculated for the hydrogen atom abstraction reaction of ethylbenzene by **1** for the replacement of one or more hydrogen atoms of the substrate by deuterium atoms. Initially the semi-classical Eyring equation (Eq 5.1) was used to calculate KIE_E from the difference in free energies of activation ($\Delta G^{\ddagger}$) of the substrate and its deuterium substituted form following previously reported methods.[50,51] Eq 5.1 uses the gas constant (R) and the actual temperature (273.15 K).

$$KIE_E = k_H/k_D = \exp\{(\Delta G^{\ddagger}_D - \Delta G^{\ddagger}_H)/RT\} \qquad (5.1)$$

Further corrections due to tunnelling were applied using the Wigner model [52] that corrects KIE_E with the tunnelling ratio (Q_{tH}/Q_{tD}) as described in Eq 5.2 and 5.3.

$$\text{KIE}_W = \text{KIE}_E \times Q_{tH}/Q_{tD} \tag{5.2}$$

$$Q_t = 1 + \frac{1}{24}\left(\frac{h\nu}{k_B T}\right)^2 \tag{5.3}$$

In Eq 5.3, k_B represents the Boltzmann's constant, h is Planck's constant and ν is the imaginary frequency in the transition state.

5.3: Results

5.3.1: Isolated reactants 1 and 2.

Our study uses density functional theory (DFT) methods and is focused on the chemical systems of Ref. 33 as described in Figure 5.1, where we included an acetonitrile solvent molecule in the sixth ligand position of the metal: $[\text{Fe(O)(BQEN)(NCCH}_3)]^{2+}$ (**1**) and $[\text{Fe(O)(BQEN)(NCCH}_3)]^{3+}$ (**2**). These structures have the metal in formal oxidation state iron(IV) and iron(V), respectively. Before looking into the reactivity patterns of structures **1** and **2** with substrates, we describe the electronic properties of the optimized geometries of **1** and **2**, Figure 5.2.

The lowest lying singlet, triplet and quintet spin states of **1** were calculated, but the singlet state was found to be high in energy. Similarly, **2** was investigated in the doublet and quartet spin states only. Figure 5.2 displays the molecular valence orbitals of **1** and **2**, which are determined by the mixing of the metal 3d orbitals with its ligands. Thus, there are three π* molecular orbitals (π^*_{xy}, π^*_{yz}, π^*_{xz}) representing the anti-bonding interactions of the 3d iron orbitals with 2p orbitals on the oxo group. High in energy are two σ* orbitals for the anti-bonding interactions of the metal with the ligands in the *xy*-plane (σ^*_{x2-y2}) and with ligands along the *z*-axis (σ^*_{z2}), whereby the *z*-axis is defined as parallel to the Fe–O bond. In the iron(IV)-oxo complex, i.e. ^{3,5}**1**, the set of orbitals shown in Figure 5.2 is occupied by four electrons, which gives two low-lying solutions with either triplet or quintet spin: **1** has a triplet spin ground state with electronic configuration $\pi^*_{xy}{}^2\pi^*_{xz}{}^1\pi^*_{yz}{}^1$ (^{3}**1**) that is somewhat lower in energy than the quintet spin state with configuration $\pi^*_{xy}{}^1\pi^*_{xz}{}^1\pi^*_{yz}{}^1\sigma^*_{x2-y2}{}^1$ (^{5}**1**), *vide supra*. In both spin states **1** has the metal in formal oxidation state iron(IV). The spin state ordering matches previous studies on hexa-coordinated nonheme iron biomimetic model complexes and also supports the experimentally reported absorption band at λ_{max} = 740 nm characteristic for triplet iron(IV)-oxo species and assigned by Nam *et al.* on $[Fe(O)(BQEN)(NCCH_3)]^{2+}$.[15-20,33,53-55]

Upon oxidation of ^{3,5}**1**, however, several possibilities arise for the electronic configuration of **2**. Firstly, ^{3}**1** can lose an electron from π^*_{yz} to give a doublet spin configuration with $\pi^*_{xy}{}^2\pi^*_{xz}{}^1$ orbital occupation or lose an electron from the doubly occupied π^*_{xy} orbital to give a quartet spin complex with $\pi^*_{xy}{}^1\pi^*_{xz}{}^1\pi^*_{yz}{}^1$ configuration. These two states have the metal in formal oxidation state iron(V) and are labelled as ^{2,4}**2** in Figure 5.2. In addition, the oxidation of ^{3}**1** can expel an electron from a ligand π-type orbital, such as π^*_{BQEN}, and lead to an electronic configuration

$\pi^*_{xy}{}^2\pi^*_{xz}{}^1\pi^*_{yz}{}^1\pi^*_{BQEN}{}^1$, whereby the radical on the ligand can be either ferromagnetically or anti-ferromagnetically coupled to the metal-based unpaired electrons in an overall quartet or doublet spin state (^{4,2}**2’**). The latter, therefore, can be seen as an iron(IV)-oxo ligand cation radical species with configuration $[Fe^{IV}(O)(BQEN^{+\bullet})(NCCH_3)]^{3+}$ and is reminiscent of Compound I of cytochrome P450 enzymes, which was characterized as an iron(IV)-oxo heme cation radical species, i.e. $[Fe^{IV}(O)(heme^{+\bullet})Cys]$.[56-58]

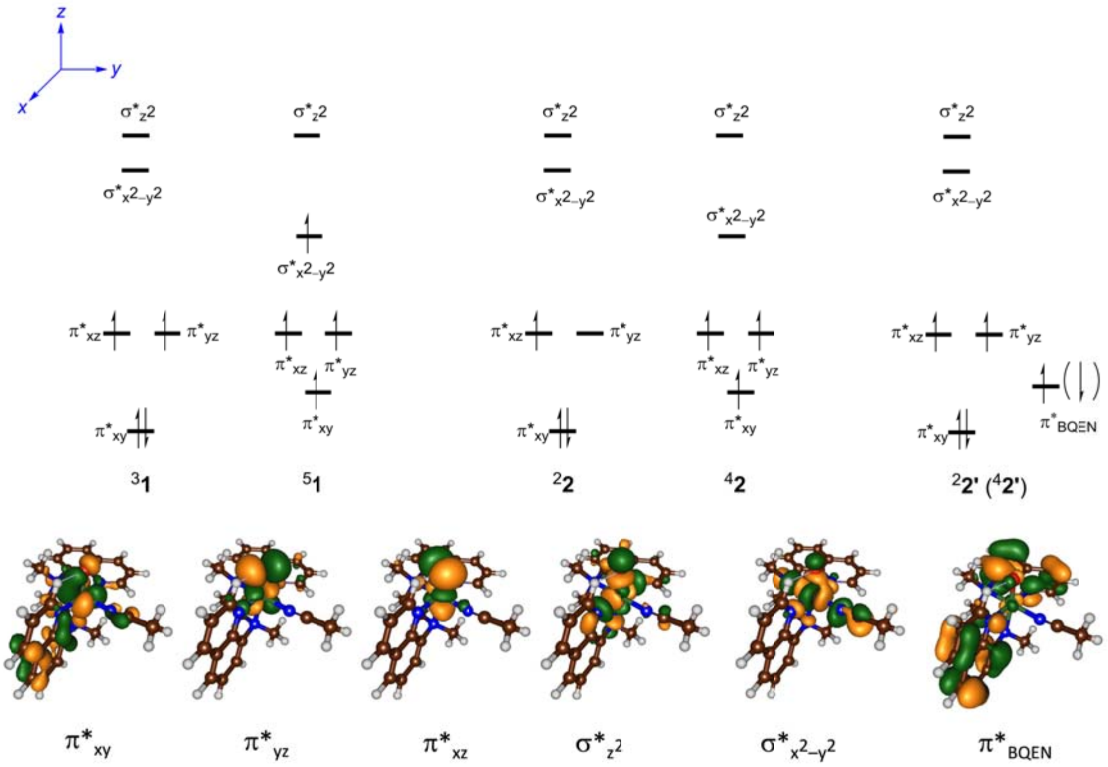

Figure 5.2: High-lying occupied and low-lying virtual orbitals of **1** and **2**. The top panel gives the different electronic configurations of **1** and **2** considered and the bottom gives the orbital shapes of the valence orbitals.

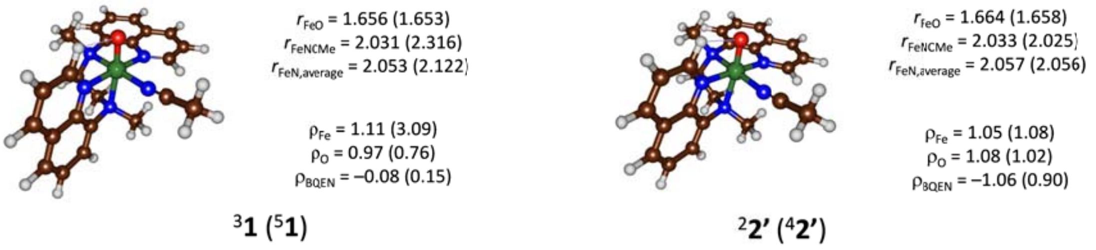

Figure5.3: Gas-phase optimized geometries (UB3LYP/BS1) of ^{3,5}**1** and ^{2,4}**2** with bond lengths in angstroms and group spin densities (ρ) in atomic units.

Details of the optimized geometries of ^{3,5}**1** and ^{2,4}**2’** in the gas phase are reported in Figure 5.3. In the gas-phase the triplet spin state is the ground state by ΔE+ZPE (ΔG) = 2.0 (0.2) kcal mol^{-1}. Optimized geometries are in line with previously reported structures on non-heme iron(IV)-oxo complexes with a short Fe–O bond of 1.66 Å, which implicates a double bond.[53-55,59-63] Group spin densities and charges confirm the orbital assignment of ^{3,5}**1** as described in Figure 5.3 with electronic configuration of $\pi^*_{xy}{}^2\pi^*_{xz}{}^1\pi^*_{yz}{}^1$ for ^{3}**1** and $\pi^*_{xy}{}^1\pi^*_{xz}{}^1\pi^*_{yz}{}^1\sigma^*_{x2-y2}{}^1$ for ^{5}**1**.

Nam and co-workers [33] using absorption and infrared spectroscopy and extended X-ray absorption fine structure (EXAFS) studied the [Fe(O)(BQEN)(NCCH$_3$)]$^{2+}$ complex experimentally. They identified an iron-oxo bond of 1.67 Å and an average Fe–N distance of 1.97 Å. Our calculated Fe–O distances for ^{3,5}**1** in Figure 5.3 match the experimental values excellently. The experimentally reported Fe–N distances are in good agreement with the triplet spin structures, but not with the quintet spin state structures due to single occupation of the σ^*_{x2-y2} orbital that elongates the distances between the metal and its ligands. Therefore, the computational studies support the characterization of a triplet spin ground state of **1**.

Geometry optimizations of ^{2,4}**2’**, however, gives a low-lying solution with two singly occupied π* orbitals coupled to a radical on the BQEN unit with spin densities of $\rho_{BQEN} = -1.06$ (0.90) in the doublet and quartet spin states. The optimized geometries, therefore, correspond to an electronic state $[Fe^{IV}(O)(BQEN^{+\bullet})(NCCH_3)]^{3+}$, i.e. ^{2,4}**2’** in Figure 5.2, rather than an iron(V)-oxo species. Although we attempted to swap molecular orbitals to generate the iron(V) solution (^{2,4}**2**) these calculations converged back to ^{2,4}**2’**, which therefore is the molecular ground state.

As the complex has a large overall charge of +3, it was decided to re-optimize these structures using the polarized continuum model mimicking an acetonitrile solution. However, the new model did not affect the spin state ordering and electronic configuration of the ground state and the same electronic state was found. It appears, therefore, that ^{2,4}**2’** is the electronic ground state that can be described as $[Fe^{IV}(O)(BQEN^{+\bullet})(NCCH_3)]^{3+}$ with an iron(IV)-oxo group coupled to a ligand radical. As both doublet and quartet spin states represent the same orbital occupation, namely $\pi^*_{xy}{}^2\pi^*_{xz}{}^1\pi^*_{yz}{}^1\pi^*_{BQEN}{}^1$, we calculate them within 2 kcal mol^{-1}. This result is similar to the spin state energies of ferromagnetically versus antiferromagnetically coupled doublet and quartet spin states of Compound I of P450, where these spin states were also found to be within a couple of kcal mol^{-1} from each other. Moreover, the energy gap was found to be sensitive to the local environment, including hydrogen bonding interactions to the oxidant as well as solvent effects.[64-67] Furthermore, these two spin states result in two-state-reactivity patterns with substrates on competing spin-state surfaces.[68] Analogously to P450 Compound I, the iron(V)-oxo species is an excited state of the molecular ground state with configuration

$[Fe^{IV}(O)(BQEN^{+\bullet})(NCCH_3)]^{3+}$. Geometrically ^{2,4}**2'** has metal-ligand bond lengths close to those found for ^{3}**1**, which also is an iron(IV)-oxo species.

5.3.2: Reactant complexes

Subsequently, ethylbenzene (EB) was added to the model complexes to create a long-range reactant complex (**RC**) as this was one of the substrates used in the experimental study and the benzyl hydroxylation processes were investigated. The electronic features of ^{3,5}**RC**$_1$ or $^{3,5}[Fe(O)(BQEN)(NCCH_3)\text{---}EB]^{2+}$ and ^{2,4}**RC**$_2$ or $^{2,4}[Fe(O)(BQEN)(NCCH_3)\text{---}EB]^{3+}$ will be discussed prior to the investigation of the catalytic mechanism. Considering that computational modelling occasionally is sensitive to the choice of the density functional used as well as on environmental variables,[69] some thorough testing of the structures, spin-state energetics and electronic configurations of ^{3,5}**RC**$_1$ and ^{2,4}**RC**$_2$ using a selection of density functional methods and procedures was carried out. Thus, geometry optimizations of all complexes in the gas-phase at UB3LYP/BS1 were performed, but also a full geometry optimization in a dielectric constant mimicking acetonitrile at UB3LYP/BS2 was done and finally a full geometry optimization in a dielectric constant at the UB3LYP-D3/BS2 was performed. In addition, single point calculations on the UB3LYP/BS2 optimized geometries using B3LYP with 15% HF exchange (B3LYP*), UB3LYP-D3 and OPBE were performed. Finally, single point calculations in the gas-phase with additional counter-ions or point charges included in the model at a distance of 15Å that neutralize the chemical systems were carried out.

Table 5.1 presents the optimized Fe–O distance and spin-state energies as obtained using these different DFT models and methods. As can be seen all methods, models and optimization techniques give the same spin state ordering, but a certain degree of variation in the relative energies is observed typical for DFT calculated iron complexes.[69] In all cases ^{3}**RC**$_1$ and ^{5}**RC**$_1$ are characterized as $[\mathrm{Fe^{IV}(O)(BQEN)(NCCH_3)}\text{---}\mathrm{EB}]^{2+}$ with orbital occupation $\pi^*_{xy}{}^2\pi^*_{xz}{}^1\pi^*_{yz}{}^1$ and $\pi^*_{xy}{}^1\pi^*_{xz}{}^1\pi^*_{yz}{}^1\sigma^*_{x2-y2}{}^1$, respectively, in agreement with what was found for structure ^{3,5}**1** above. Regardless of the method and whether the optimization is done in the gas-phase or in solvent, a triplet spin ground state that is well separated from the quintet spin state by 2.4 – 10.3 kcal mol^{-1} is found. Although this appears to be a large variation in spin state energies, actually for transition metal complexes, and, in particular iron(IV)-oxo complexes a strong variation of the ordering and relative energies is normal in DFT upon changing the density functional method or environmental effects.[70-72] Nevertheless, all methods give a triplet spin ground state in support of experimental studies.[45,46]

Table 5.1: Spin state energies and optimized geometries of reactant complexes as calculated with various DFT methods.

Structure	$r_{FeO}{}^{a,b}$	$r_{FeO}{}^{b,c}$	$r_{FeO}{}^{b,e}$	ΔE+ZPE UB3LYP Gas^{a,d}	 UB3LYP Solv^{c,d}	 UB3LYP-D3 Solv^{c,d}	 UB3LYP-D3 Solv^{d,e}	 UB3LYP PC^{c,f}	 UB3LYP* Solv^{c,d}	 OPBE Solv^{c,d}
^{3}RC$_1$	1.656	1.633	1.657	0.0	0.0	0.0	0.0	0.0	0.0	0.0
^{5}RC$_1$	1.653	1.627	1.653	10.3	2.5	7.4	8.2	8.7	6.0	2.4
^{2}RC$_2$	1.664	1.638	1.656	0.0	0.0	0.0	0.0	0.0	0.0	0.0
^{4}RC$_2$	1.664	1.631	1.653	0.6	-3.6	10.0	8.4	10.0	6.9	3.8

^{a}UB3LYP/BS1 geometry optimization in the gas-phase. ^{b} Values in Å. ^{c} UB3LYP/BS2 geometry optimization in solvent, ^{d}ΔE+ZPE value with energies at BS2 level of theory in kcal mol^{-1}. ^{e} UB3LYP-D3/BS2 geometry optimization in solvent, ^{f}Structure with added point charges that neutralize the system at 15Å

The situation is dramatically changed when $^{2,4}\mathbf{RC}_2$ is investigated with these methods and models. Whereas ^{2,4}**2’** was found as the electronic ground state with configuration $[Fe^{IV}(O)(BQEN^{+\bullet})(NCCH_3)]^{3+}$ with two unpaired π* electrons coupled to a radical on the ligand, by contrast, in $^{2,4}\mathbf{RC}_2$ we find yet another electronic configuration with two unpaired π* electrons that are coupled to an ethylbenzene radical, i.e. orbital occupation $\pi^*_{xy}{}^2\pi^*_{xz}{}^1\pi^*_{yz}{}^1\pi^*_{BQEN}{}^2\pi_{EB}{}^1$, where the latter orbital is a singly occupied π-orbital on ethylbenzene. Therefore, addition of an ethylbenzene molecule to ^{2,4}**2’** results in an intermolecular electron transfer from the substrate into the π^*_{BQEN} orbital of the oxidant and the creation of a complex $[Fe^{IV}(O)(BQEN)(NCCH_3)]^{2+}$---$EB^{+\bullet}$. This happens regardless of the method and whether gas-phase or solvent models are used. It implies that $[Fe^{IV}(O)(BQEN^{+\bullet})(NCCH_3)]^{3+}$ is a strong oxidant and can abstract electrons from substrates readily. Most probably this is caused by its extremely large electron affinity, *vide supra*

Note that outer-sphere electron transfer upon approach of a substrate onto a metal-oxo species has been calculated before on metal-porphyrins,[73,74] including a potential intermediate of nitric oxide synthase, where the arginine substrate was found to donate an electron to an iron(IV)-oxo heme cation radical species quickly. Furthermore, approach of a Zn^{2+} ion onto a high-valent manganese(V)-oxo corrolazine also led to the formation of a manganese(IV)-oxo corrolazine cation radical through valence tautomerization.[74] Finally, studies on the comparative electronic features of the iron(IV)-oxo heme species of cytochrome *c* peroxidase (C*c*P) versus ascorbate peroxidase implicated differences in electronic configuration as a result of a bound cation at a distance of 15 Å from the heme. DFT modelling on

Compound I of C*c*P tested the effect of a point charge with magnitude $Q = -1/+1$ on the electronic configuration.[75] It was found that a charge of $Q = +1$ gave an electronic state $[\mathrm{Fe}^{\mathrm{IV}}(\mathrm{O})(\mathrm{heme}^{+\bullet})\text{---}\mathrm{Trp}_{191}]$, whereas a value of $Q = -1$ resulted in an alternative state corresponding to $[\mathrm{Fe}^{\mathrm{IV}}(\mathrm{O})(\mathrm{heme})\text{---}\mathrm{Trp}_{191}{}^{+\bullet}]$. These studies have shown that seemingly small external (but long-range) perturbations can have a major impact on the electronic configuration of the oxidant and consequently on its ability to react with substrates. However, for nonheme metal-oxo species this would be the first example of outer-sphere electron transfer upon substrate approach and is likely caused by the large electron affinity of the ligand. In the following we will describe whether the change in electronic configuration is beneficial or disadvantageous to the catalysis.

5.3.3: Ethylbenzene hydroxylation by 1 and 2

Subsequently, the benzyl hydroxylation of ethylbenzene by $^{3,5}\mathbf{RC}_1$ and $^{2,4}\mathbf{RC}_2$ was calculated. Figure 5.4 displays the calculated reaction mechanism with optimized geometries of the rate determining transition states of the reaction starting from $^{3,5}\mathbf{RC}_1$. A stepwise mechanism with an initial hydrogen atom abstraction from the benzyl position of ethylbenzene via a transition state ($\mathbf{TS}_{\mathrm{HA}}$) to form a radical intermediate (**I**) followed by hydroxyl rebound via a transition state ($\mathbf{TS}_{\mathrm{reb}}$) to form alcohol products (**P**) was calculated. In all cases the hydrogen atom abstraction is rate determining and the rebound barriers are small or negligible, so that we will focus on $\mathbf{TS}_{\mathrm{HA}}$ pathway only here. In the gas phase very little energy difference between hydrogen atom abstraction from the *pro-S* versus *pro-R* site of the benzyl position of ethylbenzene by iron(IV)-oxo complexes was found. Recent computational studies on

S-mandalate synthase showed that the shape and size of the substrate binding pocket determines whether the *pro-R* or *pro-S* hydrogen atom can be abstracted.[76] Indeed, site-selective mutations confirmed the computationally proposed hypothesis.

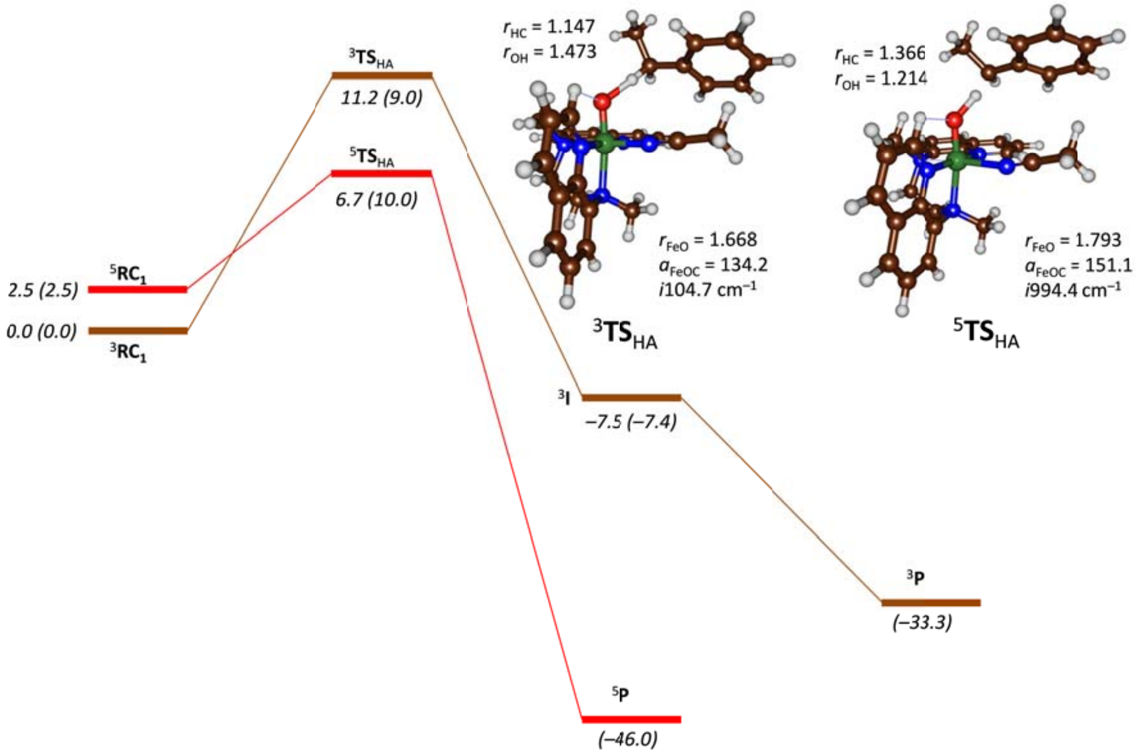

Figure5.4: DFT calculated potential energy profile for the hydrogen atom abstraction from EB by ^{3,5}**1** with energies given in kcal mol^{-1}. Also shown are optimized UB3LYP/BS2(solvent) geometries of ^{3,5}**TS**$_{\text{HA}}$ with bond lengths in angstroms, angles in degrees and the imaginary frequency in wave numbers. Relative energies represent ΔE+ZPE+E$_{\text{solv}}$ values obtained after a full geometry optimization in solvent at UB3LYP/BS2 (out of parenthesis) or at UB3LYP/BS2//UB3LYP/BS1 level of theory on a gas-phase optimized geometry

---

Geometrically, the ^{3,5}**TS**$_{\text{HA}}$ structures are quite distinct due to differences in electron transfer processes that happen in these transition states. In the triplet spin state the hydrogen atom transfer is accompanied with electron transfer from the substrate into the π^*_{xz} orbital and hence the substrate attacks under an angle (a_{FeOC} = 134.2°) to get ideal orbital overlap between donor and acceptor orbitals.[77] In the quintet spin state the hydrogen atom abstraction is accompanied with electron transfer from substrate into the vacant σ^*_{z2} orbital and hence the substrate attacks from the top with considerably larger Fe-O-C angles than found in the triplet spin state (a_{FeOC} = 151.1°), which gives an iron(III)-hydroxo complex with fully exchange coupled metal 3d system with five singly occupied orbitals that is anti-ferromagnetically coupled to a benzyl radical: ^{5}**I** has electronic configuration $\pi^*_{xy}{}^1\pi^*_{xz}{}^1\pi^*_{yz}{}^1\sigma^*_{x2-y2}{}^1\sigma^*_{z2}{}^1\pi_{EB}{}^1$. This exchange stabilization makes ^{5}**I** considerably lower in energy than the corresponding triplet spin complex. As a consequence, ^{5}**TS**$_{\mathrm{HA}}$ is stabilized over ^{3}**TS**$_{\mathrm{HA}}$, although dispersion corrections make them almost degenerate. Nevertheless, the barrier heights on both spin state surfaces are small and implicate an efficient hydrogen atom abstraction process in agreement with experiment.[33] When the enthalpy values from Figure 5.4 are converted to a free energy of activation, a value of ΔG_{solv} = 10.8 kcal mol^{-1} on the triplet spin state surface is found, which is in reasonable agreement with the experimentally reported free energy of activation of Nam et al.[33]

The experimental studies on ethylbenzene hydroxylation by **RC**$_1$ were found to proceed with a kinetic isotope effect (KIE) of 10 for the replacement of hydrogen atoms by deuterium in the substrate. To estimate the isotope effects for replacement of the transferrable hydrogen atom by deuterium in the reaction passing ^{3}**TS**$_{\mathrm{HA}}$ the Eyring and Wigner models (see Methods section) were used to estimate the KIE. Values of $\mathrm{KIE_E}$ and $\mathrm{KIE_W}$ of 4.9 and 5.4 were obtained, whereas these values increased unto 5.1 and 5.7, respectively when the fully deuterated substrate was used. Our calculated isotope effect is, therefore, predicts the same trends as experiment.

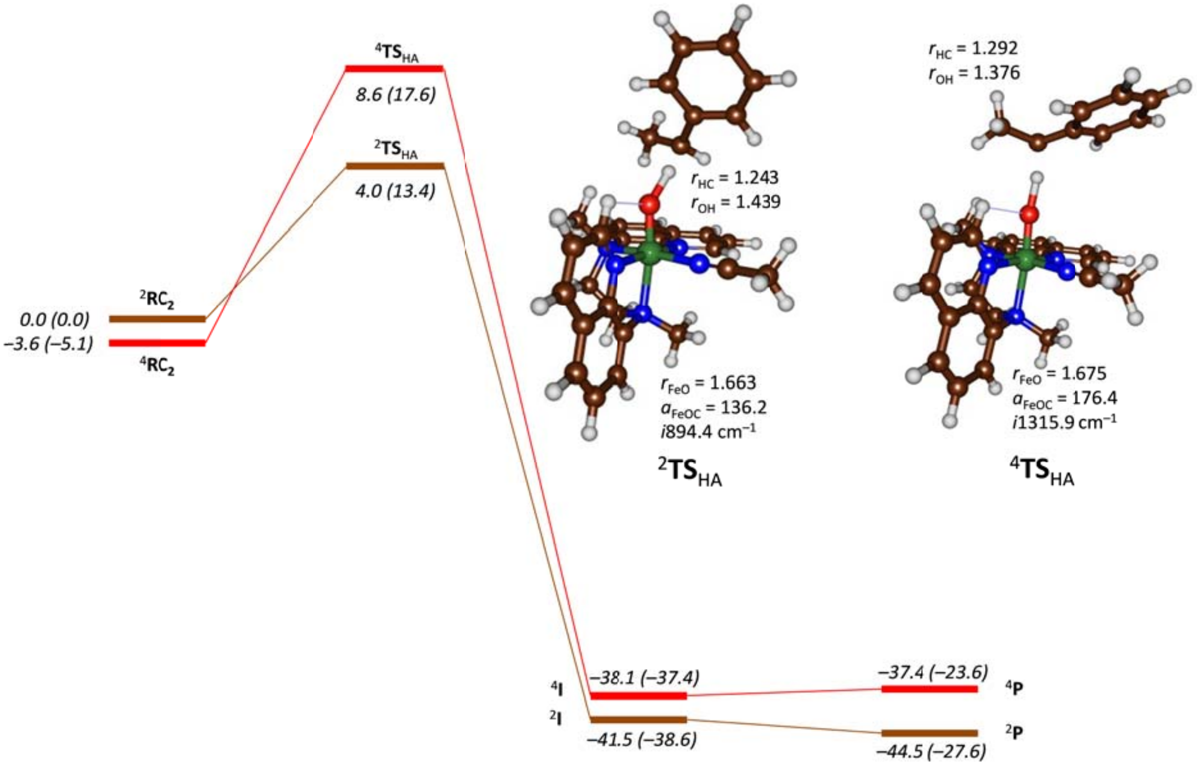

Figure 5.5. DFT calculated potential energy profile for the hydrogen atom abstraction from EB by ^{2,4}**2** with energies given in kcal mol^{-1}. Also shown are optimized UB3LYP/BS2(solvent) geometries of ^{2,4}**TS**$_{HA}$ with bond lengths in angstroms, angles in degrees and the imaginary frequency in wave numbers. Relative energies represent $\Delta E+ZPE+E_{solv}$ values obtained after a full geometry optimization in solvent at UB3LYP/BS2 (out of parenthesis) or at UB3LYP/BS2//UB3LYP/BS1 level of theory on a gas-phase optimized geometry.

Then a reaction complex of **2** with ethylbenzene (^{2,4}**RC**$_2$) in the gas phase as well as with solvent models included during the geometry optimizations was calculated. As mentioned above, the optimized geometry and group spin densities of ^{2}**RC**$_2$ characterize the reactant complex as $^3[Fe^{IV}(O)(BQEN)(NCCH_3)]^{2+}$---$^2EB^{+\bullet}$. The hydrogen atom abstraction from $EB^{+\bullet}$ by the iron(IV)-oxo complex then leads to electron transfer from the substrate into the π^*_{xz} orbital of the oxidant and spin density changes that are very similar to those observed for ^{3}**TS**$_{HA}$. Technically, the differences in hydrogen atom abstraction barrier between $^3\mathbf{RC}_1$ and $^2\mathbf{RC}_2$ should be very small as both are an iron(IV)-oxo oxidant. However, the outer-sphere electron transfer from the substrate to the oxidant has oxidized the approaching substrate, and hence the differences in barrier heights observed in Figs 5.4 and 5.5 relate to hydrogen atom abstraction of the C–H bonds of EB and $EB^{+\bullet}$, respectively. Previously, it was shown that the hydrogen atom abstraction barrier correlates with the strength of the C–H bond of the substrate that is broken in the process.[78] Indeed, experimentally determined rate constants of hydrogen atom abstraction reactions by nonheme iron oxidants were shown to correspond to the bond dissociation energy (BDE_{CH}) for the breaking of the C–H bond of the substrate.[79] It was, therefore, decided to calculate the BDE_{CH} values of EB and $EB^{+\bullet}$ into $C_6H_5CHCH_3^{\bullet/+}$ and a hydrogen atom and find values of $\Delta E+ZPE = 82.3$ and 41.2 kcal mol^{-1} in the gas phase, respectively. Thus, the oxidized ethylbenzene substrate has considerably weaker benzyl C–H bond strength as compared to the neutral system, and, therefore, the barrier heights for hydrogen atom abstraction obtained for **2’** are significantly lower than those for **1** in agreement with the differences in BDE_{CH}. Although, the higher reactivity of **2’** versus **1** is perceived as due to differences in oxidation state of the two oxidants, it actually represents the same oxidant but a difference in ionization state of the substrate with weakened BDE_{CH}. Also the reaction of **2’** with ethylbenzene incurs a significant KIE value, where a $KIE_E = 5.6$ and a $KIE_W = 7.2$ was found. These values, therefore, are similar to those found for **1** above.

Also an alternative quartet spin state of **2’** and the hydrogen atom abstraction via $^4\mathbf{TS}_{HA}$ was calculated. Thus, $^4\mathbf{RC}_2$ has orbital occupation $\pi^*_{xy}{}^2\pi^*_{xz}{}^\uparrow\pi^*_{yz}{}^\uparrow\pi_{EB}{}^\uparrow$ and similarly refers $^{3}[Fe^{IV}(O)(BQEN)(NCCH_3)]^{2+}$---$^{2}EB^{+\bullet}$, but in contrast to ^{2}**RC**$_2$ the spin on EB is ferromagnetically coupled to the unpaired electrons on the metal. Energetically, ^{2}**RC**$_2$ and ^{4}**RC**$_2$ are close in energy. However, during the hydrogen atom abstraction in ^{2}**TS**$_{HA}$ the unpaired electron from $EB^{+\bullet}$ is transferred with down-spin to give a $\pi^*_{xy}{}^{2}\pi^*_{xz}{}^{2}\pi^*_{yz}{}^{1}$ configuration, but in ^{4}**TS**$_{HA}$ the unpaired electron has up-spin so a $\pi^*_{xy}{}^{2}\pi^*_{xz}{}^{1}\pi^*_{yz}{}^{1}\sigma^*_{z2}{}^{1}$ configuration is formed. As this involves a higher lying orbital than in the corresponding doublet spin pathway, the barrier height for ^{4}**TS**$_{HA}$ is higher in energy than that for ^{2}**TS**$_{HA}$.

5.4: Discussion

Our DFT calculations on ^{3,5}**1** and ^{2,4}**2’** reported above show that both systems are in the iron(IV) oxidation state and the oxidation of **2’** does not oxidize the metal to iron(VI) but rather keeps it at iron(IV) due to electron release from the BQEN macrocycle rather than the metal. Therefore, although **2’** is perceived as an iron(V)-oxo species, it actually is an iron(IV)-oxo with BQEN cation radical. Moreover, the DFT calculations reported in this chapter show that approach of a substrate, e.g. ethylbenzene, onto ^{4,2}**2’**, leads to a long-range electron transfer upon formation of the reactant complex ^{4,2}**RC**$_2$: $^{3}[Fe^{IV}(O)(BQEN)(NCCH_3)]^{2+}$---$^{2}EB^{+\bullet}$, Figure 5.6. The subsequent hydrogen atom abstraction then gives an iron(III)-hydroxo complexes and a $C_6H_5CH^+CH_3$ cation.

In previous studies, it was shown that the driving force of a hydrogen atom abstraction correlates linearly with the free energy of activation.[67,72,78] Therefore, to understand the thermodynamics and kinetics of the reaction mechanisms reported in Figures 5.3 and 5.4 above, a detailed analysis of the individual thermodynamic reaction steps for electron and hydrogen atom transfer processes was done, which are summarized in Figure 5.7. Panel (a) in Figure 5.7 starts on the top left with ^{2}**2’** and the reaction to the right reflects a one-electron abstraction to form ^{3}**1** and the subsequent one-electron abstraction to form $[Fe^{III}(O)(BQEN)(NCCH_3)]^{+}$. The vertical arrows reflect the hydrogen atom abstraction processes from both ^{2}**2’** and ^{3}**1**. Thermodynamically, the energy for these reactions is associated with the bond dissociation energy of the O–H bond in the metal-hydroxo complex to revert back into the iron-oxo and an isolated H-atom, as defined as BDE_{OH}. The calculated BDE_{OH} values for ^{2}**2’** and ^{3}**1** are virtually the same in the gas phase, which is not surprising as both complexes are iron(IV)-oxo intermediates. Therefore, geometrically very little differences in the hydrogen atom abstraction reactions will be obtained. The energy gap between the two BDE_{OH} values widens to 10.2 kcal mol^{-1} in favour of ^{2}**2’** when solvent, thermal and entropical corrections to the energy are included.

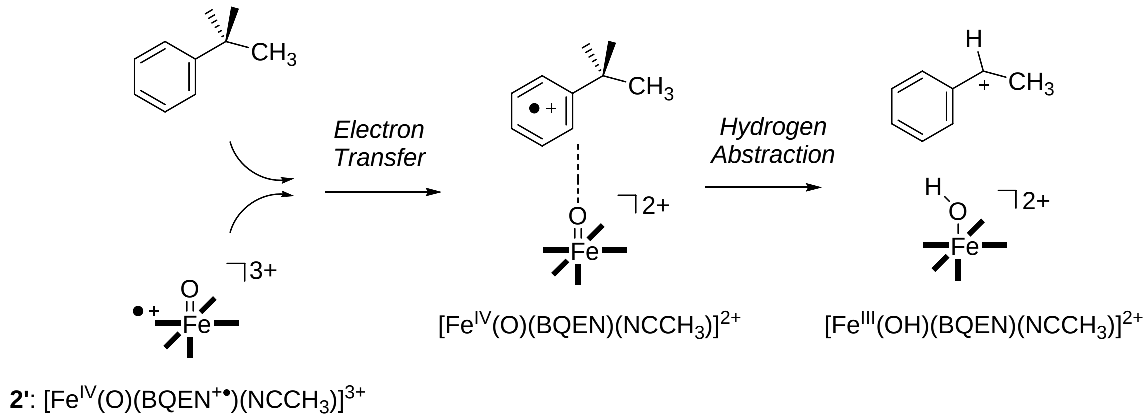

Figure 5.6: Calculated reaction mechanism for **2** with oxidation states of critical intermediates identified.

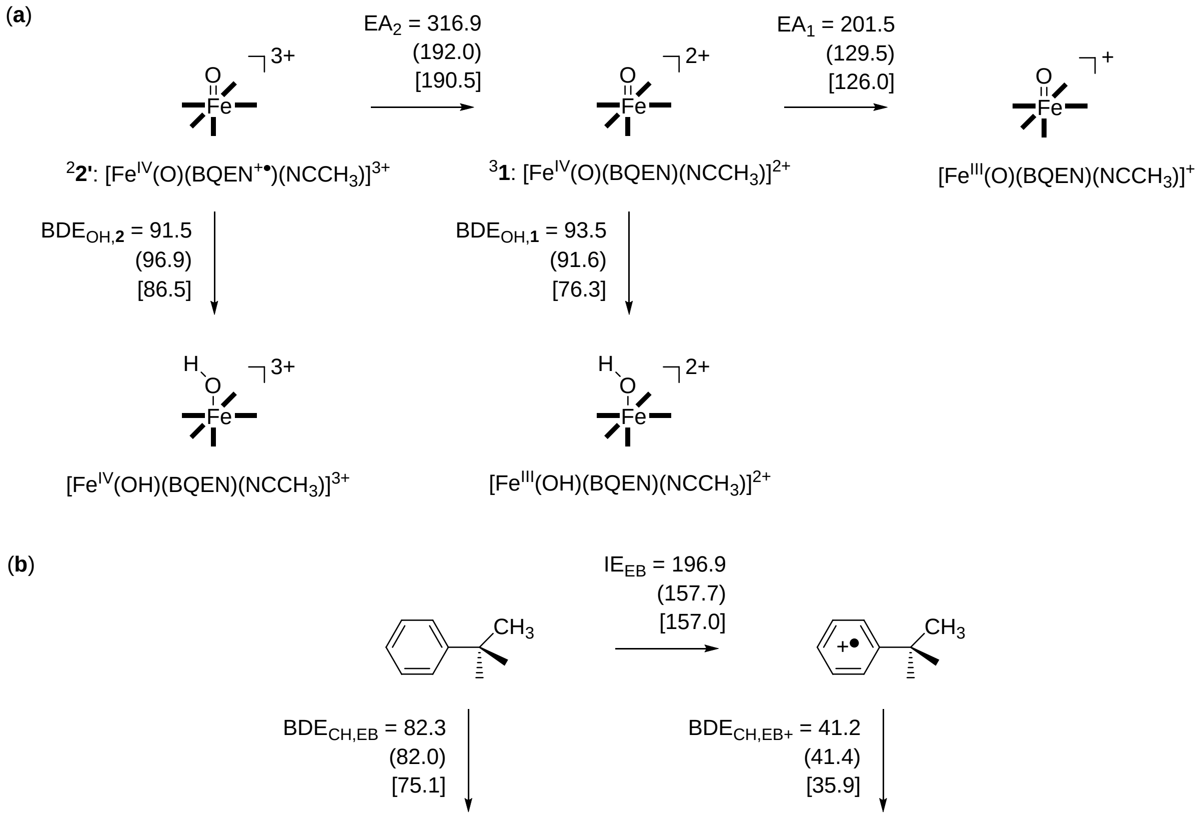

Figure 5.7: (a) Thermodynamic reaction pathways for electron and hydrogen atom abstraction by **1** and **2**. (b) Thermodynamic reaction pathways for electron and hydrogen atom abstraction by EB. All data obtained from a geometry optimization at UB3LYP/BS2. Data (in kcal mol^{-1}) reported are ΔE+ZPE in the gas-phase (ΔE+ZPE in solvent) [ΔG in solvent].

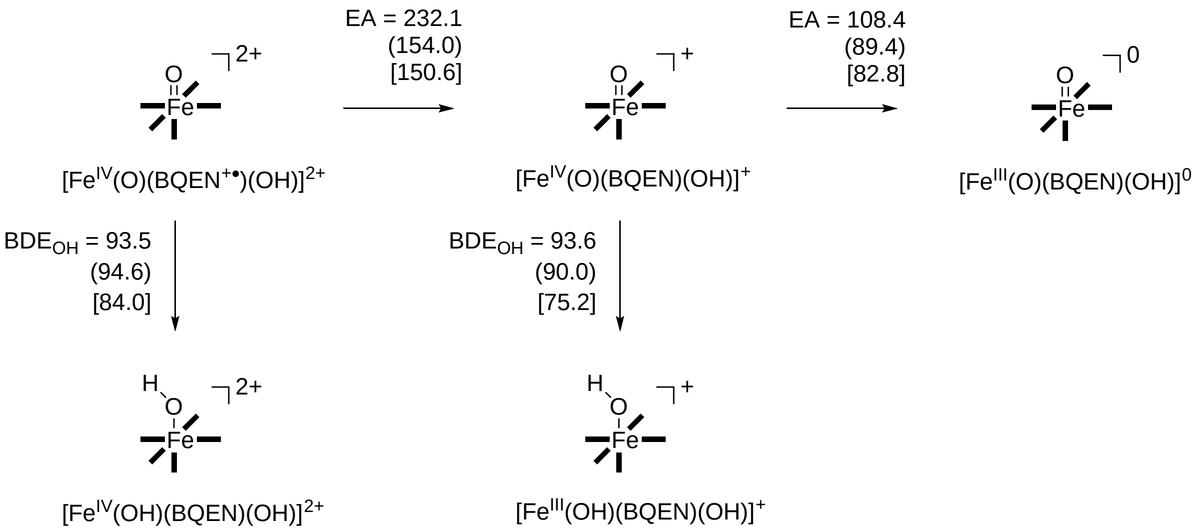

Figure 5.8: Thermodynamic reaction pathways for electron and hydrogen atom abstraction by $[Fe(O)(BQEN)(OH)]^{2+}$ and $[Fe(O)(BQEN)(OH)]^{+}$. All data obtained from a geometry optimization at UB3LYP/BS2. Data (in kcal mol^{-1}) reported are ΔE+ZPE in the gas-phase (ΔE+ZPE in solvent) [ΔG in solvent].

In the case of BDE_{OH}, solvent corrections stabilizes the value of **2’** over **1** by 7.3 kcal mol^{-1}, whereas thermal and entropic corrections add a further 4.9 kcal mol^{-1}. These BDE_{OH} values, therefore, would predict higher reactivity of ^{2}**2’** over ^{3}**1** in solvent for hydrogen atom abstraction reactions.

The major differences between **1** and **2’**, however, are related to their electron affinities or reduction potentials. Thus, ^{2}**2’** has a large electron affinity ($EA_{\mathbf{2}}$) of 316.9 kcal mol^{-1} in the gas-phase and ΔG_{solv} = 190.5 kcal mol^{-1}. It is worth noting that for all calculations, equal values for $\Delta E+ZPE+E_{solv}$ and ΔG_{solv} were found, therefore, entropic and thermal corrections to the solvent corrected enthalpies have a negligible effect on the individual reactions studied. The electron affinity of ^{2}**2’** is considerably larger than that found for ^{3}**1**, where values of $EA_{\mathbf{1}}$ = 201.5 kcal mol^{-1} in the gas-phase and ΔG_{solv} = 126.0 kcal mol^{-1} are found. Consequently, ^{2}**2'** has a ΔG_{solv} = 63.5 kcal mol^{-1} larger electron affinity than ^{3}**1** and will be more susceptible to react by electron abstraction from substrates.

For completeness we also include in Figure 5.8 the thermodynamics for ethylbenzene substrate for removal of an electron and the C–H bond strengths of the benzyl group of ethylbenzene and ethylbenzene cation radical. As already mentioned above ethylbenzene cation radical has a considerably weakened C–H bond strength of ΔG_{solv} = 35.9 kcal mol^{-1} as compared to EB. Consequently, hydrogen atom abstraction from $EB^{+\bullet}$ will have a low barrier.

To find out whether a reaction of ^{2}**2'** and ^{3}**1** with EB would lead to a large thermodynamic driving force for electron transfer, the free energy in solvent for the reactions given in Eqs 5.4 and 5.5 was calculated. Thus, the electron transfer from EB to ^{2}**2'** is calculated to be exergonic by 33.5 kcal mol^{-1}, whereas the one originating from ^{3}**1** is endergonic by 31.0 kcal mol^{-1} instead. These two reactions implicate that in a collision between ^{2}**2'** and EB the driving force will trigger an electron abstraction from EB, whereas that will not be the case in a collision between ^{3}**1** and EB. The large $EA_{\mathbf{2}}$ value will, therefore, lead to a large driving force for electron transfer from suitable substrates including ethylbenzene to **2'**. Moreover, the thermodynamic reaction pathways given in Figure 5.7 give further evidence of a likely electron transfer between EB and ^{2}**2'**.

$$^{2}\mathbf{2'} + \mathrm{EB} \rightarrow {}^{3}\mathbf{1} + \mathrm{EB}^{+\bullet} \qquad [\Delta G_{solv} = -33.5 \text{ kcal mol}^{-1}] \qquad (5.4)$$

$$^{3}\mathbf{1} + \mathrm{EB} \rightarrow {}^{4}[\mathrm{Fe^{III}(O)(BQEN)(NCCH_3)}]^{+} + \mathrm{EB}^{+\bullet} \quad [\Delta G_{solv} = +31.0 \text{ kcal mol}^{-1}] \qquad (5.5)$$

Despite the fact that the BDE_{OH} values of **1** and **2'** are virtually the same, actually at the free energy level with solvent included they are separated by about 10 kcal mol^{-1}. However, much more dramatic differences in the electron affinity of both complexes are found. Thus, the bond dissociation energy to break the A–H bond (BDE_{AH}) – or hydrogen atom abstraction ability of compound A – can be split into an individual electron and proton transfer via Eq 5.6, whereby ΔG_{acid} the acidity of the weak acid AH represents, EA_A is the electron affinity of A, and IE_H the ionization energy of a H-atom. The experimentally reported value of IE_H is 13.598 eV.[80]

$$\mathrm{A{-}H} \rightarrow \mathrm{A} + \mathrm{H} + BDE_{AH} \qquad (5.6a)$$

$$BDE_{AH} = \Delta G_{acid,AH} - EA_A - IE_H \qquad (5.6b)$$

Using the data from Figure 5.7 and the known IE_H value, a ΔG_{acid} of 590.5 kcal mol^{-1} for $[\mathrm{Fe^{IV}(OH)(BQEN)(NCCH_3)}]^{3+}$ was calculated, whereas proton transfer to **1** gives the complex $[\mathrm{Fe^{III}(OH)(BQEN)(NCCH_3)}]^{2+}$ with ΔG_{acid} = 515.9 kcal mol^{-1}. The large difference between $EA_{\mathbf{2}}$ and $EA_{\mathbf{1}}$, therefore, has a direct impact on the acidity of the iron(III)-hydroxo group and makes it considerably more acidic. The origin of the difference in electron affinity of **1** and **2'** is due to difference in electron transfer processes. Upon reduction of ^{2}**2'** an electron is transferred into the low-lying π^*_{BQEN} orbital to form a triplet spin $\pi^*_{xy}{}^{2}\pi^*_{xz}{}^{1}\pi^*_{yz}{}^{1}\pi^*_{BQEN}{}^{2}$ configuration. On the other hand, reduction of ^{3}**1** leads to filling of the virtual σ^*_{z2} orbital with a single electron. As the σ^*_{z2} orbital is significantly higher in energy than the π^*_{BQEN} orbital this means the reduction of **1** will incur a much smaller electron affinity than adding an electron to π^*_{BQEN}, which is indeed what is found in Figure 5.7.

To find out whether the *cis*-ligand of the metal-oxo group affects the EA and ΔG_{acid} values, we did a further set of calculations on the electron and hydrogen atom transfer reactions for complexes $[Fe^{IV}(O)(BQEN^{+\bullet})(OH)]^{2+}$ and $[Fe^{IV}(O)(BQEN)(OH)]^{+}$, i.e. complexes **2'** and **1** that have the acetonitrile ligand replaced by OH^{-}. We should note here that replacement of the acetonitrile equatorial ligand by hydroxide does not change the spin state ordering and electronic configuration and these complexes are characterized like **2'** and **1** above. Figure 5.8 displays the thermodynamic reaction pathways for $[Fe^{IV}(O)(BQEN^{+\bullet})(OH)]^{2+}$ and $[Fe^{IV}(O)(BQEN)(OH)]^{+}$.Firstly, very little effect of replacing the acetonitrile with hydroxide is found on the BDE_{OH} values of the complexes. For $[Fe^{IV}(OH)(BQEN)(OH)]^{2+}$ we find a BDE_{OH} value of ΔG_{solv} = 84.0 kcal mol^{-1}, whereas its one-electron reduced counterpart has a ΔG_{solv} = 75.2 kcal mol^{-1}. These values are within 2.5 kcal mol^{-1} from those obtained with an acetonitrile molecule in the *cis*-position. The situation, however, changes dramatically for the electron affinities and acidity values of the complexes when the acetonitrile ligand is replaced by hydroxide. Thus, $[Fe^{IV}(O)(BQEN^{+\bullet})(OH)]^{2+}$ has an electron affinity of ΔG_{solv} = 150.6 kcal mol^{-1}, whereas the much lower value of 82.8 kcal mol^{-1} is found for $[Fe^{IV}(O)(BQEN)(OH)]^{+}$. These lowered electron affinities with respect to complexes **2’** and **1** also mean reduced acidity of the protonated complexes, for which values of 548.2 and 471.6 kcal mol^{-1}, respectively were found.

In addition, a reaction of $[Fe^{IV}(O)(BQEN^{+\bullet})(OH)]^{2+}$ with ethylbenzene is calculated to give an endergonic electron transfer of 6.4 kcal mol^{-1} using the data given in Figures 5.7 and 5.8. Therefore, replacing the acetonitrile equatorial ligand in complex **2’** with an anion such as a hydroxide will affect the stability and reactivity of the complex and will prevent a long-range electron transfer with substrates like ethylbenzene. The electron transfer from ethylbenzene to $[Fe^{IV}(O)(BQEN)(OH)]^{+}$ is calculated to be even more endergonic (ΔG_{solv} = 74.2 kcal mol^{-1}) and consequently is not likely to happen.

In summary, we establish reasons for the large thermodynamic driving force for electron transfer from ethylbenzene to **2’** as originating from a high electron affinity of the oxidant of ΔG_{solv} = 190.5 kcal mol^{-1}. This implies that the electron transfer to the approaching substrate could be spontaneous for substrates with an ionization potential below 190.5 kcal mol^{-1} or 8.26 eV. Although, an ionization energy of 8.54 eV in the gas phase was calculated, actually in solution the value drops to ΔG_{solv} = 6.81 eV. Therefore, in solution the ionization potential of ethylbenzene is sufficiently low to incur a long-range electron transfer to the oxidant and create $^{3}[Fe^{IV}(O)(BQEN)(NCCH_3)]^{2+}$---$^{2}EB^{+\bullet}$.

Finally, the thermodynamics values of Figures 5.8 and 5.9 also enable us to predict the hydrogen atom transfer driving force in complexes $\mathbf{RC}_2$ and $\mathbf{RC}_1$. As described above, **RC**$_2$ undergoes a long-range electron transfer and converts to $[Fe^{IV}(O)(BQEN)(NCCH_3)]^{2+}$ and $EB^{+\bullet}$. This complex reacts via hydrogen atom transfer via Eq 5.7 with a free energy change of –40.4 kcal mol^{-1}. The DFT calculations for this process implicated a free energy change of ΔG_{solv} = -42.4 kcal mol^{-1} for the formation of the radical intermediate ^{2}**I**, and therefore its calculated value is in good agreement with the value estimated from our thermodynamic cycles.

$$[Fe^{IV}(O)(BQEN)(NCCH_3)]^{2+} + EB^{+\bullet} \rightarrow$$
$$[Fe^{III}(OH)(BQEN)(NCCH_3)]^{2+} + C_6H_5CH^+CH_3$$
$$[\Delta G_{solv} = -40.4 \text{ kcal mol}^{-1}] \qquad (5.7)$$

By contrast, if the same for complex **RC**$_1$ is done and the difference in free energy between the BDE_{CH} and BDE_{OH} values of oxidant and substrate is taken, an almost thermoneutral hydrogen atom abstraction reaction, Eq 5.8 is found. Indeed, the DFT calculations above predict a radical intermediate with exergonicity of 6.9 kcal mol^{-1} with respect to the reactant complex in good agreement with the thermodynamically estimated value.

$$[Fe^{IV}(O)(BQEN)(NCCH_3)]^{2+} + EB \rightarrow [Fe^{III}(OH)(BQEN)(NCCH_3)]^{2+}$$
$$+C_6H_5CH^{\bullet}CH_3$$
$$[\Delta G_{solv} = -1.2 \text{ kcal mol}^{-1}] \qquad (5.8)$$

To test whether the electron transfer observed here in our reactant complexes is a general feature that could be found in alternative iron(V)-oxo complexes as well, it was decided to also investigate the well-studied $[Fe(O)(TPA)(OH)]^{2+}$, TPA = tris-(2-pyridylmethyl)amine, system of Costas and co-workers.[8] Previously, $[Fe(O)(TPA)(X)]^{2+}$ with X = halide or OH^- has been used in studies of the *cis*-effect on substrate activation by metal-oxo species, but also as a model for non-heme iron halogenases. Technically the $[Fe(O)(TPA)(OH)]^{2+}$ is an iron(V)-oxo complex as indeed confirmed by DFT calculations.[81-84] The question, of course, arises whether the oxidation state of the complex stays in the iron(V) state upon approach of an ethylbenzene molecule. Thus, we optimized the reactant complex $[Fe(O)(TPA)(OH)---EB]^{2+}$ in the doublet and quartet spin states at UB3LYP-D3/BS2 level of theory and show the structures and group spin densities of the complexes alongside those of ^{4,2}**RC**$_2$ in Figure 5.9.

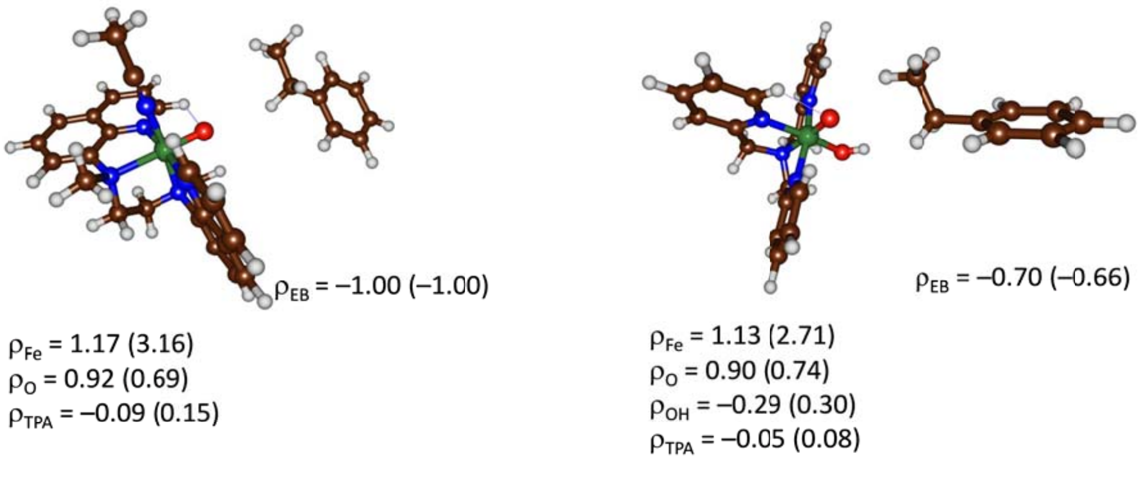

RC_2, $[Fe(O)(BQEN)(NCCH_3)---EB]^{3+}$

$[Fe(O)(TPA)(OH)---EB]^{2+}$

Figure 5.9. Group spin densities of ^{4,2}**RC**$_2$ and $[Fe(O)(TPA)(OH)---EB]^{2+}$ as calculated with UB3LYP/BS2 in solvent. High-spin data in parenthesis.

The results in Figure 5.9 show that upon approach of an ethylbenzene molecule to an iron(V)-oxo center, a long-range electron transfer takes place from substrate to oxidant. Therefore, the group spin densities of $^{2,4}\mathbf{RC}_2$ and $[\mathrm{Fe(O)(TPA)(OH)}\text{---}\mathrm{EB}]^{2+}$ both refer to an iron(IV)-oxo complex with a nearby $\mathrm{EB}^{+\bullet}$ ion. Both complexes have a doublet spin state with $\pi^*_{xy}{}^2\pi^*_{xz}{}^1\pi^*_{yz}{}^1\pi_{EB}{}^1$ configuration, i.e. a triplet spin iron(IV)-oxo complex with a nearby doublet cation radical ethylbenzene. By contrast the quartet spin state configurations of these complexes have orbital occupation $\pi^*_{xy}{}^2\pi^*_{xz}{}^1\pi^*_{yz}{}^1\sigma^*_{z2}{}^1\pi_{EB}{}^1$ configuration with the ethylbenzene radical anti-ferromagnetically coupled to three unpaired electrons on the iron(IV)-oxo complex. Note that in absence of ethylbenzene, the $[\mathrm{Fe(O)(TPA)(OH)}]^{2+}$ complex converges to an iron(V)-oxo species and no ligand radical is found. The TPA ligand, therefore, has much lower lying molecular orbitals than a BQEN ligand system and as a result the π_{BQEN} orbitals become competitive with the π^*_{xz}/π^*_{yz} orbitals on the FeO group. As a result of this $[\mathrm{Fe(O)(BQEN)(NCCH_3)}]^{3+}$ has an electronic configuration representing an iron(IV)-oxo coupled to a ligand radical, whereas $[\mathrm{Fe(O)(TPA)(OH)}]^{2+}$ is an iron(V)-oxo species.

5.5: Conclusions

In summary, we present here the first comparative study on the reactivity patterns of nonheme iron(IV)-oxo versus iron(V)-oxo intermediates. Upon approach of the substrate to the iron(IV)-oxo ligand cation radical it abstracts an electron from substrate readily, and thereby creates an iron(IV)-oxo ligand cation radical species.

The perceived reactivity of the iron(V)-oxo species, therefore, is due to activity of the iron(IV)-oxo ligand cation radical instead. It was also shown that oxidation of ethylbenzene weakens the C–H bond strength of the substrate and thereby lowers the hydrogen atom abstraction barriers and leads to higher reactivity. This is an example of how outer-sphere (long-range) electron transfer can change the C–H bond strength of the substrate so that a more efficient H-transfer becomes possible. The outer-sphere electron transfer may be a common feature in transition metal catalysis, but further research will be needed to find more examples of this type of reactivity patterns.

References:

1 E. I. Solomon, T. C. Brunold, M. I. Davis, J. N. Kemsley, S.-K. Lee, N. Lehnert, F. Neese, A. J. Skulan, Y.-S. Yang, J. Zhou, *Chem. Rev.*, **100**, 235 (2000).

2 T. D. H. Bugg, S. Ramaswamy, *Curr. Opin. Chem. Biol.*, **12**, 134 (2008).

3 M. J. Ryle, R. P. Hausinger, *Curr. Opin. Chem. Biol.*, **6**, 193 (2002).

4 Y. Mishina, E. M. Duguid, C. He, *Chem. Rev.*, **106**, 215 (2006).

5 S. P. de Visser, D. Kumar (Eds.) *Iron-containing enzymes: Versatile catalysts of hydroxylation reactions in nature*. RSC Publishing, Cambridge (UK) (2011).

6 P. He, G. R. Moran, *Curr. Opin. Chem. Biol.*, **13**, 443 (2009).

7 D. Buongiorno, G. D. Straganz, *Coord. Chem. Rev.*, **257**, 541 (2013).

8 M. Costas, M. P. Mehn, M. P. Jensen, L. Que Jr., *Chem. Rev.*, **104**, 939 (2004).

9 S. V. Kryatov, E. V. Rybak-Akimova, S. Schindler, *Chem. Rev.*, **105**, 2175 (2005).

10 M. M. Abu-Omar, A. Loaiza, N. Hontzeas, *Chem. Rev.*, **105**, 2227 (2005).

11 R. van Eldik, *Coord. Chem. Rev.*, **251**, 1649 (2007).

12 P. C. A. Bruijnincx, G. van Koten, R. J. M. Klein Gebbink, *Chem. Soc. Rev.*, **37**, 2716 (2008).

13 S. P. de Visser, J.-U. Rohde, Y.-M. Lee, J. Cho, W. Nam, *Coord. Chem. Rev.*, **257**, 381 (2013).

14 W. Nam, Y.-M. Lee, S. Fukuzumi, *Acc. Chem. Res.*, **47**, 1146 (2014).

15 M. R. Bukowski, K. D. Koehntop, A. Stubna, E. L. Bominaar, J. A. Halfen, E. Münck, W. Nam, L. Que Jr., *Science*, **310**, 1000 (2005).

16 J.-U. Rohde, J.-H. In, M. H. Lim, W. W. Brennessel, M. R. Bukowski, A. Stubna, E. Münck, W. Nam, L. Que Jr, *Science*, **299**, 1037 (2003).

17 M. Martinho, F. Banse, J.-F. Bartoli, T. A. Mattioli, P. Battioni, P.; Horner, S. Bourcier, J.-J. Girerd, *Inorg. Chem.*, **44**, 9592 (2005).

18 C. V. Sastri, M. S. Seo, M. J. Park, K. M. Kim, W. Nam, *Chem. Commun.*, 1405 (2005).

19 F. T. De Oliveira, A. Chanda, D. Banerjee, X. Shan, S. Mondal, L. Que Jr, E. L. Bominaar, E. Münck, T. J. Collins, *Science*, **315**, 835 (2007).

20 T. A. Jackson, J.-U. Rohde, M. S. Seo, C. V. Sastri, R. DeHont, A. Stubna, T. Ohta, T. Kitagawa, E. Münck, W. Nam, L. Que Jr, *J. Am. Chem. Soc.*, **130**, 12394 (2008).

21 K. Chen, M. Costas, J. Kim, A. K. Tipton, L. Que Jr, *J. Am. Chem. Soc.*, **124**, 3026 (2002).

22 A. Company, L. Gómez, M. Güell, X. Ribas, J. M. Luis, L. Que Jr, M. Costas, *J. Am. Chem. Soc.*, **129**, 15766 (2007).

23 R. Mas-Ballesté, M. Fujita, L. Que Jr, *Dalton Trans.*, 1828 (2008).

24 P. Comba, M. Maurer, P. Vadivelu, *Inorg. Chem.*, **48**, 10348 (2009).

25 A. Company, Y. Feng, M. Güell, X. Ribas, J. M. Luis, L. Que Jr, M. Costas, *Chem. Eur. J.*, **15**, 3359 (2009).

26 I. Prat, J. S. Mathieson, M. Güell, X. Ribas, J. M. Luis, L. Cronin, M. Costas, *Nature Chem.*, **3**, 788 (2011).

27 K. Chen, L. Que Jr, *J. Am. Chem. Soc.*, **123**, 6327 (2001).

28 A. D. Ryabov, *Adv. Inorg. Chem.*, **65**, 117 (2013).

29 A. Nielsen, F. B. Larsen, A. D. Bond, C. J. McKenzie, *Angew. Chem. Int. Ed.*, **45**, 1602 (2006).

30 A. Lennartson, C. J. McKenzie, *Angew. Chem. Int. Ed.*, **51**, 6767 (2012).

31 S. H. Lee, J. H. Han, H. Kwak, S. J. Lee, E. Y. Lee, H. J. Kim, J. H. Lee, C. Bae, S. N. Lee, Y. Kim, C. Kim, *Chem. Eur. J.*, **13**, 9393 (2007).

32 S. Kundu, J. Van Kirk Thompson, A. D. Ryabov, T. J. Collins, *J. Am. Chem. Soc.*, **133**, 18546 (2011).

33 J. Yoon, S. A. Wilson, Y. K. Jang, M. S. Seo, K. Nehru, B. Hedman, K. O. Hodgson, E. Bill, E. I. Solomon, W. Nam, *Angew. Chem. Int. Ed.*, **48**, 1257 (2009).

34 *Jaguar*, version 7.9, Schrodinger, LLC, New York (2011).

35 *Gaussian*-09, Revision C.01, Gaussian Inc., Wallingford CT (2010).

36 A. D. Becke, *J. Chem. Phys.*, **98**, 5648 (1993).

37 C. Lee, W. Yang, R. G. Parr, *Phys. Rev. B*, **37**, 785 (1988).

38 S. P. de Visser, *Angew. Chem. Int. Ed.*, **45**, 1790 (2006).

39 D. Kumar, W. Thiel, S. P. de Visser, *J. Am. Chem. Soc.*, **133**, 3869 (2011).

40 S. Grimme, *J. Chem. Phys.*, **124**, 034108 (2006).

41 M. Reiher, O. Salomon, B. A. Hess, *Theor. Chem. Acc.*, **107**, 48 (2001).

42 N. C. Handy, A. J. Cohen, *Mol. Phys.*, **99**, 403 (2001).

43 J. P. Perdew, K. Burke, M. Ernzerhof, *Phys. Rev. Lett.*, **77**, 3865 (1996).

44 S. P. de Visser, M. G. Quesne, B. Martin, P. Comba, U. Ryde, *Chem. Commun.*, **50**, 262 (2014).

45 P. J. Hay, W. R. Wadt, *J. Chem. Phys.*, **82**, 270 (1985).

46 W. J. Hehre, R. Ditchfield, J. A. Pople, *J. Chem. Phys.*, **56**, 2257 (1972).

47 A. K. Vardhaman, C. V. Sastri, D. Kumar, S. P. de Visser, *Chem. Commun.*, **47**, 11044 (2011).

48 A. K. Vardhaman, P. Barman, S. Kumar, C. V. Sastri, D. Kumar, S. P. de Visser, *Angew. Chem. Int. Ed.*, **52**, 12288 (2013).

49 A. K. Vardhaman, P. Barman, S. Kumar, C. V. Sastri, D. Kumar, S. P. de Visser, *Chem. Commun.*, **49**, 10926 (2013).

50 S. P. de Visser, *Chem. Eur. J.*, **12**, 8168 (2006).

51 D. J. Heyes, M. Sakuma, S. P. de Visser, N. S. Scrutton, *J. Biol. Chem.*, **284**, 3762 (2009).

52 D. Kumar, S. P. de Visser, P. K. Sharma, S. Cohen, S. Shaik, *J. Am. Chem. Soc.*, **126**, 1907 (2004).

53 D. Kumar, H. Hirao, L. Que Jr, S. Shaik, *J. Am. Chem. Soc.*, **127**, 8026 (2005).

54 S. P. de Visser, *J. Am. Chem. Soc.*, **128**, 15809 (2006).

55 S. Ye, F. Neese, *Proc. Natl. Acad. Sci. USA*, **108**, 1228 (2011).

56 M. T. Green, *J. Am. Chem. Soc.*, **121**, 7939 (1999).

57 J. Rittle, M. T. Green, *Science*, **330**, 933 (2010).

58 K. Yoshizawa, Y. Shiota, T. Yamabe, *J. Am. Chem. Soc.*, **121**, 147 (1999).

59 S. P. de Visser, *J. Am. Chem. Soc.*, **128**, 9813 (2006).

60 L. Bernasconi, E.-J. Baerends, *Eur. J. Inorg. Chem.*, 1672 (2008).

61 C. Y. Geng, S. Ye, F. Neese, *Angew. Chem. Int. Ed.*, **49**, 5717 (2010).

62 S. Shaik, H. Chen, D. Janardanan, *Nature Chem.*, **3**, 19 (2011).

63 P. Comba, M. Maurer, P. Vadivelu, *Inorg. Chem.*, **48**, 10389 (2009).

64 J. C. Schöneboom, H. Lin, N. Reuter, W. Thiel, S. Cohen, F. Ogliaro, S. Shaik, *J. Am. Chem. Soc.*, **124**, 8142 (2002).

65 S. P. de Visser, S. Shaik, P. K. Sharma, D. Kumar, W. Thiel, *J. Am. Chem. Soc.*, **125**, 15779 (2003).

66 S. P. de Visser, L. Tahsini, W. Nam, *Chem. Eur. J.*, **15**, 5577 (2009).

67 D. Kumar, G. N. Sastry, S. P. de Visser, *Chem. Eur. J.*, **17**, 6196 (2011).

68 S. Shaik, H. Hirao, D. Kumar, *Nat. Prod. Rep.*, **24**, 533 (2007).

69 M. G. Quesne, R. Latifi, L. E. Gonzalez-Ovalle, D. Kumar, S. P. de Visser, *Chem. Eur. J.*, **20**, 435 (2014).

70 M. Güell, J. M. Luis, M. Solà, M. Swart, *J. Phys. Chem. A*, **112**, 6384 (2008).

71 R. Latifi, M. A. Sainna, E. V. Rybak-Akimova, S. P. de Visser, *Chem. Eur. J.*, **19**, 4058 (2013).

72 D. Kumar, R. Latifi, S. Kumar, E. V. Rybak-Akimova, M. A. Sainna, S. P. de Visser, *Inorg. Chem.*, **52**, 7968 (2013).

73 S. P. de Visser, L. S. Tan, *J. Am. Chem. Soc.*, **130**, 12961 (2008).

74 P. Leeladee, R. A. Baglia, K. A. Prokop, R. Latifi, S. P. de Visser, D. P. Goldberg, *J. Am. Chem. Soc.*, **134**, 10397 (2012).

75 S. P. de Visser, *J. Phys. Chem. A*, **109**, 11050 (2005).

76 S. M. Pratter, C. Konstantinovics, C. L. M. DiGiuro, E. Leitner, D. Kumar, S. P. de Visser, G. Grogan, G. D. Straganz, *Angew. Chem. Int. Ed.*, **52**, 9677 (2013).

77 S. Sahu, L. R. Widger, M. G. Quesne, S. P. de Visser, H. Matsumura, P. Moënne-Loccoz, M. A. Siegler, D. P. Goldberg, *J. Am. Chem. Soc.*, **135**, 10590 (2013).

78 R. Latifi, M. Bagherzadeh, S. P. de Visser, *Chem. Eur. J.*, **15**, 6651 (2009).

79 X. Wu, M. S. Seo, K. M. Davis, Y.-M. Lee, J. Chen, K.-B. Cho, Y. N. Pushkar, W. Nam, *J. Am. Chem. Soc*., **133**, 20088 (2011).

80 S. G. Lias, in *Ionization Energy Evaluation in NIST Chemistry WebBook*, NIST Standard Reference Database Number 69: P. J. Linstrom, W. G. Mallard (Eds.), National Institute of Standards, Technology: Gaithersburg MD, 20899 (2005) (http://webbook.nist.gov).

81 Y. Ma, P. B. Balbuena, *J. Phys. Chem. B*, **111**, 2711 (2007).

82 P. Comba, G. Rajaraman, H. Rohwer, *Inorg. Chem*., **46**, 3826 (2007).

83 A. Bassan, M. R. A. Blomberg, P. E. M. Siegbahn, L. Que Jr, *J. Am. Chem. Soc*., **124**, 11056 (2002).

84 S. P. de Visser, W. Nam, *J. Phys. Chem. A*, **112**, 12887 (2008).

CHAPTER 6

A TRIMETAL CARBENE WITH REACTIVITY REMINISCENT OF FISCHER-TROPSCH CATALYSIS

CHAPTER 6

A TRIMETAL CARBENE WITH REACTIVITY REMINISCENT OF FISCHER-TROPSCH CATALYSIS

6.1: Introduction

In Industrial Fischer-Tropsch catalysis alkanes are being synthesized from H_2 and CO gas on a metal surface, which is a process that was developed and exploited in Germany in the 1920s and 1930s as an alternative to fossil fuels.[1-4] With dwindling supplies of fossil fuels, urgent alternative sources are needed, however, the Fischer-Tropsch process is energetically demanding and usually requires high pressures and/or temperatures as well as expensive heterogeneous catalysts.[5-7] Research on improving Fischer-Tropsch catalysis is hampered due to the lack of knowledge of details of the reaction mechanism and the properties played by the metal surface. In addition, few homogeneous catalysts are known that perform a Fischer-Tropsch-type reaction.[8-9]

Recently, the Matsuzaka group [10] reported the synthesis and spectroscopic characterization of $[(Cp^*Ru)_2(\mu_2\text{-}CH_2)(\mu_3\text{-}NPh)Pt(P(CH_3)_3)_2]$, which was treated with CH_3OTf in diethyl ether and after heating in toluene produced a unique structure (labelled as **3** in Ref 10) with a trigonal sp^2 hybridized carbon atom linked to three transition metal atoms. It was reported that structure **3** reacted via a Fischer-Tropsch-type reaction via H and CH_3 migration from the RuH and $PtCH_3$ ligands to form $\mu_2\text{-}CHCH_3$ products, Figure 6.1. Therefore, structure **3** catalyzes the C–C and C–H bond formation reactions for the synthesis of alkanes alike to the Fischer-Tropsch process, which are thermodynamically difficult processes. As such, structure **3** is one of the few homogeneous Fischer-Tropsch catalysts available currently. However, little is known on the reaction process and the overall potential of this type of chemical system. In order to explore its possibilities further, it is important to fully understand the origin of the reaction mechanism and the chemical properties that drive the process. Currently, however, there is limited knowledge on the chemical system displayed in Figure 6.1 and experimental studies failed to identify intermediates along the reaction mechanism. Hence it is unclear how and why this chemical system operates and how it can be further improved. Moreover, there are very few examples in the literature of analogous processes and this chemical system may pose a novel synthetic route for the generation of alkanes on a carbene center.

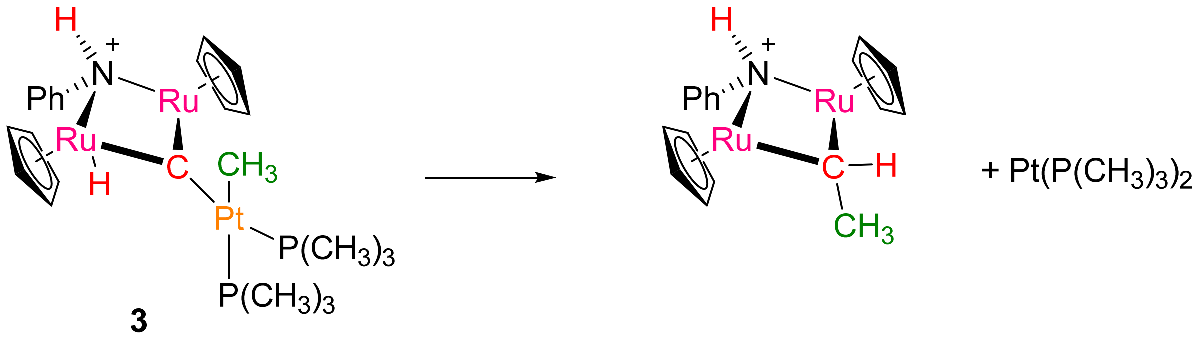

Figure 6.1: Chemical reaction investigated in this work.

The aim of the studies in this work, therefore, is focused on establishing the reaction mechanism of alkyl chain growth on the carbene center and the chemical properties of the reaction center shown in Figure 6.1. Firstly, the chemical properties of the tri-metal carbene center are poorly understood and this theory may give insight into, whether it would be a suitable catalytic center. Secondly, it is unclear whether there is an initial H-transfer followed by CH_3-transfer or the reverse. Moreover, it may very well be that both mechanisms are kinetically and thermodynamically possible. Thirdly, as shown in iron-porphyrin chemistry for many examples the reaction can take place via proton transfer, hydrogen atom transfer or hydride transfer.[11,12] Furthermore, hydrogen atom and hydride transfer processes may happen via proton-coupled-electron-transfer (PCET), whereby the electrons move to a different donor site than the protons involved in the reaction. Theory is the ideal tool to distinguish between these mechanistic pathways and to establish the electronic features that drive this important mechanism. In addition to the reactivity questions and the synthesis of alkyl groups on this carbon center, there are also questions related to the chemical structure of the central carbon atom in **3** itself. Thus, an sp^2 hybridized carbon atom would make **3** a carbocation with planar conformation, which is unlikely given the fact that the carbon atom is surrounded by positively charged metal ions. On the other hand, if the carbon atom is negatively charged, i.e. a carbanion, it would have pyramidal structure because of its sp^3 hybridization, which is in disagreement with the experimental crystal structure coordinates. Clearly, the structural and reactivity features of this complex are poorly understood and theory may provide insight into its electronic and structural features.

The Ru_2PtC core of structure **3** is an unusual structure in chemical catalysis but shows some resemblance to Grubbs catalyst,[13-15] where the metal is covalently linked to a carbon atom through either a single, a double or a triple bond. However, as far as we know, there are no reported catalysts in the literature, where the carbon atom is ligated to two Ru atoms and a Pt atom. There are several examples in the literature of carbido centered structures, where the carbon atom is bound to three or more metal atoms,[16-23] but very few of these show catalytic activity. It, therefore, remains unclear why structure **3** is reactive for the formation of alkyl groups from individual methyl, hydrogen and carbon groups. In order to gain insight into the peculiar structure and reactivity of **3**, it was decided to do a computational study and establish the electronic and thermochemical features. As we will show here, our studies give fundamental insight into the nature of the metal-carbon bond and characterizes structure **3** as a tri-metal carbene that can react via sequential methyl and hydrogen atom transfer to form μ_2-$CHCH_3$. These results may have direct relevance to heterogeneous catalysis on metal surfaces.

6.2: Methods

The calculations reported in this chapter were performed using density functional theory (DFT) methods as used previously on transition metal complexes by our groups.[24,25] DFT methods as implemented in the *Jaguar* 7.7 [26] and *Gaussian*-09 [27] program packages were used. Initial geometries were optimized (without constraints) in *Jaguar* using the hybrid density functional theory method B3LYP [28,29] coupled with an LACVP basis set (including a core potential) on ruthenium and platinum and 6-31G on the rest of the atoms: basis set BS1.[30] A subsequent analytical frequency in Gaussian confirmed the structures as local minima with real frequencies only or first order saddle points with one imaginary frequency for the correct mode. Energies were then improved by running a single point calculation in *Jaguar* using a triple-ζ quality LACV3P+ basis set on iron and 6-311+G* on the rest of the atoms: basis set BS2. The effect of dispersion on the reaction energies was also tested by doing a UB3LYP-D3 single point calculation in *Jaguar* using the model of Grimme and co-workers.[31] For a selection of chemical systems, i.e. reactants and transition states, geometry optimizations at UB3LYP/BS2 and UB3LYP-D3/BS2 were also carried out, but found very little changes with respect to those obtained at UB3LYP/BS1. Since, transition metal complexes often react via multi state reactivity,[32,33] the complete potential energy profile on the lowest lying singlet, triplet and quintet spin states was also calculated, however, in all cases the singlet spin state was the ground state and well separated from the other spin states. Energies reported in this work contain B3LYP/BS2 energies and contain zero-point and solvent corrections (calculated with B3LYP/BS2 using the polarized continuum model with a dielectric constant mimicking toluene).

As occasionally DFT calculations on spin state ordering and relative energies of transition metal complexes shows fluctuations depending on the choice of the density functional method,[34,35] it was decided to do a series of test calculations with alternative DFT methods, namely B3LYP-D3,[31] BP86,[36,37] M06,[38] OPBE and PBE0.[39,40] Similar to previously reported calculations on analogous systems,[41,42] these studies confirmed the trends and did not change the conclusions.

The methods described here were used previously for analogous transition metal containing systems in comparison with experimentally determined data and reproduced free energies of activation within 4 kcal mol^{-1},[43,44] but also gave reasonable agreement for spectroscopic data, where they reproduced resonance Raman, EXAFS and Mössbauer data excellently.[45-48] To locate transition state structures, extensive geometry scans were run between the various local minima, and used the maximum of those scans as a starting point for the actual transition state searches. Moreover, these scans confirmed that reactants and products indeed connect via the transition state.

Our chemical model, Figure 6.2, is based on the crystal structure coordinates of $[(Cp^{*}Ru)_2(\mu_2\text{-}H)(\mu_2\text{-}NHPh)(\mu_3\text{-}C)PtCH_3(P(CH_3)_3)_2]^{+}$,[10] whereby we replaced the Cp* groups with Cp and phenyl by methyl: Structure **A**. The stereo-chemical effects of the methyl groups of the $P(CH_3)_3$ groups on the reaction mechanism was investigated by replacement of the $P(CH_3)_3$ groups with PH_3. The latter structures are identified as **A'**, $\mathbf{I}_{A,Me}$**'** and $\mathbf{I}_{A,H}$**'**. As the chemical system is saturated in carbon monoxide, we also created a model with two CO molecules bound (one on each Ru center): Structure **B**. We investigated the pathways starting from structures **A** and **B** for hydrogen atom abstraction to form $\mathbf{I}_{A,H1}/\mathbf{I}_{B,H1}$ intermediates via transition state $\mathbf{TS}_{A,H1}/\mathbf{TS}_{B,H1}$ as well as the alternative pathway for initial methyl transfer via transition states $\mathbf{TS}_{A,Me1}/\mathbf{TS}_{B,Me1}$ to form intermediates $\mathbf{I}_{A,Me1}/\mathbf{I}_{B,Me1}$. Subsequently, the methyl group is transferred to $\mathbf{I}_{A,H1}/\mathbf{I}_{B,H1}$ via transition state $\mathbf{TS}_{A,Me2}/\mathbf{TS}_{B,Me2}$ to form products or the hydrogen atom is relayed to $\mathbf{I}_{A,Me1}/\mathbf{I}_{B,Me1}$ via transition state $\mathbf{TS}_{A,H2}/\mathbf{TS}_{B,H2}$ (Figure 6.2).

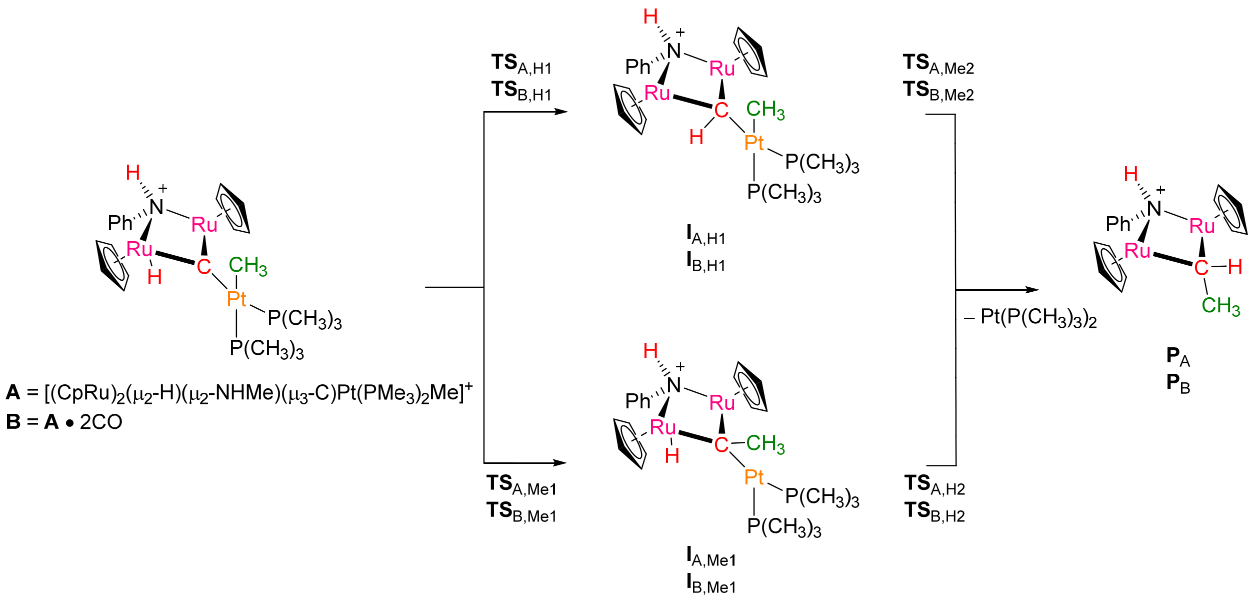

Figure 6.2: Definition of the chemical model, and nomenclature of structures along the reaction mechanism.

Charges reported in this work were obtained from a Natural Bond Occupation (NBO) calculation as implemented in *Gaussian* program package at B3LYP/BS2 level of theory.[49]

In order to fully understand the thermodynamics and kinetics of the mechanism of the overall chemical reaction, we calculated the bond dissociation free energies (BDFE) of key Ru/C–H and Pt/C–CH_3 bonds in complexes **A**, **B**, $\mathbf{I}_{A,Me1}$, $\mathbf{I}_{B,Me1}$, $\mathbf{I}_{A,H1}$, $\mathbf{I}_{B,H1}$, $\mathbf{P}_{A,H}$ and $\mathbf{P}_{B,H}$. The release of either $H^{\bullet}$, H^+, $CH_3^{\bullet}$ and CH_3^+ from these four complexes as described by Eqs 6.1 – 6.4, whereby each individual structure was calculated through a full geometry optimization to give the adiabatic bond dissociation free energies. In addition, the methylenium transfer Gibbs free energy (MTFE) and the proton transfer Gibbs free energy (PTFE) were calculated. The latter was calculated through the use of H_2O/H_3O^+

couple to balance the equation. As there were large structural changes upon H/CH_3 bond breaking on the various complexes we also calculated the diabatic bond dissociation free energies, or vertical bond dissociation free energies, whereby we took the optimized geometries of **A**, **B**, $\mathbf{I}_{A,Me1}$, $\mathbf{I}_{B,Me1}$, $\mathbf{I}_{A,H1}$, $\mathbf{I}_{B,H1}$, $\mathbf{P}_{A,H}$ and $\mathbf{P}_{B,H}$ and ran single point calculations with either $H^{\bullet}$, H^{+}, $CH_3^{\bullet}$ or CH_3^{+} removed.

$$\mathbf{A}^{+} \rightarrow [\mathbf{A} - H]^{+} + H^{\bullet} + BDFE_{H} \qquad (6.1)$$

$$\mathbf{A}^{+} \rightarrow [\mathbf{A} - CH_3]^{+} + CH_3^{\bullet} + BDFE_{Me} \qquad (6.2)$$

$$\mathbf{A}^{+} + H_2O \rightarrow [\mathbf{A} - H]^{0} + H_3O^{+} + PTFE \qquad (6.3)$$

$$\mathbf{A}^{+} \rightarrow [\mathbf{A} - CH_3]^{0} + CH_3^{+} + MTFE \qquad (6.4)$$

6.3: Results and Discussion

Before discussing our calculated reaction mechanisms, let us briefly summarize the main results on our reactant structures, **A** and **B**, and establish their chemical properties. The optimized geometries of **A** and **B** are shown in Figure 6.3. The obtained bond distances of **A** are to within 0.011 Å of the crystal structure coordinates reported in Ref 10 and as such the DFT calculations give reasonable chemical structures. The Pt–C bond of 1.960/1.947Å in **A/B** represents a single bond and is in good agreement with several reported Pt–C containing crystal structures from the literature.[50-53] The two Ru–C bonds are very close in bond length in **A** and the fact that one of the two atoms is protonated, therefore, appears to have little effect on its interaction with carbon. However, addition of two CO molecules strongly affects the Ru–C bond lengths and one of those is elongated to 2.126 Å in **B**. Ru–C bond lengths found here are typical for a single bond and compare to analogous structures reported before.[54-59] Therefore, addition of two CO molecules to structure **A** does not appear to have drastically changed the molecular geometry and keeps its original features.

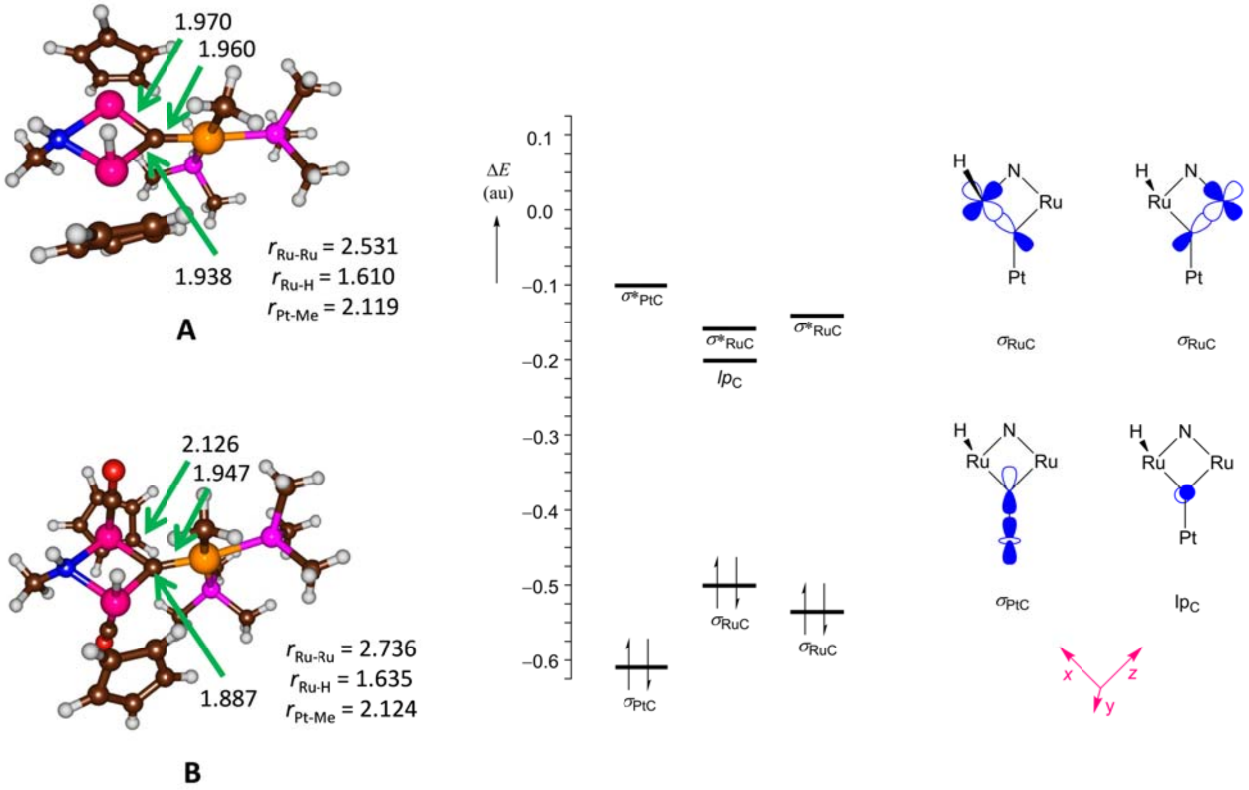

Figure 6.3: Optimized geometry of **A** and **B** as calculated with B3LYP with bond lengths given in angstroms. The right-hand-side displays the natural bond orbitals of **A** and their ordering for those involving the central carbon atom with it ligands.

The experimental studies of reference 10 implicate the hydride to bind as a bridging ligand to both Ru atoms, whereas Figure 6.3 gives a terminal-hydride atom that is linked to a single Ru atom. We created starting structures for a geometry optimization using both a bridging hydride atom as well as a terminal hydride atom. However, both of these calculations (whether CO was used as ligands or not) converged to the structure with a terminal hydride atom. This implies that a structure with bridging hydride atom will be a higher energy state and possibly inaccessible.

As transition metal complexes containing iron or ruthenium generally contain close-lying spin states and often react via multistate reactivity patterns,[32,33] structure **A** was optimized in the singlet, triplet and quintet spin states. The closed-shell singlet spin state is the ground state and is well separated from the triplet and quintet spin states by ΔG_{gas} = 17.1 and 44.8 kcal mol^{-1}, respectively. These values change by less than 1 kcal mol^{-1} when solvent corrections are included. Clearly, structure **A** is a closed-shell species that will react via single-state reactivity in contrast to metal(IV)-oxo and metal(IV)-nitrido complexes from the literature.[60,61]

In order to shed light on the bonding pattern of the central carbon atom, Natural Bond Orbital (NBO) analysis of structure **A** was done. Thus, the NBO analysis reveals three bonding type orbitals for the central carbon atom, namely three single bonds for the interaction with the two Ru atoms and the Pt atom. The σ_{PtC} orbital represents the σ-bonding orbital between Pt and C and is built up from the interaction of the $5d_{z2}$ orbital on Pt with the $2p_z$ orbital on C. In addition, there are two single bonds between the carbido atom and the two Ru atoms, which result from the mixing of the 2s, $2p_x$ and $2p_z$ atomic orbitals on C with the $4d_{z2}$ orbital on Ru or the $4d_{x2-z2}$ on Ru(H). As such the central carbon atom is sp^2 hybridized. However, the fourth valence orbital on carbon is a virtual $2p_y$ atomic orbital. The NBO analysis, therefore, assigns the central carbon atom as a carbene with three sp^2 hybridized orbitals that are occupied with two electrons in an orbital donating to Pt (σ_{PtC}), and two bonding orbitals where both C and Ru donate one electron each into the bond (σ_{RuC}, σ_{RuC}). This hybridization scheme gives the central carbon atom its planar structure, Figure 6.4. As such the chemical structure of Ru_2CPt represents a Fischer-carbene, where the lone pair of the carbon atom interacts with an empty Pt orbital and the π-type Pt orbitals give back-bonding into the empty $2p_y$ orbital of the carbene.[62-64] The NBO charges displayed in Figure 6.3 reveal a charge-neutral carbon atom ($Q_C = 0.04$) that is surrounded by slightly negatively charged metal atoms. Consequently, there is very little charge built-up in this chemical system.

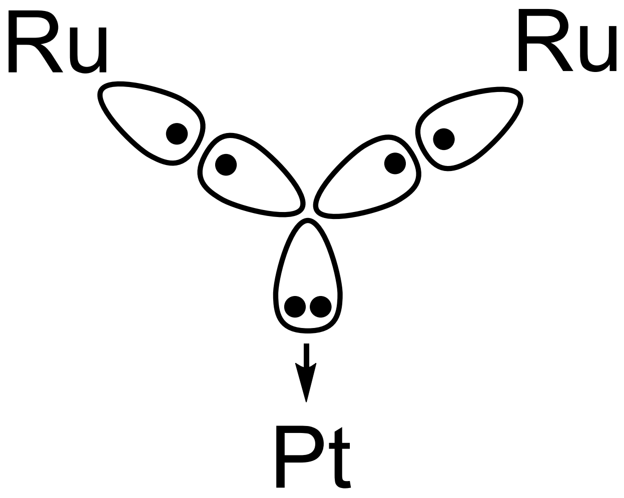

Figure 6.4: Hybridization scheme of **A** and **B**.

Subsequently, the potential energy profile for μ_2-$CHCH_3$ formation starting from **A** and **B** was calculated. Two mechanisms were tested as shown in Figure 6.5: (i) initial hydrogen transfer from RuH to the carbene followed by methyl abstraction and (ii) initial methyl transfer from $PtCH_3$ followed by hydrogen/proton transfer. Figure 6.5 starts from the center with **A**/**B** and follows the two possible reaction mechanisms: The initial H-transfer (mechanism to the right) and the initial CH_3 transfer (mechanism to the left). The two mechanisms are described as follows: In the first case, the metal-carbene group abstracts a hydrogen atom from the RuH group via a transition state $\mathbf{TS}_{H1}$ to form the H-transfer intermediate $\mathbf{I}_{H1}$. A subsequent CH_3 transfer from the $PtCH_3$ group via a barrier $\mathbf{TS}_{Me2}$ gives the μ_2-$CHCH_3$ bound product **P**. We also tested the alternative pathway starting with an initial CH_3 abstraction by the metal-carbene group via transition state $\mathbf{TS}_{Me1}$ leading to the methyl-transfer intermediate $\mathbf{I}_{Me1}$. This intermediate then reacts further by H-abstraction from RuH via a transition state $\mathbf{TS}_{H2}$ to form product **P**.

We attempted to also locate the alternative synchronous transfer of both hydrogen and methyl group at the same time to the carbene atom, however, all calculations converged to one of the lower lying transition states (or local minima) described in this work. Previously, we calculated the concerted epoxidation reaction of an olefin by an iron(IV)-oxo heme cation radical system and found it to be a second order saddle point that is well higher in energy than the stepwise transition states.[65,66]

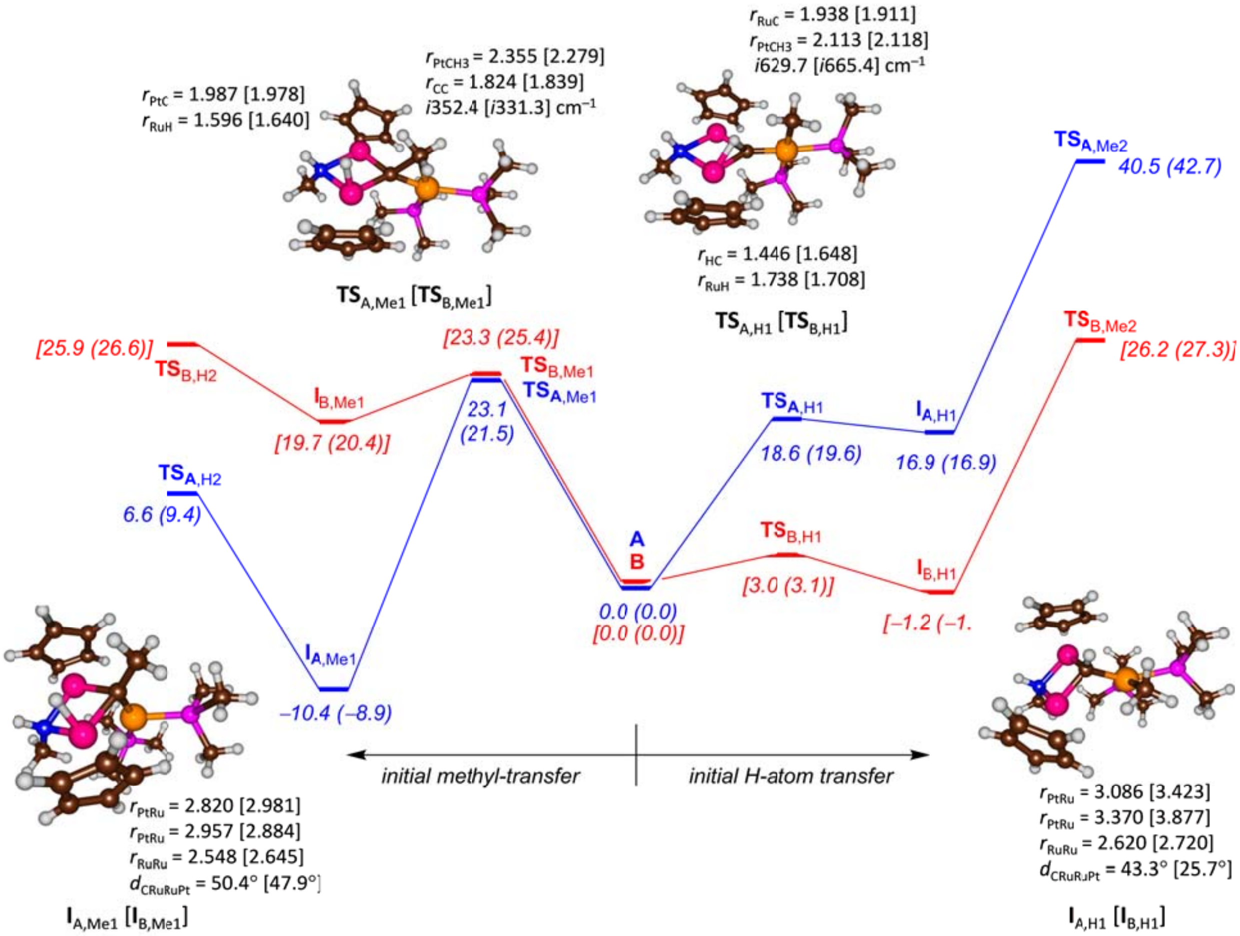

Figure 6.5: Gibbs free energy profile of alkyl chain growth on **A** and **B** via either (*i*) CH_3-transfer followed by H-transfer (mechanism from the center to the left) or (*ii*) H-transfer followed by CH_3-transfer (mechanism from the center to the right). Energies (ΔE+ZPE) and free energies (ΔG, in parenthesis) obtained with B3LYP/BS2 with values in kcal mol^{-1}. All data include solvent corrections to the energy. Optimized geometries report bond lengths in angstroms, angles in degrees and the imaginary frequency in the transition states in wave numbers.

Dramatic differences in relative energies and optimized structures are found for the pathways starting from **A** or **B**, however, in both cases the H-atom transfer reaction has the lowest Gibbs free energy of activation of $\Delta G^{\ddagger}$ = 19.6 (3.1) kcal mol^{-1} for **A** (**B**).

Nevertheless, in both the cases it is not the rate determining step as the subsequent CH_3-transfer to form products gives an additional barrier with a maximum of 23.1 (24.2) kcal mol^{-1}. Therefore, the reaction that is initiated with H-atom transfer from **A** has an unfeasible Gibbs free energy of activation of 42.7 kcal mol^{-1} for $\mathbf{TS}_{A,Me2}$ with respect to **A** and will not be able to proceed through that pathway. On the other hand this barrier for structure **B** is much lower in energy, but still would imply a relatively slow reaction process. This is in agreement with experimental observation that found evidence of a structure with analogy to $\mathbf{I}_H$, but the methyl group bound to one of the Ru atoms, which would imply a fast hydrogen abstraction followed by a much slower methyl transfer. The origin of the enhanced stabilization of CO bound intermediate $\mathbf{I}_{B,H1}$ with respect to $\mathbf{I}_{A,H1}$ comes from the structural differences. Thus, without CO bound the carbene carbon atom pyramidalizes much more and the dihedral angle $d_{CRuRuPt}$ = 43.3° in $\mathbf{I}_{A,H1}$, whereas it is 25.7° in $\mathbf{I}_{B,H1}$. The large pyramidalization causes contraction of the chemical system and more stereochemical repulsions of the $P(CH_3)_3$ groups with the RuCp groups that destabilize the structure.

The alternative pathway with an initial CH_3-transfer, on the other hand, has a calculated Gibbs free energy of activation of $\Delta G^\ddagger = 21.5$ (25.4) kcal mol^{-1} for **A** (**B**) and, therefore, is disfavored over the initial H-atom transfer process. However, this reaction leads to a very stable intermediate $\mathbf{I}_{A,Me1}$ with an exergonicity of almost 10 kcal mol^{-1}, whereas the reaction is endothermic for the formation of $\mathbf{I}_{B,Me1}$. Its subsequent H-atom transfer leading to products only has a Gibbs free energy of activation of 18.3 (6.2) kcal mol^{-1} from intermediates for **A** (**B**). Therefore, product formation is a viable, but kinetically slow, pathway through this channel for both structures **A** and **B**, whereby it is the dominant mechanism for **A** and competitive with initial hydrogen atom abstraction for **B**. Binding of CO molecules to the reaction center, therefore, changes the regioselectivity of the chemical reaction in favor of initial hydrogen atom abstraction. In previous work on the regioselectivity of substrate epoxidation versus hydroxylation by iron(IV)-oxo complexes we showed that changes to the ligand system of the iron or even replacing hydrogen atoms of the substrate by deuterium atoms can reverse a regioselectivity and as such the Ru_2Pt-carbene complex is another example of a chemical catalyst that changes its reactivity upon ligand modifications.[67,68]

The origin of the differences in stability of $\mathbf{I}_{A,Me1}$ versus $\mathbf{I}_{B,Me1}$ stems from differences in location of the transferring hydrogen atom. Thus, in $\mathbf{I}_{A,Me1}$ the hydrogen atom is located close to one Ru atom with distances Ru1–H and Ru2–H of 1.604 and 2.521 Å, whereas they change to 1.736 and 1.943 Å, respectively, in $\mathbf{I}_{B,Me1}$. The structure with the bridging proton is considerably destabilized with respect to singly protonated Ru atom.

In summary, DFT establishes a possible alkyl synthesis mechanism for **A** as a stepwise mechanism with an initial CH_3-transfer followed by H-atom transfer, whereas structure **B** proceeds with competitive mechanisms via either initial CH_3- or H-transfer processes. An analysis of the group spin densities and charges along the complete reaction mechanism shows that all local minima and transition states are closed-shell singlet species with no radical built-up during the reaction. Accordingly, the reaction starts with either proton transfer or CH_3^+ transfer.

So why is the reaction displayed in Figure 6.5 stepwise with consecutive CH_3 or H-transfer processes and what is the function of the Ru_2Pt scaffold? These questions will be answered in the following discussion. Structurally, there are major changes happening at the Ru_2Pt-carbene center during the reaction mechanism. Although **A** and **B** have an sp^2 hybridized carbon atom that lies in the plane of the Ru_2Pt atoms, upon H/CH_3-transfer the planarity is distorted and the carbon atom relaxes to a pyramidal conformation due to sp^3 hybridization. The pyramidalization is considerably more pronounced for the CH_3-transfer process than in the H-atom transfer pathway as dihedral angles C–Ru–Ru–Pt of 50.4° for $\mathbf{I}_{A,Me1}$ and 43.3° for $\mathbf{I}_{A,H1}$ are found. At the same time the Pt–Ru distances in $\mathbf{I}_{A,Me1}$ shorten by as much as 0.8Å with respect to **A** to well below 3Å, while in $\mathbf{I}_{A,H1}$ they stay considerably longer: r_{PtRu} = 3.086 and 3.370Å. These large structural changes for the CH_3-transfer pathway will have an effect on the reaction energetics and kinetics as well as on the relative stability of $\mathbf{I}_{A,Me1}$ versus $\mathbf{I}_{A,H1}$. Thus, the Pt atom in $\mathbf{I}_{A,Me1}$ only has three ligands due to CH_3-transfer to the carbon atom, which means limited stereochemical interactions between the two $P(CH_3)_3$ groups and the rest of the molecule so that the Pt atom can approach the two Ru atoms closely. In $\mathbf{I}_{A,H1}$ the Pt atom remains tetra-coordinated and the stereochemical interactions between all ligands and the rest of the molecule prevent a close approach to the Ru_2C center. As a consequence of the stereochemical repulsions $\mathbf{I}_{A,H1}$ is considerably destabilized over $\mathbf{I}_{A,Me1}$ and the reaction pathway with initial H-atom transfer is energetically disfavored.

To further establish these stereochemical interactions in $\mathbf{I}_{A,H1}$ versus $\mathbf{I}_{A,Me1}$, a subsequent set of calculations on these structures was done, but with the $P(CH_3)_3$ groups replaced by PH_3: structures $\mathbf{I}_{A,H1}$**’** and $\mathbf{I}_{A,Me1}$**’**, Figure 6.6. The optimized geometry of **A’** (Figure 6.6) is very close to that reported above for **A** in Figure 6.3 and only minor changes in bond lengths are obtained. Clearly, the $P(CH_3)_3$ groups have little effect on the structure of the

Ru_2PtC core of our chemical system. A similar situation occurs for $\mathbf{I}_{\mathrm{A,Me1}}$**'**, which has large structural similarities with $\mathbf{I}_{\mathrm{A,Me}}$ reported in Figure 6.2. Major changes, however, are seen when $\mathbf{I}_{\mathrm{A,H1}}$ is compared to $\mathbf{I}_{\mathrm{A,H1}}$**'**. Thus, one of the Ru–Pt distances decreases from 3.370 to 3.116 Å and as a consequence the pyramidality of the carbon center changes from $d_{\mathrm{CRuRuPt}} = 43.3°$ in $\mathbf{I}_{\mathrm{A,H1}}$ to a value of 51.9° in $\mathbf{I}_{\mathrm{A,H1}}$**'**. This has a major effect on the stability of $\mathbf{I}_{\mathrm{A,H1}}$**'** and it is stabilized by 6.0 kcal mol^{-1} with respect to **A'**, however, the $\mathbf{I}_{\mathrm{A,Me1}}$**'** remains the most stable conformation. This implies that the $P(CH_3)_3$ groups incur a destabilizing effect on the reaction mechanism, but will not reverse the preference of initial CH_3-transfer over H-atom transfer.

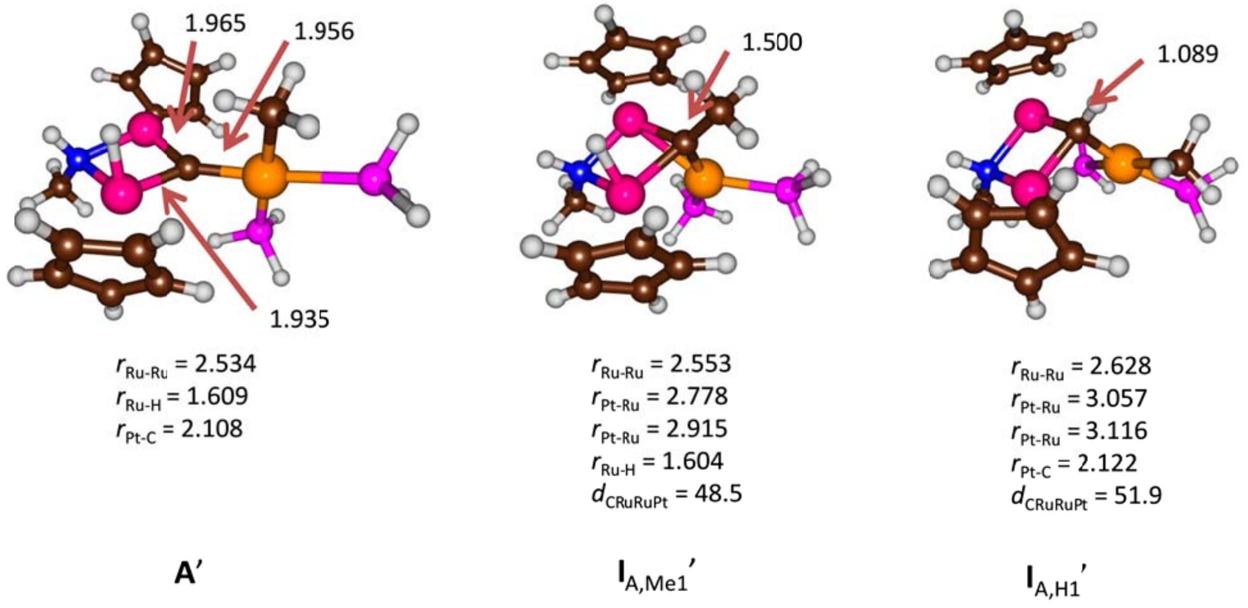

Figure 6.6: Optimized geometries of **A'**, $\mathbf{I}_{\mathrm{A,Me1}}$**'** and $\mathbf{I}_{\mathrm{A,H1}}$**'** with bond lengths in angstroms.

To gain insight into the electronic changes during the reaction mechanism, a NBO analysis was also performed on the intermediate and product complexes. The NBO calculation reveals a configuration on the central carbon atom of $2s^{1.08}$ $2p^{2.92}$for $\mathbf{I}_{A,Me1}$ and $2s^{1.18}$ $2p^{3.10}$ for $\mathbf{I}_{A,H1}$. Both intermediate complexes, therefore, have an electronic configuration close to sp^3 hybridization, and as a consequence their geometries have changed from planar to pyramidal in agreement with the optimized structures.

In order to fully understand the thermodynamics and kinetics of the mechanism displayed in Figure 6.2, and, in particular, gain insight into the electron transfer mechanisms during the reaction processes we set up Valence Bond (VB) curve crossing diagrams (Figure 6.7) for the methyl transfer and hydrogen atom transfer steps. These VB curve crossing diagrams were applied previously to rationalize the reaction mechanisms of substrate activation (hydroxylation, epoxidation, desaturation and sulfoxidation) by Compound I of cytochrome P450 enzymes as well as the nonheme iron(IV)-oxo species of dioxygenases.[69-72] These studies rationalized reaction mechanisms, and, for instance, explained why a reaction was stepwise via a radical intermediate rather than synchronous (concerted). Furthermore, in the case of P450 Compound I several possible electron transfer pathways in substrate hydroxylation by Compound I were identified via either an iron(IV)-hydroxo intermediate or an iron(III)-hydroxoheme cation radical, and different activation barriers (and consequently rate constants) were identified that passed these individual intermediates.[73] VB diagrams explained the differences in electron transfer pathways and rationalized the ordering of the various electronic and spin states. Finally, the VB diagrams were used to find patterns in activation energies/rate constants and create predictive models. As such these VB curve crossing diagrams may also find its use in organometallic chemistry and, therefore, we applied it to the chemical system described here.

The VB curve crossing diagrams start at the bottom-left with the reactant electronic configuration and wave function (Ψ_R) of **A**/**B**, which is a carbene where two sp^2 electrons form bonding orbitals with electrons on the two ruthenium atoms and the other two electrons represent a lone pair orbital that donates a bond to Pt. Each of the dots in Figure 6.7 represents one of these valence electrons. In part (*a*) in Figure 6.7 the reaction follows the methyl transfer from Pt to carbene and the structure on the right-hand-side gives the electronic configuration of $\mathbf{I}_{Me}$ with wave function Ψ_{Me}. In $\mathbf{I}_{Me}$ the central carbon atom is sp^3 hybridized and forms a single bond with Ru, Ru, Pt and CH_3. In VB theory the wave functions of the reactant and product complexes cross, i.e. Ψ_R and Ψ_{Me} in Figure 6.7a, and lead to an avoided crossing and a transition state for the reaction from reactants to intermediates.[74] Thus, the curve crossing energy (ΔE_X) is above the actual transition state ($\Delta E_{Me}^{\ddagger}$) by a factor *B*, which is called the resonance energy. It has been shown that the barrier height can be described by the difference in energy by a fraction (*f*) of the promotion gap (*G*) and the resonance energy *B*: $\Delta E_{Me}^{\ddagger} = fG_{MT} - B$. The promotion gap signifies the excitation energy from the ground state wave function to the product wave function in the geometry of the reactants, i.e. G_{MT} is the energy difference between Ψ_R and Ψ_R* in the reactant geometry. The VB diagrams also give chemical structures of the reactant and product wave functions of the ground and excited state species with valence electrons identified with a dot.

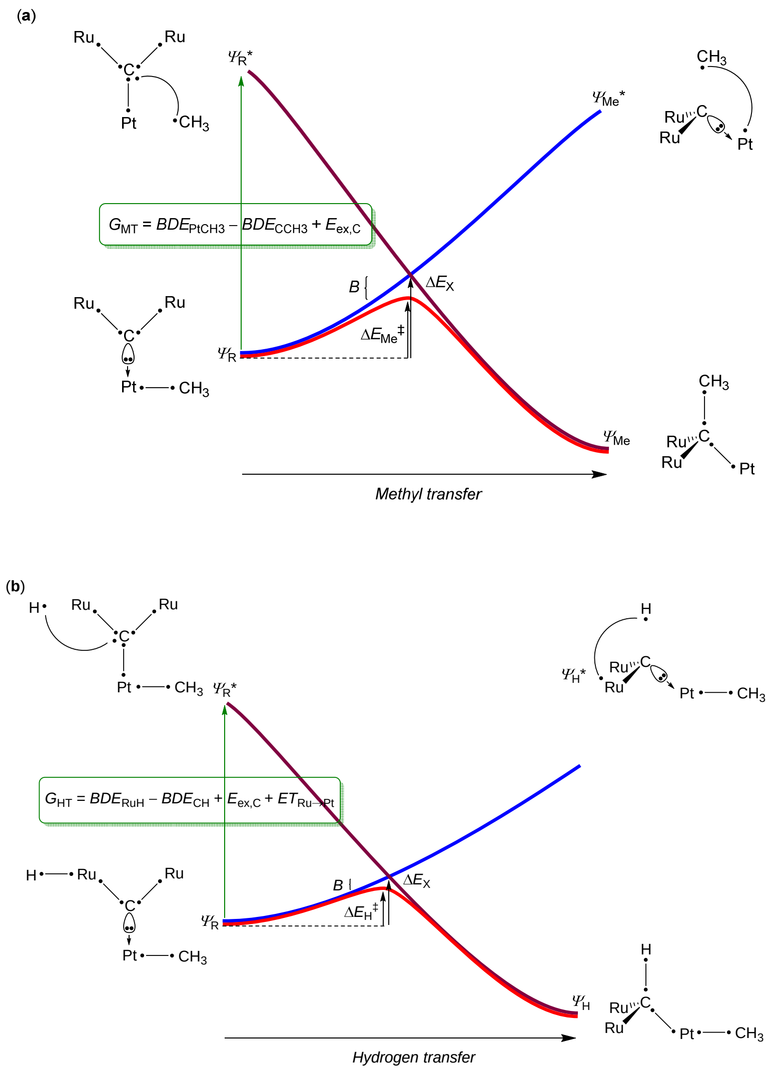

Figure 6.7: Valence bond curve crossing diagrams for methyl transfer (part **a**) and hydrogen atom transfer (part **b**) from reactants (**A** or **B**). Valence electrons are identified with a dot.

A close inspection of the VB diagrams in Figure 6.7 shows that the promotion gap for methyl transfer (G_{MT}) represents the breaking of the Pt–CH_3 bond and the formation of a new C–CH_3 bond. In addition, the VB structures of Ψ_R and Ψ_R* shows that the carbene carbon is rehybridized from sp^2 to sp^3 hybridization and one electron of the lone pair orbital pointing toward Pt is promoted into the new sp^3 orbital. At the same time the electron from the broken Pt–CH_3 bond moves into the carbene-Pt bond. Thus, the promotion gap also contains a component for the excitation energy of the carbene from sp^2 to sp^3 hybridization ($E_{ex,C}$), which essentially requires a promotion of an electron from the σ_{PtC} orbital to the virtual $2p_y$ molecular orbital on carbon. Energetically G_{MT} can be described in terms of the bond dissociation energies (BDEs) of the respective bonds that are broken and formed in the reaction process, Eq 6.5, whereby BDE_{PtCH3} represents the Gibbs free energy to break the Pt–CH_3 bond in **A**/**B** and BDE_{CCH3} is the Gibbs free energy to form the C–CH_3 bond in $\mathbf{I}_{A,Me1}$/$\mathbf{I}_{B,Me1}$.

$$G_{MT} \propto BDE_{PtCH3} - BDE_{CCH3} + E_{ex,C} \tag{6.5}$$

The situation is dramatically different for hydrogen atom transfer from **A**/**B** as shown in Figure 6.7b. Thus, the barrier height for hydrogen atom transfer ($\Delta E_H^{\ddagger}$) is proportional to the promotion gap for hydrogen atom transfer (G_{HT}), which correlates with the strength of the Ru–H bond that is broken (BDE_{RuH}), the strength of the C–H bond that is formed (BDE_{CH}) and again the excitation energy for the carbene to change from sp^2 to sp^3 hybridization. In addition to these three terms, the promotion gap G_{HT} also contains a component for the electron transfer energy from Ru to Pt ($ET_{Ru\rightarrow Pt}$). The hydrogen atom transfer process, therefore, incurs extra electron reorganization energy in the Ru_2Pt-carbene scaffold, which is not necessary for the methyl transfer step. The overall preference of hydrogen atom transfer versus methyl transfer will depend on the relative strengths of the bonds that are broken and formed in the process and the electron reorganization energy. To find out whether there are major differences between the BDE values in Eq 6.5 and those in Eq 6.6, we decided to calculate their values with DFT.

$$G_{\mathrm{HT}} \propto \mathrm{BDE}_{\mathrm{RuH}} - \mathrm{BDE}_{\mathrm{CH}} + E_{\mathrm{ex,C}} + \mathrm{ET}_{\mathrm{Ru}\rightarrow\mathrm{Pt}} \qquad (6.6)$$

As the VB drawings in Figure 6.7 only give qualitative analysis of electron transfer processes and no actual quantitative values, it was decided to calculate BDEs and bond dissociation free energies (BDFEs) of key Ru/C–H and Pt/C–CH_3 bonds in complexes **A**,**B**,$\mathbf{I}_{\mathrm{A,Me1}}$, and $\mathbf{I}_{\mathrm{A,H1}}$ by calculating the release of a $H^{\bullet}$, H^{+}, $CH_3^{\bullet}$ and CH_3^{+} from these four complexes according to Eqs 6.1 – 6.4 above. Figure 6.8 displays the diabatic driving forces for H/CH_3 release from complexes **A**, **B**, $\mathbf{I}_{\mathrm{A,H1}}$ and $\mathbf{I}_{\mathrm{A,Me1}}$. We initially calculated the adiabatic BDFE calculations, whereby we did a full geometry optimization of all individual chemical structures in Eqs 6.1 – 6.4 and then took the difference in Gibbs free energy for each of these reactions. However, due to considerable rehybridization of the central carbon atom and as a consequence large geometrical changes in some of the structures, the adiabatic BDFE values gave unrealistic results. For instance, the adiabatic bond dissociation energy for the breaking of the Ru–H bond in **A** appears negative, which would imply spontaneous dissociation in disagreement with the experimental crystal structure. However, this did not happen during the geometry optimization and consequently there is a significant barrier for this process. Another reason why the adiabatic energies give unrealistic results is the dramatic structural changes upon removal of one ligand, i.e. H or CH_3, which changes systems from hexacoordination to pentacoordination, i.e. from octahedral to trigonal bipyramical structure, which leads to major changes in electronic structure.[75] Conversely, when we calculate the diabatic Gibbs free energy change by taking the H and [**A** – H] products in the geometry of **A** then the

BDFE is positive. The same is found for the dissociation of a methyl group from **A**. By contrast to structure **A**, the adiabatic and diabatic bond energies in structures $\mathbf{I}_{\mathrm{A,Me1}}$ and $\mathbf{I}_{\mathrm{A,H1}}$ are very similar and vary by less than 6 kcal mol^{-1}. In the following, however, we will focus on the diabatic bond dissociation free energies.

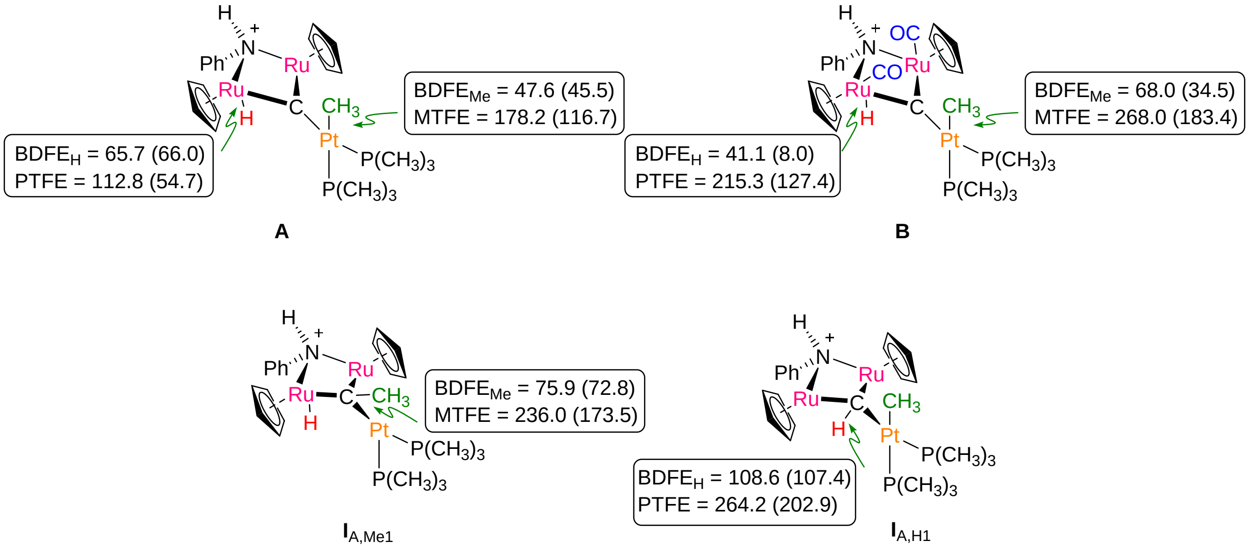

Figure 6.8: Bond dissociation free energies (BDFEs in kcal mol^{-1}) of key bonds in structures **A**, **B**, $\mathbf{I}_{\mathrm{A,Me1}}$ and $\mathbf{I}_{\mathrm{A,H1}}$. Reactions calculated according to Eqs 6.1 – 6.4. Values in parenthesis are solvent corrected free energies, whereas those out of parenthesis are gas-phase data. PTFE and MTFE are the proton and methyl transfer Gibbs free energies, respectively.

As can be seen the strength of the C–H bond in **A** is considerably different from that obtained for **B**. This, the BDFE$_{H}$ for **A** is 45.5 kcal mol^{-1} in solvent, whereas a value of 34.5 kcal mol^{-1} is found for **B** and as a consequence the hydrogen atom transfer should be much easier with the CO bound complex than with complex **A**. Indeed, the potential energy landscape in Figure 6.2 shows that formation of $\mathbf{I}_{\mathrm{B,H1}}$ is exergonic by –1.2 kcal mol^{-1}, while it is endergonic for $\mathbf{I}_{\mathrm{A,H1}}$. Thus, CO binding affects the chemical structure of the Ru centers and weakens the Ru–H bond and makes it more susceptible for hydrogen atom transfer. Despite the fact that the subsequent methyl transfer still has a barrier of about 28 kcal mol^{-1} (virtually unchanged with respect to **A**), it is now sufficiently low to cross at ambient temperatures and pressures. On the other hand, the platinum-methyl bond is much stronger in the CO bound structures and results in a considerable raise in the $\mathbf{I}_{\mathrm{B,Me1}}$ energy.

Thermodynamically, the driving force to form $\mathbf{I}_{\mathrm{A,Me1}}$/$\mathbf{I}_{\mathrm{A,H1}}$ from **A** represents the breaking of a weak Pt–CH_3 or Ru–H bond and the formation of a much stronger C–CH_3/C–H bond. Hence the reaction should be strongly exergonic, which is seen for the reaction via $\mathbf{I}_{\mathrm{A,Me1}}$ in Figure 6.2, but not for the one via $\mathbf{I}_{\mathrm{A,H1}}$. Thus, the hydrogen atom transfer from Ru in **A** to the carbine to form $\mathbf{I}_{\mathrm{A,H1}}$ results in the breaking of the Ru–H bond of $\mathrm{BDFE_H}$ = 65.7 kcal mol^{-1} in the gas-phase and the formation of a C–H bond with a diabatic value of 108.6 kcal mol^{-1} and, if the driving force was solely dependent on the change in bond strength the reaction would have been exergonic by 42.9 kcal mol^{-1}. As shown in Figure 6.2, however, this reaction is endergonic by 17.2 kcal mol^{-1}, which implies that the stereochemical and electronic effects, i.e. the sp^2 to sp^{3}rehybridization($E_{\mathrm{ex,C}}$) and the Ru → PT electron transfer ($\mathrm{ET_{Ru\rightarrow Pt}}$) accounts for a destabilization of $\mathbf{I}_{\mathrm{A,H1}}$ by about 60 kcal mol^{-1} in Gibbs free energy. This is explained schematically in Figure 6.9, where we deconvolute the processes from **A** to $\mathbf{I}_{\mathrm{A,Me1}}$ and from **A** to $\mathbf{I}_{\mathrm{A,H1}}$ into factors for bond breaking and formation (δBDFE) and quantum mechanical effects (E_{QM}). Thus, the methyl transfer reaction from **3** results in the breaking of the Pt–CH_3 bond, which requires a $\mathrm{BDFE_{Me,diabatic}}$ = 47.6 kcal mol^{-1}, and at the same time the formation of the C–CH_3 bond ($\mathrm{BDFE_{Me,diabatic}}$ = 75.9 kcal mol^{-1}). Therefore, the change in bond dissociation

Gibbs free energy for the methyl transfer is –28.3 kcal mol^{-1}. The reaction mechanism in Figure 6.2 found the methyl transfer process to be exergonic by 9.9 kcal mol^{-1}, which implies that the quantum mechanical effect of the process accounts for 18.4 kcal mol^{-1}. The quantum mechanical effect includes the rehybridization energy of the carbene group and the geometric and stereochemical factors associated with the methyl transfer. By comparison, the hydrogen atom transfer shows a much larger change in bond dissociation energy due to the strong C–H bond that is formed ($\delta BDFE_{H,diabatic} = -42.9$ kcal mol^{-1}). However, this reaction incurs a large quantum mechanical effect of 60.1 kcal mol^{-1} and thereby makes the overall process highly endergonic. The quantum mechanical effect includes the rehybridization of the carbon atom, which will probably be of the same order of magnitude as that found for the methyl transfer process, i.e. about 18 kcal mol^{-1}. In addition, there are the above mentioned stereochemical repulsions of the methyl groups of the $P(CH_3)_3$ moieties that raise $\mathbf{I}_{A,H1}$ by about 6 kcal mol^{-1}. Finally, the electronic effects (E_{QM}) for the hydrogen atom transfer reaction include the electron transfer energy from Ru to Pt as described in the VB diagram in Figure 6.7.

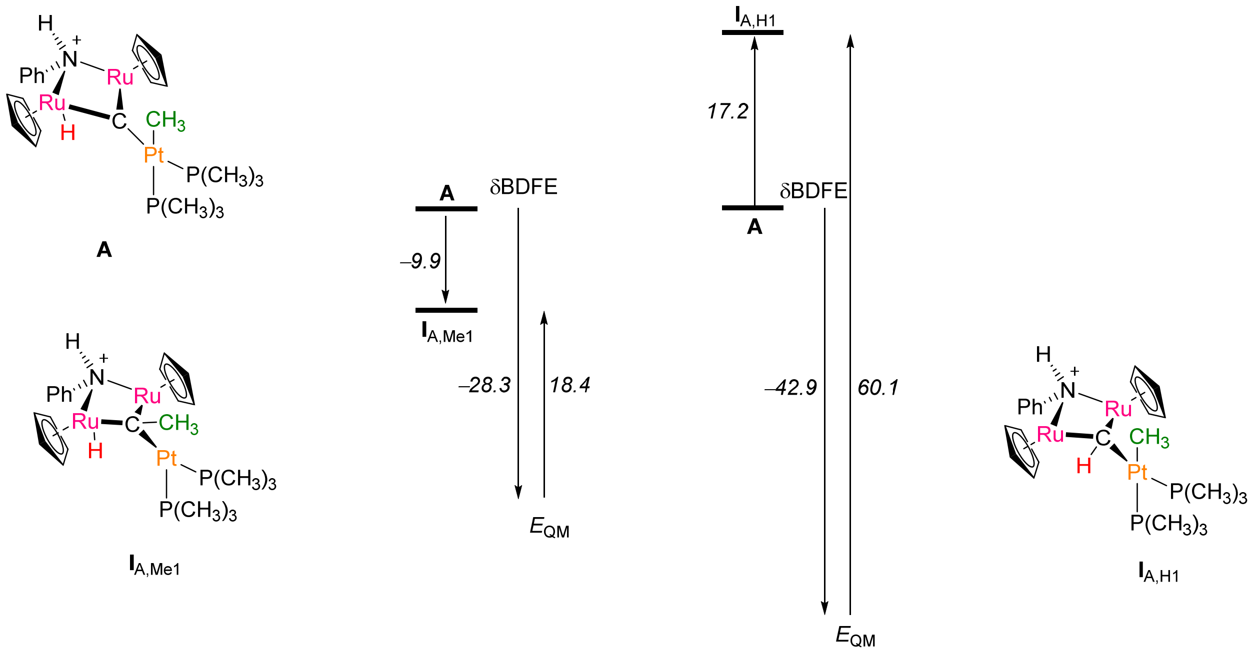

Figure 6.9: Energy decomposition of the methyl and hydrogen atom transfer reaction from **A**. Gibbs free energies given are in kcal mol^{-1}.

In addition to removal of H/CH_3 from our reactant complexes and intermediates, the breaking of the bond into two ions was also investigated and is described as the proton transfer Gibbs free energy (PTFE) and methyl transfer Gibbs free energy (MTFE). As follows from the data in Figure 6.8, it requires considerably more energy to break the Ru–H and Pt–CH_3 bonds than a homogeneous splitting into $Ru^{\bullet}$+$H^{\bullet}$ and $Pt^{\bullet}$+$CH_3^{\bullet}$. The thermodynamic analysis confirms the results described above in Figure 6.5 where either $H^{\bullet}$ or $CH_3^{\bullet}$ is transferred rather than H^{+} and CH_3^{+}.

So what about the next step for the formation of μ_2-$CHCH_3$ products? The reaction from **I**$_{A,Me1}$ to products results in the breaking of the Ru–H bond and the formation of a new C–H bond. By contrast, the pathway from **I**$_{A,H1}$ leads to the breaking of the Pt–CH_3 bond and the transfer of the methyl group to carbon. However, this process breaks the C–Pt bond and the $Pt(P(CH_3)_3)_2$ group is left behind with two unpaired electrons. Thus, an electron on Pt is promoted into a virtual orbital and the reaction proceeds via a high energy pathway. Indeed, the DFT calculated potential energy profile in Figure 6.5 gives a high barrier for $\mathbf{TS}_{A,Me2}$ in agreement with this.

In summary, DFT calculations presented here show a novel pathway for the synthesis of linear alkanes on a trimetal-carbene center. The chemical system discussed here, however, is inefficient as the lowest lying initial barrier is for hydrogen atom transfer, which leads to a dead-end reaction intermediate. By contrast, the initial methyl transfer can be followed by hydrogen atom transfer to lead to products. The question is how this catalyst may be improved for alkane synthesis. The thermodynamic and VB Schemes above give some clear indication to this. As shown in Eqs 6.5 and 6.6 above, the barrier heights $\mathbf{TS}_{H1}$ and $\mathbf{TS}_{Me1}$ are dependent on the Ru–H and Pt–CH_3 bonds that are broken and the C–H and C–CH_3 bonds being formed. Consequently, a chemical system with a weaker metal-CH_3 bond should react predominantly via initial methyl transfer and may be more efficient. The work described here may have relevance to biological and heterogeneous catalysis for the synthesis of alkanes. In particular, in heterogeneous catalysis linear alkanes are generated on a metal surface using often CO and H_2 are reactants. It may very well be that the trimetal-carbene structure discussed here is a common type intermediate in heterogeneous catalysis, but further research will have to be performed to establish this.

6.4: Conclusions

In summary, the calculations establish the key features of a synthetic homogeneous catalyst for alkyl chain growth. A combination of DFT, NBO, VB and thermochemical studies has been performed and established the intrinsic chemical properties of **A** or **B**. Firstly, reactants were characterized as having a Ru_2Pt-carbene core where the lone-pair is donated to Pt via bonding/back-bonding configuration. Secondly, we find a low energy mechanism of alkyl formation through consecutive $CH_3^{\bullet}$ and $H^{\bullet}$ transfer to the carbene with low Gibbs free energy of activation and exergonic driving force. We show that the reverse process is thermochemically hampered and would lead to an excited triplet configuration.

Overall, our work identifies a novel reaction for the synthesis of alkanes that starts from a trimetal carbene. This unique structure is shown to be capable of intramolecular methyl and hydrogen atom transfer to the carbene to form μ_2-$CHCH_3$ products as precursor to alkanes.

References:

1 C. K. Rofer-de Poorter, *Chem. Rev*., **81**, 447 (1981).

2 H. Schulz, *Appl. Catal. A: General*, **186**, 3, (1999).

3 A. Y. Khodakov, W. Chu, P. Fongarland, *Chem. Rev*., **107**, 1692 (2007).

4 P. M. Maitlis, V. Zanotti, *Chem. Commun*., 1619 (2009).

5 N. E. Tsakoumis, M. Rønning, Ø Borg, E. Rytter, A. Holmen, *Catal. Today*, **154**, 162 (2010).

6 S. Shetty, R. A. van Santen, *Catal. Today*, **171**, 168 (2011).

7 O. R. Inderwildi, S. J. Jenkins, *Chem. Soc. Rev*., **37**, 2274 (2008).

8 P. Perkins, K. P. C. Vollhardt, *J. Am. Chem. Soc*., **101**, 3985 (1979).

9 O. R. Inderwildi, D. A. King, S. J. Jenkins, *Phys. Chem. Chem. Phys*., **11**, 11110 (2009).

10 S. Takemoto, H. Morita, K. Karitani, H. Fujiwara, H. Matsuzaka, *J. Am. Chem. Soc*., **131**, 18026 (2009).

11 J. M. Mayer, *Acc. Chem. Res*., **31**, 441 (1998).

12 D. R. Weinberg, C. J. Gagliardi, J. F. Hull, C. F. Murphy, C. A. Kent, B. C. Westlake, A. Paul, D. H. Ess, D. G. McCafferty, T. J. Meyer, *Chem. Rev*., **112**, 4016 (2012).

13 J. A. Love, M. S. Sanford, M. W. Day, R. H. Grubbs, *J. Am. Chem. Soc*., *125*, 10103 (2003).

14 B. Alcaide, P. Almendros, A. Luna, *Chem. Rev*., **109**, 3817 (2009).

15 M. J. Bernal, O. Torres, M. Martín, E. Sola, *J. Am. Chem. Soc*., **135**, 19008 (2013).

16 R. L. Miller, P. T. Wolczanski, A. L. Rheingold, *J. Am. Chem. Soc*., **115**, 10422 (1993).

17 C.-J. Su, P.-C. Su, Y. Chi, S.-M. Peng, G.-H. Lee, *J. Am. Chem. Soc*., **118**, 3289 (1996).

18 J. C. Peters, A. L. Odom, C. C. Cummins, *Chem. Commun*., 1995 (1997).

19 A. Caselli, E. Solari, R. Scopelliti, C. Floriani, *J. Am. Chem. Soc*., **122**, 538

(2000).

20 W. Buchowicz, B. Herbaczyńska, L. B. Jerzykiewicz, T. Lis, S. Pasynkiewicz, A. Pietrzykowski, *Inorg. Chem.*, **51**, 8292 (2012).

21 D. J Harding, C. Kerpal, G. Meijer, A. Fielicke, *J. Phys. Chem. Lett.*, **4**, 892 (2013).

22 E. S. Borren, A. F. Hill, R. Shang, M. Sharma, A. C, Willis, *J. Am. Chem. Soc.*, **135**, 4942 (2013).

23 X. Li, L.-S. Wang, A. I. Boldyrev, J. Simons, *J. Am. Chem. Soc.*, **121**, 6033 (1999).

24 S. P. de Visser, L. S. Tan, *J. Am. Chem. Soc.*, **130**, 12961 (2008).

25 R. Latifi, M. Bagherzadeh, S. P. de Visser, *Chem. Eur. J.*, **15**, 6651 (2009).

26 Jaguar 7.7, version 7.9, Schrodinger, LLC, New York, NY (2011).

27 M. J. Frisch, G. W. Trucks, H. B. Schlegel, G. E. Scuseria, M. A. Robb, J. R. Cheeseman, G. Scalmani, V. Barone, B. Mennucci, G. A. Petersson, H. Nakatsuji, M. Caricato, X. Li, H. P. Hratchian, A. F. Izmaylov, J. Bloino, G. Zheng, J. L. Sonnenberg, M. Hada, M. Ehara, K. Toyota, R. Fukuda, J. Hasegawa, M. Ishida, T. Nakajima, Y. Honda, O. Kitao, H. Nakai, T. Vreven, J. A. Montgomery Jr., J. E. Peralta, F. Ogliaro, M. Bearpark, J. J. Heyd, E. Brothers, K. N. Kudin, V. N. Staroverov, R. Kobayashi, J. Normand, K. Raghavachari, A. Rendell, J. C. Burant, S. S. Iyengar, J. Tomasi, M. Cossi, N. Rega, J. M. Millam, M. Klene, J. E. Knox, J. B. Cross, V. Bakken, C. Adamo, J. Jaramillo, R. Gomperts, R. E. Stratmann, O. Yazyev, A. J. Austin, R. Cammi, C. Pomelli, J. W. Ochterski, R. L. Martin, K. Morokuma, V. G. Zakrzewski, G. A. Voth, P. Salvador, J. J. Dannenberg, S. Dapprich, A. D. Daniels, Ö.Farkas, J. B. Foresman, J. V. Ortiz, J. Cioslowski, D. J. Fox, *Gaussian-09, Revision A.1, Gaussian, Inc.*, Wallingford CT (2009).

28 A. D. Becke, *J. Chem. Phys.*, **98**, 5648 (1993).

29 C. Lee, W. Yang, R. G. Parr, *Phys. Rev. B*, **37**, 785 (1988).

30 P. J. Hay, W. R. Wadt, *J. Chem. Phys.*, **82**, 299 (1985).

31 S. Grimme, J. Antony, S. Ehrlich, H. Krieg, *J. Chem. Phys.*, **132**, 154104 (2010).

32 S. Shaik, S. P. de Visser, F. Ogliaro, H. Schwarz, D. Schröder, *Curr. Opin. Chem. Biol.*, **6**, 556 (2002).

33 S. P. de Visser, *Angew. Chem. Int. Ed.*, **45**, 1790 (2006).

34 S. P. de Visser, M. G. Quesne, B. Martin, P. Comba, U. Ryde, *Chem. Commun.*, **50**, 262 (2014).

35 M. G. Quesne, R. Latifi, L. E. Gonzalez-Ovalle, D. Kumar, S. P. de Visser, *Chem. Eur. J.*, **20**, 435 (2014).

36 A. D. Becke, *Phys. Rev. A*, **38**, 3098 (1988).

37 J. P. Perdew, *Phys. Rev. B*, **33**, 8822 (1986).

38 Y. Zhao, D. G. Truhlar, *Theor. Chem. Acc.*, **120**, 215 (2008).

39 C. Adamo, V. Barone, *J. Chem. Phys.*, **110**, 6158 (1999).

40 J. P. Perdew, K. Burke, M. Ernzerhof, *Phys. Rev. Lett.*, **77**, 3865 (1996).

41 M. A. Sainna, S. Kumar, D. Kumar, S. Fornarini, M. E. Crestoni, S. P. de Visser, *Chem. Sci*, **6**, 1516 (2015).

42 M. A.Sainna, D. Sil, D. Sahoo, B. Martin, S. P. Rath, P. Comba, S. P. de Visser, *Inorg. Chem.*, **54**, 1919 (2015).

43 A. K. Vardhaman, C. V. Sastri, D. Kumar, S. P. de Visser, *Chem. Commun.*, **47**, 11044 (2011).

44 S. Kumar, A. S. Faponle, P. Barman, A. K. Vardhaman, C. V. Sastri, D. Kumar, S. P. de Visser, *J. Am. Chem. Soc.*, **136**, 17102 (2014).

45 B. Karamzadeh, D. Kumar, G. N. Sastry, S. P. de Visser, *J. Phys. Chem. A*, **114**, 13234 (2010).

46 D. Kumar, R. Latifi, S. Kumar, E. V. Rybak-Akimova, M. A. Sainna, S. P. de Visser, *Inorg. Chem.*, **52**, 7968 (2013).

47 A. Draksharapu, D. Angelone, M. G. Quesne, S. K. Padamati, L. Gómez, R. Hage, M. Costas, W. R. Browne, S. P. de Visser, *Angew. Chem. Int. Ed.*, **54**, 4357 (2015).

48 M. Sallmann, S. Kumar, P. Chernev, J. Nehrkorn, A. Schnegg, D. Kumar, H. Dau, C. Limberg, S. P. de Visser, *Chem. Eur. J.*, ***21***, 7470 (2015).

49 F. Weinhold, J. E. Carpenter, *The Natural Bond Orbital Lewis Structure Concept*

for Molecules, Radicals, and Radical Ions. In *The Structure of Small Molecules and Ions*, R. Naaman, Z.Vager, (Eds.), Plenum Press, New York, pp 227 (1988).

50 L. de Quadras, E. B. Bauer, J. Stahl, F. Zhuravlev, F. Hampel, J. A. Gladysz, *New. J. Chem*., **31**, 1594 (2007).

51 C.-M. Che, J.-S. Huang, *Coord. Chem. Rev*., **231**, 151 (2002).

52 R. K. Das, B. Saha, S. M. W. Rahaman, J. K. Bera, *Chem. Eur. J*., **16**, 14459 (2010).

53 A. G. Algarra, V. V. Grushin, S. A. MacGregor, *Organometal.*, **31**, 1467 (2012).

54 S. T. Mutter, J. A. Platts, *J. Phys. Chem. A*, **115**, 11293 (2011).

55 D. Conner, K. N. Jayaprakash, M. B. Wells, S. Manzer, T. B. Gunnoe, P. D. Boyle, *Inorg. Chem*., **42**, 4759 (2003).

56 S. K. Patra, N. Sadhukhan, J. K. Bera, *Inorg. Chem*., **45**, 4007 (2006).

57 S. K. Patra, J. K. Bera, *Organometallics*, **25**, 6054 (2006).

58 S. A. MacGregor, D. McKay, J. A. Panetier, M. K. Whittlesey, *Dalton Trans*., **42**, 7386 (2013).

59 P. K. Sharma, S. P. de Visser, F. Ogliaro, S. Shaik, *J. Am. Chem. Soc*., **125**, 2291 (2003).

60 R. Latifi, M. A. Sainna, E. V. Rybak-Akimova, S. P. de Visser, *Chem. Eur. J*., **19**, 4058 (2013).

61 A. K. Vardhaman, P. Barman, S. Kumar, C. V. Sastri, D. Kumar, S. P. de Visser, *Angew. Chem. Int. Ed*., **52**, 12288 (2013).

62 S. T. Diver, *Coord. Chem. Rev*., **251**, 671 (2007).

63 J. Barluenga, M. A. Fernández-Rodríguez, E. Aguilar, *J. Organometal. Chem*., **690**, 539 (2005).

64 C. F. Bernasconi, *Chem. Soc. Rev*., **26**, 299 (1997).

65 S. P. de Visser, F. Ogliaro, S. Shaik, *Angew. Chem. Int. Ed*., **40**, 2871 (2001).

66 S. P. de Visser, F. Ogliaro, S. Shaik, *Chem. Commun*., 2322 (2001).

67 S. P. de Visser, *Chem. Eur. J*., **12**, 8168 (2006).

68 S. P. de Visser, L. Tahsini, W. Nam, *Chem. Eur. J*., **15**, 5577 (2009).

69 S. Shaik, D. Kumar, S. P. de Visser, *J. Am. Chem. Soc*., **130**, 10128 (2008).

70 S. P. de Visser, *J. Am. Chem. Soc.*, **132**, 1087 (2010).

71 D. Kumar, B. Karamzadeh, G. N. Sastry, S. P. de Visser, *J. Am. Chem. Soc.*, **132**, 7656 (2010).

72 L. Ji, A. S. Faponle, M. G. Quesne, M. A. Sainna, J. Zhang, A. Franke, D. Kumar, R. van Eldik, W. Liu,S. P. de Visser, *Chem. Eur. J.*, **21**, 9083 (2015).

73 S. P. de Visser, F. Ogliaro, P. K. Sharma, S. Shaik, *J. Am. Chem. Soc.*, **124**, 11809 (2002).

74 S. Shaik, P. C. Hiberty, *A Chemist's Guide to Valence Bond Theory*, Wiley-Interscience, New York, NY, (2007).

75 M. G. Quesne, S. P. de Visser, *J. Biol. Inorg. Chem.*, **17**, 841 (2012).

CHAPTER 7

CONCLUSIONS

CHAPTER 7

CONCLUSIONS

The work done in this thesis highlights following general conclusions:

A. Technological advancements and recent developments in theory have enabled evolution of highly accurate, efficient and inexpensive methods applicable to ‘real life’ systems. Now enzymatic intermediates and synthetic catalytic reactions may be modeled successfully even in absence of full experimental verification. The latter is not possible due to ultrafast nature of these reactions but these modeled reaction pathways have been validated as and when experimentalists became capable of suitable measurements.

B. The reaction studies established mechanisms for hydrogen and oxygen atom transfer reactions and electron transfer mechanism in transition metal containing complexes. Active oxidants were characterized in given reaction processes and rate determining step was established. Models were devised to rationalize reaction processes and barrier heights to predict rate constants of processes.

C. The difference in reactivity of heme and nonheme iron-oxo intermediates was established. The rate constants and reaction mechanisms were established. The electron transfer and hydrogen abstraction mechanism was found out.

D. The extensively tested and highly benchmarked methods used by our research group were proven to be in consonance with experimental data and helped draw useful inferences for biomimetic chemical systems presented in this thesis.

E. The studies present in this thesis work are expected to bridge the computational and experimental work being carried out in biomimetic/enzymatic reactions. Also they are expected to meet challenges of drug synthesis (pharmaceutical reactions), methane hydroxylation (environmental pollutants) and hydroxylation and oxidation of common chemical warfare agents (cyanides, mustard gas etc.).

LIST OF PUBLICATIONS

---

[1] Properties and reactivities of nonheme iron (IV)-oxo versus iron (V)-oxo: long-range electron transfer versus hydrogen atom abstraction, Physical Chemistry Chemical Physics, **16**(41), 22611-22622, (2014).

Baharan Karamzadeh, **Devendra Singh**, Wonwoo Nam, Devesh Kumar, Sam P. de Visser

[2] A Trimetal Carbene with Reactivity Reminiscent of Fischer-Tropsh Catalysis, Organometallics, **34**(9), 1651-1660, (2015).

Mala A. Sainna, **Devendra Singh**, Devesh Kumar, Sam P. de Visser

[3] Origin of the Enhanced Reactivity of µ–Nitrido-Bridged Diiron(IV)-Oxo Porphyrinoid Complexes over Cytochrome P450 Compound I, ACS Catalysis, **6**(4), 2230-2243, (2016).

Matthew G. Quesne, Dhurairajan Senthilnathan, **Devendra Singh**, Devesh Kumar, Pascale Maldivi, Alexander B. Sorokin, Sam P. de Visser

[4] Methane hydroxylation by axially ligated iron (IV)-oxo porphyrin cation radical models, International Journal of Science, Technology & Society **1**(2), 26-40, (2015).

Devendra Singh, Devesh Kumar, Sam P. de Visser

ACS Catalysis

Research Article

pubs.acs.org/acscatalysis

Origin of the Enhanced Reactivity of μ-Nitrido-Bridged Diiron(IV)-Oxo Porphyrinoid Complexes over Cytochrome P450 Compound I

Matthew G. Quesne,[†] Dhurairajan Senthilnathan,[‡,$] Devendra Singh,[&] Devesh Kumar,[&]
Pascale Maldivi,[*,‡,◇] Alexander B. Sorokin,[*,⊥] and Sam P. de Visser[*,†]

[†] Manchester Institute of Biotechnology and School of Chemical Engineering and Analytical Science, The University of Manchester, 131 Princess Street, Manchester M1 7DN, United Kingdom

[‡] Univ. Grenoble Alpes, INAC-SCIB, Reconnaissance Ionique et Chimie de Coordination, F-38000 Grenoble, France

[◇] CEA, INAC-SCIB, F-38000 Grenoble, France

[$] Center for Computational Chemistry, CRD, PRIST University, Vallam, Thanjavur, Tamilnadu 613403, India

[&] Department of Applied Physics, Babasaheb Bhimrao Ambedkar University, School for Physical Sciences, Vidya Vihar, Rae Bareilly Road, Lucknow, Uttar Pradesh 226025, India

[⊥] Institut de Recherches sur la Catalyse et l'Environnement de Lyon (IRCELYON), UMR 5256, CNRS-Université Lyon 1, 2, av. A. Einstein, 69626 Villeurbanne, France

Ⓢ *Supporting Information*

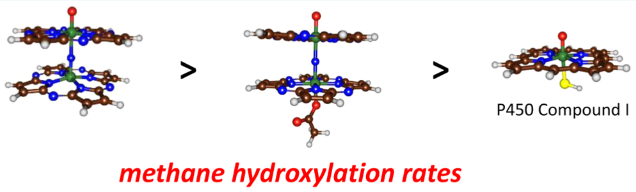

ABSTRACT: μ-Nitrido-bridged diiron porphyrins and phthalocyanines are known to be efficient oxidants that are able to oxidize some of the strongest C−H bonds in nature, such as the one in methane. The origin of their catalytic efficiency is poorly understood, and in order to gain insight into the structural and electronic features of this chemical system, we performed a detailed and systematic study into their chemical properties and reactivities using density functional theory. Our work shows that μ-nitrido-bridged diiron porphyrins and phthalocyanines are highly active catalytic oxidants, which react with methane with very low reaction barriers and a rate-determining hydrogen-atom-abstraction step. Furthermore, the μ-nitrido-bridged diiron porphyrin and phthalocyanine complexes react with a free energy of activation that is more than 10 kcal mol^{-1} lower in energy than that found for cytochrome P450 Compound I, which is known to be one of the most efficient C−H hydroxylating agents in Nature. We have analyzed the electronic configuration of reactants and transition states in detail and have identified the key properties of the oxidants that lead to this rate enhancement. In particular, the potency of the oxidant is related to the orbital mixing patterns along the Fe−O axis, whereby the axial iron(IV)-nitrido group donates sufficient electron density to affect the pK_a of the oxo group as well as the strength of the O−H bond formed in the iron(IV)-hydroxo complex. The studies confirm that μ-nitrido diiron-oxo complexes should react via oxygen atom transfer readily even with strong C−H bonds as in methane. The results are analyzed with orbital diagrams, valence bond, and thermochemical cycles and explain the intricate details of the mechanism and the properties of the oxidant.

KEYWORDS: *biomimetic models, hydrogen abstraction, hydroxylation, iron, ligand effects*

■ INTRODUCTION

Cytochrome P450 enzymes are versatile enzymes in human physiology that mainly react with compounds through oxygen atom transfer, including the hydroxylation of C−H bonds. P450s activate their substrates with the aim to initiate their metabolism and detoxification but, on the other hand, also assist in biosynthetic pathways of e.g., hormones.[1] Thus, the biodegradation of long chain fatty acids and xenobiotics is catalyzed by P450 liver isozymes through a mechanism that is considered to proceed via an iron(IV)-oxo heme cation radical intermediate called Compound I (CpdI). To understand the fundamental features of the oxidant in the P450-enzyme-catalyzed reaction mechanism, synthetic models have been prepared that model the enzyme active site composition and coordination.[2] These so-called biomimetic model complexes enable one to study the reactivity patterns and the intrinsic chemical properties of iron porphyrins and gain understanding into the intricate structural and electronic features of the active site. Biomimetic work indeed confirmed a high-valent iron(IV)-oxo porphyrin cation radical to be the active oxidant in chemical transformations of substrates and ruled out many alternative suggestions.[3]

Recent biochemical studies isolated and characterized Compound I in a P450 isozyme and established the electronic

Received: November 30, 2015
Revised: January 11, 2016

DOI: 10.1021/acscatal.5b02720
ACS Catal. 2016, 6, 2230−2243

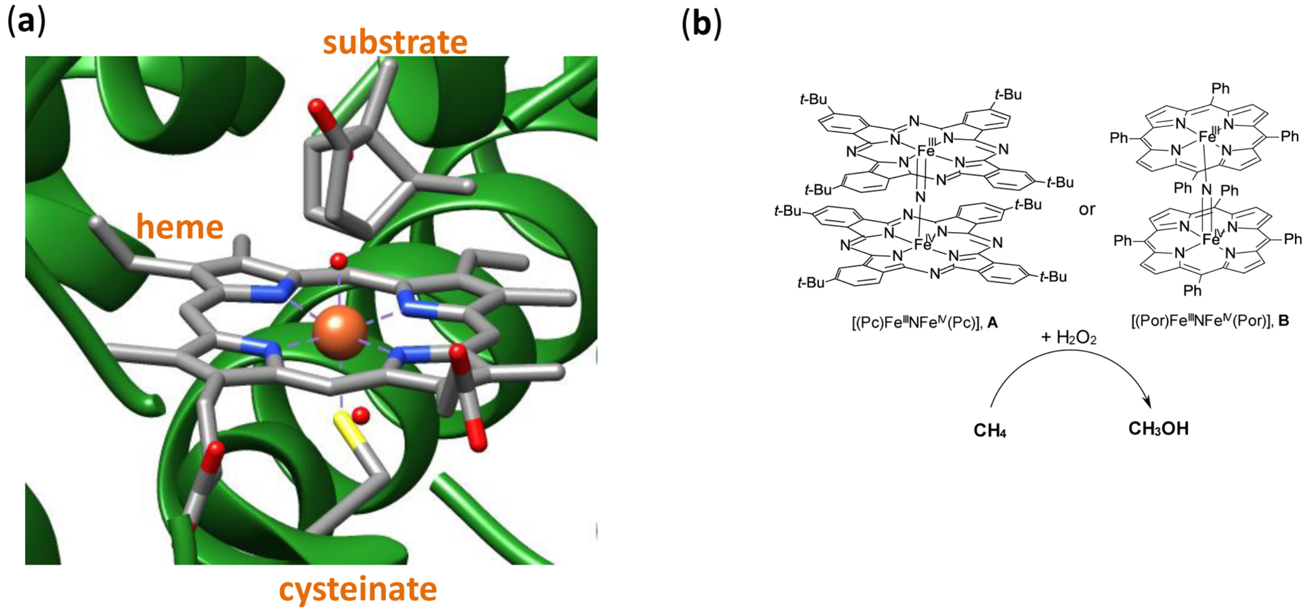

Figure 1. Comparative structural features of the active site of $P450_{cam}$ (a) and μ-nitrido-bridged diiron-oxo porphyrin and phthalocyanine complexes (b).

configuration with spectroscopic methods.[4] Although the P450s are known to be efficient and powerful oxidants in nature, native enzymes do not catalyze the conversion of methane to methanol, which requires the breaking of a very strong C−H bond with a bond dissociation energy (BDE) of 104.9 kcal mol^{-1}. However, using iodosylbenzene as an oxidant, it was shown that CYP153A6 is able to oxidize methane at room temperature, although very low turnover numbers of 0.02−0.05 were obtained.[5] On the other hand, guest/host activation of $P450_{BM3}$ with perfluorocarboxylic acids as decoy molecules enabled the oxidation of all short alkanes tested except for methane.[6,7]

Structurally, the P450s all contain an active heme group (Figure 1a) linked to the protein through a cysteinate bridge. To mimic the active site features of P450 CpdI, over the years, work on synthetic iron porphyrins has been performed with the aim of improving the oxidative power of the active species through modifications of the porphyrin scaffold. In particular, research was done to find a metal porphyrin system able to hydroxylate methane, but so far, only a few of these studies have been successful. Thus, several μ-nitrido-bridged diiron-oxo phthalocyanines and porphyrin (**A** and **B**, Figure 1b) complexes prepared using H_2O_2 or *m*-chloroperbenzoic acid (m-CPBA) are able to oxidize methane to methanol efficiently.[8,9] Experimental and computational studies on these exciting catalysts also show that these μ-nitrido-bridged systems are stable and maintain their dimerization throughout the reactions that they catalyze, unlike many of the μ-oxo dimers.[8]

It appears, therefore, that these diiron complexes are more potent oxidants than the active species of P450 enzymes, an example of which is shown using the active site structure from $P450_{cam}$ as taken from the protein databank[10] for structural comparison in Figure 1. The question is, then, what makes **A**/**B** a stronger oxidant than the enzyme, and what is the effect of the bridging μ-nitrido group on the chemical properties of the oxidant and the catalysis?

The origin of the reactivity differences between μ-nitrido-bridged diiron complexes and P450 CpdI may derive from a range of chemical and structural differences. First, some P450 isozymes have a tight substrate binding pocket and selectively activate substrates,[11] and the pocket may not be setup to hydroxylate methane efficiently, resulting in an uncoupling reaction. However, the use of decoy molecules, such as inert perfluorocarboxylic acids, makes it possible to accommodate methane into the cavity, but this did not lead to the oxidation of methane.[7] On the other hand, there are clear structural differences between **A**/**B** and P450 CpdI and particularly related to the axial ligand (i.e., cysteinate versus nitrido-iron(IV)-phthalocyanine).

It is known that the axial ligand of iron-porphyrins has a major effect on catalysis as well as on the spectroscopic properties (e.g., Fe−O vibrations) of the oxidant.[12] These biomimetic studies on axial ligand effects in iron(IV)-oxo complexes are in analogy to those derived from biochemical work on enzymes including heme-peroxidases and heme-monoxygenases. Thus, peroxidases generally have a histidine axial ligand coordinating the heme, whereas heme-monooxygenases such as the P450s have a cysteinate axial ligand. The axial ligand incurs a push- or a pull effect of electron density and thereby gives fundamental differences between the two heme enzyme classes.[13] This difference in function of P450 monoxygenases, heme peroxidases, and catalases has been assigned to the axial ligand bound to the heme.[14] In addition, biomimetic work has shown equatorial ligand may also have an effect on reactivity patterns but usually to a lesser extent than the axial ligand.[15]

Clearly, the reactivity and electronic properties of iron porphyrin/heme complexes is sensitive to the axial ligand bound and, in particular, experimental evidence appears to suggest that an axial μ-nitrido iron(IV) makes the oxidant so powerful that it can even hydroxylate methane. Therefore, we decided to investigate the electronic properties and reactivity patterns of μ-nitrido-bridged diiron-oxo complexes and find out the key factors that influence their catalytic activity with strong C−H bonds. The work shows that the axial μ-nitrido iron(IV) group has π and π^* orbitals that mix with the iron(IV)-oxo π/π^* orbitals and thereby make the oxidant more reactive.

DOI: 10.1021/acscatal.5b02720
ACS Catal. 2016, 6, 2230−2243

Scheme 1. Models of μ-Nitrido-Bridged Diiron Porphyrazine (1) and Porphyrin (2) as well as P450 CpdI (3) Investigated in This Work

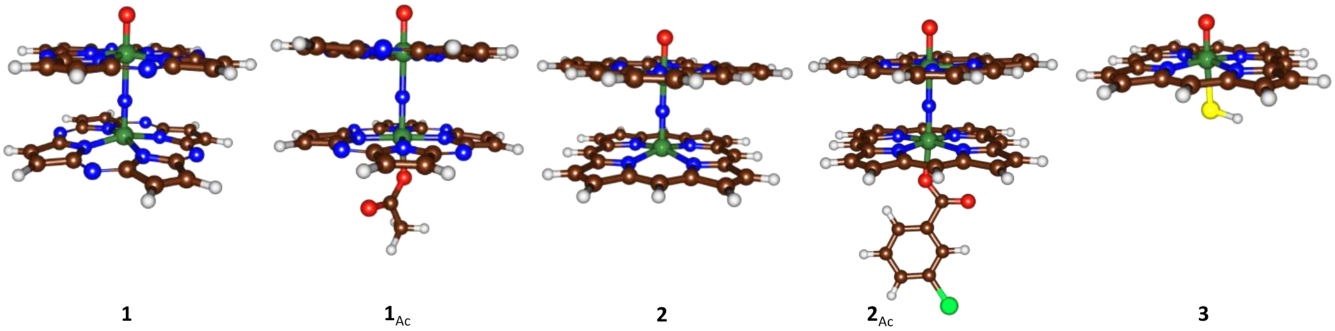

1 $\mathbf{1}_{\mathrm{Ac}}$ **2** $\mathbf{2}_{\mathrm{Ac}}$ **3**

METHODS

Models. To understand the chemical properties of **A**/**B**, we created a number of models with different equatorial and axial ligands included, see Scheme 1. First, we created a "small" μ-nitrido-bridged diiron-oxo chemical structure of 68 atoms, whereby the phthalocyanine units were abbreviated to porphyrazine macrocycles (**1**). However, experimental Mössbauer studies indicated the possible presence of an anionic axial ligand in μ-nitrido-bridged high-valent diiron porphyrin oxo species,[9] when a concentrated solution of the complex and m-CPBA was used at very low temperatures. Although the presence of the axial ligand could not be ascertained under catalytic conditions in the experiments, we decided to include a model with an axial acid anion ligand and investigated its possible influence on the oxidizing properties of the oxo species in model $\mathbf{1}_{\mathrm{Ac}}$. As a comparison, we also investigated the properties of μ-nitrido-bridged diiron-oxo porphyrin without an anionic axial ligand attached to Fe_2 (structure **2**) and with 3-chlorobenzoate ligated (structure $\mathbf{2}_{\mathrm{Ac}}$) to reflect the use of m-CPBA experimentally. Structures **1** and **2** are overall charge neutral, whereas $\mathbf{1}_{\mathrm{Ac}}$ and $\mathbf{2}_{\mathrm{Ac}}$ have a total charge of −1.

A complete model with tetraphenylporphyrin (TPP) ligands ($\mathbf{2}_{\mathrm{TPP}}$) was also studied, but the addition of substituents to the *meso*-position of the porphyrin had little effect on the optimized geometries and electronic configuration of the reactant complexes, see Supporting Information for details.

All structures and reactivities were compared with model complexes of P450 CpdI, which was modeled, as before,[16] as an iron(IV)-oxo-porphyrin cation radical ($\mathbf{3}_{\mathrm{SH}}$, $[Fe^{IV}(O)\ (Por^{+\bullet})\text{-}SH]$) but also with an elaborate cysteinate axial ligand description ($\mathbf{3}_{\mathrm{Cys}}$, $[Fe^{IV}(O)\ (Por^{+\bullet})Cys]$). In previous work, we extensively tested various enzyme models and compared those to results obtained from QM/MM studies and experiment.[17] Indeed, in recent work, model clusters were compared to QM/MM results with increasing QM size.[17b] The energy differences upon the barrier heights fluctuated within a range of a few kcal mol^{-1} and did not affect the shape of the landscape or the overall conclusions. The models discussed here were shown to reproduce QM/MM obtained results well and gave similar electronic configuration as well as reactivity patterns with barrier heights reproduced within 1.1 kcal mol^{-1}.[17a] For example, the charge and spin distributions of CpdI and the spin-state ordering and relative energies follow similar trends. In addition, studies on product isotope effects through bifurcation pathways gave excellent agreement with experimentally determined values.[18] The small model complexes used here enable one to understand the fundamental chemical differences between the active site of P450 and the synthetic μ-nitrido-bridged diiron-oxo complexes described here by elimination of the protein interactions. The P450 models were overall charge neutral and were calculated in the lowest-lying doublet and quartet spin states. Our study produced a comprehensive set of data of which the highlights are presented here, and all the details can be found in the Supporting Information.

Computational Procedures. The studies presented in this work used density functional theory methods as implemented in the Gaussian-09, Jaguar 7.8, and ORCA program packages.[19] The potential energy surfaces of the reaction of methane with **1**, $\mathbf{1}_{\mathrm{Ac}}$, $\mathbf{2}_{\mathrm{TPP}}$, and **3** on all low-lying spin states were initially explored at the UB3LYP level of theory[20] in Gaussian-09 in combination with a double-ζ quality LACVP basis set on iron with core potential and 6-31G on the rest of the atoms: basis set BS1.[21] Subsequently, full geometry optimizations of local minima and transition states were calculated at UB3LYP[20] and UBP86[22] level of theory and followed by an analytical frequency, see Supporting Information for details. Transition states were characterized with a single imaginary frequency for the correct mode, while local minima had real frequencies only. Subsequently, single-point calculations were done using a triple-ζ type LACV3P+ basis set on iron with core potential and 6-311+G* on the rest of the atoms: basis set BS2. Test calculations, whereby the geometries were optimized with UB3LYP/BS2 gave a potential energy profile of substrate hydroxylation that was within a few tenths of a kcal mol^{-1} from those obtained with UB3LYP/BS2//UB3LYP/BS1;[23] therefore, the rest of the systems were geometry optimized with UB3LYP/BS1.

As the experimental work used acetonitrile as a solvent, we performed solvent calculations using the polarized continuum model (PCM) with a dielectric constant of $\varepsilon = 37.5$ and a probe radius of 2.183 Å as implemented in Jaguar using a triple-ζ or better basis set on all atoms. Test calculations, whereby the geometry was optimized with a solvent model included, were performed (see Supporting Information Figure S19). However, this did not lead to changes in the electronic structure of the local minima and gave very similar optimized geometries.

Detailed geometry scans along one degree of freedom were performed between reactants and intermediates as well as between intermediates and products. These constrained geometry optimizations had one degree of freedom fixed, while all other coordinates were optimized. Geometry scans confirmed the reaction mechanisms and electron-transfer processes. Due to the size of the chemical systems investigated here, we only were able to run Intrinsic Reaction Coordinate (IRC) scans for a selection of systems. Those studies confirmed the mechanism and did not give results that were dramatically different from the geometry scans. The methods and procedures used in this work were extensively tested and benchmarked. For instance, in previous work, we reproduced experimental free energies of activation within 3 kcal mol^{-1},[24] but also experimental rate enhancements,[25] as well as kinetic isotope effects.[26]

The calculations of the reaction mechanism of methane with **2** and **2**$_{Ac}$ were explored at the UB3LYP/BS1 level of theory in Jaguar with basis set BS1, and with Orca using a basis set that contains LANL2DZ on iron and 6-31G on the rest of the atoms. As for the porphyrazine species, stationary points were characterized with a frequency calculation with minima and transition states having all real or one imaginary frequency, respectively. In the latter case, the imaginary mode was displayed using the Orca Pltvib utility[19c] and GOpenMol[19d] to check its nature. Solvent effects were incorporated through the Conductor-like Screening Model (Cosmo) as implemented in Orca using a dielectric constant of 37 mimicking acetonitrile. Optimizations for both minima and transition states were done in solvent at the UB3LYP/BS1 level of theory, but the resulting structures, spin densities, and energy differences were very similar to the gas-phase results. Single points at the UB3LYP/BS2 level of theory were also performed on stationary points. Natural bond order analysis calculations were performed in Gaussian-09.

Structure **1** and **1**$_{Ac}$ were investigated in Gaussian-09 on all low lying spin states: doublet, quartet, sextet and octet. As before,[27] we tested a range of ferromagnetically and antiferromagnetically coupled spin-state occupations of the reactant complexes. In particular, we attempted to create a P450 CpdI-type electronic configuration with a metal radical coupled to a ligand radical. However, all our attempts to generate an electronic state with ligand radical failed, and converted back to a state with only radical character on the OFe_1NFe_2 atoms. The same efforts were also done for **2** and **2**$_{Ac}$ in Orca and Jaguar with the same effects: namely, no radical character on the macrocycle was obtained. Although several spin states were investigated, the doublet spin state was found to be the ground state and well separated from the nearest quartet, sextet, and octet spin states. Therefore, the other models were calculated in the doublet spin state only.

To test the reproducibility of the work, we did a range of single-point calculations on the UB3LYP/BS1 optimized geometries in Gaussian using a number of (unrestricted) density functional methods with basis set BS2, namely B3LYP,[20] BP86,[22] B3LYP* (B3LYP with 15% HF),[28] dispersion-corrected B3LYP (B3LYP-D3),[29] M06-L,[30] and PBE0.[31] In general, the same spin-state ordering is obtained regardless of the density functional method, and all chemical trends are reproduced. For clarity, we will focus in the main text on the B3LYP results, but all other results can be found in the Supporting Information.

Multireference perturbation theory of the N-electron valence type (NEVPT2) was applied to test the electronic configuration of the reactant and radical intermediate complexes. These calculations were done in Orca using procedures described previously.[32]

Kinetic Isotope Effects. We estimated the kinetic isotope effect (KIE) for the hydrogen-atom-abstraction reactions by replacing one or more of the hydrogen atoms of the substrate by deuterium atoms. Thus, the ratio of the rate constants of the substrate and the deuterated substrate (k_H/k_D) is a measure of the KIE, whereby we estimated the primary KIE for replacing the transferring hydrogen atom by deuterium as well as the secondary KIE, where the other hydrogen atoms of the substrate were replaced.[33] Semiclassical KIEs (eq 1) were estimated from the Eyring equation using the free energies of activation ($\Delta G^{\ddagger}_{H}$) of the deuterium substituted and reference systems.

$$\mathrm{KIE_E} = k_H/k_D = \exp\{(\Delta G^{\ddagger}_{D} - \Delta G^{\ddagger}_{H})/RT\} \qquad (1)$$

In this equation, R is the gas constant, and T the temperature (298.15 K). Further corrections due to tunneling were obtained from the Wigner model ($\mathrm{KIE_W}$, eq 2) by multiplying $\mathrm{KIE_E}$ with the tunneling ratio (Q_{tH}/Q_{tD}, eq 3) as follows:

$$\mathrm{KIE_W} = \mathrm{KIE_E} \times Q_{tH}/Q_{tD} \qquad (2)$$

$$Q_t = 1 + (h\nu/k_BT)^2/24 \qquad (3)$$

Here, k_B is Boltzmann's constant, h is Planck's constant, and ν is the magnitude of the imaginary frequency in the transition state. Kinetic isotope effects were calculated using the data from the Gaussian frequency calculations for the hydrogen-atom-abstraction process from methane by **1**, **1**$_{Ac}$ and **3**.

Thermochemistry. The O−H and C−H bond dissociation energies ($\mathrm{BDE_{OH}}$ and $\mathrm{BDE_{CH}}$) were determined from the relative energy (ΔE + ZPE + E_{solv}) for the following two equations:

$$\mathrm{Fe^{IV}=O(L) + H^{\bullet} \rightarrow Fe^{III}OH(L) + BDE_{OH}} \qquad (4)$$

$$\mathrm{A^{\bullet} + H^{\bullet} \rightarrow A - H + BDE_{CH}} \qquad (5)$$

Electron affinities (EA) and ionization energies (IE) reported here are adiabatic values calculated with UB3LYP/BS2 with ZPE and solvent included.

RESULTS

In this work, we focus on the chemical properties of the μ-nitrido bound diiron complexes and their reactivity with methane and, in particular, aim to elucidate why **A**/**B** react faster by hydrogen atom abstraction than P450 CpdI. We used extensively benchmarked and calibrated methods, which on analogous chemical systems are known to give the correct spin-state ordering and kinetics.[34] Subsequently, the electronic properties and the origin of the reactivity differences of **1**/**2** versus **3** were elucidated through thermochemical cycles, valence bond schemes and electronic properties of the various species involved.

Substrate Hydroxylation Mechanism. Let us start with evaluating the reactivity differences of methane hydroxylation by **1**, **1**$_{Ac}$, **2**, **2**$_{Ac}$, and **3** as obtained with B3LYP. We investigated the methane hydroxylation by **1**, **1**$_{Ac}$, **2**, and **2**$_{Ac}$ and compare the obtained result with those calculated previously for [Fe^{IV}(O) (Por$^{+\bullet}$)SH] or **3**.[35] We initially created a long-range complex (**Re**) of structures **1**, **1**$_{Ac}$, **2**, and **2**$_{Ac}$ with methane and optimized the geometries in the doublet, quartet, sextet, and octet spin states. However, the doublet spin state was the ground state in isolated reactants as well as the reactant complexes and remained the lowest-lying spin state along the full reaction mechanism. The results of the alternative spin states are given in the Supporting Information Figures S2−S4 and S6−S8, Tables S5 and S9−S16.

The reaction is stepwise with an initial hydrogen atom abstraction via transition state **TS**$_{HA}$ to form the radical

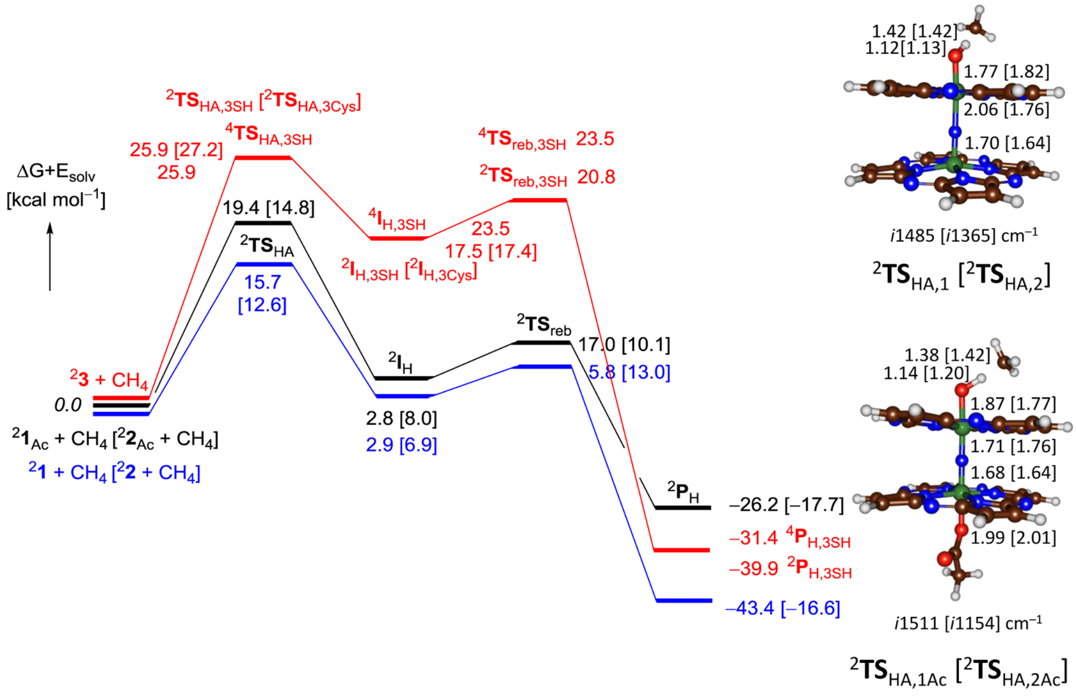

Figure 2. DFT calculated methane hydroxylation pathway by ^{2}**1**, ^{2}**1**$_{Ac}$, ^{2}**2**, ^{2}**2**$_{Ac}$, and ^{2,4}**3**. Data for **1**/**1**$_{Ac}$ and **3** were calculated in Gaussian at the UB3LYP/BS2//UB3LYP/BS1 level of theory, whereas the values for **2**/**2**$_{Ac}$ are obtained in Orca at UB3LYP/BS2//UB3LYP/BS1. Free energies are in kcal mol^{-1} and include ZPE, entropic, thermal, and solvent corrections. Also shown are optimized geometries of the rate-determining transition states with bond lengths in Å and the imaginary frequency of the **TS** in wave numbers. Data for model **1**/**2** are given in blue, **1**$_{Ac}$/**2**$_{Ac}$ in black and values for complex **3** are shown in red.

intermediate **I**$_H$, which is a complex of iron(IV)-hydroxo with $CH_3^•$. In the next step, the OH rebounds to the $CH_3^•$ group via transition state **TS**$_{reb}$ to form the methanol-bound product complex **P**$_H$. In all cases, **TS**$_{HA}$ is the rate-determining reaction step, and **TS**$_{reb}$ is smaller. This is in agreement with previous aliphatic hydroxylation mechanisms for iron(IV)-oxo complexes.[36]

Figure 2 shows the free energy landscape for methane hydroxylation by ^{2}**1**, ^{2}**1**$_{Ac}$, ^{2}**2**, ^{2}**2**$_{Ac}$, and ^{2,4}**3**. For comparison, in previous work, a free energy of activation of 25.9 kcal mol^{-1} in solvent using the same computational methods was obtained for the reaction of [Fe^{IV}(O) (Por$^{+•}$)SH] + CH_4.[35b] However, the free energy of activation of hydrogen atom abstraction from methane by **1**, in contrast, only has a value of $\Delta G^‡$ = 15.7 kcal mol^{-1}, which raises to 19.4 kcal mol^{-1} when acetate binds as an axial ligand. The ratio of the rate constants for methane hydroxylation by **3** versus **1** would imply a rate enhancement of about 10^7 for this reaction. As such, it appears that μ-nitrido-bridged diiron-oxo complexes are highly effective oxidants of substrate hydroxylation reactions and should be able to hydroxylate methane at ambient temperatures and pressures. Indeed, experimental work of Sorokin and co-workers confirmed methanol products from the reaction of μ-nitrido-bridged diiron phthalocyanine with methane.[8b,c] To further ascertain that this rate enhancement is not due to the choice of the density functional method, we repeated the calculations of all rate-determining steps with alternative density functional methods (see Supporting Information Tables S9, S10, and S60−S63 for details). However, in all cases, the free energy of activation for the reaction of methane with **1**/**1**$_{Ac}$ was considerably lower than that with a P450 CpdI model.

In order to test whether the rate enhancement from **3** to **1**/**1**$_{Ac}$ is due to the phthalocyanine ligand or the μ-nitrido-bridged diiron arrangement, we decided to also investigate the reactivity of the analogous porphyrin complexes **2**/**2**$_{Ac}$. As follows from the data shown in Figure 2, the same trend is obtained for the couple ^{2}**2**/^{2}**2**$_{Ac}$, where the hydrogen-atom-abstraction barrier is raised by 2.2 kcal mol^{-1} for the latter. Consequently, all μ-nitrido-bridged diiron-oxo complexes (**1**, **1**$_{Ac}$, **2**, **2**$_{Ac}$) give low free energies of activation for methane hydroxylation, which implies that they should catalyze the reaction at room temperature, which is in agreement with experimental data.[8b]

Geometrically, all transition states are product-like with considerably longer C−H than O−H distances. Previous studies on aliphatic hydrogen abstraction reactions by iron(IV)-oxo complexes showed that methane hydroxylation generally proceeds with a barrier characterized by a short O−H distance, a much longer C−H distance, and a geometry resembling the radical intermediate.[35,36] The two Fe$_1$−N and Fe$_2$−N distances for the bridging nitrido group in **TS**$_{HA,1}$ and **TS**$_{HA,1Ac}$ are considerably different due to the electron-donating properties of the acetate ligand that pull Fe$_2$ into the plane of the phthalocyanine/porphyrin ring.

All hydrogen-atom-abstraction transition states are characterized with a single large imaginary frequency of well over i1100 cm^{-1} that reflects a mode for the asymmetrical stretch vibration along the O−H−C bond and hence corresponds to a hydrogen atom transfer. These values are typical of hydrogen-atom-abstraction barriers by metal-oxo oxidants and implicate a narrow barrier with potentially significant amount of tunneling.[37] The nature of the barrier and its connection to reactants and radical intermediates was further established by initially running constraint geometry scans (with one degree of freedom fixed) as well as IRCs, see Supporting Information for details, which confirmed the mechanism shown in Figure 2.

Interestingly, we find a considerably larger dipole moment for $\mathbf{TS}_{HA,1}$ of 4.7 D versus that for $\mathbf{TS}_{HA,3}$ [0.8 D], and additionally, it points in the opposite direction. Similar dipole moments are found for the reactant complexes. Obviously, an enlarged dipole moment will lead to stabilization of the complex in solution and interactions with polar solvent molecules, which may affect the relative reactivities through their environment. To find further electronic factors that contribute to the transition state energy, we calculated the change in polarizability volume ($\delta\alpha$) for the geometric change from reactants to $\mathbf{TS}_{HA}$, eq 6.[38] The value $\delta\alpha$ was calculated from the difference in polarizability volume between the transition state structure and those of the isolated reactants.

$$\delta\alpha_i = \alpha_{TS} - \alpha_i - \alpha_{CH4}, \ \mathbf{i} = \mathbf{1}, \mathbf{1}_{Ac} \tag{6}$$

Previously, we showed that the polarizability change correlates linearly with enthalpy change for chemical reactions as well as for transition state formation.[23,39] This polarizability change is then plotted as a function of barrier height for a range of hydrogen-atom-abstraction reactions by $[Fe^{IV}(O)\ (Por^{+\bullet})\text{-}SH]$ in the doublet and quartet spin states (Figure 3). As can be seen, the correlation is reasonably linear, which implies that all transition states are characterized as electronically similar and are connected through the same electron-transfer processes. The calculated values for $^2\mathbf{TS}_{HA,1}$ and $^2\mathbf{TS}_{HA,1Ac}$ fit the trend and support the obtained correlation.

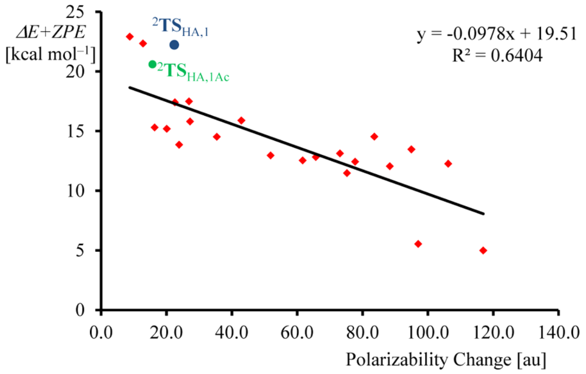

Figure 3. Plot of the change in polarizability volume ($\delta\alpha$) as a function of barrier height (ΔE + ZPE) for the reaction of $[Fe^{IV}(O)\ (Por^{+\bullet})SH]$ with aliphatic substrates.

As the rate-determining step in the reaction mechanism is a hydrogen atom abstraction, we investigated the kinetic isotope effects (KIE) by replacing one or more hydrogen atoms of the CH_4 reactant with deuterium atoms. Thus, we replaced the transferring hydrogen atom of methane by deuterium to get the primary KIE but also the three other hydrogen atoms (secondary KIE); lastly, we replaced all hydrogen atoms of CH_4 by deuterium atoms and the obtained results for reactions with **1**, $\mathbf{1}_{Ac}$, and **3** are given in Table 1. We calculated KIE values using the semiclassical Eyring model but also the Wigner model with tunneling corrections included. The KIE values are dependent on the magnitude of the imaginary frequency in the transition state and the free energy of activation, see Methods section for details. Although a considerably larger imaginary frequency in the transition state for $^2\mathbf{TS}_{HA,1}$ (i1485 cm^{-1}) is found as compared to $^{2,4}\mathbf{TS}_{HA,3}$ (values of i946 and i791 cm^{-1} for doublet and quartet spin states, respectively), actually, the Wigner KIE effects are not dramatically different for the two complexes. Nevertheless, replacement of the transferring hydrogen atom by deuterium leads to major differences in KIE values. We calculated KIE values of 7.0 (9.9) using the Eyring (Wigner) models for **1** for replacement of the transferring hydrogen atom by deuterium. Note that a significant secondary KIE value of about 1.4−2.3 for replacing the nontransferrable hydrogen atoms by deuterium atoms is obtained for all systems. The results in Table 1 show that **1** should give a considerably larger KIE value than $\mathbf{1}_{Ac}$ and **3** for hydrogen atom abstraction from unactivated, sp^3 hybridized, carbon centers.

Table 1. Calculated Kinetic Isotope Effects Using the Eyring (Wigner) Models for Replacing Hydrogen Atoms in Methane by Deuterium Atoms[a]

oxidant	O−D−CH_3	O−H−CD_3	O−D−CD_3
1	7.0 (9.9)	2.2 (2.3)	16.3 (23.4)
$\mathbf{1}_{Ac}$	7.1 (10.1)	1.4 (1.4)	10.3 (14.9)
3	5.7 (9.2)	1.4 (2.3)	8.6 (13.7)

[a] Data from Gaussian frequency calculation at 298 K for doublet spin states.

DISCUSSION

As shown in the previous section and in agreement with experimental observation, μ-nitrido-bridged diiron-oxo complexes are efficient oxidants of aliphatic hydroxylation reactions and can even hydroxylate methane at room temperature. To understand the origin of these reactivity differences with P450 CpdI, which does not hydroxylate methane at room temperature, we did a detailed analysis of the physicochemical properties of the reactants and an evaluation of the obtained transition states, which will be covered in detail in the following.

Electronic Configuration of the Reactants. To gain insight into the nature of the reactivity differences observed above, let us start our analysis with an evaluation of the electronic configuration of the isolated reactants (i.e., without methane) and compare $\mathbf{1}/\mathbf{1}_{Ac}/\mathbf{2}/\mathbf{2}_{Ac}$ on the one hand with **3** on the other hand.

Figure 4 displays the orbital energy levels of P450 CpdI, that is, $[Fe^{IV}(O)\ (Por^{+\bullet})Cys]$, and how the mixing with an axial iron(IV)-nitrido group of $[Fe^{IV}(N)\ (Por)]$ gives the new orbital energy levels for the μ-nitrido diiron-oxo complexes **1** and **2**. Thus, P450 CpdI is a triradical system with two unpaired electrons in π^*_{FeO} orbitals and a third one in a heme orbital with a_{2u} symmetry (Figure 4: left-hand-side). These three orbitals are either ferromagnetically coupled into a quartet spin state or antiferromagnetically coupled into a doublet spin state and usually DFT calculations find the two states within 1 kcal mol^{-1}.[17,40]

The π_{FeO}/π^*_{FeO} orbitals reflect the interaction of the $3d_{xz}/3d_{yz}$ atomic orbitals on iron with the $2p_x/2p_y$ orbitals on oxygen, whereas the a_{2u} orbital is a nonbonding heme orbital. Addition of an axial ligand to CpdI leads to mixing of orbitals on the ligand with both the a_{2u} and π^*_{FeO} orbitals. In particular, a cysteinate axial ligand results in mixing of the $3p_z$ orbital of the sulfur atom with the a_{2u} orbital on the porphyrin and the antibonding combination ($3p_z$−a_{2u}) is raised in energy with respect to the original a_{2u} orbital.[41] This change in orbital energy lowers the electron affinity of CpdI and it has been

DOI: 10.1021/acscatal.5b02720
ACS Catal. 2016, 6, 2230−2243

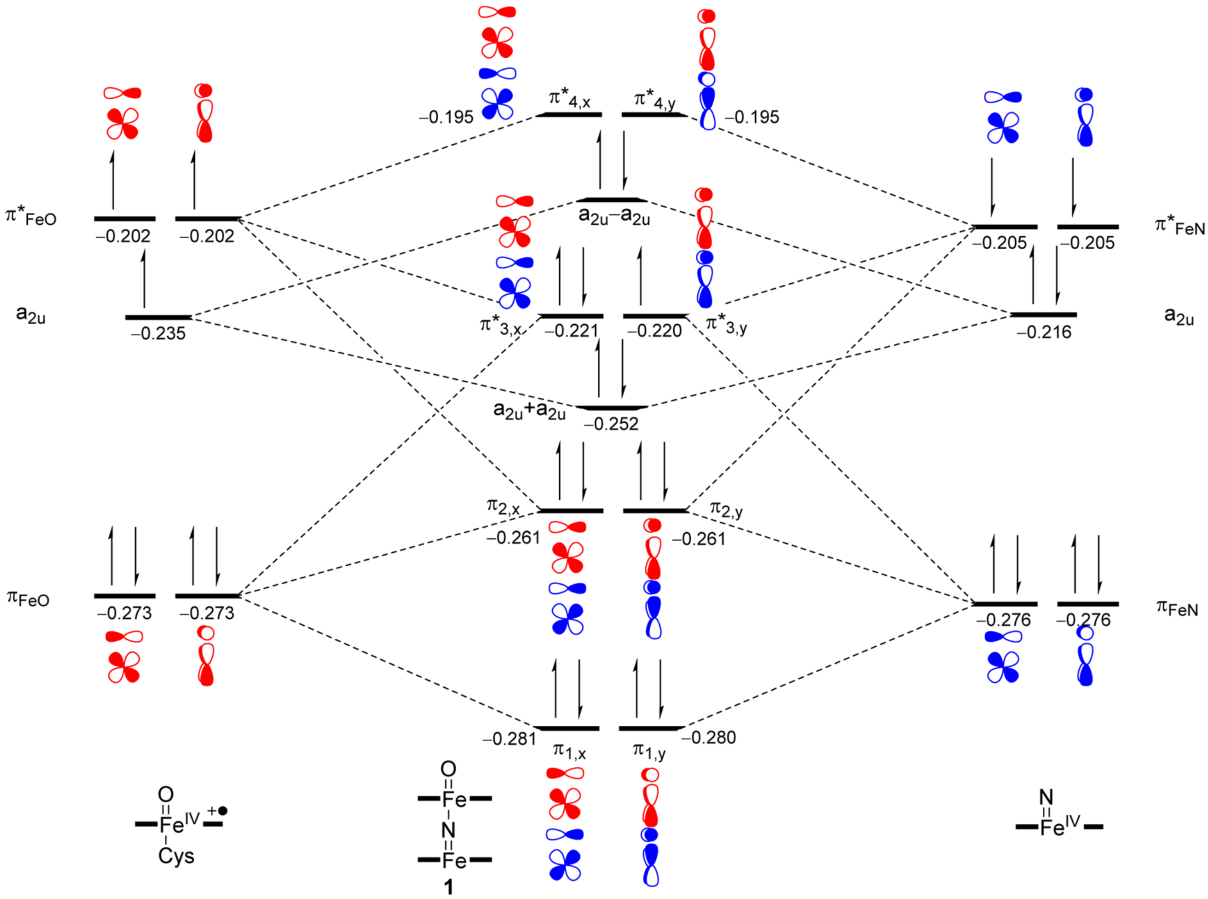

Figure 4. Orbital energy splitting of μ-nitrido-bridged diiron(IV)-oxo phthalocyanine and porphyrin species and how the orbital mixing originates from iron(IV)-oxo porphyrin cation radical (left-hand-side) and iron(IV)-nitrido (right-hand-side). Orbital energies are given for ^{2}**2** in au.

proposed that this could make it a better oxidant than an iron(IV)-oxo porphyrin without axial ligand.[26,41]

On the right-hand-side of Figure 4, we give the orbital occupation of the iron(IV)-nitrido group, which is essentially the one-electron reduced form of CpdI with orbital occupation $\pi_{FeN,xz}{}^2\ \pi_{FeN,yz}{}^2\ a_{2u}{}^2\ \pi^*_{FeN,xz}{}^1\ \pi^*_{FeN,yz}{}^1$. The iron(IV)-nitrido group has the same orbital shapes as the iron(IV)-oxo species with a pair of π_{FeN}/π^*_{FeN} orbitals and a close-lying a_{2u} orbital.

Upon formation of a μ-nitrido-bridged diiron-oxo complex, the orbitals along the molecular z-axis (i.e., along the O−Fe$_1$−N−Fe$_2$ axis) will mix and form a new set of orbitals, as shown in the middle panel of Figure 4. Thus, addition of an axial iron(IV)-nitrido group to an iron(IV)-oxo porphyrin cation radical changes the orbital interactions and energies along the z-axis dramatically. Due to alignment of the O, Fe$_1$, N, and Fe$_2$ atoms along the molecular z-axis in **1**, their atomic orbitals interact and form new molecular orbitals that span the complete molecular z-axis. The orbital interactions of the two iron $3d_{xz}/3d_{yz}$ atomic orbitals with the $2p_x/2p_y$ orbitals on the oxo and bridging nitrido groups leads to a set of bonding and antibonding combinations; namely four sets of molecular orbitals along the x and y-axis labeled as $\pi_{1,x}/\pi_{1,y}$, $\pi_{2,x}/\pi_{2,y}$, $\pi^*_{3,x}/\pi^*_{3,y}$, and $\pi^*_{4,x}/\pi^*_{4,y}$. In addition, the porphyrin π-orbitals, such as the a_{1u} and a_{2u} orbitals, mix and form bonding and antibonding sets of orbitals due to π-stacking interactions as well as the mixing with the $\sigma_{z2}/\sigma^*_{z2}$ orbitals on Fe$_1$ and Fe$_2$.

The orbital diagram in Figure 4 shows that complexes **1**/**2** should have a dominant doublet spin state with a singly occupied $\pi^*_{3,y}$ orbital and a closed-shell ligand system. This contrast of the orbital occupation and energy levels of P450 CpdI, where the high-lying π^*_{FeO} orbitals are close in energy to the a_{2u} orbital, so that a combination of ferromagnetically and antiferromagnetically coupled spin states are possible. In structures **1**/**1**$_{Ac}$/**2**/**2**$_{Ac}$, the separation between the a_{2u} and π^*_3 orbitals is large, and no low-lying states were found with radical character spread over metal and ligands. In particular, antiferromagnetic (or ferromagnetic) coupling of spin states where unpaired electrons on the metal(s) is coupled to an unpaired electron on the porphyrazine group was attempted but did not converge to stable, low-energy conformations. Furthermore, the spin-state ordering, relative energies, and group spin densities of the calculated doublet, quartet, sextet, and octet spin states of **1** and **1**$_{Ac}$ all show little radical character on the porphyrazine ligand (see Supporting Information, Tables S11 and S15).

Experimental Mössbauer spectra implicated a doublet spin ground state, which is reproduced excellently by our calculations. We attempted to create an electronic state with porphyrazine or porphyrin radical by swapping molecular orbitals or imposing local spin polarizations. Therefore, an extensive series of additional calculations were done to locate the alternative $^2A_{2u}$ state with occupation (core) $\pi^*_{3,x}{}^2\ \pi^*_{3,y}{}^2\ \pi^*_{4,x}{}^0\ (a_{2u}-a_{2u})^1$. However, in all cases during the SCF convergence the system reverted back to the $^2\Pi$ state described in Figure 4. Test calculations with a range of unrestricted density functional theory methods, i.e. B3LYP, B3LYP-D3, BP86, M06, PBE0 and B3LYP*, either after a full geometry optimization or a single-point calculation at the UB3LYP/BS1 geometry consistently gave the same spin state ordering and predicted the $^2\Pi$ state as the ground state, Supporting Information Table S17. Group spin densities obtained with these methods show small differences as seen in Table 2. In all cases the spin density on the equatorial ligand, i.e. porphyrazine or porphyrin, is negligible and all radical character is dominantly located on the OFeNFe group. The spin density contributions in Table 2 characterize all structures as a $^2\Pi$ state with a single unpaired electron in the $\pi^*_{3,y}$ orbital.

Table 2. Group Spin Densities of Reactant Configurations of **1**, **1**$_{Ac}$, **2**, and **2**$_{Ac}$ As Calculated with Various Computational Methods[a]

oxidant	method	ρ_{OFeNFe}	ρ_{Por}/ρ_{Pz}
1	UB3LYP	1.16	−0.10
	UBP86	1.01	0.00
	UB3LYP*	1.11	−0.01
	UB3LYP-D3	0.85	0.02
	M06-L	1.12	−0.12
1$_{Ac}$	UB3LYP	1.18	−0.04
	UBP86	1.02	−0.01
	UB3LYP*	1.20	−0.04
	UB3LYP-D3	1.20	−0.04
	NEVPT2	1.00	0.00
2	UB3LYP	1.16	−0.05
	UBP86	1.01	0.00
	UB3LYP*	1.11	−0.01
	UB3LYP-D3	0.86	0.01
2$_{Ac}$	UB3LYP	1.18	−0.02
	UBP86	1.02	0.00
	UB3LYP*	1.20	−0.02
	UB3LYP-D3	1.21	−0.02

[a] Data obtained for **1**/**1**$_{Ac}$ are from a Gaussian single-point calculation with basis set BS2 on a UB3LYP/BS1 optimized geometry, whereas data for **2**/**2**$_{Ac}$ were calculated in Orca.

The optimized geometries appear reasonably consistent between the various density functional theory methods (Supporting Information, Table S17). Thus, without an axial ligand bound, the $Fe_1{-}O$ and $Fe_2{-}N$ bond lengths are short (most values are between 1.62 and 1.66 Å) and implicate a double bond for both the $Fe_1{=}O$ and $Fe_2{=}N$ groups. Interestingly, upon addition of an acetate ligand to **1**, the nitrido group moves more to the center of the $Fe_1{-}Fe_2$ atoms at distances of 1.81 and 1.88 Å. Although to a much lesser extent, the same is true for structure **2**, where binding of an chlorobenzoate axial ligand leads to $Fe_2{-}N$ bond elongation. Optimized geometries of **1** and **2** are virtually the same for each density functional method and implicate little changes upon replacing the porphyrin ligand with porphyrazine. This is in line with previous studies on *meso*-substituted metal-oxo porphyrinoid systems that showed little changes upon ligand substitution.[12d,32,42] The BP86 optimized geometries of the μ-nitrido diiron oxo species supported by phthalocyanine ligands provided the following distances: $Fe_1{-}O$ = 1.73 Å, $Fe_1{-}N$ = 1.77 Å, and $Fe_2{-}N$ = 1.61 Å.[42b] These values are very close to those obtained for **1** and **2** with the same BP86 functional.

To test the effect of the environment on the spin state ordering and the nature of the electronic state of ^{2}**1**$_{Ac}$, we performed a full UB3LYP/BS2 optimization in solvent, for structure ^{2}**1**$_{Ac}$; however, there was very little structural or spin density change during the optimization as compared to the structure minimized in the gas-phase with basis set BS1 (Supporting Information Figure S19).

In a final attempt to unequivocally establish the molecular ground state of complexes **1** and **1**$_{Ac}$, we performed a NEVPT2 single-point calculation on these chemical systems. In support of the DFT studies, a molecular ground state with $^2\Pi$ configuration with no radical character on the porphyrin/porphyrazine ligands observed. Therefore, the most likely ground state of complexes **1**, **1**$_{Ac}$, **2**, and **2**$_{Ac}$ is the $^2\Pi$ state in the gas-phase. However, the presence of explicit solvent molecules, electric, and/or magnetic fields as well as the inclusion of entropy and interactions of the oxidant with ions and solvent may change the ordering of the electronic states.[43] Thus, DFT calculations of P450 CpdI models showed that hydrogen bonding interactions toward the thiolate ligand, or an electric field effect changed the electronic description of CpdI and moved radical character from the axial ligand to the porphyrin manifold.[43b] Furthermore, CpdI models of both of cytochrome *c* peroxidase and ascorbate peroxidase, showed that the addition of a point charge at 12 Å distance from the iron center changed the electronic configuration from a heme cation radical to a tryptophan radical.[44] As such, environmental

Scheme 2. Electron-Transfer Pathways for the Hydrogen Atom Abstraction from Methane by CpdI (top) and μ-Nitrido-Bridged Diiron-Oxo Species (bottom)

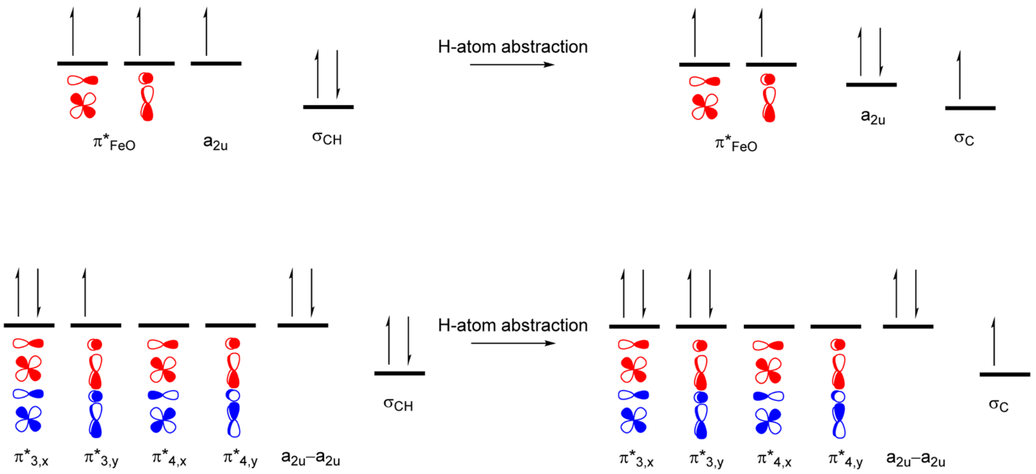

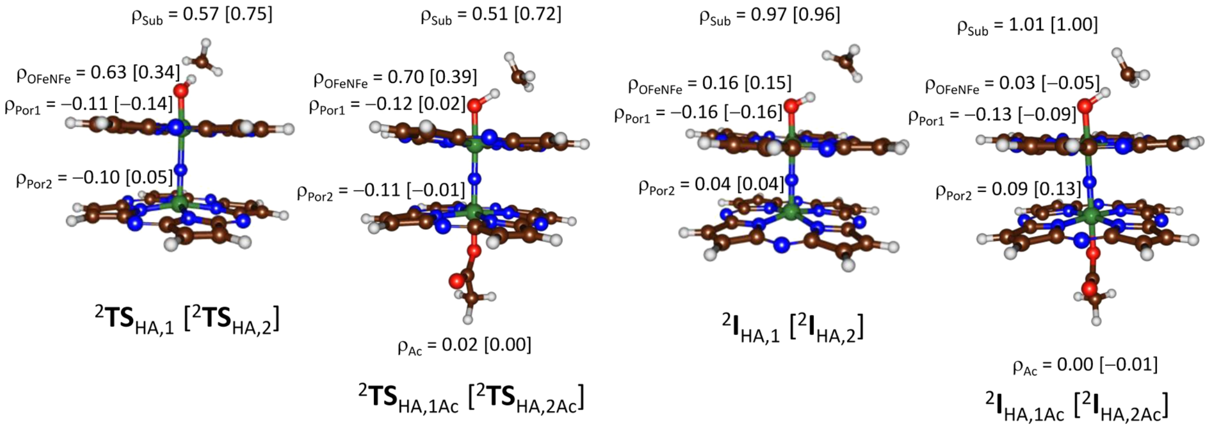

Figure 5. Group spin densities of hydrogen-atom-abstraction barriers and radical intermediates as taken from the B3LYP/BS2 results.

perturbations can have a major effect on spin-state ordering and relative energies. However, single-point calculations using the conductor-like polarized continuum model (CPCM) on species **1**, $\mathbf{1}_{\mathrm{Ac}}$, **2**, and $\mathbf{2}_{\mathrm{Ac}}$ did not change the electronic ground states.

Our DFT studies on **1** are in good agreement with calculations reported in the literature.[45] All these reports predict a doublet spin ground state, in agreement with experiment, with most unpaired spin density located on the O−Fe$_1$−N−Fe$_2$ group. Interestingly, Anasari et al.[45b] report an electronic ground state of ^{2}**1** with spin densities of 3.78 and −2.92 on Fe$_1$ and Fe$_2$, respectively, which implicates a state with four unpaired electrons on Fe$_1$ antiferromagnetically coupled to three unpaired electrons on Fe$_2$. This state is different from the state proposed on the basis of experimental Mössbauer and EPR spectra[9,46] and also to the considerably larger chemical model studied here.

Electron Transfer during the Mechanism. The hydrogen-atom-abstraction reaction from a substrate leads to formation of a hydroxo bond and the transfer of an electron from the oxo group into the metal−ligand system. Scheme 2 summarizes the main electron-transfer pathways that were observed in the hydrogen-atom-abstraction step from methane by **3** (top) and **1**/$\mathbf{1}_{\mathrm{Ac}}$ (bottom). Thus, the breaking of the C−H bond leads to the splitting of the σ_{CH} orbital into an atomic hydrogen orbital ($1s_{\mathrm{H}}$) and a substrate radical orbital (σ_{C}). The $1s_{\mathrm{H}}$ orbital then mixes with a 2p orbital on oxygen to form the σ_{OH} bond with two electrons. This process results in the one electron transferred from the oxo group into a metal or ligand type orbital and in P450 it moves into the a_{2u} orbital.

In the μ-nitrido-bridged diiron-oxo species the electron transfer is different from P450 CpdI due to a closed-shell a_{2u} orbital in the reactant state. As a result the electron moves into the $\pi^*_{3,y}$ orbital to fill it with a second electron. Indeed, the group spin densities of the hydrogen-atom-abstraction transition states (Figure 5) give a considerable reduction of the spin on the OFe$_1$NFe$_2$ group, which drops to almost zero in the radical intermediates. At the same time, a spin density of about +1 on the substrate rest-group is obtained.

We tested several possibilities for alternative radical intermediates and electron-transfer pathways with ferromagnetically and antiferromagnetically coupled states, but all those attempts gave higher energy structures. Therefore, the lowest-lying electron transfer appeared to lead to a radical intermediate with configuration $\pi^{*2}_{3,x}\ \pi^{*2}_{3,y}\ \sigma_{\mathrm{C}}^{\uparrow}$. A subsequent NEVPT2 single-point calculation gave spin density contributions corresponding to the same electronic state and confirms it to be the lowest-lying radical intermediate and hydrogen-atom-abstraction barrier. Attempts to swap molecular orbitals were done to generate the electronic state with occupation $\pi^{*2}_{3,x}\ \pi^{*\uparrow}_{3,y}\ \pi^{*\uparrow}_{4,x}\ \sigma_{\mathrm{C}}^{\downarrow}$; however, during the SCF convergence, they fell back to the state shown in Scheme 2, and hence, it is an excited state. Similarly, attempts to swap orbitals and generate a state with the (a_{2u}−a_{2u}) orbital singly occupied failed and led to the radical intermediate described above.

Group spin densities of the hydrogen abstraction transition states and radical intermediates are given in Figure 5. As can be seen, significant radical character on the CH$_3$ group is accumulating already in the transition state, which grows to a value of around 1 for the radical intermediates. The growth in spin density on the CH$_3$ group happens simultaneously with the loss of total spin density on the OFe$_1$NFe$_2$ group. The radical character on both porphyrin or porphyrazine groups remains small and never grows beyond a value of 0.2. Therefore, the calculations, in contrast to those on P450 CpdI, give no porphyrin radical in the oxidant and also not along the calculated reaction mechanism.

Physicochemical Properties of Reactant Complexes. The above studies show that structures **1** and **2** have well-separated electronic states, which are fundamentally different from the electronic ground state ($^{2,4}A_{2u}$ state) found in P450 Cpd I with three unpaired electrons and $\pi^{*1}_{\mathrm{FeO},x}\ \pi^{*1}_{\mathrm{FeO},y}\ a_{2u}^{1}$ occupation. Therefore, the difference in molecular valence orbitals between **1** or **2**, on the one hand, with **3**, on the other hand, will affect the relative energies of the molecular orbitals, such as the HOMO−LUMO energy gap, and as a consequence also the ionization potential, the electron affinity and pK_{a} values of the oxidant. This means that the spectroscopic and catalytic properties of the oxidants will be dramatically different as well as the H atom abstraction reaction, which involves a combined proton and electron transfer.[47] These factors influence the reactivity patterns with substrates and in this particular case enhance the reactivity. In addition, the potential energy landscapes shown in Figure 2 above shows that the binding of an axial ligand raises the hydrogen-atom-abstraction barriers by several kcal mol^{-1} and hence make it a weaker oxidant.

To understand how the intricate details of individual components can cause a change in the electron affinity of **1** and $\mathbf{1}_{\mathrm{Ac}}$ as compared to P450 CpdI, we dissected the electron affinities into several factors, namely the electric field effect due to the axial ligand (E_{field}), a quantum mechanical effect from orbital overlap between the oxidant and the axial ligand (E_{QM}) and a π-stacking effect of the two porphyrazine groups (E_{π_π}),

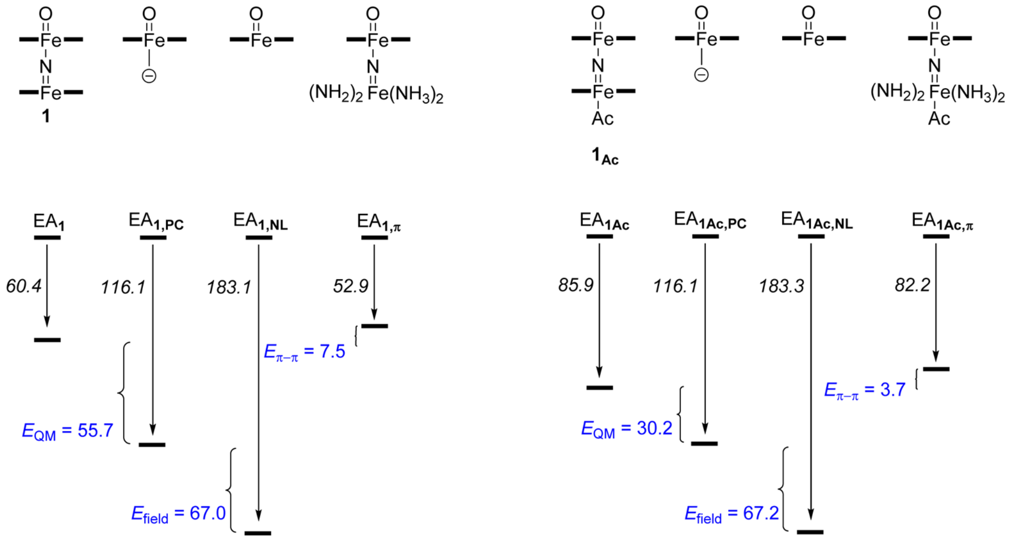

Figure 6. Axial ligand effects contributing to the electron affinity of **1** (left) and $\mathbf{1}_{\mathrm{Ac}}$ (right). All values represent ΔE + ZPE + E_{solv} energies (in kcal mol^{-1}) and contain solvent corrections.

see Figure 6. Thus, we took the optimized structures of **1** and $\mathbf{1}_{\mathrm{Ac}}$ and in one set of calculations removed the axial nitrido-iron(IV)porphyrazine group (no ligand, NL) and did a single-point electron affinity calculation to give $\mathrm{EA}_{\mathrm{NL}}$.

Subsequently, we did another set of single-point electron affinity calculations on these systems without axial ligand, where a point charge (PC) was placed in the position of the nitrido group ($\mathrm{EA}_{\mathrm{PC}}$). The difference in energy between EA and $\mathrm{EA}_{\mathrm{PC}}$, represents the quantum mechanical effect (E_{QM}) of the axial ligand group due to mixing of axial ligand orbitals with the iron(IV)-oxo group, eq 7. On the other hand, the difference in energy between $\mathrm{EA}_{\mathrm{PC}}$ and $\mathrm{EA}_{\mathrm{NL}}$ gives the electric field effect of the interaction of the charges of the axial ligand with the iron(IV)-oxo group, eq 8.

$$E_{\mathrm{QM}} = \mathrm{EA} - \mathrm{EA}_{\mathrm{PC}} \qquad (7)$$

$$E_{\mathrm{field}} = \mathrm{EA}_{\mathrm{PC}} - \mathrm{EA}_{\mathrm{NL}} \qquad (8)$$

In a final set of calculations we attempted to estimate the π-stacking contribution for the two porphyrazine ligands. To this end, we replaced the porphyrazine group of the iron(IV)-nitrido group by $(\mathrm{NH_3})_2(\mathrm{NH_2}^-)_2$, which keeps the same charge and coordination number but lacks the second porphyrazine unit, and calculated the electron affinity of $[\mathrm{O{=}Fe(Pz){-}N{=}Fe(NH_3)_2(NH_2^-)_2}]$ with and without Ac axial ligand. We call this electron affinity, the π-stacking electron affinity, EA_{π}, as it lacks the π-stacking interactions. The resulting data on EA, $\mathrm{EA}_{\mathrm{PC}}$, $\mathrm{EA}_{\mathrm{NL}}$, and EA_{π} as well as the values of E_{QM} and E_{field} are depicted in Figure 6 for comparison. On the basis of the orbital energy levels above, we predict an increased EA upon axial ligand binding, which indeed is confirmed with the calculations in Figure 2. This contrasts the behavior of P450 CpdI that sees a decrease in electron affinity upon addition of an axial ligand (cysteinate) or replacing it with a neutral molecule or solvent molecule.[23] The reason for this disparity comes from the orbital interactions that raise the antibonding $\mathrm{a}_{2\mathrm{u}}$-axial ligand interaction in P450 CpdI, whereas the π^*_3 orbitals are stabilized (and π^*_4 orbitals destabilized) in $\mathbf{1}_{\mathrm{Ac}}$ with respect to **1** due to the additional acetate ligand.

The latter also is highlighted from our dissection of the electron affinity contributions, where **1** has a much larger quantum mechanical contribution of the axial ligand than $\mathbf{1}_{\mathrm{Ac}}$ (E_{QM} is 55.7 kcal mol^{-1} for **1** and 30.2 kcal mol^{-1} for $\mathbf{1}_{\mathrm{Ac}}$). As such, binding of an acetate group has a major influence on the electron distribution within the oxidant and changes the orbital interactions so drastically that the electron affinity is raised by about 25 kcal mol^{-1}, which will affect its oxidation potential with substrates. Needless to say, the electric field effect due to the iron(IV)-nitrido porphyrazine group is virtually the same for $\mathbf{1}/\mathbf{1}_{\mathrm{Ac}}$ at a value of 67.0/67.2 kcal mol^{-1}. By contrast, the π-stacking energy ($E_{\pi\text{–}\pi}$) is small, and only in the order of 3.7–7.5 kcal mol^{-1}, and hence will not be the dominant factor. However, the electron affinity of both complexes **1** and $\mathbf{1}_{\mathrm{Ac}}$ are larger with a porphyrazine group attached to the iron(IV)-nitrido unit (compare $\mathrm{EA}_{1,\pi}$ vs EA_1), which confirms an important interaction between the axial ligand and the porphyrazine moiety exists.

The values of E_{field} and E_{QM} calculated previously for the axial ligand effect of $[\mathrm{Fe^{IV}(O)\ (Por^{+\bullet})SH}]$ were 54.0 and 38.8 kcal mol^{-1}, respectively.[48] The field effect calculated here is somewhat larger as the point charge was placed in the position of the bridging nitrogen atom at 2.06 Å, whereas in P450 CpdI, it was in the position of the sulfur atom at 2.49 Å.[48] Obviously, a shorter distance will lead to a larger Coulomb interaction and a larger field effect. In addition to an increased field effect, a comparison of **1** and $[\mathrm{Fe^{IV}(O)\ (Por^{+\bullet})SH}]$ also gives an increased quantum chemical effect by 16.9 kcal mol^{-1} due to better orbital interactions along the $\mathrm{O{-}Fe_1{-}N{-}Fe_2}$ system. However, most of this benefit is lost when acetate binds to $\mathrm{Fe_2}$. Nevertheless, **1** has a considerably lower electron affinity than P450 CpdI ($\mathrm{EA}_{\mathrm{CpdI}}$ = 92.9 kcal mol^{-1}), which is partially due to a larger electric field effect and partially as a result of a quantum mechanical effect. Based on the much smaller electron affinity of **1** versus **3**, one would expect the former to be a much weaker oxidant in hydrogen-atom-abstraction reactions. Nevertheless, as will be shown later in this work, system **1** has also a decreased $\mathrm{p}K_{\mathrm{a}}$ value, which makes it more basic and leads to a larger driving force for hydrogen atom abstraction as shown previously.[25]

Thermochemical Properties Affecting Reactivities. In order to assign the origin of reactivity differences one has to take the thermochemical properties of the oxidant and substrate into consideration. Experimental studies on hydrogen-atom-abstraction reactivities showed that the rate constant generally correlates with the strength of the C−H bond of the substrate that is broken (BDE_{CH}) as well as with the strength of the O−H bond that is formed (BDE_{OH}).[49] The BDE_{OH} and BDE_{CH} values are defined for the reactions described in eq 4 and 5 above. However, the BDE_{OH} value can be split into an electron transfer (electron affinity, EA of the oxidant), a proton affinity of the reduced oxidant (ΔG_{acid}) and the ionization energy (IE_H) of a hydrogen atom as described in eqs 9−11.

$$AH \rightarrow A^- + H^+ + \Delta G_{acid} \tag{9}$$

$$A \rightarrow A^- + EA_A \tag{10}$$

$$H \rightarrow H^+ + IE_H \tag{11}$$

Combination of reactions 9−11 adds up to reaction 4 and will give a BDE_{OH} description as given in eq 12.

$$-BDE_{OH} = \Delta G_{acid} - EA_{FeO} - IE_H \tag{12}$$

The ionization energy of a hydrogen atom is taken here from the NIST database.[50] Subsequently, we calculated the EA, ΔG_{acid}, and BDE_{OH} values of **1**, $\mathbf{1}_{Ac}$, and **3** and give the results graphically in Figure 7 but also tabulate the results in Table 3.

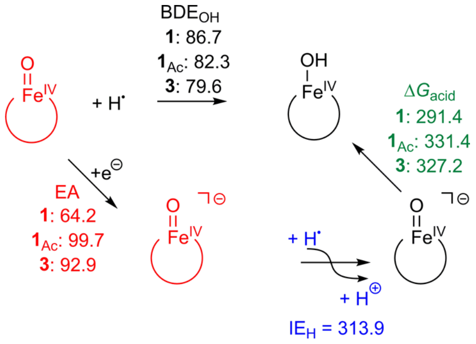

Figure 7. Calculated thermochemical variables for **1** and $\mathbf{1}_{Ac}$. Data represents $\Delta G + E_{solv}$ values with free energies that include solvent, thermal, and entropic corrections (in kcal mol^{-1}).

Table 3. Calculated Thermochemical Variables for 1, $\mathbf{1}_{Ac}$, and 3[a]

oxidant	BDE_{OH}	ΔG_{acid}	EA
1	86.7	291.4	64.2
$\mathbf{1}_{Ac}$	82.3	331.4	99.7
$\mathbf{3}_{SH}$	79.6	327.2	92.9

[a] Free energies with solvent corrections given in kcal mol^{-1}.

Extensive experimental studies implicated that the dominant component to the BDE_{OH} trends relates to the acidity of the oxo group (i.e., ΔG_{acid}).[51] With a solvent model included, we calculated a value of $BDE_{OH}(\mathbf{1})$ = 86.7 kcal mol^{-1}, which is only slightly higher in energy than the value we calculated before for $\mathbf{1}_{Ac}$, $BDE_{OH}(\mathbf{1}_{Ac})$ = 82.3 kcal mol^{-1} and the one for $\mathbf{3}_{SH}$, $BDE_{OH}(\mathbf{3}_{SH})$ = 79.6 kcal mol^{-1}.[43a] This change is likely due to the push-effect of electron density from the axial ligand to the metal-oxo group, which affects the orbital energies and consequently the electron affinity as well as the acidity of the iron(IV)-hydroxo group. However, **1** has an electron affinity that is about 35 kcal mol^{-1} lower in energy than that for $\mathbf{1}_{Ac}$, and as a consequence, **1** has a 40 kcal mol^{-1} lower ΔG_{acid} value. It is this acidity change that will make **1** a much better oxidant than either $\mathbf{1}_{Ac}$ or $\mathbf{3}_{SH}$ for substrate hydroxylation reactions.

Therefore, **1** is found to be a more powerful oxidant of hydrogen-atom-abstraction reactions than **3** due to an increased basicity of the iron(IV)-hydroxo complex that is formed, which is mainly due to orbital reorganization that affects the electron affinity of the oxidant. Figure 7 breaks down this basicity change into BDE_{OH} and EA components for species **1**, $\mathbf{1}_{Ac}$, and **3**.

In summary, the *μ*-nitrido diiron(IV)-oxo complexes have dramatically altered electronic configurations with respect to P450 CpdI, which is mainly due to charge and orbital delocalization along the O−Fe_1−N−Fe_2 axis. Because of this, the electron affinity of **1** is much lower than that of P450 CpdI; however, its interaction with ligands bound to the iron(IV)-nitrido group is also less. These orbital interactions lower the ability to abstract hydrogen atoms efficiently and make **1** a considerably better oxidant of hydrogen-atom-abstraction reactions than P450 CpdI. In addition, these electronic effects also influence the pK_a value of the corresponding iron(IV)-hydroxo group. As such, both thermochemical and electronic analysis point to the reasons for the reactivity differences of *μ*-nitrido-bridged diiron oxo complexes with respect to P450 CpdI.

Valence Bond Rationalization of the Reaction Mechanism. Finally, we have tried to understand the reaction mechanism obtained and rationalize why structures **1** and **2** are better oxidants than P450 CpdI in methane hydroxylation processes by setting up a valence bond (VB) curve crossing diagram, see Figure 8. These diagrams were used previously to rationalize hydrogen-atom-abstraction barriers and double bond epoxidation barriers by iron(IV)-oxo complexes and explained the obtained rate constant trends, but also identified the origin of the stepwise processes.[23,36,37,39] The figure starts on the bottom left with the reactant states, and in the case of **1** and **2**, the system has orbital occupation (core) $\pi^*_{3,x}{}^2\ \pi^*_{3,y}{}^1\ (a_{2u}-a_{2u})^2$ in a doublet spin ground state, which essentially implicates an iron(V)-oxo that is connected to an iron(IV)-nitrido group. This system has electrons in the $\pi_{1,x}$, $\pi_{2,x}$, and $\pi^*_{3,x}$ orbitals as identified by the dots next to the O, Fe_1, N, and Fe_2 atoms. The dots on the right-hand-side of the labels refer to the six electrons in $\pi_{1,x}{}^2\ \pi_{2,x}{}^2\ \pi^*_{3,x}{}^2$, and those on the left-hand-side of the labels represent the five electrons in $\pi_{1,y}{}^2\ \pi_{2,y}{}^2\ \pi^*_{3,y}{}^1$. In the VB structures, the equatorial ligand is given as a bold horizontal bar and both doubly occupied a_{2u} orbitals on each of the porphyrazine groups are identified with two dots next to these bars. Lastly, the C−H bond is occupied with two electrons and is given as a bar connected with two dots.

In the transition state for hydrogen atom abstraction, the C−H bond splits back into atomic orbitals, whereby the up-spin electron is retained by the CH_3 radical, while the down-spin electron leaves as a $1s_H$ orbital with hydrogen. In addition, in the transition state the $\pi_{1,x}/\pi_{2,x}/\pi^*_{3,x}/\pi^*_{4,x}$ set of orbitals is rehybridized and separated into a $2p_y$ orbital on oxygen with two electrons and three new orbitals for the interaction between Fe_1, N, and Fe_2 ($\pi'_{1,x}/\pi'_{2,x}/\pi^{*\prime}_{3,x}$). One of the electrons of the $2p_x$ orbital forms a bond (σ_{OH}) with the incoming $1s_H$ orbital of hydrogen, whereas the other electron is transferred into the $\pi'_{1,x}/\pi'_{2,x}/\pi^{*\prime}_{3,x}$ that ends up with five electrons. In the subsequent step in the reaction mechanism, namely, the OH rebound step (not shown in Figure 8), the set of $\pi_{1,y}/\pi_{2,y}/\pi^*_{3,y}/\pi^*_{4,y}$ orbitals is split into a $2p_y$ and a set of new π'_y orbitals. The radical on the substrate then forms a bond

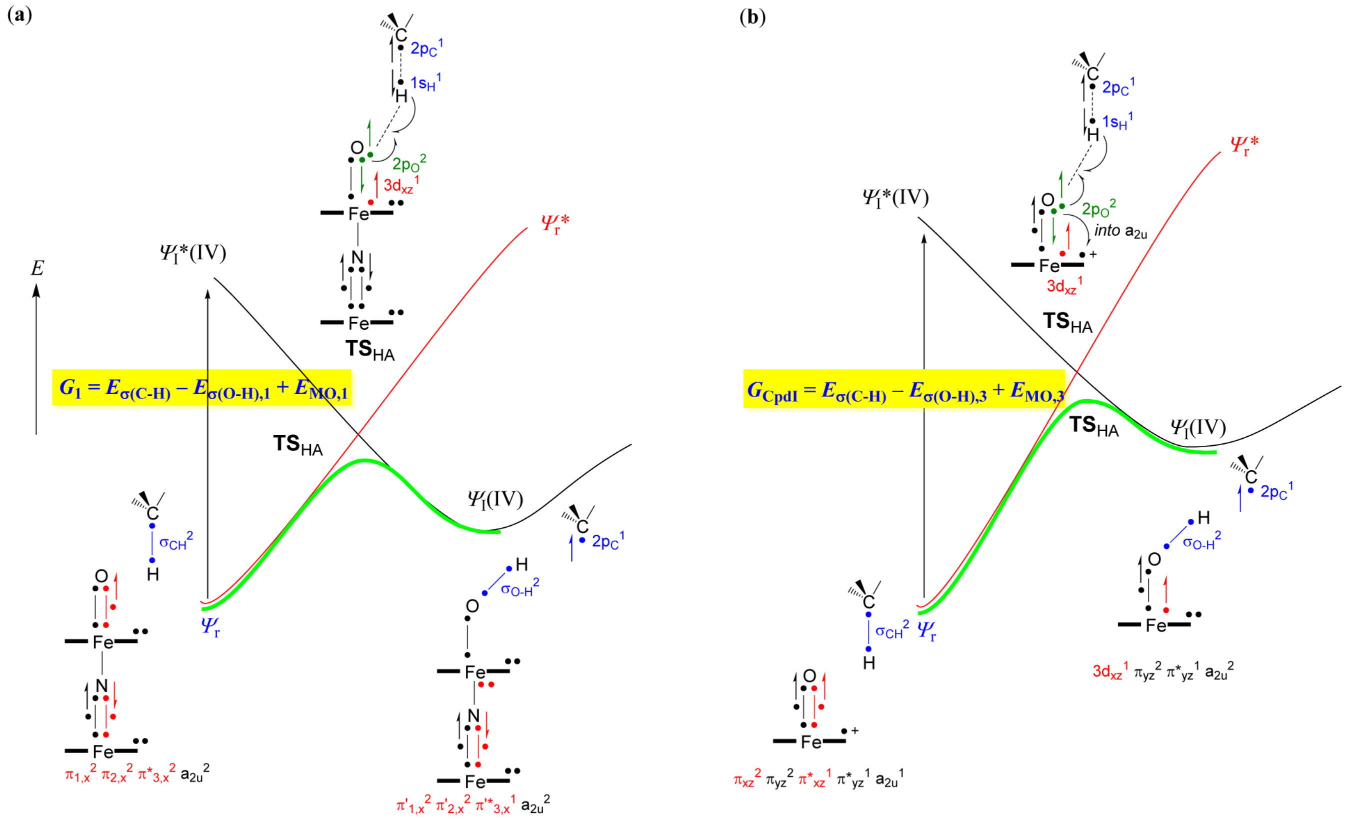

Figure 8. Valence bond curve crossing diagram for the methane hydroxylation by **1** (panel a) and P450 Cpd I (panel b). Dots represent valence electrons and lines (curved or straight) implicate chemical bonds.

with the electron in $2p_y$ to form the methanol product complex. These electron-transfer pathways and orbital occupations agree with the spin densities reported above.

The reactant configuration can be described quantum mechanically with a reactant wave function (Ψ_r) and the radical intermediate with the intermediate wave function Ψ_I. In valence bond theory, the reactant wave function represents an excited state in the intermediate geometry (i.e., Ψ_r*), whereas the intermediate configuration links to an excited state in the reactant geometry (i.e., Ψ_I*).

It has been shown that the barrier height from reactants to products is proportional to the excitation energy (or promotion gap G) from Ψ_r to Ψ_I*.[52] A comparison of the VB structures of the Ψ_r and Ψ_I* (i.e., TS) configurations gives insight into the chemical and physical components that determine the transition state for the reaction and enable us to estimate the promotion gap of **1** or **2**. Thus, the barrier is determined by the energy of the σ_{CH} bond of the substrate that is broken into atomic orbitals (i.e., $E_{\sigma(C-H)}$). In addition, it is based on the energy of the σ_{OH} bond that is formed (i.e., $E_{\sigma(O-H)}$). As discussed above, the barrier height is also dependent on molecular orbital changes (E_{MO}) in the oxidant and particularly on the electron-transfer energies and rehybridization of some of the orbitals due to bond formation and breaking. For instance, the E_{MO} value contains the energy to split the $\pi_{1,x}/\pi_{2,x}/\pi^*_{3,x}/\pi^*_{4,x}$ set of orbitals into a $2p_x$ on oxygen and a $\pi'_{1,x}/\pi'_{2,x}/\pi^{*\prime}_{3,x}$ set of orbitals along the Fe_1-N-Fe_2 axis. The overall value of the promotion gap of **1** or **2** is given in eq 13.

$$G_{\mathbf{1}} = E_{\sigma(C-H)} - E_{\sigma(O-H),\mathbf{1}} + E_{MO,\mathbf{1}} \qquad (13)$$

On the right-hand-side of Figure 8, we show the analogous VB curve crossing diagram for methane hydroxylation by P450 CpdI. Thus, the dots along the Fe−O bond represent the three electrons in the π_{xz}/π^*_{xz} (in red) and the three electrons in the π_{yz}/π^*_{yz} (in black) orbitals. Similarly, as discussed above for **1** and $\mathbf{1}_{Ac}$, the $\pi_{xz}{}^2\ \pi^*_{xz}{}^1$ orbitals split into atomic orbitals with two electrons in $2p_x(O)$ and one in the metal $3d_{xz}$. One of the electrons of $2p_x(O)$ forms the σ_{OH} bond with the incoming $1s_H$ hydrogen atom, whereas the other atom of $2p_x(O)$ is promoted to the nearest available electronic orbital, namely, the a_{2u} orbital. The promotion gap for this reaction (G_{CpdI}) is described in eq 14. Obviously, since we use the same substrate (methane) as in the reaction with **1**, the value $E_{\sigma(C-H)}$ will be the same for **1** and **3**.

$$G_{\mathbf{CpdI}} = E_{\sigma(C-H)} - E_{\sigma(O-H),\mathbf{3}} + E_{MO,\mathbf{3}} \qquad (14)$$

In principle, the $E_{\sigma(O-H)}$ represents the strength of the O−H bond that is formed and will be proportional to the BDE_{OH} value. As shown above in Table 3, the BDE_{OH} value for **1** is about 4.4 kcal mol^{-1} larger than that for $\mathbf{1}_{Ac}$ and 7.1 kcal mol^{-1} larger than that found for **3**. Therefore, we expect a smaller promotion gap for **1** than for $\mathbf{1}_{Ac}$ and **3**, which should result in a lower hydrogen-atom-abstraction barrier for **1** than for **3**. Indeed, the potential energy profiles (Figure 2) show a $\mathbf{TS}_{HA}$ ordering of $\mathbf{TS}_{HA,1} < \mathbf{TS}_{HA,1Ac} < \mathbf{TS}_{HA,3}$ in agreement with the promotion gap differences. Thus, part of the differences in BDE_{OH} values relate to differences in the acidity of the iron-hydroxo complex. However, part of this benefit is canceled out by changes in the electron affinity of the oxidants, Table 3.

The major difference between complex **1** and **3** is related to the rehybridization energy or E_{MO}, which is determined by the difference in electron affinity of **1** versus **3**. Thus, in **3**, the π_{xz}/π^*_{xz} couple is rehybridized into atomic orbitals $2p_x$(O) and $3d_{xz}$(Fe) of which the $2p_x$(O) mixes with the $1s_H$ orbital to form the new σ_{CH} orbital. By contrast, in **1** the set of four coupled orbitals $(\pi_{1,x}/\pi_{2,x}/\pi^*_{3,x}/\pi^*_{4,x})$ is reduced to a set of three coupled orbitals and the atomic $2p_x$(O) orbital, which amounts to a much lesser orbital reorganization and consequently a much smaller E_{MO} value. Therefore, **1** will have a smaller E_{MO} value than **3** and hence also a smaller excitation energy as well as higher reactivity in H atom abstraction reactions. Because of the larger quantum chemical changes upon reduction of **3** versus the reduction of **1** and the increased stability of the product, it is evident that **3** will be a lesser good oxidant of hydrogen-atom-abstraction reactions. Indeed, that is what is observed by the relative methane hydrogen-atom-abstraction reactions when **1** and **3** are compared.

■ CONCLUSION

The calculations presented in this work highlight how small external perturbations, such as those of an axially coordinated nitrido iron porphyrin ligand can lead to dramatic changes in molecular orbital interactions of the metal(IV)-oxo group with aligned ligand-orbitals as well as the dipole moment of the oxidant. In particular, an μ-nitrido-bridged diiron-oxo complex, with either porphyrin or phthalocyanine, has an increased basicity of the oxo group that is highly susceptible to hydrogen atom abstraction. This explains the enhanced reactivity observed for **A**/**B** over P450 Compound I. Moreover, these insights will assist in the design of efficient and powerful oxidants of hydrogen-atom-abstraction reactions. A detailed thermochemical, valence bond, and orbital analysis has given insight into the intricate details of μ-nitrido-bridged diiron(IV) complexes and gives hints on how this complex can be further modified to improve its catalytic properties.

■ ASSOCIATED CONTENT

Ⓢ Supporting Information

The Supporting Information is available free of charge on the ACS Publications website at DOI: 10.1021/acscatal.5b02720.

> Computational details, including tables with absolute and relative energies, group spin densities and charges, as well as figures with geometry scans, IRCs, and Cartesian coordinates of optimized geometries (PDF)

■ AUTHOR INFORMATION

Corresponding Authors

*E-mail: sam.devisser@manchester.ac.uk.
*E-mail: alexander.sorokin@ircelyon.univ-lyon1.fr.
*E-mail: pascale.maldivi@cea.fr.

Notes

The authors declare no competing financial interest.

■ ACKNOWLEDGMENTS

The National Service of Computational Chemistry Software (NSCCS) is thanked for CPU time provided. M.G.Q. thanks the BBSRC for a studentship. D.K. holds the Ramanujan Fellowship (SR/S2/RJN-11/2008) from the Department of Science and Technology (DST), New Delhi (India). A.B.S. is indebted to ANR (France) for financial support (grant ANR-08-BLANC-0183-01). P.M. is grateful to the French National Agency for Research (ANR) "Programme Labex" (ARCANE project no. ANR-11-LABX-003) for partial funding. D.S. wishes to thank Prof Sason Shaik for fruitful discussions and support in this study. S.d.-V. and P.M. also thank Prof Jean-Marc Latour for useful discussions on the structure and spectroscopy of the reactant complex. The COST action CM1305 ECostBio is acknowledged for support. This work was partially performed using HPC resources from GENCI- CINES (Grant 2015-089173).

■ REFERENCES

(1) (a) Sono, M.; Roach, M. P.; Coulter, E. D.; Dawson, J. H. *Chem. Rev.* **1996**, *96*, 2841−2888. (b) Groves, J. T. *Proc. Natl. Acad. Sci. U. S. A.* **2003**, *100*, 3569−3574. (c) Ortiz de Montellano, P. R., Ed., *Cytochrome P450: Structure, Mechanism and Biochemistry*, 3rd ed.; Kluwer Academic/Plenum Publishers: New York, 2005. (d) Munro, A. W.; Girvan, H. M.; McLean, K. J. *Nat. Prod. Rep.* **2007**, *24*, 585−609. (e) Kadish, K. M., Smith, K. M., Guilard, R., Eds.; *Handbook of Porphyrin Science*; World Scientific Publishing Co.: Singapore, 2010. (f) de Visser, S. P., Kumar, D., Eds.; *Iron-containing enzymes: Versatile catalysts of hydroxylation reaction in nature*; RSC Publishing: Cambridge, U.K., 2011. (g) Grogan, G. *Curr. Opin. Chem. Biol.* **2011**, *15*, 241−248. (h) Poulos, T. L. *Chem. Rev.* **2014**, *114*, 3919−3962. (i) Blomberg, M. R. A.; Borowski, T.; Himo, F.; Liao, R.-Z.; Siegbahn, P. E. M. *Chem. Rev.* **2014**, *114*, 3601−3658.

(2) (a) Costas, M. *Coord. Chem. Rev.* **2011**, *255*, 2912−2932. (b) Bruijnincx, P. C. A.; van Koten, G.; Klein Gebbink, R. J. M. *Chem. Soc. Rev.* **2008**, *37*, 2716−2744. (c) Kryatov, S. V.; Rybak-Akimova, E. V.; Schindler, S. *Chem. Rev.* **2005**, *105*, 2175−2226. (d) McDonald, A. R.; Que, L., Jr *Coord. Chem. Rev.* **2013**, *257*, 414−428. (e) Nam, W.; Lee, Y.-M.; Fukuzumi, S. *Acc. Chem. Res.* **2014**, *47*, 1146−1154.

(3) (a) Groves, J. T. Models and Mechanisms of Cytochrome P450 Action. In *Cytochrome P450: Structure, Mechanism and Biochemistry*, 3rd ed.; Ortiz de Montellano, P. R., Ed.; Kluwer Academic/Plenum Publishers: New York, 2005; Chapter 1, pp 1−44. (b) Nam, W. *Acc. Chem. Res.* **2007**, *40*, 522−531. (c) Denisov, I. G.; Makris, T. M.; Sligar, S. G.; Schlichting, I. *Chem. Rev.* **2005**, *105*, 2253−2277.

(4) Rittle, J.; Green, M. T. *Science* **2010**, *330*, 933−937.

(5) Chen, M. M.; Coelho, P. S.; Arnold, F. H. *Adv. Synth. Catal.* **2012**, *354*, 964−968.

(6) Zilly, F. E.; Acevedo, J. P.; Augustyniak, W.; Deege, A.; Häusig, U. W.; Reetz, M. T. *Angew. Chem., Int. Ed.* **2011**, *50*, 2720−2724; Corrigendum: *Angew. Chem., Int. Ed.* **2013**, *52*, 13503.

(7) (a) Kawakami, N.; Shoji, O.; Watanabe, Y. *Angew. Chem., Int. Ed.* **2011**, *50*, 5315−5318. (b) Kawakami, N.; Shoji, O.; Watanabe, Y. *Chem. Sci.* **2013**, *4*, 2344−2348.

(8) (a) Sorokin, A. B.; Mangematin, S.; Pergrale, C. *J. Mol. Catal. A: Chem.* **2002**, *182-183*, 267−281. (b) Sorokin, A. B.; Kudrik, E. V.; Bouchu, D. *Chem. Commun.* **2008**, 2562−2564. (c) Sorokin, A. B.; Kudrik, E. V.; Alvarez, L. X.; Afanasiev, P.; Millet, J. M. M.; Bouchu, D. *Catal. Today* **2010**, *157*, 149−154. (d) Sorokin, A. B. *Chem. Rev.* **2013**, *113*, 8152−8191. (e) Afanasiev, P.; Kudrik, E. V.; Millet, J-M. M.; Bouchu, D.; Sorokin, A. B. *Dalton Trans.* **2011**, *40*, 701−740. (f) Colomban, C.; Kudrik, E. V.; Afanasiev, P.; Sorokin, A. B. *J. Am. Chem. Soc.* **2014**, *136*, 11321−11330.

(9) Kudrik, E. V.; Afanasiev, P.; Alvarez, L. X.; Dubourdeaux, P.; Clémancey, M.; Latour, J.-M.; Blondin, G.; Bouchu, D.; Albrieux, F.; Nefedov, S. E.; Sorokin, A. B. *Nat. Chem.* **2012**, *4*, 1024−1029.

(10) Berman, H. M.; Westbrook, J.; Feng, Z.; Gilliland, G.; Bhat, T. N.; Weissig, H.; Shindyalov, I. N.; Bourne, P. E. *Nucleic Acids Res.* **2000**, *28*, 235−242.

(11) (a) Butler, C. F.; Peet, C.; Mason, A. E.; Voice, M. W.; Leys, D.; Munro, A. W. *J. Biol. Chem.* **2013**, *288*, 25387−25399. (b) Batabyal, D.; Poulos, T. L. *Biochemistry* **2013**, *52*, 8898−8906. (c) Müller, C. S.; Knehans, T.; Davydov, D. R.; Bounds, P. L.; von Mandach, U.; Halpert, J. R.; Caflisch, A.; Koppenol, W. H. *Biochemistry* **2015**, *54*, 711−721. (d) Xu, K.; Wang, Y.; Hirao, H. *ACS Catal.* **2015**, *5*, 4175−4179.

(12) (a) Gross, Z.; Nimri, S. *Inorg. Chem.* **1994**, *33*, 1731−1732. (b) Czarnecki, K.; Nimri, S.; Gross, Z.; Proniewicz, L. M.; Kincaid, J. R. *J. Am. Chem. Soc.* **1996**, *118*, 2929−2935. (c) Song, W. J.; Ryu, Y. O.; Song, R.; Nam, W. *JBIC, J. Biol. Inorg. Chem.* **2005**, *10*, 294−304. (d) Takahashi, A.; Yamaki, D.; Ikemura, K.; Kurahashi, T.; Ogura, T.; Hada, M.; Fujii, H. *Inorg. Chem.* **2012**, *51*, 7296−7305.

(13) For examples, see the following: (a) Alfonso-Prieto, M.; Biarnés, X.; Vidossich, P.; Rovira, C. *J. Am. Chem. Soc.* **2009**, *131*, 11751−11761. (b) Colin, J.; Wiseman, B.; Switala, J.; Loewen, P. C.; Ivancich, A. *J. Am. Chem. Soc.* **2009**, *131*, 8557−8563. (c) Raven, E. L. *Nat. Prod. Rep.* **2003**, *20*, 367−381. (d) Veitch, N. C. *Phytochemistry* **2004**, *65*, 249−259.

(14) (a) Dawson, J. H.; Holm, R. H.; Trudell, J. R.; Barth, G.; Linder, R. E.; Bunnenberg, E.; Djerassi, C.; Tang, S. C. *J. Am. Chem. Soc.* **1976**, *98*, 3707−3709. (b) Poulos, T. L. *JBIC, J. Biol. Inorg. Chem.* **1996**, *1*, 356−359.

(15) (a) Zhou, Y.; Shan, X.; Mas-Ballesté, R.; Bukowski, M. R.; Stubna, A.; Chakrabarti, M.; Slominski, L.; Halfen, J. A.; Münck, E.; Que, L., Jr *Angew. Chem., Int. Ed.* **2008**, *47*, 1896−1899. (b) de Visser, S. P.; Nam, W. *J. Phys. Chem. A* **2008**, *112*, 12887−12895. (c) Takahashi, A.; Kurahashi, T.; Fujii, H. *Inorg. Chem.* **2011**, *50*, 6922−6928.

(16) Shaik, S.; Kumar, D.; de Visser, S. P.; Altun, A.; Thiel, W. *Chem. Rev.* **2005**, *105*, 2279−2328.

(17) (a) Porro, C. S.; Sutcliffe, M. J.; de Visser, S. P. *J. Phys. Chem. A* **2009**, *113*, 11635−11642. (b) Hernández-Ortega, A.; Quesne, M. G.; Bui, S.; Heyes, D. J.; Steiner, R. A.; Scrutton, N. S.; de Visser, S. P. *J. Am. Chem. Soc.* **2015**, *137*, 7474−7487. (c) Quesne, M. G.; Borowski, T.; de Visser, S. P. *Chem. - Eur. J.* **2016**, *22*, 2562−2581.

(18) (a) de Visser, S. P.; Quesne, M. G.; Martin, B.; Comba, P.; Ryde, U. *Chem. Commun.* **2014**, *50*, 262−282. (b) Kumar, D.; de Visser, S. P.; Sharma, P. K.; Cohen, S.; Shaik, S. *J. Am. Chem. Soc.* **2004**, *126*, 1907−1920. (c) Kumar, D.; de Visser, S. P.; Shaik, S. *J. Am. Chem. Soc.* **2004**, *126*, 5072−5073.

(19) (a) Frisch, M. J. et al. *Gaussian 09*, revision D.01; Gaussian, Inc.: Wallingford, CT, 2009. (b) *Jaguar*, version 8.4; Schrodinger, Inc.: New York, NY, 2013. (c) Neese, F. *ORCA − an ab initio, DFT and semiempirical SCF-MO package*, version 2.9; University of Bonn: Bonn, Germany, 2009. (d) Visualizing Molecules with gOpenMol. http://www.chem.utah.edu/directory/anderson/research-group/gopen/ (accessed January 2016).

(20) (a) Becke, A. D. *J. Chem. Phys.* **1993**, *98*, 5648−5652. (b) Lee, C.; Yang, W.; Parr, R. G. *Phys. Rev. B: Condens. Matter Mater. Phys.* **1988**, *37*, 785−789.

(21) (a) Hay, P. J.; Wadt, W. R. *J. Chem. Phys.* **1985**, *82*, 299−310. (b) Hehre, W. J.; Ditchfield, K.; Pople, J. A. *J. Chem. Phys.* **1972**, *56*, 2257−2261.

(22) (a) Becke, A. D. *Phys. Rev. A: At., Mol., Opt. Phys.* **1988**, *38*, 3098−3100. (b) Perdew, J. P. *Phys. Rev. B: Condens. Matter Mater. Phys.* **1986**, *33*, 8822−8824.

(23) de Visser, S. P. *J. Am. Chem. Soc.* **2010**, *132*, 1087−1097.

(24) (a) Vardhaman, A. K.; Sastri, C. V.; Kumar, D.; de Visser, S. P. *Chem. Commun.* **2011**, *47*, 11044−11046. (b) Vardhaman, A. K.; Barman, P.; Kumar, S.; Sastri, C. V.; Kumar, D.; de Visser, S. P. *Angew. Chem., Int. Ed.* **2013**, *52*, 12288−12292. (c) Vardhaman, A. K.; Barman, P.; Kumar, S.; Sastri, C. V.; Kumar, D.; de Visser, S. P. *Chem. Commun.* **2013**, *49*, 10926−10928.

(25) Prokop, K. A.; de Visser, S. P.; Goldberg, D. P. *Angew. Chem., Int. Ed.* **2010**, *49*, 5091−5095.

(26) de Visser, S. P. *Chem. - Eur. J.* **2006**, *12*, 8168−8177.

(27) (a) Sainna, M. A.; Kumar, S.; Kumar, D.; Fornarini, S.; Crestoni, M. E.; de Visser, S. P. *Chem. Sci.* **2015**, *6*, 1516−1529. (b) Sainna, M. A.; Sil, D.; Sahoo, D.; Martin, B.; Rath, S. P.; Comba, P.; de Visser, S. P. *Inorg. Chem.* **2015**, *54*, 1919−1930.

(28) Reiher, M.; Salomon, O.; Hess, B. A. *Theor. Chem. Acc.* **2001**, *107*, 48−55.

(29) Grimme, S.; Antony, J.; Ehrlich, S.; Krieg, H. *J. Chem. Phys.* **2010**, *132*, 154104−154104.

(30) Zhao, Y.; Truhlar, D. G. *J. Chem. Phys.* **2006**, *125*, 194101−194101.

(31) Adamo, C.; Barone, V. *J. Chem. Phys.* **1999**, *110*, 6158−6169.

(32) Neu, H. M.; Quesne, M. G.; Yang, T.; Prokop-Prigge, K. A.; Lancaster, K. M.; Donohoe, J.; DeBeer, S.; de Visser, S. P.; Goldberg, D. P. *Chem. - Eur. J.* **2014**, *20*, 14584−14588.

(33) Heyes, D. J.; Sakuma, M.; de Visser, S. P.; Scrutton, N. S. *J. Biol. Chem.* **2009**, *284*, 3762−3767.

(34) For examples, see the following: Neu, H. M.; Yang, T.; Baglia, R. A.; Yosca, T. H.; Green, M. T.; Quesne, M. G.; de Visser, S. P.; Goldberg, D. P. *J. Am. Chem. Soc.* **2014**, *136*, 13845−13852.

(35) (a) Yoshizawa, K.; Kamachi, T.; Shiota, Y. *J. Am. Chem. Soc.* **2001**, *123*, 9806−9816. (b) de Visser, S. P.; Kumar, D.; Cohen, S.; Shacham, R.; Shaik, S. *J. Am. Chem. Soc.* **2004**, *126*, 8362−8363.

(36) Shaik, S.; Kumar, D.; de Visser, S. P. *J. Am. Chem. Soc.* **2008**, *130*, 10128−10140.

(37) For examples, see the following: Kumar, S.; Faponle, A. S.; Barman, P.; Vardhaman, A. K.; Sastri, C. V.; Kumar, D.; de Visser, S. P. *J. Am. Chem. Soc.* **2014**, *136*, 17102−17115.

(38) de Visser, S. P. *Phys. Chem. Chem. Phys.* **1999**, *1*, 749−754.

(39) (a) Kumar, D.; Karamzadeh, B.; Sastry, G. N.; de Visser, S. P. *J. Am. Chem. Soc.* **2010**, *132*, 7656−7667. (b) Kumar, D.; Sastry, G. N.; de Visser, S. P. *Chem. - Eur. J.* **2011**, *17*, 6196−6205.

(40) de Visser, S. P.; Shaik, S.; Sharma, P. K.; Kumar, D.; Thiel, W. *J. Am. Chem. Soc.* **2003**, *125*, 15779−15788.

(41) Ogliaro, F.; de Visser, S. P.; Cohen, S.; Kaneti, J.; Shaik, S. *ChemBioChem* **2001**, *2*, 848−851.

(42) (a) Kumar, D.; Tahsini, L.; de Visser, S. P.; Kang, H. Y.; Kim, S. J.; Nam, W. *J. Phys. Chem. A* **2009**, *113*, 11713−11722. (b) Colomban, C.; Kudrik, E. V.; Briois, V.; Shwarbrick, J. C.; Sorokin, A. B.; Afanasiev, P. *Inorg. Chem.* **2014**, *53*, 11517−11530.

(43) (a) de Visser, S. P.; Tan, L. S. *J. Am. Chem. Soc.* **2008**, *130*, 12961−12974. (b) Shaik, S.; de Visser, S. P.; Kumar, D. *J. Am. Chem. Soc.* **2004**, *126*, 11746−11749.

(44) de Visser, S. P. *J. Phys. Chem. A* **2005**, *109*, 11050−11057.

(45) (a) Silaghi-Dumitrescu, R.; Makarov, S. V.; Uta, M.-M.; Dereven'kov, I. A.; Stuzhin, P. A. *New J. Chem.* **2011**, *35*, 1140−1145. (b) Ansari, M.; Vyas, N.; Ansari, A.; Rajaraman, G. *Dalton Trans.* **2015**, *44*, 15232−15243. (c) İşci, Ü.; Faponle, A. S.; Afanasiev, P.; Albrieux, F.; Briois, V.; Ahsen, V.; Dumoulin, F.; Sorokin, A. B.; de Visser, S. P. *Chem. Sci.* **2015**, *6*, 5063−5075.

(46) Bocian, D. F.; Findsen, E. W.; Hofmann, J. A., Jr; Schick, G. A.; English, D. R.; Hendrickson, D. N.; Suslick, K. S. *Inorg. Chem.* **1984**, *23*, 800−807.

(47) For examples, see the following: (a) Latifi, R.; Bagherzadeh, M.; de Visser, S. P. *Chem. - Eur. J.* **2009**, *15*, 6651−6662. (b) Faponle, A. S.; Quesne, M. G.; Sastri, C. V.; Banse, F.; de Visser, S. P. *Chem. - Eur. J.* **2015**, *21*, 1221−1236.

(48) Ogliaro, F.; de Visser, S. P.; Shaik, S. *J. Inorg. Biochem.* **2002**, *91*, 554−567.

(49) (a) Friedrich, L. E. *J. Org. Chem.* **1983**, *48*, 3851−3852. (b) Bordwell, F. G.; Cheng, J.-P. *J. Am. Chem. Soc.* **1991**, *113*, 1736−1743. (c) Mayer, J. M. *Acc. Chem. Res.* **1998**, *31*, 441−450.

(50) *NIST Chemistry WebBook*, NIST Standard Reference Database, Number 69; Linstrom, P. J., Mallard, W. G., Eds.; National Institute of Standards and Technology: Gaithersburg, MD, 2016. http://webbook.nist.gov.

(51) (a) Green, M. T.; Dawson, J. H.; Gray, H. B. *Science* **2004**, *304*, 1653−1656. (b) Parsell, T. H.; Yang, M.-Y.; Borovik, A. S. *J. Am. Chem. Soc.* **2009**, *131*, 2762−2763.

(52) Shaik, S. S. *J. Am. Chem. Soc.* **1981**, *103*, 3692−3701.

Methane hydroxylation by axially ligated iron(IV)-oxo porphyrin cation radical models

Devendra Singh[1], Devesh Kumar[1], and Sam P. de Visser[2]*

Abstract

Methane hydroxylation is a thermochemically difficult process due to the strength of the C–H bond that needs to be broken in the process. In Nature only the methane monoxygenases have a catalytic center that is active enough to perform this task. Other metalloenzymes, such as, mononuclear iron monoxygenases and dioxygenases, including the cytochromes P450, are not known to catalyze methane hydroxylation. The cytochromes P450 contain an iron heme group that in a catalytic cycle is converted into an iron(IV)-oxo heme cation radical (Compound I). To gain insight into the features that affect methane hydroxylation by Compound I and synthetic model complexes, we have done a detailed computational study. Thus, we investigated the chemical properties of iron(IV)-oxo porphyrins with varying axial ligands, including SH^-, F^-, OH^-, CN^-, CF_3COO^- and CH_3COO^-. In addition, we calculated the methane hydroxylation pathways for a selection of these oxidants and rationalize the obtained trends with thermochemical cycles and valence bond schemes. In general, the rate determining hydrogen atom abstraction barrier is dependent on the π_{xz}/π^*_{xz} energy splitting along the Fe–O bond, the excitation energy from π_{xz} to a_{2u}, as well as the bond dissociation energies of the methane C–H bond and the newly formed O–H bond. Our studies predict that iron(IV)-oxo porphyrin cation radical models with hydroxide as axial ligand should be efficient oxidants of substrate hydroxylation reactions and able to activate methane at room temperature. However, changing the axial ligand to a weaker electron donating group decreases its activity and raises the hydrogen atom abstraction barriers dramatically. These studies show that subtle modifications to the oxidant can have a great impact on the catalytic ability of the active center.

Keywords: cytochrome P450, Compound I, hydroxylation, hydrogen abstraction, valence bond, density functional theory.

1. Introduction

Methane hydroxylation is a challenging chemical process that few enzymatic systems are able to perform due to the strength of the methyl C–H bond that needs to be broken in the process. Nature has developed only a single class of enzymes that perform this task efficiently, namely the methane monoxygenases (Balasubramanian *et al.,* 2007; Shiota *et al.,.,* 2009; Himes *et al.,* 2010). These are generally dicopper enzymes that utilize molecular oxygen and convert methane to methanol. Nature utilizes a large range of metalloenzymes with a broad functional scope, yet most of these enzymes cannot activate methane. For instance, non-heme iron dioxygenases are efficient oxidants of hydrogen atom abstraction and oxygen atom transfer reactions and therefore are well studied. In particular, the non-heme iron enzymes taurine/α-ketoglutarate dioxygenase (de Visser,

---

[1] Department of Applied Physics, School for Physical Sciences, Babasaheb Bhimrao Ambedkar University, VidyaVihar, Rai Bareilly Road, Lucknow 226 025, India.

[2] Manchester Institute of Biotechnology and School of Chemical Engineering and Analytical Science, The University of Manchester, 131 Princess Street, Manchester M1 7DN, United Kingdom.

*Corresponding Author Email: sam.devisser@manchester.ac.uk

2006a,b; de Visser, 2007a; de Visser, 2009), prolyl-4-hydroxylase (Karamzadeh *et al.,* 2010) and cysteine dioxygenase (Aluri *et al.,* 2007; de Visser *et al.,* 2009a; Kumar *et al.,* 2011a; Kumar *et al.,* 2012a; Sallmann *et al.,* 2015) are known to react with substrates efficiently with large turnover numbers. Our computational modelling predicted relatively small hydrogen atom abstraction barriers of methane by the high-valent iron(IV)-oxo intermediate of taurine/α-ketoglutarate dioxygenase (Latifi *et al.,*., 2009), but so far no experimental support of methane hydroxylation by non-heme iron enzymes exists. Similarly, heme monoxygenases, which are considered as highly efficient in hydrogen atom abstraction processes, do not naturally utilize methane during their activity either (Meunier *et al.,* 2004; Abu-Omar *et al.,* 2005; Kryatov *et al.,* 2005; Shaik *et al.,* 2005; de Visser *et al.,* 2011a).

Cytochrome P450 enzymes are heme-based monoxygenases found in all forms of life and have important biochemical functions that essentially include the chemical modification of substrates. Thus, they are involved in the biosynthesis of hormones, such as estrogen.In addition, the P450s catalyze the metabolism of drugs (Ji *et al.,* 2015) and the detoxification of xenobiotics in the liver (Munro *et al.,* 2007). The P450s have a characteristic structure with a central protoporphyrin IX group (heme) that is attached to the protein via an Fe–S linkage using a conserved cysteinate residue of the protein; the axial ligand. Figure 1 displays the active site structure of the mammalian P450 isozyme P450$_{2C5}$ with the drug molecule diclofenac bound, as taken from the crystal structure coordinates (Wester *et al.,* 2003). The substrate is located in a tight binding pocket and is positioned in such a way that promotes a regioselective and stereospecific oxidation. The heme is linked to the protein via an interaction of the metal with a cysteinate group in the axial position. In addition, the heme is placed in position through a number of hydrogen bonding interactions, for instance, toward the propionate side chains of the heme. Molecular oxygen binds *trans* to the cysteinate moiety, i.e. on the distal site.Prior to substrate hydroxylation, however, the heme needs to be activated and an active species is generated. This process includes the binding of molecular oxygen, two reduction and two protonation steps and ultimately leads to the formation of a high-valent iron(IV)-oxo heme cation radical species, called Compound I (Cpd I) (Meunier *et al.,* 2004; Shaik *et al.,* 2005; de Visser *et al.,* 2003). The P450s, therefore, have an intricate hydrogen bonding network surrounding the heme active site that delivers protons (Kumar *et al.,* 2005b). Interestingly, hydrogen bonding interactions, for instance through water molecules, were found to affect also reaction barriers of substrate activation, and, hence they are often non-innocent (Sharma *et al.,* 2003b; Sharma *et al.,* 2004; Kumar *et al.,* 2005c). Moreover, the spin state ordering and relative energies often gives a dependence on environmental effects, such as hydrogen bonding (Sahoo *et al.,* 2015) or a point charge (de Visser, 2005).

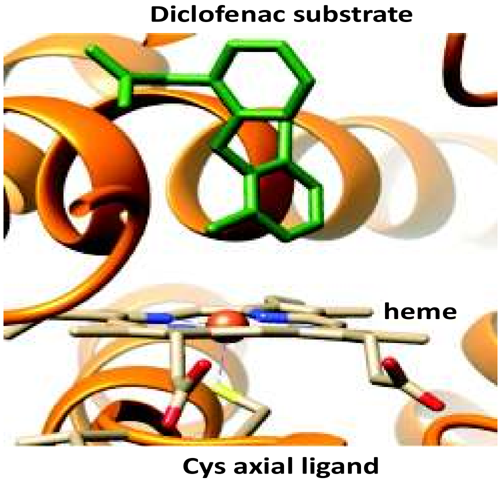

Figure 1: Extract of the active site of P450$_{2C5}$ with substrate diclofenac bound.

P450s are efficient oxidants in nature and react with substrates via aliphatic hydroxylation (Shaik *et al.,* 2005), aromatic hydroxylation (de Visser *et al.,* 2003b; de Visser 2006e; de Visser *et al.,* 2007; Hazan*et al.,* 2007; de Visser *et al.,* 2009b; Kumar *et al.,* 2012b; Latifi *et al.,* 2012a; Sahu *et al.,* 2013), olefin epoxidation (de Visser*et al.,* 2001a,b,c; Ogliaro *et al.,* 2002b; de Visser *et al.,* 2002a,b; de Visser *et al.,* 2003c; de Visser *et al.,* 2004b; Kumar *et al.,* 2005a,d; de Visser 2006a,b,c,d,g; de Visser 2008; de Visser *et al.,* 2008b; Kumar *et al.,* 2010; Kumar *et al.,* 2013;Sainna*et al.,* 2015a)) and sulfoxidation (Sharma *et al.,* 2003b; Kumar *et al.,* 2005e; Kumar *et al.,* 2011b; Prokop *et al.,* 2011).

Enzymes with a structure closely resembling the P450 active site feature, are, for instance, the peroxidases and catalases, but these systems lack the cysteinate axial ligand of P450.Instead, the peroxidases and catalases contain either a histidine or a tyrosinate axial ligand, respectively (Veitch *et al.,* 2000; Vidossich *et al.,* 2012). The difference in chemical structure of the P450s, on the one hand, and peroxidases and catalases, on the other hand, has led to speculation that the axial ligand is responsible for the change in reactivity and the chemical properties of these enzymes. Indeed, quantum chemical calculations of Cpd I with either a cysteinate, a histidine or a tyrosinate axial ligand as mimics of Cpd I of P450, horseradish peroxidase and catalase, respectively, showed dramatic differences in their electron affinities, and, consequently their ability to pick up electrons from substrates (de Visser *et al.,* 2003a; de Visser 2005; de Visser 2006f). This was further highlighted through a push-effect of electron density from the axial ligand upon the heme and, in particular, the mixing of a lone pair of the axial ligand with the heme a_{2u} orbital (Ogliaro *et al.,* 2002a).

In order to understand spectroscopic and reactivity differences of these enzyme classes, synthetic model complexes have been developed: the so-called biomimetic models (Bruijnincx *et al.,* 2008; Costas 2011). Thus, Gross *et al.,* (Gross *et al.,* 1994) showed that for synthetic iron(III)-porphyrins, there was an axial ligand effect on the reactivity differences of the various complexes but there also were spectroscopic differences as a result of binding an alternative axial ligand. Theoretical modelling can assist in understanding the fundamental differences inreactivities and establish the key factors that determine the reaction mechanism. To gain insight into the axial ligand effect of iron-porphyrins, we investigated the properties and reactivities of a range of iron(IV)-oxo porphyrin cation radical models with varying axial ligand description:**1**$_X$, X = F$^-$, Cl$^-$, CN$^-$, OH$^-$, CH$_3$COO$^-$, CF$_3$COO$^-$ and SH$^-$, see Figure 2. We then studied the reaction of a selection of these oxidants with methane on the doublet and quartet spin state surfaces and compare reactivity differences and how this is affected by the axial ligand of the oxidant.

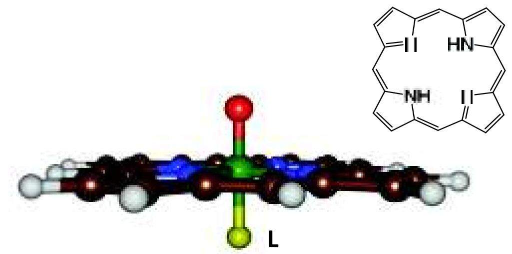

L = F$^-$, Cl$^-$, CN$^-$, OH$^-$, CH$_3$COO$^-$, CF$_3$COO$^-$, SH$^-$

Figure 2: Chemical structure of the reactants studied in this work.

2. Methods

The studies presented in this work use density functional theory methods as implemented in the *Gaussian*-03 program package (Frisch *et al.,* 2013). Following previous experience in the field (Quesne *et al.,* 2014; de Visser *et al.,* 2014; Sainna *et al.,* 2015b), we use the unrestricted hybrid density functional method UB3LYP (Becke, 1993; Lee *et al.,* 1988) in combination with a double-ζ quality LACVP basis set on iron and 6-31G on the rest of the atoms: basis set BS1 (Hay *et al.,* 1985). We performed a full geometry optimization (without constraints) followed by an analytical frequency. All reactant structures were confirmed as local minima and had no imaginary frequencies. Single point calculations using a triple-ζ quality LACV3P+ basis set on iron and 6-311+G* on the rest of the atoms energies were used throughout: basis set BS2. All data reported here include zero-point corrections and solvent corrections using an acetonitrile solvent.

Subsequently, we investigated methane hydroxylation by several iron (IV)-oxo oxidants. We optimized a reactant complex, radical intermediate and product complex at UB3LYP/BS1 on the doublet and quartet spin state surfaces. Extensive geometry scans linking reactants with radical intermediates and of radical intermediates with products were performed. The maxima of these scans were used as starting points for the transition state searches and established first order saddle points characterized by a single imaginary frequency for the correct mode.

Previously, we tested the effect of substituents to the periphery of the porphyrin scaffold and found few changes to the chemical structures and reactivities (Kumar *et al.,* 2009; Neu *et al.,* 2014). Furthermore, full geometry optimization with basis set BS2 reproduced all calculations well. The methods and procedures used here were extensively tested and benchmarked and, for instance, were found to reproduce experimental rate constants within about 4 kcal mol^{-1} (Vardhaman *et al.,* 2011; Vardhaman *et al.,* 2013a; Jastrzebski *et al.,* 2014) but also reproduce experimental infrared spectra (de Visser 2008,) and resonance Raman spectra (Draksharapu *et al.,* 2015).

3. Results and Discussion

Before going through the reactivity studies, let us first discuss one of the reactant complexes, namely (Fe^{IV}(O)(Por$^{+\bullet}$)F) or $\mathbf{1}_F$, in more detail as an example of a Compound I model. Figure 3 displays the high-lying occupied and low-energy virtual orbitals that are relevant for the electronic description and the subsequent reactivity with methane. The molecular orbitals follow close analogy to those found for P450 Compound I (Ogliaro *et al.,* 2000b; Ogliaro *et al.,* 2001a,b; Sainna *et al.,* 2015a). The metal orbitals form bonding and antibonding pairs of orbitals, e.g. there is a pair of π_{xz}/π^*_{xz} set of orbitals for the interaction of the 3d$_{xz}$(Fe) with 2p$_x$(O). Similarly, the atomic 3d$_{yz}$(Fe) and 2p$_y$(O) mix to form the π_{yz}/π^*_{yz} pair of orbitals. In addition, there is a nonbonding orbital in the plane of the porphyrin ring: δ_{x2-y2}. Finally, two virtual orbitals for the σ* interactions along the O–Fe axis (σ^*_{z2}) and in the plane of the porphyrin ring (σ^*_{xy}) complete the set of iron-type orbitals. In addition to the metal-type orbitals there are two π-orbitals for the conjugated porphyrin system high-lying, which under D$_{4h}$ symmetry have the labels a$_{1u}$ and a$_{2u}$. The latter orbital strongly mixes with a lone-pair orbital on the axial ligand and influences the electron affinity of the oxidant strongly, see below.

The set of orbitals displayed in Figure 3 is occupied with the following configuration: ^{4,2}Compound I = $\pi_{xz}{}^{2}\pi_{yz}{}^{2}\delta_{x2-y2}{}^{2}\pi^*_{xz}{}^{1}\pi^*_{yz}{}^{1}\sigma^*_{z2}{}^{0}\sigma^*_{xy}{}^{0}a_{1u}{}^{2}\ a_{2u}{}^{1}$. The three unpaired electrons in the system are either ferromagnetically coupled into a quartet spin state (^{4}A$_{2u}$ state) or the two π* electrons are up-spin and the a$_{2u}$ electron down-spin to give it an overall doublet spin state (^{2}A$_{2u}$ state). These two spin states are close in energy and for all systems considered here they fall within 1 kcal mol^{-1}.

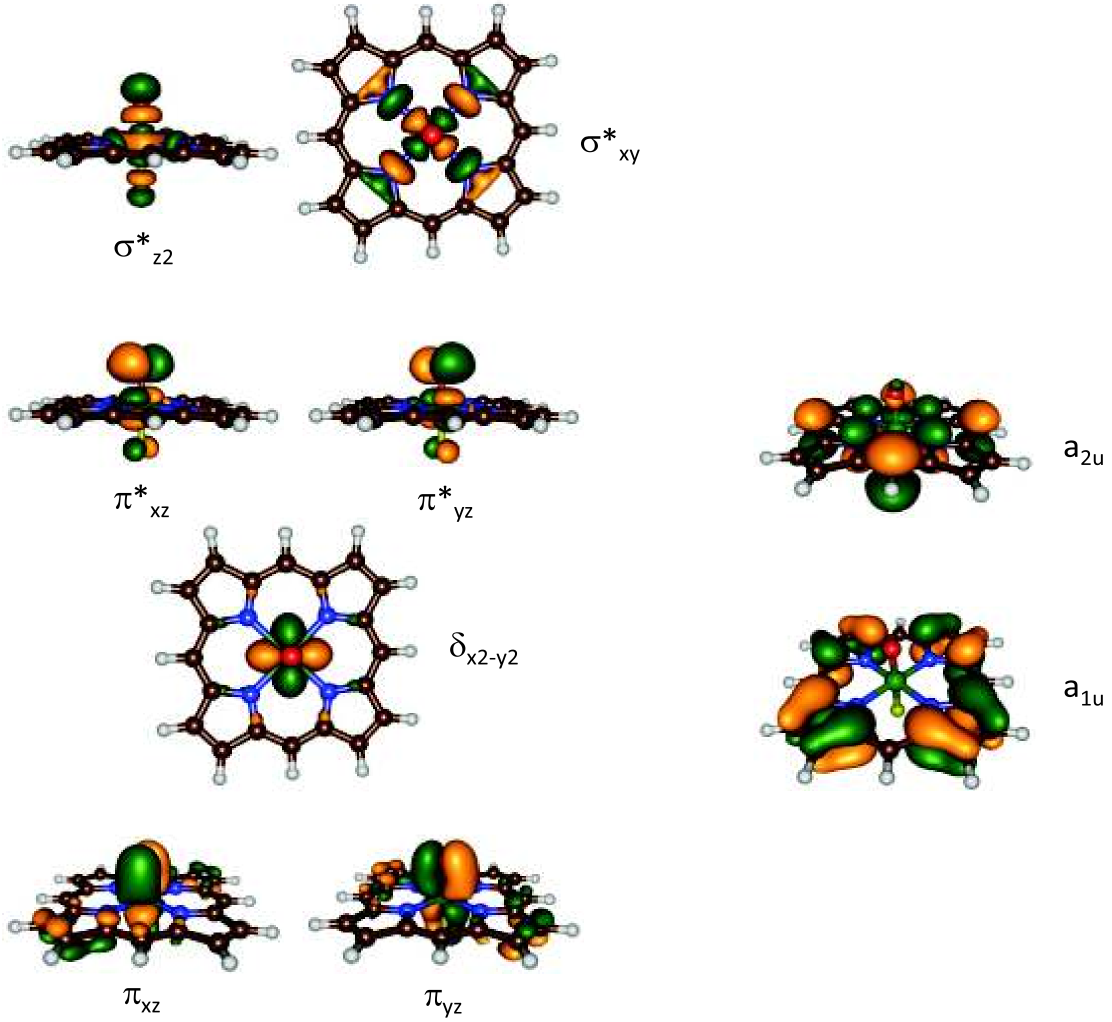

Figure 3: Molecular orbitals of $\mathbf{1}_F$.

Next, we did a geometry optimization of doublet and quartet iron(IV)-oxo porphyrin cation radical models with varying axial ligands, namely, $^{2,4}\mathbf{1}_X$ with X = CF_3COO^-, CH_3COO^-, Cl^-, F^-, ImH (imidazole), acetonitrile, OH^- and SH^-.Key geometric and vibrational parameters obtained for the doublet spin state structures are given in Figure 4. As follows from the data shown in Figure 4, the Fe–O distances vary strongly dependent on the axial ligand bound to the iron-porphyrin system. Thus, an axially ligated fluoride ligand gives a relatively long Fe–O distance of 1.681 Å, whereas a neutral acetonitrile molecule bound gives a much shorted Fe–O bond of 1.645 Å. This is further reduced to 1.630 Å when the axial ligand is removed altogether (Sainna *et al.,* 2015a). The opposite trends are found for the Fe–O stretch vibration (π_{FeO}), whereby an axial thiolate ligand gives the highest mode at 870.6 cm^{-1}. Strong electron-donating axial ligands, such as F^- and OH^-, by contrast, give dramatically reduced Fe–O stretch vibrations of the order of 817.7 and 816.6 cm^{-1}, respectively. Note that without an axial ligand the Fe–O vibration is located at 920.0 cm^{-1}. Consequently, the axial ligand affects the strength of the Fe–O bond and as a result the Fe–O frequency is shifted by about 100 cm^{-1}. This will have major effects on the oxygen atom transfer reaction with substrates.

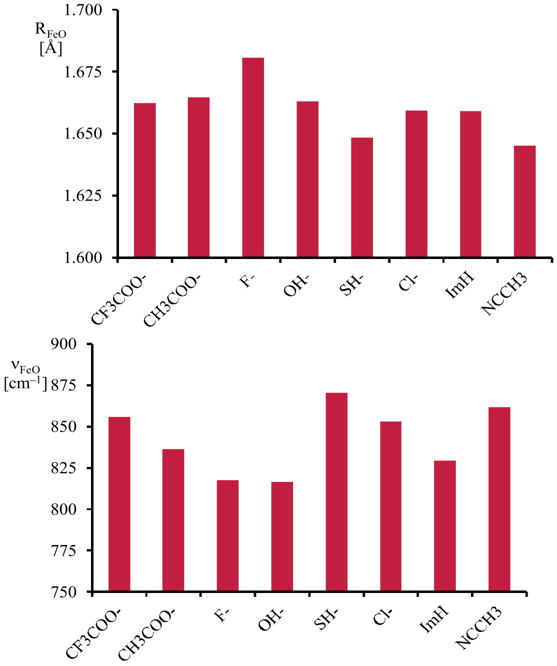

Figure 4: (a) Fe–O bond distance (R_{FeO}) for various complexes $^{2}\mathbf{1}_X$. (b) Fe–O stretch vibration (□$_{FeO}$) for various complexes $^{2}\mathbf{1}_X$.

We subsequently investigated the methane hydroxylation mechanism by $^{2,4}\mathbf{1}_X$ with X = OH^{-}, F^{-} and CN^{-}. As an example, the potential energy profile of methane hydroxylation by $^{2,4}\mathbf{1}_{OH}$ is shown in Figure 5, the results for $^{2,4}\mathbf{1}_F$ and $^{2,4}\mathbf{1}_{CN}$ are very similar. The reaction is stepwise with an initial hydrogen atom abstraction via transition state **TS**$_{HA}$ leading to an iron(IV)-hydroxo complex with a radical, **IM**. The OH and radical are combined via a rebound transition state **TS**$_{reb}$ to form the alcohol products **P**. This mechanism is analogous to earlier hydrogen atom abstraction reactions calculated for similar complexes and substrates (Ogliaro *et al.,* 2000; de Visser *et al.,* 2002a,b; Sharma *et al.,* 2003a; Kumar *et al.,* 2003; Kumar *et al.,* 2004a,b; de Visser *et al.,* 2004a; Shaik *et al.,* 2004b; Kumar *et al.,* 2005a; de Visser 2006a,b,c,d,e; Wang *et al.,* 2007; de Visser, 2007b; de Visser *et al.,* 2008a; Godfrey *et al.,* 2008; Shaik *et al.,* 2008; Heyes *et al.,* 2009; Kim *et al.,* 2009; de Visser *et al.,* 2009; Latifi*et al.,* 2009; Tahsini *et al.,* 2009; Kumar *et al.,* 2009; de Visser, 2010; Prokop *et al.,* 2010; Karamzadeh *et al.,* 2010; de Visser *et al.,* 2011b; Latifi *et al.,* 2011a,b; de Visser 2012; Latifi *et al.,* 2012a,b; de Visser, 2013; de Visser *et al.,* 2013; Latifi *et al.,* 2013; Pratter *et al.,* 2013; Vardhaman *et al.,* 2013b; Kumar *et al.,* 2014; Karamzadeh *et al.,* 2014; Ji *et al.,* 2015). As described before, the rebound barriers are small on the high-spin surface and negligible on the low-spin surface, which is also seen here (Shaik *et al.,* 2004a).

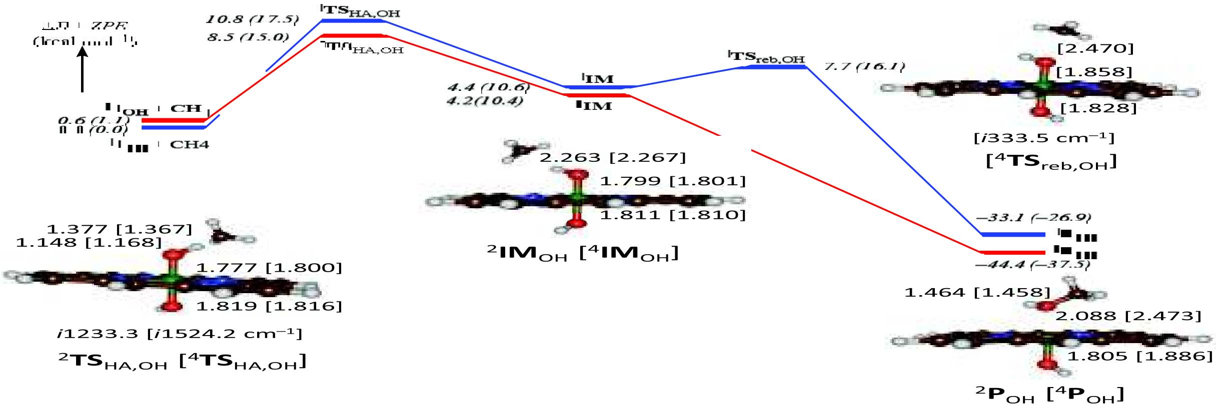

Figure 5: Potential energy landscape of methane hydroxylation by $^{2,4}\mathbf{1}_{OH}$ with energies in kcal mol^{-1}. All energies obtained with UB3LYP/BS2//UB3LYP/BS1 and contain ZPE corrections. Values given out of parenthesis refer to gas-phase data and those inside parenthesis include solvent corrections. Optimized geometries of local minima and transition states give bond lengths in angstroms and the imaginary frequency in the transition state in wave numbers.

For ^{2,4}**1**$_{OH}$, small hydrogen atom abstraction barriers of 8.5 (10.8) kcal mol^{-1} on the doublet (quartet) spin states are found in the gas-phase, whereas those with a dielectric continuum included with □= 4.7 are raised to 15.0 (17.5) kcal mol^{-1}. Nevertheless, these barriers are accessible at room temperature and imply that ^{2,4}**1**$_{OH}$ should be able to hydroxylate methane efficiently. The hydrogen atom abstraction barriers are narrow with a large imaginary frequency of *i*1233.3 (*i*1524.2) cm^{-1}, which implies they will proceed with a large kinetic isotope effect for replacing the transferring hydrogen atom by deuterium (Kumar *et al.,* 2004a; de Visser, 2006e). Geometrically, the barriers are late with long C–H bonds and much shorter O–H bonds, similarly to H-atom abstraction barriers calculated before for methane by (Fe^{IV}(O)(Por$^{+\bullet}$)SH), (de Visser *et al.,* 2004).

After H-atom abstraction a radical intermediate is formed representing an (Fe^{IV}(OH)(Por)OH) complexed to $CH_3^{\bullet}$ with a small exothermicity of 4.2 (4.4) kcal mol^{-1} for ^{2}**IM**$_{OH}$ (^{4}**IM**$_{OH}$), respectively. The rebound barrier is negligible on the low-spin surface, whereas a OH rebound barrier of 3.5 kcal mol^{-1} is obtained in the high-spin state. The overall mechanism to form alcohols is strongly exothermic as expected.

Subsequently, we replaced the OH axial ligand of ^{2,4}**1**$_{L}$ by alternative ligands, namely $L = F^{-}$ and CN^{-} and the results are given in Table 1. In general, the potential energy profile for all complexes follows the same pattern as that seen in Figure 5, with a rate determining hydrogen atom abstraction barrier and negligible rebound barrier at the low-spin pathway. The only differences obtained are due to the axial ligand interactions with the metal and oxygen atom.

Table 1: Relative energies (ΔE+ZPE, in kcal mol^{-1}) of local minima and transition states for methane hydroxylation by ^{2,4}1$_{L}$, L = OH^{-}, F^{-}, and CN^{-}. Values in the gas-phase and in solvent are in given.

	$L = OH^{-}$		$L = F^{-}$		$L = CN^{-}$	
	gas	solvent	gas	solvent	gas	solvent
^{4}**1**$_{L}$	0.0	0.0	0.0	0.0	0.0	0.0
^{2}**1**$_{L}$	0.6	1.1	2.1	2.6	0.6	1.1
^{4}**TS**$_{HA}$	10.8	17.5	15.5	22.2	18.4	25.1
^{4}**IM**	4.4	10.6	9.2	15.4	13.0	19.2
^{4}**TS**$_{reb}$	7.7	16.1	ND	ND	ND	ND
^{4}**P**$_{L}$	-33.1	-26.9	ND	ND	ND	ND
^{2}**TS**$_{HA}$	8.5	15.0	26.2	32.7	16.3	22.8
^{2}**IM**	4.2	10.4	9.0	15.2	13.2	19.4
^{2}**P**$_{L}$	-44.4	-37.5	ND	ND	ND	ND

ND = not determined.

The studies presented in Table 1 implicate that the axial ligand has a profound effect on the catalytic efficiency and performance of the active oxidant. This is not surprising and has been seen before for the reactivity of iron (IV)-oxo porphyrin radical cation models with substrates (de Visser, 2006d; Wang *et al.,* 2007; de Visser *et al.,* 2009b; de Visser 2010; Kumar *et al.,* 2013). To understand the electronic features of the reaction mechanism and find factors that determine the rate constant we set up a valence bond (VB) curve crossing diagram, see Figure 6. Previously, we used the VB technique to rationalize the hydrogen atom abstraction reactions of heme and non-heme iron(IV)-oxo complexes (Shaik *et al.,* 2008; Latifi *et al.,* (2009); de Visser, 2010; Ji *et al.,* 2015) as well as double bond epoxidation reactions (Kumar *et al.,* 2010; Sainna*et al.,* 2015a) and sulfoxidation reactions (Kumar *et al.,* 2011b).

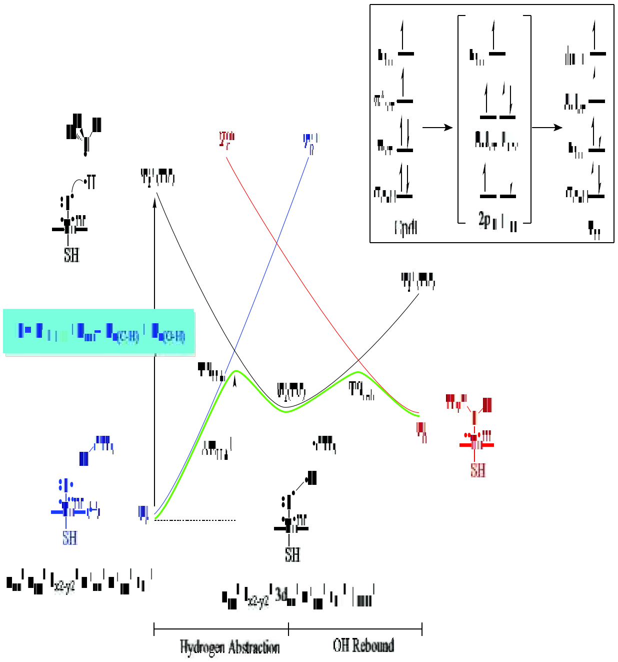

Figure 6: Valence bond curve crossing diagram rationalizing the methane hydroxylation reaction by P450 Cpd I. Dots represent valence electrons and lines (curved or straight) are chemical bonds.

Thus, in VB one starts on the left-hand-side with the reactant state $\square_{r}$, which in our case is Compound I and substrate (methane). The reactant state is connected to an excited state in the radical intermediate as well as in the product geometry. Similarly, the product state $\square_{p}$, although the ground state in the product geometry, is an excited state in the radical intermediate and reactant geometries. The radical intermediate state ($\square_{I}$) bisects the reactant and product wave functions and creates a stepwise hydrogen atom abstraction-radical rebound mechanism by creating a stable radical intermediate. The height of the barrier for hydrogen atom abstraction ($\Delta E_{HA}^{\ddagger}$) is equal to the energy where the two curves cross, e.g. crossing point of the blue and black lines, minus the geometric distortion (resonance energy *B*) upon moving from reactants to the transition state. It has been shown previously (Shaik *et al.,* 2008) that the curve crossing energy is a fraction (usually with value of 0.3) of the excitation energy (*G*) from the reactant state ($\square_{r}$) to the radical intermediate state ($\square_{I}$*) in the geometry of the reactants. The analysis of the VB structures for the reactant and excited states enables one to determine the factors that influence the barrier. The VB structures give dots for key valence electrons. For instance, in Compound I the π_{xz}/π^*_{xz} set of orbitals has three electrons, which is given on the right-hand-side of the Fe–O bond with three dots. Similarly, the π_{yz}/π^*_{yz} pair of orbitals have three electrons and these are given with three dots on the left-hand-side of the Fe–O bond. In addition, there is of course a radical on the porphyrin ring for single occupation of the a_{2u} orbital. Two electrons occupy the C–H bond of the substrate.

A look at the VB structure of the radical intermediate shows the same π_{yz}/π^*_{yz} occupation with three electrons, however, the π_{xz}/π^*_{xz} set of orbitals has ceased to exist and has reverted back into atomic orbitals ($3d_{xz}$ and $2p_{x}$). The $3d_{xz}$ orbitals remains as a nonbonding orbital and singly occupied, while the $2p_{x}$ orbital on the oxo group pairs up with the 1s orbital of the incoming hydrogen atom to form the new O–H bond (σ_{OH}). As the π_{xz}/π^*_{xz} set of orbitals had three electrons, this implies that one of these electrons will have to move to another orbital and indeed fills the a_{2u} orbital with a second electron. This change in orbitals is summarized and highlighted in the inset of Figure 6.

As a result, the hydrogen atom abstraction barrier will depend on the energy to split the π_{xz}/π^*_{xz} orbitals back into atomic orbitals (E_{π/π^*xz}) and an electron excitation from π_{xz} to a_{2u} (E_{exc}). In addition, the excitation energy refers to the breaking of the C–H bond and the formation of the O–H bond. The bond dissociation energy (BDE_{CH}) of the C–H bond of methane is ΔE+ZPE = 101.6 kcal mol^{-1} (Shaik *et al.,* 2008). We calculated the O–H bond strength from Eq 1 for $\mathbf{1}_L$ with L = F^-, Cl^-, OH^-, CH_3COO^-, CF_3COO^- and SH^-, see Table 2. As follows the strength of the O–H bond that is formed varies by as much as 14 kcal mol^{-1} between L = CF_3COO^- and L = OH^-.

$$(Fe^{IV}(OH)(Por)L) \rightarrow (Fe^{IV}(O)(Por^{+\bullet})L) + H^{\bullet} + BDE_{OH} \quad (1)$$

Table 2: Calculated thermochemical properties (ΔE+ZPE) for selected $\mathbf{1}_L$ species (L = CF_3COO^-, Cl^-, SH^-, CH_3COO^-, F^- and OH^-). All energies are in kcal mol^{-1}.

	BDE_{OH}	$EA(\mathbf{1}_L)$	ΔH_{acid}	BDE_{FeL}	$E\pi/\pi^*_{xz}$	E_{exc}
CF_3COO^-	85.4	85.8	314.3	90.7	ND	ND
Cl^-	87.6	79.2	305.5	ND	ND	ND
SH^-	89.3	71.6	296.3	112.2	81.2	88.2
CH_3COO^-	89.4	80.5	305.0	103.6	75.5	84.8
F^-	94.0	78.9	298.8	128.4	86.3	86.0
OH^-	99.4	76.0	290.5	137.5	75.2	79.4

In addition to the BDE_{OH} values for the oxidants, we calculated several other thermochemical properties. Firstly, we calculated the electron affinity (EA) of all complexes $\mathbf{1}_L$ from the difference in energy of $^4\mathbf{1}_L$ and its one-electron reduced species ($^3\mathbf{1}_L^-$). Technically, a hydrogen atom transfer is the sum of an electron and a proton transfer, so that the BDE_{OH} can be split into a the electron affinity of the oxidant, the acidity of the iron(IV)-hydroxo complex (ΔH_{acid}) and the ionization potential of a hydrogen atom (IE_H), Eq 2. The latter we took from the NIST database (Linstrom *et al.,* 2014) and has a value IE_H = 313.9 kcal mol^{-1}.

$$BDE_{OH} = EA(\mathbf{1}_L) - \Delta H_{acid} + IE_H \quad (2)$$

As discussed above, the electron affinity of $\mathbf{1}_L$ is dependent on the amount of mixing of the axial ligand orbitals with the a_{2u} orbital on the porphyrin. With L = SH^- this interaction is strong and as a consequence $\mathbf{1}_{SH}$ has a very low EA of 71.6 kcal mol^{-1}. A weak anionic ligand like CF_3COO^- gives weak interactions with the a_{2u} orbital and has a considerably higher EA of 85.8 kcal mol^{-1}. Neutral axial ligands, such as a solvent molecule or a imidazole group of a histidine give a further rise in electron affinity and removal of the axial ligand altogether gives a maximum electron affinity of about 8.2 eV (Sainna *et al.,* 2015a) as determined by mass spectrometry.

The BDE_{OH} value of the various complexes depends on the electron affinity and ΔH_{acid} differences of the complex. As mentioned the electron affinity differences depend on the mixing of axial ligand and a_{2u} orbitals. The ΔH_{acid} value, however, contains an electronic component for the splitting of the π_{xz}/π^*_{xz} orbitals back into atomic orbitals and formation of the O–H bond. We analyzed the orbitals of the complexes in detail and determined the $E\pi/\pi^*_{xz}$ and E_{exc} energy gaps and report those in the last two columns of Table 2. Both parameters vary by as much as 10 kcal mol^{-1} for the four iron (IV)-oxo species studied. The smaller the π_{xz}/π^*_{xz} energy splitting and the smaller the excitation energy from π_{xz} to a_{2u}, the lower in energy the hydrogen atom abstraction barrier will be.

4. Conclusions

In this work a series of computational studies are presented on the methane hydroxylation mechanism of models of Compound I of cytochrome P450, whereby the axial ligand is replaced by alternative anionic ligands. The work shows that an axial ligand at a distance well over 4 Å from the reaction center has a profound effect on the catalytic properties of the oxidant. We identified several key components. Firstly, there are thermochemical impacts on the electron affinity and iron (IV)-hydroxo acidity due to differences in orbital occupation. In addition, during the rate determining hydrogen atom abstraction the π-bond of the iron-oxo group needs to be broken and the π_{xz}/π^*_{xz} energy splitting affect the hydrogen atom abstraction. Finally, during the hydrogen atom abstraction step an electron migrates from the oxo group to the heme. In general, a hydroxide axial ligand gives small reaction barriers, and should be the best oxidant.

Acknowledgements

The National Service of Computational Chemistry Software (NSCCS) is thanked for providing CPU time.

References

1. Abu-Omar MM, Loaiza A and Hontzeas N (2005). Reaction mechanisms of mononuclear non-heme iron oxygenases. *Chem. Rev.*, 105: 2227–2252.
2. AluriS and de Visser SP (2007).The mechanism of cysteine oxygenation by cysteine dioxygenase enzymes. *J. Am. Chem. Soc.*, 129: 14846–14847.
3. Balasubramanian R and Rosenzweig AC (2007).Structural and mechanistic insights into methane oxidation by particulate methane monooxygenase. *Acc. Chem. Res.*, 40: 573–580.
4. Becke AD (1993). Density functional thermochemistry. III. The role of exact exchange. *J. Chem. Phys.*, 98: 5648–5652.
5. Bruijnincx PCA, van Koten G and Klein Gebbink RJM (2008). Mononuclear non-heme iron enzymes with the 2-His-1-carboxylate facial triad: recent developments in enzymology and modeling studies. *Chem. Soc. Rev.*, 37: 2716–2744.
6. Costas M (2011). Selective C–H oxidation catalyzed by metalloporphyrins. *Coord. Chem. Rev.*, 255: 2912–2932.
7. de Visser SP (2005). What affects the quartet-doublet energy splitting in peroxidase enzymes? *J. Phys. Chem. A*, 109: 11050–11057.
8. de Visser SP (2006a). Propene activation by the oxo-iron active species of taurine/□-ketoglutarate dioxygenase (TauD) enzyme. How does the catalysis compare to heme-enzymes? *J. Am. Chem. Soc.*, 128: 9813–9824.
9. de Visser SP (2006b). Differences in and comparison of the catalytic properties of heme and non-heme enzymes with a central oxo-iron group.*Angew. Chem. Int. Ed.*, 45: 1790–1793.
10. de Visser SP (2006c). What factors influence the ratio of C–H hydroxylation versus C=C epoxidation by a nonheme cytochrome P450 biomimetic? *J. Am. Chem. Soc.*, 128: 15809–15818.
11. de Visser (2006d). The axial ligand effect of oxo-iron porphyrin catalysts. How does chloride compare to thiolate? *J. Biol. Inorg. Chem.*, 11: 168–178.
12. de Visser (2006e). Substitution of hydrogen by deuterium changes the regioselectivity of ethylbenzene hydroxylation by an oxo-iron-porphyrin catalyst. *Chem. Eur. J.*, 12: 8168–8177.
13. de Visser SP (2006f). What external perturbations influence the electronic properties of catalase Compound I?*Inorg. Chem.*, 45: 9551–9557.
14. de Visser SP (2006g). Can the replacement of a single atom in the enzyme horseradish peroxidase convert it into a monoxygenase? A density functional study. *J. Phys. Chem. B*, 110: 20759–20761.
15. de Visser SP (2007a). Can the peroxosuccinate complex in the catalytic cycle of taurine/□-ketoglutarate dioxygenase (TauD) act as an alternative oxidant? *Chem. Commun.*: 171–173.
16. de Visser SP (2007b). Preferential hydroxylation over epoxidation catalysis by a horseradish peroxidase mutant: a cytochrome P450 mimic. *J. Phys. Chem. B*, 111: 12299–12302.
17. de Visser SP (2008). Is the □-oxo-□-peroxodiiron intermediate of a ribonucleotide reductase biomimetic a possible oxidant of epoxidation reactions? *Chem. Eur. J.*, 14: 4533–4541.
18. de Visser SP (2009). Elucidating enzyme mechanism and intrinsic chemical properties of short-lived intermediates in the catalytic cycles of cysteine dioxygenase and taurine/□-ketoglutarate dioxygenase. *Coord. Chem. Rev.*, 253: 754–768.
19. de Visser SP (2010). Trends in substrate hydroxylation reactions by heme and nonheme iron(IV)-oxo oxidants give correlations between intrinsic properties of the oxidant with barrier height. *J. Am. Chem. Soc.*, 132: 1087–1097.
20. de Visser SP (2012). Predictive studies of oxygen atom transfer reactions by Compound I of cytochrome P450: aliphatic and aromatic hydroxylation, epoxidation and sulfoxidation. *Adv. Inorg. Chem.*, 64: 1–31.
21. de Visser SP (2013). Differences in chemical properties and reactivity patterns of mono- and dioxomanganese(V) porphyrins as revealed by density functional theory. *J. Porph. Phthalocyanines*, 17: 954–963.

22. de Visser SP, Ogliaro F, Harris N and Shaik S (2001a). Multi-state epoxidation of ethene by cytochrome P450: a quantum chemical study. *J. Am. Chem. Soc*., 123: 3037–3047.
23. de Visser SP, Ogliaro F and Shaik S (2001b). How does ethene inactivate cytochrome P450 en route to its epoxidation? A density functional study. *Angew. Chem. Int. Ed*., 40: 2871–2874.
24. de Visser SP, Ogliaro F and Shaik S (2001c). Stereospecific oxidation by Compound I of cytochrome P450 does not proceed in a concerted synchronous manner? *Chem. Commun*.: 2322–2323.
25. de Visser SP, Ogliaro F, Sharma PK and Shaik S (2002a). Hydrogen bonding modulates the selectivity of enzymatic oxidation by P450: a chameleon oxidant behavior of Compound I. *Angew. Chem. Int. Ed*., 41: 1947–1951.
26. de Visser SP, Ogliaro F, Sharma PK and Shaik S (2002b). What factors affect the regioselectivity of oxidation by cytochrome P450? A DFT study of allylic hydroxylation and double bond epoxidation in a model reaction.*J. Am. Chem. So*c., 124: 11809–11826.
27. de Visser SP, Shaik S, Sharma PK, Kumar D and Thiel W (2003a). Active species of horseradish peroxidase (HRP) and cytochrome P450: two electronic chameleons.*J. Am. Chem. Soc*., 125: 15779–15788.
28. de Visser SP and Shaik S (2003b). A proton-shuttle mechanism mediated by the porphyrin in benzene hydroxylation by cytochrome P450 enzymes.*J. Am. Chem. Soc*., 125: 7413–7424.
29. de Visser SP, Kaneti J, Neumann R and Shaik S (2003c). Fluorinated alcohols enable olefin epoxidation by H2O2: template catalysis.*J. Org. Chem*., 68: 2903–2912.
30. de Visser SP, Kumar D, Cohen S, Shacham R and Shaik S (2004a). A predictive pattern of computed barriers for C–H hydroxylation by Compound I of cytochrome P450.*J. Am. Chem. Soc*., 126: 8362–8363.
31. de Visser SP, Kumar D and Shaik S (2004b). How do aldehyde side products occur during alkene epoxidation by cytochrome P450? Theory reveals a state-specific multi-state scenario where the high-spin component leads to all side products.*J. Inorg. Biochem*., 98: 1183–1193.
32. de Visser SP, Oh K, Han A-R and Nam W (2007). Combined experimental and theoretical study on aromatic hydroxylation by mononuclear nonheme iron(IV)-oxo complexes. *Inorg. Chem*., 46: 4632–4641.
33. de Visser SP and Tan LS (2008a). Is the bound substrate in nitric oxide synthase protonated or neutral and what is the active oxidant that performs substrate hydroxylation? *J. Am. Chem. Soc*., 130: 12961–12974.
34. de Visser SP and Nam W (2008b). The effect and influence of cis-ligands on the electronic and oxidizing properties of nonheme oxoironbiomimetics. A density functional study. *J. Phys. Chem. A*, 112: 12887–12895.
35. de Visser SP and Straganz GD (2009a), Why do cysteine dioxygenase enzymes contain a 3-His ligand motif rather than a 2His/1Asp motif like most nonheme dioxygenases? *J. Phys. Chem. A*, 113: 1835–1846.
36. de Visser SP, Tahsini L and Nam W (2009b). How does the axial ligand of cytochrome P450 biomimetics influence the regioselectivity of aliphatic versus aromatic hydroxylation? *Chem. Eur. J*., 15: 5577–5587.
37. de Visser SP and Kumar D (eds) (2011a). Iron-containing enzymes: Versatile catalysts of hydroxylation reactions in nature. Royal Society of Chemistry Publishing: Cambridge (UK).
38. de Visser SP, Latifi R, Tahsini L and Nam W (2011b). The axial ligand effect on aliphatic and aromatic hydroxylation by nonheme iron(IV)-oxo biomimetic complexes. *Chem. Asian J*., 6: 493–504.
39. de Visser SP, Rohde J-U, Lee Y-M, Cho J and Nam W (2013). Intrinsic properties and reactivities of mononuclear nonheme iron–oxygen complexes bearing the tetramethylcyclam ligand.*Coord. Chem. Rev*., 257: 381–393.
40. de Visser SP, Quesne MG, Martin B, Comba P and Ryde U (2014). Computational modelling of oxygenation processes in enzymes and biomimetic model complexes. *Chem. Commun*., 50: 262–282.
41. Draksharapu A, Angelone D, Quesne MG, Padamati SK, Gómez L, Hage R, Costas M, Browne WR and de Visser SP (2015). Identification and spectroscopic characterization of nonheme iron(III) hypochlorite intermediates. *Angew. Chem. Int. Ed*., 54: 4357–4361.
42. Faponle AS, Quesne MG, Sastri CV, BanseF and de Visser SP (2015).Differences and comparisons of the properties and reactivities of iron(III)-hydroperoxo complexes with saturated coordination sphere. *Chem. Eur. J*., 21: 1221–1236.
43. Frisch MJ, Trucks GW, Schlegel HB, Scuseria GE, Robb MA, Cheeseman JR, Scalmani G, Barone V, Mennucci B, Petersson GA, Nakatsuji H, Caricato M, Li X, Hratchian HP, Izmaylov AF, Bloino J, Zheng G, Sonnenberg JL, Hada M, Ehara M, Toyota

K, Fukuda R, Hasegawa J, Ishida M, Nakajima T, Honda Y, Kitao O, Nakai H, Vreven T, Montgomery Jr JA, Peralta JE, Ogliaro F, Bearpark M, Heyd JJ, Brothers E, Kudin KN, Staroverov VN, Keith T, Kobayashi R, Normand J, Raghavachari K, Rendell A, Burant JC, Iyengar SS, Tomasi J, Cossi M, Rega N, Millam JM, Klene M, Knox JE, Cross JB, Bakken V, Adamo C, Jaramillo J, Gomperts R, Stratmann RE, Yazyev O, Austin AJ, Cammi R, Pomelli C, Ochterski JW, Martin RL, Morokuma K, Zakrzewski VG, Voth GA, Salvador P, Dannenberg JJ, Dapprich S, Daniels AD, Farkas O, Foresman JB, Ortiz JV, Cioslowski J and Fox DJ (2013).Gaussian 09, Revision D.01, Gaussian, Inc., Wallingford CT.

44. Godfrey E, Porro CS and de Visser SP (2008). Comparative quantum mechanics/molecular mechanics (QM/MM) and density functional theory calculations on the oxo-iron species of taurine/□-ketoglutarate dioxygenase. *J. Phys. Chem. A*, 112: 2464–2468.
45. Gross Z and Nimri S (1994).A pronounced axial ligand effect on the reactivity of oxoiron(1V) porphyrin cation Radicals. *Inorg. Chem.*, 33: 1731–1732.
46. Hay PJ and Wadt WR (1985). Ab initio effective core potentials for molecular calculations. Potentials for K to Au including the outermost core orbitals. *J. Chem. Phys.*, 82: 299–310.
47. Hazan C, Kumar D, de Visser SP and Shaik S (2007).A density functional study of the factors that influence the regioselectivity of toluene hydroxylation by cytochrome P450 enzymes. *Eur. J. Inorg. Chem.*: 2966–2974.
48. Heyes DJ, Sakuma M, de Visser SP and Scrutton NS (2009). Nuclear quantum tunneling in the light-activated enzyme protochlorophyllide oxidoreductase. *J. Biol. Chem.*, 284: 3762–3767.
49. Himes RA, Barnese K and Karlin KD (2010). One is lonely and three is a crowd: two coppers are for methane oxidation. *Angew. Chem. Int. Ed.*, 49: 6714–6716.
50. Jastrzebski R, Quesne MG, Weckhuysen BM, de Visser SP and Bruijnincx PCA (2014). Experimental and computational evidence for the mechanism of intradiol catechol dioxygenation by non-heme iron(III) complexes.*Chem. Eur. J.*, 20: 15686–15691.
51. Ji L, Faponle AS, Quesne MG, Sainna MA, Zhang J, Franke A, Kumar D, van Eldik R, Liu W and de Visser SP (2015). Drug metabolism by cytochrome P450 enzymes: What distinguishes the pathways leading to substrate hydroxylation over desaturation? *Chem. Eur. J.*, 21: in press.
52. Karamzadeh B, Kumar D, Sastry GN and de Visser SP (2010).Steric factors override thermodynamic driving force in regioselectivity of proline hydroxylation by prolyl-4-hydroxylase enzymes. *J. Phys. Chem. A*, 114: 13234–13243.
53. Karamzadeh B, Singh D, Nam W, Kumar D and de Visser SP (2014). Properties and reactivities of nonheme iron(IV)-oxo versus iron(V)-oxo: Long-range electron transfer versus hydrogen atom abstraction. *Phys. Chem. Chem. Phys.*, 16: 22611–22622.
54. Kim SJ, Latifi R, Kang HY, Nam W and de Visser SP (2009). Activation of hydrocarbon C–H bonds by iodosylbenzene: how does it compare with iron(IV)-oxo oxidants? *Chem. Commun.*, 1562–1564.
55. Kryatov SV, Rybak-Akimova EV and Schindler S (2005). Kinetics and mechanisms of formation and reactivity of non-heme iron oxygen intermediates. *Chem. Rev.*, 105: 2175–2226.
56. Kumar D, de Visser SP and Shaik S (2003). How does product isotope effect prove the operation of a two-state “rebound” mechanism in C–H hydroxylation by cytochrome P450? *J. Am. Chem. Soc.*, 125: 13024–13025.
57. Kumar D, de Visser SP, Sharma PK, Cohen S and Shaik S (2004a). Radical clock substrates, their C–H hydroxylation mechanism by cytochrome P450 and other reactivity patterns: what does theory reveal about the clocks’ behavior? *J. Am. Chem. Soc.*, 126: 1907–1920.
58. Kumar D, de Visser SP and Shaik S (2004b). Oxygen economy of cytochrome P450: what is the origin of the mixed functionality as a dehydrogenase–oxidase enzyme compared with its normal function? *J. Am. Chem. Soc.*, 126: 5072–5073.
59. Kumar D, de Visser SP, Sharma PK, Derat E and Shaik S (2005a). The intrinsic axial ligand effect on propene oxidation by horseradish peroxidase versus cytochrome P450 enzymes. *J. Biol. Inorg. Chem.*, 10: 181–189.
60. Kumar D, Hirao H, de Visser SP, Zheng J, Wang D, Thiel W and Shaik S (2005b). New features in the catalytic cycle of cytochrome P450 during the formation of Compound I from Compound 0. *J. Phys. Chem. B*, 109: 19946–19951.
61. Kumar D, de Visser SP and Shaik S (2005c). Theory favors a stepwise mechanism of porphyrin degradation by a ferric hydroperoxide model of the active species of heme oxygenase. *J. Am. Chem. Soc.*, 127: 8204–8213.
62. Kumar D, de Visser SP and Shaik S (2005d).Multistate reactivity in styrene epoxidation

by Compound I of cytochrome P450: mechanisms of products and side products formation. *Chem. Eur. J.*, 11: 2825–2835.

63. Kumar D, de Visser SP, Sharma PK, HiraoH and Shaik S (2005e). Sulfoxidation mechanisms catalyzed by cytochrome P450 and horseradish peroxidase models: spin selection induced by the ligand. *Biochemistry*, 44: 8148–8158.
64. Kumar D, Tahsini L, de Visser SP, Kang HY, Kim SJ and Nam W (2009). The effect of porphyrin ligands on the regioselective dehydrogenation versus epoxidation of olefins by oxoiron(IV) mimics of cytochrome P450. *J. Phys. Chem. A*, 113: 11713–11722.
65. Kumar D, Karamzadeh B, Sastry GN and de Visser SP (2010).What factors influence the rate constant of substrate epoxidation by Compound I of cytochrome P450 and analogous iron (IV)-oxo oxidants. *J. Am. Chem. Soc.*, 132: 7656–7667.
66. Kumar D, Thiel W and de Visser SP (2011a). Theoretical study on the mechanism of the oxygen activation process in cysteine dioxygenase enzymes. *J. Am. Chem. Soc.*, 133: 3869–3882.
67. Kumar D, SastryGN and de Visser SP (2011b). Effect of the axial ligand on substrate sulfoxidation mediated by iron(IV)-oxo porphyrin cation radical oxidants. *Chem. Eur. J.*, 17: 6196–6205.
68. Kumar D, Sastry GN, Goldberg DP and de Visser SP (2012a). Mechanism of S-oxygenation by a cysteine dioxygenase model complex.*J. Phys. Chem. A*, 116: 582–591.
69. Kumar D, SastryGN and de Visser SP (2012b). Axial ligand effect on the rate constant of aromatic hydroxylation by iron(IV)-oxo complexes mimicking cytochrome P450 enzymes. *J. Phys. Chem. B*, 116: 718–730.
70. Kumar D, Latifi R, Kumar S, Rybak-Akimova EV, Sainna MA and de Visser SP (2013). Rationalization of the barrier height for para-Z-styrene epoxidation by iron(IV)-oxo porphyrins with variable axial ligands.*Inorg. Chem.*, 52: 7968–7979.
71. Kumar S, Faponle AS, Barman P, Vardhaman AK, Sastri CV, Kumar D and de Visser SP (2014). Long-range electron transfer triggers mechanistic differences between iron(IV)-oxo and iron(IV)-imido oxidants. *J. Am. Chem. Soc.*, 136: 17102–17115.
72. Latifi R, Bagherzadeh M and de Visser SP (2009). Origin of the correlation of the rate constant of substrate hydroxylation by nonheme iron(IV)-oxo complexes with the bond-dissociation energy of the C–H bond of the substrate. *Chem. Eur. J.*, 15: 6651–6662.
73. Latifi R, Tahsini L, Karamzadeh B, Safari N, Nam W and de Visser SP (2011a). Manganese substituted Compound I of cytochrome P450 biomimetics: A comparative reactivity study of Mn^V-oxo versus MnIV-oxo species. *Arch. Biochem. Biophys.*, 507: 4–13.
74. Latifi R, Tahsini L, Kumar D, Sastry GN, Nam W and de Visser SP (2011b). Oxidative properties of a nonheme $Ni^{II}(O_2)$ complex: Reactivity patterns for C–H activation, aromatic hydroxylation and heteroatom oxidation. *Chem. Commun.*, 47: 10674–10676.
75. Latifi R, Tahsini L, Nam W and de Visser SP (2012a). Regioselectivity of aliphatic versus aromatic hydroxylation by a nonheme iron(II)-superoxo complex. *Phys. Chem. Chem. Phys.*, 14: 2518–2524.
76. Latifi R, Valentine JS, Nam W and de Visser SP (2012b). Predictive studies of H-atom abstraction reactions by an iron(IV)-oxo corrole cation radical oxidant. *Chem. Commun.*, 48: 3491–3493.
77. Latifi R, Sainna MA, Rybak-Akimova EV and de Visser SP (2013). Does hydrogen bonding-donation to manganese(IV)-oxo and iron(IV)-oxo oxidants affect the oxygen atom transfer ability? A computational study. *Chem. Eur. J.*, 19: 4058–4068.
78. Lee C, Yang W, and Parr RG (1988). Development of the Colle-Salvetti correlation-energy formula into a functional of the electron density. *Phys. Rev. B*, 37: 785–789.
79. Linstrom PJ and Mallard WG (2015). NIST Chemistry WebBook, NIST Standard Reference Database, Number 69, National Institute of Standards and Technology, Gaithersburg MD, 20899, http://webbook.nist.gov.
80. Meunier B, de Visser SP and Shaik S (2004). Mechanism of oxidation reactions catalyzed by cytochrome P450 enzymes.*Chem. Rev.*, 104: 3947–3980.
81. Munro AW, Girvan HM and McLean KJ (2007). Variations on a (t)heme – novel mechanisms, redox partners and catalytic functions in the cytochrome P450 superfamily. *Nat. Prod. Rep.*, 24: 585–609.
82. Neu HM, Quesne MG, Yang T, Prokop-Prigge KA, Lancaster KM, Donohoe J, DeBeer S, de Visser SP and Goldberg DP (2014). Dramatic influence of an anionic donor on the oxygen-atom-transfer reactivity of an Mn(V)-oxo complex. *Chem. Eur. J.*, 20: 14584–14588.
83. Ogliaro F, Harris N, Cohen S, Filatov M, de Visser SP and Shaik S (2000a). A model “rebound” mechanism of hydroxylation by cytochrome P450: stepwise and effectively concerted pathways, and

their reactivity patterns. *J. Am. Chem. Soc.*, 122: 8977–8989.

84. Ogliaro F, Cohen S, de Visser SP and Shaik S (2000b).Medium polarization and hydrogen bonding effects on Compound I of cytochrome P450: what kind of a radical is it really? *J. Am. Chem. Soc.*, 122: 12892–12893.
85. Ogliaro F, de Visser SP, Groves JT and Shaik S (2001a). Chameleon states: high-valent metal-oxo species of cytochrome P450 and its ruthenium analog. *Angew. Chem. Int. Ed.*, 40: 2874–2878.
86. Ogliaro F, de Visser SP, Cohen S, Kaneti J and Shaik S (2001b). The experimentally elusive oxidant of cytochrome P450: A theoretical "trapping" defining more closely the "real" species. *ChemBioChem.*, 2: 848–851.
87. Ogliaro F, de Visser SP and Shaik S (2002a). The "push" effect of the thiolate ligand in cytochrome P450: a theoretical gauging. *J. Inorg. Biochem.*, 91: 554–567.
88. Ogliaro F, de Visser SP, Cohen S, Sharma PK and Shaik S (2002b). Searching for the second oxidant in the catalytic cycle of cytochrome P450: a theoretical investigation of the iron(III)-hydroperoxo species and its epoxidation pathways. *J. Am. Chem. Soc.*, 124: 2806–2817.
89. Porro CS, Sutcliffe MJ and de Visser SP (2009).Quantum mechanics/molecular mechanics studies on the sulfoxidation of dimethyl sulfide by Compound I and Compound 0 of Cytochrome P450: which is the better oxidant? *J. Phys. Chem. A*, 113: 11635–11642.
90. Pratter SM, Konstantinovics C, DiGiuro CLM, Leitner E, Kumar D, de Visser SP, Grogan G and Straganz GD (2013). Inversion of enantio-selectivity of a mononuclear non-heme iron(II)-dependent hydroxylase by tuning the interplay of metal-center geometry and protein structure. *Angew. Chem. Int. Ed.*, 52: 9677–9681.
91. Prokop KA, de Visser SP and Goldberg DP (2010). Unprecedented rate enhancements of hydrogen-atom transfer to a manganese(V)-oxo corrolazine complex. *Angew. Chem. Int. Ed.*, 49: 5091–5095.
92. Prokop KA, Neu HM, de Visser SP and Goldberg DP (2011). A manganese(V)-oxo □-cation radical complex: Influence of one-electron oxidation on oxygen-atom transfer. *J. Am. Chem. Soc.*, 133, 15874–15877.
93. Quesne MG, Latifi R, Gonzalez-Ovalle LE, Kumar D and de Visser SP (2014). Quantum mechanics/molecular mechanics study on the oxygen binding and substrate hydroxylation step in AlkB repair enzymes. *Chem. Eur. J.*, 20: 435–446.
94. SahooD, Quesne MG, de Visser SP and Rath SP (2015).Hydrogen bonding interactions trigger a spin-flip iniron(III)-porphyrin complexes.*Angew. Chem. Int. Ed.*, 54: 4796–4800.
95. Sahu S, Widger LR, Quesne MG, de Visser SP, Matsumura H, Moënne-Loccoz P, Siegler MA and Goldberg DP (2013). Secondary coordination sphere influence on the reactivity of nonheme iron(II) complexes: An experimental and DFT approach. *J. Am. Chem. Soc.*, 135: 10590–10593.
96. Sahu S, Quesne MG, Davies CG, Dürr M, Ivanović-Burmazović I, Siegler MA, Jameson GNL, de Visser SP and Goldberg DP (2014). Direct observation of a non-heme iron(IV)-oxo complex that mediates aromatic C-F hydroxylation. *J. Am. Chem. Soc.*, 136: 13542–13545.
97. Sainna MA, Kumar S, Kumar D, Fornarini S, Crestoni ME and de Visser SP (2015a). A comprehensive test set of epoxidation rate constants by iron(IV)-oxo porphyrin complexes. *Chem. Sci.*, 6: 1516–1529.
98. Sainna MA, Sil D, Sahoo D, Martin B, Rath SP,CombaP and de Visser SP (2015b). Spin state ordering in hydroxo-bridged diiron(III)bisporphyrin complexes. *Inorg. Chem.*, 54: 1919–1930.
99. Sallmann M, Kumar S, Chernev P,Nehrkorn J, Schnegg A, Kumar D, Dau H, Limberg C and de Visser SP (2015). Structure and mechanism leading to formation of the cysteine sulfinate product complex of a biomimetic cysteine dioxygenase model. *Chem. Eur. J.*, 21: 7470–7479.
100. Shaik S, Cohen S, de Visser SP, Sharma PK, Kumar D, Kozuch S, Ogliaro F and Danovich D (2004a). The "rebound controversy": An overview and theoretical modeling of the rebound step in C–H hydroxylation by cytochrome P450.*Eur. J. Inorg. Chem.*: 207–226.
101. Shaik S, de Visser SP and Kumar D (2004b). External electric field will control the selectivity of enzymatic-like bond activations. *J. Am. Chem. Soc.*, 126: 11746–11749.
102. Shaik S, Kumar D, de Visser SP, Altun A and Thiel W (2005). Theoretical perspective on the structure and mechanism of cytochrome P450 enzymes. *Chem. Rev.*, 105: 2279–2328.
103. Shaik S, Kumar D and de Visser SP (2008). A valence bond modeling of trends in hydrogen abstraction barriers and transition states of hydroxylation reactions catalyzed by cytochrome P450 enzymes. *J. Am. Chem. Soc.*, 130: 10128–10140.
104. Sharma PK, de Visser SP, Ogliaro F and Shaik S (2003a). Is the ruthenium analogue of Compound I

105. of cytochrome P450 an efficient oxidant? A theoretical investigation of the methane hydroxylation reaction. *J. Am. Chem. Soc.*, 125: 2291–2300.
106. Sharma PK, de Visser SP and Shaik S (2003b). Can a single oxidant with two spin states masquerade as two different oxidants? A study of the sulfoxidation mechanism by cytochrome P450. *J. Am. Chem. Soc.*, 125: 8698–8699.
107. Sharma PK, Kevorkiants R, de Visser SP, Kumar D and Shaik S (2004). Porphyrin trap its own terminator! Concerted and stepwise porphyrin degradation mechanisms induced by heme-oxygenase vs. cytochrome P450. *Angew. Chem. Int. Ed.*, 43: 1129–1132.
108. Shiota Y and Yoshizawa K (2009). Comparison of the reactivity of bis(□-oxo)Cu^{II}Cu^{III} and Cu^{III}Cu^{III} species to methane. *Inorg. Chem.*, 48: 838–845.
109. Tahsini L, Bagherzadeh M, Nam W and de Visser SP (2009). Fundamental differences of substrate hydroxylation by high-valent iron(IV)-oxo models of cytochrome P450. *Inorg. Chem.*, 48: 6661–6669.
110. Vardhaman AK, Sastri CV, Kumar D and de Visser SP (2011). Nonheme ferric hydroperoxo intermediates are efficient oxidants of bromide oxidation.” *Chem. Commun.*, 47: 11044–11046.
111. Vardhaman AK, Barman P, Kumar S, Sastri CV, Kumar D and de Visser SP (2013a). Mechanistic insight into halide oxidation by non-heme iron complexes. Haloperoxidase versus halogenase activity. *Chem. Commun.*, 49: 10926–10928.
112. Vardhaman AK, Barman P, Kumar S, Sastri CV, Kumar D and de Visser SP (2013b). Comparison of the reactivity of nonheme iron(IV)-oxo versus iron(IV)-imido complexes: Which is the better oxidant? *Angew. Chem. Int. Ed.*, 52: 12288–12292.
113. Veitch NC and Smith AT (2000). Horseradish peroxidase. *Adv. Inorg. Chem.*, 51: 107–162.
114. VidossichP, Mercedes Alfonso-Prieto M and Rovira C (2012). Catalases versus peroxidases: DFT investigation of H_2O_2 oxidation in models systems and implications for heme protein engineering. *J. Inorg. Biochem.*, 117: 292–297.
115. Wang R and de Visser SP (2007). How does the push/pull effect of the axial ligand influence the catalytic properties of Compound I of catalase and cytochrome P450? *J. Inorg. Biochem.*, 101: 1464–1472.
116. Wester MR, Johnson EF, Marques-Soares C, Dijols S, Dansette PM, Mansuy D and Stout CD (2003). Structure of mammalian cytochrome P450 2C5 complexed with diclofenac at 2.1Å resolution: Evidence for an induced fit model of substrate binding. *Biochemistry*, 42: 9335–9345.

PCCP

ROYAL SOCIETY OF CHEMISTRY

PAPER

Cite this: *Phys. Chem. Chem. Phys.*, 2014, **16**, 22611

Properties and reactivities of nonheme iron(IV)–oxo *versus* iron(V)–oxo: long-range electron transfer *versus* hydrogen atom abstraction†

Baharan Karamzadeh,[a] Devendra Singh,[b] Wonwoo Nam,*[c] Devesh Kumar*[b] and Sam P. de Visser*[a]

Received 11th July 2014,
Accepted 8th September 2014

DOI: 10.1039/c4cp03053b

www.rsc.org/pccp

Recent work of Nam and co-workers [J. Yoon, S. A. Wilson, Y. K. Jang, M. S. Seo, K. Nehru, B. Hedman, K. O. Hodgson, E. Bill, E. I. Solomon and W. Nam, *Angew. Chem., Int. Ed.*, 2009, **48**, 1257] on a biomimetic iron complex implicated a mixture of iron(IV)–oxo and iron(V)–oxo intermediates but the latter could not be spectroscopically characterized, hence its involvement was postulated. To gain insight into the relative activity of these iron(IV)–oxo *versus* iron(V)–oxo intermediates, we have performed an extensive density functional theory (DFT) study on the chemical properties of the chemical system of Nam *et al.*, namely $[\mathrm{Fe(O)(BQEN)(NCCH_3)}]^{2+/3+}$ with BQEN = *N*,*N*′-dimethyl-*N*,*N*′-bis(8-quinolyl)ethane-1,2-diamine and their reactivity in hydrogen atom abstraction from ethylbenzene. We show that the perceived iron(V)–oxo species actually is an iron(IV)–oxo ligand cation radical, similar to cytochrome P450 compound I. Moreover, this intermediate has an extremely large electron affinity and therefore can abstract electrons from substrates readily. In our particular system, this means that prior to the hydrogen atom abstraction, an electron is abstracted to form an iron(IV)–oxo species, which subsequently abstracts a hydrogen atom from the substrate. Thus, our calculations show for the first time how some nonheme iron complexes react by long-range electron transfer and others directly *via* hydrogen atom abstraction. We have rationalized our results with detailed thermochemical cycles that explain the observed reactivity patterns.

Introduction

Nonheme iron dioxygenases are important enzymes for human health with essential functions that include DNA base repair mechanisms and oxidative cleavage of carotenoids.[1] In several organisms, natural product biosynthesis is catalysed by nonheme iron dioxygenases, and, therefore, they have important functions in biology as well as in biotechnology. In order to understand enzymatic reaction processes, synthetic model complexes have been developed and designed.[2] These biomimetic model complexes of nonheme iron oxidants are well studied and many biomimetic high-valent catalytic intermediates have been characterized in recent years.[3] For instance, to tackle the controversy in Rieske dioxygenases regarding the active oxidant in the reaction process, several biomimetic model complexes with iron(V)–oxo(hydroxo) as reactive features have been studied and their reactivity patterns established.[4]

All biomimetic Rieske dioxygenase models contain a hydroxo group in a *cis*-position of the iron(IV/V)–oxo group. Only few examples exist of biomimetic iron(V)–oxo intermediates without this *cis*-hydroxo ligand and spectroscopic studies gave indirect evidence of its existance.[5] Thus, McKenzie and co-workers reported the structural characterization of an iron(V)–oxo species with a monoionic multidentate ligand and found it to react with thioanisole efficiently.[6] Kim and co-workers used a tetradentate ligand system and formed the corresponding iron(V)–oxo species by heterolytic cleavage of an iron–acylperoxo intermediate.[7] They determined kinetic isotope effects (KIE, k_H/k_D), $H_2{}^{18}O$ exchange reactions and measured product distributions. Using a tetraamido macrocyclic ligand, Collins and co-workers studied the sulfoxidation of substrates by an iron(V)–oxo species and compared the rates with analogous iron(IV)–oxo species.[8] Finally, Nam and co-workers studied the reaction of $[\mathrm{Fe^{II}(BQEN)}]^{2+}$, BQEN = *N*,*N*′-dimethyl-*N*,*N*′-bis(8-quinolyl) ethane-1,2-diamine, with CH_3CO_3H and found evidence of competing reaction mechanisms originating from

---

[a] Manchester Institute of Biotechnology and School of Chemical Engineering and Analytical Science, the University of Manchester, 131 Princess Street, Manchester M1 7DN, UK. E-mail: sam.devisser@manchester.ac.uk; Fax: +44 (0)1613065201; Tel: +44 (0)1613064882

[b] Department of Applied Physics, School for Physical Sciences, Babasaheb Bhimrao Ambedkar University, Vidya Vihar, Rai Bareilly Road, Lucknow 226 025, India. E-mail: dkclcre@yahoo.com

[c] Department of Chemistry and Nano Science, Ewha Womans University, Seoul 120-750, Korea. E-mail: wwnam@ewha.ac.kr

† Electronic supplementary information (ESI) available: Tables with absolute and relative energies as well as group spin densities and charges. See DOI: 10.1039/c4cp03053b

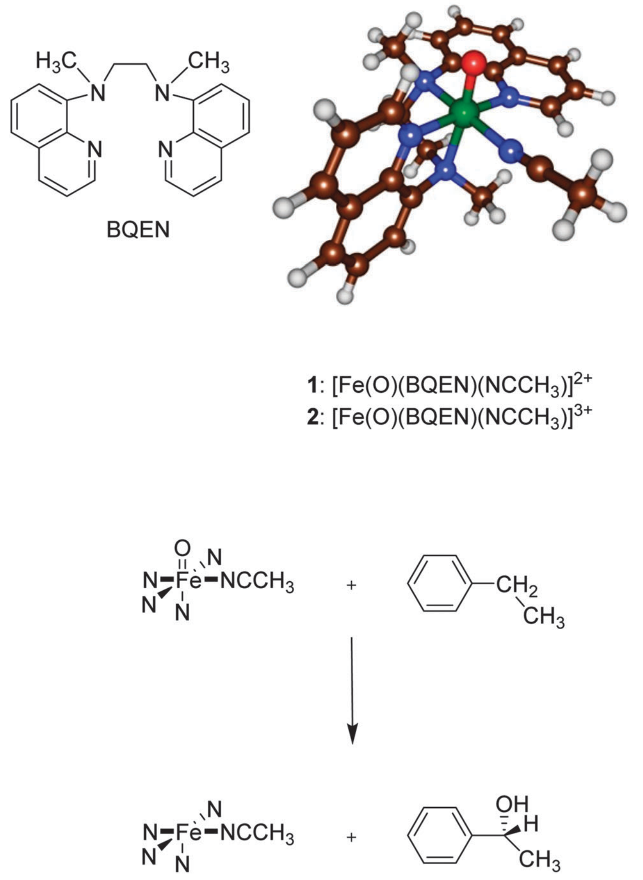

1: $[\mathrm{Fe(O)(BQEN)(NCCH_3)}]^{2+}$
2: $[\mathrm{Fe(O)(BQEN)(NCCH_3)}]^{3+}$

Scheme 1 Iron–oxo oxidants and ligand system studied in this work.

two oxidants in the reaction mixture that were tentatively assigned as $[\mathrm{Fe^{IV}(O)(BQEN)}]^{2+}$ and $[\mathrm{Fe^{V}(O)(BQEN)}]^{3+}$.[9] Their studies failed to unequivocally assign the active oxidant in the reaction mechanism, and therefore could not determine the relative reactivity of iron(IV)–oxo *versus* iron(V)–oxo. In order to resolve this dichotomy and gain general insight into the relative reactivity of iron(IV)–oxo *versus* iron(V)–oxo with nonheme ligand systems a computational study was conducted using the $[\mathrm{Fe^{IV}(O)(BQEN)(NCCH_3)}]^{2+}$ (**1**) and $[\mathrm{Fe^{V}(O)(BQEN)(NCCH_3)}]^{3+}$ (**2**) systems, Scheme 1.

Currently, very little is known regarding the catalytic activity of iron(V)–oxo intermediates and to the best of our knowledge, no direct comparison in reactivity between iron(IV)–oxo and iron(V)–oxo has been reported. We present here a DFT study to gain insight into the potential use of iron(V)–oxo intermediates as catalytic oxidants with ethylbenzene as the selected substrate. We present the first comparative study on the aliphatic hydroxylation by iron(IV)–oxo *versus* iron(V)–oxo using the BQEN ligand system shown in Scheme 1 and follow the mechanism of ethylbenzene activation leading to benzyl alcohol product complexes.

Methods

All studies reported here utilize density functional theory (DFT) methods as implemented in the Jaguar and Gaussian program packages.[10] We initially did exploratory gas-phase optimizations on $[\mathrm{Fe(O)(BQEN)(NCCH_3)}]^{3+/2+}$ in Jaguar at the UB3LYP level of theory[11] and explored the catalytic mechanism of ethylbenzene hydroxylation. However, as most of our chemical systems are multiply charged ions we decided to do a subsequent set of calculations, where the complete project was done using a polarized continuum solvent model included during the geometry optimizations. These studies gave considerable differences from the gas-phase results and therefore we will focus on the solvent optimized calculations mainly. Details of the gas-phase calculations can be found in the ESI.† Thus, all geometry optimizations and frequencies were performed with a solvent model included with a dielectric constant mimicking acetonitrile. All local minima are characterized with a frequency calculation and have real frequencies only, whereas the transition states have one imaginary frequency for the correct mode. As transition metal containing complexes give close-lying electronic and spin states,[12] we calculated the $[\mathrm{Fe(O)(BQEN)(NCCH_3)}]^{3+}$ complexes in the lowest lying doublet, quartet and sextet spin states and the $[\mathrm{Fe(O)(BQEN)(NCCH_3)}]^{2+}$ complexes in the singlet, triplet and quintet spin states.

We tested the reproducibility and reliability of the density functional method by applying a range of unrestricted DFT methods, including B3LYP,[11] B3LYP-D3,[13] B3LYP*,[14] and OPBE.[15] There is a certain degree of fluctuation observed in the relative energies, spin state ordering and geometric details as commonly observed in nonheme iron complexes.[16] However, the results confirmed the assignment of the electron configuration of all complexes and reproduce experimental trends.

All optimizations and frequencies use a triple-ζ quality basis set (BS2) with LACV3P+ on iron and 6-311+G* on the rest of the atoms.[17] Previously, we used these methods extensively for the description of nonheme iron complexes and reproduced experimental free energies of activation within several kcal mol^{-1}.[18] To test the effect of the overall charge on the calculations we also performed a set of test calculations on charge neutral complexes, whereby the reactants and rate determining transition states were modified by counter-ions at a fixed distance of 15 Å from the axial nitrogen atom and with an angle of 120 degrees with respect to iron and the axial nitrogen atom. Point charges, $\mathrm{Cl^-}$ counter-ions and $\mathrm{OH^-}$ counter-ions were applied, but all results reproduced the solvent optimized results and did not give changes to the charge and spin distributions.

Kinetic isotope effects (KIEs) were calculated for the hydrogen atom abstraction reaction of ethylbenzene by **1** for the replacement of one or more hydrogen atoms of the substrate by deuterium atoms. We initially used the semi-classical Eyring equation (eqn (1)) to calculate $\mathrm{KIE_E}$ from the difference in free energies of activation ($\Delta G^{\ddagger}$) of the substrate and its deuterium substituted form following previously reported methods.[19] Eqn (1) uses the gas constant (R) and the actual temperature (273.15 K).

$$\mathrm{KIE_E} = k_{\mathrm{H}}/k_{\mathrm{D}} = \exp\left\{\left(\Delta G_{\mathrm{D}}^{\ddagger} - \Delta G_{\mathrm{H}}^{\ddagger}\right)\Big/RT\right\} \tag{1}$$

Further corrections due to tunnelling were applied using the Wigner model[20] that corrects $\mathrm{KIE_E}$ with the tunnelling ratio ($Q_{\mathrm{tH}}/Q_{\mathrm{tD}}$) as described in eqn (2) and (3).

$$\mathrm{KIE_W} = \mathrm{KIE_E} \times Q_{\mathrm{tH}}/Q_{\mathrm{tD}} \tag{2}$$

$$Q_{\mathrm{t}} = 1 + \frac{1}{24}\left(\frac{h\nu}{k_{\mathrm{B}}T}\right)^2 \tag{3}$$

In eqn (3), k_B represents the Boltzmann's constant, h is Planck's constant and ν is the imaginary frequency in the transition state.

Results

Isolated reactants 1 and 2

Our study uses density functional theory (DFT) methods and is focused on the chemical systems of ref. 9 as described in Scheme 1, where we included an acetonitrile solvent molecule in the sixth ligand position of the metal: $[\mathrm{Fe(O)(BQEN)(NCCH_3)}]^{2+}$ (**1**) and $[\mathrm{Fe(O)(BQEN)(NCCH_3)}]^{3+}$ (**2**). These structures have the metal in formal oxidation state iron(IV) and iron(V), respectively. Before we will look into the reactivity patterns of structures **1** and **2** with substrates, we will describe the electronic properties of the optimized geometries of **1** and **2**, Fig. 1.

The lowest lying singlet, triplet and quintet spin states of **1** were calculated, but the singlet state was found to be high in energy. Similarly, **2** was investigated in the doublet and quartet spin states only. Fig. 1 displays the molecular valence orbitals of **1** and **2**, which are determined by the mixing of the metal 3d orbitals with its ligands. Thus, there are three π* molecular orbitals (π^*_{xy}, π^*_{yz}, π^*_{xz}) representing the anti-bonding interactions of the 3d iron orbitals with 2p orbitals on the oxo group. High in energy are two σ* orbitals for the anti-bonding interactions of the metal with the ligands in the *xy*-plane ($\sigma^*_{x^2-y^2}$) and with ligands along the *z*-axis ($\sigma^*_{z^2}$), whereby the *z*-axis is defined as parallel to the Fe–O bond. In the iron(IV)–oxo complex, *i.e.* ^{3,5}**1**, the set of orbitals shown in Fig. 1 is occupied by four electrons, which gives two low-lying solutions with either triplet or quintet spin: **1** has a triplet spin ground state with electronic configuration $\pi^*_{xy}{}^2\ \pi^*_{xz}{}^1\ \pi^*_{yz}{}^1$ (^{3}**1**) that is somewhat lower in energy than the quintet spin state with configuration $\pi^*_{xy}{}^1\ \pi^*_{xz}{}^1\ \pi^*_{yz}{}^1\ \sigma^*_{x^2-y^2}{}^1$ (^{5}**1**), *vide infra*. In both spin states **1** has the metal in formal oxidation state iron(IV). The spin state ordering matches previous studies on hexacoordinated non-heme iron biomimetic model complexes and also supports the experimentally reported absorption band at $\lambda_{\max}$ = 740 nm characteristic for triplet iron(IV)–oxo species and assigned by Nam *et al.* on $[\mathrm{Fe(O)(BQEN)(NCCH_3)}]^{2+}$.[3,9,21]

Upon oxidation of ^{3,5}**1**, however, several possibilities arise for the electronic configuration of **2**. Firstly, ^{3}**1** can lose an electron from π^*_{yz} to give a doublet spin configuration with $\pi^*_{xy}{}^2\ \pi^*_{xz}{}^1$ orbital occupation or lose an electron from the

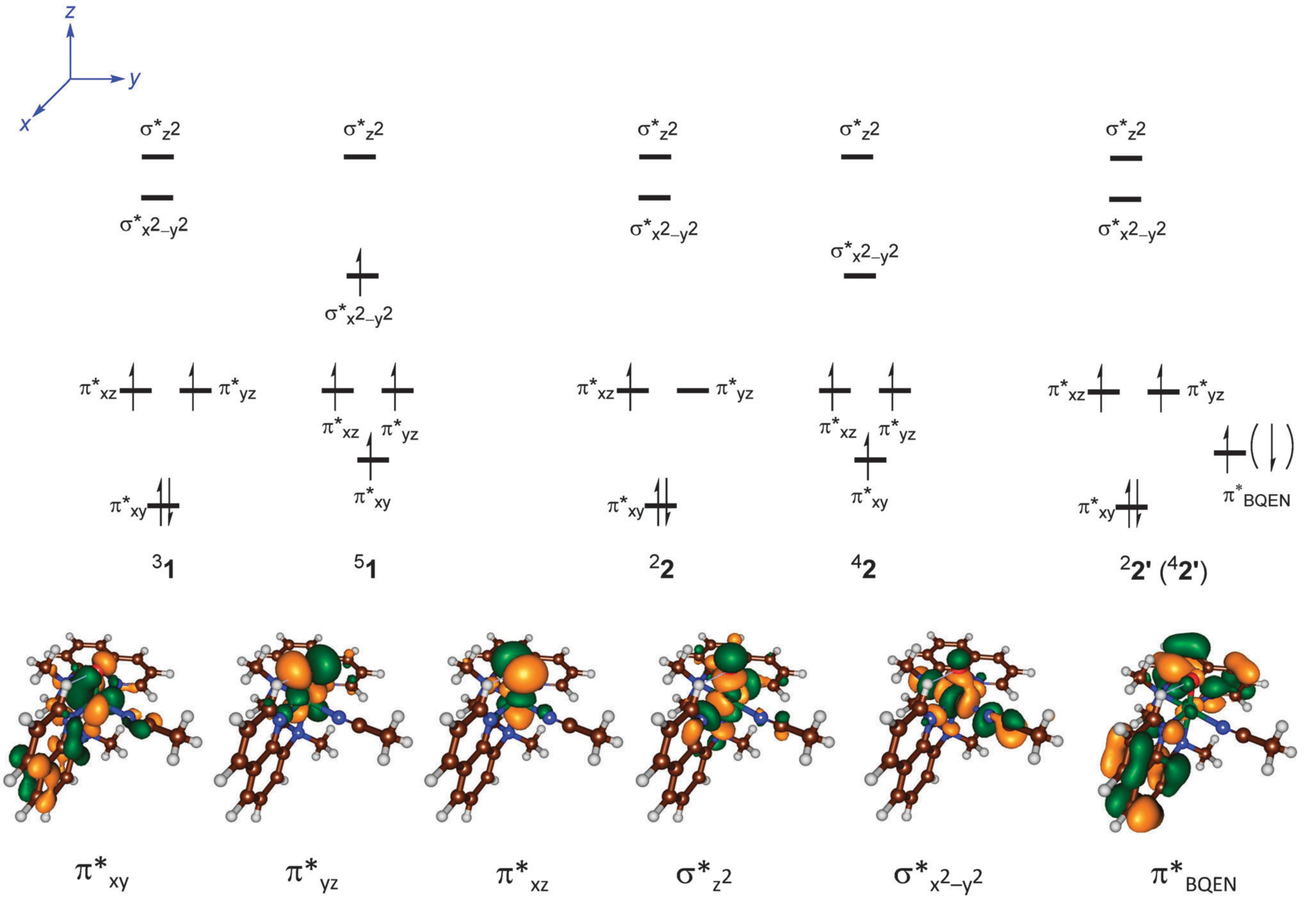

Fig. 1 High-lying occupied and low-lying virtual orbitals of **1** and **2**. The top panel shows the different electronic configurations of **1** and **2** considered and the bottom shows the orbital shapes of the valence orbitals.

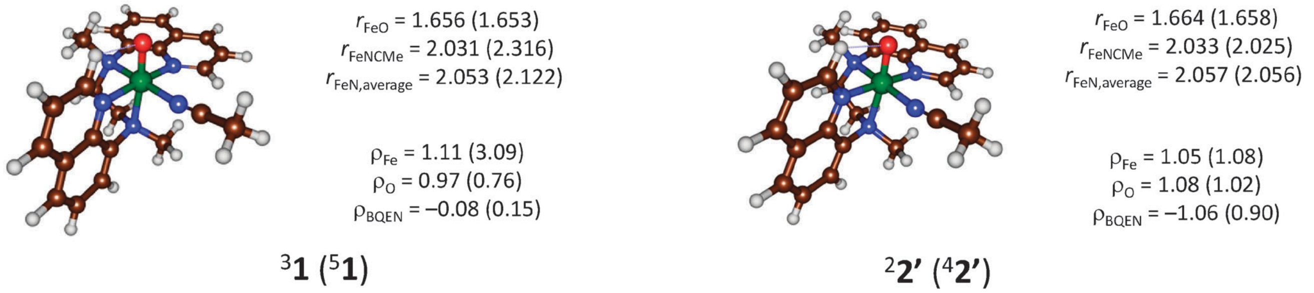

Fig. 2 Gas-phase optimized geometries (UB3LYP/BS1) of ^{3,5}**1** and ^{2,4}**2** with bond lengths in angstroms and group spin densities (ρ) in atomic units.

doubly occupied π^*_{xy} orbital to give a quartet spin complex with $\pi^*_{xy}{}^1\ \pi^*_{xz}{}^1\ \pi^*_{yz}{}^1$ configuration. These two states have the metal in formal oxidation state iron(V) and are labelled as ^{2,4}**2** in Fig. 1. In addition, the oxidation of ^{3}**1** can expel an electron from a ligand π-type orbital, such as π^*_{BQEN}, and lead to an electronic configuration $\pi^*_{xy}{}^2\ \pi^*_{xz}{}^1\ \pi^*_{yz}{}^1\ \pi^*_{BQEN}{}^1$, whereby the radical on the ligand can be either ferromagnetically or anti-ferromagnetically coupled to the metal-based unpaired electrons in an overall quartet or doublet spin state (^{4,2}**2′**). The latter, therefore, can be seen as an iron(IV)–oxo ligand cation radical species with configuration $[Fe^{IV}(O)(BQEN^{+\bullet})(NCCH_3)]^{3+}$ and is reminiscent of compound I of cytochrome P450 enzymes, which was characterized as an iron(IV)–oxo heme cation radical species, *i.e.* $[Fe^{IV}(O)(heme^{+\bullet})Cys]$.[22]

Details of the optimized geometries of ^{3,5}**1** and ^{2,4}**2′** in the gas phase are reported in Fig. 2. In the gas-phase the triplet spin state is the ground state by ΔE + ZPE (ΔG) = 2.0 (0.2) kcal mol^{-1}. Optimized geometries are in line with previously reported structures on non-heme iron(IV)–oxo complexes with a short Fe–O bond of 1.66 Å, which implicates a double bond.[21,23] Group spin densities and charges confirm the orbital assignment of ^{3,5}**1** as described in Fig. 2 with electronic configuration of $\pi^*_{xy}{}^2\ \pi^*_{xz}{}^1\ \pi^*_{yz}{}^1$ for ^{3}**1** and $\pi^*_{xy}{}^1\ \pi^*_{xz}{}^1\ \pi^*_{yz}{}^1\ \sigma^*_{x^2-y^2}{}^1$ for ^{5}**1**.

Nam and co-workers[9] using absorption and infrared spectroscopy and extended X-ray absorption fine structure (EXAFS) studied the $[Fe(O)(BQEN)(NCCH_3)]^{2+}$ complex experimentally. They identified an iron–oxo bond of 1.67 Å and an average Fe–N distance of 1.97 Å. Our calculated Fe–O distances for ^{3,5}**1** in Fig. 2 match the experimental values excellently. The experimentally reported Fe–N distances are in good agreement with the triplet spin structures, but not with the quintet spin state structures due to single occupation of the $\sigma^*_{x^2-y^2}$ orbital that elongates the distances between the metal and its ligands. Therefore, the computational studies support the characterization of a triplet spin ground state of **1**.

Geometry optimizations of ^{2,4}**2′**, however, gives a low-lying solution with two singly occupied π* orbitals coupled to a radical on the BQEN unit with spin densities of $\rho_{BQEN} = -1.06$ (0.90) in the doublet and quartet spin states. The optimized geometries, therefore, correspond to an electronic state $[Fe^{IV}(O)(BQEN^{+\bullet})(NCCH_3)]^{3+}$, *i.e.* ^{2,4}**2′** in Fig. 1, rather than the anticipated iron(V)–oxo species. Although we attempted to swap molecular orbitals to generate the iron(V) solution (^{2,4}**2**) these calculations converged back to ^{2,4}**2′**, which therefore is the molecular ground state.

As the complex has a large overall charge of +3, we decided to reoptimize these structures using the polarized continuum model mimicking an acetonitrile solution. However, the new model did not affect the spin state ordering and electronic configuration of the ground state and the same electronic state was found. It appears, therefore, that ^{2,4}**2′** is the electronic ground state that can be described as $[Fe^{IV}(O)(BQEN^{+\bullet})(NCCH_3)]^{3+}$ with an iron(IV)–oxo group coupled to a ligand radical. As both doublet and quartet spin states represent the same orbital occupation, namely $\pi^*_{xy}{}^2\ \pi^*_{xz}{}^1\ \pi^*_{yz}{}^1\ \pi^*_{BQEN}{}^1$, we calculate them within 2 kcal mol^{-1}. This result is similar to the spin state energies of ferromagnetically *versus* antiferromagnetically coupled doublet and quartet spin states of compound I of P450, where these spin states were also found to be within a couple of kcal mol^{-1} from each other. Moreover, the energy gap was found to be sensitive to the local environment, including hydrogen bonding interactions to the oxidant as well as solvent effects.[24] Furthermore, these two spin states result in two-state-reactivity patterns with substrates on competing spin-state surfaces.[25] Analogously to P450 compound I, the iron(V)–oxo species is an excited state of the molecular ground state with configuration $[Fe^{IV}(O)(BQEN^{+\bullet})(NCCH_3)]^{3+}$. Geometrically ^{2,4}**2′** has metal–ligand bond lengths close to those found for ^{3}**1**, which is also an iron(IV)–oxo species.

Reactant complexes

Subsequently, ethylbenzene (EB) was added to the model complexes to create a long-range reactant complex (**RC**) as this was one of the substrates used in the experimental study and we investigated the benzyl hydroxylation processes. The electronic features of ^{3,5}**RC**$_1$ or $^{3,5}[Fe(O)(BQEN)(NCCH_3)\cdots EB]^{2+}$ and ^{2,4}**RC**$_2$ or $^{2,4}[Fe(O)(BQEN)(NCCH_3)\cdots EB]^{3+}$ will be discussed prior to the investigation of the catalytic mechanism. Considering that computational modelling occasionally is sensitive to the choice of the density functional used as well as on environmental variables,[26] some thorough testing of the structures, spin-state energetics and electronic configurations of ^{3,5}**RC**$_1$ and ^{2,4}**RC**$_2$ using a selection of density functional methods and procedures was carried out. Thus, we performed geometry optimizations of all complexes in the gas-phase at UB3LYP/BS1, but also did a full geometry optimization in a dielectric constant mimicking acetonitrile at UB3LYP/BS2 and finally a full geometry optimization in a dielectric constant at the UB3LYP-D3/BS2. In addition, single point calculations on the UB3LYP/BS2 optimized geometries using B3LYP with 15% HF exchange (B3LYP*), UB3LYP-D3 and OPBE were

Table 1 Spin state energies and optimized geometries of reactant complexes as calculated using various DFT methods

				ΔE + ZPE						
				UB3LYP	UB3LYP	UB3LYP-D3	UB3LYP-D3	UB3LYP	UB3LYP*	OPBE
Structure	r_{FeO} [a,b]	r_{FeO} [b,c]	r_{FeO} [b,e]	Gas[a,d]	Solv[c,d]	Solv[c,d]	Solv[d,e]	PC[c,f]	Solv[c,d]	Solv[c,d]
^{3}**RC**$_1$	1.656	1.633	1.657	0.0	0.0	0.0	0.0	0.0	0.0	0.0
^{5}**RC**$_1$	1.653	1.627	1.653	10.3	2.5	7.4	8.2	8.7	6.0	2.4
^{2}**RC**$_2$	1.664	1.638	1.656	0.0	0.0	0.0	0.0	0.0	0.0	0.0
^{4}**RC**$_2$	1.664	1.631	1.653	0.6	−3.6	10.0	8.4	10.0	6.9	3.8

[a] UB3LYP/BS1 geometry optimization in the gas-phase. [b] Values in Å. [c] UB3LYP/BS2 geometry optimization in solvent. [d] ΔE + ZPE value with energies at the BS2 level of theory in kcal mol^{-1}. [e] UB3LYP-D3/BS2 geometry optimization in solvent. [f] Structure with added point charges that neutralize the system at 15 Å.

performed. Finally, single point calculations in the gas-phase with additional counter-ions or point charges included in the model at a distance of 15 Å that neutralize the chemical systems were carried out.

Table 1 presents the optimized Fe–O distance and spin-state energies as obtained using these different DFT models and methods. As can be seen all methods, models and optimization techniques give the same spin state ordering, but a certain degree of variation in the relative energies is observed typical for DFT calculated iron complexes.[26] In all cases ^{3}**RC**$_1$ and ^{5}**RC**$_1$ are characterized as [Fe$^{\text{IV}}$(O)(BQEN)(NCCH$_3$)···EB]$^{2+}$ with orbital occupation $\pi^*_{xy}{}^2\ \pi^*_{xz}{}^1\ \pi^*_{yz}{}^1$ and $\pi^*_{xy}{}^1\ \pi^*_{xz}{}^1\ \pi^*_{yz}{}^1\ \sigma^*_{x^2-y^2}{}^1$, respectively, in agreement with what was found for structure ^{3,5}**1** above. Regardless of the method and whether the optimization is done in the gas-phase or in solvent, a triplet spin ground state that is well separated from the quintet spin state by 2.4–10.3 kcal mol^{-1} is found. Although this appears to be a large variation in spin state energies, actually for transition metal complexes, and, in particular iron(IV)–oxo complexes a strong variation of the ordering and relative energies is normal in DFT upon changing the density functional method or environmental effects.[27] Nevertheless, all methods give a triplet spin ground state in support of experimental studies.[17]

The situation is dramatically changed when ^{2,4}**RC**$_2$ is investigated with these methods and models. Whereas ^{2,4}**2′** was found as the electronic ground state with configuration [Fe$^{\text{IV}}$(O)(BQEN$^{+\bullet}$)(NCCH$_3$)]$^{3+}$ with two unpaired π^* electrons coupled to a radical on the ligand, by contrast, in ^{2,4}**RC**$_2$ we find yet another electronic configuration with two unpaired π^* electrons that are coupled to an ethylbenzene radical, *i.e.* orbital occupation $\pi^*_{xy}{}^2\ \pi^*_{xz}{}^1\ \pi^*_{yz}{}^1\ \pi^*_{\text{BQEN}}{}^2\ \pi_{\text{EB}}{}^1$, where the latter orbital is a singly occupied π-orbital on ethylbenzene. Therefore, addition of an ethylbenzene molecule to ^{2,4}**2′** results in an intermolecular electron transfer from the substrate into the π^*_{BQEN} orbital of the oxidant and the creation of a complex [Fe$^{\text{IV}}$(O)(BQEN)(NCCH$_3$)]$^{2+}$···EB$^{+\bullet}$. This happens regardless of the method and whether gas-phase or solvent models are used. It implies that [Fe$^{\text{IV}}$(O)(BQEN$^{+\bullet}$)(NCCH$_3$)]$^{3+}$ is a strong oxidant and can abstract electrons from substrates readily. Most probably this is caused by its extremely large electron affinity, *vide infra*.

Note that outer-sphere electron transfer upon approach of a substrate onto a metal–oxo species has been calculated before on metal–porphyrins,[28,29] including a potential intermediate of nitric oxide synthase, where the arginine substrate was found to donate an electron to an iron(IV)–oxo heme cation radical species quickly. Furthermore, approach of a Zn^{2+} ion onto a high-valent manganese(V)–oxo corrolazine also led to the formation of a manganese(IV)–oxo corrolazine cation radical through valence tautomerization.[29] Finally, studies on the comparative electronic features of the iron(IV)–oxo heme species of cytochrome *c* peroxidase (C*c*P) *versus* ascorbate peroxidase implicated differences in electronic configuration as a result of a bound cation at a distance of 15 Å from the heme. DFT modelling on compound **I** of C*c*P tested the effect of a point charge with magnitude $Q = -1/+1$ on the electronic configuration.[30] It was found that a charge of $Q = +1$ gave an electronic state [Fe$^{\text{IV}}$(O)(heme$^{+\bullet}$)···Trp$_{191}$], whereas a value of $Q = -1$ resulted in an alternative state corresponding to [Fe$^{\text{IV}}$(O)(heme)···Trp$_{191}{}^{+\bullet}$]. These studies have shown that seemingly small external (but long-range) perturbations can have a major impact on the electronic configuration of the oxidant and consequently on its ability to react with substrates. However, for nonheme metal–oxo species this would be the first example of outer-sphere electron transfer upon substrate approach and is likely caused by the large electron affinity of the ligand. In the following we will describe whether the change in electronic configuration is beneficial or disadvantageous to the catalysis.

Ethylbenzene hydroxylation by 1 and 2

Subsequently, the benzyl hydroxylation of ethylbenzene by ^{3,5}**RC**$_1$ and ^{2,4}**RC**$_2$ was calculated. Fig. 3 displays the calculated reaction mechanism with optimized geometries of the rate determining transition states of the reaction starting from ^{3,5}**RC**$_1$. We calculate a stepwise mechanism with an initial hydrogen atom abstraction from the benzyl position of ethylbenzene *via* a transition state (**TS**$_{\text{HA}}$) to form a radical intermediate (**I**) followed by hydroxyl rebound *via* a transition state (**TS**$_{\text{reb}}$) to form alcohol products (**P**). In all cases the hydrogen atom abstraction is rate determining and the rebound barriers are small or negligible, so that we will focus on the **TS**$_{\text{HA}}$ pathway only here. Full details of the rest of the mechanism are given in the ESI.† In the gas phase very little energy difference between hydrogen atom abstraction from the *pro-S versus pro-R* site of the benzyl position of ethylbenzene by iron(IV)–oxo complexes was found. Recent computational studies on *S*-mandalate synthase showed that the shape and size of the substrate binding pocket determines

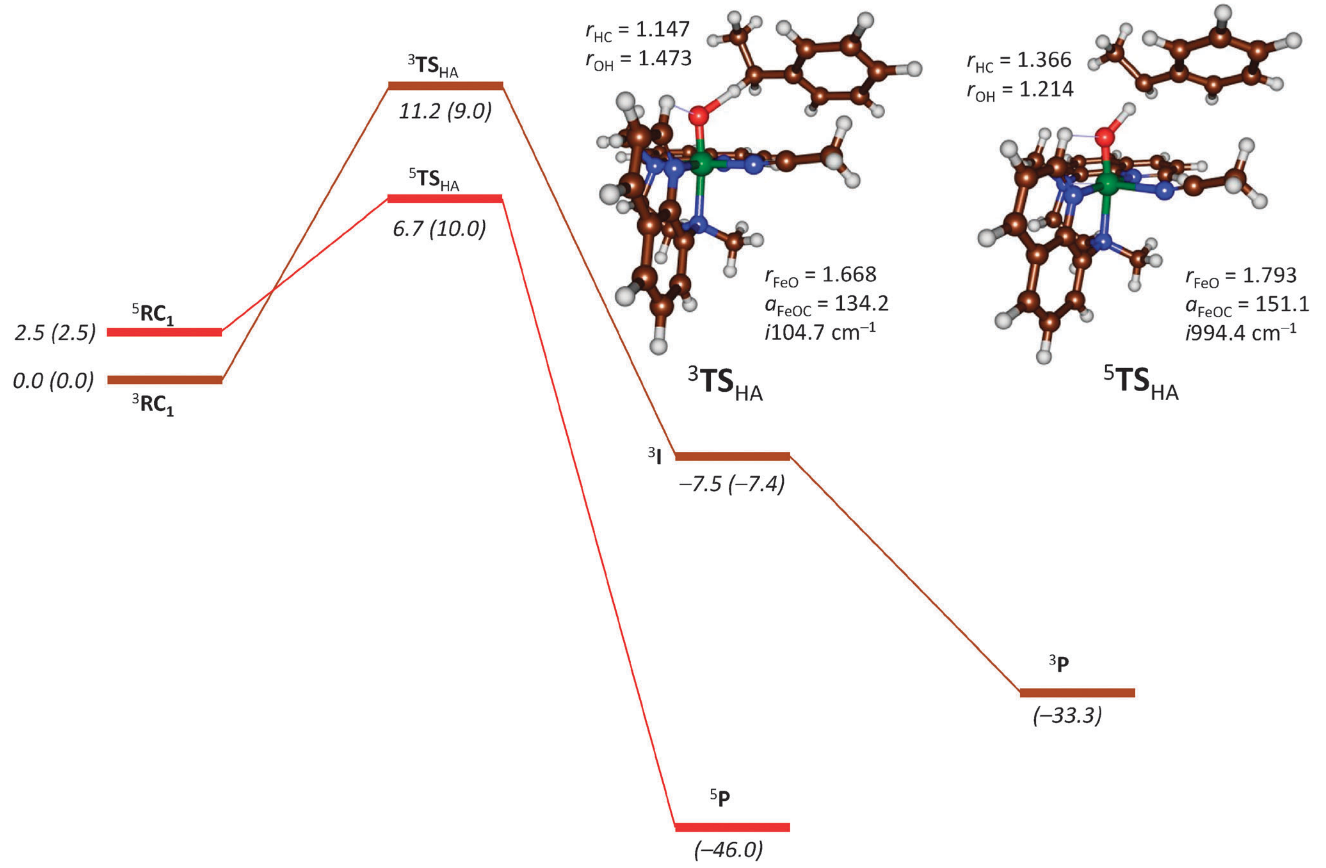

Fig. 3 DFT calculated potential energy profile for the hydrogen atom abstraction from EB by ^{3,5}**1** with energies given in kcal mol^{-1}. Also shown are optimized UB3LYP/BS2(solvent) geometries of ^{3,5}**TS**$_{\text{HA}}$ with bond lengths in angstroms, angles in degrees and the imaginary frequency in wave numbers. Relative energies represent ΔE + ZPE + E_{solv} values obtained after a full geometry optimization in solvent at the UB3LYP/BS2 (out of parenthesis) or at UB3LYP/BS2//UB3LYP/BS1 level of theory on a gas-phase optimized geometry.

whether the *pro-R* or *pro-S* hydrogen atom can be abstracted.[31] Indeed, site-selective mutations confirmed the computationally proposed hypothesis.

Geometrically, the ^{3,5}**TS**$_{\text{HA}}$ structures are quite distinct due to differences in electron transfer processes that happen in these transition states. In the triplet spin state the hydrogen atom transfer is accompanied with electron transfer from the substrate into the π^*_{xz} orbital and hence the substrate attacks under an angle (a_{FeOC} = 134.2°) to get ideal orbital overlap between donor and acceptor orbitals.[32] In the quintet spin state the hydrogen atom abstraction is accompanied with electron transfer from the substrate into the vacant $\sigma^*_{z^2}$ orbital and hence the substrate attacks from the top with considerably larger FeOC angles than found in the triplet spin state (a_{FeOC} = 151.1°), which gives an iron(III)–hydroxo complex with a fully exchange coupled metal 3d system with five singly occupied orbitals that is antiferromagnetically coupled to a benzyl radical: ^{5}**I** has electronic configuration $\pi^*_{xy}{}^1\ \pi^*_{xz}{}^1\ \pi^*_{yz}{}^1\ \sigma^*_{x^2-y^2}{}^1\ \sigma^*_{z^2}{}^1\ \pi_{\text{EB}}{}^1$. This exchange stabilization makes ^{5}**I** considerably lower in energy than the corresponding triplet spin complex. As a consequence, ^{5}**TS**$_{\text{HA}}$ is stabilized over ^{3}**TS**$_{\text{HA}}$, although dispersion corrections make them almost degenerate. Nevertheless, the barrier heights on both spin state surfaces are small and implicate an efficient hydrogen atom abstraction process in agreement with experiment.[9] When the enthalpy values from Fig. 3 are converted to a free energy of activation, a value of ΔG_{solv} = 10.8 kcal mol^{-1} on the triplet spin state surface is found, which is in reasonable agreement with the experimentally reported free energy of activation of Nam *et al.*[9]

The experimental studies on ethylbenzene hydroxylation by **RC**$_1$ were found to proceed with a kinetic isotope effect (KIE) of 10 for the replacement of hydrogen atoms by deuterium in the substrate. To estimate the isotope effects for replacement of the transferrable hydrogen atom by deuterium in the reaction passing ^{3}**TS**$_{\text{HA}}$ we used the Eyring and Wigner models (see Methods section) to estimate the KIE. Values of KIE$_{\text{E}}$ and KIE$_{\text{W}}$ of 4.9 and 5.4 were obtained, whereas these values increased up to 5.1 and 5.7, respectively, when the fully deuterated substrate was used. Our calculated isotope effect, therefore, predicts the same trends as experiment.

We then calculated a reaction complex of **2** with ethylbenzene (^{2,4}**RC**$_2$) in the gas phase as well as with solvent models included during the geometry optimizations. As mentioned above, the optimized geometry and group spin densities of ^{2}**RC**$_2$ characterize the reactant complex as $^3[\text{Fe}^{\text{IV}}(\text{O})(\text{BQEN})(\text{NCCH}_3)]^{2+}\cdots{}^2\text{EB}^{+\bullet}$. The hydrogen atom abstraction from EB$^{+\bullet}$ by the iron(IV)–oxo complex then leads to electron transfer from the substrate into the π^*_{xz} orbital of the oxidant and spin density changes that are

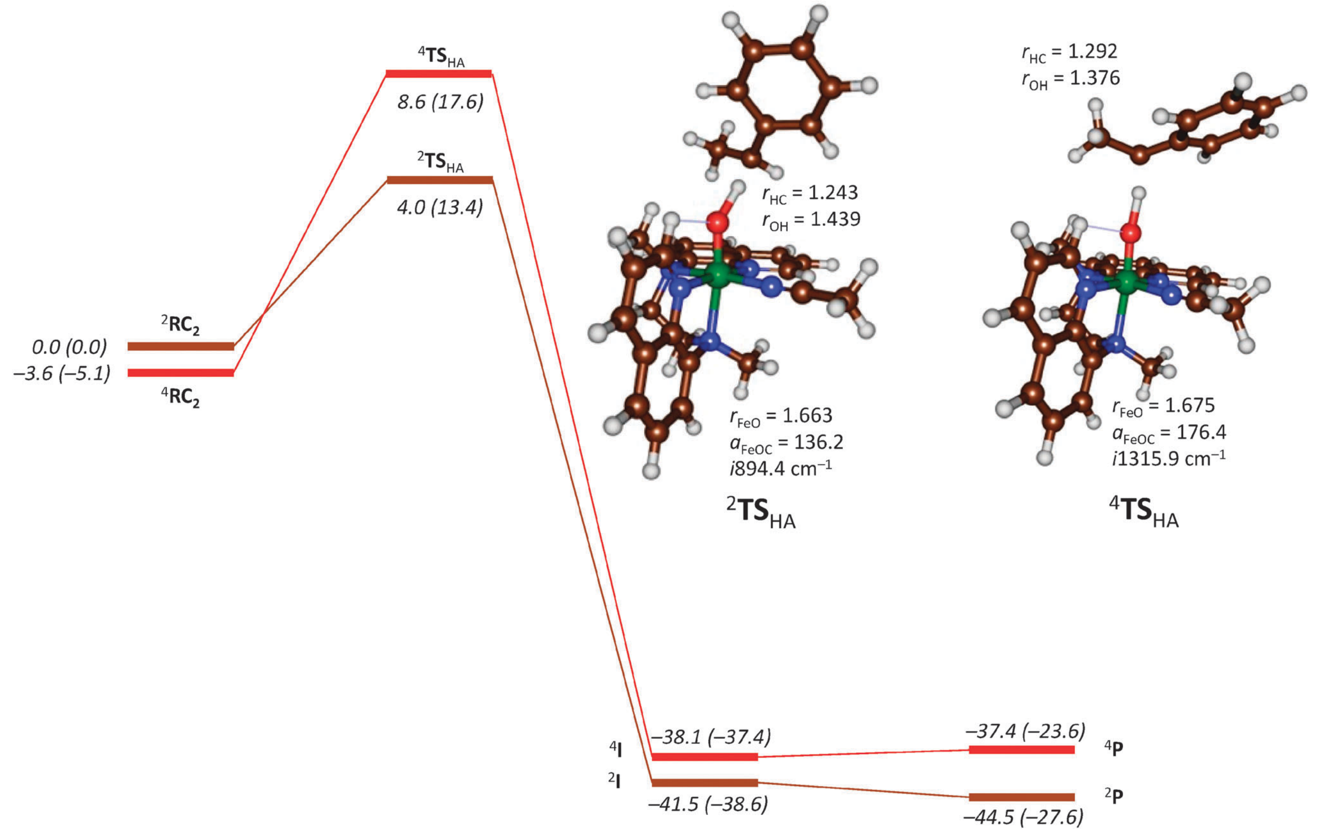

Fig. 4 DFT calculated potential energy profile for the hydrogen atom abstraction from EB by ^{2,4}**2** with energies given in kcal mol^{-1}. Also shown are optimized UB3LYP/BS2(solvent) geometries of ${}^{2,4}\mathbf{TS}_{\mathrm{HA}}$ with bond lengths in angstroms, angles in degrees and the imaginary frequency in wave numbers. Relative energies represent ΔE + ZPE + E_{solv} values obtained after a full geometry optimization in solvent at the UB3LYP/BS2 (out of parenthesis) or at UB3LYP/BS2//UB3LYP/BS1 level of theory on a gas-phase optimized geometry.

very similar to those observed for ${}^{3}\mathbf{TS}_{\mathrm{HA}}$. Technically, the differences in the hydrogen atom abstraction barrier between ${}^{3}\mathbf{RC}_{1}$ and ${}^{2}\mathbf{RC}_{2}$ should be very small as both are an iron(IV)–oxo oxidant. However, the outer-sphere electron transfer from the substrate to the oxidant has oxidized the approaching substrate, and hence the differences in barrier heights observed in Fig. 3 and 4 relate to hydrogen atom abstraction of the C–H bonds of EB and $\mathrm{EB}^{+\bullet}$, respectively. Previously, it was shown that the hydrogen atom abstraction barrier correlates with the strength of the C–H bond of the substrate that is broken in the process.[33] Indeed, experimentally determined rate constants of hydrogen atom abstraction reactions by nonheme iron oxidants were shown to correspond to the bond dissociation energy ($\mathrm{BDE}_{\mathrm{CH}}$) for the breaking of the C–H bond of the substrate.[34] We, therefore, decided to calculate the $\mathrm{BDE}_{\mathrm{CH}}$ values of EB and $\mathrm{EB}^{+\bullet}$ into $\mathrm{C_6H_5CHCH_3}^{\bullet/+}$ and a hydrogen atom and find values of ΔE + ZPE = 82.3 and 41.2 kcal mol^{-1} in the gas phase, respectively. Thus, the oxidized ethylbenzene substrate has considerably weaker benzyl C–H bond strength as compared to the neutral system, and, therefore, the barrier heights for hydrogen atom abstraction obtained for **2′** are significantly lower than those for **1** in agreement with the differences in $\mathrm{BDE}_{\mathrm{CH}}$. Although, the higher reactivity of **2′** *versus* **1** is perceived as due to differences in the oxidation state of the two oxidants, it actually represents the same oxidant but a difference in the ionization state of the substrate with weakened $\mathrm{BDE}_{\mathrm{CH}}$. Also the reaction of **2′** with ethylbenzene incurs a significant KIE value, where we find a $\mathrm{KIE}_{\mathrm{E}} = 5.6$ and a $\mathrm{KIE}_{\mathrm{W}} = 7.2$. These values, therefore, are similar to those found for **1** above.

We also calculated the alternative quartet spin state of **2′** and the hydrogen atom abstraction *via* ${}^{4}\mathbf{TS}_{\mathrm{HA}}$. Thus, ${}^{4}\mathbf{RC}_{2}$ has orbital occupation $\pi^{*}{}_{xy}{}^{2}\ \pi^{*}{}_{xz}{}^{\uparrow}\ \pi^{*}{}_{yz}{}^{\uparrow}\ \pi_{\mathrm{EB}}{}^{\uparrow}$ and refers to ${}^{3}[\mathrm{Fe^{IV}(O)(BQEN)(NCCH_3)}]^{2+}\cdots{}^{2}\mathrm{EB}^{+\bullet}$, but in contrast to ${}^{2}\mathbf{RC}_{2}$ the spin on EB is ferromagnetically coupled to the unpaired electrons on the metal. Energetically, ${}^{2}\mathbf{RC}_{2}$ and ${}^{4}\mathbf{RC}_{2}$ are close in energy. However, during the hydrogen atom abstraction in ${}^{2}\mathbf{TS}_{\mathrm{HA}}$ the unpaired electron from $\mathrm{EB}^{+\bullet}$ is transferred with down-spin to give a $\pi^{*}{}_{xy}{}^{2}\ \pi^{*}{}_{xz}{}^{2}\ \pi^{*}{}_{yz}{}^{1}$ configuration, but in ${}^{4}\mathbf{TS}_{\mathrm{HA}}$ the unpaired electron has up-spin so a $\pi^{*}{}_{xy}{}^{2}\ \pi^{*}{}_{xz}{}^{1}\ \pi^{*}{}_{yz}{}^{1}\ \sigma^{*}{}_{z^2}{}^{1}$ configuration is formed. As this involves a higher lying orbital than in the corresponding doublet spin pathway, the barrier height for ${}^{4}\mathbf{TS}_{\mathrm{HA}}$ is higher in energy than that for ${}^{2}\mathbf{TS}_{\mathrm{HA}}$.

Discussion

Our DFT calculations on ^{3,5}**1** and ^{2,4}**2′** reported above show that both systems are in the iron(IV) oxidation state and the oxidation

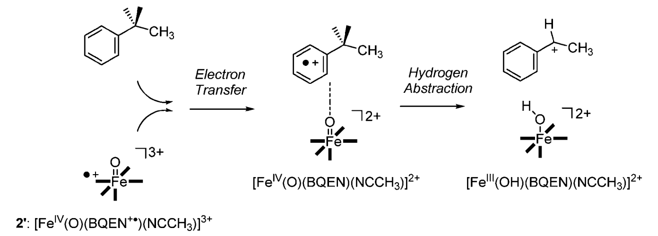

Scheme 2 Calculated reaction mechanism for **2** with oxidation states of critical intermediates identified.

of **2**′ does not oxidize the metal to iron(VI) but rather keeps it at the lower oxidation state of iron(IV) due to electron release from the BQEN macrocycle rather than the metal. Therefore, although **2**′ is perceived as an iron(V)–oxo species, it actually is an iron(IV)–oxo with BQEN cation radical. Moreover, the DFT calculations reported in this work show that approach of a substrate, *e.g.* ethylbenzene, onto $^{4,2}\mathbf{2}'$, leads to a long-range electron transfer upon formation of the reactant complex $^{4,2}\mathbf{RC}_2$: $^{3}[\mathrm{Fe^{IV}(O)(BQEN)(NCCH_3)}]^{2+}\cdots{}^{2}\mathrm{EB}^{+\bullet}$, Scheme 2. The subsequent hydrogen atom abstraction then gives an iron(III)–hydroxo complex and a $C_6H_5CH^+CH_3$ cation.

In previous studies, we showed that the driving force of a hydrogen atom abstraction correlates linearly with the free energy of activation.[24d,27c,33] Therefore, to understand the thermodynamics and kinetics of the reaction mechanisms reported in Fig. 2 and 3 above, we did a detailed analysis of the individual thermodynamic reaction steps for electron and hydrogen atom transfer processes, which are summarized in Fig. 5. Panel (a) in Fig. 5 starts on the top left with $^{2}\mathbf{2}'$ and the reaction to the right reflects a one-electron abstraction to form $^{3}\mathbf{1}$ and the subsequent one-electron abstraction to form $[\mathrm{Fe^{III}(O)(BQEN)(NCCH_3)}]^{+}$. The vertical arrows reflect the hydrogen atom abstraction processes from both $^{2}\mathbf{2}'$ and $^{3}\mathbf{1}$. Thermodynamically, the energy for these reactions is associated with the bond dissociation energy of the O–H bond in the metal–hydroxo complex to revert back into the iron–oxo and an isolated H-atom, as defined as $\mathrm{BDE_{OH}}$. The calculated $\mathrm{BDE_{OH}}$ values for $^{2}\mathbf{2}'$ and $^{3}\mathbf{1}$ are virtually the same in the gas phase, which is not surprising as both complexes are iron(IV)–oxo intermediates. Therefore, geometrically very little differences in the hydrogen atom abstraction reactions will be obtained. The energy gap between the two $\mathrm{BDE_{OH}}$ values widens to 10.2 kcal mol^{-1} in favour of $^{2}\mathbf{2}'$ when solvent, thermal and entropical corrections to the energy are included.

In the case of $\mathrm{BDE_{OH}}$, solvent corrections stabilize the value of **2**′ over **1** by 7.3 kcal mol^{-1}, whereas thermal and entropic

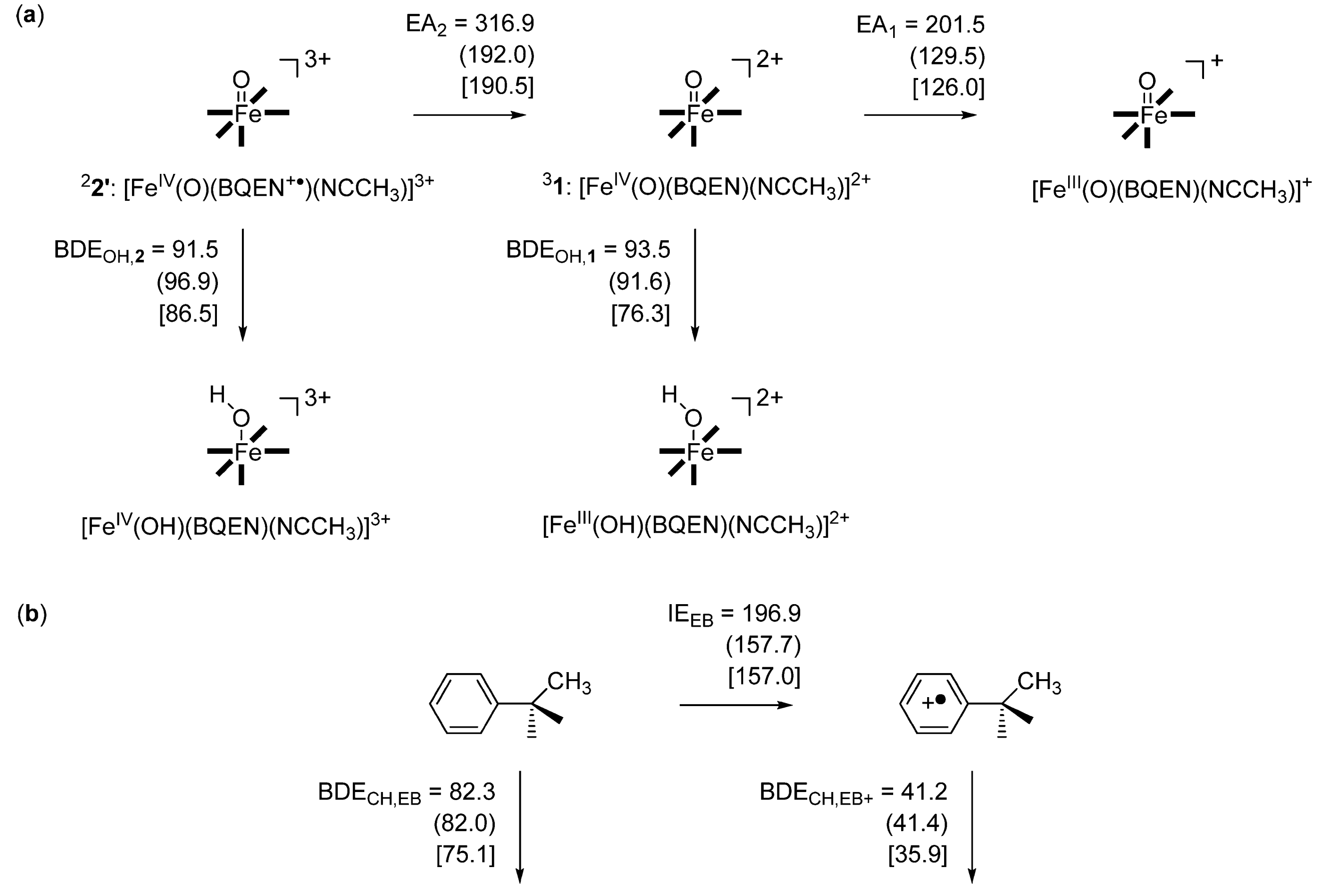

Fig. 5 (a) Thermodynamic reaction pathways for electron and hydrogen atom abstraction by **1** and **2**. (b) Thermodynamic reaction pathways for electron and hydrogen atom abstraction by EB. All data obtained from a geometry optimization at UB3LYP/BS2. Data (in kcal mol^{-1}) reported are ΔE + ZPE in the gas-phase (ΔE + ZPE in solvent) [ΔG in solvent].

corrections add a further 4.9 kcal mol^{-1}. These BDE$_{OH}$ values, therefore, would predict higher reactivity of ^{2}**2′** over ^{3}**1** in solvent for hydrogen atom abstraction reactions.

The major differences between **1** and **2′**, however, are related to their electron affinities or reduction potentials. Thus, ^{2}**2′** has a large electron affinity (EA$_2$) of 316.9 kcal mol^{-1} in the gas-phase and ΔG_{solv} = 190.5 kcal mol^{-1}. It is worth noting that for all calculations we find almost equal values for ΔE + ZPE + E_{solv} and ΔG_{solv}, therefore, entropic and thermal corrections to the solvent corrected enthalpies have a negligible effect on the individual reactions studied. The electron affinity of ^{2}**2′** is considerably larger than that found for ^{3}**1**, where values of EA$_1$ = 201.5 kcal mol^{-1} in the gas-phase and ΔG_{solv} = 126.0 kcal mol^{-1} are found. Consequently, ^{2}**2′** has a ΔG_{solv} = 63.5 kcal mol^{-1} larger electron affinity than ^{3}**1** and will be more susceptible to react by electron abstraction from substrates.

For completeness we also include in Fig. 6 the thermodynamics for the ethylbenzene substrate for removal of an electron and the C–H bond strengths of the benzyl group of ethylbenzene and the ethylbenzene cation radical. As already mentioned above the ethylbenzene cation radical has a considerably weakened C–H bond strength of ΔG_{solv} = 35.9 kcal mol^{-1} as compared to EB. Consequently, hydrogen atom abstraction from EB$^{+\bullet}$ will have a low barrier.

To find out whether a reaction of ^{2}**2′** and ^{3}**1** with EB would lead to a large thermodynamic driving force for electron transfer, the free energy in solvent for the reactions given in eqn (4) and (5) was calculated. Thus, the electron transfer from EB to ^{2}**2′** is calculated to be exergonic by 33.5 kcal mol^{-1}, whereas the one originating from ^{3}**1** is endergonic by 31.0 kcal mol^{-1} instead. These two reactions implicate that in a collision between ^{2}**2′** and EB the driving force will trigger an electron abstraction from EB, whereas that will not be the case in a collision between ^{3}**1** and EB. The large EA$_2$ value will, therefore, lead to a large driving force for electron transfer from suitable substrates including ethylbenzene to **2′**. Moreover, the thermodynamic reaction pathways given in Fig. 5 give further evidence of a likely electron transfer between EB and ^{2}**2′**.

$$^{2}\mathbf{2'} + \mathrm{EB} \rightarrow {}^{3}\mathbf{1} + \mathrm{EB}^{+\bullet} \quad [\Delta G_{solv} = -33.5\ \mathrm{kcal\ mol^{-1}}] \tag{4}$$

$$^{3}\mathbf{1} + \mathrm{EB} \rightarrow {}^{4}[\mathrm{Fe^{III}(O)(BQEN)(NCCH_3)}]^{+} + \mathrm{EB}^{+\bullet} \quad [\Delta G_{solv} = +31.0\ \mathrm{kcal\ mol^{-1}}] \tag{5}$$

Despite the fact that the BDE$_{OH}$ values of **1** and **2′** are virtually the same, actually at the free energy level with solvent included they are separated by about 10 kcal mol^{-1}. However, much more dramatic differences in the electron affinity of both complexes are found. Thus, the bond dissociation energy to break the A–H bond (BDE$_{AH}$) – or hydrogen atom abstraction ability of compound A – can be split into an individual electron and proton transfer *via* eqn (6), whereby ΔG_{acid} represents the acidity of the weak acid AH, EA$_A$ is the electron affinity of A, and IE$_H$ the ionization energy of a H-atom. The experimentally reported value of IE$_H$ is 13.598 eV.[35]

$$\mathrm{A{-}H} \rightarrow \mathrm{A} + \mathrm{H} + \mathrm{BDE_{AH}} \tag{6a}$$

$$\mathrm{BDE_{AH}} = \Delta G_{\mathrm{acid,AH}} - \mathrm{EA_A} - \mathrm{IE_H} \tag{6b}$$

Using the data from Fig. 5 and the known IE$_H$ value we calculate a ΔG_{acid} of 590.5 kcal mol^{-1} for [Fe^{IV}(OH)(BQEN)(NCCH$_3$)]$^{3+}$, whereas proton transfer to **1** gives the complex [Fe^{III}(OH)(BQEN)(NCCH$_3$)]$^{2+}$ with ΔG_{acid} = 515.9 kcal mol^{-1}. The large difference between EA$_2$ and EA$_1$, therefore, has a direct impact on the acidity of the iron(III)–hydroxo group and makes it considerably more acidic. The origin of the difference in electron affinity of **1** and **2′** is due to difference in electron transfer processes. Upon reduction of ^{2}**2′** an electron is transferred into the low-lying π^*_{BQEN} orbital to form a triplet spin $\pi^{*2}_{xy}\ \pi^{*1}_{xz}\ \pi^{*1}_{yz}\ \pi^{*2}_{BQEN}$ configuration.

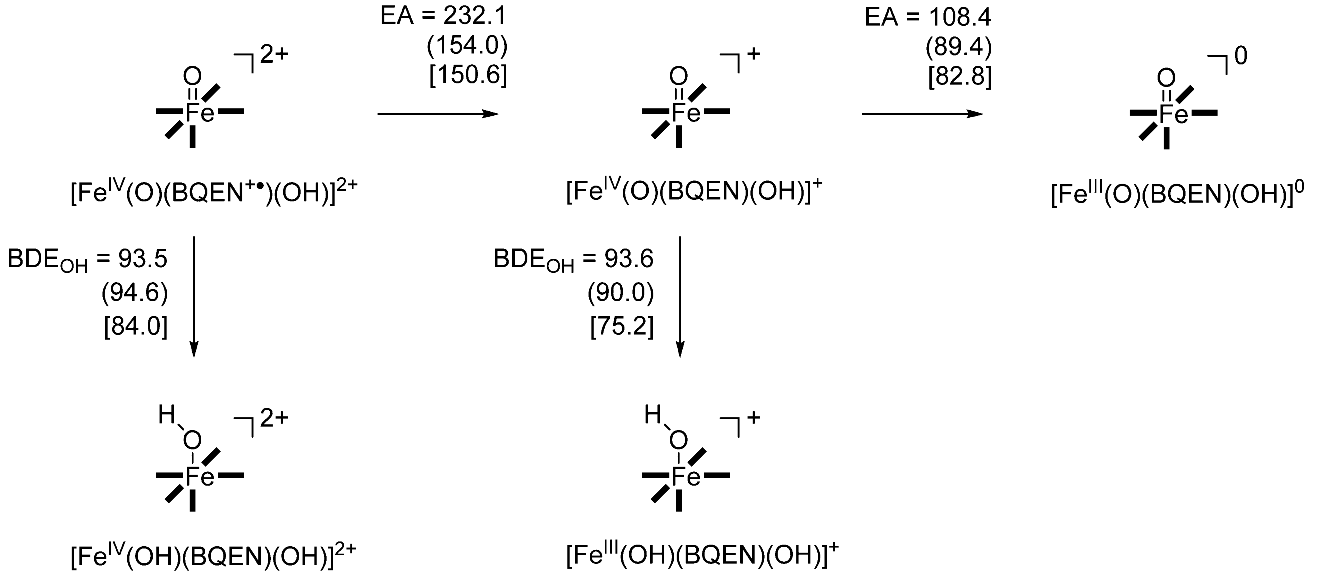

Fig. 6 Thermodynamic reaction pathways for electron and hydrogen atom abstraction by [Fe(O)(BQEN)(OH)]$^{2+}$ and [Fe(O)(BQEN)(OH)]$^{+}$. All data obtained from a geometry optimization at UB3LYP/BS2. Data (in kcal mol^{-1}) reported are ΔE + ZPE in the gas-phase (ΔE + ZPE in solvent) [ΔG in solvent].

On the other hand, reduction of ^{3}**1** leads to filling of the virtual $\sigma^*_{z^2}$ orbital with a single electron. As the $\sigma^*_{z^2}$ orbital is significantly higher in energy than the π^*_{BQEN} orbital this means the reduction of **1** will incur a much smaller electron affinity than adding an electron to π^*_{BQEN}, which is indeed what is found in Fig. 5.

To find out whether the *cis*-ligand of the metal–oxo group affects the EA and ΔG_{acid} values, we did a further set of calculations on the electron and hydrogen atom transfer reactions for complexes $[\mathrm{Fe^{IV}(O)(BQEN^{+\bullet})(OH)}]^{2+}$ and $[\mathrm{Fe^{IV}(O)(BQEN)(OH)}]^{+}$, *i.e.* complexes **2′** and **1** that have the acetonitrile ligand replaced by $\mathrm{OH^-}$. We should note here that replacement of the acetonitrile equatorial ligand by hydroxide does not change the spin state ordering and electronic configuration and these complexes are characterized like **2′** and **1** above. Fig. 6 displays the thermodynamic reaction pathways for $[\mathrm{Fe^{IV}(O)(BQEN^{+\bullet})(OH)}]^{2+}$ and $[\mathrm{Fe^{IV}(O)(BQEN)(OH)}]^{+}$. Firstly, a very little effect of replacing the acetonitrile with hydroxide is found on the $\mathrm{BDE_{OH}}$ values of the complexes. For $[\mathrm{Fe^{IV}(OH)(BQEN)(OH)}]^{2+}$ we find a $\mathrm{BDE_{OH}}$ value of $\Delta G_{\mathrm{solv}} = 84.0$ kcal mol^{-1}, whereas its one-electron reduced counterpart has a $\Delta G_{\mathrm{solv}} = 75.2$ kcal mol^{-1}. These values are within 2.5 kcal mol^{-1} from those obtained with an acetonitrile molecule in the *cis*-position. The situation, however, changes dramatically for the electron affinities and acidity values of the complexes when the acetonitrile ligand is replaced by hydroxide. Thus, $[\mathrm{Fe^{IV}(O)(BQEN^{+\bullet})(OH)}]^{2+}$ has an electron affinity of $\Delta G_{\mathrm{solv}} =$ 150.6 kcal mol^{-1}, whereas the much lower value of 82.8 kcal mol^{-1} is found for $[\mathrm{Fe^{IV}(O)(BQEN)(OH)}]^{+}$. These lowered electron affinities with respect to complexes **2′** and **1** also mean reduced acidity of the protonated complexes, for which we find values of 548.2 and 471.6 kcal mol^{-1}, respectively.

In addition, a reaction of $[\mathrm{Fe^{IV}(O)(BQEN^{+\bullet})(OH)}]^{2+}$ with ethylbenzene is calculated to give an endergonic electron transfer of 6.4 kcal mol^{-1} using the data given in Fig. 5 and 6. Therefore, replacing the acetonitrile equatorial ligand in complex **2′** with an anion such as a hydroxide will affect the stability and reactivity of the complex and will prevent a long-range electron transfer with substrates like ethylbenzene. The electron transfer from ethylbenzene to $[\mathrm{Fe^{IV}(O)(BQEN)(OH)}]^{+}$ is calculated to be even more endergonic ($\Delta G_{\mathrm{solv}} = 74.2$ kcal mol^{-1}) and consequently is not likely to happen.

In summary, we establish reasons for the large thermodynamic driving force for electron transfer from ethylbenzene to **2′** as originating from a high electron affinity of the oxidant of $\Delta G_{\mathrm{solv}} = 190.5$ kcal mol^{-1}. This implies that the electron transfer to the approaching substrate could be spontaneous for substrates with an ionization potential below 190.5 kcal mol^{-1} or 8.26 eV. Although, we calculate an ionization energy of 8.54 eV in the gas phase actually in solution the value drops to $\Delta G_{\mathrm{solv}} =$ 6.81 eV. Therefore, in solution the ionization potential of ethylbenzene is sufficiently low to incur a long-range electron transfer to the oxidant and create $^3[\mathrm{Fe^{IV}(O)(BQEN)(NCCH_3)}]^{2+}\cdots{}^2\mathrm{EB^{+\bullet}}$.

Finally, the thermodynamics values of Fig. 6 and 7 also enable us to predict the hydrogen atom transfer driving force in complexes $\mathbf{RC_2}$ and $\mathbf{RC_1}$. As described above, $\mathbf{RC_2}$ undergoes a long-range electron transfer and converts to $[\mathrm{Fe^{IV}(O)(BQEN)(NCCH_3)}]^{2+}$ and $\mathrm{EB^{+\bullet}}$. This complex reacts *via* hydrogen atom transfer *via* eqn (7) with a free energy change of −40.4 kcal mol^{-1}. The DFT calculations for this process, see ESI,† implicated a free energy change of $\Delta G_{\mathrm{solv}} = -42.4$ kcal mol^{-1} for the formation of the radical intermediate ^{2}**I**, and therefore its calculated value is in good agreement with the value estimated from our thermodynamic cycles.

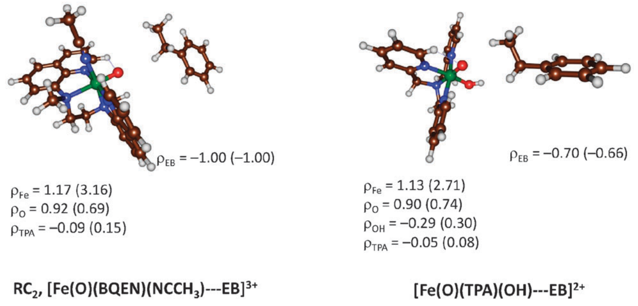

Fig. 7 Group spin densities of $^{4,2}\mathbf{RC_2}$ and $[\mathrm{Fe(O)(TPA)(OH)\cdots EB}]^{2+}$ as calculated with UB3LYP/BS2 in solvent. High-spin data in parenthesis.

$$[\mathrm{Fe^{IV}(O)(BQEN)(NCCH_3)}]^{2+} + \mathrm{EB^{+\bullet}} \rightarrow [\mathrm{Fe^{III}(OH)(BQEN)(NCCH_3)}]^{2+} + \mathrm{C_6H_5CH^{+}CH_3}\ [\Delta G_{\mathrm{solv}} = -40.4\ \mathrm{kcal\ mol^{-1}}] \quad (7)$$

By contrast, if we do the same for complex $\mathbf{RC_1}$ and take the difference in free energy between the $\mathrm{BDE_{CH}}$ and $\mathrm{BDE_{OH}}$ values of oxidant and substrate, we find an almost thermoneutral hydrogen atom abstraction reaction, eqn (8). Indeed, the DFT calculations above predict a radical intermediate with an exergonicity of 6.9 kcal mol^{-1} with respect to the reactant complex in good agreement with the thermodynamically estimated value.

$$[\mathrm{Fe^{IV}(O)(BQEN)(NCCH_3)}]^{2+} + \mathrm{EB} \rightarrow [\mathrm{Fe^{III}(OH)(BQEN)(NCCH_3)}]^{2+} + \mathrm{C_6H_5CH^{\bullet}CH_3}\quad [\Delta G_{\mathrm{solv}} = -1.2\ \mathrm{kcal\ mol^{-1}}] \quad (8)$$

To test whether the electron transfer observed here in our reactant complexes is a general feature that could be found in alternative iron(V)–oxo complexes as well, we also decided to investigate the well-studied $[\mathrm{Fe(O)(TPA)(OH)}]^{2+}$, TPA = tris-(2-pyridylmethyl)amine, system of Costas and co-workers.[10b] Previously, $[\mathrm{Fe(O)(TPA)(X)}]^{2+}$ with X = halide or $\mathrm{OH^-}$ has been used in studies of the *cis*-effect on substrate activation by metal–oxo species, but also as a model for non-heme iron halogenases. Technically the $[\mathrm{Fe(O)(TPA)(OH)}]^{2+}$ is an iron(V)–oxo complex as indeed confirmed by DFT calculations.[36] The question, of course, arises whether the oxidation state of the complex stays in the iron(V) state upon approach of an ethylbenzene molecule. Thus, we optimized the reactant complex $[\mathrm{Fe(O)(TPA)(OH)\cdots EB}]^{2+}$ in the doublet and quartet spin states at UB3LYP-D3/BS2 level of theory and show the structures and group spin densities of the complexes alongside those of $^{4,2}\mathbf{RC_2}$ in Fig. 7.

The results in Fig. 7 show that upon approach of an ethylbenzene molecule to an iron(V)–oxo center, a long-range electron transfer takes place from substrate to oxidant. Therefore, the group spin densities of $^{2,4}\mathbf{RC_2}$ and $[\mathrm{Fe(O)(TPA)(OH)\cdots EB}]^{2+}$ both refer to an iron(IV)–oxo complex with a nearby $\mathrm{EB^{+\bullet}}$ ion. Both complexes have a doublet spin state with $\pi^{*}_{xy}{}^{2}\ \pi^{*}_{xz}{}^{1}\ \pi^{*}_{yz}{}^{1}\ \pi_{\mathrm{EB}}{}^{1}$ configuration, *i.e.* a triplet spin iron(IV)–oxo complex with a nearby doublet cation radical ethylbenzene. By contrast the quartet spin state configurations of these complexes have orbital occupation $\pi^*_{xy}{}^2$ $\pi^*_{xz}{}^1$ $\pi^*_{yz}{}^1$ $\sigma^*_{z^2}{}^1$ $\pi_{EB}{}^1$ configuration with the ethylbenzene radical anti-ferromagnetically coupled to three unpaired electrons on the iron(IV)–oxo complex. Note that without ethylbenzene the $[Fe(O)(TPA)(OH)]^{2+}$ complex converges to an iron(V)–oxo species and no ligand radical is found. The TPA ligand, therefore, has much lower lying molecular orbitals than a BQEN ligand system and as a result the π_{BQEN} orbitals become competitive with the π^*_{xz}/π^*_{yz} orbitals on the FeO group. As a result of this $[Fe(O)(BQEN)(NCCH_3)]^{3+}$ has an electronic configuration representing an iron(IV)–oxo coupled to a ligand radical, whereas $[Fe(O)(TPA)(OH)]^{2+}$ is an iron(V)–oxo species.

Conclusions

In summary, we present here the first comparative study on the reactivity patterns of nonheme iron(IV)–oxo *versus* iron(V)–oxo intermediates. Upon approach of the substrate to the iron(IV)–oxo ligand cation radical it abstracts an electron from the substrate readily, and thereby creates an iron(IV)–oxo ligand cation radical species. The perceived reactivity of the iron(V)–oxo species, therefore, is due to the activity of the iron(IV)–oxo ligand cation radical instead. We also show that oxidation of ethylbenzene weakens the C–H bond strength of the substrate and thereby lowers the hydrogen atom abstraction barriers and leads to higher reactivity. This is an example of how outer-sphere (long-range) electron transfer can change the C–H bond strength of the substrate so that a more efficient H-transfer becomes possible. The outer-sphere electron transfer may be a common feature in transition metal catalysis, but further research will be needed to find more examples of this type of reactivity patterns.

Acknowledgements

SdV thanks the Royal Society for an International Exchanges with Korea grant. The National Service of Computational Chemistry Software (NSCCS) is acknowledged for cpu time. DK acknowledges Department of Science and Technology (New Delhi) for a Ramanujan Fellowship. The research at EWU was supported by NRF of Korea through CRI (NRF-2012R1A3A2048842) and GRL (NRF-2010-00353).

Notes and references

1 (*a*) E. I. Solomon, T. C. Brunold, M. I. Davis, J. N. Kemsley, S.-K. Lee, N. Lehnert, F. Neese, A. J. Skulan, Y.-S. Yang and J. Zhou, *Chem. Rev.*, 2000, **100**, 235; (*b*) T. D. H. Bugg and S. Ramaswamy, *Curr. Opin. Chem. Biol.*, 2008, **12**, 134; (*c*) M. J. Ryle and R. P. Hausinger, *Curr. Opin. Chem. Biol.*, 2002, **6**, 193; (*d*) Y. Mishina, E. M. Duguid and C. He, *Chem. Rev.*, 2006, **106**, 215; (*e*) *Iron-containing enzymes: Versatile catalysts of hydroxylation reactions in nature*, ed. S. P. de Visser and D. Kumar, RSC Publishing, Cambridge (UK), 2011; (*f*) P. He and G. R. Moran, *Curr. Opin. Chem. Biol.*, 2009, **13**, 443; (*g*) D. Buongiorno and G. D. Straganz, *Coord. Chem. Rev.*, 2013, **257**, 541.

2 (*a*) M. Costas, M. P. Mehn, M. P. Jensen and L. Que Jr, *Chem. Rev.*, 2004, **104**, 939; (*b*) S. V. Kryatov, E. V. Rybak-Akimova and S. Schindler, *Chem. Rev.*, 2005, **105**, 2175; (*c*) M. M. Abu-Omar, A. Loaiza and N. Hontzeas, *Chem. Rev.*, 2005, **105**, 2227; (*d*) R. van Eldik, *Coord. Chem. Rev.*, 2007, **251**, 1649; (*e*) P. C. A. Bruijnincx, G. van Koten and R. J. M. Klein Gebbink, *Chem. Soc. Rev.*, 2008, **37**, 2716; (*f*) S. P. de Visser, J.-U. Rohde, Y.-M. Lee, J. Cho and W. Nam, *Coord. Chem. Rev.*, 2013, **257**, 381; (*g*) W. Nam, Y.-M. Lee and S. Fukuzumi, *Acc. Chem. Res.*, 2014, **47**, 1146.

3 See, *e.g.*, (*a*) M. R. Bukowski, K. D. Koehntop, A. Stubna, E. L. Bominaar, J. A. Halfen, E. Münck, W. Nam and L. Que Jr, *Science*, 2005, **310**, 1000; (*b*) J.-U. Rohde, J.-H. In, M. H. Lim, W. W. Brennessel, M. R. Bukowski, A. Stubna, E. Münck, W. Nam and L. Que Jr, *Science*, 2003, **299**, 1037; (*c*) M. Martinho, F. Banse, J.-F. Bartoli, T. A. Mattioli, P. Battioni, P. Horner, S. Bourcier and J.-J. Girerd, *Inorg. Chem.*, 2005, **44**, 9592; (*d*) C. V. Sastri, M. S. Seo, M. J. Park, K. M. Kim and W. Nam, *Chem. Commun.*, 2005, 1405; (*e*) F. T. De Oliveira, A. Chanda, D. Banerjee, X. Shan, S. Mondal, L. Que Jr, E. L. Bominaar, E. Münck and T. J. Collins, *Science*, 2007, **315**, 835; (*f*) T. A. Jackson, J.-U. Rohde, M. S. Seo, C. V. Sastri, R. DeHont, A. Stubna, T. Ohta, T. Kitagawa, E. Münck, W. Nam and L. Que Jr, *J. Am. Chem. Soc.*, 2008, **130**, 12394.

4 (*a*) K. Chen, M. Costas, J. Kim, A. K. Tipton and L. Que Jr, *J. Am. Chem. Soc.*, 2002, **124**, 3026; (*b*) A. Company, L. Gómez, M. Güell, X. Ribas, J. M. Luis, L. Que Jr and M. Costas, *J. Am. Chem. Soc.*, 2007, **129**, 15766; (*c*) R. Mas-Ballesté, M. Fujita and L. Que Jr, *Dalton Trans.*, 2008, 1828; (*d*) P. Comba, M. Maurer and P. Vadivelu, *Inorg. Chem.*, 2009, **48**, 10348; (*e*) A. Company, Y. Feng, M. Güell, X. Ribas, J. M. Luis, L. Que Jr and M. Costas, *Chem. – Eur. J.*, 2009, **15**, 3359; (*f*) I. Prat, J. S. Mathieson, M. Güell, X. Ribas, J. M. Luis, L. Cronin and M. Costas, *Nat. Chem.*, 2011, **3**, 788.

5 (*a*) K. Chen and L. Que Jr, *J. Am. Chem. Soc.*, 2001, **123**, 6327; (*b*) A. D. Ryabov, *Adv. Inorg. Chem.*, 2013, **65**, 117.

6 (*a*) A. Nielsen, F. B. Larsen, A. D. Bond and C. J. McKenzie, *Angew. Chem., Int. Ed.*, 2006, **45**, 1602; (*b*) A. Lennartson and C. J. McKenzie, *Angew. Chem., Int. Ed.*, 2012, **51**, 6767.

7 S. H. Lee, J. H. Han, H. Kwak, S. J. Lee, E. Y. Lee, H. J. Kim, J. H. Lee, C. Bae, S. N. Lee, Y. Kim and C. Kim, *Chem. – Eur. J.*, 2007, **13**, 9393.

8 S. Kundu, J. Van Kirk Thompson, A. D. Ryabov and T. J. Collins, *J. Am. Chem. Soc.*, 2011, **133**, 18546.

9 J. Yoon, S. A. Wilson, Y. K. Jang, M. S. Seo, K. Nehru, B. Hedman, K. O. Hodgson, E. Bill, E. I. Solomon and W. Nam, *Angew. Chem., Int. Ed.*, 2009, **48**, 1257.

10 (*a*) *Jaguar, version 7.9*, Schrodinger, LLC, New York, NY, 2011; (*b*) *Gaussian-09, Revision C.01*, Gaussian Inc., Wallingford CT, 2010.

11 (*a*) A. D. Becke, *J. Chem. Phys.*, 1993, **98**, 5648; (*b*) C. Lee, W. Yang and R. G. Parr, *Phys. Rev. B: Condens. Matter Mater. Phys.*, 1988, **37**, 785.

12 (*a*) S. P. de Visser, *Angew. Chem., Int. Ed.*, 2006, **45**, 1790; (*b*) D. Kumar, W. Thiel and S. P. de Visser, *J. Am. Chem. Soc.*, 2011, **133**, 3869.

13 S. Grimme, *J. Chem. Phys.*, 2006, **124**, 034108.

14 M. Reiher, O. Salomon and B. A. Hess, *Theor. Chem. Acc.*, 2001, **107**, 48.

15 (*a*) N. C. Handy and A. J. Cohen, *Mol. Phys.*, 2001, **99**, 403; (*b*) J. P. Perdew, K. Burke and M. Ernzerhof, *Phys. Rev. Lett.*, 1996, **77**, 3865.

16 S. P. de Visser, M. G. Quesne, B. Martin, P. Comba and U. Ryde, *Chem. Commun.*, 2014, **50**, 262.

17 (*a*) P. J. Hay and W. R. Wadt, *J. Chem. Phys.*, 1985, **82**, 270; (*b*) W. J. Hehre, R. Ditchfield and J. A. Pople, *J. Chem. Phys.*, 1972, **56**, 2257.

18 (*a*) A. K. Vardhaman, C. V. Sastri, D. Kumar and S. P. de Visser, *Chem. Commun.*, 2011, **47**, 11044; (*b*) A. K. Vardhaman, P. Barman, S. Kumar, C. V. Sastri, D. Kumar and S. P. de Visser, *Angew. Chem., Int. Ed.*, 2013, **52**, 12288; (*c*) A. K. Vardhaman, P. Barman, S. Kumar, C. V. Sastri, D. Kumar and S. P. de Visser, *Chem. Commun.*, 2013, **49**, 10926.

19 (*a*) S. P. de Visser, *Chem. – Eur. J.*, 2006, **12**, 8168; (*b*) D. J. Heyes, M. Sakuma, S. P. de Visser and N. S. Scrutton, *J. Biol. Chem.*, 2009, **284**, 3762.

20 D. Kumar, S. P. de Visser, P. K. Sharma, S. Cohen and S. Shaik, *J. Am. Chem. Soc.*, 2004, **126**, 1907.

21 (*a*) D. Kumar, H. Hirao, L. Que Jr and S. Shaik, *J. Am. Chem. Soc.*, 2005, **127**, 8026; (*b*) S. P. de Visser, *J. Am. Chem. Soc.*, 2006, **128**, 15809; (*c*) S. Ye and F. Neese, *Proc. Natl. Acad. Sci. U. S. A.*, 2011, **108**, 1228.

22 (*a*) M. T. Green, *J. Am. Chem. Soc.*, 1999, **121**, 7939; (*b*) J. Rittle and M. T. Green, *Science*, 2010, **330**, 933; (*c*) K. Yoshizawa, Y. Shiota and T. Yamabe, *J. Am. Chem. Soc.*, 1999, **121**, 147.

23 (*a*) S. P. de Visser, *J. Am. Chem. Soc.*, 2006, **128**, 9813; (*b*) L. Bernasconi and E.-J. Baerends, *Eur. J. Inorg. Chem.*, 2008, 1672; (*c*) C. Y. Geng, S. Ye and F. Neese, *Angew. Chem., Int. Ed.*, 2010, **49**, 5717; (*d*) S. Shaik, H. Chen and D. Janardanan, *Nat. Chem.*, 2011, **3**, 19; (*e*) P. Comba, M. Maurer and P. Vadivelu, *Inorg. Chem.*, 2009, **48**, 10389.

24 (*a*) J. C. Schöneboom, H. Lin, N. Reuter, W. Thiel, S. Cohen, F. Ogliaro and S. Shaik, *J. Am. Chem. Soc.*, 2002, **124**, 8142; (*b*) S. P. de Visser, S. Shaik, P. K. Sharma, D. Kumar and W. Thiel, *J. Am. Chem. Soc.*, 2003, **125**, 15779; (*c*) S. P. de Visser, L. Tahsini and W. Nam, *Chem. – Eur. J.*, 2009, **15**, 5577; (*d*) D. Kumar, G. N. Sastry and S. P. de Visser, *Chem. – Eur. J.*, 2011, **17**, 6196.

25 S. Shaik, H. Hirao and D. Kumar, *Nat. Prod. Rep.*, 2007, **24**, 533.

26 M. G. Quesne, R. Latifi, L. E. Gonzalez-Ovalle, D. Kumar and S. P. de Visser, *Chem. – Eur. J.*, 2014, **20**, 435.

27 See, *e.g.*, (*a*) M. Güell, J. M. Luis, M. Solà and M. Swart, *J. Phys. Chem. A*, 2008, **112**, 6384; (*b*) R. Latifi, M. A. Sainna, E. V. Rybak-Akimova and S. P. de Visser, *Chem. – Eur. J.*, 2013, **19**, 4058; (*c*) D. Kumar, R. Latifi, S. Kumar, E. V. Rybak-Akimova, M. A. Sainna and S. P. de Visser, *Inorg. Chem.*, 2013, **52**, 7968.

28 S. P. de Visser and L. S. Tan, *J. Am. Chem. Soc.*, 2008, **130**, 12961.

29 P. Leeladee, R. A. Baglia, K. A. Prokop, R. Latifi, S. P. de Visser and D. P. Goldberg, *J. Am. Chem. Soc.*, 2012, **134**, 10397.

30 S. P. de Visser, *J. Phys. Chem. A*, 2005, **109**, 11050.

31 S. M. Pratter, C. Konstantinovics, C. L. M. DiGiuro, E. Leitner, D. Kumar, S. P. de Visser, G. Grogan and G. D. Straganz, *Angew. Chem., Int. Ed.*, 2013, **52**, 9677.

32 S. Sahu, L. R. Widger, M. G. Quesne, S. P. de Visser, H. Matsumura, P. Moënne-Loccoz, M. A. Siegler and D. P. Goldberg, *J. Am. Chem. Soc.*, 2013, **135**, 10590.

33 R. Latifi, M. Bagherzadeh and S. P. de Visser, *Chem. – Eur. J.*, 2009, **15**, 6651.

34 X. Wu, M. S. Seo, K. M. Davis, Y.-M. Lee, J. Chen, K.-B. Cho, Y. N. Pushkar and W. Nam, *J. Am. Chem. Soc.*, 2011, **133**, 20088.

35 S. G. Lias, in *Ionization Energy Evaluation in NIST Chemistry WebBook*, NIST Standard Reference Database Number 69: ed. P. J. Linstrom and W. G. Mallard, National Institute of Standards and Technology, Gaithersburg MD, 2005, p. 20899, http://webbook.nist.gov.

36 (*a*) Y. Ma and P. B. Balbuena, *J. Phys. Chem. B*, 2007, **111**, 2711; (*b*) P. Comba, G. Rajaraman and H. Rohwer, *Inorg. Chem.*, 2007, **46**, 3826; (*c*) A. Bassan, M. R. A. Blomberg, P. E. M. Siegbahn and L. Que Jr, *J. Am. Chem. Soc.*, 2002, **124**, 11056; (*d*) S. P. de Visser and W. Nam, *J. Phys. Chem. A*, 2008, **112**, 12887.

ORGANOMETALLICS
Article
pubs.acs.org/Organometallics

A Trimetal Carbene with Reactivity Reminiscent of Fischer–Tropsch Catalysis

Mala A. Sainna,[†,§] Devendra Singh,[‡,§] Devesh Kumar,*[,‡] and Sam P. de Visser*[,†]

[†]Manchester Institute of Biotechnology and School of Chemical Engineering and Analytical Science, The University of Manchester, 131 Princess Street, Manchester M1 7DN, United Kingdom

[‡]Department of Applied Physics, School for Physical Sciences, Babasaheb Bhimrao Ambedkar University, Vidya Vihar, Rae Bareilly Road, Lucknow (U. P.) 226 025, India

Supporting Information

ABSTRACT: Metal-carbenes are common reaction intermediates in chemical catalysis; however, very few catalysts are known with a trimetal-carbene active center. In this work, we describe a computational study into the chemical and catalytic properties of a unique trimetal carbene containing a Ru_2Pt-carbene core, $[(CpRu)_2(\mu_2\text{-}CH_2)(\mu_3\text{-}NCH_3)Pt(P(CH_3)_3)_2]$, with and without bound CO. The chemical structure and individual orbital interactions are identified from a natural bond orbital analysis, and the reaction pathways for consecutive intramolecular CH_3 and H transfer (or vice versa) are investigated. The studies show that CO binding has dramatic effects on the reaction mechanism and weakens the Ru–H bond strength. The reaction processes are rationalized by valence bond models and thermochemical bond strength studies. The work leads to suggestions on how to improve this chemical system for enhanced alkane synthesis.

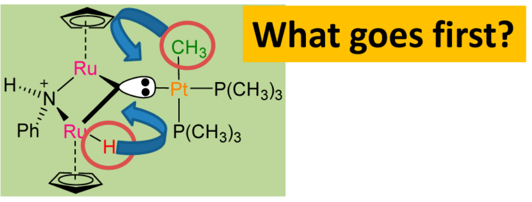

■ INTRODUCTION

In industrial Fischer–Tropsch catalysis, alkanes are being synthesized from H_2 and CO gas on a metal surface, which is a process that was developed and exploited in Germany in the 1920s and 1930s as an alternative to fossil fuels.[1] With dwindling supplies of fossil fuels, urgent alternative sources are needed; however, the Fischer–Tropsch process is energetically demanding and usually requires high pressures and/or temperatures as well as expensive heterogeneous catalysts.[2] Research on improving Fischer–Tropsch catalysis is hampered due to the lack of knowledge of details of the reaction mechanism and the properties played by the metal surface. In addition, few homogeneous catalysts are known that perform a Fischer–Tropsch-type reaction.[3]

Recently, the Matsuzaka group[4] reported the synthesis and spectroscopic characterization of $[(Cp^*Ru)_2(\mu_2\text{-}CH_2)(\mu_3\text{-}NPh)Pt(P(CH_3)_3)_2]$, which was treated with CH_3OTf in diethyl ether and, after heating in toluene, produced a unique structure (labeled as **3** in ref 4) with a trigonal sp^2 hybridized carbon atom linked to three transition-metal atoms. It was reported that structure **3** reacted via a Fischer–Tropsch-type reaction via H and CH_3 migration from the RuH and $PtCH_3$ ligands to form $\mu_2\text{-}CHCH_3$ products (Scheme 1). Therefore, structure **3** catalyzes the C–C and C–H bond formation reactions for the synthesis of alkanes alike to the Fischer–Tropsch process, which are thermodynamically difficult processes. As such, structure **3** is one of the few homogeneous Fischer–Tropsch catalysts available currently. However, little is known of the reaction process and the overall potential of this type of chemical system. In order to explore its possibilities further, it is important to fully understand the origin of the reaction mechanism and the chemical properties that drive the process. Currently, there is limited knowledge on the chemical system displayed in Scheme 1, and experimental studies failed to identify intermediates along the reaction mechanism. Hence, it is unclear how and why this chemical system operates and how it can be further improved. Moreover, there are very few examples in the literature of analogous processes, and this chemical system may pose a novel synthetic route for the generation of alkanes on a carbene center.

Scheme 1. Chemical Reaction Investigated in This Work

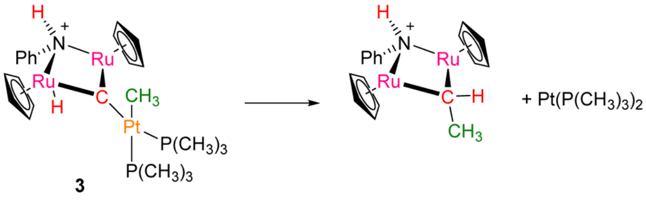

The aim of the studies in this work, therefore, is focused on establishing the reaction mechanism of alkyl chain growth on the carbene center and the chemical properties of the reaction center shown in Scheme 1. First, the chemical properties of the trimetal carbene center are poorly understood, and theory may give insight into whether it would be a suitable catalytic center. Second, it is unclear whether there is an initial H transfer, followed by a CH_3 transfer or the reverse. Moreover, it may very well be that both mechanisms are kinetically and thermodynamically possible. Third, as shown in iron-porphyrin

Received: February 7, 2015
Published: April 30, 2015

DOI: 10.1021/acs.organomet.5b00305
Organometallics 2015, 34, 1651–1660

Scheme 2. Definition of the Chemical Model, and Nomenclature of Structures along the Reaction Mechanism

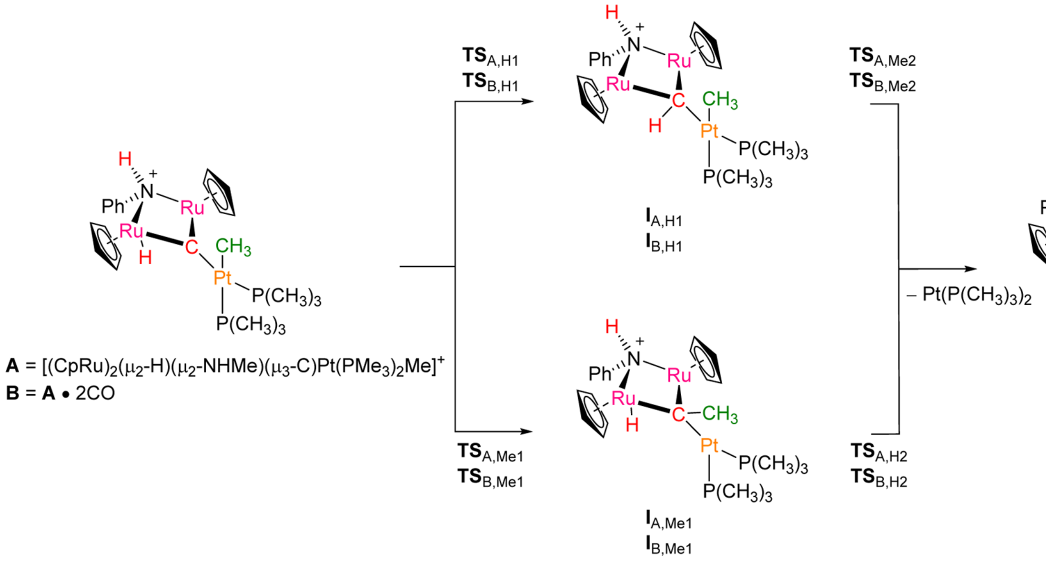

chemistry, for many examples, the reaction can take place via proton transfer, hydrogen atom transfer, or hydride transfer.[5] Furthermore, hydrogen atom and hydride transfer processes may happen via proton-coupled electron transfer (PCET), whereby the electrons move to a different donor site than the protons involved in the reaction. Theory is the ideal tool to distinguish between these mechanistic pathways and to establish the electronic features that drive this important mechanism. In addition to the reactivity questions and the synthesis of alkyl groups on this carbon center, there are also questions related to the chemical structure of the central carbon atom in **3** itself. Thus, an sp^2 hybridized carbon atom would make **3** a carbocation with a planar conformation, which is unlikely given the fact that the carbon atom is surrounded by positively charged metal ions. On the other hand, if the carbon atom is negatively charged, i.e., a carbanion, it would have a pyramidal structure because of its sp^3 hybridization, which is in disagreement with the experimental crystal structure coordinates. Clearly, the structural and reactivity features of this complex are poorly understood, and theory may provide insight into its electronic and structural features.

The Ru$_2$PtC core of structure **3** is an unusual structure in chemical catalysis but shows some resemblance to Grubbs catalyst,[6] where the metal is covalently linked to a carbon atom through either a single, a double, or a triple bond. However, as far as we know, there are no reported catalysts in the literature, where the carbon atom is ligated to two Ru atoms and a Pt atom. There are several examples in the literature of carbido centered structures, where the carbon atom is bound to three or more metal atoms,[7] but very few of these show catalytic activity. It, therefore, remains unclear why structure **3** is reactive for the formation of alkyl groups from individual methyl, hydrogen, and carbon groups. In order to gain insight into the peculiar structure and reactivity of **3**, we decided to do a computational study and establish the electronic and thermochemical features. As we will show here, our studies give fundamental insight into the nature of the metal−carbon bond and characterizes structure **3** as a trimetal carbene that can react via sequential methyl and hydrogen atom transfer to form μ_2-CHCH$_3$. These results may have direct relevance to heterogeneous catalysis on metal surfaces.

■ METHODS

The calculations reported in this work were performed using density functional theory (DFT) methods as used previously on transition-metal complexes by our groups,[8] and are implemented in the Jaguar 7.7[9] and Gaussian 09[10] program packages. Initial geometries were optimized (without constraints) in Jaguar using the hybrid density functional theory method B3LYP[11] coupled with an LACVP basis set (including a core potential) on ruthenium and platinum and 6-31G on the rest of the atoms: basis set BS1.[12] A subsequent analytical frequency in Gaussian confirmed the structures as local minima with real frequencies only or first-order saddle points with one imaginary frequency for the correct mode. Energies were then improved by running a single point calculation in Jaguar using a triple-ζ quality LACV3P+ basis set on iron and 6-311+G* on the rest of the atoms: basis set BS2. We also tested the effect of dispersion on the reaction energies by doing a UB3LYP-D3 single point calculation in Jaguar using the model of Grimme and co-workers.[13] For a selection of chemical systems, i.e., reactants and transition states, we did geometry optimizations at UB3LYP/BS2 and UB3LYP-D3/BS2, but found very little changes with respect to those obtained at UB3LYP/BS1. Since transition-metal complexes often react via multistate reactivity,[14] we calculated the complete potential energy profile on the lowest-lying singlet, triplet, and quintet spin states; however, in all cases, the singlet spin state was the ground state and well separated from the other spin states. Energies reported in this work contain B3LYP/BS2 energies and include zero-point and solvent corrections (calculated with B3LYP/BS2 using the polarized continuum model with a dielectric constant mimicking toluene).

As occasionally DFT calculations on spin state ordering and relative energies of transition-metal complexes show fluctuations depending on the choice of the density functional method,[15] we decided to do a series of test calculations with alternative DFT methods, namely, B3LYP-D3,[13] BP86,[16] M06,[17] OPBE, and PBE0; see the Supporting Information.[18] Similar to previously reported calculations on analogous systems,[19] these studies confirmed the trends and did not change the conclusions.

The methods described here were benchmarked previously on transition-metal-containing systems and compared with experimentally determined data, which gave free energies of activation within 4 kcal mol^{-1} from experiment,[20] but also gave reasonable agreement for spectroscopic data, where they reproduced resonance Raman, EXAFS, and Mössbauer data excellently.[21] To locate transition-state structures, we ran extensive geometry scans between the various local minima and used the maximum of those scans as a starting point for the actual transition state searches. Moreover, these scans confirmed that

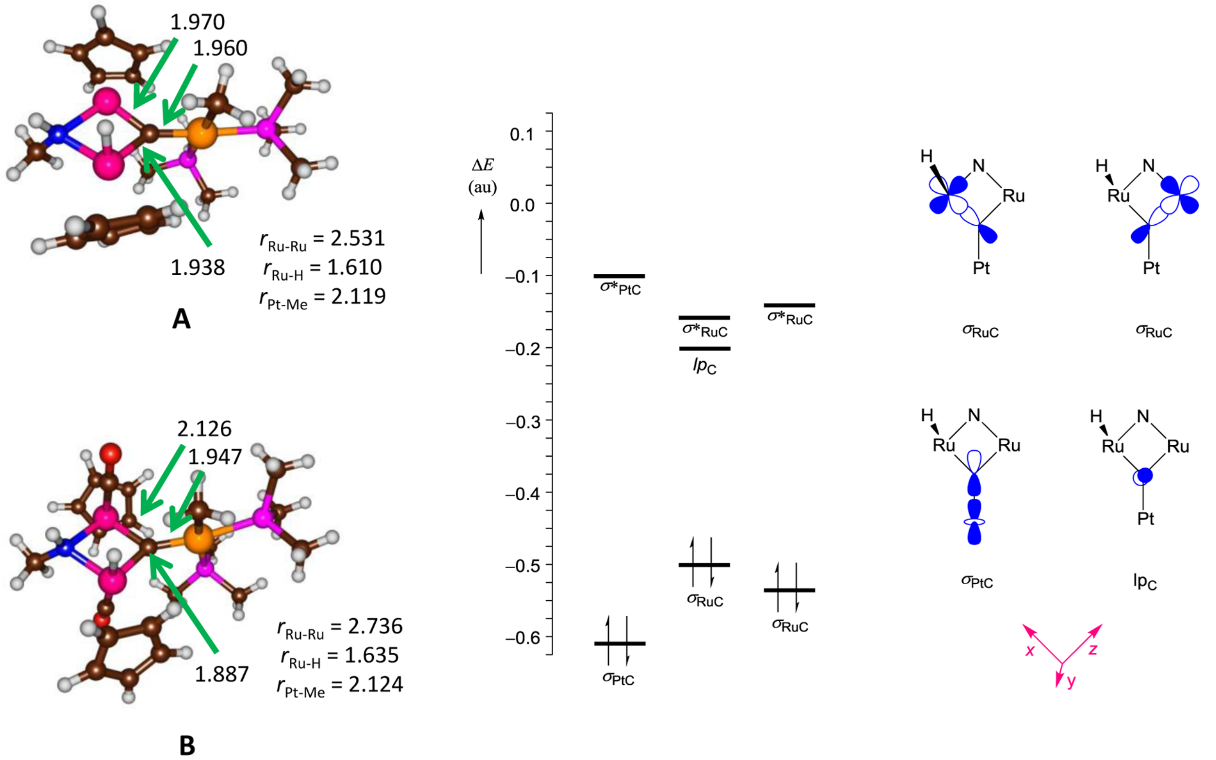

Figure 1. Optimized geometry of **A** and **B** as calculated with B3LYP with bond lengths given in angstroms. The right-hand side displays relative energies of the natural orbitals of **A** and gives drawings of the metal-carbon interactions.

reactants and products indeed connect via the reported transition state.

Our chemical model (Scheme 2) is based on the crystal structure coordinates of $[(Cp^*Ru)_2(\mu_2\text{-}H)(\mu_2\text{-}NHPh)(\mu_3\text{-}C)PtCH_3(P(CH_3)_3)_2]^+$,[4] whereby we replaced the Cp* groups with Cp and phenyl by methyl: Structure **A**. The stereochemical effects of the methyl groups of the $P(CH_3)_3$ groups on the reaction mechanism were investigated by replacement of the $P(CH_3)_3$ groups with PH_3. The latter structures are identified as **A**′, $\mathbf{I}_{A,Me}$′, and $\mathbf{I}_{A,H}$′. As the chemical system is saturated in carbon monoxide, we also created a model with two CO molecules bound (one on each Ru center): Structure **B**. We investigated the pathways starting from structures **A** and **B** for hydrogen atom abstraction to form $\mathbf{I}_{A,H1}$/$\mathbf{I}_{B,H1}$ intermediates via transition state $\mathbf{TS}_{A,H1}$/$\mathbf{TS}_{B,H1}$ as well as the alternative pathway for initial methyl transfer via transition states $\mathbf{TS}_{A,Me1}$/$\mathbf{TS}_{B,Me1}$ to form intermediates $\mathbf{I}_{A,Me1}$/$\mathbf{I}_{B,Me1}$. Subsequently, the methyl group is transferred to $\mathbf{I}_{A,H1}$/$\mathbf{I}_{B,H1}$ via transition state $\mathbf{TS}_{A,Me2}$/$\mathbf{TS}_{B,Me2}$ to form products. Alternatively, in the reactant, a methyl group is relayed to form $\mathbf{I}_{A,Me1}$/$\mathbf{I}_{B,Me1}$, followed by a hydrogen atom migration via transition state $\mathbf{TS}_{A,H2}$/$\mathbf{TS}_{B,H2}$ to form products (Scheme 2).

Charges reported in this work were obtained from a natural bond occupation (NBO) calculation as implemented in the Gaussian program package at the B3LYP/BS2 level of theory.[22]

In order to fully understand the thermodynamics and kinetics of the mechanism of the overall chemical reaction, we calculated the bond dissociation free energies (BDFEs) of key Ru/C−H and Pt/C−CH_3 bonds in complexes **A**, **B**, $\mathbf{I}_{A,Me1}$, $\mathbf{I}_{B,Me1}$, $\mathbf{I}_{A,H1}$, $\mathbf{I}_{B,H1}$, $\mathbf{P}_{A,H}$, and $\mathbf{P}_{B,H}$. The release of either $H^\bullet$, H^+, $CH_3^\bullet$, or CH_3^+ from these four complexes as described by eqs 1−4, whereby each individual structure was calculated through a full geometry optimization to give the adiabatic bond dissociation free energies. In addition, we calculated the methylenium transfer Gibbs free energy (MTFE) and the proton transfer Gibbs free energy (PTFE). The latter was calculated through the use of the H_2O/H_3O^+ couple to balance the equation. As there were large structural changes upon H/CH_3 bond breaking on the various complexes, we also calculated the diabatic bond dissociation free energies, or vertical bond dissociation free energies, whereby we took the optimized geometries of **A**, **B**, $\mathbf{I}_{A,Me1}$, $\mathbf{I}_{B,Me1}$, $\mathbf{I}_{A,H1}$, $\mathbf{I}_{B,H1}$, $\mathbf{P}_{A,H}$, and $\mathbf{P}_{B,H}$ and ran single point calculations with either $H^\bullet$, H^+, $CH_3^\bullet$, or CH_3^+ removed.

$$\mathbf{A}^+ \rightarrow [\mathbf{A} - \mathrm{H}]^+ + \mathrm{H}^\bullet + \mathrm{BDFE_H} \tag{1}$$

$$\mathbf{A}^+ \rightarrow [\mathbf{A} - \mathrm{CH_3}]^+ + \mathrm{CH_3}^\bullet + \mathrm{BDFE_{Me}} \tag{2}$$

$$\mathbf{A}^+ + \mathrm{H_2O} \rightarrow [\mathbf{A}\text{–}\mathrm{H}]^0 + \mathrm{H_3O}^+ + \mathrm{PTFE} \tag{3}$$

$$\mathbf{A}^+ \rightarrow [\mathbf{A} - \mathrm{CH_3}]^0 + \mathrm{CH_3}^+ + \mathrm{MTFE} \tag{4}$$

■ RESULTS AND DISCUSSION

Before we discuss our calculated reaction mechanisms, let us briefly summarize the main results on our reactant structures, **A** and **B**, and establish their chemical properties. The optimized geometries of **A** and **B** are shown in Figure 1. The obtained bond distances of **A** are to within 0.011 Å of the crystal structure coordinates reported in ref 4, and as such, the DFT calculations give reasonable chemical structures. The Pt−C bond of 1.960/1.947 Å in **A**/**B** represents a single bond and is in good agreement with several reported Pt−C containing crystal structures from the literature.[23] The two Ru−C bonds are very close in bond length in **A**, and the fact that one of the two atoms is protonated, therefore, appears to have little effect on its interaction with carbon. However, addition of two CO molecules strongly affects the Ru−C bond lengths, and one of those is elongated to 2.126 Å in **B**. Ru−C bond lengths found here are typical for a single bond and compare to analogous structures reported before.[24] Therefore, addition of two CO molecules to structure **A** does not appear to have drastically changed the molecular geometry and keeps its original features.

The experimental studies of ref 4 implicate the hydride to bind as a bridging ligand to both Ru atoms, whereas Figure 1 gives a terminal-hydride atom that is linked to a single Ru atom.

We created starting structures for a geometry optimization using both a bridging hydride atom as well as a terminal hydride atom. However, both of these calculations (whether CO was used as ligands or not) converged to the structure with a terminal hydride atom. This implies that a structure with a bridging hydride atom will be a higher energy state and possibly inaccessible.

As transition-metal complexes containing iron or ruthenium generally contain close-lying spin states and often react via multistate reactivity patterns,[14] structure **A** was optimized in the singlet, triplet, and quintet spin states. The closed-shell singlet spin state is the ground state and is well separated from the triplet and quintet spin states by ΔG_{gas} = 17.1 and 44.8 kcal mol^{-1}, respectively. These values change by less than 1 kcal mol^{-1} when solvent corrections are included. Clearly, structure **A** is a closed-shell species that will react via single-state reactivity in contrast to metal(IV)-oxo and metal(IV)-nitrido complexes from the literature.[25]

In order to shed light on the bonding pattern of the central carbon atom, we did a natural bond orbital (NBO) analysis of structure **A**. Thus, the NBO analysis reveals three bonding type orbitals for the central carbon atom, namely, three single bonds for the interaction with the two Ru atoms and the Pt atom. The σ_{PtC} orbital represents the σ-bonding orbital between Pt and C and is built up from the interaction of the $5d_{z^2}$ orbital on Pt with the $2p_z$ orbital on C. In addition, there are two single bonds between the carbido atom and the two Ru atoms, which result from the mixing of the 2s, $2p_x$, and $2p_z$ atomic orbitals on C with the $4d_{z^2}$ orbital on Ru or the $4d_{x^2-z^2}$ on Ru(H). As such, the central carbon atom is sp^2 hybridized. However, the fourth valence orbital on carbon is a virtual $2p_y$ atomic orbital. The NBO analysis, therefore, assigns the central carbon atom as a carbene with three sp^2 hybridized orbitals that are occupied with two electrons in an orbital donating to Pt (σ_{PtC}), and two bonding orbitals where both C and Ru donate one electron each into the bond (σ_{RuC}, σ_{RuC}). This hybridization scheme gives the central carbon atom its planar structure (Scheme 3).

Scheme 3. Hybridization Scheme of A and B

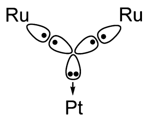

As such, the chemical structure of Ru_2CPt represents a Fischer-carbene, where the lone pair of the carbon atom interacts with an empty Pt orbital and the π-type Pt orbitals give backbonding into the empty $2p_y$ orbital of the carbene.[26] The NBO charges displayed in Figure 1 reveal a charge-neutral carbon atom (Q_C = 0.04) that is surrounded by slightly negatively charged metal atoms. Consequently, there is very little charge built up in this chemical system.

Subsequently, we calculated the potential energy profile for μ_2-$CHCH_3$ formation starting from **A** and **B**. We tested two mechanisms as shown in Figure 2: (i) initial hydrogen transfer from RuH to the carbene, followed by methyl abstraction, and (ii) initial methyl transfer from $PtCH_3$, followed by hydrogen/proton transfer. Figure 2 starts from the center with **A**/**B** and follows the two possible reaction mechanisms: The initial H transfer (mechanism to the right) and the initial CH_3 transfer (mechanism to the left). The two mechanisms are described as follows: In the first case, the metal-carbene group abstracts a hydrogen atom from the RuH group via a transition state $\mathbf{TS_{H1}}$ to form the H-transfer intermediate $\mathbf{I_{H1}}$. A subsequent CH_3 transfer from the $PtCH_3$ group via a barrier $\mathbf{TS_{Me2}}$ gives the μ_2-$CHCH_3$ bound product **P**. We also tested the alternative pathway starting with an initial CH_3 abstraction by the metal-carbene group via transition state $\mathbf{TS_{Me1}}$ leading to the methyl transfer intermediate $\mathbf{I_{Me1}}$. This intermediate then reacts further by H abstraction from RuH via a transition state $\mathbf{TS_{H2}}$ to form product **P**.

We attempted to also locate the alternative synchronous transfer of both hydrogen and methyl group at the same time to the carbene atom; however, all calculations converged to one of the lower-lying transition states (or local minima) described in this work. Previously, we calculated the concerted epoxidation reaction of an olefin by an iron(IV)-oxo heme cation radical system and found it to be a second-order saddle point that is well higher in energy than the stepwise transition states.[27]

Dramatic differences in relative energies and optimized structures are found for the pathways starting from **A** or **B**; however, in both cases, the H-atom transfer reaction has the lowest Gibbs free energy of activation of $\Delta G^{\ddagger}$ = 19.6 (3.1) kcal mol^{-1} for **A** (**B**). Nevertheless, in both cases, it is not the rate-determining step as the subsequent CH_3 transfer to form products gives an additional barrier with a maximum of 23.1 (24.2) kcal mol^{-1}. Therefore, the reaction that is initiated with H-atom transfer from **A** has an unfeasible Gibbs free energy of activation of 42.7 kcal mol^{-1} for $\mathbf{TS_{A,Me2}}$ with respect to **A** and will not be able to proceed through that pathway. On the other hand, this barrier for structure **B** is much lower in energy, but still would imply a relatively slow reaction process. This is in agreement with experimental observation that found evidence of a structure with analogy to $\mathbf{I_H}$, but the methyl group bound to one of the Ru atoms, which would imply a fast hydrogen abstraction, followed by a much slower methyl transfer. The origin of the enhanced stabilization of CO bound intermediate $\mathbf{I_{B,H1}}$ with respect to $\mathbf{I_{A,H1}}$ comes from the structural differences. Thus, without CO bound, the carbene carbon atom pyramidalizes much more and the dihedral angle $d_{CRuRuPt}$ = 43.3° in $\mathbf{I_{A,H1}}$, whereas it is 25.7° in $\mathbf{I_{B,H1}}$. The large pyramidalization causes contraction of the chemical system and more stereochemical repulsions of the $P(CH_3)_3$ groups with the RuCp groups that destabilize the structure.

The alternative pathway with an initial CH_3 transfer, on the other hand, has a calculated Gibbs free energy of activation of $\Delta G^{\ddagger}$ = 21.5 (25.4) kcal mol^{-1} for **A** (**B**) and, therefore, is disfavored over the initial H-atom transfer process. However, this reaction leads to a very stable intermediate $\mathbf{I_{A,Me1}}$ with an exergonicity of almost 10 kcal mol^{-1}, whereas the reaction is endothermic for the formation of $\mathbf{I_{B,Me1}}$. Its subsequent H-atom transfer leading to products only has a Gibbs free energy of activation of 18.3 (6.2) kcal mol^{-1} from intermediates for **A** (**B**). Therefore, product formation is a viable, but kinetically slow, pathway through this channel for both structures **A** and **B**, whereby it is the dominant mechanism for **A** and competitive with initial hydrogen atom abstraction for **B**. Binding of CO molecules to the reaction center, therefore, changes the regioselectivity of the chemical reaction in favor of initial hydrogen atom abstraction. In previous work on the regioselectivity of substrate epoxidation versus hydroxylation by iron(IV)-oxo complexes, we showed that changes to the ligand system of the iron or even replacing hydrogen atoms of the substrate by deuterium atoms can reverse a regioselectivity, and as such, the Ru_2Pt-carbene complex is another example of a

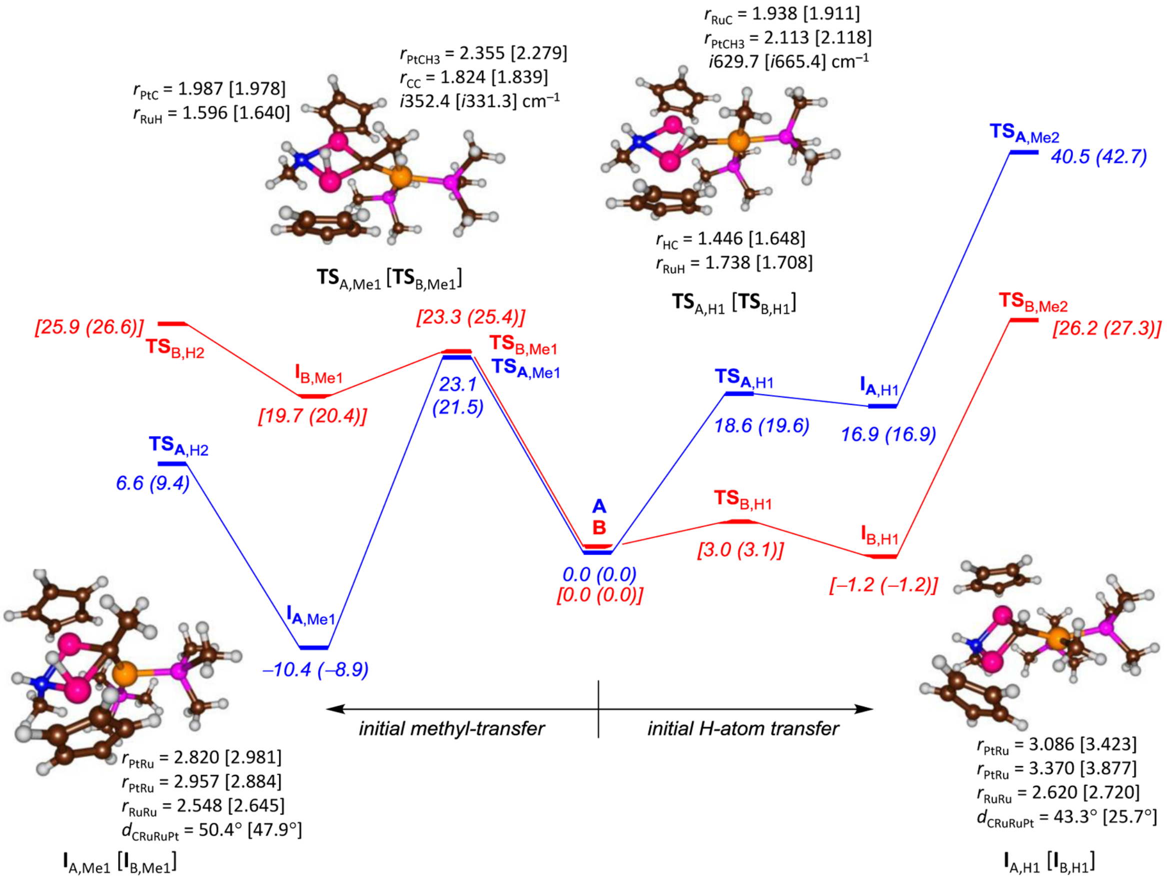

Figure 2. Gibbs free energy profile of alkyl chain growth on **A** and **B** via either (i) CH_3 transfer, followed by H transfer (mechanism from the center to the left), or (ii) H transfer, followed by CH_3 transfer (mechanism from the center to the right). Energies (ΔE + ZPE) and free energies (ΔG, in parentheses) obtained with B3LYP/BS2 with values in kcal mol^{-1}. All data include solvent corrections to the energy. Optimized geometries report bond lengths in angstroms, angles in degrees, and the imaginary frequency of the transition states in wavenumbers.

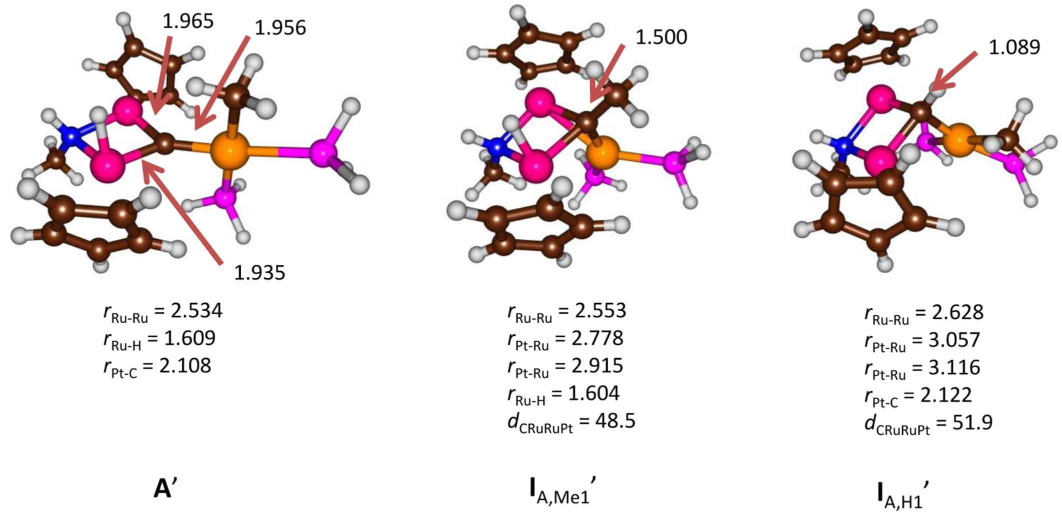

Figure 3. Optimized geometries of **A**′, **I**$_{A,Me1}$′, and **I**$_{A,H1}$′ with bond lengths in angstroms.

chemical catalyst that changes its reactivity upon ligand modifications.[28]

The origin of the differences in stability of **I**$_{A,Me1}$ versus **I**$_{B,Me1}$ stems from differences in location of the transferring hydrogen atom. Thus, in **I**$_{A,Me1}$, the hydrogen atom is located close to one Ru atom with Ru1−H and Ru2−H distances of 1.604 and 2.521 Å, whereas they change to 1.736 and 1.943 Å, respectively, in **I**$_{B,Me1}$. The structure with the bridging proton is considerably destabilized with respect to singly protonated Ru atom.

In summary, DFT establishes a possible alkyl synthesis mechanism for **A** as a stepwise mechanism with an initial CH_3 transfer, followed by H-atom transfer, whereas structure **B** proceeds with competitive mechanisms via either initial CH_3-

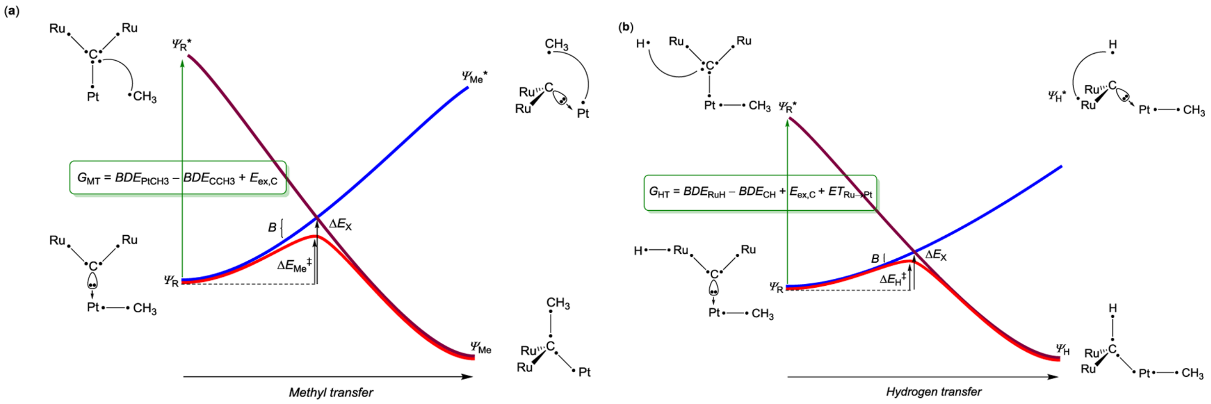

Figure 4. Valence bond curve crossing diagrams for methyl transfer (part a) and hydrogen atom transfer (part b) from reactants (**A** or **B**). Valence electrons are identified with a dot.

or H-transfer processes. An analysis of the group spin densities and charges (Supporting Information) along the complete reaction mechanism shows that all local minima and transition states are closed-shell singlet species with no radical built up during the reaction. Accordingly, the reaction starts with either proton transfer or CH_3^+ transfer.

So, why is the reaction displayed in Figure 2 stepwise with consecutive CH_3- or H-transfer processes, and what is the function of the Ru_2Pt scaffold? These questions will be answered in the following discussion. Structurally, there are major changes happening at the Ru_2Pt-carbene center during the reaction mechanism. Although **A** and **B** have an sp^2 hybridized carbon atom that lies in the plane of the Ru_2Pt atoms, upon H/CH_3 transfer, the planarity is distorted and the carbon atom relaxes to a pyramidal conformation due to sp^3 hybridization. The pyramidalization is considerably more pronounced for the CH_3-transfer process than in the H-atom transfer pathway as dihedral angles C−Ru−Ru−Pt of 50.4° for $\mathbf{I}_{A,Me1}$ and 43.3° for $\mathbf{I}_{A,H1}$ are found. At the same time, the Pt−Ru distances in $\mathbf{I}_{A,Me1}$ shorten by as much as 0.8 Å with respect to **A** to well below 3 Å, while, in $\mathbf{I}_{A,H1}$, they stay considerably longer: r_{PtRu} = 3.086 and 3.370 Å. These large structural changes for the CH_3-transfer pathway will have an effect on the reaction energetics and kinetics as well as on the relative stability of $\mathbf{I}_{A,Me1}$ versus $\mathbf{I}_{A,H1}$. Thus, the Pt atom in $\mathbf{I}_{A,Me1}$ only has three ligands due to CH_3 transfer to the carbon atom, which means limited stereochemical interactions between the two $P(CH_3)_3$ groups and the rest of the molecule so that the Pt atom can approach the two Ru atoms closely. In $\mathbf{I}_{A,H1}$, the Pt atom remains tetracoordinated and the stereochemical interactions between all ligands and the rest of the molecule prevent a close approach to the Ru_2C center. As a consequence of the stereochemical repulsions, $\mathbf{I}_{A,H1}$ is considerably destabilized over $\mathbf{I}_{A,Me1}$ and the reaction pathway with initial H-atom transfer is energetically disfavored.

To further establish these stereochemical interactions in $\mathbf{I}_{A,H1}$ versus $\mathbf{I}_{A,Me1}$, we did a subsequent set of calculations on these structures, but with the $P(CH_3)_3$ groups replaced by PH_3: structures $\mathbf{I}_{A,H1}'$ and $\mathbf{I}_{A,Me1}'$ (Figure 3). The optimized geometry of **A′** (Figure 3) is very close to that reported above for **A** in Figure 1, and only minor changes in bond lengths are obtained. Clearly, the $P(CH_3)_3$ groups have little effect on the structure of the Ru_2PtC core of our chemical system. A similar situation occurs for $\mathbf{I}_{A,Me1}'$, which has large structural similarities with $\mathbf{I}_{A,Me}$ reported in Figure 2. Major changes, however, are seen when $\mathbf{I}_{A,H1}$ is compared to $\mathbf{I}_{A,H1}'$. Thus, one of the Ru−Pt distances decreases from 3.370 to 3.116 Å, and as a consequence, the pyramidality of the carbon center changes from $d_{CRuRuPt}$ = 43.3° in $\mathbf{I}_{A,H1}$ to a value of 51.9° in $\mathbf{I}_{A,H1}'$. This has a major effect on the stability of $\mathbf{I}_{A,H1}'$, and it is stabilized by 6.0 kcal mol^{-1} with respect to **A′**; however, the $\mathbf{I}_{A,Me1}'$ remains the most stable conformation. This implies that the $P(CH_3)_3$ groups incur a destabilizing effect on the reaction mechanism, but will not reverse the preference of initial CH_3 transfer over H-atom transfer.

To gain insight into the electronic changes during the reaction mechanism, a NBO analysis was also performed on the intermediate and product complexes. The NBO calculation reveals a configuration on the central carbon atom of $2s^{1.08}2p^{2.92}$ for $\mathbf{I}_{A,Me1}$ and $2s^{1.18}2p^{3.10}$ for $\mathbf{I}_{A,H1}$. Both intermediate complexes, therefore, have an electronic configuration close to sp^3 hybridization, and as a consequence, their geometries have changed from planar to pyramidal, in agreement with the optimized structures.

In order to fully understand the thermodynamics and kinetics of the mechanism displayed in Figure 2, and, in particular, gain insight into the electron transfer mechanisms during the reaction processes, we set up valence bond (VB) curve crossing diagrams (Figure 4) for the methyl transfer and hydrogen atom transfer steps. We applied these VB curve crossing diagrams previously to rationalize the reaction mechanisms of substrate activation (hydroxylation, epoxidation, desaturation, and sulfoxidation) by Compound I of cytochrome P450 enzymes as well as the nonheme iron(IV)-oxo species of dioxygenases.[29] These studies rationalized reaction mechanisms and, for instance, explained why a reaction was stepwise via a radical intermediate rather than synchronous (concerted). Furthermore, in the case of P450 Compound I, several possible electron transfer pathways in substrate hydroxylation by Compound I were identified via either an iron(IV)-hydroxo intermediate or an iron(III)-hydroxo heme cation radical, and different activation barriers (and consequently rate constants) were identified that passed these individual intermediates.[30] VB diagrams explained the differences in electron transfer pathways and rationalized the ordering of the various electronic and spin states. Finally, the VB diagrams were used to find patterns in activation energies/rate constants and create predictive models. As such, these VB curve crossing diagrams may also find their use in organometallic chemistry, and therefore, we applied it to the chemical system described here.

The VB curve crossing diagrams start at the bottom-left with the reactant electronic configuration and wave function (Ψ_R) of

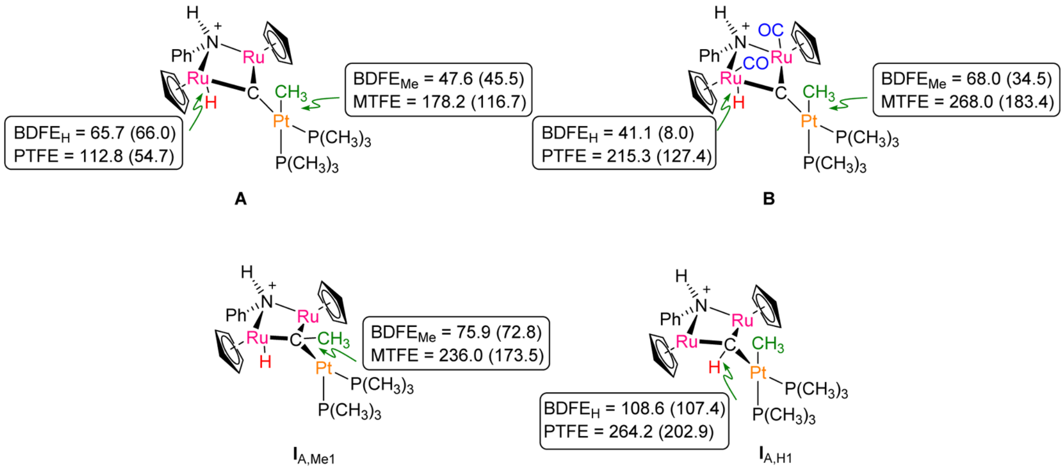

Figure 5. Bond dissociation free energies (BDFEs in kcal mol^{-1}) of key bonds in structures **A**, **B**, $\mathbf{I}_{A,Me1}$, and $\mathbf{I}_{A,H1}$. Reactions calculated according to eqs 1−4. Values in parentheses are solvent-corrected free energies, whereas those out of parentheses are gas-phase data. PTFE and MTFE are the proton and methyl transfer Gibbs free energies, respectively.

A/**B**, which is a carbene where two sp^2 electrons form bonding orbitals with electrons on the two ruthenium atoms and the other two electrons represent a lone pair orbital that donates a bond to Pt. Each of the dots in Figure 4 represents one of these valence electrons. In part (a) in Figure 4, the reaction follows the methyl transfer from Pt to carbene and the structure on the right-hand side gives the electronic configuration of $\mathbf{I}_{Me}$ with wave function Ψ_{Me}. In $\mathbf{I}_{Me}$, the central carbon atom is sp^3 hybridized and forms a single bond with Ru, Ru, Pt, and CH$_3$. In VB theory, the wave functions of the reactant and product complexes cross, i.e., Ψ_R and Ψ_{Me} in Figure 4a, and lead to an avoided crossing and a transition state for the reaction from reactants to intermediates.[31] Thus, the curve crossing energy (ΔE_X) is above the actual transition state ($\Delta E_{Me}{}^{\ddagger}$) by a factor B, which is called the resonance energy. It has been shown that the barrier height can be described by the difference in energy by a fraction (f) of the promotion gap (G) and the resonance energy B: $\Delta E_{Me}{}^{\ddagger} = fG_{MT} - B$. The promotion gap signifies the excitation energy from the ground state wave function to the product wave function in the geometry of the reactants; i.e., G_{MT} is the energy difference between Ψ_R and $\Psi_R{}^*$ in the reactant geometry. The VB diagrams also give chemical structures of the reactant and product wave functions of the ground and excited state species with valence electrons identified with a dot.

A close inspection of the VB diagrams in Figure 4 shows that the promotion gap for methyl transfer (G_{MT}) represents the breaking of the Pt−CH$_3$ bond and the formation of a new C−CH$_3$ bond. In addition, the VB structures of Ψ_R and $\Psi_R{}^*$ show that the carbene carbon is rehybridized from sp^2 to sp^3 hybridization and one electron of the lone pair orbital pointing toward Pt is promoted into the new sp^3 orbital. At the same time, the electron from the broken Pt−CH$_3$ bond moves into the carbene−Pt bond. Thus, the promotion gap also contains a component for the excitation energy of the carbene from sp^2 to sp^3 hybridization ($E_{ex,C}$), which essentially requires a promotion of an electron from the σ_{PtC} orbital to the virtual 2p$_y$ molecular orbital on carbon. Energetically, G_{MT} can be described in terms of the bond dissociation energies (BDEs) of the respective bonds that are broken and formed in the reaction process (eq 5), whereby BDE_{PtCH_3} represents the Gibbs free energy to break the Pt−CH$_3$ bond in **A**/**B** and BDE_{CCH_3} is the Gibbs free energy to form the C−CH$_3$ bond in $\mathbf{I}_{A,Me1}$/$\mathbf{I}_{B,Me1}$.

$$G_{MT} \propto \mathrm{BDE}_{PtCH_3} - \mathrm{BDE}_{CCH_3} + E_{ex,C} \qquad (5)$$

The situation is dramatically different for hydrogen atom transfer from **A**/**B**, as shown in Figure 4b. Thus, the barrier height for hydrogen atom transfer ($\Delta E_H{}^{\ddagger}$) is proportional to the promotion gap for hydrogen atom transfer (G_{HT}), which correlates with the strength of the Ru−H bond that is broken (BDE_{RuH}), the strength of the C−H bond that is formed (BDE_{CH}), and again the excitation energy for the carbene to change from sp^2 to sp^3 hybridization. In addition to these three terms, the promotion gap G_{HT} also contains a component for the electron transfer energy from Ru to Pt ($\mathrm{ET}_{Ru\rightarrow Pt}$). The hydrogen atom transfer process, therefore, incurs extra electron reorganization energy in the Ru$_2$Pt-carbene scaffold, which is not necessary for the methyl transfer step. The overall preference of hydrogen atom transfer versus methyl transfer will depend on the relative strengths of the bonds that are broken and formed in the process and the electron reorganization energy. To find out whether there are major differences between the BDE values in eq 5 and those in eq 6, we decided to calculate their values with DFT.

$$G_{HT} \propto \mathrm{BDE}_{RuH} - \mathrm{BDE}_{CH} + E_{ex,C} + \mathrm{ET}_{Ru\rightarrow Pt} \qquad (6)$$

As the VB drawings in Figure 4 only give qualitative analysis of electron transfer processes and no actual quantitative values, we decided to calculate BDEs and bond dissociation free energies (BDFEs) of key Ru/C−H and Pt/C−CH$_3$ bonds in complexes **A**, **B**, $\mathbf{I}_{A,Me1}$, and $\mathbf{I}_{A,H1}$ by calculating the release of a H$^{\bullet}$, H$^+$, CH$_3{}^{\bullet}$, and CH$_3{}^+$ from these four complexes according to eqs 1−4 above. Figure 5 displays the diabatic driving forces for H/CH$_3$ release from complexes **A**, **B**, $\mathbf{I}_{A,H1}$, and $\mathbf{I}_{A,Me1}$. We initially calculated the adiabatic BDFE calculations, whereby we did a full geometry optimization of all individual chemical structures in eqs 1−4 and then took the difference in Gibbs free energy for each of these reactions. However, due to considerable rehybridization of the central carbon atom and, as a consequence, large geometrical changes in some of the structures, the adiabatic BDFE values gave unrealistic results. For instance, the adiabatic bond dissociation energy for the breaking of the Ru−H bond in **A** appears negative, which

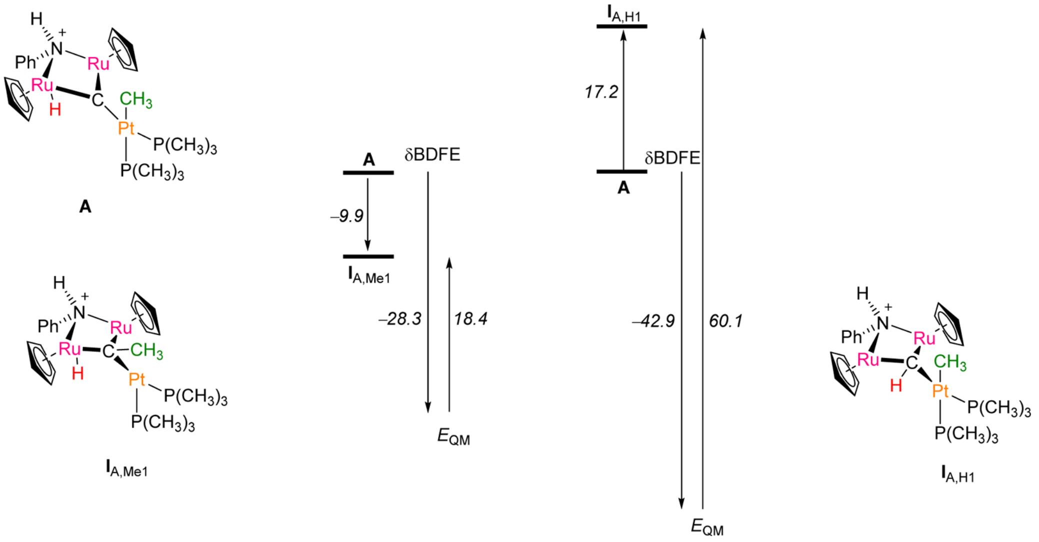

Figure 6. Energy decomposition of the methyl and hydrogen atom transfer reaction from **A**. Gibbs free energies given are in kcal mol^{-1}.

would imply spontaneous dissociation, in disagreement with the experimental crystal structure. However, this did not happen during the geometry optimization, and consequently, there is a significant barrier for this process. Another reason the adiabatic energies give unrealistic results is the dramatic structural changes upon removal of one ligand, i.e., H or CH_3, which changes systems from hexacoordination to pentacoordination, i.e., from an octahedral to a trigonal bipyramical structure, which leads to major changes in electronic structure.[32] Conversely, when we calculate the diabatic Gibbs free energy change by taking the H and [**A**−H] products in the geometry of **A**, then the BDFE is positive. The same is found for the dissociation of a methyl group from **A**. By contrast to structure **A**, the adiabatic and diabatic bond energies in structures $\mathbf{I}_{A,Me1}$ and $\mathbf{I}_{A,H1}$ are very similar and vary by less than 6 kcal mol^{-1}. In the following, however, we will focus on the diabatic bond dissociation free energies.

As can be seen, the strength of the C−H bond in **A** is considerably different from that obtained for **B**. Thus, the $BDFE_H$ for **A** is 45.5 kcal mol^{-1} in solvent, whereas a value of 34.5 kcal mol^{-1} is found for **B**, and as a consequence, the hydrogen atom transfer should be much easier with the CO bound complex then with complex **A**. Indeed, the potential energy landscape in Figure 2 shows that formation of $\mathbf{I}_{B,H1}$ is exergonic by −1.2 kcal mol^{-1}, whereas it is endergonic for $\mathbf{I}_{A,H1}$. Thus, CO binding affects the chemical structure of the Ru centers and weakens the Ru−H bond and makes it more susceptible for hydrogen atom transfer. Despite the fact that the subsequent methyl transfer still has a barrier of about 28 kcal mol^{-1} (virtually unchanged with respect to **A**), it is now sufficiently low to cross at ambient temperatures and pressures. On the other hand, the platinum−methyl bond is much stronger in the CO bound structures and results in a considerable raise in the $\mathbf{I}_{B,Me1}$ energy.

Thermodynamically, the driving force to form $\mathbf{I}_{A,Me1}/\mathbf{I}_{A,H1}$ from **A** represents the breaking of a weak Pt−CH_3 or Ru−H bond and the formation of a much stronger C−CH_3/C−H bond. Hence, the reaction should be strongly exergonic, which is seen for the reaction via $\mathbf{I}_{A,Me1}$ in Figure 2, but not for the one via $\mathbf{I}_{A,H1}$. Thus, the hydrogen atom transfer from Ru in **A** to the carbene to form $\mathbf{I}_{A,H1}$ results in the breaking of the Ru−H bond of $BDFE_H$ = 65.7 kcal mol^{-1} in the gas phase and the formation of a C−H bond with a diabatic value of 108.6 kcal mol^{-1}, and if the driving force was solely dependent on the change in bond strength, the reaction would have been exergonic by 42.9 kcal mol^{-1}. As shown in Figure 2, however, this reaction is endergonic by 17.2 kcal mol^{-1}, which implies that the stereochemical and electronic effects, i.e., the sp^2 to sp^3 rehybridization ($E_{ex,C}$) and the Ru → PT electron transfer ($ET_{Ru\rightarrow Pt}$), account for a destabilization of $\mathbf{I}_{A,H1}$ by about 60 kcal mol^{-1} in Gibbs free energy. This is explained schematically in Figure 6, where we deconvolute the processes from **A** to $\mathbf{I}_{A,Me1}$ and from **A** to $\mathbf{I}_{A,H1}$ into factors for bond breaking and formation (δBDFE) and quantum mechanical effects (E_{QM}). Thus, the methyl transfer reaction from **3** results in the breaking of the Pt−CH_3 bond, which requires a $BDFE_{Me,diabatic}$ = 47.6 kcal mol^{-1}, and, at the same time, the formation of the C−CH_3 bond ($BDFE_{Me,diabatic}$ = 75.9 kcal mol^{-1}). Therefore, the change in bond dissociation Gibbs free energy for the methyl transfer is −28.3 kcal mol^{-1}. The reaction mechanism in Figure 2 found the methyl transfer process to be exergonic by 9.9 kcal mol^{-1}, which implies that the quantum mechanical effect of the process accounts for 18.4 kcal mol^{-1}. The quantum mechanical effect includes the rehybridization energy of the carbene group and the geometric and stereochemical factors associated with the methyl transfer. By comparison, the hydrogen atom transfer shows a much larger change in bond dissociation energy due to the strong C−H bond that is formed ($\delta BDFE_{H,diabatic}$ = −42.9 kcal mol^{-1}). However, this reaction incurs a large quantum mechanical effect of 60.1 kcal mol^{-1} and thereby makes the overall process highly endergonic. The quantum mechanical effect includes the rehybridization of the carbon atom, which will probably be of the same order of magnitude as that found for the methyl transfer process, i.e., about 18 kcal mol^{-1}. In addition, there are the above-mentioned stereochemical repulsions of the methyl groups of the $P(CH_3)_3$ moieties that raise $\mathbf{I}_{A,H1}$ by about 6 kcal mol^{-1}. Finally, the electronic effects (E_{QM}) for the hydrogen atom transfer reaction include the electron transfer energy from Ru to Pt, as described in the VB diagram in Figure 4.

In addition to removal of H/CH_3 from our reactant complexes and intermediates, the breaking of the bond into two ions was also investigated and is described as the proton transfer Gibbs free energy (PTFE) and methyl transfer Gibbs free energy (MTFE). As follows from the data in Figure 5, it requires considerably more energy to break the Ru−H and Pt−CH_3 bonds than a homogeneous splitting into $Ru^•$ + $H^•$ and $Pt^•$ + $CH_3^•$. The thermodynamic analysis confirms the results described above in Figure 2, where either an $H^•$ or $CH_3^•$ is transferred rather than H^+ and CH_3^+.

So what about the next step for the formation of μ_2-$CHCH_3$ products? The reaction from $\mathbf{I}_{A,Me1}$ to products results in the breaking of the Ru−H bond and the formation of a new C−H bond. By contrast, the pathway from $\mathbf{I}_{A,H1}$ leads to the breaking of the Pt−CH_3 bond and the transfer of the methyl group to carbon. However, this process breaks the C−Pt bond and the $Pt(P(CH_3)_3)_2$ group is left behind with two unpaired electrons. Thus, an electron on Pt is promoted into a virtual orbital and the reaction proceeds via a high energy pathway. Indeed, the DFT calculated potential energy profile in Figure 2 gives a high barrier for $\mathbf{TS}_{A,Me2}$, in agreement with this.

In summary, DFT calculations presented here show a novel pathway for the synthesis of linear alkanes on a trimetal-carbene center. The chemical system discussed here, however, is inefficient as the lowest-lying initial barrier is for hydrogen atom transfer, which leads to a dead-end reaction intermediate. By contrast, the initial methyl transfer can be followed by hydrogen atom transfer to lead to products. The question is how this catalyst may be improved for alkane synthesis. The thermodynamic and VB schemes above give some clear indication to this. As shown in eqs 5 and 6, above, the barrier heights $\mathbf{TS}_{H1}$ and $\mathbf{TS}_{Me1}$ are dependent on the Ru−H and Pt−CH_3 bonds that are broken and the C−H and C−CH_3 bonds being formed. Consequently, a chemical system with a weaker metal−CH_3 bond should react predominantly via initial methyl transfer and may be more efficient. The work described here may have relevance to biological and heterogeneous catalysis for the synthesis of alkanes. In particular, in heterogeneous catalysis, linear alkanes are generated on a metal surface using often CO and H_2 as reactants. It may very well be that the trimetal-carbene structure discussed here is a common type intermediate in heterogeneous catalysis, but further research will have to be performed to establish this.

■ CONCLUSIONS

In summary, our calculations establish the key features of a synthetic homogeneous catalyst for alkyl chain growth. A combination of DFT, NBO, VB, and thermochemical studies has been performed and establish the intrinsic chemical properties of **A** or **B**. First, we characterize reactants as having a Ru_2Pt-carbene core where the lone pair is donated to Pt via a bonding/backbonding configuration. Second, we find a low energy mechanism of alkyl formation through consecutive $CH_3^•$ and $H^•$ transfer to the carbene with low Gibbs free energy of activation and exergonic driving force. We show that the reverse process is thermochemically hampered and would lead to an excited triplet configuration.

Overall, our work identifies a novel reaction for the synthesis of alkanes that starts from a trimetal carbene. This unique structure is shown to be capable of intramolecular methyl and hydrogen atom transfer to the carbene to form μ_2-$CHCH_3$ products as precursor to alkanes.

■ ASSOCIATED CONTENT

Ⓢ Supporting Information

Supporting Information with Cartesian coordinates as well as tables with group spin densities, charges, and absolute and relative energies is provided. The Supporting Information is available free of charge on the ACS Publications website at DOI: 10.1021/acs.organomet.5b00305.

■ AUTHOR INFORMATION

Corresponding Authors

*E-mail: Sam.devisser@manchester.ac.uk (S.P.d.V.).
*E-mail: dkclcre@yahoo.com (D.K.).

Author Contributions

§These authors contributed equally.

Notes

The authors declare no competing financial interests.

■ ACKNOWLEDGMENTS

The National Service of Computational Chemistry Software is thanked for CPU time provided. D.K. holds the Ramanujan Fellowship (SR/S2/RJN-11/2008) from the Department of Science and Technology (DST), New Delhi (India). M.A.S. thanks the Petroleum Technology Development Fund in Nigeria for a studentship.

■ REFERENCES

(1) (a) Rofer-de Poorter, C. K. *Chem. Rev.* **1981**, *81*, 447−474. (b) Schulz, H. *Appl. Catal., A* **1999**, *186*, 3−12. (c) Khodakov, A. Y.; Chu, W.; Fongarland, P. *Chem. Rev.* **2007**, *107*, 1692−1744. (d) Maitlis, P. M.; Zanotti, V. *Chem. Commun.* **2009**, 1619−1634.

(2) See, e.g.: (a) Tsakoumis, N. E.; Rønning, M.; Borg, Ø.; Rytter, E.; Holmen, A. *Catal. Today* **2010**, *154*, 162−182. (b) Shetty, S.; van Santen, R. A. *Catal. Today* **2011**, *171*, 168−173. (c) Inderwildi, O. R.; Jenkins, S. J. *Chem. Soc. Rev.* **2008**, *37*, 2274−2309.

(3) (a) Perkins, P.; Vollhardt, K. P. C. *J. Am. Chem. Soc.* **1979**, *101*, 3985−3987. (b) Inderwildi, O. R.; King, D. A.; Jenkins, S. J. *Phys. Chem. Chem. Phys.* **2009**, *11*, 11110−11112.

(4) Takemoto, S.; Morita, H.; Karitani, K.; Fujiwara, H.; Matsuzaka, H. *J. Am. Chem. Soc.* **2009**, *131*, 18026−18027.

(5) (a) Mayer, J. M. *Acc. Chem. Res.* **1998**, *31*, 441−450. (b) Weinberg, D. R.; Gagliardi, C. J.; Hull, J. F.; Murphy, C. F.; Kent, C. A.; Westlake, B. C.; Paul, A.; Ess, D. H.; McCafferty, D. G.; Meyer, T. J. *Chem. Rev.* **2012**, *112*, 4016−4093.

(6) See, e.g.: (a) Love, J. A.; Sanford, M. S.; Day, M. W.; Grubbs, R. H. *J. Am. Chem. Soc.* **2003**, *125*, 10103−10109. (b) Alcaide, B.; Almendros, P.; Luna, A. *Chem. Rev.* **2009**, *109*, 3817−3858. (c) Bernal, M. J.; Torres, O.; Martín, M.; Sola, E. *J. Am. Chem. Soc.* **2013**, *135*, 19008−19015.

(7) (a) Miller, R. L.; Wolczanski, P. T.; Rheingold, A. L. *J. Am. Chem. Soc.* **1993**, *115*, 10422−10423. (b) Su, C.-J.; Su, P.-C.; Chi, Y.; Peng, S.-M.; Lee, G.-H. *J. Am. Chem. Soc.* **1996**, *118*, 3289−3290. (c) Peters, J. C.; Odom, A. L.; Cummins, C. C. *Chem. Commun.* **1997**, 1995−1996. (d) Caselli, A.; Solari, E.; Scopelliti, R.; Floriani, C. *J. Am. Chem. Soc.* **2000**, *122*, 538−539. (e) Buchowicz, W.; Herbaczyńska, B.; Jerzykiewicz, L. B.; Lis, T.; Pasynkiewicz, S.; Pietrzykowski, A. *Inorg. Chem.* **2012**, *51*, 8292−8297. (f) Harding, D. J.; Kerpal, C.; Meijer, G.; Fielicke, A. *J. Phys. Chem. Lett.* **2013**, *4*, 892−896. (g) Borren, E. S.; Hill, A. F.; Shang, R.; Sharma, M.; Willis, A. C. *J. Am. Chem. Soc.* **2013**, *135*, 4942−4945. (h) Li, X.; Wang, L.-S.; Boldyrev, A. I.; Simons, J. *J. Am. Chem. Soc.* **1999**, *121*, 6033−6038.

(8) (a) de Visser, S. P.; Tan, L. S. *J. Am. Chem. Soc.* **2008**, *130*, 12961−12974. (b) Latifi, R.; Bagherzadeh, M.; de Visser, S. P. *Chem.—Eur. J.* **2009**, *15*, 6651−6662.

(9) *Jaguar 7.7*, version 7.9; Schrodinger, LLC: New York, NY, 2011.

(10) Frisch, M. J.; Trucks, G. W.; Schlegel, H. B.; Scuseria, G. E.; Robb, M. A.; Cheeseman, J. R.; Scalmani, G.; Barone, V.; Mennucci, B.; Petersson, G. A.; Nakatsuji, H.; Caricato, M.; Li, X.; Hratchian, H. P.; Izmaylov, A. F.; Bloino, J.; Zheng, G.; Sonnenberg, J. L.; Hada, M.; Ehara, M.; Toyota, K.; Fukuda, R.; Hasegawa, J.; Ishida, M.; Nakajima, T.; Honda, Y.; Kitao, O.; Nakai, H.; Vreven, T.; Montgomery, J. A., Jr.;

Peralta, J. E.; Ogliaro, F.; Bearpark, M.; Heyd, J. J.; Brothers, E.; Kudin, K. N.; Staroverov, V. N.; Kobayashi, R.; Normand, J.; Raghavachari, K.; Rendell, A.; Burant, J. C.; Iyengar, S. S.; Tomasi, J.; Cossi, M.; Rega, N.; Millam, J. M.; Klene, M.; Knox, J. E.; Cross, J. B.; Bakken, V.; Adamo, C.; Jaramillo, J.; Gomperts, R.; Stratmann, R. E.; Yazyev, O.; Austin, A. J.; Cammi, R.; Pomelli, C.; Ochterski, J. W.; Martin, R. L.; Morokuma, K.; Zakrzewski, V. G.; Voth, G. A.; Salvador, P.; Dannenberg, J. J.; Dapprich, S.; Daniels, A. D.; Farkas, Ö.; Foresman, J. B.; Ortiz, J. V.; Cioslowski, J.; Fox, D. J. *Gaussian 09*, Revision A.1; Gaussian, Inc.: Wallingford, CT, 2009.

(11) (a) Becke, A. D. *J. Chem. Phys.* **1993**, *98*, 5648−5652. (b) Lee, C.; Yang, W.; Parr, R. G. *Phys. Rev. B* **1988**, *37*, 785−789.

(12) Hay, P. J.; Wadt, W. R. *J. Chem. Phys.* **1985**, *82*, 299−310.

(13) Grimme, S.; Antony, J.; Ehrlich, S.; Krieg, H. *J. Chem. Phys.* **2010**, *132*, 154104.

(14) (a) Shaik, S.; de Visser, S. P.; Ogliaro, F.; Schwarz, H.; Schröder, D. *Curr. Opin. Chem. Biol.* **2002**, *6*, 556−567. (b) de Visser, S. P. *Angew. Chem., Int. Ed.* **2006**, *45*, 1790−1793.

(15) (a) de Visser, S. P.; Quesne, M. G.; Martin, B.; Comba, P.; Ryde, U. *Chem. Commun.* **2014**, *50*, 262−282. (b) Quesne, M. G.; Latifi, R.; Gonzalez-Ovalle, L. E.; Kumar, D.; de Visser, S. P. *Chem.—Eur. J.* **2014**, *20*, 435−446.

(16) (a) Becke, A. D. *Phys. Rev. A* **1988**, *38*, 3098−3100. (b) Perdew, J. P. *Phys. Rev. B* **1986**, *33*, 8822−8824.

(17) Zhao, Y.; Truhlar, D. G. *Theor. Chem. Acc.* **2008**, *120*, 215−241.

(18) (a) Adamo, C.; Barone, V. *J. Chem. Phys.* **1999**, *110*, 6158−6169. (b) Perdew, J. P.; Burke, K.; Ernzerhof, M. *Phys. Rev. Lett.* **1996**, *77*, 3865−3868.

(19) (a) Sainna, M. A.; Kumar, S.; Kumar, D.; Fornarini, S.; Crestoni, M. E.; de Visser, S. P. *Chem. Sci.* **2015**, *6*, 1516−1529. (b) Sainna, M. A.; Sil, D.; Sahoo, D.; Martin, B.; Rath, S. P.; Comba, P.; de Visser, S. P. *Inorg. Chem.* **2015**, *54*, 1919−1930.

(20) (a) Vardhaman, A. K.; Sastri, C. V.; Kumar, D.; de Visser, S. P. *Chem. Commun.* **2011**, *47*, 11044−11046. (b) Kumar, S.; Faponle, A. S.; Barman, P.; Vardhaman, A. K.; Sastri, C. V.; Kumar, D.; de Visser, S. P. *J. Am. Chem. Soc.* **2014**, *136*, 17102−17115.

(21) (a) Karamzadeh, B.; Kumar, D.; Sastry, G. N.; de Visser, S. P. *J. Phys. Chem. A* **2010**, *114*, 13234−13243. (b) Kumar, D.; Latifi, R.; Kumar, S.; Rybak-Akimova, E. V.; Sainna, M. A.; de Visser, S. P. *Inorg. Chem.* **2013**, *52*, 7968−7979. (c) Draksharapu, A.; Angelone, D.; Quesne, M. G.; Padamati, S. K.; Gómez, L.; Hage, R.; Costas, M.; Browne, W. R.; de Visser, S. P. *Angew. Chem., Int. Ed.* **2015**, *54*, 4357−4361. (d) Sallmann, M.; Kumar, S.; Chernev, P.; Nehrkorn, J.; Schnegg, A.; Kumar, D.; Dau, H.; Limberg, C.; de Visser, S. P. *Chem.—Eur. J.* **2015**, DOI: 10.1002/chem.201500644.

(22) Weinhold, F.; Carpenter, J. E. The Natural Bond Orbital Lewis Structure Concept for Molecules, Radicals, and Radical Ions. In *The Structure of Small Molecules and Ions*; Naaman, R., Vager, Z., Eds.; Plenum Press: New York, 1988; pp 227−236.

(23) (a) de Quadras, L.; Bauer, E. B.; Stahl, J.; Zhuravlev, F.; Hampel, F.; Gladysz, J. A. *New. J. Chem.* **2007**, *31*, 1594−1604. (b) Che, C.-M.; Huang, J.-S. *Coord. Chem. Rev.* **2002**, *231*, 151−164. (c) Das, R. K.; Saha, B.; Rahaman, S. M. W.; Bera, J. K. *Chem.—Eur. J.* **2010**, *16*, 14459−14468. (d) Algarra, A. G.; Grushin, V. V.; MacGregor, S. A. *Organometallics* **2012**, *31*, 1467−1476.

(24) (a) Mutter, S. T.; Platts, J. A. *J. Phys. Chem. A* **2011**, *115*, 11293−11302. (b) Conner, D.; Jayaprakash, K. N.; Wells, M. B.; Manzer, S.; Gunnoe, T. B.; Boyle, P. D. *Inorg. Chem.* **2003**, *42*, 4759−4772. (c) Patra, S. K.; Sadhukhan, N.; Bera, J. K. *Inorg. Chem.* **2006**, *45*, 4007−4015. (d) Patra, S. K.; Bera, J. K. *Organometallics* **2006**, *25*, 6054−6060. (e) MacGregor, S. A.; McKay, D.; Panetier, J. A.; Whittlesey, M. K. *Dalton Trans.* **2013**, *42*, 7386−7395. (f) Sharma, P. K.; de Visser, S. P.; Ogliaro, F.; Shaik, S. *J. Am. Chem. Soc.* **2003**, *125*, 2291−2300.

(25) (a) Latifi, R.; Sainna, M. A.; Rybak-Akimova, E. V.; de Visser, S. P. *Chem.—Eur. J.* **2013**, *19*, 4058−4068. (b) Vardhaman, A. K.; Barman, P.; Kumar, S.; Sastri, C. V.; Kumar, D.; de Visser, S. P. *Angew. Chem., Int. Ed.* **2013**, *52*, 12288−12292.

(26) See, e.g.: (a) Diver, S. T. *Coord. Chem. Rev.* **2007**, *251*, 671−701. (b) Barluenga, J.; Fernández-Rodríguez, M. A.; Aguilar, E. *J. Organomet. Chem.* **2005**, *690*, 539−587. (c) Bernasconi, C. F. *Chem. Soc. Rev.* **1997**, *26*, 299−307.

(27) (a) de Visser, S. P.; Ogliaro, F.; Shaik, S. *Angew. Chem., Int. Ed.* **2001**, *40*, 2871−2874. (b) de Visser, S. P.; Ogliaro, F.; Shaik, S. *Chem. Commun.* **2001**, 2322−2323.

(28) (a) de Visser, S. P. *Chem.—Eur. J.* **2006**, *12*, 8168−8177. (b) de Visser, S. P.; Tahsini, L.; Nam, W. *Chem.—Eur. J.* **2009**, *15*, 5577−5587.

(29) Previous work that used VB diagrams to explain reaction mechanisms: (a) Shaik, S.; Kumar, D.; de Visser, S. P. *J. Am. Chem. Soc.* **2008**, *130*, 10128−10140. (b) de Visser, S. P. *J. Am. Chem. Soc.* **2010**, *132*, 1087−1097. (c) Kumar, D.; Karamzadeh, B.; Sastry, G. N.; de Visser, S. P. *J. Am. Chem. Soc.* **2010**, *132*, 7656−7667. (d) Ji, L.; Faponle, A. S.; Quesne, M. G.; Sainna, M. A.; Zhang, J.; Franke, A.; Kumar, D.; van Eldik, R.; Liu, W.; de Visser, S. P. *Chem. Eur. J.* **2015**, DOI: 10.1002/chem.201500329.

(30) de Visser, S. P.; Ogliaro, F.; Sharma, P. K.; Shaik, S. *J. Am. Chem. Soc.* **2002**, *124*, 11809−11826.

(31) Shaik, S.; Hiberty, P. C. *A Chemist's Guide to Valence Bond Theory*; Wiley-Interscience: New York, NY, 2007.

(32) Quesne, M. G.; de Visser, S. P. *J. Biol. Inorg. Chem.* **2012**, *17*, 841−852.